



SAPP XXII

22nd Symposium on Application of Plasma Processes
and
11th EU-Japan Joint Symposium on Plasma
Processing

Book of Contributed Papers

Štrbské Pleso, Slovakia
18-24 January, 2019

Edited by V. Medvecká, J. Országh, P. Papp, Š. Matejčík



Book of Contributed Papers: 22nd Symposium on Application of Plasma Processes and 11th EU-Japan Joint Symposium on Plasma Processing, Štrbské Pleso, Slovakia, 18-24 January 2019.

Symposium organised by Department of Experimental Physics, Faculty of Mathematics, Physics and Informatics, Comenius University in Bratislava and Society for Plasma Research and Applications in hotel SOREA TRIGAN***, Štrbské Pleso, Slovakia, 18-24 January 2019.

Editors: V. Medvecká, J. Országh, P. Papp, Š. Matejčík

Publisher: Department of Experimental Physics, Faculty of Mathematics, Physics and Informatics, Comenius University in Bratislava; Society for Plasma Research and Applications in cooperation with Library and Publishing Centre CU, Bratislava, Slovakia

Issued: January 2019, Bratislava, first issue

Number of pages: 386

ISBN 978-80-8147-089-9

URL: http://neon.dpp.fmph.uniba.sk/sappxxii/download/SAPP_XXII_JSPP_XI_Book_of_Contributed_Papers.pdf

Local Organizers

Department of Experimental Physics

Faculty of Mathematics, Physics and Informatics

Comenius University in Bratislava

Mlynská dolina F2

842 48 Bratislava, Slovakia

URL: <http://www.fmph.uniba.sk/>

Tel.: +421 2 602 95 686

Fax: +421 2 654 29 980



Society for plasma research and applications

Faculty of Mathematics, Physics and Informatics

Comenius University Bratislava

Mlynská dolina F2

842 48 Bratislava, Slovakia

URL: <https://spvap.eu/>

E-mail: spvap@neon.dpp.fmph.uniba.sk

Tel.: +421 2 602 95 686



Local Organizing Committee

Štefan Matejčík (chair)

František Krčma

Peter Papp

Juraj Országh

Veronika Medvecká

Ladislav Moravský

International Scientific Committee

22nd Symposium on Application of Plasma Processes

Prof. J. Benedikt	Christian-Albrechts-University, Kiel, Germany
Dr. R. Brandenburg	INP, Greifswald, Germany
Dr. Z. Donkó	Hungarian Academy of Sciences, Budapest, Hungary
Dr. T. Field	Queen's University, Belfast, United Kingdom
Prof. S. Hamaguchi	Osaka University, Japan
Prof. F. Krčma	Brno University of Technology, Brno, Czech Republic
Prof. N. Mason	University of Kent, United Kingdom
Prof. Š. Matejčík	Comenius University in Bratislava, Slovakia
Prof. J. Pawlat	University of Technology, Lublin, Poland
Prof. M. Radmilović-Radjenović	Institute of Physics, Belgrade, Serbia
Prof. P. Scheier	Leopold-Franzens University, Innsbruck, Austria

11th EU-Japan Joint Symposium on Plasma Processing

Prof. S. Hamaguchi	Osaka University, Japan
Prof. N. Mason	University of Kent, United Kingdom
Prof. Z. Petrović	Institute of Physics, Belgrade, Serbia

Reading Committee

Prof. Š. Matejčík	Comenius University in Bratislava, Slovakia
Prof. F. Krčma	Brno University of Technology, Brno, Czech Republic
Prof. N. Mason	University of Kent, United Kingdom
Dr. P. Papp	Comenius University in Bratislava, Slovakia
Dr. J. Országh	Comenius University in Bratislava, Slovakia
Dr. V. Medvecká	Comenius University in Bratislava, Slovakia

Conference Topics

- 1. Electrical discharges and other plasma sources**
- 2. Elementary processes and plasma chemical reactions**
- 3. Plasma-surface interactions**
- 4. Plasma treatment of polymer and biological materials**
- 5. Nanometer-scaled plasma technology**
- 6. Ion mobility spectrometry**

Table of Content

	INVITED LECTURES	10
IL-01	Chris Mayhew <i>SOFT CHEMICAL IONISATION AND THE HUMAN VOLATILOME: APPLICATIONS TO MEDICAL SCIENCE AND HUMAN DETECTION</i>	11
IL-02	Douyan Wang <i>BIOLOGICAL APPLICATIONS USING PULSED ELECTRIC FIELD AND PLASMAS</i>	21
IL-03	Milan Simek <i>NANOSECOND DISCHARGE IN LIQUID WATER AT IPP: OVERVIEW OF RECENT RESULTS</i>	23
IL-04	Mario Janda <i>CHEMICAL KINETIC MODEL OF TRANSIENT SPARK: SPARK PHASE AND NOX FORMATION</i>	25
IL-05	Ana Sobota <i>ATMOSPHERIC PRESSURE PLASMAS IN CONTACT WITH TARGETS: ELECTRIC FIELDS AND ELECTRON PROPERTIES</i>	35
IL-06	Timo Gans <i>TAILORING REACTIVE SPECIES PRODUCTION IN COLD ATMOSPHERIC PRESSURE PLASMAS FOR ENVIRONMENTAL AND HEALTHCARE TECHNOLOGIES</i>	36
IL-07	Sander Nijdam <i>PHYSICS OF TRANSIENT PLASMAS</i>	38
IL-08	Patrik Španěl <i>MASS SPECTROMETRY FOR REAL TIME MEASUREMENT OF TRACE CONCENTRATIONS OF VOLATILE COMPOUNDS IN AIR AND BREATH</i>	39
IL-09	Mahmoud Tabrizchi <i>DEVELOPMENT OF SEVERAL NON-RADIOACTIVE IONIZATION SOURCES FOR ION MOBILITY SPECTROMETRY</i>	45
IL-10	Yuzuru Ikehara <i>A PRINCIPLE OF BLOOD COAGULATION INDUCED BY LOW- TEMPERATURE PLASMA TREATMENT</i>	46
IL-11	Masaaki Matsukuma <i>PLASMA PROCESSES FOR MANUFACTURING SEMICONDUCTOR DEVICES AND SIMULATIONS</i>	49
IL-12	Sasa Dujko <i>NON-EQUILIBRIUM TRANSPORT OF ELECTRONS IN GASES AND LIQUIDS AND ITS APPLICATIONS IN MODELING OF PARTICLE DETECTORS</i>	57
IL-13	Naoki Shirai <i>PLASMA LIQUID INTERACTION INDUCED BY ATMOSPHERIC PRESSURE DC GLOW DISCHARGE</i>	63
IL-14	Uros Cvelbar <i>HOW TO DESIGN NANOCATALYSTS WITH PLASMA?</i>	67
IL-15	Nevena Puač <i>DIAGNOSTICS OF ATMOSPHERIC PRESSURE PLASMAS AND THEIR APPLICATION IN AGRICULTURE</i>	68
IL-16	Peter Awakowicz <i>REDUCTION OF VOLATILE ORGANIC COMPOUNDS WITH THE CONCEPT OF A SURFACE DIELECTRIC BARRIER DISCHARGE</i>	70
IL-17	Petr Synek <i>UNRAVELING THE COMPLEXITY OF BARRIER DISCHARGES: ROTATIONAL NON-EQUILIBRIA AND MICRO-AMPERE CURRENTS</i>	71
IL-18	Johannes Berndt <i>SOME GENERAL ASPECTS CONCERNING THE PLASMA BASED DEPOSITION OF THIN FILMS</i>	76
	TOPICAL LECTURES	77
TL-01	Zoltan Donkó <i>PARTICLE SIMULATION OF ATMOSPHERIC PRESSURE TRANSIENT DISCHARGES INCLUDING VUV PHOTON TRANSPORT</i>	78
TL-02	Lenka Zajíčková <i>GLIDING ARC WITH SIDE GAS INLET: PLASMA DIAGNOSTICS AND APPLICATION IN POLYMER TREATMENT</i>	83
TL-03	Viktor Schneider <i>MICROPARTICLES TRAPPED BY OPTICAL TWEEZERS - MEASUREMENTS WITH AND WITHOUT A PLASMA</i>	89
TL-04	Matej Klas <i>DISCHARGE BREAKDOWN STUDIED UNDER HIGH PRESSURE IN ARGON</i>	90

TL-05	Hans Höft	<i>CONTROLLING DISCHARGE REGIMES IN PULSED, SINGLE-FILAMENT DIELECTRIC BARRIER DISCHARGES</i>	93
TL-06	Satoshi Hamaguchi	<i>SURFACE REACTIONS OF ATOMIC LAYER ETCHING PROCESSES</i>	100
TL-07	Miroslav Michlíček	<i>MASS SPECTROMETRY OF CAPACITIVELY COUPLED PLASMA IGNITED IN CYCLOPROPYLAMINE/ARGON MIXTURE</i>	104
TL-08	Zoran Petrović	<i>THE EFFECT OF ATTACHMENT ON RF BREAKDOWN</i>	110
TL-09	Michal Ďurian	<i>CONSTRUCTION OF A FOURIER TRANSFORM SPECTROMETER FOR THE UV-VIS REGION</i>	114
TL-10	Samuel Omasta	<i>DETERMINATION OF ELECTRIC FIELD IN HUMID AIR PLASMA FROM NITROGEN FNS AND SPS BANDS RATIO</i>	118
TL-11	Abdulrahman Basher	<i>THE FIRST PRINCIPLE CALCULATIONS OF THE INTERACTION BETWEEN HEXAFLUOROACETYLACETONE (HFAC) WITH Ni AND NiO SURFACES FOR ATOMIC LAYER ETCHING (ALE) APPLICATIONS</i>	122
TL-12	Stanislav Chudják	<i>FORMATION OF LIFE PRECURSOR MOLECULES IN TITAN RELATED ATMOSPHERE AT RELEVANT TEMPERATURE AND PRESSURE</i>	126
TL-13	Ladislav Moravský	<i>ION MOBILITY SPECTROMETRY MONITORING OF DECOMPOSITION OF DIMETHYL PHTHALATE BY POSITIVE CORONA DISCHARGE</i>	131
TL-14	Jarostaw Puton	<i>ELECTRON CAPTURE IN IMS DETECTORS – A COMPARISON OF ECD, DT IMS AND DMS</i>	135
TL-15	Kristian Wende	<i>SMALL MOLECULE ANALYTICS TO ELUCIDATE PLASMA – LIQUID INTERACTIONS</i>	139
TL-16	Ju Young Park	<i>INACTIVATION OF INDOOR AIRBORNE BACTERIA BY DBD</i>	145
TL-17	Kinga Kutasi	<i>TUNNING THE PAW COMPOSITION BY A SURFACE-WAVE MICROWAVE DISCHARGE</i>	147
TL-18	Jan Benedikt	<i>ATMOSPHERIC PLASMAS FOR GENERATION OF NANOSTRUCTURED MATERIALS</i>	152
TL-19	Tom Field	<i>PLASMA FORMATION IN CONDUCTING LIQUIDS: GROWTH AND NATURE OF THE VAPOUR LAYER</i>	155
TL-20	Antonina Malinina	<i>EMISION CHARACTERISTICS OF GAS-DISCHARGE PLASMA OF ATMOSPHERIC PRESSURE DIELECTRIC BARRIER DISCHARGE ON ZINC DIODIDE VAPOR WITH NEON AND XENON MIXTURES</i>	156
TL-21	Ilija Stefanovic	<i>NEW AND VERSATILE MINATURE MICROWAVE PLASMA SOURCE</i>	165
TL-22	Mikhail Yablokov	<i>HYDROPHILICITY OF PLASMA-TREATED POLYMERS AS A RESULT OF SURFACE CHARGING</i>	169
TL-23	Zbyněk Voráč	<i>INCREASING THE EFFICIENCY OF PLASMA JET TREATMENT BY THE PRECURSOR ADDITION</i>	174
TL-24	Bilel Rais	<i>μPLASMAPRINT: DIGITAL ON-DEMAND SURFACE ENGINEERING</i>	177
TL-25	Jozef Ráheľ	<i>MANIPULATION OF POWDERY MATERIALS BY A SEQUENTIALLY PULSED COPLANAR BARRIER DISCHARGE</i>	181
TL-26	Zdenko Machala	<i>GASEOUS AND AQUEOUS REACTIVE OXYGEN AND NITROGEN SPECIES OF AIR PLASMAS WITH WATER</i>	186
		POSTER PRESENTATIONS	191
P-01	Arian Fateh Borkhari	<i>DC VACUUM BREAKDOWN AT MICRO-METER SEPARATIONS</i>	192
P-02	Richard Cimerman	<i>DISCHARGE FORMATION INSIDE THE HONEYCOMB STRUCTURES ASSISTED BY SURFACE BARRIER DISCHARGE</i>	196
P-03	Aranka Derzsi	<i>HEAVY-PARTICLE INDUCED SURFACE PROCESSES IN CAPACITIVE RADIO FREQUENCY DISCHARGES DRIVEN BY TAILORED VOLTAGE WAVEFORMS</i>	200

P-04	Ján Ďurian	<i>ACCELERATING MONTE CARLO PARTICLE-IN-CELL (MCC-PIC) SIMULATIONS OF DISCHARGES</i>	205
P-05	Tom Field	<i>PLASMA FORMATION IN CONDUCTING LIQUIDS: TIME TO BREAKDOWN</i>	211
P-06	Milan Simek	<i>NANOSECOND DISCHARGE IN LIQUID WATER AT IPP: OVERVIEW OF RECENT RESULTS</i>	23
P-07	Ján Blaško	<i>ELECTRON INDUCED FRAGMENTATION OF 2,6 - DICHLOROANISOLE</i>	212
P-08	Beáta Feilhauerová	<i>DISSOCIATION OF DIMETHYL PHTHALATE MOLECULE INDUCED BY LOW-ENERGY ELECTRON IMPACT</i>	217
P-09	Michal Lacko	<i>INFLUENCE OF ELECTRIC FIELD ON ION CHEMISTRY OF GLYOXAL</i>	221
P-10	Dušan Mészáros	<i>LOW ENERGY ELECTRON ATTACHMENT TO OCTAFLUOROCYCLOBUTANE MOLECULES AND CLUSTERS</i>	226
P-11	Juraj Országh	<i>EXCITATION OF WATER INDUCED BY ELECTRON IMPACT</i>	230
P-12	Peter Papp	<i>THE PROTON AFFINITIES OF DIMETHYL PHTALATE ISOMERS</i>	234
P-13	Barbora Stachová	<i>ELECTRON IMPACT EXCITATION OF HELIUM</i>	238
P-14	Veronika Medvecká	<i>LOW-TEMPERATURE PLASMA TREATMENT OF SELECTED CEREALS</i>	244
P-15	Barbora Pijáková	<i>BIOLOGICAL ACTIVITY OF PLASMA MODIFIED PROTECTIVE LAYERS ON FAÇADE USING RF SLIT NOZZLE</i>	249
P-16	Ľubomír Staňo	<i>SURFACE MODIFICATION OF POLYPROPYLENE MEMBRANES BY PLASMA-INDUCED GRAFTING FOR THEIR APPLICATION AS SEPARATORS IN ALKALINE ELECTROLYSIS CELL</i>	254
P-17	Vlasta Štěpánová	<i>ROLL-TO-ROLL ATMOSPHERIC PRESSURE PLASMA TREATMENT OF POLYAMIDE FOILS</i>	259
P-18	Juliána Tomeková	<i>LOW TEMPERATURE AIR PLASMA AND ITS EFFECT ON GERMINATION OF SOYA BEANS</i>	264
P-19	Zlata Tučeková	<i>STRUCTURING OF POLYMETHYLMETHACRYLATE SUBSTRATES BY REDUCING PLASMA</i>	269
P-20	Anna Zahoranová	<i>EFFECT OF COLD ATMOSPHERIC PRESSURE PLASMA TREATMENT ON SEED GERMINATION AND THE POTENTIAL GENOTOXIC IMPACT</i>	273
P-21	Martina Ilčíková	<i>AGEING EFFECT OF PLASMA TREATED Al_2O_3 AND ZrO_2 CERAMIC POWDERS WITH RESPECT TO ELECTROPHORETIC DEPOSITION</i>	278
P-22	Jana Hrdá	<i>DETECTION OF PHTHALATES BY ATMOSPHERIC PRESSURE CHEMICAL IONISATION ION MOBILITY SPECTROMETRY</i>	282
P-23	Bartosz Michalczuk	<i>ION MOBILITY SPECTROMETRY FOR RAPID QUANTATIVE ANALYSIS OF WHISKY LACTONE IN OAK WOOD</i>	287
P-24	Matúš Sámel	<i>IONIZATION AT ATMOSPHERIC PRESSURE USING KEV ELECTRON SOURCE</i>	290
P-25	Maria Pinteá	<i>VELOCITY MAP IMAGING TECHNIQUE AND THE DISSOCIATION PROCESSES IN $W(CO)_6$ AND $Fe(CO)_5$ NEGATIVE IONS</i>	292
P-26	Jun Choi	<i>STUDY ON ATMOSPHERIC MICROPLASMA WITH TRANSMISSION LINE RESONATORS DRIVEN BY MICROWAVE</i>	293
P-27	Faro Hechenberger	<i>NOZZLE-TYPE PLASMA ION SOURCE WITH HIGH ION FLUX FOR ION SURFACE INVESTIGATIONS</i>	295
P-28	Vladimír Held	<i>COMBUSTION EXHAUST CLEANING USING TRANSITION ELECTRIC DISCHARGE</i>	298
P-29	Petr Hoffer	<i>INTERFEROMETRIC ANALYSIS OF PRESSURE FIELDS AROUND NANOSECOND DISCHARGES IN WATER</i>	302
P-30	Benedek Horváth	<i>ELECTRON-INDUCED SECONDARY ELECTRONS IN LOW-PRESSURE CAPACITIVELY COUPLED RADIO-FREQUENCY PLASMAS</i>	306

P-31	David Olivenza Leon	<i>PROTON TRANSFER REACTION – MASS SPECTROMETRY AND ITS APPLICATIONS TO HOMELAND SECURITY: DETECTION OF COCAINE AND ITS METABOLITES</i>	311
P-32	Vaclav Prukner	<i>SURFACE DBD BASED JET SYSTEM FOR IN-LINE PROCESSING OF SOLID AND LIQUID PARTICLES</i>	316
P-33	Nail Asfandiarov	<i>DISSOCIATIVE ELECTRON ATTACHMENT TO 4-BROMOBIPHENYL MOLECULE</i>	318
P-34	Peter Čermák	<i>STABILITY OF DISCHARGES THERMOMETRY BASED ON THE EMISSION OF 2PS, NOγ, AND HIR SYSTEMS</i>	323
P-35	Kalev Erme	<i>THE EFFECT OF CATALYST ON OZONE AND NITROUS OXIDE PRODUCTION IN DIELECTRIC BARRIER DISCHARGE</i>	325
P-36	Mostafa Hassan	<i>INVESTIGATION OF THE ELECTROSPRAYED WATER MICRODROPLETS USING OPTICAL IMAGING METHODS</i>	330
P-37	František Krčma	<i>INFLUENCE OF SOLUTION PROPERTIES AND GAS ADDITION ON HYDROGEN PEROXIDE PRODUCTION BY A NOVEL PLASMA SOURCE GENERATING DC NONPULSING DISCHARGE IN LIQUIDS</i>	335
P-38	František Krčma	<i>THE ROLE OF OXYGEN AND CARBON DIOXIDE ON DISCHARGE INITIATED CHEMISTRY IN TITAN RELATED ATMOSPHERE AT RELEVANT TEMPERATURES</i>	338
P-39	Felix Duensing	<i>INVESTIGATE SURFACE STRUCTURE OF MOLYBDENUM SPUTTERING TARGETS BY LOW ENERGY ION-SURFACE COLLISIONS</i>	343
P-40	Gervais Blondel Ngiffo Yemeli	<i>PLASMA ACTIVATED WATER GENERATED BY TRANSIENT SPARK AIR DISCHARGE: CHEMICAL PROPERTIES AND APPLICATION IN SEED GERMINATION AND PLANT GROWTH</i>	345
P-41	Michal Hlína	<i>TETRAFLUOROMETHANE (CF$_4$) DECOMPOSITION USING ARGON/WATER PLASMA TORCH</i>	350
P-42	Zdenka Kolska	<i>SURFACE MODIFICATIONS OF POLYMER FOR VARIABLE APPLICATIONS</i>	354
P-43	Pavel Kříž	<i>THE EFFECT OF LOW-TEMPERATURE PLASMA TREATMENT OF SEEDS OF SELECTED CROPS ON GERMINATION AND ITS BIOLOGICAL ACTIVITY IN EARLY GROWTH</i>	357
P-44	Katarina Kučerová	<i>EFFECT OF PLASMA ACTIVATED WATER ON LETTUCE</i>	363
P-45	Alicia Marín Roldán	<i>DIAGNOSTICS OF THIN LAYERS ON Si SUBSTRATE BY CF-LIBS USING VUV AND UV-NIR SPECTRAL RANGES</i>	368
P-46	Robin Menthéour	<i>ANTIBACTERIAL EFFECTS OF PLASMA ACTIVATED WATER COUPLED WITH ELECTROPORATION</i>	371
P-47	Joanna Pawłat	<i>NON THERMAL PLASMA APPLICATION IN ANTIMICROBIAL CONDITIONING OF MUNICIPAL WASTES</i>	376
P-48	Václav Švorčík	<i>ANTIBACTERIAL PROPERTIES OF SILVER COATED REGENERATED CELLULOSE</i>	380
P-49	Barbora Tarabová	<i>NON-THERMAL PASTEURIZATION OF FRESH APPLE JUICE BY COLD AIR PLASMAS</i>	382

Invited Lectures

SOFT CHEMICAL IONISATION AND THE HUMAN VOLATILOME: APPLICATIONS TO MEDICAL SCIENCE AND HUMAN DETECTION

Paweł Mochalski,¹ Veronika Ruzsanyi,¹ Raquel Fernández del Río,² Margaret E. O'Hara,² Michaela Malásková,¹ Helmut Wiesenhofer,¹ Karl Unterkofler,^{1,3} Clemens Ager,¹ and Chris A. Mayhew^{1,2}

¹*Institute for Breath Research, University of Innsbruck, Rathausplatz 4, 6850, Dornbirn, Austria*

²*Molecular Physics Group, School of Physics and Astronomy, University of Birmingham, Edgabston, Birmingham, B15 2TT, United Kingdom*

³*University of Applied Sciences Vorarlberg, Hochschulstr. 1, A-6850 Dornbirn, Austria*

E-mail: Christopher.Mayhew@uibk.ac.at/c.mayhew@bham.ac.uk

Abstract

Soft chemical ionization mass spectrometric techniques, which include proton transfer reaction mass spectrometry, selected ion flow tube mass spectrometry, and ion mobility spectrometry, employ ions as sensitive analytical probes for use in the identification, detection and monitoring of trace compounds in complex chemical surroundings. These techniques have opened up new and exciting possibilities for applied areas of research with applications to health, food science, the environment and security, to name a few. Among these is the potential to use the trace (pptv-ppbv) volatiles contained in human breath, emitted from the skin and present in bodily fluids for diagnosing and monitoring diseases, monitoring treatments and drug therapy and for examining health in general. This is possible because these volatiles, which make up the so-called human volatilome, provide a non-invasive window to physiological and metabolic processes occurring within the body. The research being undertaken at the Institute for Breath Research, University of Innsbruck, in Dornbirn, Austria and the Molecular Physics Group, University of Birmingham, United Kingdom, is addressing the many current challenges of applying soft chemical ionization mass spectrometry for the analysis of the human volatilome for the benefit of clinical non-invasive diagnostic procedures; including sampling protocols, sample analyses, and importantly the assignment of volatile compounds with a high specificity. The unambiguous identification of volatile compounds is needed to provide the necessary information for the development of portable real time analytical instruments for the detection of specific compounds for a given application. A main focus of this paper deals with our breath volatile research activities of relevant to the health sciences and development of diagnostic techniques at the point-of-care or for laboratory based screening procedures. However, details of related projects in homeland security involving search and rescue operations, namely those involved in discovering humans trapped in buildings or hiding in containers through the volatiles that people emit, are also presented.

1. The Human Volatilome

Hundreds of volatile compounds are present in our breath, emitted through our skin and contained within bodily fluids and faeces. Collectively, these are referred to as the human volatilome [1]. However, the volatiles associated with urine, saliva, blood, sweat and faeces are transient. Hence our research activities, both in the Molecular Physics Group in the United Kingdom and the Institute for Breath Research in Austria, have concentrated predominantly on the volatiles coming from the breath and skin (figure 1).

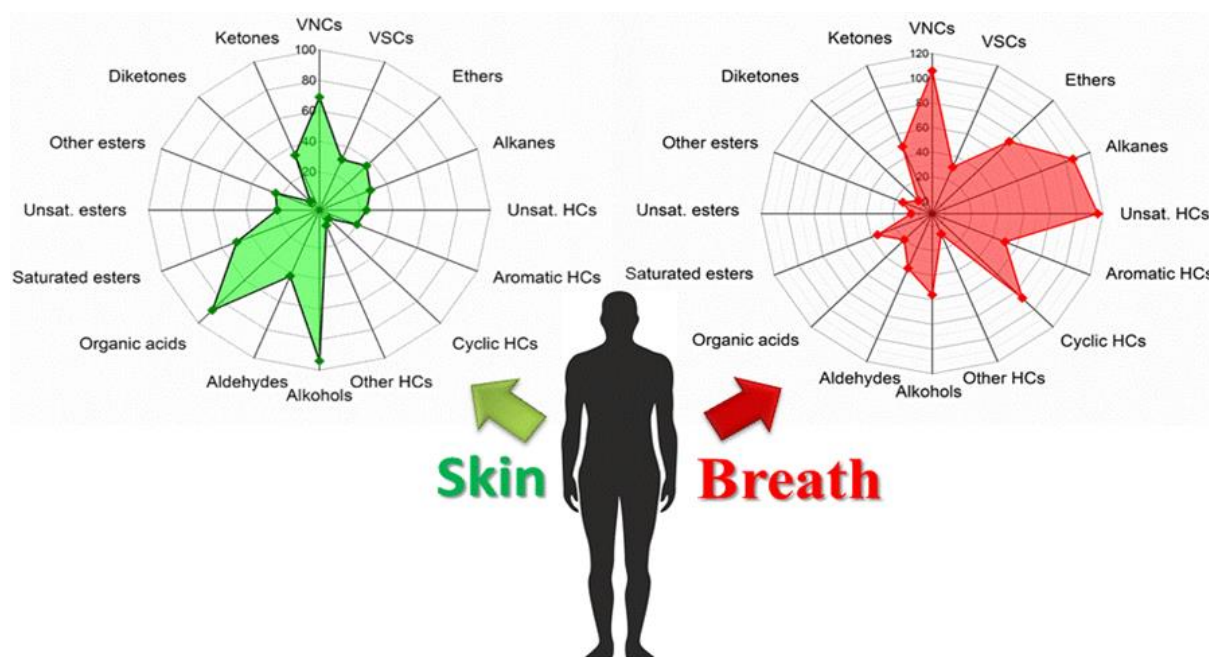


Figure 1. The human volatilome for breath and skin. The type of volatile organic compounds (VOCs) and their detected number are given. An indication of the numbers of the less abundant volatile nitrogen compounds (VNCs) and volatile sulphur compounds (VSCs) are also provided.

This volatilome contains not only volatile metabolites derived endogenously but also those originating from exogenous sources, which independently or together can provide unique non-invasive information on processes occurring within a human body for use in the health sciences [1-3]. These same volatiles can also be used to detect the presence of entrapped or hidden people [4, 5]. Of course, this requires real time sampling and analysis, which can be done quickly and cheaply by electronic sensors. However, before adopting such technologies, the volatile compounds need to be identified and quantified using more powerful analytical chemical techniques. The same is true in the use of VOCs for medical applications, using real time measurements or not. This identification of volatile biomarkers is a key objective of the research being undertaken at the Institute for Breath Research in Dornbirn, Austria, using not only soft chemical ionization mass spectrometric techniques, such as proton transfer reaction mass spectrometry (PTR-MS) [2, 6] and ion mobility spectrometry (IMS) [7], but also what is referred to as the gold standard for analytical chemistry, Gas Chromatography Mass Spectrometry (GC-MS). Once the volatiles, or their fingerprint patterns, have been determined, machine-learning and pattern recognition algorithms could then be used in sensors to identify disease states or to monitor therapy.

We illustrate here some of our recent research activities by highlighting results obtained predominantly using the soft chemical ionization techniques of PTR-MS and IMS to identify and monitor volatiles in the human volatilome from breath and skin.

2. The Human Volatilome and Medical Uses

To date human volatilome medical research has predominantly focused on volatiles contained in breath [1, 2], although some work has also been done on volatile emissions from skin [1, 2] and volatiles coming from the head space of blood [1, 2], urine [1, 2], fluids in the gut [8], saliva [1] and fecal matter [1, 9]. In this section, we will provide information on some of our recent activities involving breath analysis and its applications to the health sciences.

Volatile biomarkers produced by disease, changes in metabolism and drugs present in the bloodstream pass from the blood capillaries into the alveoli in the lungs and then are carried out in the breath. The exhaled volatiles on breath therefore provide a non-invasive window into the physiological and metabolic processes occurring within the whole body and to any drugs present in the bloodstream. Thus, the development of breath tests for the non-invasive detection of early stage disease and for the monitoring of treatment have the potential of having a significant impact on our society, in terms of improving the quality of life and therapy and for reducing the cost of health care.

There are four main areas for the applications of breath analysis (figure 2), but the major research focus by groups world-wide has been on its use as a non-invasive probe to disease. This is not surprising, because it holds great potential for early diagnosis and monitoring of disease, screening and determination of effects therapy, without the need for invasive procedures. However, despite intensive world-wide activities for many decades, both in laboratories and in clinical programmes involving multidisciplinary teams, to date the potential of breath research has not been realised, and has only been exploited in just a few applications, such as the ^{13}C -urea breath test for helicobacter pylori infection or the fructose hydrogen breath test for carbohydrate malabsorption.

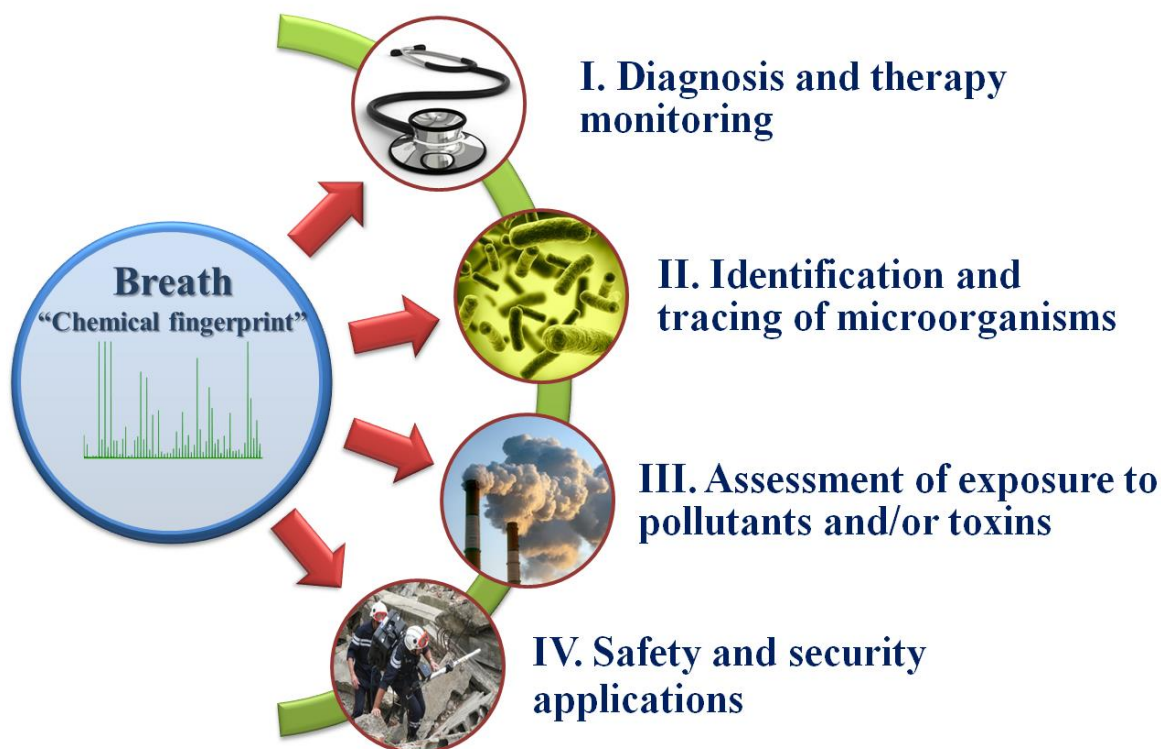


Figure 2. Key applications for breath analysis.

Numerous studies have looked for endogenous volatiles that can be related to a specific disease. But this is a challenging task owing to issues of breath sampling and confounding factors, such as medication, treatment, diet, age, and environmental factors. There are also issues of applying appropriate statistical approaches when dealing with multiple compound analysis using a small sample set, so that care must be taken to ensure that “voodoo” (coincidental) correlations do not occur. Hence, whilst individual studies claim to have provided evidence for the use of endogenous breath volatiles to diagnose diseases few, if any, have shown reproducibility and predictability.

Exogenous volatiles are easier to use in breath analysis, because of the reduction in confounding and voodoo factors. Their metabolites, or the lack of production of metabolites, give a direct insight into the state of the human body. A recent example is the reduction in the metabolism of limonene owing to chronic liver disease and, hence, higher concentrations of limonene in breath are found compared to healthy controls as illustrated in figure 3 [10-12].

RESULTS: 1st PHASE 31 Patients versus 30 controls

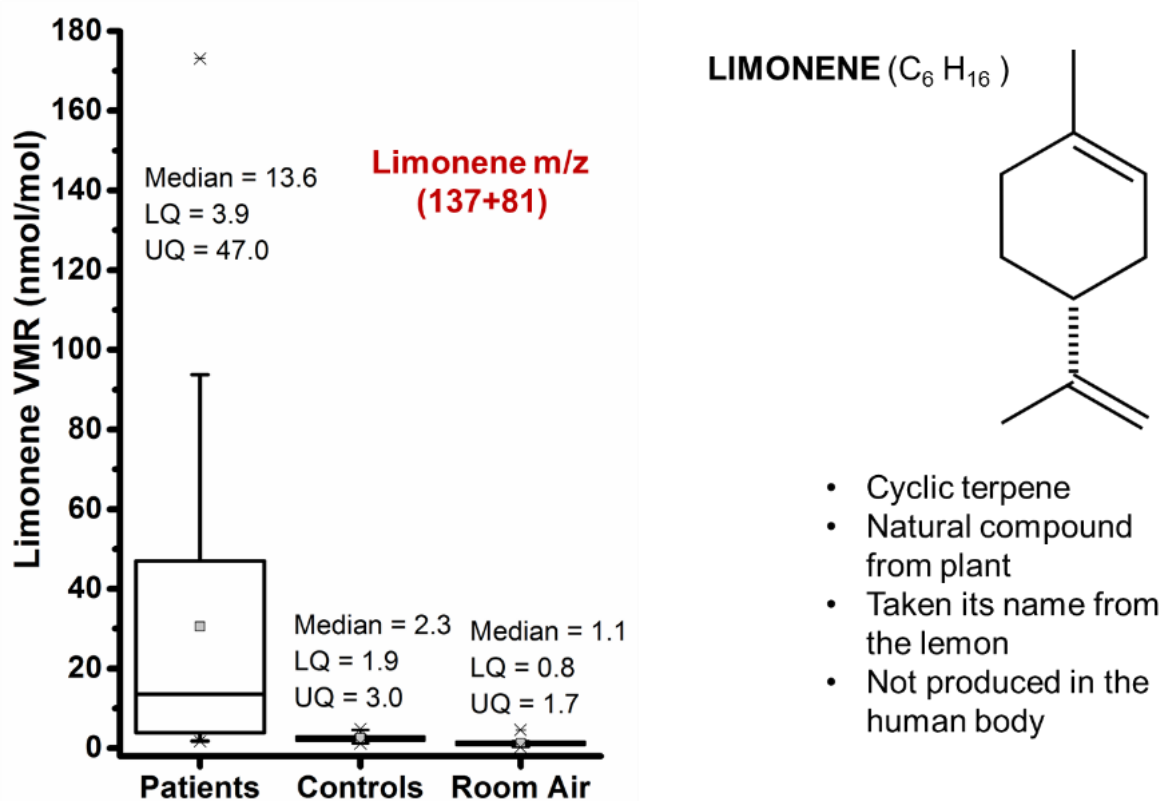


Figure 3. Boxplots showing in units of nmol/mol the lower quartile (LQ), median, mean and upper quartile (UQ) calculated volume mixing ratios (VMR) for limonene on the breath of 31 patients with liver cirrhosis, compared to 30 controls and room air samples [11]. Whiskers are 1.5 times the inter-quartile range and an outlier is depicted by a star. First phase refers to patients prior to liver transplants.

Our studies link limonene with the diseased organ itself, rather than simply the diseased patient as a whole. That limonene is a marker for liver disease has been positively validated, because of a post-transplant (2nd phase) follow-up for a number of patients. Moreover, we have a plausible mechanistic link between liver disease and the observed increases in limonene levels in the breath. It has been documented that the production of the enzyme

CYP2C19, which metabolizes limonene in the human body, is reduced when a liver is cirrhotic [13]. Limonene is thus a specific biomarker, resulting from the effects of liver disease, rather than liver disease itself, and assesses the health of the whole liver, rather than a localized biopsy, which is expensive, invasive and carries a risk.

The importance of this discovery lies in the fact that the burden of liver disease has risen dramatically in the United Kingdom in the last few decades as highlighted in a recent Lancet report [14]. This is mainly caused by changes in western life-styles (particularly from over-eating leading to obesity and from alcohol abuse). For example, in the United Kingdom liver disease is the 3rd most common cause of preventable death for the under 65 years. Furthermore, evidence shows that approximately 95% of liver cancers are a result of liver cirrhosis, and liver cancer is one of the most rapidly increasing forms of cancer in the United Kingdom. Therefore, if liver disease can be detected in its early stages, changes in life styles and the use of new drugs that are becoming available can reverse liver damage before it destroys lives. Of course, the increase in liver disease is not just a United Kingdom problem. According to presentations made at the 2017 European Society for Medical Oncology, liver cancer is set to become the 3rd biggest cancer worldwide in the next ten years [15]. Among the key recommendations in the Lancet report is the need to strengthen the detection of early-stage liver disease [14]. We propose that the analysis of volatiles in breath has the potential to provide this, and unlike an invasive liver biopsy, which samples only a small portion of the liver, breath analysis provides a non-invasive measure of the health of the whole liver.

Although we have focused on an exogenous compound, limonene, with regards to liver disease, there is strong evidence from our studies [11] that there are two endogenous volatiles which are diagnostically useful to the cirrhotic organ itself, namely methanol and 2-pentagon. However, unlike limonene, we do not know the biochemical route for the production of these volatiles, and hence we cannot be certain of how specific or useful they are for use in detecting liver disease or monitoring liver function.

We consider that our discovery of limonene as a biomarker for liver disease is a major finding because it raises the potential for using the detection of limonene as a non-invasive method for detecting early-stage liver disease, to assess liver function before, during and after any treatment or medication, and to assess the success of a liver transplant, all via pharmacokinetic-based tests. This holds enormous promise for improved healthcare, the implications of which are far-reaching both for patients and for the health providers.

3. The Human Volatilome for Detecting Entrapped or Hidden People

The trafficking and smuggling of people into Europe have reached epidemic proportions in recent years, with the people being smuggled often risking their lives. Consequently, there is a need for highly portable, rapid security devices for the non-intrusive monitoring of containers and trucks to detect the presence of hidden people who are either being smuggled or trafficked. Such a device would also be useful to first responders to help rapidly find buried or trapped people under collapsed buildings resulting from natural (e.g. earthquakes, accidental (e.g. poor construction) or man-made (e.g. terrorist's attacks) disasters .

Towards the above goal, our research activities at the Institute for Breath Research in Austria are focusing on providing the key fundamental data to help in the development of portable field devices, such as e-noses or IMS systems, based on assessing a human volatile chemical fingerprint, which could be used to rapidly identify the presence of hidden, smuggled or entrapped people with a high level of confidence.

The volatile species forming this human footprint during entrapment can stem from compounds present in human breath or emitted from urine, feces, blood, sweat and skin. However, as mentioned earlier, the volatiles from urine, saliva, blood, sweat and feces are transient and more variable than obtained from breath and skin. Hence, our research activities

in this area have concentrated on investigating the volatiles contained in breath and those emitted from the skin. These volatiles also have the added advantages that they are associated with living people and that in an enclosed environment their concentrations will build up with time.

To be ideal markers of human presence, volatiles need to have a number of characteristics; namely, the selected volatiles should be omnipresent in the human volatilome, distinguishable from background levels, relatively non-reactive (i.e. not absorbed significantly by building material, packing material etc.), continuously emitted by the human body (so that concentrations can build-up), be reliably identified and present in the proximity of an entrapped or hidden person at levels detectable by a field analyser. To date, our studies suggest that fewer than 50 volatile species are useful potential markers of buried or hidden people. These species consist of aldehydes, hydrocarbons, ketones and inorganic compounds. These proposed volatiles and their emission rates are summarised in figure 4. The detection of such a large number of volatiles places major requirements and limitations on any analytical device. Hence, further investigations are needed to draw-up an ideal subset of human volatile trace compounds that are necessary and sufficient for use in the detection of people with a high level of confidence. Of those compounds so far selected, we suggest that eleven metabolites, namely CO₂, NH₃, acetone, 6-methyl-5-hepten-2-one, isoprene, n-propanal, n-hexanal, n-heptanal, n-octanal, n-nonanal, and acetaldehyde may be the most useful for finding trapped people, because they are systemic species exhibiting high emission rates from a human body, which should make them distinguishable from urban background levels [16].

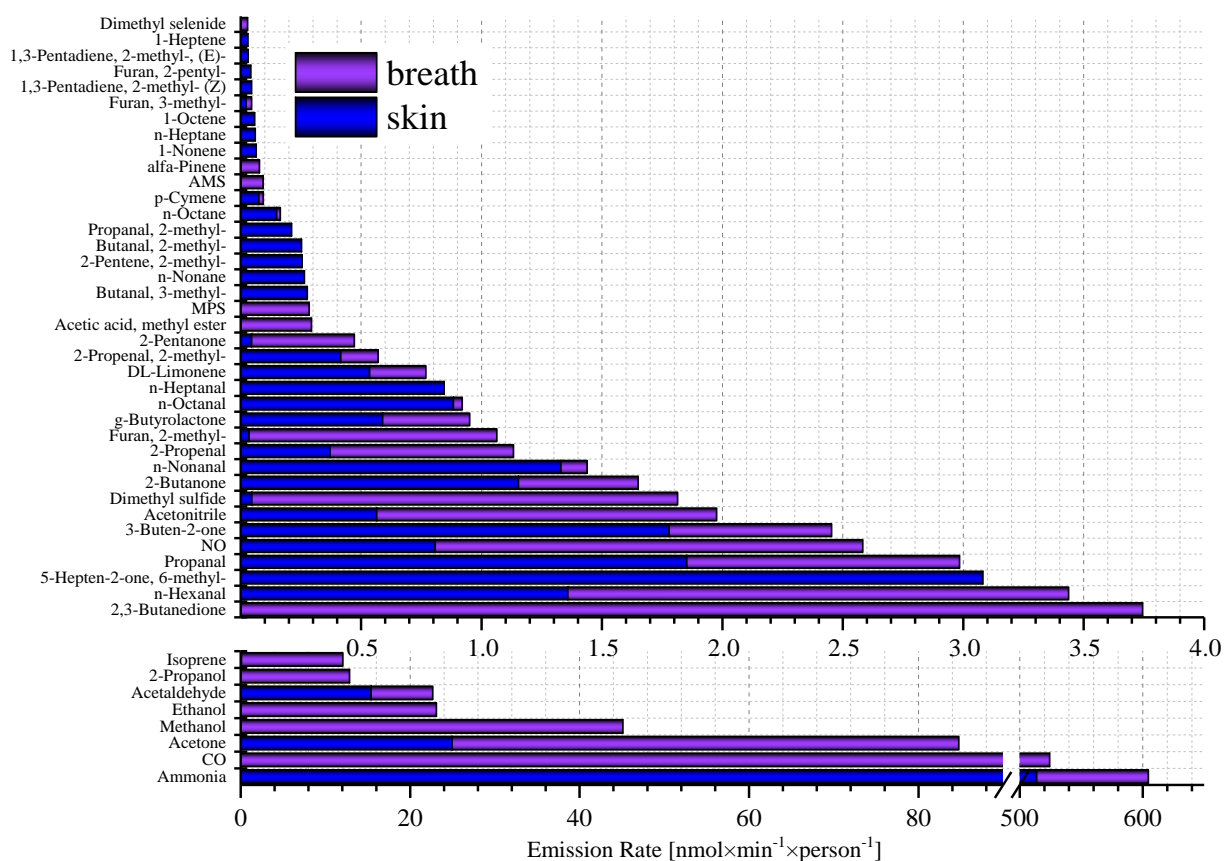


Figure 4. Illustrative potential volatile markers of human presence and their total emission rates (breath (blue) and skin (purple)). This figure has been adapted from the work of Pawel Mochalski et al. [16]. Note that CO₂ has a high emission rate in the range of 10⁶-10⁷ nmol×min⁻¹×person⁻¹, and hence has been excluded from this figure for reasons of clarity.

Two analytical techniques arguably have the greatest potential in this context of finding humans via volatile emissions in the field (e.g. at border controls or earthquake sites), namely IMS, which uses soft chemical ionisation approaches [5], and chemoresistive sensors [17]. Recently we have used an IMS coupled with gas chromatography (GC-IMS) to monitor the volatiles released from the human body under conditions that mimic entrapment [5]. Figure 5 provides an illustrative chromatogram from this instrument. In total seventeen VOCs were identified and quantified from thirty-five ion mobility peaks corresponding to a human being present, thereby adding to the list above. These VOCs are 7 aldehydes (acrolein, 2-methylpropanal, 3-methylbutanal, 2-ethacrolein, n-hexanal, n-heptanal, benzaldehyde), 3 ketones (acetone, 2-pentanone, 4-methyl-2-pentanone), 5 esters (ethyl formate, ethyl propionate, vinyl butyrate, butyl acetate, ethyl isovalerate), one alcohol (2-methyl-1-propanol) and one organic acid (acetic acid).

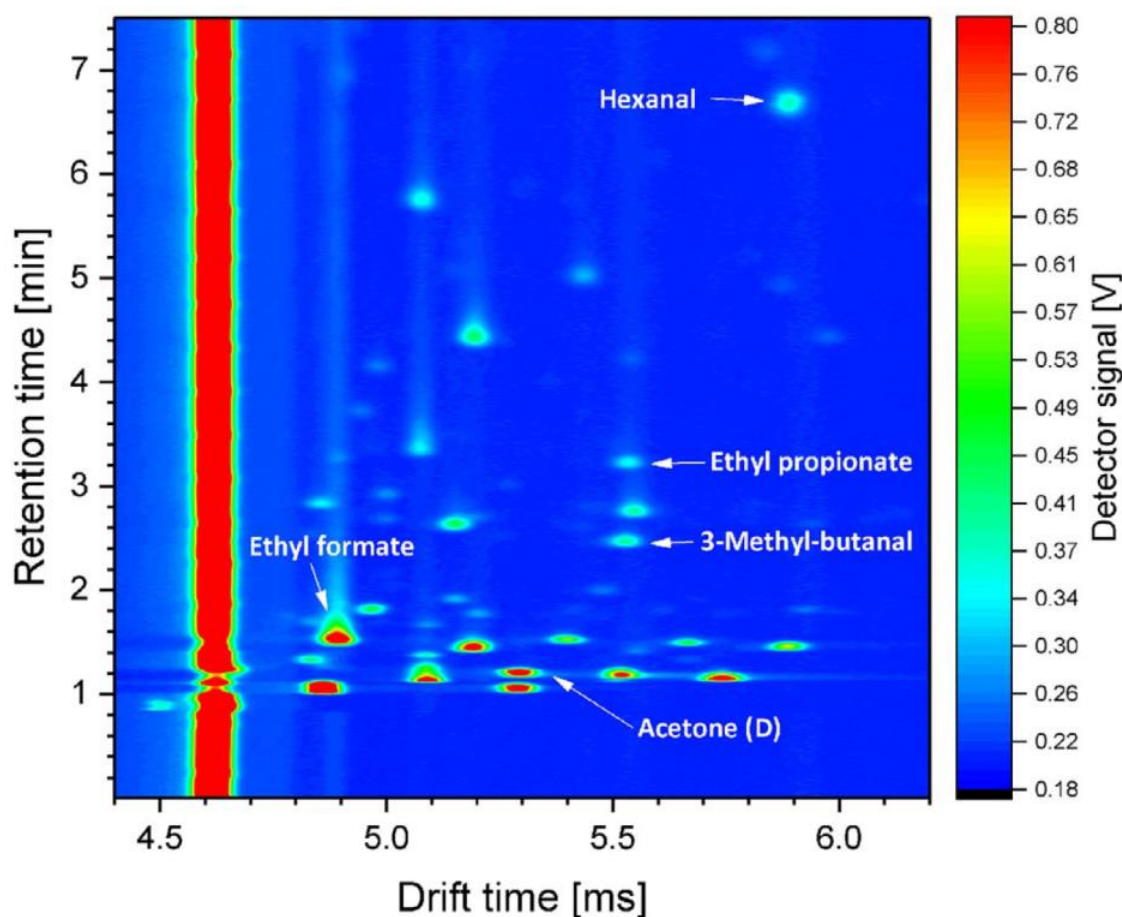


Figure 5. Fragment of an exemplary 2D GC-IMS chromatogram from the analysis of human-borne VOCs detected in a closed plethysmography chamber containing a human volunteer [5]. Some of the key volatiles are identified.

This proof-of-principle study demonstrates that GC-IMS can be used as a portable field detector of hidden or entrapped people. Compared to soft chemical Ionisation studies, there is less published work on the capabilities chemoresistive sensor arrays for use in detecting volatiles associated with the human volatilome. Therefore with colleagues at ETH, Zurich, we undertook a study using state-of-the-art sensor arrays developed by ETH at our breath research facility in Dornbirn, Austria. A proton transfer reaction mass spectrometer was used in parallel to cross-validate the sensor array's accuracy, selectivity and sensitivity.

This work showed that novel ETH sensors have the required sensitivity (low ppb) to find people in enclosed environments [17].

4. Concluding Remarks

The analysis of volatiles contained in the breath and emitted by skin has a considerable potential for use as non-invasive probes in the health sciences, ranging from determining the type of bacterial infection through to disease diagnosis and determining the efficacy of drug therapy. However, research in this area is fraught with major challenges, and that has resulted in a lack of progress and the development of clinically useful endogenous (untargeted) volatile diagnostic tests. There have been numerous “fishing” expeditions to look for specific endogenous volatiles or patterns of these volatiles that are characteristic of a disease. Yet none have been reproducible and it is not clear how specific the discovered volatiles are to a given disease. It still needs to be ascertained whether there are unique patterns of endogenous VOCs, made up of specific and/or non-specific biomarkers, for a particular disease that can be discerned from the complex chemical environment of breath. This is because of the fact that the large number of endogenous VOCs in the breath makes it challenging to identify and validate breath volatiles with a specific disease.

The use of exogenous volatile compounds has been more successful, and there are a number of approved breath tests for clinical utilization [18, 19], but the majority of these make use of expensive isotopically labelled compounds. And it is just not the expense that is an issue with the use of isotopes other than ^{13}C . For example, a recent study by us has illustrated that in the case of using deuterated compounds and proton transfer reaction mass spectrometry, care must be taken in the choice of an exogenous deuterated compound for use in breath pharmacokinetic studies using proton transfer reaction mass spectrometry, D/H exchange processes in the reaction region this instrument impose interpretative problems for breath analysis [20].

Given the complications associated with the use of endogenous and isotopically labelled exogenous compounds, we consider that the application of non-labelled exogenous compounds for clinical use, for examples to determine the effectiveness of therapy and drugs or to monitor organ function, holds the greatest future for the use of breath volatile biomarkers in the medical arena. We can simply monitor how externally introduced compounds are absorbed, metabolised or excreted by the body. They provide targeted probes to biological processes through either the production or the lack of production of metabolites in breath following the oral administration of a compound which then subsequently is or is not metabolised in the body, the volatiles of which are measured in the breath. This often produces compounds which are not present naturally in the environment, leading to the required reduction in confounding factors and the use of simple statistical analysis, rather than multivariate statistics frequently used when looking at endogenous compounds to find correlations between volatile patterns and a disease state.

5. References

- [1] A. Amann, B. de L Costello, W. Miekisch, J. Schubert, B. Buszewski, J. Pleil, N. Ratcliffe, and T. A. Risby, “The human volatilome: volatile organic compounds (VOCs) in exhaled breath, skin emanations, urine, feces and saliva”, *Journal of Breath Research* 8(3), 034001 (2014). doi: 10.1088/1752-7155/8/3/034001.
- [2] A. M. Ellis and C. A. Mayhew, “Proton Transfer Reaction Mass Spectrometry Principles and Applications” (2014) John Wiley & Sons Ltd., UK. doi: 10.1002/9781118682883.

- [3] S. Sethi, R. Nanda and T. Chakraborty, “Clinical Application of Volatile Organic Compound Analysis for Detecting Infectious Diseases”, *Clinical Microbiology Reviews* 26(3), 462-475 (2013). doi: 10.1128/CMR.00020-13.
- [4] P. Mochalski, V. Ruzsanyi, H. Wiesenhofer, and C. A. Mayhew, “Instrumental sensing of trace volatiles – a new promising tool for detecting the presence of entrapped or hidden people”, *Journal of Breath Research* 12, 027107 (2018). doi: 10.1088/1752-7163/aa9769.
- [5] P. Mochalski, H. Wiesenhofer, M. Allers, S. Zimmermann, A. T. Güntner, N. J. Pineauc, W. Lederer, A. Agapiou, C. A. Mayhew, V. Ruzsanyi, “Monitoring of selected skin- and breath-borne volatile organic compounds emitted from the human body using gas chromatography ion mobility spectrometry (GC-IMS)”, *Journal of Chromatography B* 1076, 29-34 (2018). doi: 10.1016/j.jchromb.2018.01.013.
- [6] A. D. J. Critchley, T. S. Elliott, G. Harrison, C. A. Mayhew, J. M. Thompson, and T. Worthington, “The Proton Transfer Reaction Mass Spectrometer and its use in Medical Science: applications to drug assays and the monitoring of bacteria”, *Int. J. Mass Spectrom.* 239 (2004) 235-241.
- [7] G.A. Eiceman, Z. Karpas, Herbert H. Hill, Jr. “Ion Mobility Spectrometry 3rd Edition ISBN: 978-1-4398-5998-8 (CRC Press (2013))”.
- [8] M. Lechner, H. P. Colvin, C. Ginzel, et al., “Headspace screening of fluid obtained from the gut during colonoscopy and breath analysis by proton transfer reaction-mass spectrometry: a novel approach in the diagnosis of gastro-intestinal diseases”, *International Journal of Mass Spectrometry* 243, 151-154 (2005). doi: 10.1016/j.ijms.2005.02.002.
- [9] C. A. Batty, M. Cauchi, C. Lourenço, J. O. Hunter, C. Turner, “Use of the Analysis of the Volatile Faecal Metabolome in Screening for Colorectal Cancer”, *PLoS ONE* 10(6), e0130301 (2015). doi: 10.1371/journal.pone.0130301.
- [10] P. A. Brown, PhD Thesis “Investigations of Proton Transfer Reaction Mass Spectrometry for Applications in organophosphate Detection and Breath Analysis”, Molecular Physics Group, University of Birmingham, UK (<http://etheses.bham.ac.uk/3839/>).
- [11] R. Fernández del Río, M. E. O’Hara, A. Holt, P. Pemberton, T. Shah, T. Whitehouse, and C. A. Mayhew, “Volatile biomarkers in breath associated with liver cirrhosis - comparisons of pre- and post-liver transplant breath samples”, *EBioMedicine* 2, 1243-1250 (2015). doi: 10.1016/j.ebiom.2015.07.027.
- [12] M. E O’Hara, R. Fernández del Río, A. Holt, P. Pemberton, T. Shah, T. Whitehouse, and C .A. Mayhew “Limonene in exhaled breath is elevated in Hepatic Encephalopathy” *Journal of Breath Research J. Breath Res.* 2016 Nov 21;10(4):046010.
- [13] R. F. Frye, N. K. Zgheib, G. R. Matzke, D. Chaves-Gnecco, M. Rabinovitz, O. S. Shaikh, and R. A. Branch “Liver disease selectively modulates cytochrome P450--mediated metabolism” *Clinical pharmacology and therapeutics.* 80(3) (2006) 235–245.
- [14] R. Williams, R. Aspinall R, M. Bellis, G. Camps-Walsh, M. Cramp, A. Dhawan, J. Ferguson, D. Forton, G. Foster, I. Gilmore, M. Hickman, M. Hudson, D. Kelly, A. Langford,

M. Lombard, L. Longworth, N. Martin, K. Moriarty, P. Newsome, J. O'Grady, R. Pryke, H. Rutter, S. Ryder, N. Sheron, T. Smith. "Addressing liver disease in the UK: A blueprint for attaining excellence in health care and reducing premature mortality from lifestyle issues of excess consumption of alcohol, obesity, and viral hepatitis" *Lancet* 384 (2014) 1953-1997.

[15] Medical Oncology Congress: Integrating science into oncology for a better patient outcome, Madrid Spain 8th – 12th September 2017.

[16] P. Mochalski, K. Unterkofler, G. Teschl, and A. Amann, "Potential of volatile organic compounds as markers of entrapped humans for use in urban search-and-rescue operations" *Trends in Anal. Chem.* 68 (2015) 88.

[17] A. T. Güntner, N. J. Pineau, P. Mochalski, H. Wiesenhofer, A. Agapiou, C. A. Mayhew, and S. E. Pratsinis "Sniffing Entrapped Humans with Sensor Arrays" *Anal. Chem.* 90 (8) (2018) 4940–4945.

[18] K. M. Paschke¹, A. Mashir¹ and R. A. Dweik, "Clinical applications of breath testing", *F1000 Medicine Reports* 2: 56 (2010).

[19] I. Siddiqui, S. Ahmed, and S. Abid, "Update on diagnostic value of breath test in gastrointestinal and liver diseases", *World J. Gastrointest. Pathophysiol.* 7(3) (2016) 256-265.

[20] P. Mochalski, S. Mirmigkou, K. Unterkofler, P. Sulzer, C. A. Mayhew, and T. D. Märk, "PTR-MS studies of the reactions of H_3O^+ with a number of deuterated volatile organic compounds and the subsequent sequential reactions of the primary product ions with water under normal and humid drift tube conditions: implications for use of deuterated compounds for breath analysis" *Int. J. Mass Spectrom.* 436 (2019) 65-70.

Acknowledgements

The work presented in this paper in part supported by the PIMMS and IMPACT ITNs which are in turn supported by the European Commission's seventh Framework Programme under Grant Agreement Numbers 287382 and 674911, respectively. We also gratefully acknowledge financial support from the Austrian Research Promotion Agency (FFG) for the program KIRAS Security Research under the grant DHS-AS (grant agreement no. 859586). For the liver disease work presented, Margaret O'Hara thanks the Daphne Jackson Trust for a Fellowship and the Engineering and Physical Sciences Research Council and University of Birmingham for her sponsorship, and we thank the Wellcome Trust (grant number 097825/Z/11/B) for an Institutional Strategic Support Fund and the National Institute of Health Research Clinical Research Network (NIHR CRN) for support.

BIOLOGICAL APPLICATIONS USING PULSED ELECTRIC FIELD AND PLASMAS

Douyan Wang¹, Takao Namihira¹

¹ Institute of Pulsed Power Science, Kumamoto University, JAPAN

E-mail: douyan@cs.kumamoto-u.ac.jp

Pulsed power is an instantaneous ultra-high power with high energy density (10^5 - 10^7 J/m³). By controlling and utilizing it in a narrow space and an instantaneous time, phenomena and reactions that are not attained by conventional and ordinary methods can be achieved. Due to this unique characteristic, it enables a wide variety of applications which cover the solids, liquids, super critical fluids, gases, and bioelectrics fields. Various topics related to biological applications will be introduced in the presentation.

1. Pulsed power generation

Pulsed power technology which enables to control the time duration and peak-to-average power ratio of output signal. It can deliver a single short pulse or multi pulses with a controllable repetition rate. The highest energy and power that have been achieved in a single pulse are the order of 100 MJ and a few hundred terawatts, respectively. Figure 1 shows a schematic diagram of pulsed power generation system [1]. Pulsed power can generate high electric field of discharge plasma both in gaseous and in liquid phases. In addition, the generation of either non-thermal plasma or thermal plasma can be controlled by designing circuit parameters of the generation system. Discharge plasma in liquids is known to generate some physical phenomena such as extremely high electric fields at the tip of streamers, as well as high energy electrons, ozone, other chemically active species, ultraviolet rays and shock waves [2].

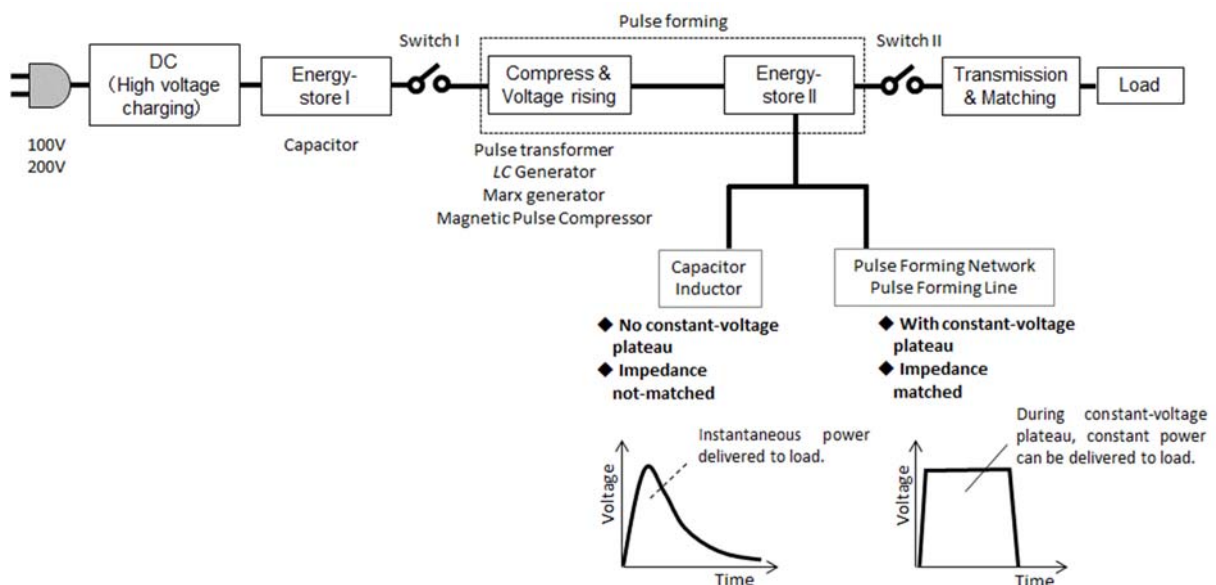


Fig. 1. Schematic diagram of pulsed power generation system [1].

2. Applications using pulse electric field and plasmas

Bioelectrics refers to the use of pulsed power, non-thermal plasmas in gases or liquids and shock waves, to give novel physical stresses to biological cells, tissues and/or organisms as well as bacteria. For biological applications, the main effect is either spatially distributed electric field or chemically active species produced by discharge plasma, sometimes the superimposed effects are expected. By controlling the degree of electrical stimulations, it is possible to either inactivate biological targets or keep them alive and activate their functions. Due to the excellent controllability, its research fields have a wide

range such as medical applications [3-6], veterinary medicine, food processing, agriculture [7-8], sterilization [9] and marine industries [10-13].

3. References

- [1] Wang D, Namihira T and Akiyama H 2015 *J. Inst. Electrostat. Jpn.* **39** 6 230-236.
- [2] Akiyama H 2000 *IEEE Trans. Electr. Insul.* **7** 5 646-653.
- [3] Higashi H, Wang D, Matsuoka T, Namihira T, Akiyama H, Saitoh H 2016 *IEEE Transactions on Plasma Science* **44** 7 1137-1143.
- [4] Sonoda T, Umeda K, Wang D, Namihira T Akiyama H 2015 *Plasma Medicine* **5** 2-4 271-281.
- [5] Takamura N, Wang D, Satoh T, Namihira T, Saitoh H and Akiyama H 2014 *Electronics and Communications in Japan* **97** 11 65-73.
- [6] Takamura N, Wang D, Seki D, Namihira T, Yano K, Saitoh H and Akiyama H 2012 *International Journal of Plasma Environmental Science & Technology* **6** 1 59-62.
- [7] Sonoda T, Higashi Y, Yamada Y, Wang D, Namihira T and Akiyama H 2017 *International Journal of Plasma Environmental Science & Technology* **11** 1 81-86.
- [8] Sonoda T, Takamura N, Wang D, Namihira T and Akiyama H 2014 *IEEE Transactions on Plasma Science* **42** 10 3202-3208.
- [9] Choi J, Wang D, Namihira T, Katsuki S, Akiyama H, Lin X, Sato H, Seta H, Matsubara H and Saeki T 2008 *Journal of Applied Physics* **104** 094701.
- [10] Hirayama K, Wang D, Namihira T, Takano H, Takio S and Akiyama H 2012 *International Journal of Plasma Environmental Science & Technology* **6** 3 272-277.
- [11] Wang D, Lin X, Hirayama K, Li Z, Ohno T, Zhang W, Namihira T, Katsuki S, Takano H, Takio S and Akiyama H 2010 *IEEE Transactions on Plasma Science* **38** 1 39-46.
- [12] Wang D, Hirayama K, Takamura N, Goto T, Namihira T and Akiyama H 2011 *Proceeding of the XXX International Conference on Phenomena in Ionized Gases (ICPIG), Belfast, Northern Ireland, UK* D16.
- [13] Li Z, Sakai S, Yamada C, Wang D, Chung S, Lin X, Namihira T, Katsuki S and Akiyama H 2006 *IEEE Transactions on Plasma Science* **34** 5 1719-1724.

NANOSECOND DISCHARGE IN LIQUID WATER AT IPP: OVERVIEW OF RECENT RESULTS

Milan Šimek, Petr Hoffer, Václav Prukner, Jiří Schmidt,
Václav Babický, and Petr Lukeš

Department of Pulse Plasma Systems, Institute of Plasma Physics CAS, Prague, Czech Republic
E-mail: simek@ipp.cas.cz

This presentation reports on recent experimental research carried out in the field of discharge generation in liquids at the Department of Pulse Plasma Systems, Institute of Plasma Physics (IPP). We have employed emission and laser based diagnostic techniques to reveal basic fingerprints of nanosecond discharges developing in liquid water by applying periodic high-voltage pulses in a point-to-plane electrode configuration.

1. Introduction

Fundamentals of electrical discharges generated in aqueous liquid solutions are less understood compared with gaseous discharges. Electrical breakdown of liquid/gaseous dielectrics is conditioned by physical properties, such as the mass density, electrical permittivity and conductivity [1–2]. Discharges inside liquids can be initiated through bubbles (gas breakdown) that can be formed due to the local heating of the liquid. The bubble breakdown in water typically occurs in the discharge systems driven by slow high-voltage (HV) waveforms (such as AC or pulsed waveforms of microsecond duration) [1–3]. In the case of discharges driven by short HV waveforms of nanosecond duration applied at low repetition rate however, it is frequently assumed that the discharge develops due to the presence of voids or that direct ionization of water without phase change (no bubbles) takes place.

2. Time-resolved optical-based diagnostics

We have explored basic emission and electrical characteristics of the discharge produced in deionized liquid water in point-to-plane electrode geometry by applying 5 ns (FWHM) HV pulses at 1–10 Hz repetition rate [4–6]. We employed techniques of time-resolved ICCD spectroscopy and microscopy to register basic emission and morphological fingerprints (Fig.1). Time resolved ICCD images evidence typical tree-like morphology while emission spectra show broad-band continua evolving during the first few nanoseconds while the later phase (tens of ns) is characterized by the well-known atomic lines (H_{α} or O^I). The ICCD based techniques were complemented by fast (sub-ns) PMT measurements of emission waveform evolution and propagation velocity at selected wavelengths.

Very recently, the concept of Mach-Zehnder interferometer was applied to detect the pressure field developing during the discharge. The Katana 05 (Onefive) laser, producing pulses 532 nm/30 ps/4 nJ was used to produce probe and reference beams. The 12 bit CCD SensiCam (PCO) camera was used as detector [7].

3. Summary of achieved results

- The nanosecond discharge in liquid water is characterised by many isolated primary (mostly 2–4 channels) and secondary micro-filaments creating a tree-like structure similar to the corona discharges in air.
- An inception of a few isolated micro-discharges is followed by an approximately linear initial expansion of the luminous discharge filaments, with propagation velocity of luminous front of $\sim 10^5$ m/s.
- After initial expansion and branching of primary filaments, the length of luminous filaments collapses.

- Bound-free/free-free radiative transitions might be the most important emission characteristics of the nanosecond discharge initiation mechanism, which does not involve formation of vapour bubbles, in liquid water.
- Bound-bound (atomic) emission (by hydrogen and oxygen) occurs much later during subsequent discharge initiated by reflected HV pulses, and probably indicates (together with the Stark and pressure broadening) the discharge mechanism with participation of bubbles.
- The discharge visual characteristics and behaviour is not significantly influenced by water conductivity but the length of the filaments was increasing with the increasing voltage amplitude and reached the maximum value of 1.8 mm for 90 kV.
- The propagation velocity of luminous filaments increases with the voltage amplitude for all conductivities due to the electric field amplification near the needle.
- There is no systematic dependence of the propagation velocity on the water conductivity and thus we cannot definitely conclude if the water conductivity does play a significant role in the filament propagation velocity. Our results show that the effect of conductivity is negligible.
- Interference patterns captured just after the discharge initiation show opaque areas with no visible fringes. This means that the laser beam was deflected out of the field of view of the optical system due to very strong refractive index gradients indicating presence of extremely strong shock waves.
- Compared to results and experimental setups of other authors we conclude that our type of discharge is very similar in nature to theirs and propagates in the liquid phase as well.

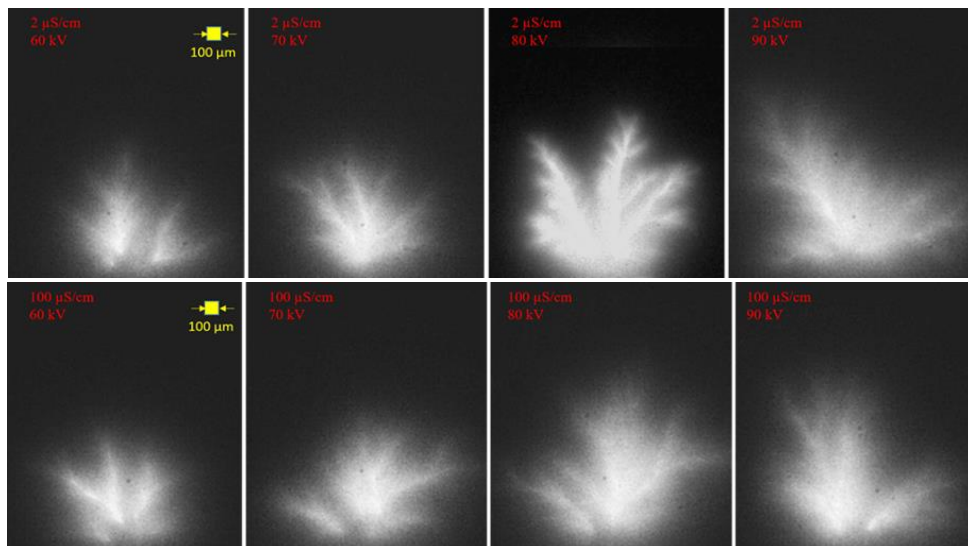


Fig. 1. Typical time-resolved ICCD images of single discharge events for two different water conductivities and various HV amplitudes. All images were captured using the shortest gate of the ICCD intensifier of 2 ns and with background subtracted during the acquisition.

Acknowledgements

This work was supported by the Czech Science Foundation (Project ID 18-04676S).

4. References

- [1] Šunka P *et al.* 1999 *Plasma Sources Science & Technology* **8** 258.
- [2] Locke B R *et al.* 2006 *Ind. Eng. Chem. Res.* **45** 882.
- [3] Šimek M *et al.* 2012 *Plasma Sources Science & Technology* **21** 055031.
- [4] Šimek M *et al.* 2017 *Plasma Sources Science & Technology* **26** 07LT01.
- [5] Pongráč B *et al.* 2018 *Journal of Physics D-Applied Physics* **51** 124001.
- [6] Pongráč B *et al.* 2019 *Plasma Sources Science & Technology* **28** xxxxxx.
- [7] Hoffer P *et al.* 2019 *SAPP XXII Book_of_Contributed_Papers*

CHEMICAL KINETIC MODEL OF TRANSIENT SPARK: SPARK PHASE AND NO_x FORMATION

Mário Janda, Karol Hensel, Zdenko Machala

*Division of Environmental physics, Faculty of Mathematics, Physics and Informatics,
Comenius University, Mlynská dolina F2, 842 48 Bratislava, Slovakia
E-mail: janda@fmph.uniba.sk*

Transient Spark (TS) discharge generated in atmospheric air is an efficient source of NO_x for biomedical applications with a negligible O₃ production. The TS discharge is characteristic by short (~10 ns) and high current (~A) spark pulses initiated by streamers. The paper presents chemical kinetic model of the TS that simulates electron density evolution during both streamer and spark phases and studies generation of selected reactive oxygen and nitrogen species (RONS), e.g. O, N, NO, NO₂, and O₃, that are important for their antibacterial and other biomedical effects. The dominant intermediate product of the streamer chemistry is atomic O. Without the following spark phase, this would lead to the generation of O₃ as the dominant final product. In the spark phase, unlike in the streamer phases, the chemistry is twisted towards production of reactive nitrogen species (RNS), as the density of N atoms exceeds the atomic O density. This is in agreement with the experimental observation that TS generates more NO_x than O₃, although the generation of NO_x occurs mainly during the relaxation phase following the TS pulse, which is not yet included in the presented model.

1. Introduction

The transient spark (TS) is a dc-operated, self-pulsing and filamentary discharge with typical repetition frequency in the range 1-10 kHz. Fundamental research of the positive polarity TS revealed that it is characteristic by the short (~10-100 ns) spark current pulses, having maximum amplitude in the range of a few Amps [1]. Thanks to the short spark pulse duration and limited amount of deposited energy (~1 mJ/pulse), significant heating of the treated gas is avoided and the generated plasma is non-equilibrium and highly reactive, with the electron density above 10¹⁷ cm⁻³ [2].

The reactive plasma properties predetermine the TS for environmental and biomedical applications or generation of nanoparticles [3, 4]. In biomedical applications, the major antibacterial role in TS discharge is attributed to reactive oxygen and nitrogen species (RONS) [5]. We recently reported the efficient generation of nitrogen oxides (NO_x) by TS discharge [6]. The NO_x production rate ~7×10¹⁶ molecules/J was achieved. We assume that further optimization of NO_x formation by TS is also possible. It requires further study of TS including its chemical kinetic modeling.

The modeling of chemical kinetics aiming to calculate the temporal density evolution of all species included in the kinetic model is an effective tool for plasma chemistry [7-10]. It is commonly used not only for the modeling of cold plasma chemistry including RONS generation [7], but also for the description of high-temperature steady-state arc plasmas [8], nanosecond duration of streamer propagation [9], or fast gas heating in pulsed discharges [10]. The chemical kinetic modeling could also help us to better understand the TS discharge physical and chemical characteristics.

We presented a chemical kinetic model developed for TS discharge with a focus on the initial streamer phase recently [11]. Here we present an updated version of this model including the spark phase. The validity of the model was tested by comparing the calculated electron density with experimental data [2]. This model is further used to analyse the generation of selected RONS: O, N, O₃, NO, and NO₂.

2. Transient Spark

Figure 1 shows a schematic of the electric circuit used to generate the positive TS discharge by a positive polarity dc high-voltage (HV) power supply connected to a metal needle HV electrode via a series resistor ($R = 5-10$ M Ω). In the same way, the negative TS can be generated using negative dc HV power supply [12]. The usual distance d between the tip of the HV electrode and a grounded electrode is 4-10 mm. For the grounded electrode we typically use plate, mesh, or blunt tip.

The TS is initiated by a streamer current pulse with the amplitude 50-100 mA (blue dots in Fig. 2, top-right corner), appearing when the potential on the stressed electrode reaches the voltage V_{TS} characteristic for the TS discharge. The optical visualization of the TS temporal evolution revealed two events during the initial TS phase, identified as primary and secondary streamers [13, 14]. The primary streamer creates a relatively conductive plasma bridge between the electrodes. This enables partial discharging of the internal capacitance C of the electric circuit generating TS, and heating of the gas inside this plasma channel during the streamer-to-spark transition phase. The spark current pulse appears when the gas temperature inside the plasma channel increases up to ~ 1000 K [15].

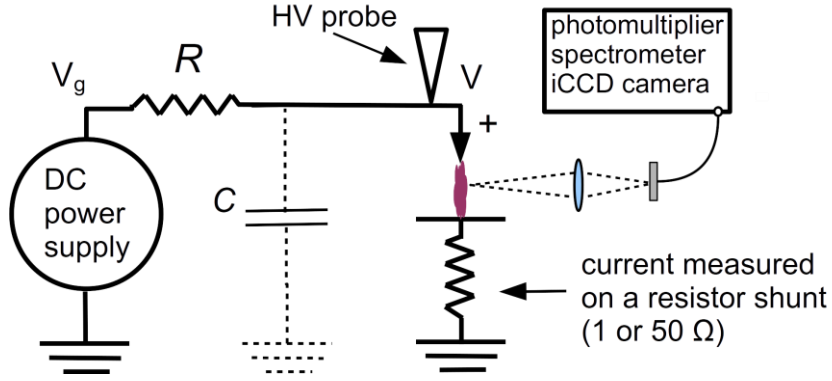


Fig. 1. Schematic of the set-up used for generation and diagnostics of the TS.

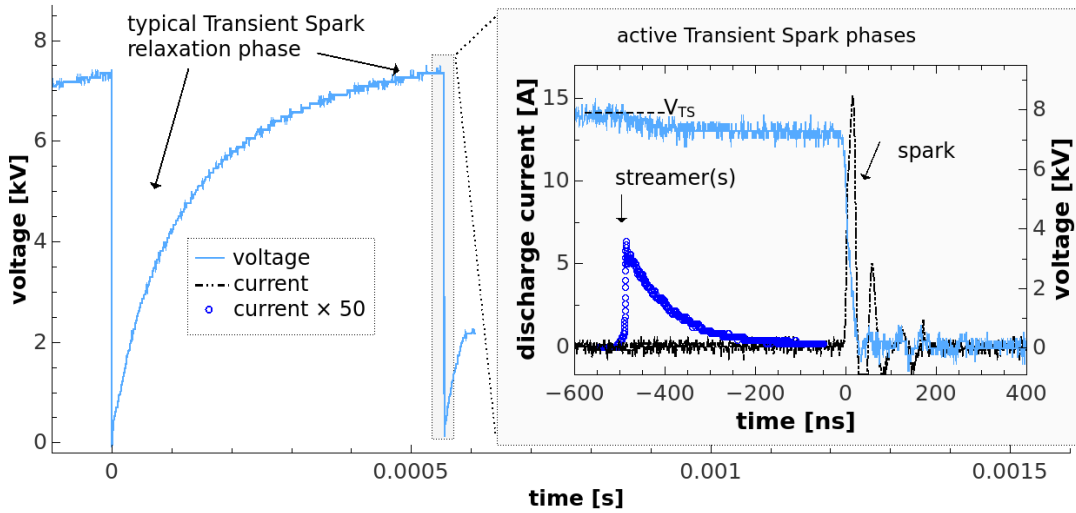


Fig. 2. Typical voltage and current waveforms of the TS.

During the spark phase, the electric circuit internal capacitance discharges completely, the voltage on the HV electrode drops to almost zero, and the discharge current reaches a high value ($\sim 1-10$ A) for a short time. The electron density n_e during the TS spark phase can exceed 10^{17} cm^{-3} [2]. The gas temperature in the plasma channel shortly after the spark increases to at least 1500-3500 K [6]. However, complete thermalization of plasma is most probably not possible due to small amount of energy stored in C that is delivered to the gap during the spark phase.

The large ballast resistor R limits the dc current delivered to the plasma after the spark current pulse when C is discharged. As a result, the plasma starts to decay after the spark pulse. Eventually, the plasma resistance exceeds R and the potential V on the stressed electrode gradually increases (long time scale voltage waveform in Fig. 2), as the capacitance C recharges during the TS relaxation phase. A new TS pulse, initiated by a new streamer, occurs when V reaches again the characteristic voltage V_{TS} . The TS is thus based on repetitive charging and discharging of C . The repetition frequency f of this process can be controlled by generator voltage V_g approximately in the range 1-10 kHz [1].

3. Model Description

The aim of the chemical kinetic model is to calculate density evolution of studied species interacting via defined set of chemical reactions. For this purpose we used ZDPlasKin software code [16]. Authors of ZDPlasKin also provide a ready-to-use list of chemical processes in N₂-O₂ plasmas with all necessary rate coefficients. We used this set of reactions (version 1.03) in our simulations too. This set includes ~650 chemical reactions for 53 species, namely, molecules N₂ (X¹, v = 0-8), N₂ (A³, B³, a¹, C³), O₂ (X³, v = 0-4), O₂ (a¹, b¹, 4.5 eV), O₃, NO, N₂O, NO₂, NO₃ and N₂O₅, atoms N (⁴S, ²D, ²P) and O (³P, ¹D, ¹S), positive ions N⁺, N₂⁺, N₃⁺, N₄⁺, O⁺, O₂⁺, O₄⁺, NO⁺, N₂O⁺, NO₂⁺ and O₂⁺N₂, negative ions O⁻, O₂⁻, O₃⁻, O₄⁻, NO⁻, N₂O⁻, NO₂⁻ and NO₃⁻, and electrons. The electron impact excitation of other electronic states of nitrogen is also included, but the model assumes their instantaneous relaxation: N₂(W³, B³) → N₂(B³); N₂(a¹, w¹) → N₂(a¹), and N₂(E³, a¹) → N₂(C³). The generalized level O₂(4.5 eV) corresponds to O₂(A³, C³) and O₂(c¹) states.

The rate constants of reactions between heavy species are specified in the input file. The rate constants for electron impact reactions are calculated from electron energy distribution function (EEDF). The ZDPlasKin module enables to use either Maxwellian distribution functions defined by the electron temperature T_e , or the EEDF obtained by solving the Boltzmann equation for free electrons. The ZDPlasKin package includes a Bolsig+ solver [17] for this purpose. A set of required electron scattering cross sections was taken from the LXCat project database [18].

Finally, ZDPlasKin module requires to use additional subroutines for more comprehensive control of simulation conditions, e.g. changes in the gas temperature and reduced electric field. Our major goal was to create a module compatible with ZDPlasKin with subroutines that would take into account fast changes in the reduced electric field strength E/N , gas temperature T_g , electron temperature T_e and total density of neutrals N characteristic for a TS discharge. The time evolution of E/N , T_g , T_e and N simulating the TS were constructed based on our experimental results and the literature, as it is explained in the next sections.

3.1. Streamer phase

The streamer phase is relatively short (<200 ns) initial phase of the TS discharge consisting of the primary and the secondary streamer. The streamer phase of the TS is mainly characterized by fast changes of E/N . It is therefore necessary to determine the density of many species that could influence the plasma induced chemistry with good temporal resolution (~ns), while processes such as diffusion can be neglected on this short time scale.

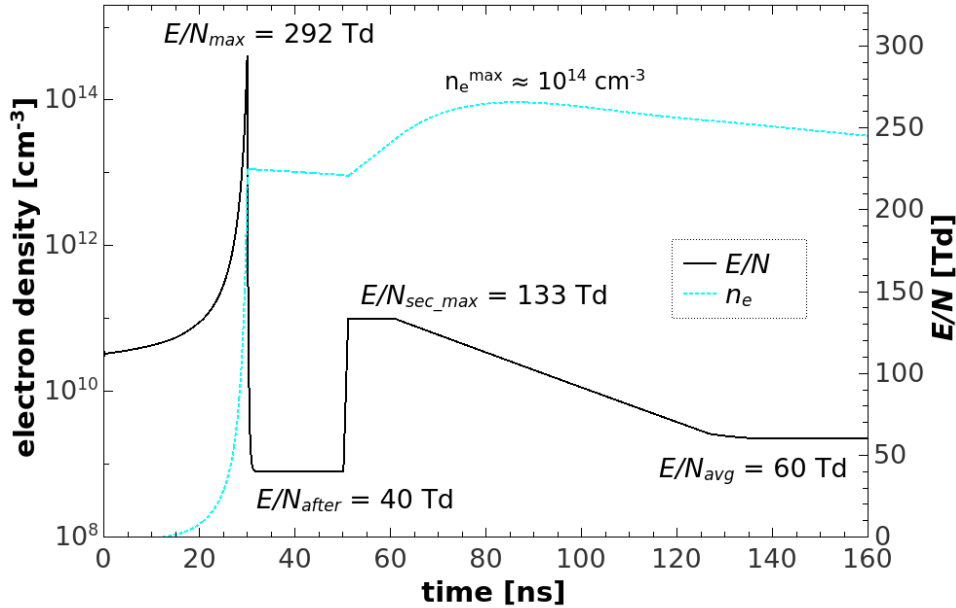


Fig. 3. The modeled reduced electric field strength profiles and calculated electron density during the primary and the secondary streamer phase of the TS discharge.

The influence of the primary and the secondary streamer on the rates of chemical reactions in our 0-D kinetic model can be introduced by using appropriate temporal evolution of E/N . The temporal evolution of E/N used in our model (Fig. 3) is based on published primary and secondary streamer characteristics and our experimental results (see [11] and references therein). The aim was to achieve the peak electron density during the TS streamer phase close to the experimentally observed $n_e \approx 10^{14} \text{ cm}^{-3}$ [2].

3.2 Streamer-to-spark transition phase

An average streamer-to-spark transition time τ depends strongly on TS repetition frequency f . At lower frequencies ($< 3 \text{ kHz}$), τ is very random and it can vary from a few hundred ns up to several μs [15]. With increasing frequency, τ drops below $\sim 100 \text{ ns}$ and at $\sim 10 \text{ kHz}$, we even observed an almost instantaneous formation of a spark after the streamer [13]. Here we study "low" frequency TS ($\sim 1 \text{ kHz}$), where the streamer and spark current pulses are well separated, and the current before the spark falls down to a few mA [15].

Decrease of the current and n_e (Fig. 3) results from relatively low $E/N_{\text{avg}} = 60 \text{ Td}$ in the plasma channel established after the disappearance of the secondary streamer. Transition to the spark requires the increase of E/N to accelerate the ionization processes. In TS, it can be achieved only by the significant decrease in N . We thus assume that the breakdown and spark formation in TS at low frequencies proceeds via mechanism postulated by Marode et al. [19]. It can be summarized as follows: heating of the channel \rightarrow increase in the pressure \rightarrow hydrodynamic expansion \rightarrow decrease in N in the core of the channel \rightarrow increase in E/N \rightarrow acceleration of ionization processes \rightarrow gas breakdown.

We are not able to calculate the time evolution of gas density $N(t)$ with our 0-D kinetic model. For this reason, we tested the N profile (Fig. 4) from the simulations of Naidis [20]. Besides the hydrodynamic expansion, it also handles the radial diffusion of particles from the discharge channel. We suppose that this profile is the closest match to the TS discharge we found in the literature.

The changes of N according to the profile taken from Naidis starts in the calculation time 650 ns, so that the fastest rate of N decrease is reached in the moment when $T_g = 1000 \text{ K}$ (Fig. 4, calculation time 800 ns). We extrapolated this profile and the N starts to decrease from initial N_o ($\approx 2.09 \times 10^{19} \text{ cm}^{-3}$ for initial gas temperature $T_g^{\text{ini}} = 350 \text{ K}$ at atmospheric pressure) already after the primary streamer (from the calculation time 40 ns). The rate of the extrapolated gas density decrease is proportional to the difference between the T_g and T_g^{ini} . The T_g increases linearly during the calculation time 40 ns to 800 ns from T_g^{ini} to 1000 K. The temperature remains constant for very short time till the end of the streamer-to-spark transition phase.

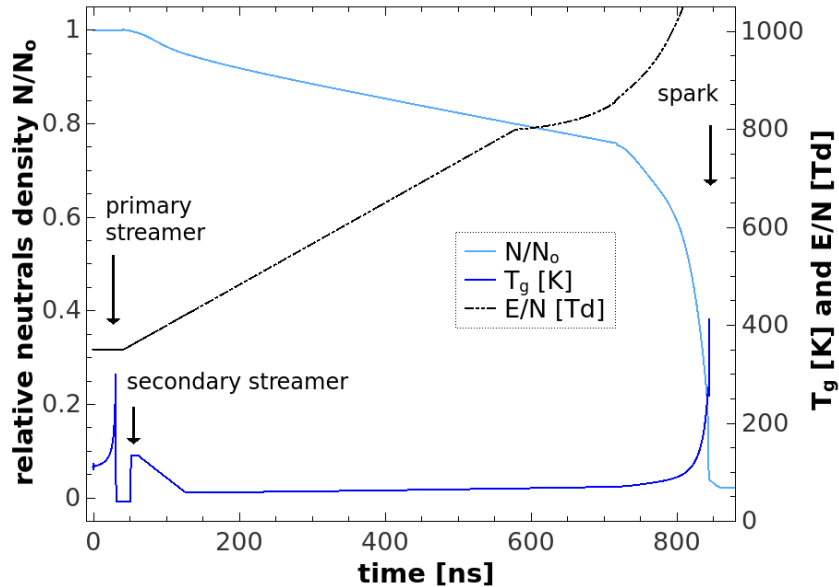


Fig. 4. The evolution of reduced electric field strength E/N , gas temperature T_g and relative density of heavy particles N/N_o during the streamer-to-spark transition phase used in model.

The streamer-to-spark transition phase in our model stops when the ionization degree ζ reaches 2×10^{-2} . We use this limit because the Bolsig+ solver can reliably calculate EEDFs and rate of electron-molecule impact processes only for $\xi < 2 \times 10^{-2}$. We calculate ζ as

$$\zeta = \frac{n_e}{n_e + N + N_{ion}}, \quad (2)$$

where N_{ion} is the density of ions.

For calculation of E/N required by Bolsig+ solver, we must also calculate the evolution of the electric field E inside the plasma channel. First, our model calculates the time evolution of potential $V(t)$ between the electrodes. We actually simulate the discharging of C via the plasma resistance R_p . The advantage of this approach is that besides n_e , we calculate another variable that can be compared with experimental data: $V(t)$.

The decrease in potential ΔV^i for the i -th calculation step can be expressed as

$$\Delta V^i = -V^{i-1} \times \frac{\Delta t}{C R_p^{i-1}}. \quad (3)$$

The R_p is related to the plasma conductivity σ_p by

$$R_p = \frac{4d}{\sigma_p \pi D_p^2}, \quad (4)$$

where d and D_p are the plasma channel length and the diameter, respectively. For approximation of D_p we used the experimentally obtained value defined as the full-width at half-maximum of the spectrally unresolved radial intensity profile of the plasma channel after the Abel inversion [2]. At low TS repetition frequencies (below 4 kHz), we observed shrinking of the discharge channel diameter during the streamer-to-spark transition from $D_p^{\text{streamer}} \approx 150 \pm 40 \mu\text{m}$ in the streamer phase, down to $D_p^{\text{spark}} \approx 50 \pm 20 \mu\text{m}$ in the spark phase.

The plasma conductivity σ_p is calculated by the model from n_e

$$\sigma_p = \frac{e^2 n_e}{m_e v_m}. \quad (5)$$

Here e and m_e are the electron charge and mass, respectively, and v_m is the effective collision frequency of electrons with heavy particles, provided by Bolsig+ solver. Finally, $E/N(t)$ is derived from $V(t)$ and $N(t)$ assuming homogeneous axial potential distribution.

3.3 Spark phase

The spark phase in our model starts when the ionization degree ξ reaches 2×10^{-2} and it continues to increase further. Unlike in the previous phases, plasma is thus highly ionized. The duration of the spark phase in our model can be defined in the configuration files. We used 400 ns duration, as we found it is long enough for plasma to become weakly ionized again. On the other side, we assume that it is short enough to neglect processes such as diffusion or mixing with the surrounding air during this phase.

Thanks to the high degree of ionization we can use Maxwellian EEDFs during the spark phase. The usage of Bolsig+ solver is not preferable because of the high degree of ionization, but also because of high degree of atomization during this phase. The available sets of electron scattering cross sections for O and N atoms are simply not adequate to calculate EEDFs accurately. Using Maxwellian EEDFs, the knowledge of the E/N evolution is not important anymore and thus also the evolution of N is not crucial unlike in the previous phase when we rely on N evolution taken from external source [20]. Fur-

ther evolution of N during the spark phase is handled by our model itself, i. e. the density of neutrals changes only via chemical processes.

The crucial parameter during the spark phase is the electron temperature that defines the Maxwellian EEDF. We calculate T_e from the mean electron energy ε . The evolution of ε is calculated numerically starting from the last value calculated by Bolsig+ solver at the end of the streamer-to-spark transition phase using electron energy balance equation [21]

$$\frac{d\varepsilon}{dt} = \frac{e^2 E^2}{m_e v_m} - \delta(\varepsilon - \varepsilon_g) v_m \quad (6)$$

The first term on the right side represents the energy gained from the electric field; the second term represents the energy losses due to collisions with heavy particles having mean energy ε_g . The collision frequency v_m includes collisions of electrons with both neutrals and ions, and the coefficient δ determines relative amount of energy lost per single collision.

If we take into account only elastic collisions, then $\delta = \delta_e = 2m_e/M_{avg}$, where M_{avg} is a weighted average mass of heavy particles. Since $m_e \ll M_{avg}$, the typical value of δ_e is only $\sim 5 \times 10^{-5}$. This explains why elastic collisions do not efficiently transfer energy from electrons to heavy particles in weakly ionized plasma. Our model takes into account inelastic collisions of electrons when calculating δ , therefore this parameter is much higher before the spark phase ($\sim 10^{-2}$). The δ decreases in strongly ionized plasma with high frequency of elastic electron-ion collisions, which are characterized by large coulomb cross sections. In our simulations we can see this situation in Figure 5 in calculation time 850-900 ns. Here δ drops down to $\sim 10^{-4}$ and there is a peak of v_m due to increasing amount of electron-ion collisions.

Later (calculation time >1000 ns), δ slightly increases but it remains relatively low despite decreasing degree of ionization. This is due to gas composition changes. Molecules with many vibrational levels consuming lot of energy decompose to O and N atoms. In highly atomized gas, the vibrational excitation processes are negligible and δ can be increased only by electronic excitations and ionizations of atoms. Unfortunately, we lack electron scattering cross sections for most excitation levels of O and N atoms. Therefore, the parameter δ is probably underestimated in our model when gas is highly atomized. However, it is probably not crucial for calculation of δ , because the mean energy of electrons is relatively low in this phase (~ 1 eV), and the excitation probability of higher energy levels is thus low.

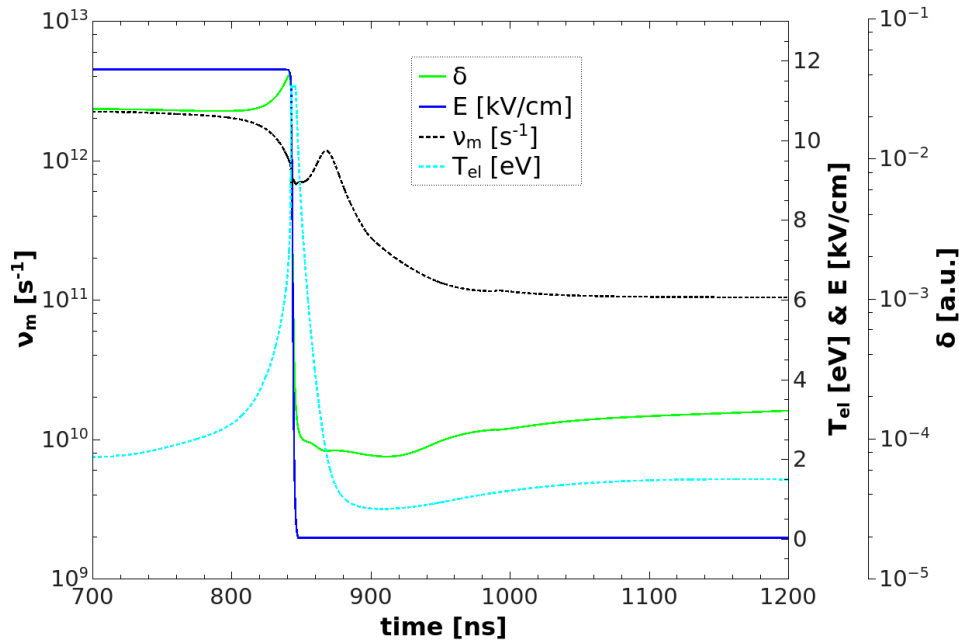


Fig. 5. The evolution of electric field E , electron temperature T_e , electron collision frequency and relative energy loss per collision δ during the spark phase used in the model.

The electric field evolution $E(t)$ during the spark phase is derived from calculated $V(t)$ similarly as it is done with $E/N(t)$ during the streamer-to-spark transition phase (see section 3.2, eq. 3-5). The main difference is that $V(t)$ changes slowly during the streamer-to-spark transition phase, while it drops quickly to almost zero during the spark phase. Since spark can be considered as an arc discharge with short duration, we decided to stop the voltage drop in our model in the moment when V reaches minimal voltage $V_{min} = 40$ V, characteristic for an arc discharge [21]. We further subtract 25 V from V_{min} when calculating E , taking into account typical cathode and anode fall voltages.

The fast drop of E when plasma becomes strongly ionized is accompanied by almost equally fast decrease of δ (Fig. 5). The electron temperature T_e decreases to ~ 1 eV within ~ 40 ns. The fast decrease of T_e means a fast transfer of energy to heavy particles, i.e. gas heating. In our model, the gas temperature during this short period (initial 40 ns of the spark phase) increases exponentially from 1000 K to 3000 K. Later, when T_e drops to ~ 1 eV and δ is low, the energy transfer from electrons to heavy particles should be also much slower. For this reason we also slowed down further increase of T_g , from exponential growth to logarithmic-like growth from 3000 K up to 3500 K at the end of the spark phase. The $T_g = 3500 \pm 500$ K was the highest temperature observed experimentally in TS.

4. RONS Generation

The presented model reasonably calculates voltage drop during the spark phase. More important is that a good agreement was achieved (Fig. 6) when comparing the calculated electron densities with experimental data [1, 2]. We thus assume that this model can be used to determine reliably the density evolution of various species, which we are not able to measure using available experimental techniques. Next, we focus on temporal evolution of the selected RONS, namely NO, NO₂, N, O, and O₃.

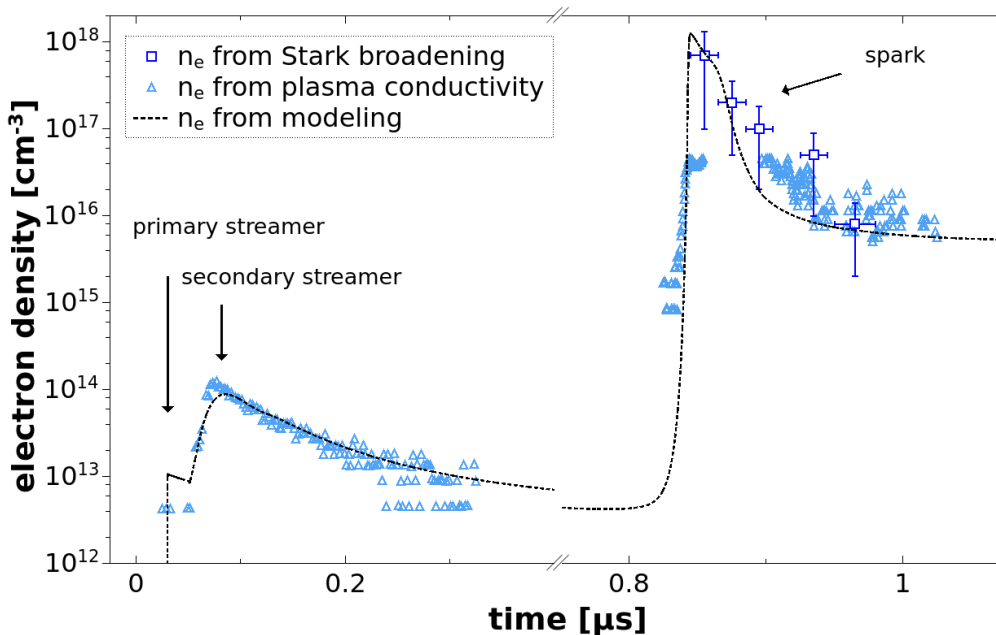


Fig. 6. Comparison of the measured and calculated electron density.

4.1. Evolution of RONS before the spark phase

Each TS spark pulse is initiated by the primary streamer propagating from the HV electrode towards the grounded electrode with strong electric field in its head. With $E/N \approx 300$ Td, electrons gain high energy and are able to initiate various chemical processes. During the secondary streamer phase, the field is lower, but the duration of the secondary streamer is longer and therefore higher electron density is achieved (Fig. 6). For this reason, the secondary streamer strongly influences the density of produced reactive species (Fig. 7). Later, during the streamer-to-spark transition phase, the changes of selected RONS densities are relatively slow.

The density of NO is higher than the density of O₃ before the spark phase, and the NO₂ density is even lower than O₃. However the density of atomic O is the highest among the reactive species and this indicates that NO must be converted to NO₂ in later phases. We really observed this process when we simulated a hypothetical situation with primary and secondary streamer phases but no spark phase [11]. More importantly we observed that the final dominant product was ozone, since the atomic O density after the streamer phase highly exceeded the density of atomic N. Thus, only the following spark and relaxation phases can explain why the TS generates preferentially NO_x and not O₃ [6].

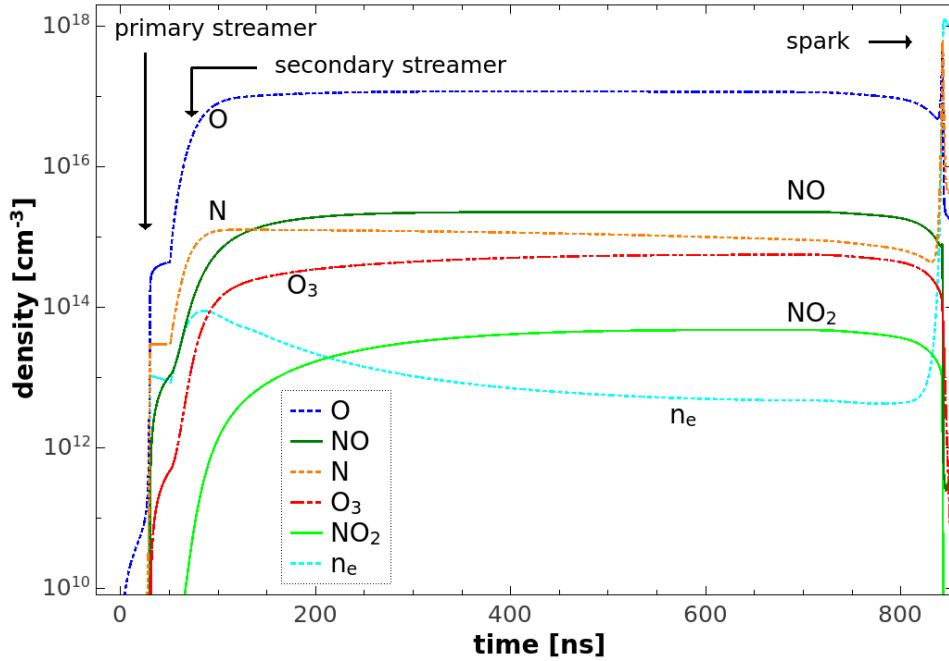


Fig. 7. Calculated densities of electrons and selected RONS before transition to spark.

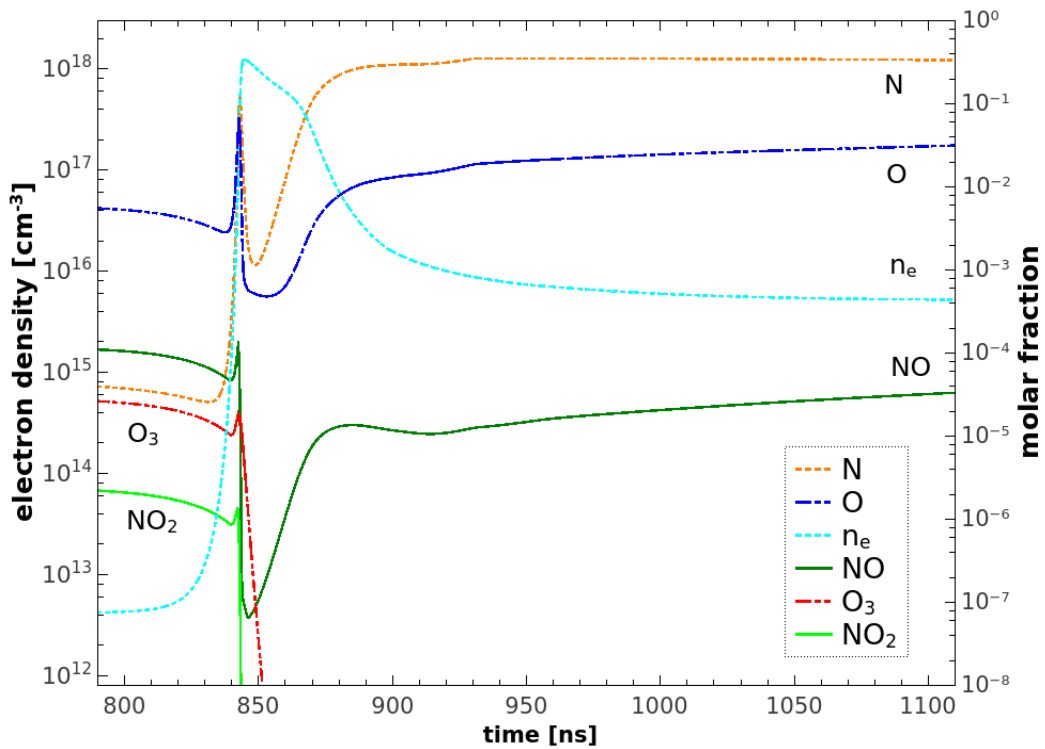


Fig. 8. Calculated electron density and molar fraction of selected RONS during the spark phase.

4.2. Evolution of RONS during the spark phase

The spark pulse in our model is induced by the gas density decrease causing the increase of E/N and T_e . The densities of all neutrals thus change due to two different processes, chemical reactions and hydrodynamic expansion simulated by the decrease of N . In order to show only the changes due to chemical processes, we present here evolution of molar fractions of studied RONS during the spark phase (Fig. 8).

The spark phase is characterized by a strong increase of ionization degree, gas temperature and decomposition of molecules. The dissociation degree of three-atomic molecules (NO_2 , O_3) is approximately by two orders of magnitude higher than the dissociation of two-atomic molecules such as NO . However, even the molar fraction of NO decreases by three orders of magnitude during the initial part of the spark phase. Thus, we can say that NO , NO_2 and O_3 densities achieved during the previous streamer phase have almost no influence on the final densities of these species. Their final densities will be established later during the relaxation phase, which is not included in the model yet. During the spark phase, we mostly see generation of their precursors: N and O atoms. Unlike in the previous phases, the amount of N exceeds the amount of O atoms during the spark phase (Fig. 8). This is the first indicator of the experimentally observed result that TS generates more NO_x than O_3 .

5. Conclusions

The transient spark (TS) discharge has been successfully used for various biomedical and environmental applications. The TS can be used as relatively cheap and simple NO_x generator, however its further optimization requires better understanding of basic chemical processes that take place during different phases of the TS. Therefore, we studied TS discharge using chemical kinetic modeling. The 0-D model based on ZDPlasKin module was successfully used to model plasma induced chemistry during the transient events propagating in space, such as primary and secondary streamers. The ZDPlasKin was also used to model plasma chemistry during the spark phase characterized by highly ionized non-thermal plasma. The electron density calculated in our model agrees well with experimental observations.

We further focused on the production of selected RONS playing important roles in biomedical applications of electrical discharges in air: O , N , NO , NO_2 and O_3 . We found out that the secondary streamer strongly influences the densities of these reactive species. The density of NO is higher than the density of O_3 shortly after the secondary streamer. However, the density of atomic O after the secondary streamer is even higher than NO and O_3 densities, and it strongly exceeds the density of atomic N . When we simulated a hypothetical situation with primary and secondary streamer phases but no spark phase, the final dominant product was O_3 . In transient spark, however, the experimental data shows that NO_x are dominant products and there is no O_3 . We assume that this results from the enhancement of atomic N generation and gas heating during the spark phase. Our model shows that the amount of N exceeds the amount of O atoms during the spark phase. Due to the strong degree of atomization during the spark phase, the densities achieved during the streamer phase has almost no influence on the final densities of NO , NO_2 and O_3 .

Our results indicate that the production of stable products NO , NO_2 and O_3 determining their final densities must occur later, during the TS relaxation phase. We are planning further development of our kinetic model to be able to reliably simulate the relaxation phase of the TS discharge to prove this hypothesis and find better correlation with experiments.

Acknowledgement: This work was supported by Slovak Research and Development Agency APVV-17-0382, and Slovak Grant Agency VEGA 1/0419/18.

6. References

- [1] Janda M et al. 2011 *Plasma Sources Sci. Technol.* **20** 035015.
- [2] Janda M et al. 2014 *Plasma Sources Sci. Technol.* **23** 065016.
- [3] Hontanon E et al. 2013 *J. Nanopart. Res.* **15** 1957.
- [4] Hensel K et al. 2015 *Biointerphases* **10** 029515.
- [5] Graves D B 2012 *J. Phys. D: Appl. Phys.* **45** 263001.
- [6] Janda M et al. 2016 *Plasma Chem. Plasma Process.* **36** 767.

- [7] Gaens W Van and Bogaerts A 2014 *Plasma Sources Sci. Technol.* **23** 035015.
- [8] Jenista J 1999 *J. Phys. D: Appl. Phys.* **32** 2763.
- [9] Barni R et al. 2005 *J. Appl. Phys.* **97** 073301.
- [10] Flitti A and Pancheshnyi S 2009 *Eur. Phys. J.: Appl. Phys.* **45** 21001.
- [11] Janda M, Hensel K and Machala Z 2018 *J. Phys. D: Appl. Phys.* **51** 334002.
- [12] Gerling T et al. 2013 *Plasma Sources Sci. Technol.* **22** 065012.
- [13] Janda M et al. 2017 *Plasma Sources Sci. Technol.* **26** 055010.
- [14] Janda M et al. 2017 *J. Phys. D: Appl. Phys.* **50** 425207.
- [15] Janda M et al. 2012 *Plasma Sources Sci. Technol.* **21** 045006.
- [16] Pancheshnyi S et al. 2008 Computer Code ZDPlasKin, Univ. Toulouse, Toulouse, LAPLACE, CNRS-UPS-INP, France. [Online]. Available: <https://www.zdplaskin.laplace.univ-tlse.fr>
- [17] Hagelaar G J M and Pitchford L C 2005 *Plasma Sources Sci. Technol.* **14** 722.
- [18] LXCAT database. [Online]. Available: www.lxcat.net
- [19] Marode E, Bastien F and Bakker M 1979 *J. Appl. Phys.* **50** 141.
- [20] Naidis G V 2009 *Eur. Phys. J. Appl. Phys.* **47** 22803.
- [21] Raizer Y P 1991 *Gas Discharge Physics*, Springer-Verlag Berlin Heidelberg.

ATMOSPHERIC PRESSURE PLASMAS IN CONTACT WITH TARGETS: ELECTRIC FIELDS AND ELECTRON PROPERTIES

Ana Sobota

¹Eindhoven University of Technology, Netherlands

There is ample published work on non-thermal atmospheric pressure plasmas, because of their diverseness in application as well as the low cost and the ease with which they can be generated and applied. The applications are variations on surface treatment or modification of substrates that are either sensitive to low pressures, high temperatures or high currents, or the less sensitive substrates with options of treatment in the open atmosphere. It is the rich chemistry and the electrical properties of these plasmas that are responsible for their effectiveness. It is, however, important to note that the plasma and the substrate should be researched together, or while in interaction, as the non-thermal atmospheric pressure plasmas are sensitive to the vicinity of the substrates. This work brings absolute values for some of the fundamental properties of a non-thermal atmospheric pressure plasma, such as the electric field, electron density and temperature, in the presence of different types of targets. The plasma source in question was a kHz He plasma jet. High- and low-permittivity targets were researched and have been shown to have an influence not only on the absolute values of electric fields and electron properties, but also on the temporal development of the plasma. In the case of the metallic target the plasma-surface interaction was significantly prolonged when compared to the low-permittivity and liquid target.

TAILORING REACTIVE SPECIES PRODUCTION IN COLD ATMOSPHERIC PRESSURE PLASMAS FOR ENVIRONMENTAL AND HEALTHCARE TECHNOLOGIES

Timo Gans¹

¹*York Plasma Institute, Department of Physics, University of York, YO10 5DD York, UK*
E-mail: timo.gans@york.ac.uk

Abstract

Atmospheric pressure plasmas are versatile and efficient sources for reactive species production at ambient room temperature. This enables the development of new plasma technologies for various environmental and healthcare applications. The non-equilibrium chemical kinetics is initiated and determined by the electron dynamics. Due to the strongly collisional environment and associated short electron energy relaxation times the electron dynamics can be tailored using multi-frequency power coupling techniques, enabling separate control of key parameters like electron density and electron mean energy. Reactive atomic species play key roles in the chemical kinetics and details strongly depend on the feed-gas composition. Measurements and predictive simulations of key reactive species are equally challenging due to the strongly collisional environment and their multi-scale nature in space and time. The most promising approach is the exploitation of complementary advantages in direct measurements combined with specifically designed numerical simulations. Picosecond two-photon absorption laser induced fluorescence (TALIF) spectroscopy allows us to measure absolute densities of atomic oxygen (O), nitrogen (N) and hydrogen (H), even in chemical environments with complex reaction kinetics and associated collisional quenching processes, through directly resolving the effective lifetime with sub-nanosecond resolution. This is particularly important in realistic situations for technological applications with plasma operation and species penetration into ambient air. The picosecond TALIF measurements are compared with direct VUV synchrotron absorption spectroscopy under well-defined gas compositions showing very good agreement. Further insight into the chemical kinetics is obtained through additional UV & IR absorption spectroscopy (OH, O₃, CO₂, CO) measurements and synergistic combination with multi-scale numerical simulations of the chemical kinetics. The presentation will focus on examples of He-O₂-N₂-H₂O mixtures for bio-medical applications and He/Ar-CO₂ mixtures for CO₂ conversion into value-added chemicals.

Acknowledgement

This work was supported by the EPSRC through grant EP/K018388/1

Related Publications

[1] C. O'Neill, J. Waskoenig, T. Gans, *Tailoring electron energy distribution functions through energy confinement in dual radio-frequency driven atmospheric pressure plasmas*, Applied Physics Letters, 2012, **101** (15), 154107.

[2] A. Greb, K. Niemi, D. O'Connell, T. Gans, *Energy resolved actinometry for simultaneous measurement of atomic oxygen densities and local mean electron energies in radio-frequency driven plasmas*, Applied Physics Letters, 2014, **105**, 234105.

[3] T. Murakami, K. Niemi, T. Gans, D. O'Connell, W. G. Graham, *Afterglow chemistry of atmospheric-pressure helium-oxygen plasmas with humid air impurity*, Plasma Sources Sci. Technol., 2014, **23**, 025005.

- [4] J. Golda, J. Held, B. Redeker, M. Konkowski, P. Beijer, A. Sobota, G. Kroesen, N. St. J. Braithwaite, S. Reuter, M. M. Turner, T. Gans, D. O'Connell and V. Schulz-von der Gathen, *Concepts and characteristics of the 'COST Reference Microplasma Jet'*, J. Phys. D: Appl. Phys., 2016, **49**, 084003.
- [5] A. Wijaikhum, D. Schroeder, S. Schröter, A. R. Gibson, K. Niemi, J. Friderich, A. Greb, V. Schulz-von der Gathen, D. O'Connell and T. Gans, *Absolute ozone densities in a radio-frequency driven atmospheric pressure plasma using two-beam UV-LED absorption spectroscopy and numerical simulations*, Plasma Sources Sci. Technol., 2017, **26**, 115004.
- [6] J. Dedrick, S. Schröter, K. Niemi, A. Wijaikhum, E. Wagenaars, N. de Oliveira, L. Nahon, J. P. Booth, D. O'Connell and T. Gans, *Controlled production of atomic oxygen and nitrogen in a pulsed radio-frequency atmospheric-pressure plasma*, J. Phys. D: Appl. Phys., 2017, **50**, 455204.
- [7] S. Schröter, A. Wijaikhum, A. R. Gibson, A. West, H. Davies, N. Minesi, J. Dedrick, E. Wagenaars, N. de Oliveira, L. Nahon, M. J. Kushner, J. P. Booth, K. Niemi, T. Gans, D. O'Connell, *Chemical kinetics in an atmospheric pressure helium plasma containing humidity*, Phys. Chem. Chem. Phys., 2018, **20**, 24263
- [8] L. Bischoff, G. Hübner, I. Korolov, Z. Donkó, P. Hartmann, T. Gans, J. Held, V. Schulz-von der Gathen, Y. Liu, T. Mussenbrock, J. Schulze, *Experimental and computational investigations of electron dynamics in micro atmospheric pressure radio-frequency plasma jets operated in H₂/N₂ mixtures*, Plasma Sources Sci. Technol., 2018, **27**, 125009
- [9] Z. Donkó, S. Hamaguchi, T. Gans, *The effect of photoemission on nanosecond helium microdischarges at atmospheric pressure*, Plasma Sources Sci. Technol., 2018, **27**, 054001
- [10] A.R. Gibson, Z. Donkó, L. Alelyani, L. Bischoff, G. Hübner, J. Bredin, S. Doyle, I. Korolov, K. Niemi, T. Mussenbrock, P. Hartmann, J.P. Dedrick, J. Schulze, T. Gans, D. O'Connell, *Disrupting the spatio-temporal symmetry of the electron dynamics in atmospheric pressure plasmas by voltage waveform tailoring*, Plasma Sources Sci. Technol., 2019, **28**, 01LT01

PHYSICS OF TRANSIENT PLASMAS

Sander Nijdam¹

¹*Eindhoven University of Technology, Netherlands*

E-mail: s.nijdam@tue.nl

Positive streamers require two ingredients to propagate: a sufficiently high external electric field and a constant supply of (free) electrons in front of the developing streamer head. In air, the electrons are usually provided by photo-ionization, producing free electrons in all directions around the streamer head. However, in cases with reduced photo-ionization, for example in pure gasses, the local external field direction does not necessarily coincide with the direction of sufficient electron density.

One way to create such a condition is by using a laser beam to ionize a path. Depending on parameters this can lead to a guided streamer moving almost perpendicular to the field direction.

Alternatively, a preceding discharge can have left a specific electron distribution and thereby guide the path of following discharges. This effect is very important for pulsed plasma jets or plasma bullets in pure nitrogen. We have studied this by looking at the development of the discharge during the first few pulses after ignition. Also, we have investigated what happens when an electric field is applied in the period between subsequent high voltage pulses. If the memory effect is indeed due to leftover electrons, they could be moved by an electric field and thereby the next discharge should be affected. However, this experiment has resulted in some unexpected results which I will present.

An important aspect of transient plasmas is the distribution in time and space of the electric field. We have measured this for plasma bullets using the four-wave mixing diagnostic.

Finally, a dielectric surface close to the streamer path can have a large influence on both the electric field distribution, as well as the electron density distribution and thereby can lead to specific paths that the streamer follows or avoids.

MASS SPECTROMETRY FOR REAL TIME MEASUREMENT OF TRACE CONCENTRATIONS OF VOLATILE COMPOUNDS IN AIR AND BREATH

Patrik Španěl¹

¹*J. Heyrovský Institute*

E-mail: spanel@jh-inst.cas.cz

The need for rapid and accurate measurement of trace concentrations of compounds present in air and human breath has led to construction of specialised mass spectrometers based on the Selected Ion Flow Tube Mass Spectrometry, SIFT-MS, its drift tube variant, SIFDT-MS and Proton Transfer Mass Spectrometry, PTR-MS. It is possible currently to analyse vapours of volatile organic compounds and other gases including ammoniac, hydrogen sulphide or hydrogen cyanide present in concentrations as low as a part per billion by volume (ppbv). Plasma physics is relevant in formation of the reagent ions in electrical discharges. Vacuum technology is important in these instruments to facilitate the function of the mass analyzers and to define the accurate reaction time for the ion-molecule reactions with analyte molecules in the sample that take place at buffer gas pressures of 1 – 2 mbar.

1. SIFT-MS

Selected-ion flow-tube mass spectrometry (SIFT-MS) is a quantitative mass spectrometry technique for trace gas analysis which involves the chemical ionization of trace volatile compounds by selected positive precursor ions during a well-defined time period along a flow tube.¹⁻³ Absolute concentrations of trace compounds present in air, breath or the headspace of bottled liquid samples can be calculated in real time from the ratio of the precursor and product ion signal ratios, without the need for sample preparation or calibration with standard mixtures. H_3O^+ , NO^+ and O_2^+ are most suitable reagent ions, because they do not react rapidly with the major components of air and breath viz. N_2 , O_2 , H_2O , CO_2 and Ar, but they do react rapidly with most BVOCs forming characteristic product ions that identify the various neutral molecules, M, in the air sample being analysed. However, when humid air or breath is analysed, cluster ions of the kind $\text{H}_3\text{O}^+(\text{H}_2\text{O})_{1,2,3}$, and $\text{NO}^+(\text{H}_2\text{O})_{1,2}$ can form from the simple precursor ions and these cluster ions can also act as precursor ions and lead to hydrated product ions of the kind $\text{MH}^+(\text{H}_2\text{O})_{1,2,3}$. Then it is important to recognise that all the precursor and characteristic product ion species must be included for the analysis of each M¹⁻³.

A simple example is the reaction of acetone with H_3O^+ reagent ions in SIFT-MS. It proceeds rapidly by the process of proton transfer producing protonated acetone:



When concentration of acetone, [M], is small, the fractional reduction in the large precursor ion count rate is immeasurably small, but the much smaller count rates of the product ions can still be determined accurately. It is easy to show that the number density of the product ions $[\text{MH}^+]$ are related to the number density of the precursor ions $[\text{H}_3\text{O}^+]$ as $[\text{MH}^+] = [\text{H}_3\text{O}^+]k[\text{M}]tD_e$. As before, k is the rate coefficient for the reaction of the H_3O^+ ions with the trace gas molecules present at a number density [M] and t is the reaction time. D_e is a differential diffusion enhancement coefficient that accounts for the fact that the precursor ions and the product ions diffuse at different rates to the walls of the flow tube and this influences their relative number densities at the downstream sampling orifice (see Fig. 1), and this differential diffusion must be accounted for to obtain an accurate quantification of M^{2, 4-6}. Also, mass discrimination against larger m/z ions in the analytical quadrupole mass spectrometer^{4, 6} and the formation of hydrated reagent and product ions (see section 3.1 and ^{2, 6}) must be accounted for. Thus, the concentrations of trace gases in multicomponent mixtures

in humid samples such as exhaled breath can readily be calculated from the observed count rates of each product ion species. Of great significance is that the analyses only involve the ratio of the characteristic product ion count rates to the reagent ion count rates and so any drift in the reagent ion count rate does not invalidate the analyses.

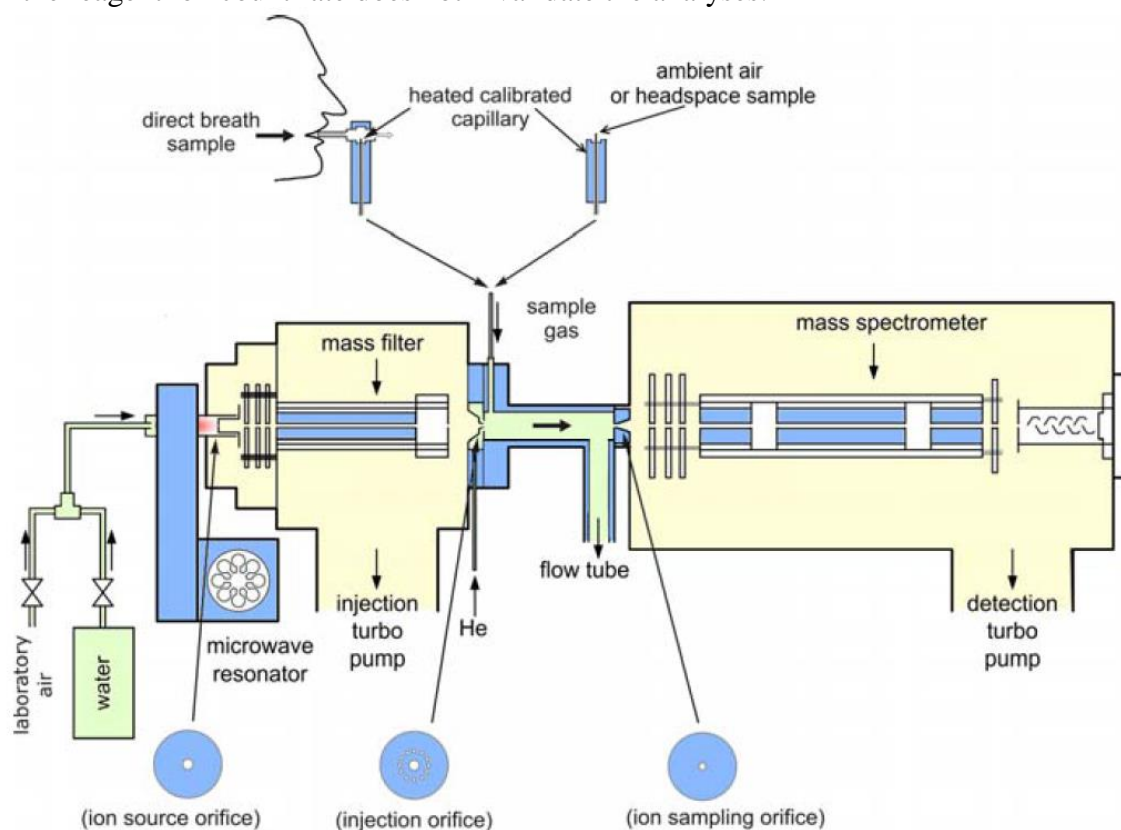


Fig. 1. Schematics of the Profile 3 SIFT-MS instrument.

The detection sensitivity of a SIFT-MS instrument depends on the count rates of the precursor ions that can be realised. For the current *Profile 3* instruments^{4,7} these are up to 3 million counts-per-second, c/s, and the sensitivity for most BVOCs is typically 10 c/s per ppbv corresponding to a practical detection limit of 1 ppbv per second of integration time. Detection limits in the sub-ppb range have been validated for aromatic hydrocarbons⁸ using longer integration times. The absolute accuracy of SIFT-MS has been validated to be better than 10%^{4,6,9} for several compounds without the need for external standards, as long as the sample and carrier gas flow rates and flow tube temperature are accurately known and mass discrimination and diffusion effects are properly accounted for. In PTR-MS instruments the precursor ion c/s are typically about 10 times higher than in SIFT-MS (principally because no upstream mass filter is used) and then the sensitivity can be commensurately greater.

SIFT-MS instruments can be operated in two modes: They are (i) the full scan (FS) mode in which a complete mass spectrum of both precursor and product ions is obtained by sweeping the analytical quadrupole mass spectrometer over a selected m/z range for a chosen time whilst a sample of air or breath is introduced into the carrier gas. The resulting mass spectrum (see the example in Figure 2, which is discussed later in Section 5.1.1) is interpreted by relating the product ions to the trace gases present in the sample using the acquired knowledge of the ion chemistry. The concentrations of the individual trace gases can be calculated using the in-built kinetics library, as described above. (ii) the multiple ion monitoring (MIM) mode in which the count rates of the reagent ions and their hydrates, such as $\text{H}_3\text{O}^+(\text{H}_2\text{O})_n$, and a number of characteristic product ions appropriate to the number of trace

compounds to be analysed are monitored as air or breath displaces the ambient air at the entrance to the sampling capillary (see Figure 1). This is achieved by rapidly switching the downstream mass spectrometer between the several m/z values of the reagent and product ions, dwelling on each m/z for a predetermined short time interval. This real-time monitoring is possible because of the fast time response of SIFT-MS, which is typically less than 20 ms. The humidity of the sampled air (for example, exhaled breath consists of 6% water vapour) is routinely obtained from the data and is an indicator of sample quality and control ¹⁰.

2. PTR-MS

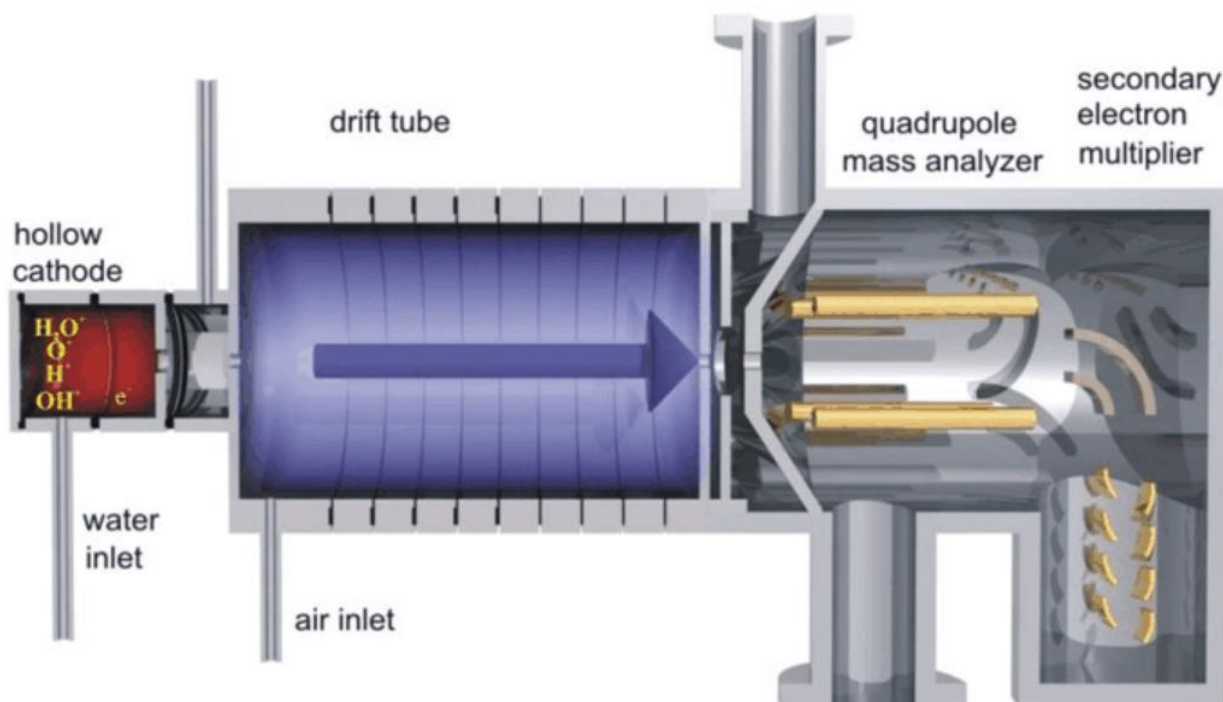


Fig. 2. Schematics of the Profile 3 SIFT-MS instrument.

The scheme of a typical device for mass spectrometry with proton transfer reactions, PTR-MS, is shown in Fig. 1. RPTR-MS is essentially a flow-drift tube CI analytical technique ¹¹⁻¹³. Ions are generated in a hollow cathode discharge and injected into a flow/drift tube buffered with the sample gas to be analysed, usually air. The ions experience an electric field coaxial with the flow tube and gain energy reaching a drift speed in the field direction and arrive at a downstream orifice where they are sampled into a differentially pumped mass spectrometer system and analysed in an analogous way to that in SIFT-MS. The precursor ions mostly used to date are H_3O^+ ions so, as explained previously; the primary reaction process utilized for analysis is proton transfer such as reaction (1). Because a mass filter is not used to select precursor ions, higher currents of precursor ions can be injected and the axial electric field results in less diffusive loss of the precursor ions to the walls of the flow-drift tube. Diffusive loss is also reduced by usage of air (the sample to be analysed) as the buffer/carrier gas rather than the lighter helium gas as used in SIFT-MS. and the pressure in the drift tube which are different for PTR-MS and SIFT-MS. The net result is that greater count rates of the precursor reagent H_3O^+ ions are available which leads to greater analytical sensitivity. Thus, detection limits can be in the parts-per-trillion by volume, pptv, to the sub-ppbv regime ^{11, 14, 15}. Since the reagent ion energies are elevated above thermal, the formation of cluster ions of the kind $H_3O^+(H_2O)_{1,2,3}$ are suppressed in comparison with SIFT-MS, although the actual count rates depend sensitively on the ratio of electric field strength to the buffer gas number density, E/N . A very good review of PTR-MS has been given recently ¹².

Kinetics of the ion-molecule reactions and the reaction time can be sensitive to E/N ; thus accurate quantification is not simply achieved. A canonical value ($2 \times 10^{-9} \text{ cm}^3\text{s}^{-1}$) for the reaction rate coefficients, k , is often used to estimate trace gas concentrations from PTR-MS data. Quantification is directly dependent on k , which can vary widely for ion-molecule reactions in the thermal energy regime (over the range $1\text{-}5 \times 10^{-9} \text{ cm}^3\text{s}^{-1}$), so a commensurate uncertainty can be introduced into PTR-MS quantification. However, such uncertainties can be minimised using calibration techniques. It is for these reasons that PTR-MS has been used only sporadically for breath analysis¹⁶ where greater accuracy is needed; rather, it has mostly been used for air analysis¹³ and environmental studies^{17,18}. A further problem is that following proton transfer from H_3O^+ , some MH^+ nascent product ions can undergo spontaneous unimolecular dissociation or collision induced dissociation, and this must be recognised to avoid false compound identifications, see for example^{19,20}. Unimolecular dissociation of MH^+ product ions can occur even under the thermal energy conditions of SIFT-MS²¹⁻²⁴, but collision induced dissociation is exacerbated in PTR-MS where the ion-molecule interaction energies are suprathreshold. Further, in conventional PTR-MS it is also impossible to separate isobaric compounds when only H_3O^+ reagent ions are used, because they simply result in MH^+ ions or fragments of these. This problem is alleviated in SIFT-MS that exploits NO^+ and O_2^+ precursor ions also (see Section 3 below). Other precursor ions can be used by changing the discharge gas composition in PTR-SRI-MS instruments¹⁴ and high resolution analytical time of flight, TOF, mass spectrometers that can separate nominally isobaric compounds²⁵⁻²⁷.

PTR-MS is a popular method for analysis of VOCs, especially in the terrestrial troposphere¹³ for which its greater sensitivity currently holds an advantage over SIFT-MS, but both these techniques have important contributions to make in ambient chemistry. The H_3O^+ ion chemistry involved is largely common to both techniques, but with obvious divergences that will be highlighted in the ion chemistry review that follows, has been largely researched using SIFT and SIFT-MS.

3. SIFDT-MS

A selected ion flow drift tube mass spectrometric analytical technique, SIFDT-MS,²⁸⁻³⁰ extends the selected ion flow tube mass spectrometry, SIFT-MS, by the inclusion of a static but variable E -field along the axis of the flow tube reactor in which the analytical ion-molecule chemistry occurs (see Fig. 3). The ion axial speed is increased in proportion to the reduced field strength E/N (N is the carrier gas number density) and the residence/reaction time, t , which is measured by Hadamard transform multiplexing, is correspondingly reduced. To ensure a proper understanding of the physics and ion chemistry underlying SIFDT-MS, ion diffusive loss to the walls of the flow-drift tube and the mobility of injected H_3O^+ ions have been studied as a function of E/N . It is seen that the derived diffusion coefficient and mobility of H_3O^+ ions are consistent with those previously reported. The rate coefficient has been determined at elevated E/N for the association reaction of the H_3O^+ reagent ions with H_2O molecules, which is the first step in the production of $\text{H}_3\text{O}^+(\text{H}_2\text{O})_{1,2,3}$ reagent hydrate ions. The production of hydrated analyte ion was also experimentally investigated.³⁰ The analytical performance of SIFDT-MS is demonstrated by the quantification of acetone and isoprene in exhaled breath. A major advance compared to SIFT-MS is that the speed of ions through the reaction zone can be achieved using the adjustable E -field, which allows the suppression of ion diffusion losses even at very low carrier gas flow speeds corresponding to helium carrier gas and sample gas flow rates more than 7 times lower than those used in *Profile 3* SIFT-MS instruments. Thus, a less powerful vacuum pump can be used to maintain the gas flow along the ion-chemical reactor and a smaller helium carrier gas pressure reservoir is needed, which facilitates production of smaller and more versatile transportable instruments. Furthermore, smaller sample flow rates can be used for analysis, which is a distinct advantage when, for example, liquid headspace is to be analysed. The simplicity of construction of the SIFDT-MS instrument is due to the use of a resistive glass flow-drift tube element and by adopting the Hadamard transform multiplexing for direct reaction time measurement, which is another improvement on SIFT-MS in which the reaction times are fixed and calculated indirectly from the gas pressure and flow rate. The presence of the E -field results in an increase of the kinetic and internal energies of the ions that influence hydrated ion formation and the initial studies confirmed that variation of E/N modifies the count rates of hydrated product ions relatively to the primary product ions. The use of low E/N values somewhat inhibits reagent and analyte ion hydration without significantly modifying the bimolecular ion chemistry, thus promising more accurate analyses.

However, it is worthy of note that increasing E/N to higher values (>20 Td) can promote controlled collisional dissociation of ions and this might ultimately allow isobaric ions to be distinguished, a technique well known in MS-MS methods.

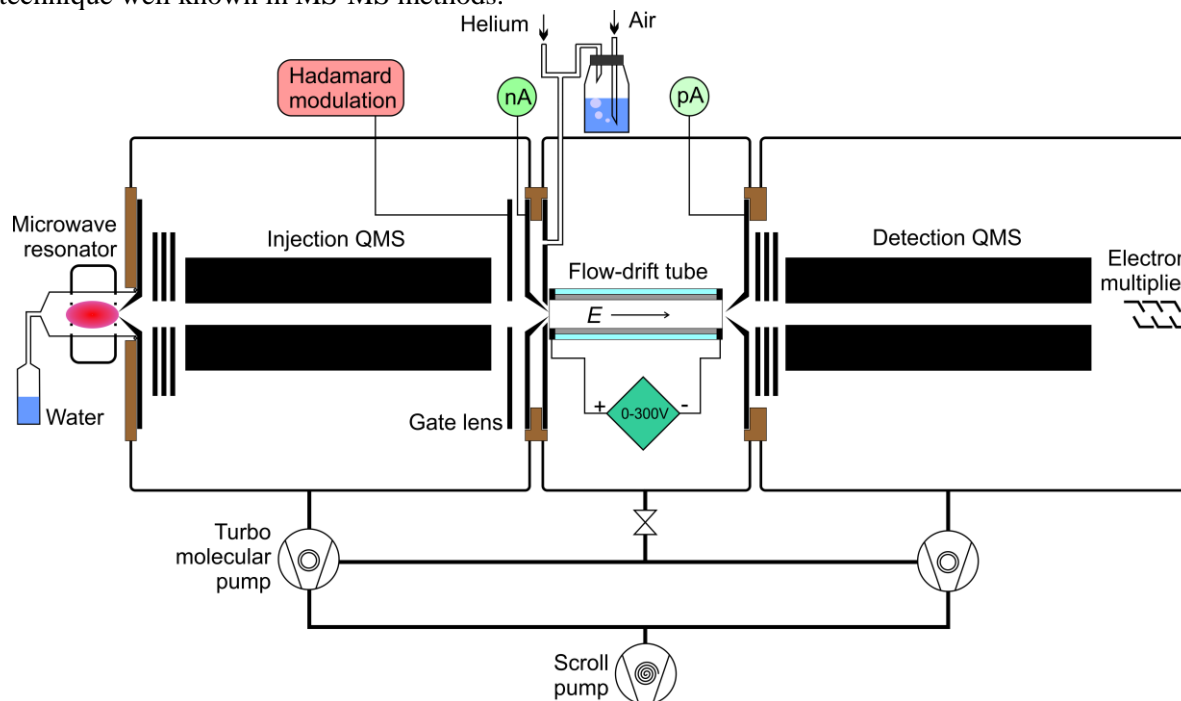


Fig. 3. Schematic drawing of the selected ion flow-drift tube, SIFDT, apparatus. Note that the speed of the helium carrier gas is reduced by a restrictive aperture between the flow-drift tube compartment and the scroll pump.

4. References

- [1] Španěl P, Smith D 1996 *Med Biol Eng Comput* **34** 409.
- [2] Španěl P, Dryahina K, Smith D 2006 *Int J Mass Spectrom* **249** 230.
- [3] Smith D, Španěl P 2005 *Mass Spectrom Rev* **24** 661.
- [4] Smith D, Pysanenko A, Španěl P 2009 *Int J Mass Spectrom* **281** 15.
- [5] Dryahina K, Španěl P 2005 *Int J Mass Spectrom* **244** 148.
- [6] Španěl P, Smith D 2001 *J Am Soc Mass Spectrom* **12** 863.
- [7] Španěl P, Smith D 2010 *Mass Spectrom Rev* In press doi: 10.1002/mas.20303.
- [8] Ross B 2008 *BMC Research Notes* **1** 41.
- [9] Španěl P, Cocker J, Rajan B, Smith D 1997 *Ann Occup Hyg* **41** 373.
- [10] Španěl P, Smith D 2001 *Rapid Commun Mass Spectrom* **15** 563.
- [11] Lindinger W, Hansel A, Jordan A 1998 *Int J Mass Spectrom Ion Process* **173** 191.
- [12] Blake R S, Monks P S, Ellis A M 2009 *Chem Rev* **109** 861.
- [13] de Gouw J, Warneke C 2007 *Mass Spectrom Rev* **26** 223.
- [14] Jordan A, Haidacher S, Hanel G, et al. 2009 *Int J Mass Spectrom* **286** 32.
- [15] Lindinger W, Jordan A 1998 *Chemical Society Reviews* **27** 347.
- [16] Karl T, Prazeller P, Mayr D, et al. 2001 *J Appl Physiol* **91** 762.
- [17] De Gouw J, Goldan P, Warneke C, et al. 2003 *J Geophys Res-Atmos* **108** 4682.
- [18] Hewitt C, Hayward S, Tani A 2003 *Journal of Environmental Monitoring* **5** 1.
- [19] Taipale R, Ruuskanen T, Rinne J, et al. 2008 *Atmos Chem Phys* **8** 6681.
- [20] Schripp T, Fauck C, Salthammer T 2010 *Int J Mass Spectrom* **289** 170.
- [21] Schoon N, Amelynck C, Debie E, Bultinck P, Arijs E 2007 *Int J Mass Spectrom* **263** 127.
- [22] Wang T S, Španěl P, Smith D 2004 *Int J Mass Spectrom* **239** 139.
- [23] Španěl P, Smith D 1997 *Int J Mass Spectrom* **167** 375.
- [24] Dhooche F, Amelynck C, Rimetz-Planchon J, Schoon N, Vanhaecke F 2009 *Int J Mass Spectrom* **285** 31.
- [25] Blake R S, Wyche K P, Ellis A M, Monks P S 2006 *Int J Mass Spectrom* **254** 85.

- [26] Wyche K, Blake R, Willis K, Monks P, Ellis A 2005 *Rapid Commun Mass Spectrom* **19** 3356.
- [27] Blake R, Whyte C, Hughes C, Ellis A, Monks P 2004 *Anal Chem* **76** 3841.
- [28] Spesyvyi A, Smith D, Spanel P 2017 *Phys Chem Chem Phys* **19** 31714.
- [29] Spesyvyi A, Sovova K, Spanel P 2016 *Rapid Commun Mass Spectrom* **30** 2009.
- [30] Spesyvyi A, Smith D, Spanel P 2015 *Anal Chem* **87** 12151.

DEVELOPMENT OF SEVERAL NON-RADIOACTIVE IONIZATION SOURCES FOR ION MOBILITY SPECTROMETRY

Mahmoud Tabrizchi

Isfahan University of Technology, Isfahan, Iran

Ion mobility spectrometry (IMS) is a fast analytical technique that works based on separation of analyte ions in atmospheric pressure. Hence, the major and essential step in application of IMS is the efficient ionization of samples in ambient pressure. The common ion source in traditional IMS based instruments are radioactive sources. However, significant attempts were made to develop different ionization sources appropriate for detection of special class of compounds in ambient condition. Corona discharge (CD) is heavily used as non-radioactive ion source for IMS. Here, the results of using CD in different gases with and without dopant in both positive and negative polarities will be discussed. In addition, time resolved corona discharge ionization spectra will be reported. Other non-radioactive ion sources such as photoionization, surface or thermal ionization, and recent progresses in developing alkali/halogen ion emitters and their use in special applications as well as the multiple ion source IMS, will also be discussed.

A PRINCIPLE OF BLOOD COAGULATION INDUCED BY LOW-TEMPERATURE PLASMA TREATMENT

Sanae Ikehara^{1,2} and Yuzuru Ikehara^{1,2,3}

¹ Graduate School of Medicine, Chiba University

² Electronics and Photonics Research Institute, National Institute of Advanced Industrial Science and Technology (AIST),

³ Biotechnology Research Institute for Drug Discovery, AIST

E-mail: yuzuru-ikehara@chiba-u.jp

The low-temperature plasma (LTP) technology at atmospheric pressure is being integrated into methodologies in the medical and biological sciences. Bleeding control using LTP was one of the applications to reduce the heat damages on hemostasis in surgery, based on the novel plasma effect to induce aggregation of soluble serum proteins. In my talk, I will introduce our concept of LTP use in hemostasis and illustrate our future plan to integrate LTP technology into the biomedical manufacture

1. Blood coagulation using LTP treatment

In the last decade, accumulating evidence has succeeded to illustrate the feasibility to use LTPs at atmosphere for oozy bleeding. Blood clot formation (blood coagulation) by low temperature plasma (LTP) treatment was pointed out in earlier reports as shorten whole-blood clotting time [1-3]. The underlying mechanism to accelerate blood coagulation was linked with the activation of platelets and coagulation factors upon LTP treatment, while no effects on the shape of erythrocytes in formed clot and serum proteins such as albumin and immune globulins were demonstrated [1-3]. On the other hand, we have focused on the plasma effects on hemolysis, and aggregation of proteins that was not involved in blood coagulation and the fibrogenesis system (Fig.1 -3), because erythrocyte volume and albumin concentration are much higher than the amounts and levels of platelets and fibrinogen[4-6]. To maximize the plasma effect that alters them to cellular and molecular “glue” in clot formation, we developed the instrument to produce plasma using a dielectric barrier discharge (66 kHz, sinusoidal peak-to-peak voltage of 6.0 kV applied to an electrode [4, 7]. In *in vivo* experiments, our plasma treatment succeeded to form clots solidly more than the naturally formed clot, and could generate aggregation on the solution that contained either albumin and immune globulins, resulting in the protein disc at 1-cm diameter with continuous contact with the plasma flare [4, 5, 8].

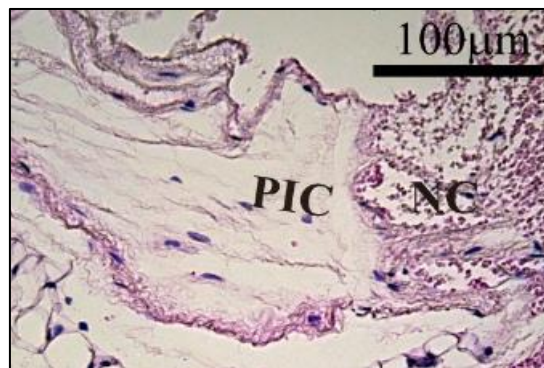


Fig. 1. Plasma Induce Coagulation(PIC) and Natural Clot (NC). Referred from Ikehara Y. et al. J, Photopolym. Sci. Technol., 26(4) 2013 (Ref. 4)

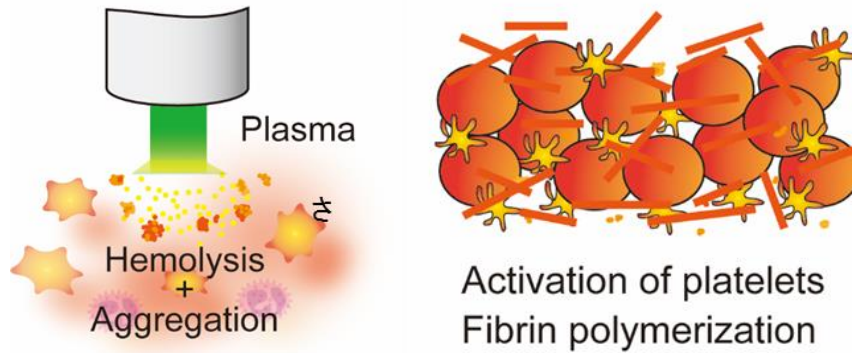


Fig. 2. Shame for Plasma Induce Coagulation(left) and Natural Clot (right).
 Referred from Miyamoto K et al Archives of Biochemistry and Biophysics, **605** 2013 (Ref. 6)

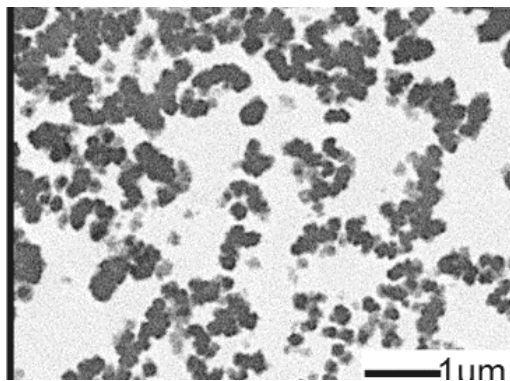


Fig. 3. Trans electron microscopic image for plasma induced protein micelle in albumin solution.
 Referred from Ikehara S. et al. *Plasma Process Polym*, **12** 2015 (Ref. 5)

2. Significance in Medicine

A basic concept on the electronic surgical devices is to evaporate water components in tissue and to close bleeding points by shrinking the tissue, and the treatment using electronic surgical devices sometimes caused severe heat damage in parenchymal tissues. On the other hand, the LTP treatment is an innovative approach with minimal invasion because it can stop blood flow by sealing the bleeding point and creating a possibly favorable healing process. Moreover, the fundamental concept behind LTP hemostasis is to provide an essential method that can suppress excessive host inflammatory responses.

3. Plasma treatment as tissue processing technology

In this paper, I have figured out a concept of using LTP at atmospheric pressure for hemostasis. From the perspective of plasma physics, controlling reactions at the bleeding points might be analogous with semiconductor fabrication technologies such as etching and surface modification, because the active elements such as reactive molecular species, charged particles, and photons appear to react with biomolecules in bleeding points. Indeed, LTP treatment shut down the following immune reaction around the blood coagulation the analogous as on the plasma passivation in the semiconductor fabrication process. I and my collaborators reported that myosin light chain (MyI) 9 and MyI12 are functional ligands for CD69 protein, suggesting that MyI9/MyI12 released from platelets might act as a mediator for inflammatory responses by interacting with CD69 on the leukocyte surface [9]. More, the interaction between MyI9/MyI12 and CD69 is a new therapeutic target for unfavorable allergic inflammatory responses such as asthma because specific antibodies blocking this interaction diminished the inflammation. It is noteworthy that the activated platelets release MyI9 and MyI12 to form intravascular net-like structures that retain inflammatory cells [9], and that our LTP treatment could block MyI9/MyI12 release from platelets because of both red blood cell clot formation and serum protein aggregations in whole blood [4-6]. Our LTP treatment but for other groups might have intervened in an inflammatory reaction cascade starting from MyI9/MyI12 net-like structure formation because LTP

treatments reported by other groups produced activated platelets [1-3] .

Plasma treatment is a kind of tissue-processing technology, insulating local inflammation to start the tissue regeneration. The difference between semiconductor manufacturing and medical applications lies in the responses triggered by LTP treatments. Indeed, it is usually sufficient in semiconductor fabrication to see transient encounters between active agents and results on a local surface, while the production of metabolites and cytokines occurs after treatment for a long duration. Nevertheless, I believe that LTP will become a conventional processing technology in tissue and biomaterial engineering with the progression of plasma science due to the expected interdisciplinary fusion between applied physics and pathology . I hope that our results will serve as a stepping-stone for the advancement of plasma science [10] .

Acknowledgments

I thank Dr. Sakakita for our collaborative research. I thank Dr. Sakakita for our collaborative research. Grant Numbers 24108006 and 15K08413 in MEXT/JSPS KAKENHI Grants-in-Aid for Scientific Research on Innovative Areas supported this study.

References

- [1] Fridman G, Peddinghaus M, Balasubramanian M *et al.* 2006 *Plasma Chemistry and Plasma Processing*; **26**:425-442.
- [2] Kalghatgi SU, Fridman G, Cooper M *et al.* 2007 *IEEE Transactions on Plasma Science*; **35**:1559-1566.
- [3] Kim J, Sakakita H, Yamada H *et al.* 2015 *Plasma Medicine*; **5**:99-108.
- [4] Ikehara Y, Sakakita H, Shimizu N, Ikehara S, Nakanishi H. 2013 *J Photopolym Sci Tehnol*; **26(4)**:555-557.
- [5] Ikehara S, Sakakita H, Ishikawa K *et al.* 2015 *Plasma Process Polym*; **12**:1348-1353.
- [6] Miyamoto K, Ikehara S, Takei H *et al.* 2016 *Arch Biochem Biophys*; **605**:95-101.
- [7] Sakakita H, Ikehara Y, Kiyama S. 2012 *WO2012/005132*.
- [8] Miyamoto K, Ikehara S, Takei H *et al.* 2016 *Arch Biochem Biophys*; **605**:95-101.
- [9] Hayashizaki K, Kimura MY, Tokoyoda K *et al.* 2016 *Science Immunology* **1**:9154.
- [10] Shimizu T, Ikehara. Y. 2017 *Journal of Physics D: Applied Physics*; **50 (50)**:503001.

PLASMA PROCESSES FOR MANUFACTURING SEMICONDUCTOR DEVICES AND SIMULATIONS

Masaaki Matsukuma

Tokyo Electron Technology Solutions Ltd.

E-mail: masaaki.matsukuma@tel.com

The semiconductor devices evolved by shrinkage of their size according to the Moore's law. However, more shrinkage is restricted by the physical limitation. Hence the semiconductor devices are now changing the choice of materials and their structures. Four scales of simulations related to the semiconductor device fabrication tools are discussed. More robust VHF-CCP simulator, chemistry datasets including the cross sections for real process gas mixtures, the quantum mechanics level accurate simulator for surface reactions, and precise feature profile simulator are needed.

1. Introduction

Plasmas have been widely used to manufacture semiconductor devices due to their unique properties. High reactivity of plasmas can lower the process temperature comparing with the thermal process and the reactive ion etching (RIE) technique with plasma is one of the key technology to fabricate the most advanced logic devices such like CPUs and large capacity memory devices. It was no exaggeration to say that the history of evolution of semiconductor devices was identical to the history of the device size shrinkage; i.e. it's well known as "Moore's law." The small transistors provided us significant benefits in aspects of their performance and productivities. The device size has been shrunken and now it reaches to 7nm. The manufacturing technology along the Moore's law is facing to the physical limitation. Furthermore, over hundreds chips which has billions of transistors on a silicon wafer with 300mm diameter must be fabricated, uniformly. The length scale of our interest is over 10^9 , hence the simulation technique must be utilized to understand and improve our tools and processes. In this paper, the plasma simulation to predict the chemical species and their uniformity, the sheath simulation to calculate the ion energy and angular distribution function, the molecular dynamics (MD) simulation to understand the mechanism of plasma induced damage formation, and the feature profile simulation to predict the results of the fabrication processes are described.

2. Plasma simulation

The capacitively coupled plasmas (CCP), the inductively couple plasmas (ICP), and the microwave plasmas (MW) are widely utilized to manufacturing the semiconductor devices. Especially, CCP is likely to be used because it easily generates a bias potential on wafer for RIE and controls the residence time and the distribution of gas supply with a shower head. The driving frequency of plasma generation have increased from the radio frequency (RF) to the very high frequency (VHF) because of demanding to reduce the plasma potential and separate controllability of the plasma density and the ion energy for better process performance. While VHF plasma gave us the good quality of deposited film or the good performance of REI, the uniformity within the wafer became poor. Sawada et al. reports that keen centre-peaked plasma density profiles are realized in VHF-CCP equipment when the electron density exceeds $5 \times 10^{16} \text{m}^{-3}$ (see figure 1).^[1] In their setup, Ar plasmas were generated with 60MHz or 106MHz CCP. The pressure range was 15mTorr to 100mTorr. The electron density was measured by the plasma absorption probe (PAP).

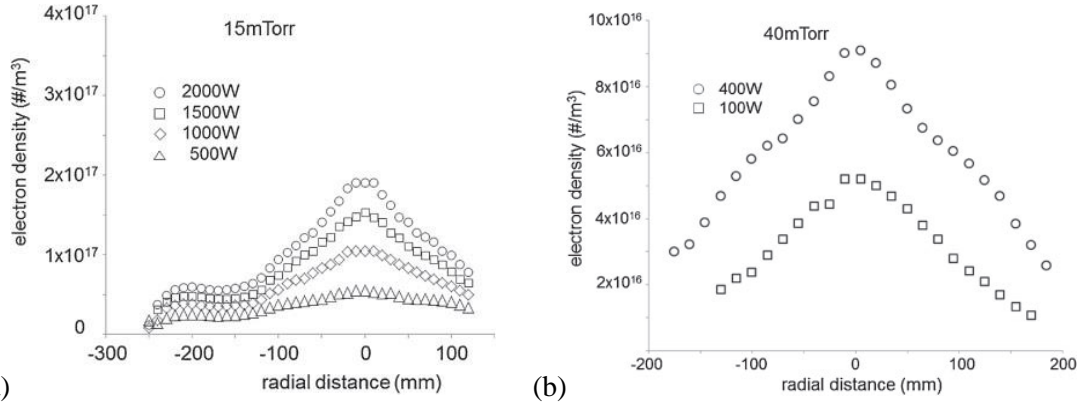


Fig. 1. The measurements of the electron density distributions adopted from Sawada 2014.

The fluid approximation of plasma failed to reproduce these centre-peaked plasma profiles. Sawada et al. found that the higher harmonics had the strong relationship to the centre-peaked profile and they succeeded to obtain the centre-peaked profile with using the VizGlow^[2]. However, the most difficult problem is how to determine the magnitude of higher harmonics components because the fluid model never self-excites them. Hence, the particle in cell (PIC) code should be promised solution, but the computational work load of two dimensional PIC simulation was unpractical, especially for industry users. Recent ten years, some PIC code accelerated by the graphics processing unit (GPU) achieves one hundred times faster than CPU parallelized PIC code.^[3-4] Eremin et al. firstly showed the centre-peaked profile as the result of the self-consistent simulation (Fig. 2).

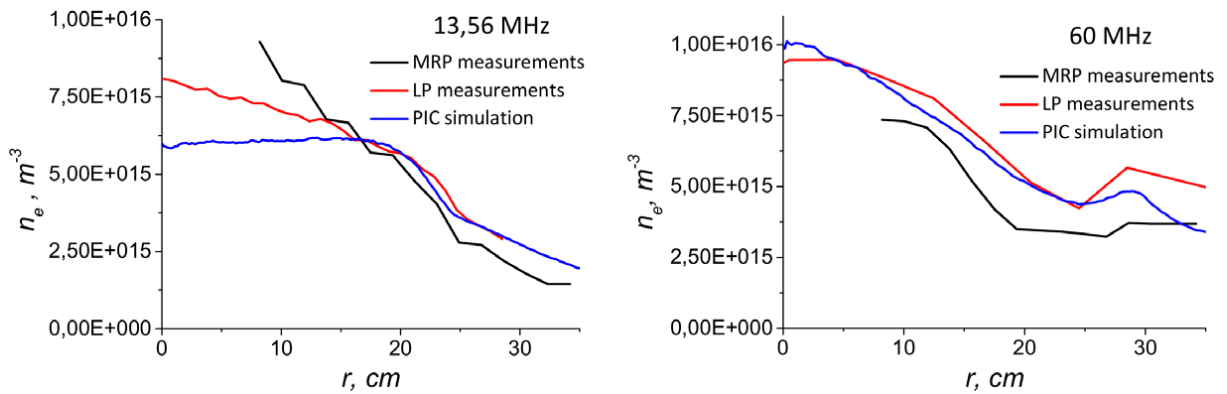


Fig.2 The comparison of simulation and measurements of the electron density profile adopted from Eremin 2016.

The chemistry data such like the cross section dataset and/or reaction kinetics database for the process gases are another problem. While Ar plasma is commonly used for both of simulations and experiments for simplicity, the actual process gases for industrial usage are 3 or more complex mixtures and it is often hard to prepare the data for those gases although there are some projects to collect those fundamental data.^[5-7]

3. Sheath simulation

The number of layers in the most advanced 3D NAND memory have been increasing and will reach 120 layers by 2020. It is needed to the precise high aspect ratio (HAR) hole and/or trench etch technology to fabricate these multi-layer memories and three dimensional transistors. For HAR etch technology, the control of the ion energy and ion incident angle distribution function (IEADF) have the primary importance. Those control at the outermost peripheral part of the wafer, since the number of obtained semiconductor chips in that region is largest in a single wafer. On the other hand, it is most difficult to control IEADF at the wafer edge due to the discontinuity of the material. Denpoh et al. have developed the IEADF simulator which the ion trajectories are simulated with a Monte Carlo method including the collision effects with neutral species. The potential boundary conditions are derived from Denpoh's

method^[8] which is an extended theory of Lieberman's single RF sheath theory^[9] to a dual-frequency RF sheath. In fig. 3, simulated IEDFs are compared with measurements obtained with on-wafer ion energy analyser^[10]. It is clearly seen that the simulator can precisely predict the IEDF all over a wide energy range. Cross section data of the charge-exchange collision plays an important role to predict the spectra of IEDF in the low energy range. From the view point of IEDF simulation, the expansion of precise cross section data is highly demanded.

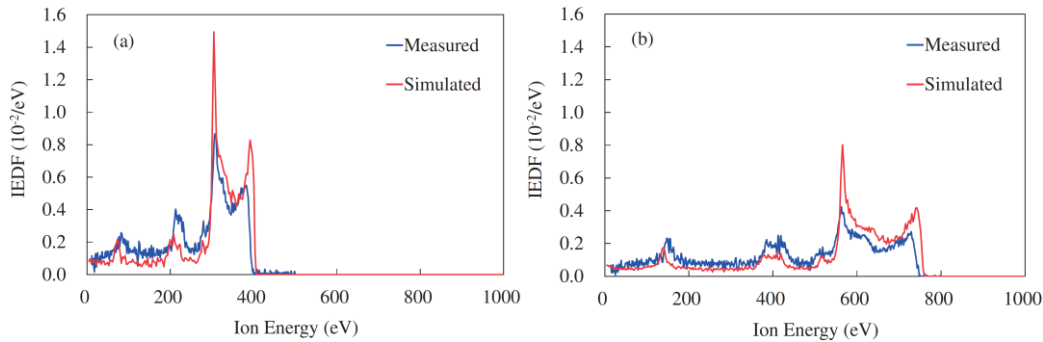


Fig. 3 The comparison of IEDF adopted from Denpoh 2014. (a) 200 and (b) 600W at 13MHz bias power for 100W of 100MHz source power and 20mTorr of Ar in a dual-frequency VHF-CCP etching reactor.

Moreover, Denpoh et al. expanded their theory to multidimensional RF sheath model for single- and dual-frequency CCPs^[11-13] utilizing a commercial finite element method (FEM) software, "COMSOL Multiphysics". This model can simulate ion trajectories in an RF sheath formed around an arbitrary surface geometry (see fig. 4) and obtain IEADF.^[14]

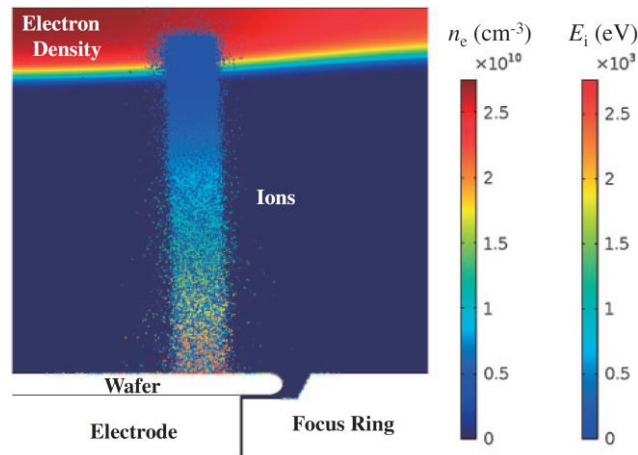


Fig. 4 Snapshot of ion transport in oscillating sheath adopted from Denpoh 2014. Simulated region is very edge of 300mm wafer in a dual-frequency VHF-CCP (40MHz of source and 3MHz of bias) etching reactor for 30mTorr of Ar.

In fig. 5 (a), there is no significant difference of IEDF between 1D simulation and 2D. However, those IADF are completely different (see fig.5 (b)). It is obvious that 1D simulation fails to take into account the distortion of sheath caused by the complex geometry. A PIC modelling is an upper compatible of this simulator, however, it is difficult to apply PIC to a complex geometry. Hence we use PIC or other plasma model to simulate the plasma distribution profile and obtain information of incident fluxes to the wafer, then incorporate those results into this simulator to predict the IEADF to optimize our equipment and processes.

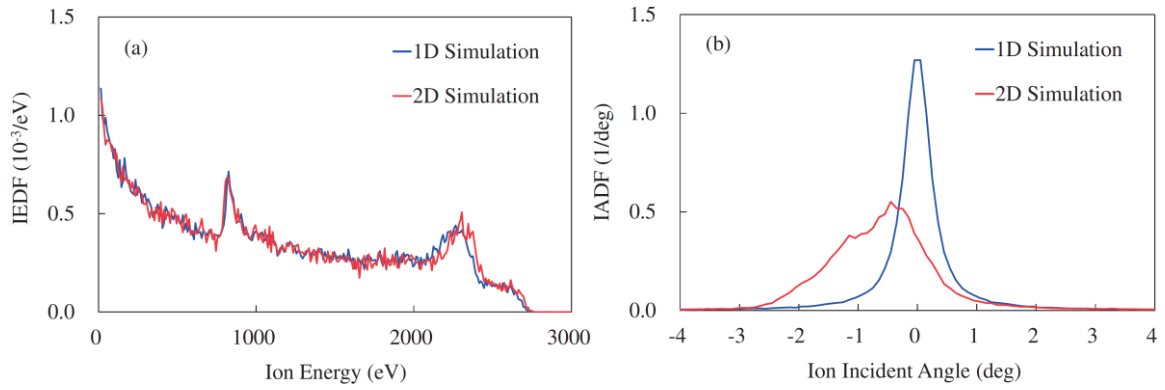


Fig. 5 (a) IEDF and (b) IADF comparison of 1D and 2D adopted from Denpoh 2014.

4. Molecular dynamics simulation

Normally it is difficult to avoidable from plasma induced physical damage (PID) during REI. For modern memory devices, the ion incident energy is quite high for HAR hole etching and a thickness of each layer become thinner than 20nm, hence this extreme condition makes PID control important. Moreover, the structure of transistor is now changing from the traditional planner type to three dimensional one. During the fabrication process of 3D transistor such like FinFET, a channel region is possibly irradiated with a direct ion bombardment while the channel region of the planner type transistor was protected by a gate structure. Additionally, the material is also changing from silicon to III-V tribes and/or Ge. While PID analysis have been studied Eriguchi et al.^[15-18], it must be reworked to obtain more precise prediction for finer transistors at these paradigm shift.

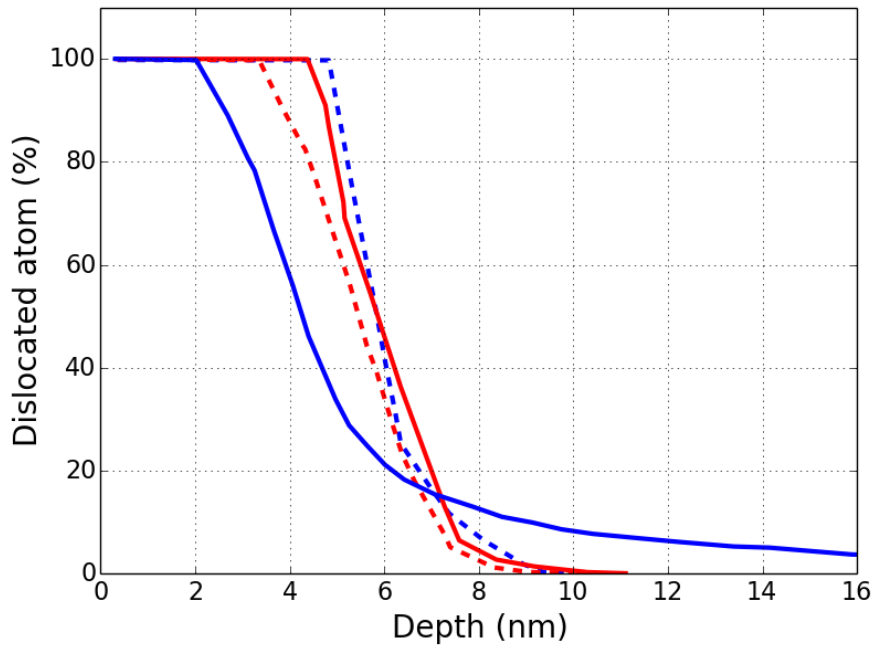


Fig. 6 The comparison of damage profiles. The blue lines are Ge substrates and the red lines are Si substrates. The solids and dashes are experiments and c-MD, respectively.

At first, the classical molecular dynamics simulation (c-MD) could be sufficient tool to reproduce those PID appropriately since the damages were created through the momentum transfer between incident ions and atoms in substrate. In fig.6, simulated damage profiles and measurements are compared. We used a in-house c-MD code with the expanded Hamaguchi-Ohta potential mode^[19-21]. Argon ions were injected into the silicon or germanium substrate with 300eV and the system was simulated with NVE ensemble to form the damage for 2ps and with NVT ensemble for 0.5ps to prepare for next ion incident. The damage formation experiments were conducted with the mass-selected ion beam apparatus in Osaka

University^[22] and the damage profiles were measured with the resolution Rutherford Backscattering Spectrometry (HRRBS). The damage profiles obtained from the experiments shows significant differences between Si and Ge. From the experiments, the thickness of completely destroyed layer of Si beneath the surface is almost half of that of Ge. In the damage profile of Ge substrate, it is clearly seen the deep tailed profile. On the other hand, the damage profile from c-MD seems to be almost identical. Although our model was verified to reproduce the sputtering yield (fig.7), it failed to simulate the damage profiles.

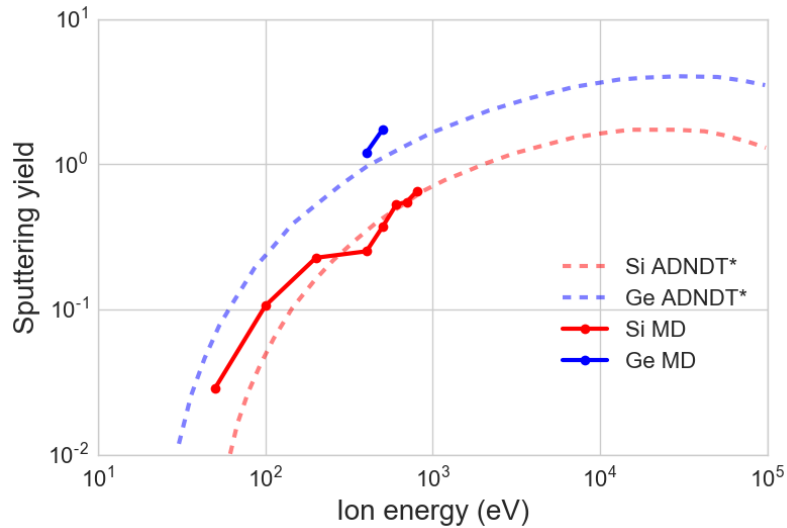


Fig. 7 The comparison of simulated sputtering yield and experiments. The experimental results are adopted from [Atomic Data Nuclear Data Tables, v.31 p.1\(1984\)](#).

Accordingly, the quantum mechanics (QM) calculation must be needed to simulate more accurately. However, our system contains around one thousand of atoms and it takes impractical time to calculate the whole system under QM rule. We developed a hybrid simulator (Quantum Mechanics/Molecular Mechanics (QM/MM) simulator). Quippy^[24] which is a python module for hybrid simulation is used as a QM/MM platform, in which the reactive region dynamically defined base on the kinetic energy is calculated with the density functional tight binding method (DFTB)^[25] and the rest part is simulated as c-MD with the Stillinger-Weber potential^[26]. DFTB parameters for atomic combination of Ar-Si/Ar-Ge/Si-Si/Ge-Ge/(H-Ar/H-Si/H-Ge) were generated with a commercial software “Materials Studio”^[27]. An atom which has highest kinetic in the system is choose as a reaction centre and a sphere with a radius of 6Å around the reaction centre is defined as a QM region. The QM region is updated every 10 timestep. Quippy can make the interatomic potential model from DFTB calculations on-the-fly and can reduce the computational workload of DFTB calculation drastically. In this study, DFTB calculation is taken place every 10 timestep. The timestep is 0.1 femtosecond.

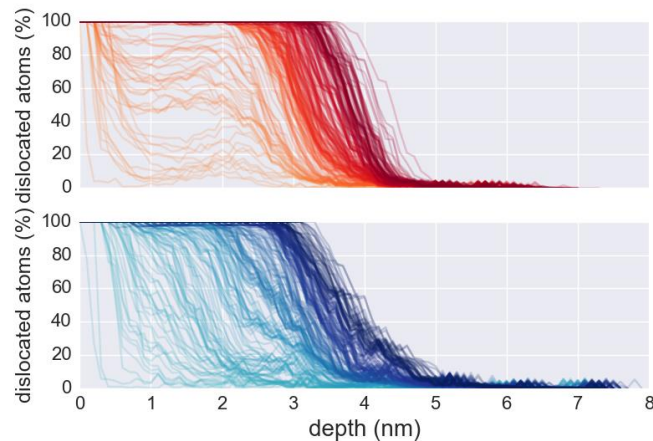


Fig. 8 The evolution of simulated damage profile: red and blue is Si and Ge, respectively

The evolution of damage profile simulated with QM/MM are shown in fig.8 and thinner amorphous layer beneath the surface and deep tailed profile can be seen in Ge substrate case. Those differences could be caused by several characteristics of each material. For silicon, Ar ions likely to deeply penetrate the silicon substrate due to the weak interaction between Ar and Si at the very beginning of the ion irradiation (see fig.9(a)) and this characteristic makes rapid growth of damage profile. After building up the surface amorphous layer, the damages are unlikely to transfer and Si atoms are also unlikely to be sputtered because of relatively strong interaction of Si-Si, hence, the Si substrate has thicker amorphous layer and no-tailed profile. On the other hand, Ar ion can be disturbed easily in Ge substrate and it is destroyed gradually from the surface (fig.9(b)). Thereafter, the thinner amorphous layer on the top is created due to the high sputtering yield and the damage easily propagate into the deeper bulk to create the tailed profile because of the weak interaction of Ge-Ge.

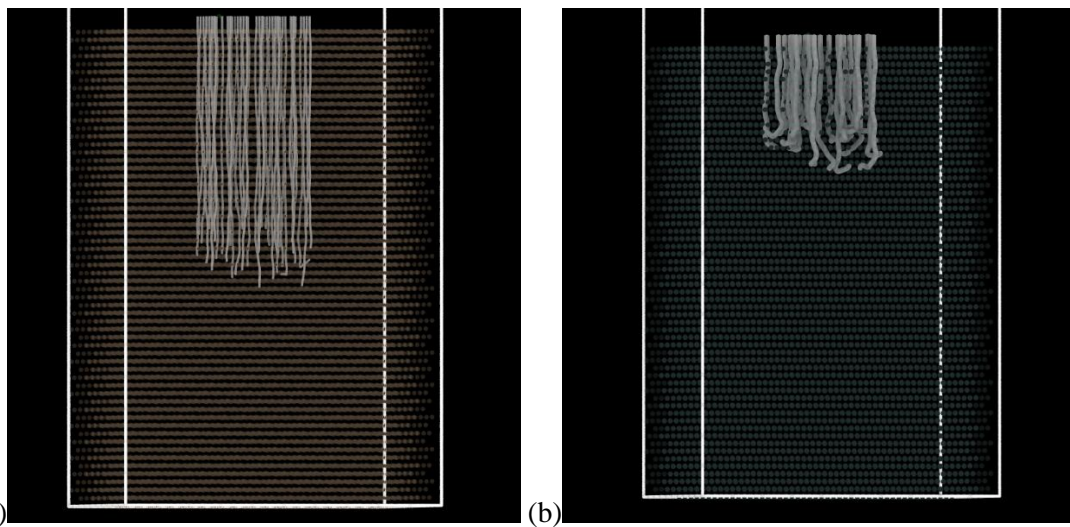


Fig. 9 The Ar ion trajectories. (a) Si, (b) Ge.

5. Feature profile simulation

To simulate the feature profile evolution is one of the ultimate goal for semiconductor manufacturing tool developers to optimize their processes and designs. Unfortunately, the feature profile simulation (FPS) is one of the hardest simulation since the incident fluxes and surface reaction mechanics are generally hard to know. Hence we extract the information of incident fluxes from the plasma simulation and sheath simulation described above and input those into FPS. And also we build the surface reaction mechanism with QM, MD, and QM/MM calculations and incorporate with FPS to simulate the feature profile evolution. We've developed in-house FPS code named FPS3D^[28] over 10 years.

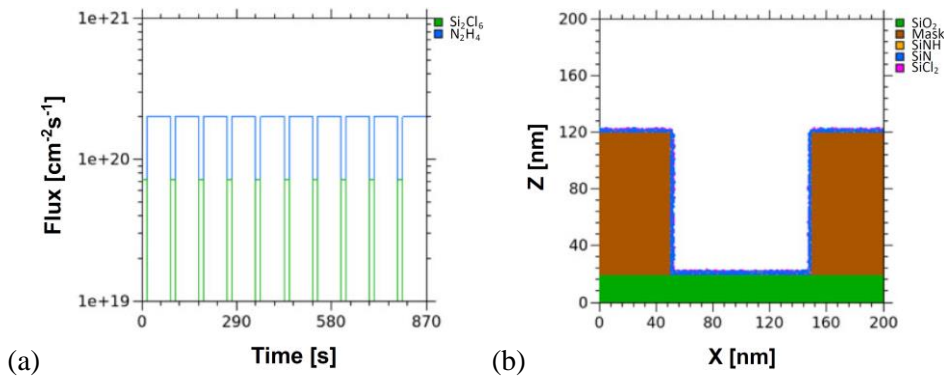


Fig. 10 SiN ALD simulation of FPS3D adopted from Moroz 2017: (a) shows example sequence and (b) show the results after 10 cycles.

Recently, the atomic layer deposition (ALD) and the atomic layer etching (ALE) attract many researchers and process engineers with shrinkage of the transistor size. FPS3D can simulate the ALD/ALE with appropriate fluxes and reaction set (fig. 10)^[29]. Not only the growth rate and/or the etch rate but also the morphology of the deposited film and/or etched shape can be predicted to optimize the process condition(fig. 11).

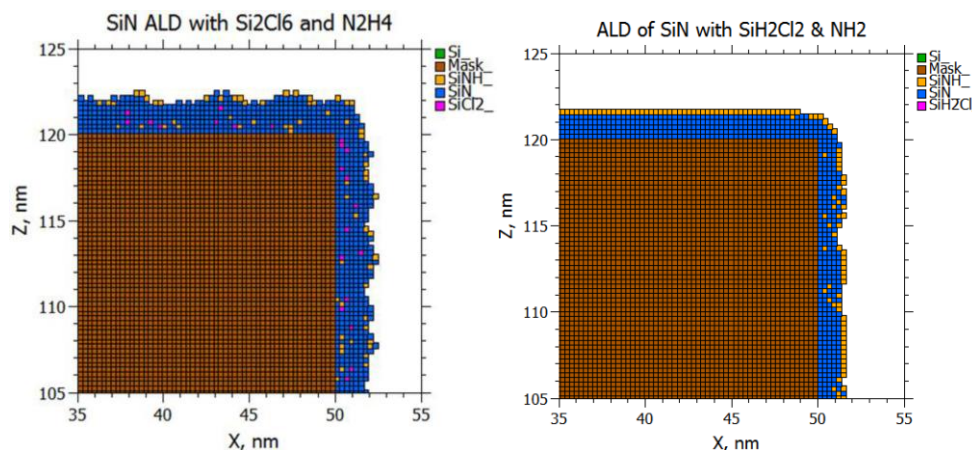


Fig. 11 Close-up of shoulder part adopted from Moroz 2017.

Moreover, now Denpoh et al. are trying to combine the plasma simulation and FPS3D for Multiscale/Multiphysics simulation. The plasma distribution is simulated with the plasma-fluid approximation and IEADFs are calculated with PIC-MCC(Mote Carlo Collision). The surface reactions are simulated with FPS3D and simulated feature profiles are compared with SEM image for fine tuning of the reaction parameters. Sequentially, the tuned surface reaction parameters are re-implemented on the plasma simulator and re-calculate the plasma distribution and incident fluxes. The simulated plasma distribution and feature profile are shown in fig.12

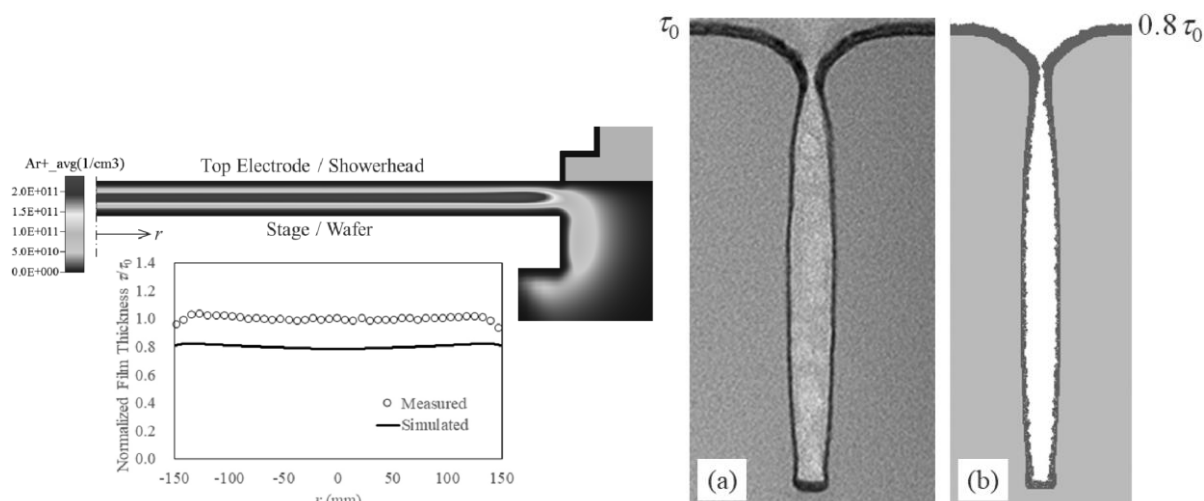


Fig. 12 The example of Multiscale/Multiphysics simulation adopted from Denpoh 2018

6. Conclusion

The simulations of four scales related to the semiconductor device fabrication are described. The chamber size scale VHF-CCP simulation had a difficulty to reproduce the plasma distribution formerly, GPU-PIC can be one of the promising solution of VHF-CCP simulation. To collect the appropriate chemistry dataset of real process gas mixture is other challenge. For the sheath size scale, the accurate simulation of IEADF taking into account the surrounding geometry is important. The damage simulation is described as the example of atomistic scale analysis. At the technology paradigm shift, the choice of materials and structure is dramatically changed and more precise simulations are highly demanded.

QM/MM hybrid simulation described above is one candidate solution. For the feature profile scale, FPS is one of our dream tool while the preparation of incident fluxes and surface reactions are critical difficulties of this simulator. The Multiscale/Multiphysics simulator can overcome this problem.

7. Acknowledgement

The author greatly thanks to Prof. Hamaguchi and Prof. Karahashi at Osaka University for their great support of the ion beam experiments and discussion of PID study. The acknowledgements are also given to Dr. Denpoh, Dr. Moroz, Dr. Ventzek, Dr. Larne, Dr. Sawada at Tokyo Electron Ltd. and Dr. Eremin at Ruhr University Bochum for their collaborative research and helpful discussions.

8. References

- [1] I. Sawada et al. 2014 *Jpn. J. Appl. Phys.* **53** 03DB01.
- [2] VizGlow: Plasma Modeling Software for Multi-Dimensional Simulations of Non-Equilibrium Glow Discharge Systems, Theory Manual, version 1.9 (Esgee Technologies Inc., 2012).
- [3] D. Eremin et al. 2010 *63rd Annual Gaseous Electronics Conference, Paris, France.*
- [4] D. Eremin et al. 2016 *Plasma Sources Sci. Technol.* **25** 025020.
- [5] LXcat <https://nl.lxcat.net/home/>
- [6] QDB <https://www.quantemoldb.com/>
- [7] NIFS DATABASE <https://dbshino.nifs.ac.jp/>
- [8] K. Denpoh et al. 2004 *Jpn. J. Appl. Phys.* **43** 5533
- [9] M. A. Lieberman 1988 *IEEE Trans. Plasma Sci.* **16** 638
- [10] M. Funk. et al. 2012 *59th Int. Symp. American Vacuum Society.*
- [11] K. Denpoh et al. 2009 *Jpn. J. Appl. Phys.* **48** 090209
- [12] K. Denpoh et al. 2010 *Jpn. J. Appl. Phys.* **49** 056202
- [13] K. Denpoh et al. 2011 *Jpn. J. Appl. Phys.* **50** 036001
- [14] K. Denpoh et al. 2014 *Jpn. J. Appl. Phys.* **53** 080304
- [15] K. Eriguchi et al. 1994 *Jpn. J. Appl. Phys.* **33** 83–7.
- [16] K. Eriguchi et al. 2008 *J. Phys. D* **41** 024002.
- [17] K. Eriguchi et al. 2010 *Jpn. J. Appl. Phys.* **49** 056203.
- [18] K. Eriguchi et al. 2017 *J. Phys. D: Appl. Phys.* **50** 333001.
- [19] H. Ohta et al. 2001 *J. Chem. Phys.* **115** No.14 6679.
- [20] H. Ohta et al. 2001 *J. Vac. Sci. & Technol. A* **19** 5 2373.
- [21] H. Ohta et al. 2004 *J. Plasma Fusion Res* **6** 399.
- [22] K. Karahashi et al. 2004 *J. Vac. Sci. & Technol. A* **22**, 1166.
- [23] [Atomic Data Nuclear Data Tables, v.31 p.1\(1984\)](#)
- [24] QUIP & Quippy <http://libatoms.github.io/QUIP/>
- [25] Density Functional based Tight Binding (DFTB) <https://www.dftb.org/>
- [26] F. Stillinger et al. 1985 *Phys. Rev. B* **31** 8.
- [27] Materials Studio® BIOVIA
- [28] P. Moroz et al. 2011 *ECS Transactions* **35** 25.
- [29] P. Moroz et al. 2017 *Jpn. J. Appl. Phys.* **56** 06HE07.
- [30] K. Denpoh et al. 2018 *40th International Symposium on Dry Process, Nagoya, Japan.*

NON-EQUILIBRIUM TRANSPORT OF ELECTRONS IN GASES AND LIQUIDS AND ITS APPLICATIONS IN MODELING OF PARTICLE DETECTORS

S. Dujko¹, D. Bošnjaković¹, I. Simonović¹, Z.Lj. Petrović^{1,2} and R.D. White³

¹*Institute of Physics, University of Belgrade, Pregrevica 118, 11080 Belgrade, Serbia*

²*Serbian Academy of Sciences and Arts, Knez Mihailova 35, 11001 Belgrade, Serbia*

³*College of Science and Engineering, James Cook University, 4811 Townsville, Australia*

E-mail: sasa.dujko@ipb.ac.rs

In this work we explore the connections between transport theory of charged particle swarms and modelling of particle detectors used in high-energy physics. In particular, we discuss the physics of resistive plate chambers (RPCs), including the electron transport and propagation of streamers in the gas filled gaps and signal induction in the electrodes. Electron transport coefficients are calculated in a variety of RPC gas mixtures as a function of the reduced electric field, using a Boltzmann equation analysis and Monte Carlo simulations. A 1.5D fluid model with photoionization is developed to investigate how the nature of transport data affects the calculated signals in various RPCs used in high-energy physics experiments at CERN. Electron transport and propagation of streamers are also considered in liquid rare gases. Solutions of Boltzmann's equation and Monte Carlo method for electrons in dilute neutral gases, are extended and generalized to consider the transport processes of electrons in liquid non-polar gases by accounting for the coherent and other liquid scattering effects.

1. Introduction

Studies of charged particle transport processes in gases and liquids in combined electric and magnetic fields are of vital interest in the modelling of non-equilibrium plasmas [1], particle detectors in high-energy physics [2], and numerous other applications. Further optimization and understanding of such applications is dependent on an accurate knowledge of the cross sections for charged particle scattering, transport coefficients and the physical processes involved. In particular, the advanced technology associated with detection of high-energy particles using various types of gaseous and liquid detectors demands the most accurate modelling of charged particle transport. Over the last two decades, there has been a lot of progress in the understanding of charged particle transport in combined electric and magnetic fields [3,4], but this has not always been taken advantage of by physicists working in high-energy physics.

One of the main goals of the present work is to discuss how to bridge the gap between the modelling of particle detectors in high-energy physics and the swarm-plasma nexus that has been thoroughly investigated in our recent reviews [3-5]. We discuss how to adopt the well know techniques in plasma physics, including the numerical solution of Boltzmann's equation [4,5], Monte Carlo simulation technique [6,7] and fluid equation based models [4,8,9], to model the particle detectors in high-energy physics. Indeed, there is a considerable overlap between the two fields and in this work we present the methodology, quantitative and qualitative procedures for modelling of gaseous and liquid detectors of high-energy particles.

2. Modeling of resistive plate chambers

In the first part of this work we discuss the transport of electrons in gases, propagation of streamers and signal induction in resistive plate chambers (RPCs). RPCs are gaseous detectors often used for timing and triggering purposes in many high-energy physics experiments [10-12]. RPCs consist of a single or multiple gas filled gaps between the electrodes of high volume resistivity, such as glass or bakelite, which are used for the suppression of destructive higher current discharges. Despite the simple construction, modeling of RPCs is not a simple task due to many physical processes occurring on different time scales, including primary ionization, charge transport and multiplication, electrode relaxation and signal formation. After passing through the detector, a high energy charged particle

(muon, charged pion and/or kaon, etc.) makes clusters of electrons in the gas, which are drifting towards the anode and multiplied in the process of ionization. Electrons move in a homogeneous electric field which is provided by the high voltage that is applied to the parallel plate electrodes. Depending on the applied electric field strength, geometry and gas mixture, RPCs can be operated in an avalanche or streamer mode. Typical gas mixtures used in RPCs are composed of tetrafluoroethane ($C_2H_2F_4$), iso-butane (iso- C_4H_{10}) and sulfur hexafluoride (SF_6). Each of these gas components has a specific purpose: $C_2H_2F_4$ is a weak electronegative gas with a high primary ionization efficiency while iso- C_4H_{10} is a UV-quencher gas. SF_6 , on the other hand, is a strongly electronegative gas, often used in avalanche mode to suppress and control the development of streamers.

The first building block in the modeling of RPCs is the analysis of cross sections for electron scattering in $C_2H_2F_4$, iso- C_4H_{10} and SF_6 . In this work, we propose a complete and consistent set of cross sections for electron scattering in $C_2H_2F_4$ [13], while for iso- C_4H_{10} and SF_6 we use the sets of cross sections found in the literature [14,15]. The set of cross sections for $C_2H_2F_4$ is validated through a series of comparisons between swarm data calculated using a multi term theory for solving the Boltzmann equation and Monte Carlo simulations, and the measurements under the pulsed Townsend conditions. Other sets of cross sections for electron scattering in $C_2H_2F_4$ were also used as input in our numerical codes with the aim of testing their completeness, consistency and accuracy. The calculated swarm parameters are compared with measurements in order to assess the quality of the cross sections in providing data for modeling.

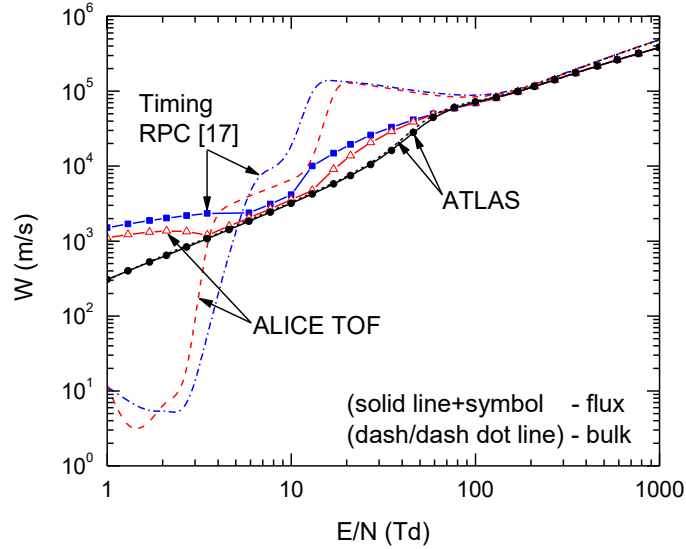


Figure 1. Bulk and flux drift velocities as a function of E/N for gas mixtures used in ATLAS triggering RPC, ALICE timing RPC and timing RPC [17].

In addition to pure gases, we investigate electron transport in various $C_2H_2F_4$ /iso- C_4H_{10} / SF_6 mixtures used in RPCs in the ALICE, CMS and ATLAS experiment using a multi term theory for solving the Boltzmann equation and Monte Carlo simulation technique [16]. The duality of transport coefficients, e.g., the existence of two different families of transport coefficients, the bulk and the flux, in the presence of non-conservative collisions, is investigated. A multitude of interesting and atypical kinetic phenomena, induced by the explicit effects of non-conservative collisions, is observed. Perhaps the most striking phenomenon is the occurrence of negative differential conductivity (NDC) in the bulk drift velocity with no indication of any NDC for the flux component in the ALICE timing RPC system. Figure 1 displays the variation of the bulk and flux drift velocities with the reduced electric field for ATLAS triggering RPC (94.7% $C_2H_2F_4$ +5% iso- C_4H_{10} +0.3% SF_6), ALICE timing RPC (90% $C_2H_2F_4$ +5% iso- C_4H_{10} +5% SF_6) and timing RPC (85% $C_2H_2F_4$ +5% iso- C_4H_{10} +10% SF_6) [17]. We systematically study the origin and mechanisms for such phenomena as well as the possible physical implications which arise from their explicit inclusion into models of RPCs.

The Boltzmann equation analysis and Monte Carlo simulations are performed assuming the hydrodynamic conditions and motion of electrons in an infinite gas. The more realistic RPC simulations with implementing gas gap boundaries and primary ionization models have been performed using a Monte Carlo simulation technique with the aim of obtaining the performance characteristics of a timing RPC [18,19]. Timing resolutions and efficiencies are calculated for a specific timing RPC with a 0.3mm gas gap and gas mixture of 85% C₂H₂F₄ + 5% iso-C₄H₁₀ + 10% SF₆.

In this work we also present our 1.5D fluid model with photoionization to investigate the transition from an electron avalanche into a streamer, propagation of streamers and signal induction in the system of electrodes [20]. In particular, we investigate how the duality of transport coefficients affects the calculated signals of the ATLAS triggering RPC and ALICE timing RPC used at CERN, and also a timing RPC [17] with high SF₆ content. Calculations are performed using the classical fluid model in which both the bulk and flux transport data are used as an input. In addition, we present a new approach in fluid modelling of RPCs based on the equation of continuity and density gradient expansion of the source term. The model requires knowledge of the coefficients in the density gradient expansion of the source term as a function of the reduced electric field. We apply the Monte Carlo method for the determination of these coefficients using the cross sections for electron scattering as a set of input data.

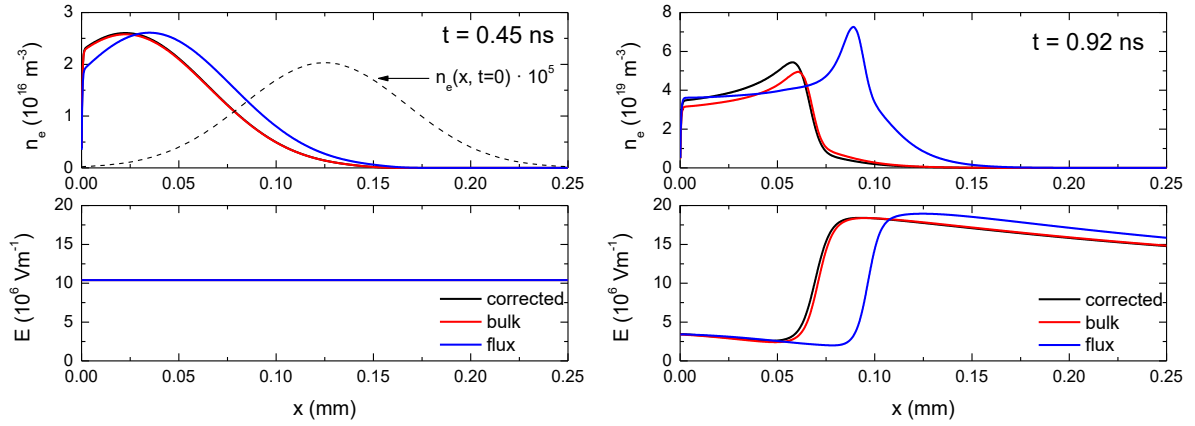


Figure 2. Electron number density and electric field along the gas gap of ALICE timing RPC at $t = 0.45$ ns during avalanche development (left panel), and $t = 0.92$ ns during positive streamer formation (right panel). The external electric field is set to 10.4 MV/m and pressure is 1 atm. Calculations are made using a corrected fluid model and classical fluid model with flux and bulk transport data as an input [20].

As an illustrative example of our fluid simulations of RPCs, in figure 2 we show the development of an electron avalanche and its transition into a positive streamer. On the left panel we show the electron number density and electric field at time instant $t = 0.45$ ns during avalanche development in ALICE timing RPC. We observe that there are no space charge effects and the profiles obtained using corrected model match very well with those obtained using classical model with bulk data. Comparing avalanches with bulk and flux data, we see that the avalanche with the flux data is slower. This might be expected, since the bulk drift velocity is greater than the flux drift velocity for a given electric field. During the avalanche phase, the induced current grows exponentially with time. However, the exponential rise gradually stops due to both space charge effects and electron absorption at the anode. At about $t = 0.92$ ns, the positive streamers starts to develop (see the right panel in figure 2) and the current rises again while the streamer progress towards the cathode. Since the positive streamer move against the electron drift direction, it requires a source of electrons ahead of the streamer to support the ionization process. This is the reason why photoionization should be included in the modelling. The positive streamer stops at about 1 ns and starts to diminish while the induced current slowly drops to zero. The differences between the profiles shown in the streamer stage are clearly evident. These differences follow from the differences between the bulk and flux drift velocities as well as due to representation of the source term employed in these models.

3. Electron transport and negative streamers in liquid rare gases

In the second part of this work we investigate electron transport, transition from an electron avalanche into a negative streamer, and propagation of negative streamers in liquid rare gases. Liquid rare gases, particularly liquid argon and liquid xenon, are very good detecting media, due to their unique physical properties [21]. The high density and high atomic numbers make them very efficient in stopping penetration radiation, while a significant abundance of many isotopes with different values of nuclear spin enables the study of both spin dependent and spin independent interactions.

In this work we extend and generalize the Monte Carlo method, initially developed for dilute neutral gases, to consider the transport processes of electrons in liquids by accounting for the coherent and other liquid scattering effects [22]. The extended code is tested through a series of benchmark calculations for the Percus-Yevick model. Values and general trends of the mean energy, drift velocity, diffusion tensor and ionization coefficient are calculated for liquid rare gases and compared to the available measurements. The comparison is also made between the liquid and gas phase results. Calculated transport coefficients are then used as an input in fluid simulations of negative streamers, which are realized in both 1D and 1.5D setups. In particular, we investigate how various scenarios of representing the inelastic energy losses in liquid rare gases affect both electron transport and propagation of streamers. We consider three different cases where: (1) the energy losses to electronic excitations are neglected, (2) certain particular excitations are taken into account, and finally (3) all electronic excitations are included. These individual cases are discussed in light of the available spectroscopy and photoconductivity experiments in liquid rare gases [22].

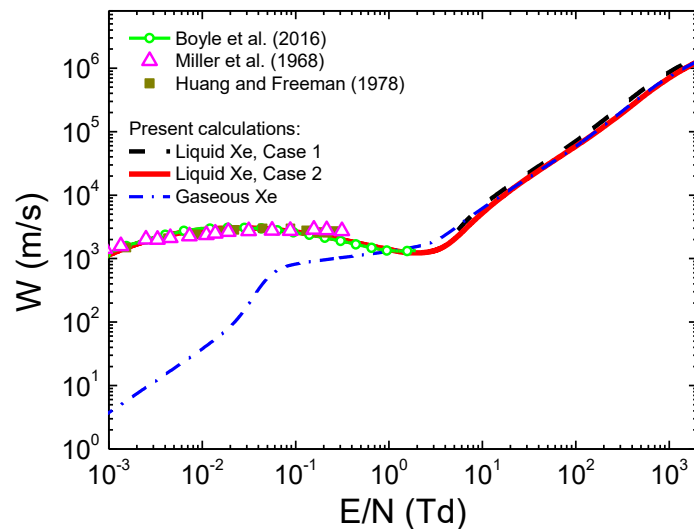


Figure 3. Comparison of the measured drift velocities in liquid xenon (Miler et al. (1968) [23] and Huang and Freeman (1978) [24] with our theoretical calculations. The theoretically calculated drift velocities in liquid xenon, include the Boltzmann equation results of Boyle et al. (2016) [25] and the present calculations obtained in Monte Carlo simulations. The bulk drift velocity of electrons in gaseous xenon is also shown in this figure for comparison [22].

In figure 3 we show the variation of the bulk drift velocity with E/N for electrons in liquid xenon. Our Monte Carlo calculations over a wide range of E/N are compared with those obtained from the numerical solution of Boltzmann's equation for the lower values of E/N , as well as with the available measurements. The Boltzmann equation results for gaseous xenon are also included in figure 3. We consider the following two cases for representing the inelastic energy losses: (1) no electronic excitations, and (2) all electronic excitations are included. The cross sections detailed in [22,25] are used in the present study. We observe that for the lower values of E/N (lower than approximately 1

Td), the drift velocity in the liquid phase significantly exceeds the drift velocity in the gas phase. This is a clear sign of the significant reduction of the rate of momentum transfer of the lower energy electrons occurring in liquids. This reduction follows from the modification of the scattering potential and the coherent scattering effects. As a consequence, the electric field accelerates electrons more efficiently in liquid xenon than in the gas phase. For the higher values of electric fields, however, this effect is reduced, as the scattering of a high energy electron on a xenon atom is significantly less perturbed by the surrounding liquid. Thus, we see that the drift velocity decreases between approximately 0.02 and 2 Td. The reduction of the drift velocity with increasing E/N is the well known phenomenon of negative differential conductivity (NDC). In the gas phase, NDC is caused by inelastic and/or non-conservative collisions, but in liquid xenon this is structure induced phenomenon. We observe that our values of the drift velocity are close to those predicted in the experiments of Miler et al. [23] and Huang and Freeman [24]. However, as we can see NDC is not observed in the experiments.

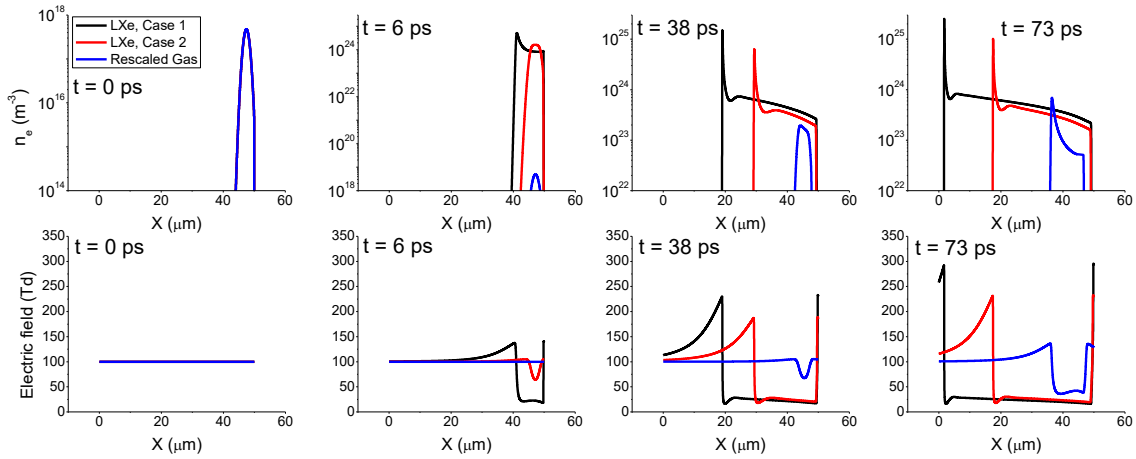


Figure 4. The formation and propagation of negative streamers in liquid xenon for $E/N=100$ Td, The presented results are determined by assuming the following two cases for representing the inelastic energy losses: (1) no electronic excitations (Case 1), and (2) all electronic excitations are included (Case 2). Streamers propagate from the right to the left.

In figure 4 we show the formation and propagation of a negative streamer in liquid xenon. In the same figure we include the simulation in which the transport data for electrons in the gas phase are scaled to liquid density (Rescaled gas). The initial condition for both electrons and positive ions is a Gaussian, which is positioned near the cathode [22]. In liquid xenon, positive charge carriers are holes, with a mobility that is several orders of magnitude less than the electron mobility. Thus, the positive holes are assumed to be stationary, on the time scales relevant for this study.

Comparing streamers in gases and liquids, we observe that the transition from an electron avalanche and formation of a negative streamer occur much faster in liquid xenon. We also observe that the formation and propagation of a streamer are reduced by including the inelastic energy losses in the model (Case 2). The number density of electrons in both the streamer head and the streamer interior is also reduced. Other streamer features in liquid xenon are similar as those in the gas phase. We see that the electron number density has a sharp peak in the streamer head where the electric field is significantly enhanced by the space charge effects. In the streamer interior, however, the number density of electrons is reduced. The reason is twofold: (1) As electric field decreases, the contribution of ionization is less pronounced, and (2) the recombination of electrons and positive holes is enhanced.

Acknowledgments

This work was supported by the Grants No. OI171037 and III41011 from the Ministry of Education, Science and Technological Development of the Republic of Serbia and also by the project 155 of the

Serbian Academy of Sciences and Arts. RDW acknowledges the support of the Australian Research Council.

4. References

- [1] Makabe T and Petrović Z Lj 2014 *Plasma Electronics: Applications in Microelectronic Device Fabrication* (New York: CRC Press).
- [2] Rolandi L, Riegler W and Blum W 2008 *Particle Detection with Drift Chambers* (Berlin: Springer).
- [3] Petrović et al. 2009 *J. Phys. D: Appl. Phys.* **42** 194002.
- [4] White R D, Robson R E, Dujko S, Nicoletopoulos P and Li B 2009 *J. Phys. D: Appl. Phys.* **42** 194001.
- [5] Dujko S, White R D, Petrović Z Lj and Robson R E 2011 *Plasma Source Sci. Technol.* **20** 024013.
- [6] Dujko S, White R D and Petrović Z Lj 2008 *J. Phys. D: Appl. Phys.* **41** 245205.
- [7] Dujko S, Raspopović Z M and Z.Lj. Petrović 2005 *J. Phys. D: Appl. Phys.* **38** 2952.
- [8] Boyle G J, White R D, Robson R E, Dujko S and Petrović Z Lj 2012 *New J. Phys.* **14** 045011.
- [9] Dujko S, Markosyan A H, White R D and Ebert U 2013 *J. Phys. D: Appl. Phys.* **46** 475202.
- [10] The ALICE Collaboration 2008 *J. Instrum.* **3** S08002.
- [11] The ATLAS Collaboration 2008 *J. Instrum.* **3** S08003.
- [12] The CMC Collaboration 2008 *J. Instrum.* **3** S08004.
- [13] Šašić O, Dupljanin S, de Urquijo J and Petrović Z Lj 2013 *J. Phys. D: Appl. Phys.* **46** 325201.
- [14] Itoh H, Matsumura T, Satoh K, Date H, Nakao Y and Tagashira H 1993 *J. Phys. D: Appl. Phys.* **26** 1975.
- [15] Biagi S, MAGBOLTZ – Program to compute electron transport parameters in gases, v.2, CERN.
- [16] Bošnjaković D, Petrović Z Lj White R D and Dujko S 2014 *J. Phys. D.* **47** 435203.
- [17] Lopes L, Fonte P and Mangiarotti A 2012 *Nucl. Instrum. Methods A* **661** S194.
- [18] Bošnjaković D, Petrović Z Lj and Dujko S 2014 *J. Instrum.* **9** P09012.
- [19] Petrović Z Lj, Simonović I, Marjanović S, Bošnjaković D, Marić D, Malović G and Dujko S 2017 *Plasma Phys. Control. Fusion* **59** 014026.
- [20] Bošnjaković D, Petrović Z Lj and Dujko S 2016 *J. Phys. D: Appl. Phys.* **49** 405201.
- [21] Aprile E and Doke T 2010 *Rev. Mod. Phys.* **82** 2053.
- [22] Simonović I, Garland N A, Bošnjaković D, Petrović Z Lj, White R D and Dujko S, accepted manuscript in *Plasma Sources Sci. Technol.*, doi: <https://doi.org/10.1088/1361-6595/aaf968>
- [23] Miller L S, Howe S, and Spear W E 1968 *Phys. Rev.* **166** 871.
- [24] Huang S S and Freeman G R 1978 *J. Chem. Phys.* **47** 1355.
- [25] Boyle G J, McEachran R P, Cocks D G, Brunger M J, Buckman S J, Dujko S and White R D 2016 *J. Phys. D: Appl. Phys.* **49** 355201

PLASMA LIQUID INTERACTION INDUCED BY ATMOSPHERIC PRESSURE DC GLOW DISCHARGE

Naoki Shirai

¹Hokkaido University

E-mail: nshirai@qe.eng.hokudai.ac.jp

Characteristics of atmospheric pressure plasma using liquid electrode were investigated. Especially, I focused on two characteristics. One is the droplet generation from the liquid surface which occur in gas phase. The other is chemiluminescence of liquid induced by plasma generation. Both characteristics are important results for understanding the fundamental study of plasma-liquid interaction.

1. Introduction

Atmospheric pressure plasma in contact with liquid is widely used for many applications such as water treatment, material process and bio-medical applications [1]. Many interesting phenomena induced by plasma are observed on liquid surface. However, these phenomena are complicated and are not understood completely. In this presentation, I reported some of the experimental results of the plasma liquid interaction induced by atmospheric pressure DC glow discharge. Previously we investigated characteristics of atmospheric pressure DC glow discharge using liquid electrode[2-4]. Using this type of plasma when liquid worked as cathode, the atomic lines of sodium dissolved in the solution appear in the spectrum emitted by the plasma[2]. Nanoparticles can be synthesized at plasma-liquid interface by using this plasma[3]. Although many researches have been reported about plasma with liquid electrode, the detail mechanism of the plasma-liquid interaction have not been understood completely. Previously we reported the optical emission of atomic metal which is component of cation in liquid. However, mechanism of metal cation (such as Na^+) transported from liquid (NaCl aq.) electrode is still unclear. In addition, in liquid phase reaction induced by plasma is also unclear because it is difficult to visualize the reaction in liquid. In this study, we investigate the characteristics of gas phase reaction and liquid phase reaction induced by plasma generation. Firstly, I report the gas phase reaction. When plasma is generated, many droplets are emitted from liquid surface. I experimentally investigate the droplet generation. Secondary, I report the liquid phase reaction. Blue chemiluminescence (CL) was observed just below the plasma-liquid interface when plasma is generated. I investigate the characteristic of CL.

2. Experimental setup

Figure 1 shows the experimental setup for obtaining electrolyte cathode discharges with a miniature helium flow. The concentration of the electrolyte electrode (NaCl aq. solution) is 0-15% or mixed solution of luminol (5 mM) and sodium hydroxide (0.1 M). The stainless-steel nozzle anode has inner and outer diameters of 500 and 800 μm , respectively. The gap length is 1-4 mm. Helium gas is fed through the nozzle anode in open air. The gas flow rate is adjusted 200 sccm using a mass flow controller. The experiment was carried out in open air, but we provided O₂ as a shielding gas around the helium plasma column in some experiments to control the ambient environment. The flow rate of O₂ was approximately 1000 ccm, and it was provided from a nozzle having an inner diameter of 5 mm. The glow discharge is generated by applying a dc voltage to the nozzle anode. The current from the power source is varied up to 120 mA. The electrolyte cathode is grounded via a platinum wire immersed in the electrolyte. The mist dynamics in plasma was observed by the scattering of laser light. The light source

is He-Ne laser with wavelength of 633 nm. The mist dynamics along the laser sheet was observed with a high-speed camera or a digital camera.

For investigation of CL, we took photographs of the chemiluminescence by watching it from the bottom through the transparent side of the liquids container using a digital CCD camera to examine the shape and size of the chemiluminescence. We also measured the optical emission spectrum of the chemiluminescence by guiding it to a spectrograph using an optical fiber. A lens was used for projecting the image of the chemiluminescence onto the input side of the optical fiber. The sensitivity of the spectrograph as a function of the wavelength was calibrated using a standard tungsten lamp. The quantity of OH radicals produced in the solution was examined by adding TA at a concentration of 5 mM. We irradiated the plasma-treated solution with UV light at 310 nm and detected the fluorescence from HTA,19,21) which was produced by the reaction between OH and TA, using the same spectrograph.

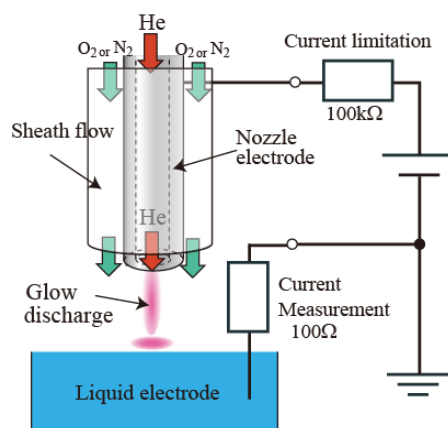


Fig. 1 Experimental setup for generation of atmospheric pressure glow discharge with liquid electrode

3. Droplet generation from liquid surface

When plasma is generated, Na emission is observed near the liquid surface with increasing discharge current, as shown in Fig. 2. The details were described in ref. [X]. Figure 3 shows visualization of the droplet emission from liquid surface induced by plasma liquid interface when plasma is generated using NaCl aq. with the concentration of 5 w%. With increasing concentration of NaCl aq., amount of droplet increased and distance of scattered droplet becomes longer. Namely, amount of droplet depend on the concentration of NaCl. When we use the NaCl aq. solution mixed with other electrolyte including metal cation such as CuSO₄, intensity of spectral emission of Cu increases compared with the case of using only CuSO₄ aq. solution. These results indicate that plasma induced droplet generation which depends on concentration of NaCl is important factor for transport metal cation in solution to gas phase. This droplet generation might relate to the explosion reaction of alkali metal with water.

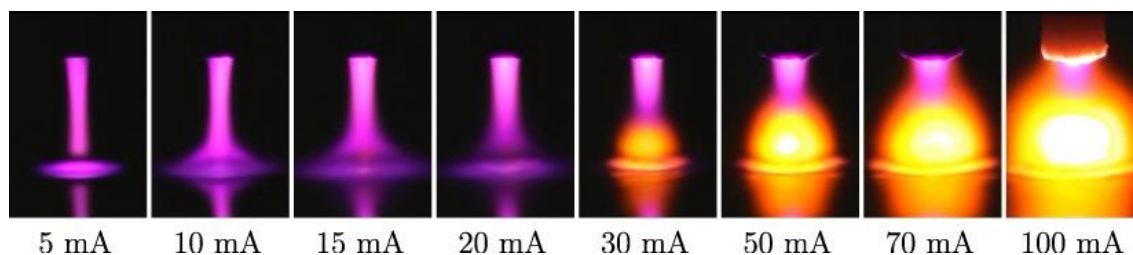


Fig. 2 Dependence of Na emission on discharge current and electrolyte temperature.

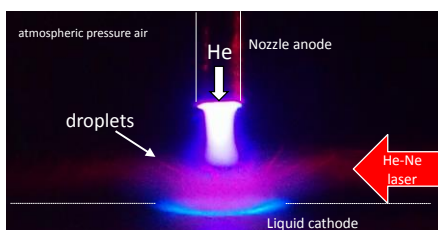


Fig. 3 Observation of droplet emission from liquid surface induced by plasma-liquid interaction.

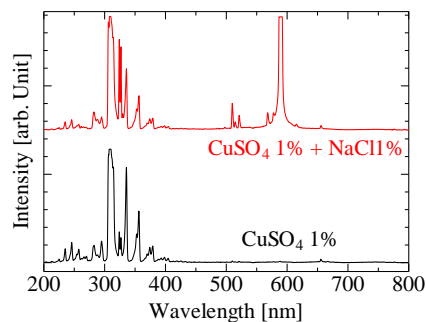


Fig. 4 Atomic lines of metal dissolved in the solution appear in the spectrum emitted by the plasma

4. Visualization of interaction in liquid by chemiluminescence

Blue chemiluminescence (CL) was observed just below the plasma-liquid interface as shown in Fig. 5, when an atmospheric-pressure plasma was in contact with an alkaline solution in which luminol was dissolved¹⁾. The shape of the area with the chemiluminescence was a thin disk. The diameter of the disk was approximately the same as that of the plasma column. The CL is considered to be originated from oxidation reaction of luminol by O_2^- and/or OH. The experimental results reveal that the chemiluminescence of luminol is useful for the real-time visualization of plasma-induced short-lived species in liquids. By using pulsed DC voltage for plasma generation, we measure the temporal change of the emission from chemiluminescence of luminol and nitrogen second positive band system which is emission from plasma, as shown in Fig. 6. The nitrogen second positive system appears immediately after plasma turns ON, and immediately disappear after plasma turns OFF. On the other hands, rising time of CL is delayed nitrogen emission, and decay time is also delayed. Delay time of decay is about 100 μs which might indicate the life-time of reactive species in liquid included by plasma. These results show that CL emission indicates the reaction in liquid phase such as short reactive radical. The understanding the chemiluminescence might be important for clarification of reaction mechanism induced by plasma.

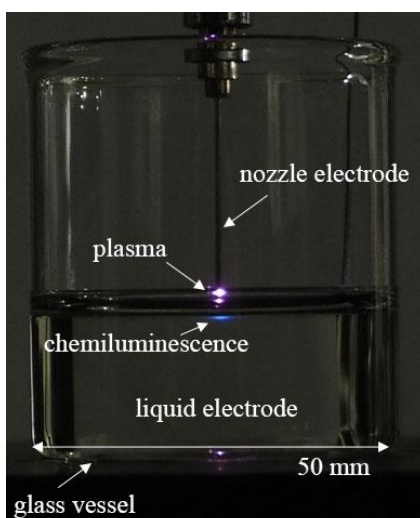


Fig. 5. Image of CL induced by plasma.

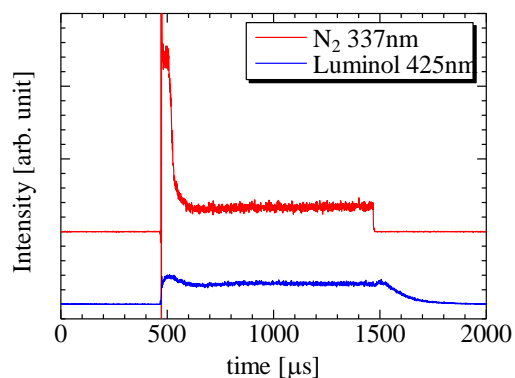


Fig. 6. Temporal change of optical emission from plasma and CL.

5. Conclusion

This study reported about the some of the experimental results of atmospheric pressure plasma using liquid electrode. Not only gas phase but liquid phase, many reactions are observed. In presentation, I will talk about the detail experimental results.

6. References

- [1] P. Bruggeman et al., Plasma–liquid interactions: a review and roadmap, *Plasma Sources Sci. Technol.* **25** 053002 (2016)
- [2] N. Shirai et al., Influence of liquid temperature on characteristics of atmospheric dc glow discharge using liquid electrode with miniature helium flow, *Plasma Source Sci. Technol.* **20** 034013 (2011)
- [3] N. Shirai et al., Synthesis of metal nanoparticles by dual plasma electrolysis using atmospheric dc glow discharge in contact with liquid, *Jpn J. Appl. Phys.* **53** 046202 (2014).
- [4] N. Shirai et al., Influence of oxygen gas on characteristics of self-organized luminous pattern formation observed in atmospheric DC glow discharge using liquid electrode, *Plasma Source Sci. Technol.* **23** 054010 (2014)
- [5] N. Shirai et al., Visualization of short-lived reactive species in liquid in contact with atmospheric-pressure plasma by chemiluminescence of luminol, *Appl. Phys. Express.* **11** 026201 (2018)

HOW TO DESIGN NANOCATALYSTS WITH PLASMA?

Uroš Cvelbar¹, Petra Stražar¹, Martin Košiček¹, Gregor Filipič¹, Janez Zavašnik¹, Jacek Jasinski², Mahendra K. Sunkara²

¹*Jožef Stefan Institute, Jamova cesta 39, SI-1000 Ljubljana, Slovenia, EU*

²*CONN Centre, University of Louisville, Louisville, KY, USA*

E-mail: uros.cvelbar@ijs.si

The presentation deals with the use of plasma for modifications and conversions of nanomaterials, more specifically nanocatalysts. To understand the plasma modifications or syntheses of different nanomaterials, we need to understand the basic processes taking place at the atomic scale. These processes depend highly on used plasma species and can produce highly unusual states of nanomaterials which can improve catalytic properties.

In the recent direction of research, plasmas are being more and more used for or in catalysis. The aim is either to find alternative routes for a large scale production of, e.g. new gases or to increase catalysis efficiency of catalytic materials. There are two systems where plasmas work for catalysis; i) in synergy systems of beneficial interactions between plasma and materials, or ii) in systems where plasmas are used for the design of catalysts. The last aspect connected with the design of nanocatalysts is opening the new opportunities for applications. Low-temperature plasmas have proven to be great sources for the surface manipulations or supplying building blocks for nanomaterials. Furthermore, the specific plasma-surface interactions are leading to synergistic effects, where very little is understood in terms of basic processes taking place. The catalytic activity of nanomaterials is determined by their size, faceting, the presence of steps, defects, strain, oxidation state and support material. In plasma catalysis, all these nanomaterial factors are influenced by plasma, thus affecting the sequent catalytic process. To understand these processes at the atomic scale and mechanisms taking place, we implemented different low-pressure plasma treatments of nanoscale materials such as nanowires or nanoparticles. As results of interactions of various plasma species including electrons or neutral atoms, the intrinsic properties of nanomaterials change. These observations are supported by analytical methods in order to unravel what is occurring on the nanomaterial surface. Through the changes in the crystalline structure of material or reorganisation of its surfaces, the functionality of materials is radically changed for applications such as gas sensing, liquid purification, etc.

DIAGNOSTICS OF ATMOSPHERIC PRESSURE PLASMAS AND THEIR APPLICATION IN AGRICULTURE

N. Puač¹, N. Škoro¹, D. Maletić¹, S. Živković², N. Selaković¹, G. Malović¹ and
Z.Lj. Petrović^{1,3}

¹*Institute of Physics, University of Belgrade, Pregrevica 118, 11080 Belgrade, Serbia*

²*Institute for Biological Research "Siniša Stanković", University of Belgrade, Bul. despota Stefana
142, 11000 Belgrade, Serbia*

³*Serbian Academy of Sciences and Arts, Knez Mihailova 35, 11000 Belgrade, Serbia*
E-mail: nevena@ipb.ac.rs

Atmospheric pressure plasmas (APPs) have been intensively studied in the last decade due to their high potential in the applications in medicine, biology and, lately, in agriculture [1, 2]. They are generated in plasma sources of various geometries and configurations and with different electrode material in order to make them efficient for large variety of applications. The types of sources used are mainly atmospheric pressure plasma jets (APPJs), but since some applications require large areas to be treated plan parallel dielectric barrier discharges [3-6] are also utilized. Typical configurations of APPJs consist of a tube for conducting the flow of the buffer gas and set of electrodes where powered one can be in the contact with the plasma or covered by dielectric. The power supplies that are most commonly used can be divided by the type of signal as continuous or pulsed and they can operate in the large range of frequencies (from several kHz to GHz). The choice of the geometry as well as the type of the power supply used is governed by the application of the APP. Regardless of the system choice and configuration, one needs to perform detailed diagnostics of the plasma system to obtain the data that could be linked to the processes significant for the particular treatment. Then, the efficiency of desired application can be assessed and, which is also important in many cases, there is an opportunity up to some extent to compare the achieved effects with the other systems used for the same application. At the same time, the detailed diagnostics allows the studies of fundamental questions of APP behaviour. For instance, in the case of APPJs an interesting feature of formation of pulsed atmospheric-pressure streamers (PAPS) was observed and investigated. The fast ICCD imaging of this phenomena revealed that PAPS have a speed of several kilometres per second and their formation and propagation still needs to be explained in more detail.

However, from the point of applications the most important feature of the APP is that they create chemically highly active media (both in gas and liquid) with the properties that can be generally tuned according to the application's demands. The active chemistry of the plasma's gas phase can directly modify the treated surface or activate specific mechanisms inside the treated target, e.g. plasma treatment of cells leading to the improved differentiation or cancer cell death [7, 8]. Also, since APP can operate in direct contact with a liquid, the chemically active environment produced in the gas phase above the liquid can modify the physical and chemical properties of the treated liquid [9-11]. Extensive research in this type of experimental configurations has led to the development of the applications of APP in the field of agriculture. Two examples of such applications are direct treatment of seeds and treatment of water in order to create plasma activated water. It was shown that in both cases plasma treatment induces higher germination percentage, less contamination of the seedlings, higher water uptake and faster plant development. These and other observed effects are the result of the interaction of plasma formed reactive oxygen and nitrogen species (RONS) with the seed and plant cells. RONS can trigger various biochemical mechanisms that can be observed also at molecular level through the activity of enzymes or hormones in the seeds and plants.

Here we will try to give the overview of the detailed characterization of the APP systems that were used for both medical applications and applications in agriculture. Results of time-resolved plasma imaging using fast ICCD camera will show the development of plasma structure within one period of the power signal and provide an insight in kinetic effects such as PAPS. Moreover, by using optical emission spectroscopy spectra of excited species in the gas phase will be obtained allowing the qualitative assessment of excited species above the treated liquid. The results of electrical measurements of APP

sources, as another important diagnostics tool, will be presented. Comparison of the two different APP (in electrode geometry and applied voltage frequency) will be done by comparing both the results of plasma diagnostics and the response of the biological system treated by these plasma sources. Also, investigations of the applications of APP in the agriculture will be shown featuring the idea of plasma decontamination of water polluted by pesticides and its influence on germination of commercial plants.

Acknowledgments: This research has been supported by the Ministry of Education and Science Serbia, project III41011 and ON171037.

References

- [1] Adamovich I. *et al. J. Phys. D. Appl. Phys.* 2017 **50** 323001.
- [2] Puač N, Gherardi M and Shiratani M 2017 *Plasma Process Polym.* e1700174.
- [3] Stoffels E, Flikweert A J, Stoffels W W and Kroesen G M W 2002 *Plasma Sources Sci. Technol.* **11** 383–8.
- [4] Winter J, Brandenburg R and Weltmann K-D 2015 *Plasma Sources Sci. Technol.* **24** 064001.
- [5] Maletić D, Puač N, Selaković N, Lazović S, Malović G, Đorđević A and Petrović Z L 2015 *Plasma Sources Sci. Technol.* **24** 025006.
- [6] Čech J, Brablec A, Černák M, Puač N, Selaković N and Petrović Z L 2017 *Eur. Phys. J. D* **71** 27.
- [7] Miletić M, Mojsilović S, Okić Đorđević I, Maletić D, Puač N, Lazović S, Malović G, Milenković P, Petrović Z L and Bugarski D 2013 *J. Phys. D. Appl. Phys.* **46** 345401
- [8] Hirst A M, Frame F M, Maitland N J and O'Connell D 2014 *Biomed Res. Int.* **2014** 878319
- [9] Bruggeman P J et al 2016 *Plasma Sources Sci. Technol.* **25** 053002.
- [10] Škoro N, Puač N, Živković S, Krstić-Milošević D, Cvelbar U, Malović G, Petrović Z. Lj. 2018 *Eur. Phys. J. D* **72** 2.
- [11] Puač N, Miletić M, Mojović M, Popović-Bijelić A, Vuković D, Miličić B, Maletić D, Lazović S, Malović G, Petrović Z. Lj. 2015 *Open Chemistry* **13**(1) 332.

REDUCTION OF VOLATILE ORGANIC COMPOUNDS WITH THE CONCEPT OF A SURFACE DIELECTRIC BARRIER DISCHARGE

Peter Awakowicz¹, Björn Offerhaus, Lars Schücke

¹*Institute for Electrical Engineering and Plasma Technology, Ruhr-University Bochum, Germany*

For environmental protection, the decrease of harmful pollutants in industrial gas flows is decisive. In particular in industrial paint shops, so called volatile organic compounds (VOC) need to be drastically oxidized to CO₂ and H₂O in an ideal case, since the emission of VOCs is strictly regulated by legislation. Conventional methods such as regenerative thermal oxidation (RTO) become inefficient to operate when dealing with low concentrations (< 1g/m³). On the other hand, energy costs of RTO are rather high, typically exceeding on third up to one half of the total energy costs of a car production facility.

A solution especially for low concentrations of VOC in exhaust may be delivered by plasma technology. Based on a surface DBD (SDBD) system, plasma is capable to drastically reduce the VOC concentration by generating oxidative radicals like O, OH, O₃ and many others.

In this talk, the concept of SDBD is presented, the plasma is quantitatively characterized by optical spectroscopy and some examples of VOC conversion, in lab and industry, are presented. abstract of the contributed paper. Short abstract of the contributed paper. Short abstract of the contributed paper. Short abstract of the contributed paper.

UNRAVELING THE COMPLEXITY OF BARRIER DISCHARGES: ROTATIONAL NON-EQUILIBRIA AND MICRO-AMPERE CURRENTS

Petr Synek, Jan Voráč, Tomáš Hoder

Department of physical electronics, Masaryk University, Brno, Czech republic
E-mail: synek@physics.muni.cz

In this contribution we present the methodologies which enable current characteristics with both temporal resolution in sub-nanosecond times and current sensitivity in the range from tens of microamperes to milliamperes, as well as way to probe the non-equilibrium rotational-vibrational state distributions of molecules from emission spectra. By application of these methods to barrier discharges we were able to find previously undocumented physical processes as sub-critical discharge pulses, to measure ion post discharge currents and strongly non-equilibrium distributions of excited molecular states.

1. Introduction

The precise analyses of fast plasma pulses formed in high-pressure micro discharges has been and still remain challenging task. Such highly non-equilibrium plasmas are of great importance in multiple traditional and novel applications (for example, optimisation of ozone generation, gas and water or surface treatment or plasma medicine). There is a constant need to have an enhanced, up-to-date and easy to access analytical methodology at our disposal. Two key approaches for discharge analysis are electrical characterization and various optical diagnostics. Precise current and charge transfer measurements reveal new phenomena, quantify energy input, determine charge transfer distribution functions, clarify memory propagation, or even estimate plasma density. Optical emission spectroscopy applied to non-equilibrium plasmas in molecular gases can give important information on basic plasma parameters, including the rotational, vibrational temperatures and densities of the investigated radiative states which give us insight into discharge chemistry.

In first part of this contribution, we compare simple self-made current probe and its performance with some commercial current probes in common usage [1]. We show that with calibration the proper (undeformed) shape of the measured nanosecond current pulse may be reconstructed. By application of this probe to a single-filament barrier discharge in atmospheric air we were able to measure the ionic currents and revealed novel features of the micro current pulses. When we have combined this method with a high-sampling-rate oscilloscope, it allowed us to analyse the statistical behaviour of the discharge over 82 consecutive unique periods with sub-ns resolution and μA sensitivity. This allowed us to address fundamental discharge phenomena as a post-streamer electric field rearrangement, isobaric gas expansion due to the temperature rise, and microscopic discharging of surface charge domains.

In next part we describe how to precisely understand the non-equilibrium of rotational-vibrational state distribution from the investigated spectra without limiting presumptions. We show that state-by-state temperature-independent fitting procedure is the ideal approach. We have developed a novel software tool, freely available for the scientific community, which offers a convenient way to construct Boltzmann plots even from overlapping molecular and atomic spectra, in a user-friendly environment [2,3]. By application of this software to the challenging case of spectra of the surface streamer discharges generated from the triple-line of the argon/water/dielectrics interface we were able to obtain spatially and phase resolved rotational populations of $\text{f N}_2(\text{C})$ and $\text{OH}(\text{A})$ and reveal the inequilibria within.

This reasearch was part of larger project which focuses on study of surface barrier discharge emerging at the triple-line (triple-junction) of the argon/water/fused silica interface. Plasmas generated at the triple-line at atmospheric pressure usually feature high temperature and electric field gradients as a result of the presence of strong charge separation in the narrow sheath. This feature can be important in the treatment of sensitive or bio-medical samples, or when trying to understand the detailed plasma-initiated chemistry in the surface treatment of polymers.

2. Electrical analysis

Before we performed the triple-junction electrical characterization it was necessary to improve the methodology of current characteristics on dielectric barrier discharges. We aimed to compare two commonly used probes Tektronix CT-1, Pearson current monitor 2877 and a self-assembled coaxial resistive probe to test their applicability to dielectric barrier discharge (DBD) in order to measure small capacitive currents. For this reason we have chosen configuration with symmetric electrodes with a gas gap of 1 mm, both electrodes were half-spherical with approximately 0.5 mm layer of Al_2O_3 as dielectric barrier. The curvature radius of both dielectrics was approximately 2 mm. All experiments were conducted in ambient atmospheric pressure air.

We have compared the probes by trial on this DBD configuration and by measuring their frequency response using a vector network analyser (Rohde & Schwarz,) to obtain the frequency response and phase shift in the 10 kHz–10 GHz range. Out of the probes the self assembled probe shown best sensitivity and frequency response.

Using high-resolution (bandwidth 2 GHz), high-sensitivity (10-bit ADC), high-sampling-rate of 20 gigasamples per second (GSs^{-1}) oscilloscope (Keysight DSO-S 204A with four input channels) and by measuring simultaneously on two oscilloscope channels with different ranges we were able to cover simultaneously both capacitive currents in order of tens of μA and discharge pulse current in order of tens of mA (see Figure 1).

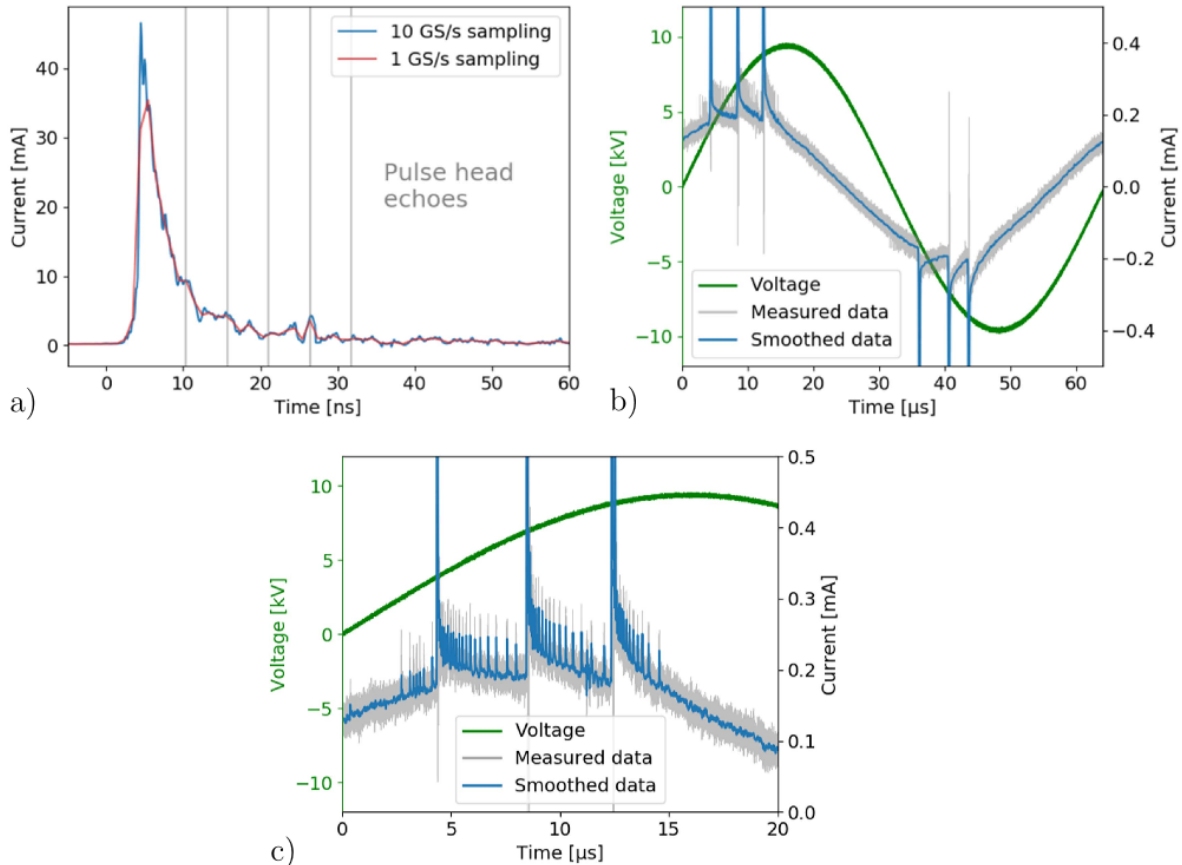


Figure 1. Current characteristics of pulse a), capacitive current b) and detail of discharge phase with low currents c) measured by BNC probe.

By post processing we have merged both current channels into one dataset. Using the data obtained from frequency response measurement we were able to ‘correct’ the error induced by probe uneven attenuation and phase response (pulse wave packet undergoes frequency dependent dispersion in the cables). This correction for example shows that 1 m high quality coaxial cable can increase observable width of 2 ns pulse up to 3 ns.

This enhanced methodology enabled us also to detect micro pulse currents with amplitudes of a few tens of μA and ion (post-electron) currents. These micro-pulses are in immediate pre-discharge times, but

mostly during the ion current. An example of such pulses is depicted in figure 1.c. As their source of origin was uncertain at first, we performed a series of tests to prove that they are discharge-related and not a glitch in the system. This low-current low-charge feature leads us to describe these micro-pulses as sub-critical pulses. A discharge with such small current cannot bridge the gap in given time and remains sub-critical with respect to the classical microdischarge bridging the millimetre gap between the dielectrics under given conditions. Moreover, it is worth noting that the transferred charge of these pulses is in the range of 10^7 electrons. This number lies under the known Raether-Meek criterion value of 10^8 electrons necessary for streamer initiation {raizer1991}.

Using high-sample rate oscilloscope we obtained continuous signal for 82 successive periods of the applied sine voltage and statistically processed these data in order to extract the information which may show the physics hidden behind it. To do so we have modelled the data using simplified pulse profile (see figure 2.) for each discharge pulse and gathered this information into the database containing all available information in accessible manner. The results show that the precise measurements of ionic currents of microsecond duration can play significant role in total transferred charge during the current pulse as they contribute up to 50% of total transferred charge.

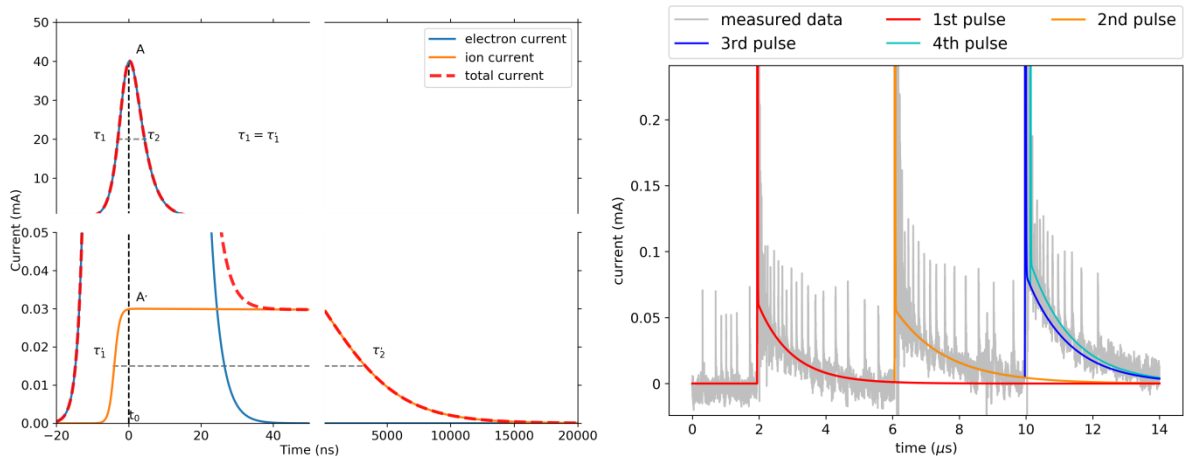


Figure 2. On the left the schematic figure describing the fitted experimental data current waveform. Final profile is created by adding the short-term intense current pulse of electrons and long-term low discharge ion. Fit variables are depicted accordingly. Please note the breaks on current and time axis. The model was applied for each discharge in the 82 periods and example of the fit results of ion currents are on the right.

3. Optical emission spectroscopy

The electrode in this case arrangement was based on the standard surface barrier discharge configuration, see figure 3. Two metal electrodes (copper foil) were glued to opposite sides of a dielectric sheet (fused silica). The dielectric sheet was curved and forms a jacket of a cylindrical cuvette such that one electrode was glued on the outside and the other was on the inside. The cuvette was filled with transformer oil, so the discharges are forced to appear on the outside. The cuvette with the electrodes is placed in a sealed chamber rinsed with argon (1.4 slm flow). The purity of the environment was checked indirectly by observing nitrogen bands in the discharge emission.

The chamber was partially flooded with deionised water such that the outer electrode is submerged. In this way, the water forms an additional dielectric barrier and the discharges were thus not in direct contact with the electrode. To obtain spatially resolved spectroscopic measurements, a real image of the discharge was formed at an input slit of a monochromator (Acton SP-500) using a spherical mirror.

The camera exposure was synchronised with the discharge driving voltage. The outer submerged electrode is earthed, whereas the inner was driven by sinusoidal alternating voltage with 5.4 kV amplitude at the resonant frequency of 15 kHz. The positive and negative half-cycles of were acquired separately.

To obtain sufficient signal-to-noise ratio, the signal was accumulated over 10^6 discharge periods on the CCD chip before readout. Electrical investigations and ICCD imaging have shown that the discharges appearing in the opposite half-cycles are of fundamentally different nature. The discharges always start at the triple-line interface in contact with the water level. At one half-cycle, positive streamer discharges

appear (average duration 30 ns). The negative streamers (average duration 15 ns) emerge in the other half-cycle.

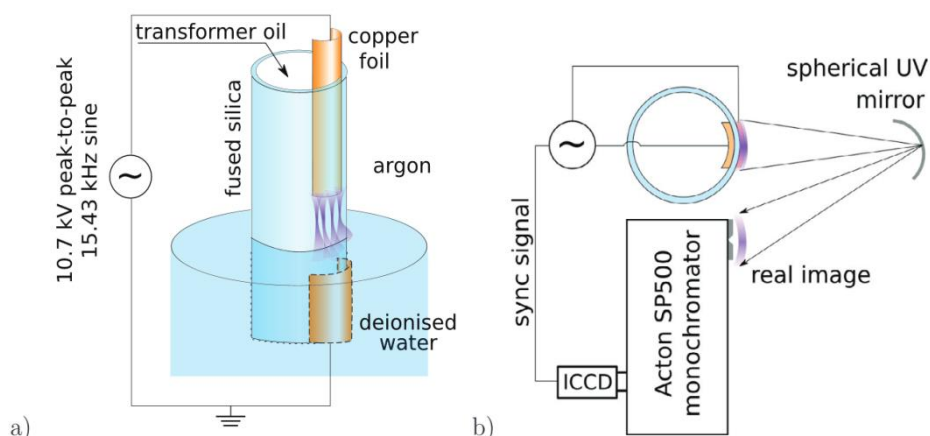


Figure 3. Experimental setup: (a) Schematic sketch of the discharge reactor (detailed description of the electrical circuit is omitted for brevity), (b) the scheme of optical detection setup

Spectra of $N_2(C-B)$ and $OH(A-X)$ transitions were recorded and analysed. Population of $N_2(C)$ states appeared to be in rotational equilibrium. Assuming, the rotational temperature reflects the temperature of the neutral gas, a temperature profile along the discharge path was constructed for the separate half-cycles. It appeared that the positive streamer discharges are slightly warmer, except for the triple-line interface, where the temperature was comparable. The temperature in the discharges was in the range of 340-440 K.

$OH(A-X)$ spectra revealed a greatly non-equilibrium rotational-vibrational distribution (see figure 4). A novel method of state-by-state fitting has been developed and used to construct Boltzmann plots for each measured spectrum. Preparing a Boltzmann plot may be a difficult task, particularly for overlapping spectra. The proposed state-by-state fitting offers a convenient way to construct Boltzmann plots even from partially overlapping spectra. As this functionality is offered for free as a part of an open-source software, it is also quite undemanding and available to the community.

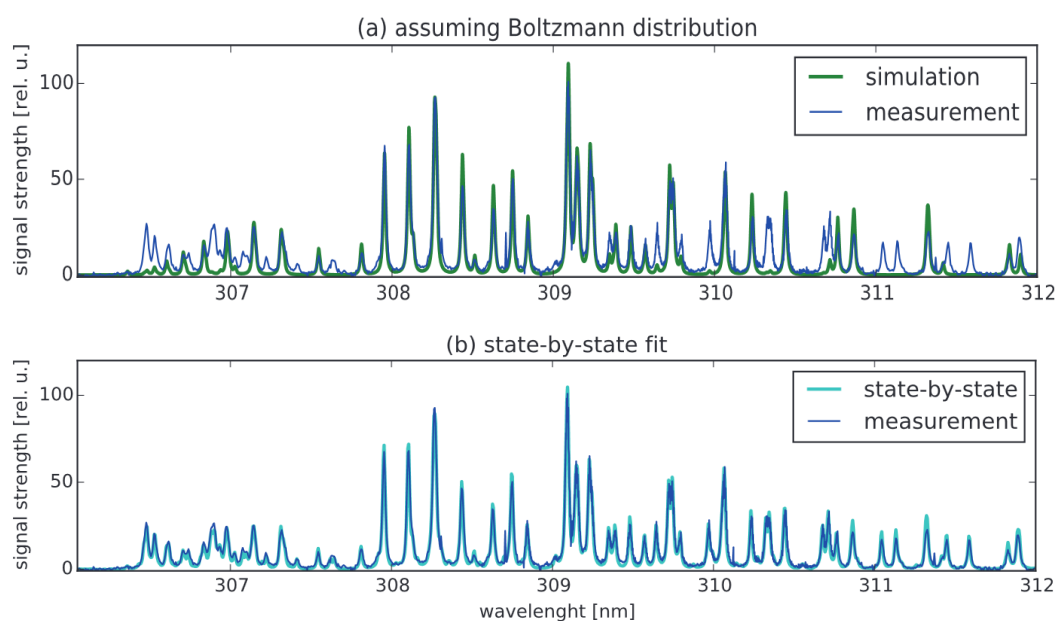


Figure 4. Example of the fits (a) assuming Boltzmann distribution, best fitting $T_{rot} = 848$ K and $T_{vib} = 5300$ K, (b) state-by-state fit not assuming any population distribution. The Boltzmann plot corresponding to (b) is in figure 5.

The Boltzmann plots were analysed assuming that the observed distribution is a sum of two Boltzmann-distributed independent populations. The states with ($v'=0, 9 < N' < 13$) were found to be overpopulated with respect to the two-Boltzmann distribution, perhaps due to fast vibrational-energy transfer. The novel approach to the OH(A-X) spectra enabled us to decouple the different groups of OH(A) and thoroughly investigate their properties.

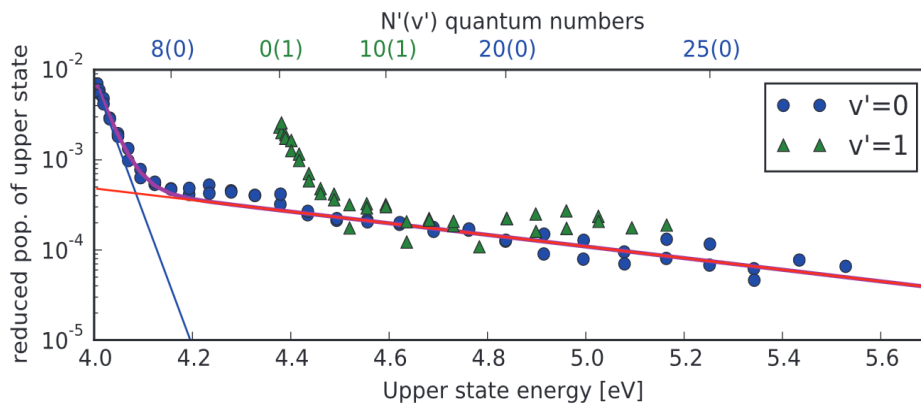


Figure 5. Boltzmann plot obtained by state-by-state analysis of spectrum in figure 4. The relative populations are divided by the respective degeneracy, i.e. reduced. The magenta curved line is a two-temperature fit, where the blue and red straight lines are its components. The two fitted rotational temperatures are $T_{rot} = 343 \pm 28$ low K and $T_{rot} = 7800 \pm 550$ high K. Fitted populations of $v' = 2$ states are not shown.

The temperature of the hot group of OH(A) was linked with the vibrational temperature estimate, as they both are believed to show an intermediate step of the E-T and E-R relaxation. This is further supported by the observation, that in the longer lasting positive streamer discharges, both vibrational and hot group rotational temperatures were lower (compared to negative streamer discharges), while the gas temperature was higher.

4. Acknowledgements

This research was funded by the Czech Science Foundation project 16-09721Y. This research has been also supported by the project CZ.1.05/2.1.00/03.0086 funded by European Regional Development Fund and project LO1411 (NPU I) funded by Ministry of Education Youth and Sports of Czech Republic.

5. References

- [1] P Synek, M Zemánek, V Kudrle, T Hoder [Advanced electrical current measurements of microdischarges: evidence of sub-critical pulses and ion currents in barrier discharge in air](#) - Plasma Sources Science and Technology, 2018
- [3] J Voráč, P Synek, V Procházka, T Hoder [State-by-state emission spectra fitting for non-equilibrium plasmas: OH spectra of surface barrier discharge at argon/water interface](#) - Journal of Physics D: Applied Physics, 2017
- [4] J Voráč, P Synek, L Potočňáková, J Hnilica, V Kudrle [Batch processing of overlapping molecular spectra as a tool for spatio-temporal diagnostics of power modulated microwave plasma jet](#) - Plasma Sources Science and Technology, 2017

SOME GENERAL ASPECTS CONCERNING THE PLASMA BASED DEPOSITION OF THIN FILMS

Johannes Berndt, Cedric Pattyn, Eva Kovacevic

¹GREMI UMR7344, CNRS & Université d'Orléans, France

E-mail: johannes.berndt@univ-orleans.fr

The distinct non-equilibrium character of low temperature plasmas makes them a breeding place for a great variety of different species in particular when they are operated in molecular gases. Depending on the nature of the gas and the external discharge parameter these species can be used as a basis for quite different processes as the deposition of thin films, the formation of nanoparticles or the etching of microstructures. In the context of surface coating plasma based techniques are in particular suitable for the production of extremely uniform and ultra thin (pin-hole free) layers that strongly adhere to a great class of different substrates. However, the plasma based deposition of thin films is a rather complex procedure, which involves many different plasma species, various timescales and several physical and chemical processes. The process starts with the fragmentation of the original parent molecule due to electron impact reactions. These reactions are responsible for the initial formation of a great variety of different radicals and ions which can induce subsequent polymerization reactions leading by and by to the formation of larger and larger molecules and eventually to the formation of nanoparticles. All these species which are formed in the plasma volume can contribute to the flux of species impinging on the substrate redounding there to the film growth. This contribution will discuss some general aspects of plasma based thin film deposition processes. The deposition of thin films performed in mixtures of argon and aniline will be used to illustrate some specific problems occurring in plasma based polymerization processes.

Acknowledgements

The authors would like to acknowledge funding through the European FETOPEN project PEGASUS and the ANR project PlasBioSENS.

Topical Lectures

PARTICLE SIMULATION OF ATMOSPHERIC PRESSURE TRANSIENT DISCHARGES INCLUDING VUV PHOTON TRANSPORT

Zoltán Donkó^{1,2}, Satoshi Hamaguchi², Timo Gans³

¹*Institute for Solid State Physics and Optics, Wigner Research Centre for Physics, Hungarian Academy of Sciences, 1121 Budapest, Konkoly-Thege Miklós str. 29-33, Hungary*

²*Center for Atomic and Molecular Technologies, Graduate School of Engineering, Osaka University, 2-1 Yamadaoka, Suita, Osaka 565-0871, Japan*

³*York Plasma Institute, Department of Physics, University of York, Heslington, York, United Kingdom*

E-mail: donko.zoltan@wigner.mta.hu

We investigate atmospheric-pressure micro-discharges excited by nanosecond high-voltage pulses, in helium-nitrogen mixtures. We use a particle-based (first-principles) approach and also include in the simulations the transport of the helium VUV resonance radiation. We find that the computed charged particle densities and fluxes, as well as the discharge current are significantly higher when electron emission from the cathode surface due to the VUV radiation is accounted for. The simulations allow us to compute the density of helium atoms in the 2^1P resonant state, the density of photons in the plasma and the line shape of the resonant VUV radiation escaping the plasma. We find significant radiation trapping in the plasma and photon escape times much longer than the duration of the excitation pulses.

1. Introduction

Short-pulse discharges excited with \sim kV voltages in various gases have been attracting considerable interest and have been studied for a wide range of pressure (extending from low, \sim mbar, to atmospheric pressure) [1] and a wide range of excitation voltage pulse width (from the picosecond domain up to tens - hundreds of nanoseconds) [2,3]. The gases that have been considered, include pure noble gases and their mixtures with molecular gases, as well as air, which is particularly important for various practical applications. Studies have been reported about, e.g., switching applications [4,5] and the effects of active species generated in such discharges, on cells and tissues [6].

The primary computational tools for investigations of high pressure discharges are based on the fluid approaches. Fluid computations are usually able to account for the complex plasma chemistry [7,8], however, particle-based kinetic approaches, like the Particle-in-Cell method complemented with Monte Carlo Collisions (PIC/MCC), have also been applied in some studies, despite the high computational requirements, because these can describe non-local kinetic effects in domains with high reduced electric field and provide access to the electron energy distribution function [9-11].

In [12] we reported the development of a particle-based simulation code for the description of short-pulse, \sim ns) discharges at atmospheric pressure mixtures of helium and molecular nitrogen (at N_2 concentrations ≤ 1 %). In this code, we have also included the photon treatment of the VUV resonance radiation of helium, based on the approach presented in [13]. We have shown that electron emission from the electrodes due to VUV photons largely enhances the charged particle densities and fluxes, and, consequently, leads to a higher plasma current. Analysis of the velocity distribution function (VDF) and the energy distribution function (EEDF) of the electrons indicated the presence of highly energetic electrons near the negative electrode and a significant anisotropy of the VDF. These observations demonstrated the usefulness (and uniqueness) of particle simulations of such physical systems. The analysis of photon trajectories indicated very strong trapping of the resonance radiation at the high pressure of 1 bar, as revealed by the escape time and the spectral distribution of the photons arriving at the electrodes. Below, we briefly describe our discharge model and its implementation, and give illustrative computational results for several discharge characteristics to give an insight into the operation of short pulse atmospheric plasma sources.

2. Discharge model and simulation

The simulations are based on the "standard" PIC/MCC approach (see e.g. [14]). Our electrostatic code describes a symmetric bounded plasma that is one dimensional in space and three dimensional in velocity space (1d3v).

We trace electrons and three ionic species: He^+ , He_2^+ , and N_2^+ . Electrons collide with He atoms and N_2 molecules of the background gas. For the electron – He atom collisions we use the cross sections from [15], while for electron – N_2 collisions, the cross section set is adopted from [16]. (We note that this latter set is largely based on the Siglo cross section set, which is now accessible at the LxCat website [17]). All electron – atom/molecule collisions are assumed to result in isotropic scattering. When electrons collide with He atoms, 50% of the excitation to singlet states is assumed to result in the formation of singlet (2^1S) metastable atoms and the other 50% is assumed to populate the 2^1P resonant state, either by direct excitation to these levels or by cascade transitions from higher-lying states [12]. For excitation in the triplet system, 50% is assumed to lead to the formation of triplet metastables (2^3S). For the three types of ion species, we only consider elastic collisions with the major constituent of the background gas, i.e. He atoms. Besides these processes only two additional heavy-particle processes are considered: Penning ionisation ($\text{He}^* + \text{N}_2 \rightarrow \text{He} + \text{N}_2^+ + e^-$) and ion conversion ($\text{He}^+ + \text{He} + \text{He} \rightarrow \text{He}_2^+ + \text{He}$). These are treated in the model in the following way: the rates of these reactions (which are adopted from [18,19]) are used to assign a random lifetime – according to the Monte Carlo approach – to each of the metastable atoms and He^+ ions upon their "birth". These particles are then placed on a "wait list" and the given conversion reaction is executed at a later time according to the (random) lifetime of the given particle. The complete list of elementary processes is given in Ref. [12].

To account for the transport of the resonant radiation we keep track of the excited atoms in the 2^1P state and trace the propagation of individual photons. The excited state is assigned to have a random lifetime according to the natural lifetime of the 2^1P level. Upon emission of the photon, natural broadening and pressure broadening, as well as Doppler broadening of the emission spectrum are considered and the actual wavelength of an individual photon is sampled randomly from the broadened spectrum. The free path of the photon is defined by the (wavelength dependent) photo-absorption cross section of the $1^1\text{S} \rightarrow 2^1\text{P}$ transition. At the high-pressure conditions considered here the photons propagate via a sequence of free flight – absorption – emission events until they eventually escape the plasma. For more details see [12].

The neutral gas temperature is kept constant at $T_g = 300$ K. The electron reflection probability at the electrodes is set to 0.2, and we adopt the following values for ion-induced secondary electron emission coefficients: $\gamma(\text{He}^+) = 0.15$, $\gamma(\text{He}_2^+) = 0.1$, $\gamma(\text{N}_2^+) = 0.05$. For the VUV photons, we take an electron emission coefficient of $\gamma(\text{ph}) = 0.1$. The simulations start from a pre-defined "seed" electron and ion density, He_2^+ and N_2^+ ions and electrons are distributed within the electrode gap according to a cosine profile. The electrode area is assumed to be 1 cm^2 .

3. Results

The characteristics of nanosecond discharges are illustrated for a trapezoidal excitation voltage pulse that has a peak amplitude of $U_0 = 1600$ V and equal rise, plateau duration, and fall times, $\tau = 5$ ns. The background gas composition is He + 0.1% N_2 at $p = 1$ bar pressure and we take an electrode distance of $L = 1$ mm. The spatial average of the initial charged particle density (of both the positive and negative species) is $n_0 = 1.5 \times 10^{11} \text{ cm}^{-3}$.

The excitation voltage pulse and the computed discharge current pulse are displayed in figure 1. For the conditions given above, the discharge current exhibits only a slow increase during the rising slope of the applied voltage pulse. When the plateau of the voltage pulse is reached, electron multiplication becomes significant and the current rises rapidly up to a peak value of ~ 10 A, which is reached at the end of the plateau. Subsequently, the current decreases and upon the termination of the voltage pulse a negative current pulse is generated due to the presence of the accumulated ion space charge that cannot respond to the voltage variation on a ns time scale.

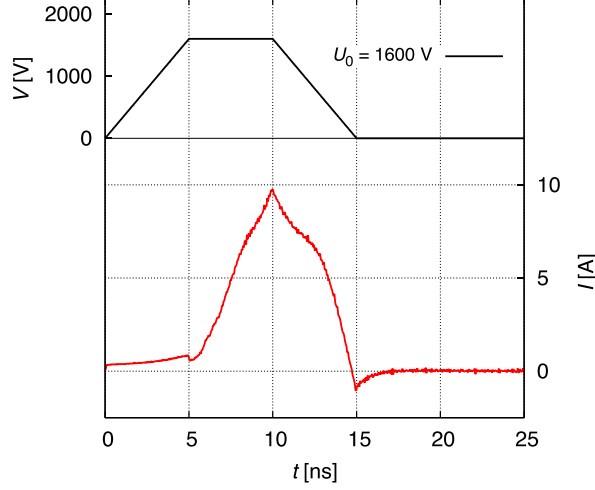


Fig. 1. Excitation voltage pulse (left scale, black line) and computed discharge current (right scale, red line) for a trapezoidal voltage pulse with parameters $U_0 = 1600$ V peak voltage and $\tau = 5$ ns, for He + 0.1% N₂ buffer gas at $p = 1$ bar, $L = 1$ mm, and $n_0 = 1.5 \times 10^{11}$ cm⁻³.

The spatio-temporal evolution of the densities of charged particles and He atoms in the excited (metastable and resonant) states, shown in figure 2 helps understanding of the details of plasma development and dynamics. At the initial phase of the discharge (at times $t < 5$ ns) we observe that the “seed” electrons are swept towards the anode – with no significant multiplication, due to the relatively low electric field at early times of the pulse (see figure 2(a)). However, as the excitation voltage reaches its plateau, the electron density grows by about an order of magnitude in a few nanoseconds and we observe that an ionisation front moves towards the cathode, and the cathode sheath develops. Upon the sheath formation, the He⁺ ion density (figure 2(b)) grows significantly and reaches a peak value of few times 10^{14} cm⁻³ near the cathode, similarly to the electrons. Some of the He⁺ ions convert to He₂⁺ ions, the density of the latter (shown in figure 2(c)) exhibits a growth in the cathode region as well. Due to the low concentration of N₂ in the buffer gas the N₂⁺ ion density (figure 2(d)) is relatively low (about two orders of magnitude lower than the densities of He ionic species). We note that this density ratio is specific to the short-pulse excitation scenario considered here, in [12] we have found that for $\tau = 30$ ns (i.e. for an excitation pulse that has a total length of 90 ns) and $U_0 = 1000$ V, but at otherwise similar conditions, the N₂⁺ ion density exceeds the He⁺ density at times beyond ~ 70 ns. The different behaviour can be understood by the relation of the pulse length vs. the characteristic conversion times associated with the Penning and helium ion conversion reactions, at longer times the number of N₂⁺ ions is increased by the former and the number of He⁺ ions is decreased by the latter reaction.

The data shown in figures 2(e) and (f) indicate that a significant density of metastable atoms and 2¹P excited atoms build up. Besides of the cathode region these species are also present in the bulk plasma region filling most of the electrode gap, with densities in the order of few times 10^{13} cm⁻³.

The time-dependence of the (resonant) photon flux at the cathode is shown in figure 3(a). These data clearly illustrate that the photon “escape time” is significantly longer than the duration of the excitation pulse – the radiation decays on the order of several hundred ns (which is not covered by the present simulations). This slow decay is the consequence of the fact that the VUV photons are many times re-absorbed / re-emitted until they escape the plasma, due to the very high photo-absorption cross section of this radiation [12]. As the photo-absorption cross section sharply peaks at the line centre, photons with $\lambda \simeq \lambda_0 = 58.4334$ nm have a very short flight before the next absorption event and have very little chance to leave the plasma. This effect gives rise to a specific line shape of the resonance radiation that leaves the plasma, characteristic for high-pressure, optically thick plasma conditions, shown in figure 3(b). The intensity of the radiation at the line centre is weak, and the radiation intensity spreads to the “wings” of the spectral line, giving rise to a significant line width.

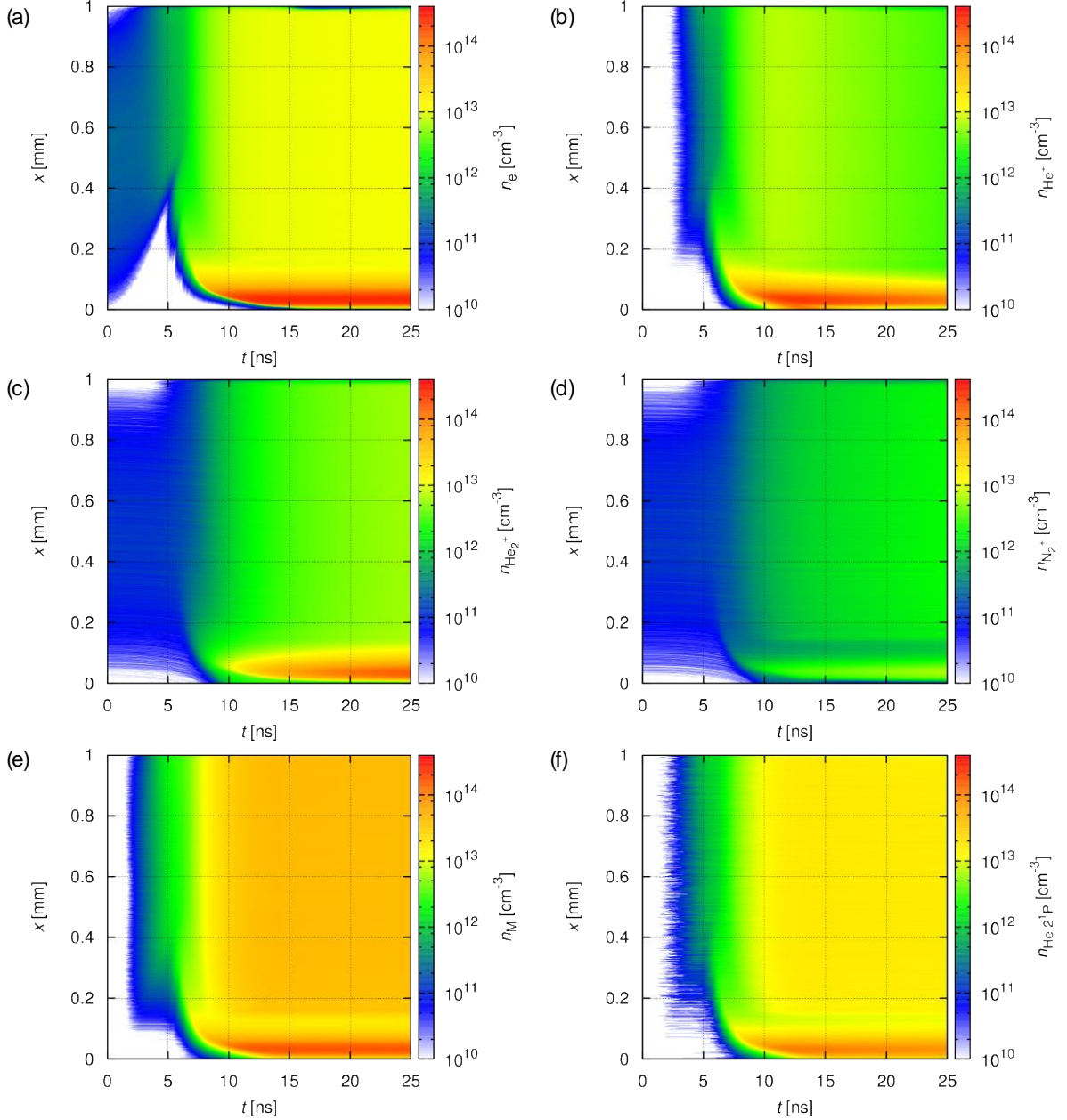


Fig. 2. Spatio-temporal evolution of the density of electrons (a), ions (b,c,d), metastable atoms (e), and He atoms in the 2^1P resonant state (f), for a trapezoidal excitation voltage pulse. Discharge conditions: $U_0 = 1600$ V and $\tau = 5$ ns, He + 0.1% N₂ buffer gas, $p = 1$ bar, $L = 1$ mm, and $n_0 = 1.5 \times 10^{11}$ cm⁻³. The cathode of the discharge is situated at $x = 0$ mm, while the anode is at $x = 1$ mm.

4. Summary

We have presented a simulation study of atmospheric-pressure nanosecond discharges in He + 0.1% N₂ buffer gas, excited by ~kV voltage pulses. Besides tracing charged species (electrons and He⁺, He₂⁺, and N₂⁺ ions) the simulation code also included the transport of the VUV helium resonance radiation by keeping track of excited atoms and trajectories of individual photons. Examples were given for the computed current pulse shape, the spatio-temporal evolution of the densities of charged species and excited atoms, the time dependence of the photon flux and the time-averaged line shape of the He resonance radiation. More complete overview of the characteristics of these discharges is given in Ref. [12].

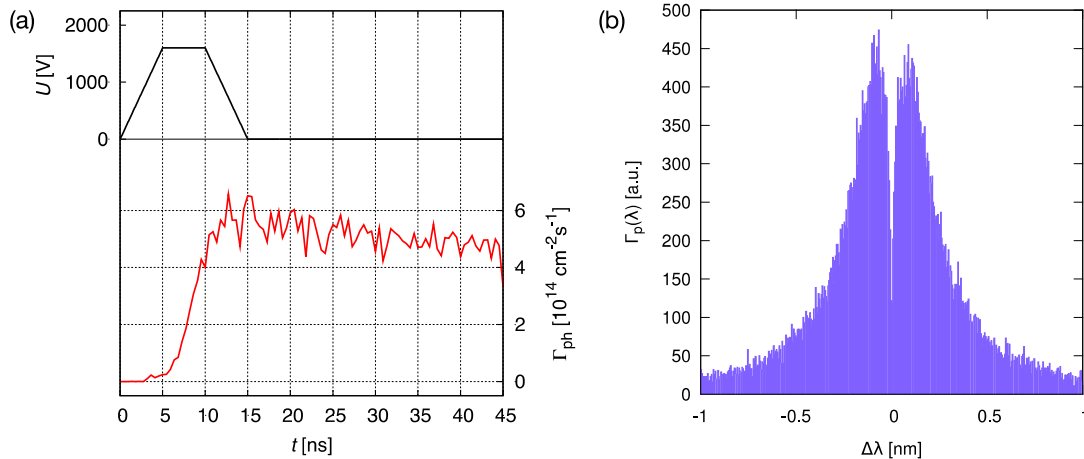


Fig. 3. The flux of VUV resonance radiation at the cathode, as a function of time (a) and the temporally averaged line shape He of the $2^1P \rightarrow 2^1S$ resonance radiation, around the central wavelength of $\lambda_0 = 58.4334$ nm (b). Discharge conditions: $U_0 = 1600$ V and $\tau = 5$ ns, He + 0.1% N₂ buffer gas, $p = 1$ bar, $L = 1$ mm, and $n_0 = 1.5 \times 10^{11}$ cm⁻³.

5. References

- [1] Starikovskaia S M 2014 *J. Phys. D, Appl. Phys.* **47** 353001.
- [2] Starikovskaia S M 2006 *J. Phys. D, Appl. Phys.* **39** R265.
- [3] Starikovskiy A 2013 *Progress in Energy and Combustion Science* **39** 61.
- [4] Bokhan P A, Gugin P P, Zakrevsky D E and Lavrukhin M A 2013 *J. Phys. D: Appl. Phys.* **49** 245202.
- [5] Bokhan P A, Gugin P P, Zakrevsky D K and Lavrukhin M A 2016 *Tech. Phys. Lett.* **42** 372.
- [6] Beebe S J, Fox P M, Rec L J, Somers K, Stark R H and Schoenbach K H 2002 *IEEE Transactions on Plasma Science* **30** 286.
- [7] Waskoenig J, Niemi K, Knake N, Graham L M, Reuter S, Schulz-von der Gathen V, Gans T 2010 *Plasma Sources Sci. Technol.* **19** 045018.
- [8] Niemi K, Waskoenig J, Sadeghi N, Gans T, O'Connell D 2010 *Plasma Sources Sci. Technol.* **20** 055005.
- [9] Schweigert I V, Alexandrov A L, Gugin P P, Lavrukhin M A, Bokhan P A and Zakrevsky D E 2017 *IEEE Trans. Plasma Sci.* **45** 3202.
- [10] Schweigert I V, Alexandrov A L, Zakrevsky D E and Bokhan P A 2014 *Phys. Rev. E* **90** 051101(R).
- [11] Lo Chieh-Wen and Hamaguchi S 2011 *J. Phys. D: Appl. Phys.* **44** 37520.
- [12] Donkó Z, Hamaguchi S and Gans T 2018 *Plasma Sources Sci. Technol.* **27** 054001.
- [13] Fierro A, Moore C, Scheiner B, Yee B T and Hopkins M M 2017 *J. Phys. D: Appl. Phys.* **50** 065202.
- [14] Birdsall C K 1991 *IEEE Trans. Plasma Sci.* **19** 65
- [15] Cross sections extracted from PROGRAM MAGBOLTZ, VERSION 7.1 JUNE 2004, downloaded from LXcat, <http://www.lxcat.laplace.univ-tlse.fr>
- [16] Gordillo-Vazquez F J and Donkó Z 2009 *Plasma Sources Sci. Technol.* **18** 34021.
- [17] www.lxcat.net/SIGLO
- [18] Brok W J M, Bowden M D, van Dijk J, van der Mullen J J A M and Kroesen G M W 2005 *J. Appl. Phys.* **98** 13302.
- [19] Sakiyama Y and Graves D B 2006 *J. Phys. D: Appl. Phys.* **39** 3644.

GLIDING ARC WITH SIDE GAS INLET: PLASMA DIAGNOSTICS AND APPLICATION IN POLYMER TREATMENT

Lenka Zajíčková^{1,2}, Petr Jelínek^{1,2}, Kateřina Polášková^{1,2}, Lukáš Dostál³, Jiří Cerman^{4,5}, Filip Jeník⁶, Zdenka Jeníková⁶, Petr Špatenka^{4,6}

¹*RG Plasma Technology, Central European Institute of Technology - CEITEC, Masaryk University, Brno, Czech Republic*

²*Dept. Phys. Electronics, Faculty of Science, Masaryk University, Brno Czech Republic*

³*Faculty of Electr. Eng. and Communication, Brno University of Technology, Czech Republic*

⁴*Surface Treat a.s., Jungmannova 695/42, České Budějovice, Czech Republic*

⁵*Dept. Mater. Sci., Faculty of Mech. Engineering, Technical University of Liberec, Czech Republic*

⁶*Dept. Mater. Eng., Faculty of Mech. Eng., Czech Technical University, Prague, Czech Republic*

E-mail: lenkaz@physics.muni.cz

Non-thermal atmospheric pressure plasma jets represent a simple technology for the modification of material nanostructure and surface chemistry. They can be applied to polymers aiming at improved adhesion of further coatings or adhesives or synthetic textiles to improved wettability and biocompatibility. We have investigated an industrial device based on gliding arc discharge working in air at 50 Hz. The novelty of our set-up consists in the addition of an extra gas from the side, i.e. into the region of non-thermal gliding-arc plasma filaments. This set-up was optimized “in silico” with the help of gas dynamics simulations and investigated experimentally by plasma diagnostics (optical emission spectroscopy and fast camera imaging) and analyses of plasma-treated polypropylene. The side addition of argon revealed an increased width and improved uniformity of the plasma treatment at higher treatment speeds. Addition of argon with vapours of chemical reactants enabled different modifications of polypropylene surface or deposition of functional thin films.

1. Introduction

Atmospheric pressure gliding arc is ignited between the divergent-shape electrodes as a thermal arc. The plasma channel slides along the electrodes and as it is pushed away it develops into a non-thermal plasma filament [1]. The sliding can be caused by (i) gravity-dependent buoyant force originating from the temperature difference between the hot plasma channel and cold surrounding atmosphere, and/or (ii) drag of gas which typically flows between the electrodes. Gliding arc is usually studied in flow regimes with relatively high flow rates (≈ 1 m/s). In such case, the gas drag governs the discharge dynamics, especially the speed of the plasma column movement [2-4] and the buoyancy, directed opposite to the gravitational force, plays only a minor role.

The efficiency of vibrational excitation pathways is high at the typical electron temperature of gliding arc, $T_e = 1$ eV, and it leads to a high concentration of active species [5]. Therefore, the gliding arc can produce a high concentration of reactive radicals available for the treatment of polymer surfaces and it is a promising candidate for a quick and efficient plasma treatment at atmospheric pressure. When applied to polymer materials aiming at an improved adhesion of top coatings, adhesive strength of joints and improved wettability.

The gliding arc can be operated in various working gases such as dry [6] and humid air [7], pure oxygen, nitrogen [8], noble gases [9] or hydrocarbons [10]. For the industrial applications, utilization of dry or humid air is preferable to maintain the process costs as low as possible. Therefore, several studies of the gliding arc jet working in the mixture of air with an additive were carried out in recent years [11, 12]. However, in all of the published studies, the additive was mixed into the air before the arc ignition point leading to its high fragmentation in the thermal region of the plasma. The opposite approach is the utilization of a post-treatment grafting that can lead to the high density of functional groups but it is time consuming [13] and thus, not suitable for the industrial process lines.

In this work, we have utilized a novel approach to achieve a complex plasmachemistry by addition of an extra gas from the side, i.e. into the region of non-thermal gliding-arc plasma filaments. The side gas inlet for the addition of gaseous additives, especially a mixture of monomer vapors with carrier gas, was proposed with the help of gas dynamics simulations and the monomer transport simulations provided a deeper insight into the mixing process. The gas-phase chemistry was studied by optical emission spectroscopy. The plasma dynamics was observed with fast camera imaging. The results of plasma-surface interaction were assessed by the surface analysis of modified polypropylene.

2. Experimental details

The experiments were carried out with the industrial gliding arc jet GVN1k-2011 (SurfaceTreat) operating at 50 Hz. Its stainless steel electrodes were enclosed in the box with the slit 40 x 12 mm² (Fig. 1). The power was set to 450 W and the gliding arc voltage was $U = 10$ kV. The compressed dry air was used as the discharge working gas at the flow rate of 11.8 slm. The distance d between the polypropylene (PP) sample and the gliding arc jet nozzle (right side of Fig. 1) was kept constant at 10 mm. During the treatment, the sample was moved with the constant speed using a conveyor belt. If not specified, two passes with the offset of 5 mm from the sample axis, i.e. with the relative vertical shift of 10 mm, were applied.

An extra gas mixture could be added from the side into the region of non-thermal gliding-arc plasma filaments by a capillary mounted at $y = 2.5$ mm below the jet nozzle (Fig. 2, right). Vapour additives were transported using two argon (99.998 %, Messer) lines (Fig. 2, left). One line passed through the bubbler with the different tested liquids (demineralized water; ethanol, Lach-Ner 96 %; isopropanol Lach-Ner ≥ 98 %, hexamethyldisiloxane, Sigma-Aldrich $\geq 99,5\%$; n-hexane). The argon flow rate was varied in order to vary the vapor flow rate according to the bubbler equation [14]. The second argon line was used to keep the total argon flow rate constant.

3. Gas dynamics simulations

The simulation was implemented using COMSOL Multiphysics platform in two steps. All the equations were solved at the atmospheric pressure dry air and the standard temperature. In the first step, the gas flow dynamics was calculated using Navier-Stokes equations (Computational Fluid Dynamics module). For simplicity, the influence of plasma or heating on the gas flow dynamics was neglected. In the second step, the transport of an additive was calculated with the Transport of Diluted Species module using the results from the previous step assuming the well-diluted mixture of 5 % benzene vapors in air at the side inlet boundary. The choice of benzene was based on the availability of necessary physical constants and in the same time, its similarity with more complex additives going to be used in the further research. The recalculation of the Navier-Stokes equations in this step was not necessary because the small additive concentration would lead to only negligible changes.

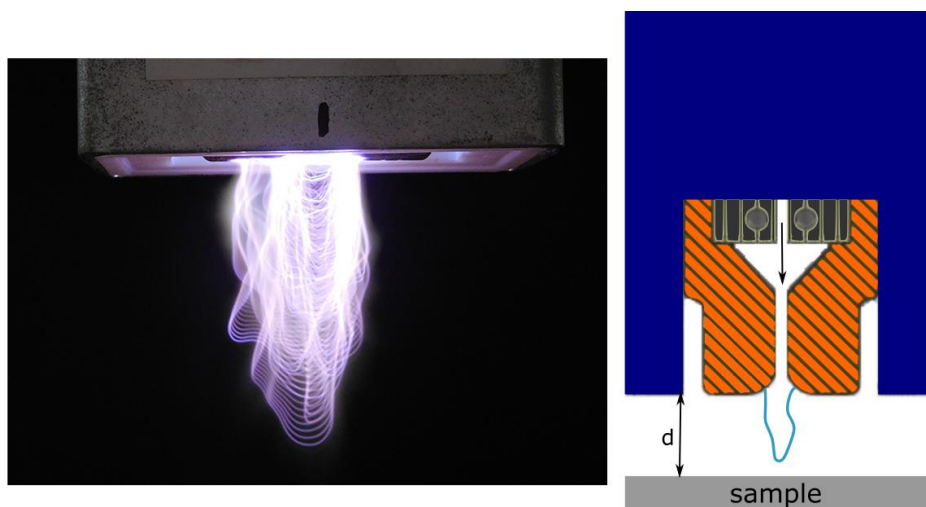


Fig. 1. Glide arc GVN1k-2011 in operation (left) and its schematic drawing illustrating the shape of electrodes, enclosing box and the distance d between the slit jet nozzle and treated surface (right).

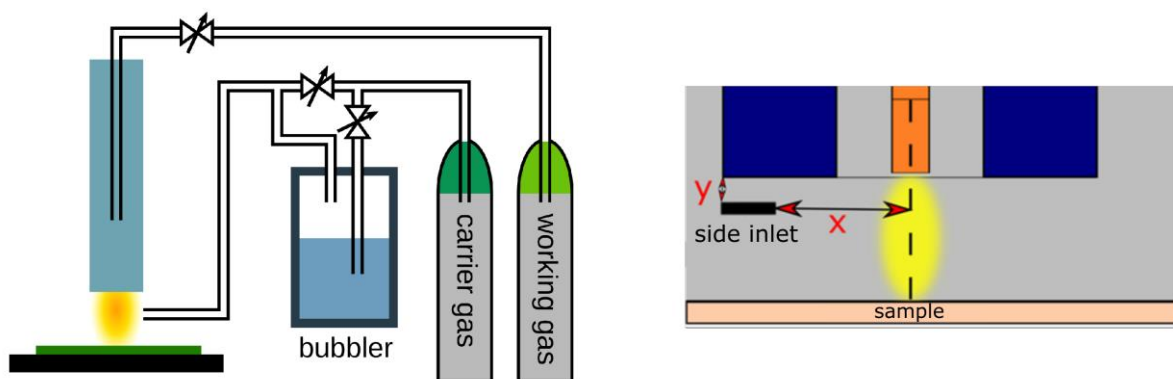


Fig. 2. Schematic sketch of the experimental configuration with the side gas injection system consisting of an alumina capillary (left) and detail of the capillary position (x and y coordinates) with respect to the gliding arc jet (right).

The differential equations were discretized using the finite element method and solved in full close-to-real three dimensional geometry. The model geometry included the gas inlet pipes (main inlet, side inlet), jet head with electrodes and the gap between jet head and sample. Tetrahedral mesh consisting of more than 800000 elements was used for discretization. Three types of boundary conditions were implemented to constrain Navier-Stokes equations. The gas flow rates were imposed at the main inlet and the side inlet. The no-slip boundary condition was imposed at all the walls (the electrodes, the walls of the gas inlet and the plane representing the surface of the sample), which effectively set the gas velocity to zero. At the outflow, the Dirichlet boundary condition for pressure was applied by setting $p = 1$ atm, representing free gas outflow.

The vertical distance of the capillary from the jet head (y -coordinate in Fig. 2) and the gas flow rate through the gliding arc were fixed for all the calculation at the values 2.5 mm and 11.8 slm, respectively. Other parameters were varied in order to find the optimum conditions. The capillary diameter was 0.8 or 1.8 mm, the gas flow rate was 0.5 - 5 slm and the distance from the central axis of the discharge (x -coordinate in Fig. 2) $x = 8.5, 11.0, 13.5$ mm.

The results for the capillary 1.8 mm and $x = 8.5$ mm are shown in Fig. 3. In this case, the optimum gas flow rate ensuring the transport of additive into the main discharge gas stream seemed to be 3 - 4 slm through the side inlet. The optimum value increased with the higher x and decreased for lower capillary diameter. Therefore, the 0.8 mm capillary and $x = 8.5$ mm were chosen for followed up experiments.

4. Plasma diagnostics

Optical emission spectra in the range 200–1000 nm were recorded with Andor spectrometer Shamrock 500i equipped with CCD Andor Newton detector. Atomic lines and molecular bands in measured emission spectra were identified according to the NIST Atomic Lines database and [15], respectively.

The relatively strong OH (A-X) bands were recorded in the range 306–310 nm. The presence of OH in the measured spectrum was attributed to the electron dissociation of water vapors which were admixed from surrounding air into the discharge region. The presence of OH emission enabled the calculation of OH radical rotational temperature $T_{rot}(OH)$ using MassiveOES software [16]. The rotational temperature was 4100 – 4200 K.

Investigation of space and time development of the plasma filaments and dynamics of its interaction with PP was carried out with ultrafast camera (Photron FASTCAM SA-X2 1080K with objective Nikon 105mm f/2,8 G NIKKOR AF) imaging with the speed of 20000 frame/s (frame exposure time of 48 μ s) or the speed of 30000 frame/s (frame exposure time of 25 μ s). Example of plasma filament development is in Fig. 4.

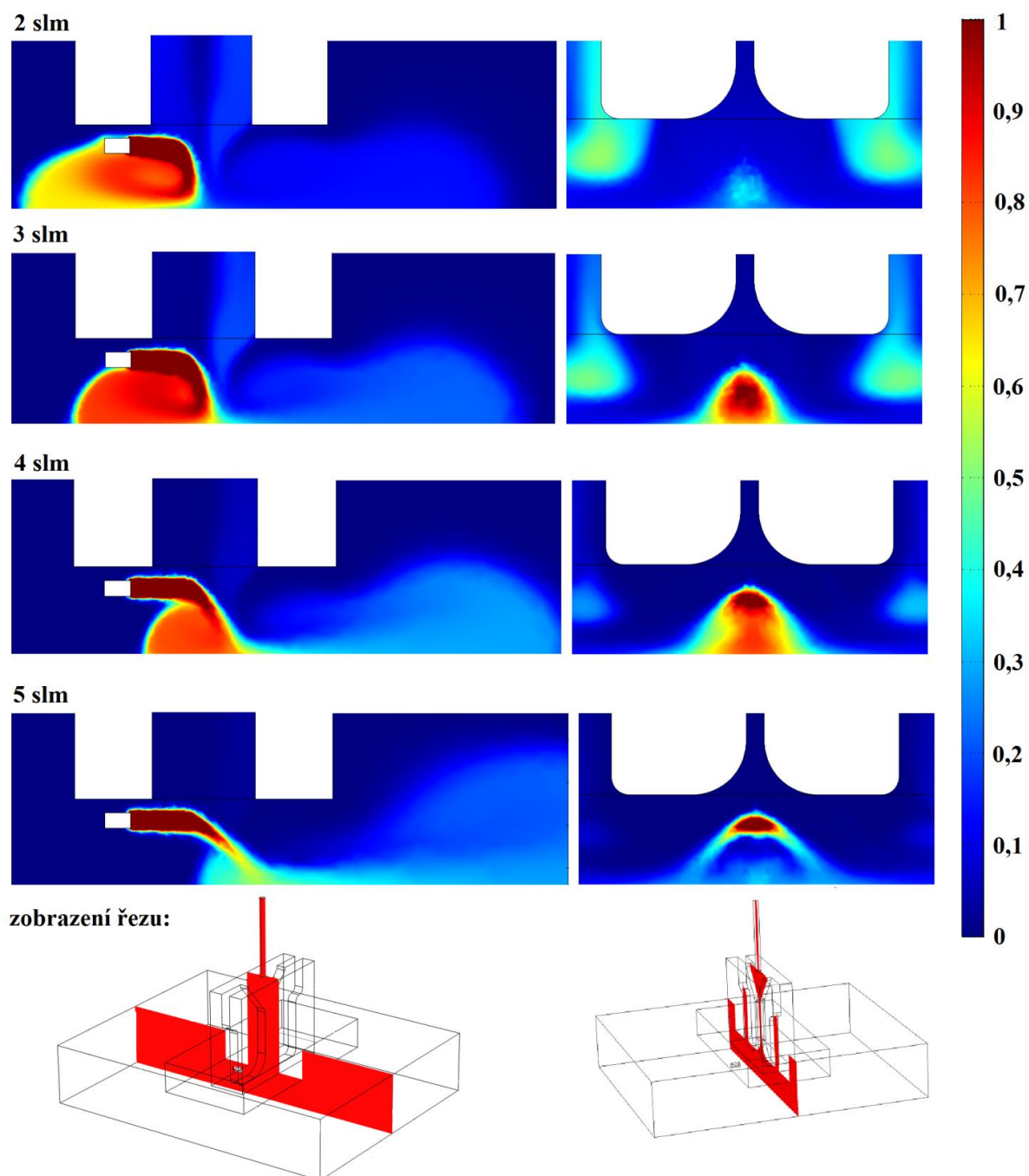


Fig. 3. Concentration of additive n (mol/m^3) calculated from the numerical simulation of gas dynamics for the capillary inlet diameter of 1.8 mm and its position $x = 8.5$ mm, $y = 2.5$ mm. The gas flow through the gliding arc was 11.8 slm.

5. Plasma modification of polypropylene

The water contact angle (WCA) of plasma treated PP was measured by the sessile drop (3 μl of demineralized water) method using the See System (Advex Instruments). The surface free energy (SFE) was roughly determined using Arcotest - testing marker QuickTest 38 (TQC) designed to discriminate polymer surfaces with the free energy above and below 38 mN/m . In some experiments, SFE was determined from CA measurements using two liquids, water and diiodomethane.

The surface chemical composition was characterized by XPS using the Axis Supra (Kratos Analytical) spectrometer with the monochromatic $K\alpha$ radiation. The survey spectrum was measured using the pass energy of 80 eV with the step of 1 eV. The pass energy of 20 eV, the step 0.1 eV and

five-time accumulation were used for the high resolution measurements. All the spectra were acquired in at least two different places (to ensure that the modified PP is measured) in the so-called slot mode in which the electrons were collected from an area of 3 x 2 mm. All the samples were analyzed maximum 1 hour after the treatment. The XPS C 1s spectra were fitted by the CASA XPS software after the subtraction of Shirley-type background.

The tensile strength of the adhesive joint between PP and aluminum stripes (25 x 100 x 5 mm and 25 x 100 x 1.5 mm, respectively) created with the epoxy adhesive DP190 (3M) was measured according to the norm (668510) CSN EN 1465 [17]. The aluminum stripe was mechanical roughed for ensuring an excellent adhesion to the epoxy glue. The dimension of the joint part was 12.5 x 25 mm. For each treatment condition, a set of 10 samples was prepared. The preparation of the PP-epoxy-Al joint was carried out one day after the plasma treatment. The joints were weighted down by the weight of 0.7 kg per sample for the next 24 hours. The tests were carried out after at least seven days when the cure of adhesive was ensured. The free ends of the stripes were gripped by claws of the ZD 10 (W + B) tensile tester and pulled away with the velocity of 20 mm/min.

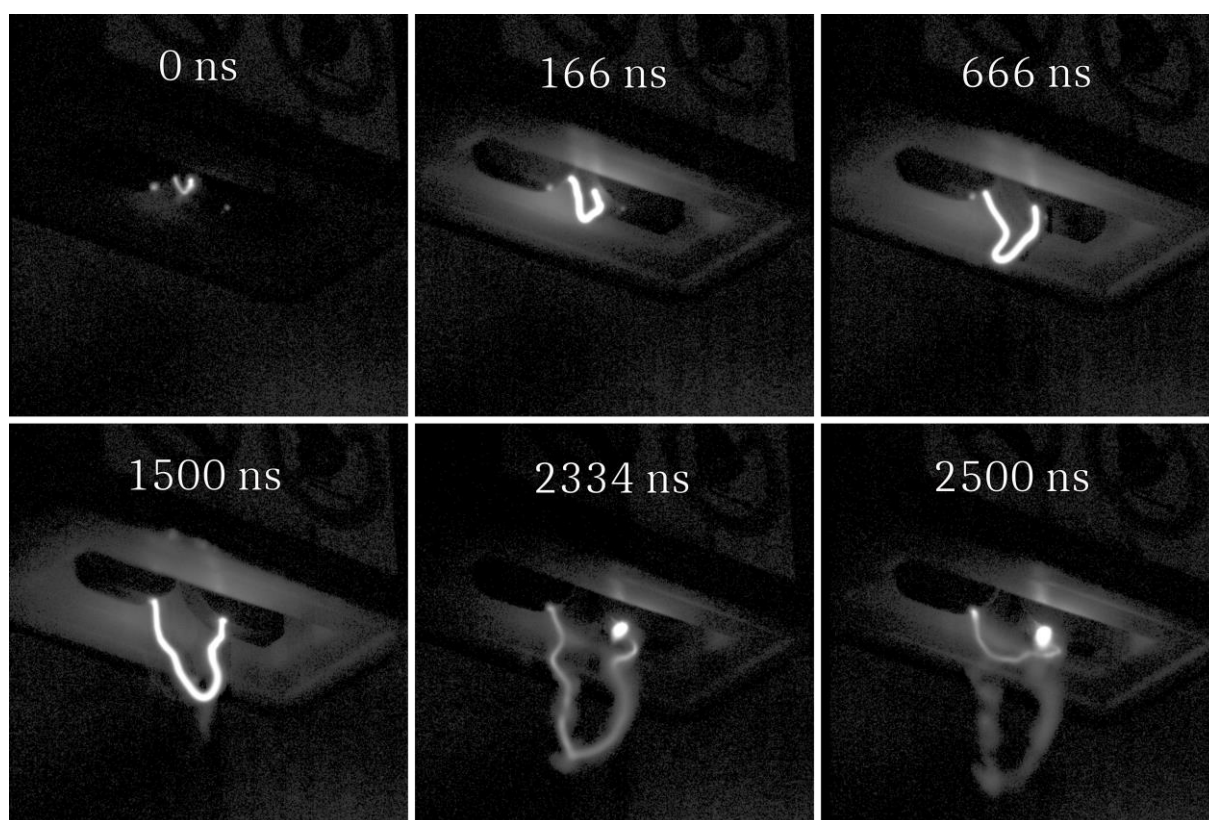


Fig. 4. Ultrafast camera imaging with 2000 frame/s and frame exposure time of 48 μ s.

Acknowledgement

This work has been supported by the Ministry of Industry and Trade in the frame of TRIO project FV10342 and by the Ministry of Education, Youth and Sports (MEYS) of the Czech Republic under the project CEITEC 2020 (LQ1601). Part of the work was carried out with the support of CEITEC Nano Research Infrastructure (ID LM2015041, MEYS, 2016-2019), Central European Institute of Technology, Brno University of Technology. The authors gratefully acknowledge also the financial support from the MEYS of the Czech Republic under NPU I program (projects No. LO1207 and No. LO1210) and under OP VVV Programme (project No. CZ.02.1.01/0.0/0.0/16 013/0001638 CVVOZE Power Laboratories - Modernization of Research Infrastructure).

References

- [1] A. Fridman, S. Nester, L. A. Kennedy, A. Saveliev, O. Mutaf-Yardimci, Gliding arc gas discharge, *Progress in Energy and Combustion Science* 25 (2) (1999) 211.
- [2] J. Zhu, Z. Sun, Z. Li, A. Ehn, M. Aldén, M. Salewski, F. Leipold, and Y. Kusano, Dynamics, OH distributions and UV emission of a gliding arc at various flow-rates investigated by optical measurements, *Journal of Physics D: Applied Physics* 47 (29) (2014) 295203.
- [3] Z. Bo, J. H. Yan, X. D. Li, Y. Chi, B. Chéron, and K. F. Cen, The dependence of gliding arc gas discharge characteristics on reactor geometrical configuration, *Plasma Chemistry and Plasma Processing* 27 (6) (2007) 691.
- [4] Z. Sun, J. Zhu, Z. Li, M. Aldén, F. Leipold, M. Salewski, and Y. Kusano, Optical diagnostics of a gliding arc, *Optics Express* 21 (5) (2013) 6028.
- [5] W. Wang, D. Mei, X. Tu, A. Bogaerts, Gliding arc plasma for co₂ conversion: Better insights by a combined experimental and modelling approach, *Chemical Engineering Journal* 330 (2017) 11.
- [6] Z. Bo, J. Yan, X. Li, Y. Chi, K. Cen, Nitrogen dioxide formation in the gliding arc discharge-assisted decomposition of volatile organic compounds, *Journal of Hazardous Materials* 166 (2-3) (2009) 1210.
- [7] B. Benstaali, P. Boubert, B. Cheron, A. Addou, J. Brisset, Density and rotational temperature measurements of the OH and NO radicals produced by a gliding arc in humid air, *Plasma Chemistry and Plasma Processing* 22 (4) (2002) 553.
- [8] R. Burlica, M. J. Kirkpatrick, B. R. Locke, Formation of reactive species in gliding arc discharges with liquid water, *Journal of Electrostatics* 64 (1) (2006) 35.
- [9] L. Potočňáková, J. Šperka, P. Zikán, J. J. van Loon, J. Beckers, V. Kudrle, Gliding arc in noble gases under normal and hypergravity conditions, *IEEE Transactions on Plasma Science* 42 (10) (2014) 2724.
- [10] A. Indarto, J.-W. Choi, H. Lee, H. K. Song, Effect of additive gases on methane conversion using gliding arc discharge, *Energy* 31 (14) (2006) 2986.
- [11] S. Liu, D. Mei, L. Wang, X. Tu, Steam reforming of toluene as biomass tar model compound in a gliding arc discharge reactor, *Chemical Engineering Journal* 307 (2017) 793.
- [12] B. S. Patil, F. Peeters, G. J. van Rooij, J. Medrano, F. Gallucci, J. Lang, Q. Wang, V. Hessel, Plasma assisted nitrogen oxide production from air: Using pulsed powered gliding arc reactor for a containerized plant, *AIChE Journal* 64 (2) (2018) 526.
- [13] K. Hori, S. Fujimoto, Y. Togashi, T. Kuroki, M. Okubo, Improvement in molecular-level adhesive strength of PTFE film treated by atmospheric plasma combined processing, in: *Industry Applications Society Annual Meeting, 2017 IEEE*, pp. 1
- [14] M. Gürsoy, M. Karaman, Wiley-VCH, *Surface Treatments for Biological, Chemical and Physical Applications*, 2016.
- [15] R. Pearse, A. Gaydon, *The identification of molecular spectra* (1950).
- [16] J. Voráč, P. Synek, V. Procházka, T. Hoder, State-by-state emission spectra fitting for non-equilibrium plasmas: Oh spectra of surface barrier discharge at argon/water interface, *Journal of Physics D: Applied Physics* 50 (29) (2017) 294002.
- [17] Adhesives - Determination of tensile lap-shear strength of bonded assemblies, Standard, European Committee for Standardization, Brussels, BE (Oct. 2009).

MICROPARTICLES TRAPPED BY OPTICAL TWEEZERS - MEASUREMENTS WITH AND WITHOUT A PLASMA

Viktor Schneider¹ and Holger Kersten¹

¹Institute of Experimental and Applied Physics, Christian-Albrechts-University Kiel, Germany
E-mail: schneider@physik.uni-kiel.de

The idea to use microparticles as electrostatic or thermal probes for plasma diagnostic purposes was implemented during the last decades by several experiments [1]-[5]. Because of their small size, microparticles can be utilized in studies of dynamic processes [6] as well as single probes in plasma sheath diagnostics [7, 8]. In this study SiO₂ microparticles are in an optical trap to manipulate them in the environment of a CCP discharge. In contrast to common plasma diagnostic tools (e.g. Langmuir probes, calorimetric probes, mass spectrometers etc.), in the μ PLASMA (microparticles in a discharge with laser assisted manipulation) experiment particles can be regarded as noninvasive single probes [9]. The displacement of the particle in the laser trap is observed to measure a force while it is moving relatively to the plasma, either deeper into the sheath or into the plasma bulk [see Fig. 1 a)]. The benefit of the presented technique is the possibility to retain the particle even after the plasma is turned off. Systematic measurements of the residual charges [10] on the particle after switching off the plasma have been performed [see Fig. 1 b)], depending on the position of the particle in the plasma bulk or the sheath, respectively. Furthermore, charging of the spheres by UV radiation in an external electric field is investigated and discussed. The measurements indicate electron induced secondary electron emission and an emission yield above unity for energies about 100 eV [11].

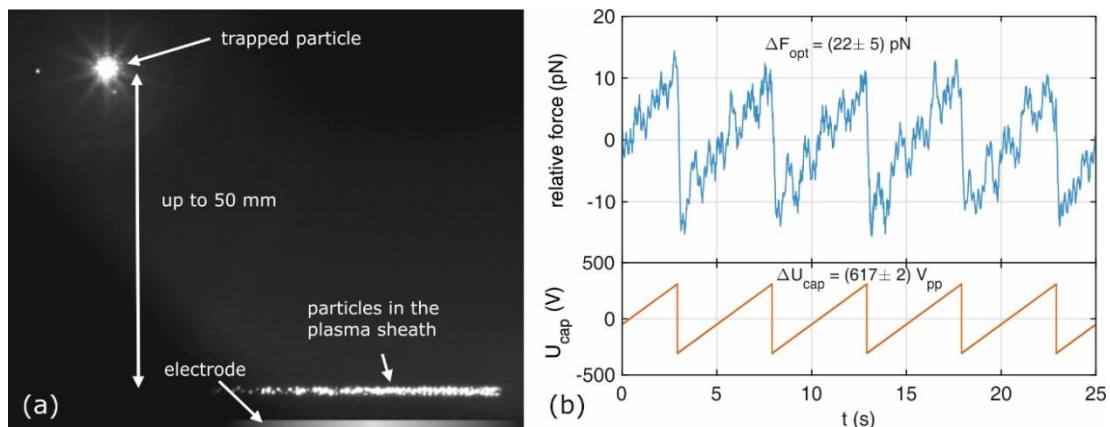


Fig. 1. a) Photo of a trapped probe particle moved into the plasma bulk ~50 mm above the other levitating particles in the plasma sheath. b) Force measured from the positions of a confined, charged particle after the plasma was switched off and a sawtooth potential is applied on a capacitor electrode to generate an electric field and to determine the residual charge.

References

- [1] A.A. Samarian, B.W. James, Plasma Phys. Control. Fusion. **47**(2005), B629.
- [2] G. Thieme et al., Faraday Discuss. **137**(2008), 157-171.
- [3] H. R. Maurer et al., Contrib. Plasma Phys. **51**(2011), 218-227.
- [4] G. Schubert et al., Contrib. Plasma Phys. **52**(2012), 827.
- [5] P. Hartmann et al., Plasma Sources Sci. Technol. **23**(2014), 045008.
- [6] J. Schablinski et al., Phys. Plasmas **22**(2015), 043703.
- [7] J. Carstensen et al., IEEE Trans. Plasma Sci. **41**(2013), 764.
- [8] A. Douglass et al., J. Plasma Phys. **82**(2016), 615820402.
- [9] V. Schneider, H. Kersten, Rev. Sci. Instrum. **89**, (2018), 103505.
- [10] L. Couëdel et al., Contrib. Plasma Phys. **49**(2009), 235-259.
- [11] B. Horváth et al., Plasma Sources Sci. Technol. **26**, (2017), 124001

DISCHARGE BREAKDOWN STUDIED UNDER HIGH PRESSURE IN ARGON

Matej Klas¹, Štefan Matejčík¹, Marija Radmilovic² Branislav Radjenovic²

¹Department of Experimental Physics, Comenius University, Mlynská dolina F-2,
842 48 Bratislava, Slovakia

²Institute of Physics, University of Belgrade - Pregrevica 118, 11080 Zemun, Serbia

E-mail: matej.klas@gmail.com

An investigation of the breakdown voltage of argon has been made at room temperature under high pressure conditions. The measurements were performed for the stainless-steel electrodes at sphere to plane geometry separated from 5 μ m up to 100 μ m with the pressure range from 1bar up to 60bar.

1. Introduction

It has been found, that Paschen's law is no longer valid in compressed gases and in high DC electric field in the order of 10-20MV/m [1-3]. This failure of Paschen's law was associated with the onset of the pre-breakdown current attributed to the field emission of electrons from the cathode. However, the surface properties of the electrodes and also the purity of the gas plays important role in the mechanism of discharge ignition [1]. In this paper we have focused on the study of the influence of the electrodes on the gradual evolution of the breakdown voltages at electric field up to 200MV/m and the temporal evolution of the breakdown.

2. Experimental setup

The measurements were carried out using Argon of 6.0 purity and high pressure chamber equipped with stainless steel electrodes of sphere to plane geometry. The schematic view of apparatus is shown in Fig. 1. One of the electrodes was fixed and the other one was movable continuously with micrometre screw with resolution of $\sim 2\mu$ m in the range of 5 μ m to 100 μ m. To avoid fast damage of the electrode surface after each discharge ignition, a shutdown mechanism was implemented in circuit released by the current probe. The breakdown voltages and the current waveforms were measured by Tektronix probe P6015A, Pearson current monitor 2877 and recorder by oscilloscope (Agilent DSO5032A).

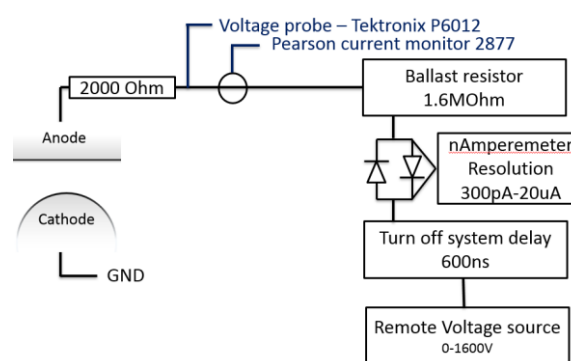


Fig. 1. Schematic view of experimental setup.

3. Results and discussion

Typical evolution of the breakdown voltage as a function of the number of the breakdowns at different pressure is shown in Fig 2. We have observed following behavior at different condition:

- 1) for fresh polished electrodes are inserted in to the chamber, the breakdown voltage is measured with uncertainty around 10-15%
- 2) after several of breakdowns, in some cases even after first breakdown the difference in breakdown voltage may reach 50 -90% of initial value.

3) at the electrode distance of 10 μ m and pressure 50bar we have observed a similar value of direct breakdown as for low pressure of 10bar.

This indicates that at high pressure a rapid change of electrode surface properties plays crucial role in breakdown voltage at high electric fields. This observation is supported as well by the state of the electrodes after the discharges as displayed in the Figure 3. The electrodes, which were well prepared (polished) prior the first discharges, show strong modifications by the electric discharges.

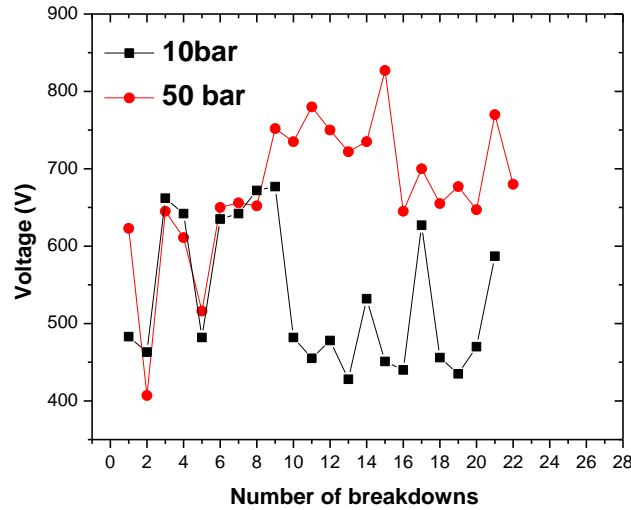


Fig. 2. Effect of conditioning on the breakdown field of compressed argon at 50bar and 10bar and electrode distance of 10 μ m

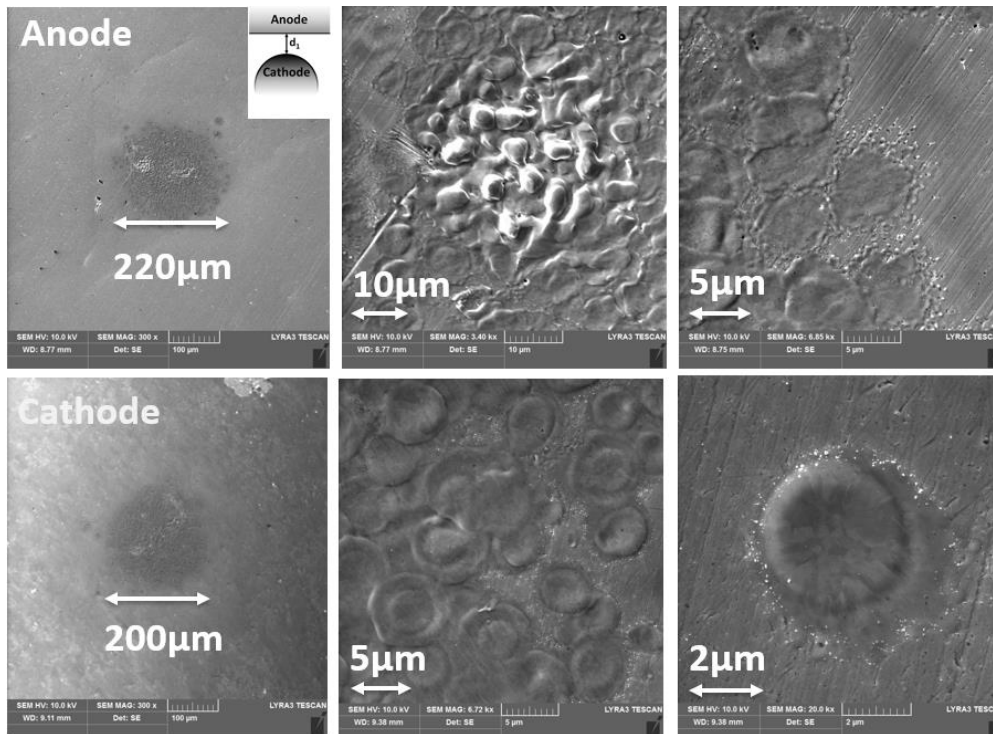


Fig. 3. Electrode surface after several thousands of breakdowns at 50bar, $d=10\mu$ m

Acknowledgements

This project has received funding from the European Union's Horizon 2020 research and innovation programme under grant agreement No. 692335. This work has been supported by Development Agency Projects Nr. APVV-15-580, No. SK-SRB-2016-0035, and Ministry of Education and Science Republic of Serbia O171036 project.

4. References

- [1] Meek J M Craggs I D 1953 *Clarendon Press, Oxford*
- [2] Howell A 1939 *Trent AIEE*, **58**, pp. 193-204
- [3] Watson P Sharbaugh, H 1969 *Journal of Applied Physics*, Volume 40, Issue 1, p.328-334, 1969
- [4] Cookson A 1970 *Proc. IEE*, Vol. **117**, No. 1

CONTROLLING DISCHARGE REGIMES IN PULSED, SINGLE-FILAMENT DIELECTRIC BARRIER DISCHARGES

Hans Höft, Manfred Kettlitz, Markus M. Becker, Ronny Brandenburg

Leibniz Institute for Plasma Science and Technology (INP Greifswald)

Felix-Hausdorff-Straße 2, 17489 Greifswald, Germany

E-mail: hans.hoeft@inp-greifswald.de

In this study, pulsed dielectric barrier discharges (DBDs) in a single-filament arrangement were investigated in N_2 - O_2 gas mixtures by means of fast optical and electrical diagnostics. The focus was on the discharge inception, i.e. what triggers the breakdown, and how it can be manipulated. It was shown, how the variation of pulse width, slope steepness and gas mixture can be used to control discharge properties down to the fundamental level, e.g. the occurrence of different breakdown regimes. It was found that all effects on the DBD characteristics are mainly connected to the manipulation of the pre-ionisation, which demonstrates the importance of volume memory processes on the breakdown and development of single-filament DBDs.

1. Introduction

Non-thermal plasmas generated in dielectric barrier discharges (DBDs) at atmospheric pressure feature high electron energies while heavier particles (molecules, atoms, ions) remain at low energies, i.e. the gas temperature stays near 300 K [1]. This allows an efficient generation of active species, which are important for industrial applications such as ozone generation, surface modification and exhaust treatment [2].

The “tailoring” of a DBD for a specific application is one of the main goals of current research. This requires a distinct control of the DBD characteristics. The inception and development of the discharge is strongly influenced by processes in the so-called (Townsend) pre-breakdown phase, i.e. the time before the actual breakdown occurs [3-5]. While in sinusoidal-operated DBDs the pre-phase lasts for at least several hundred nanoseconds, in pulsed-operated DBDs this duration is limited by the rise time of the high-voltage (HV) pulse. Pulsed-operation, however, offers an additional electrical control parameter (apart from voltage amplitude, HV slope steepness and repetition frequency): the pulse width [6,7]. In addition to the analysis of pulse width and slope steepness variation, the influence of the O_2 content in O_2/N_2 gas mixtures was investigated. Furthermore, the interrelations between the DBD control by pulse width and O_2 admixture were evaluated.

2. Experimental Set-up

For the investigations a single filament DBD arrangement (double-sided, half-sphere Al_2O_3 covered electrodes) with 1 mm gap was used, see figure 1.

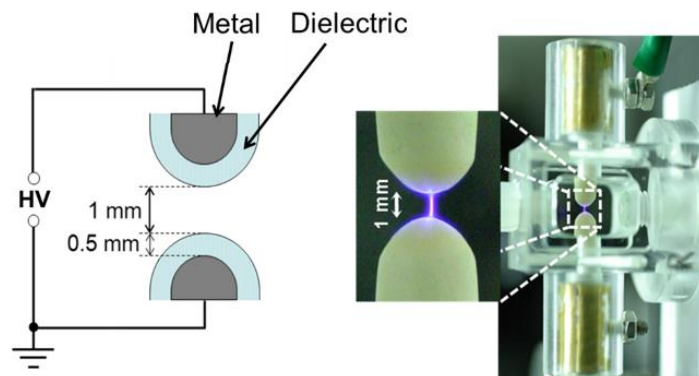


Fig. 1. Electrode configuration and discharge cell for single filament arrangement.

The DBDs were driven by unipolar positive HV pulses with 10 kV amplitude and 10 kHz repetition rate. The pulse width was varied from 50 to 0.2 μ s and the HV slope steepness from 45 to 200 ns (10-

90% rise time) for 0.1 vol% O₂ in N₂. The HV slope steepness was set by inserting a variable resistor in line between the HV pulse generator and the DBD cell. The O₂ concentration in N₂ was changed from 0.1 to 20 vol% at a fixed pulse width. Synchronised, fast electrical, iCCD and streak measurements are performed to record the electrical characteristics as well as the spatio-temporal DBD development; see figure 2 for an overview of the set-up [8].

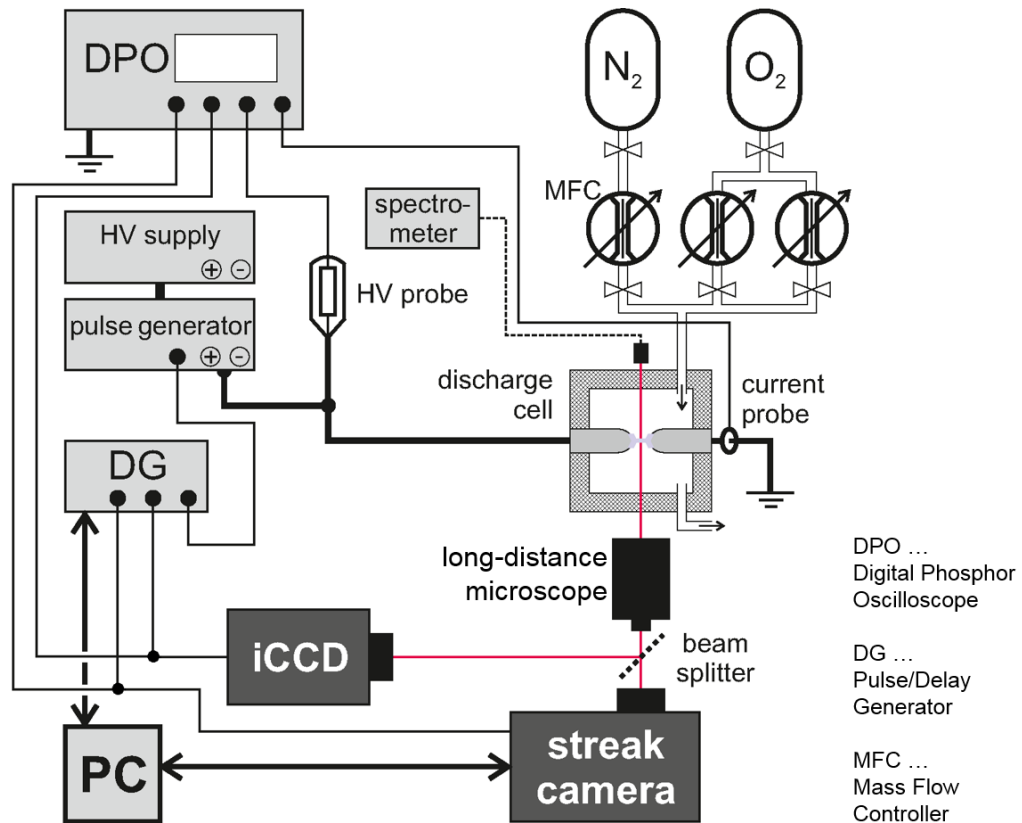


Fig. 2. Scheme of experimental set-up with HV, and gas supply, and applied, synchronised electrical and optical diagnostics.

3. Results and Discussion

In figure 3, an overview of the applied HV waveform and the total discharge current is shown. A single discharge event occurs at the rising and falling slopes of the HV pulse. The synchronised measurement of voltage and current enables e.g. the determination of breakdown voltage, transferred charge, and consumed electrical energy [8].

Increasing the HV slope steepness leads to higher discharge current peaks, transferred charge and consumed energy [9], see figure 4. A higher discharge power stabilises the discharge, i.e. the temporal discharge jitter is decreasing with increasing HV pulse slope steepness. It was found that the increase of the consumed energy for steeper HV slopes also causes an increase of the pre-ionisation, which decreases the voltage required for breakdown. On the other hand, a smoother HV slope enlarges the range, where the applied voltage is near the breakdown voltage. These data were obtained by a statistical analysis of the breakdown using 12000 single discharge events per slope and HV steepness.

All further data in this contribution concerning the pulse width and O₂ concentration variation were obtained for the steepest HV slope.

The DBD breakdown characteristics at the falling slope of the HV pulse can be controlled by the pulse width [9,10]. Besides the effects of HV slope steepness, the pulsed operation offers via the pulse width

an effective parameter to set the pre-ionisation by shifting the DBDs in the after-glow of the previous discharge using asymmetrical HV pulse waveforms (see figure 3). The breakdown characteristics of these subsequent DBDs igniting in different pre-ionised conditions defined by the residual charge carrier densities originated from the previous DBD in the gap can be controlled down to the fundamental level.

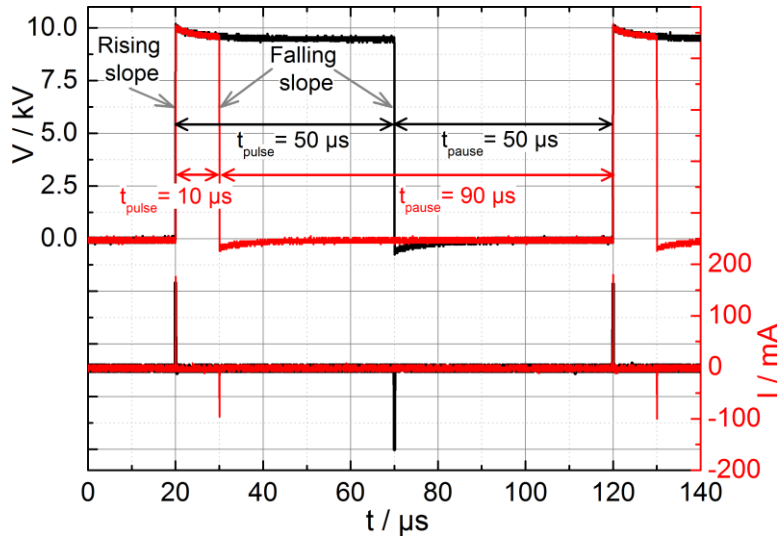


Fig. 3. Overview of applied voltage and corresponding current pulses, and visualisation of the concept of pulse width variation.

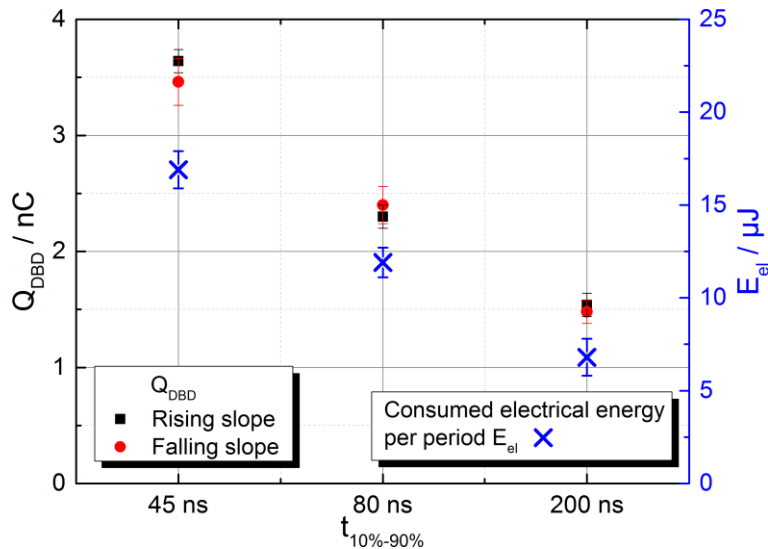


Fig. 4. Transferred charge per single discharge event and consumed electrical energy per period (obtained by Q - V plot) for three different slope steepnesses in 0.1 vol% O_2 in N_2 .

For instance, four different breakdown regimes in single filament DBDs for 0.1 vol% O_2 in N_2 were described and correlated to the processes during their pre-breakdown phases [10]. The “classical” DBD development (cathode-directed streamer followed by a transient glow discharge) can be controlled in a certain range, followed by a transition to a breakdown regime featuring a simultaneous propagation of a cathode- and an anode-directed streamer. Finally, a reignition of the previous DBDs without any propagation occurs. These regimes could be induced by reducing the pulse width (time between two subsequent DBDs), i.e. increasing the pre-ionisation level. Consequently, this manipulation of the pre-ionisation level was found to be the crucial point to affect and consequently control the DBD behaviour. This was confirmed by time-dependent, spatially one-dimensional modelling of the DBD [11].

Another control parameter is the O_2/N_2 ratio, which has a significant impact on the DBD characteristics, too [12,13]. While the transferred charge in the investigated DBDs depends not on the pulse width, but on the O_2 concentration (higher $[O_2] \rightarrow$ lower transferred charge); there are some physical quantities, which show a similar behaviour either for increasing pulse width or increasing O_2 concentration. This is shown in figure 5 for the breakdown voltage, in figure 6 for the maximal velocity of the cathode-directed streamer obtained in front of the cathode using streak camera images, and in figure 7 for the discharge emission duration (using spectrally and spatially integrated streak images). The impact of the O_2 concentration was evaluated at the rising slope for $10 \mu s$ pulse width to minimise the effect of the pre-ionisation caused by the previous discharge. The absolute values do not agree, but the same tendency is clearly visible: an increase of the pulse width as well as the O_2 concentration leads to shorter emission duration and higher propagation velocities.

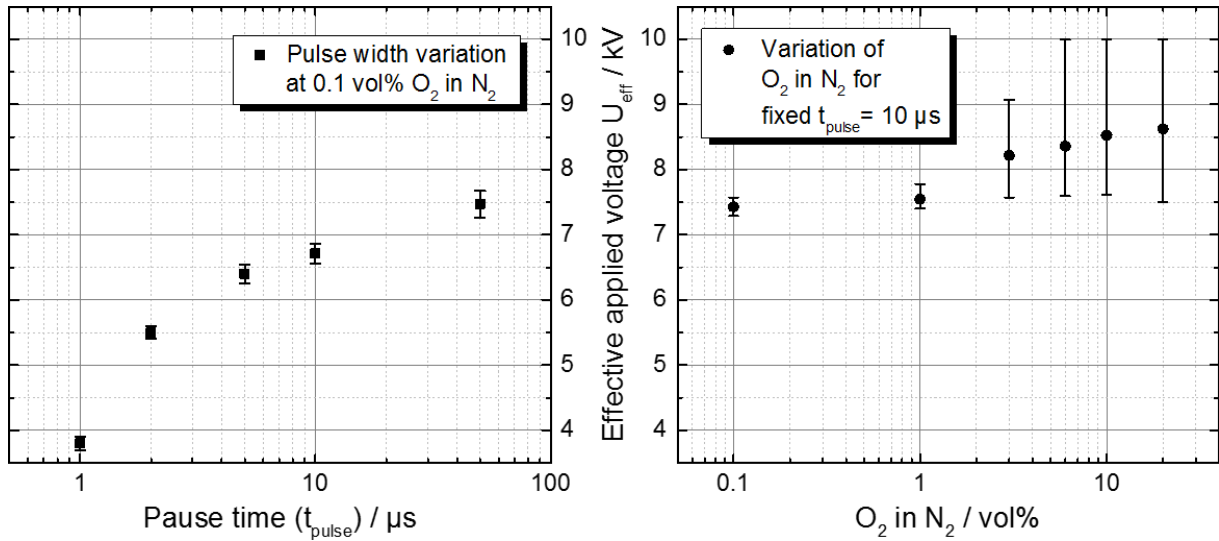


Fig. 5. Effect of pulse width (at falling slope for 0.1 vol% O_2 in N_2) and O_2/N_2 ratio variation (at rising slope for $t_{\text{pulse}} = 10 \mu s$) on the maximal propagation velocity of the cathode-directed streamer.

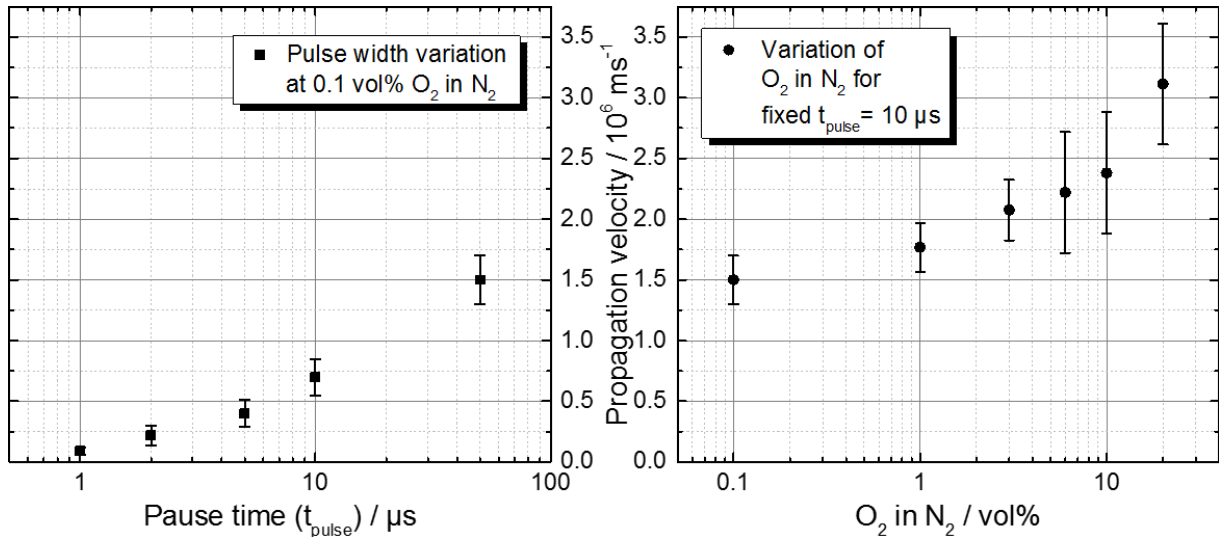


Fig. 6. Effect of pulse width (at falling slope for 0.1 vol% O_2 in N_2) and O_2/N_2 ratio variation (at rising slope for $t_{\text{pulse}} = 10 \mu s$) on the maximal propagation velocity of the cathode-directed streamer ($50 \mu m$ in front of cathode).

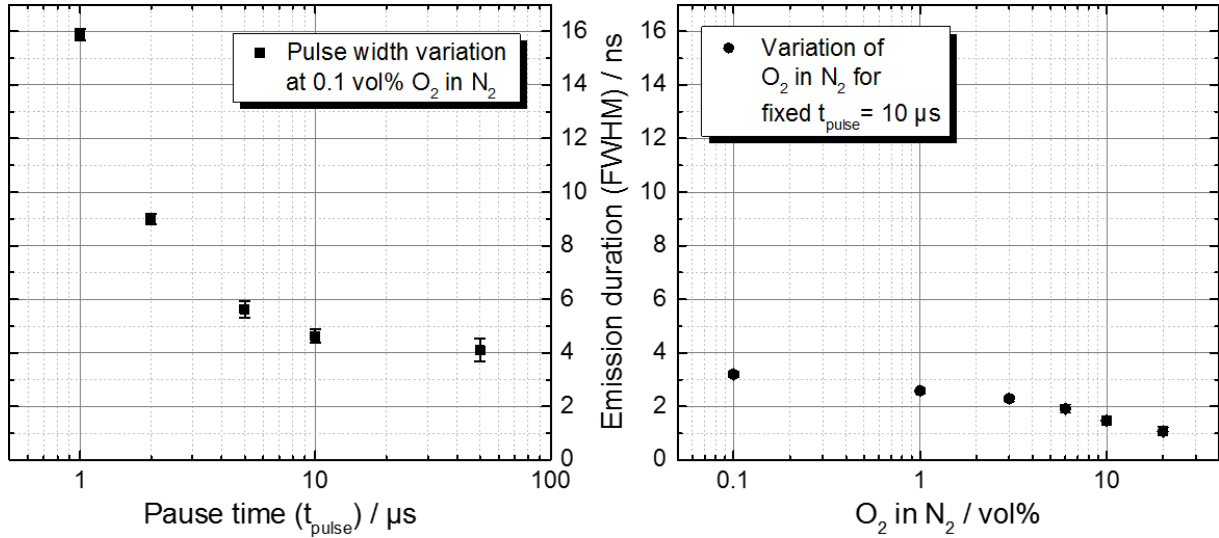


Fig. 7. Effect of pulse width (at falling slope for 0.1 vol% O₂ in N₂) and O₂/N₂ ratio variation (at rising slope for $t_{\text{pulse}} = 10 \mu\text{s}$) on the full width at half maximum (FWHM) of the emission duration.

In summary, it can be stated, that to some extent, several of the reported effects achieved by varying the pulse width at a fixed O₂ concentration in N₂ (0.1 vol%) were also observed for a fixed pulse width and changing O₂ content. To emphasise this statement, the emission structure of the DBD during the pre-breakdown phase and the following breakdown was analysed. Therefore, emission profiles obtained by spatially averaging the SPS signals (second positive system of N₂(C) at 337 nm) over 250 μm in front of the anode were used [11]. These profiles show the temporal emission structure synchronised with the applied voltage for pulse width variation at a fixed gas composition of 0.1 vol% O₂ in N₂ (figure 8, left), and for O₂ concentration variation of a fixed HV pulse width of 1 μs (figure 8, right). This specific pulse width was chosen, because a simultaneous cathode- and anode-directed (streamer) propagation occurs at $t_{\text{pulse}} = 1 \mu\text{s}$.

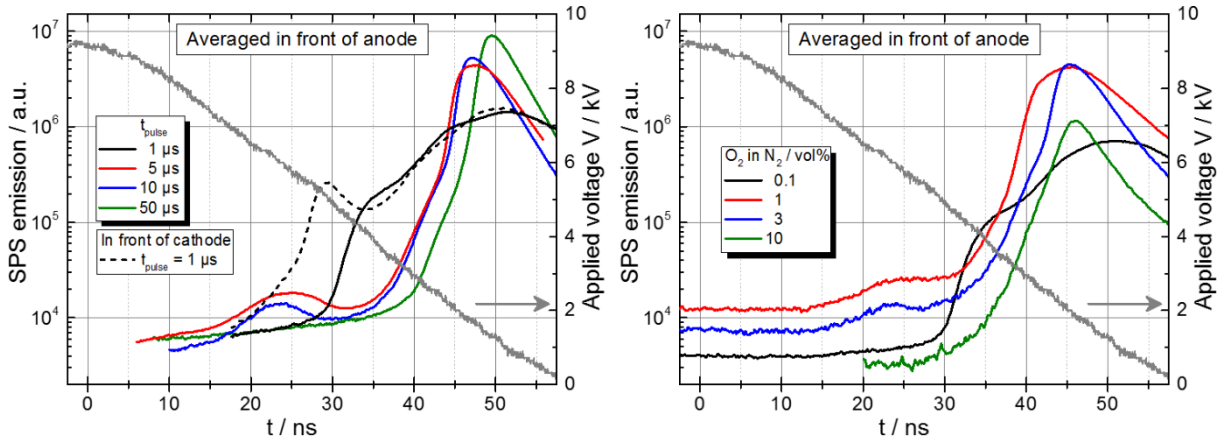


Fig. 8. Time-resolved, spatially averaged emission profiles (SPS of N₂(C) at 337 nm) at the falling slope synchronised with applied voltage for HV pulse width variation at 0.1 vol% O₂ in N₂ (left), and O₂ in N₂ variation at $t_{\text{pulse}} = 1 \mu\text{s}$ (right).

For O₂ concentrations of 1 vol% and higher, the “double-propagation” regime vanishes. A weak temporal delimited diffuse SPS emission before the actual breakdown near the anode was observed in the pre-breakdown phase for O₂ concentrations up to 3 vol% O₂ in N₂, similar to the one occurring for pulse widths of 5 and 10 μs between 25 and 35 ns, see figure 8. This isolated emission is correlated with the acceleration of residual electrons by the increasing electric field towards the anode. These residual electrons also cause a shift of the inception point of the cathode directed propagation (positive streamer)

towards the cathode [11]. The occurrence of the isolated emission in front of the anode during the pre-phase indicates an elevated pre-ionisation, which has significant consequences on the DBD properties like spatio-temporal discharge development or on duration and amplitude of the electrical discharge current. Furthermore, there is a decrease of the breakdown voltage, the streamer propagation velocity and the discharge current maximum together with an increase of the duration of the emission and the discharge current. For O_2 concentrations above 3 vol% O_2 in N_2 , no isolated emission in the pre-breakdown phase of the discharge in the falling slope was detected.

The increase of the O_2 concentration has changed the intrinsic properties of the gas, i.e. due to the high electronegativity of oxygen, negative ions are formed, which lead to a decrease in the (electron) pre-ionisation. Moreover, O_2 quenches excited N_2 molecules effectively by collisions. Some of these N_2 species contribute to the energy storage during the DBD afterglow, e.g. metastable $N_2(A)$ [14].

Consequently, a higher O_2 concentration means a decrease in space charge leading to a faster decay of the ionisation in the gap after a discharge event. Therefore, an increase of O_2 concentration leads to similar effects as a prolongation of the pulse width at 0.1 vol% O_2 in N_2 in a specific parameter range of the pulse width and O_2/N_2 ratio. Hence, the response of DBD properties to changing pre-ionisation levels seems to be a general principle of DBD control.

4. Summary and Outlook

The investigation of pulsed DBDs in a single-filament arrangement have revealed that volume memory effects are caused by residual charge carrier densities originating from previous discharge. The dynamics of residual electrons during the pre-breakdown phase have a strong impact on the discharge development leading to different breakdown regimes. Besides the energy input, which is increased with HV slope steepness, pulsed operation enables precise control of the pre-ionisation via pulse width variation, i.e. using the time between subsequent discharges. For a higher O_2/N_2 ratio, the electron attachment and faster quenching processes reduce the pre-ionisation in the gap. Consequently, pulse width reduction and O_2 concentration increase have similar effects. In figure 9, the DBD control mechanisms and their interrelation emphasising the importance of volume pre-ionisation are summarised.

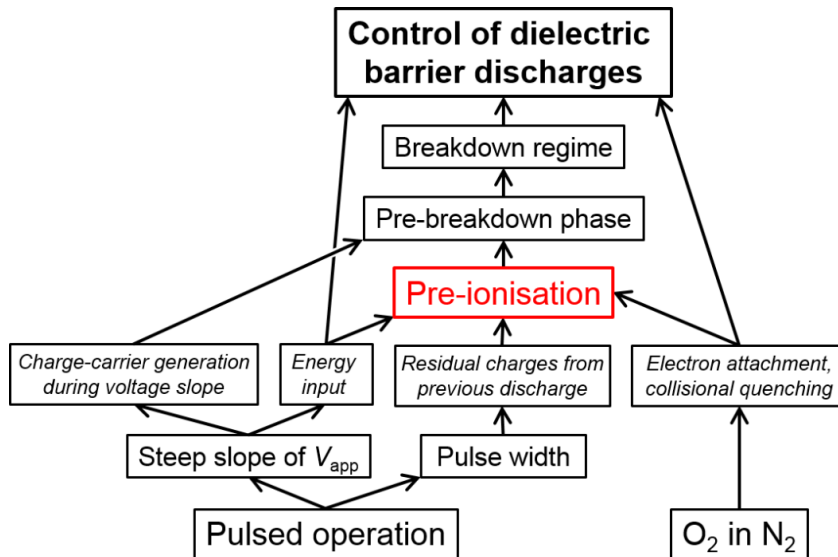


Fig. 9. Discharge control mechanisms via HV pulse width, slope steepness, and O_2/N_2 ratio.

So far, the discussion has not addressed the role of surface charges, especially their temporal development, which is assumed to be on the microsecond time scale [15]. The future inclusion of surface processes is important to evaluate the correlation between volume and surface memory effects as proposed e.g. in [16].

5. References

- [1] A. Fridman, A. Chirokov, A. Gutsol, *J. Phys. D: Appl. Phys.* **38** R1 (2005).
- [2] U. Kogelschatz, *Plasma Chem. Plasma Process.* **23** 1 (2003).
- [3] K.V. Kozlov, H.-E. Wagner, R. Brandenburg, P. Michel, *J. Phys. D: Appl. Phys.* **34** 3164 (2001).
- [4] Y.V. Yurgelenas, H.-E. Wagner, *J. Phys. D: Appl. Phys.* **39** 4031 (2006).
- [5] T. Hoder, R. Brandenburg, R. Basner, K. D. Weltmann, K. V. Kozlov, H.-E. Wagner, *J. Phys. D: Appl. Phys.* **43** 124009 (2010).
- [6] X. Lu, M. Laroussi, *J. Phys. D: Appl. Phys.* **39** 1117 (2006).
- [7] M. Kettlitz, H. Höft, T. Hoder, K.-D. Weltmann, R. Brandenburg, *Plasma Sources Sci. Technol.* **22** 025003 (2013).
- [8] M. Kettlitz, H. Höft, T. Hoder, S. Reuter, K.-D. Weltmann, R. Brandenburg, *J. Phys. D: Appl. Phys.* **45** 245201 (2012).
- [9] H. Höft, M.M. Becker, D. Loffhagen, M. Kettlitz, *Plasma Sources Sci. Technol.* **25** 064002 (2016).
- [10] T. Hoder, H. Höft, M. Kettlitz, K.-D. Weltmann, R. Brandenburg, *Phys. Plasmas* **19** 070701 (2012).
- [11] H. Höft, M. Kettlitz, M.M. Becker, T. Hoder, D. Loffhagen, R. Brandenburg, K.-D. Weltmann, *J. Phys. D: Appl. Phys.* **47** 465206 (2014).
- [12] K.V. Kozlov, R. Brandenburg, H.-E. Wagner, A.M. Morozov, P. Michel, *J. Phys. D: Appl. Phys.* **38** 518 (2005).
- [13] H. Höft, M. Kettlitz, T. Hoder, K.-D. Weltmann, R. Brandenburg, *J. Phys. D: Appl. Phys.* **46** 095202 (2013).
- [14] G. Dilecce, P. F. Ambrico, S. de Benedictis, *Plasma Sources Sci. Technol.* **16**, 070701 (2012).
- [15] R. Tschiersch, S. Nemschokmichal, M. Bogaczyk, J. Meichsner, *J. Phys. D: Appl. Phys.* **50** 105207 (2017).
- [16] Y. Akishev, G. Aponin, A. Balakirev, M. Grushin, V. Karalnik, A. Petryakov, N. Trushkin, *Plasma Sources Sci. Technol.* **20** 024005 (2011).

SURFACE REACTIONS OF ATOMIC LAYER ETCHING PROCESSES

Satoshi Hamaguchi¹, Yuki Okada¹, Shunpei Shigeno¹, Michiro Isobe¹,
Tomoko Ito¹, and Kazuhiro Karahashi¹

¹*Center for Atomic and Molecular Technologies, Graduate School of Engineering,*

Osaka University

E-mail: hamaguch@ppl.eng.osaka-u.ac.jp

Alternating application of fluorocarbon plasmas with no bias energy and Ar plasma with low bias energy to a SiO₂ film is known to cause atomic layer etching (ALE) of its surface. In this ALE process, it is assumed that a thin layer of fluorocarbon is deposited on the SiO₂ surface in the first step and low-energy Ar⁺ ion irradiation causes mixing of deposited fluorocarbon with atoms of the underlying SiO₂ surface in the second step, promoting desorption of volatile SiF_x and CO from the surface until fluorocarbon on the surface is completely exhausted. In this study, we have examined the surface reactions of such processes, using molecular dynamics (MD) simulations. It has been found, however, the actual surface reactions are not as simple as described above. In the Ar⁺ ion irradiation step, preferential sputtering of O atoms occurs even at low ion incident energy, which makes the surface more Si rich and also promotes the formation of Si-C bonds in the presence of a deposited fluorocarbon layer. In other words, in deficiency of O atoms on a SiO₂ film surface, low-energy Ar⁺ ion irradiation may not be able to remove C atoms completely from the surface. Under such conditions, more carbon atoms may remain on the surface after each ALE cycle and etch stop may eventually occur after several ALE cycles.

1. Introduction

As the sizes of semiconductor devices continue to diminish and are now approaching atomic scales, the downsizing of transistors following Moore's law is bound to end in the near future. The continuing market demand for higher performance and lower energy consumption of large-scale integrated (LSI) circuits therefore necessitates further innovation in semiconductor technologies. For example, new device technologies such as three-dimensional (3D) device structures and devices based on non-silicon materials have been invented to circumvent the requirement of further device miniaturization. The precise control of device structures at the atomic level over a large area is crucial for the manufacturing of such devices and atomic layer processes, i.e., atomic layer deposition (ALD) and atomic layer etching (ALE), are considered to be some of the most effective means to achieve such goals. Unlike conventional deposition or etching processes, an atomic layer process requires self-limiting reactions, i.e., surface reactions that limit the process only to (essentially) a monolayer in each process cycle and therefore allow a highly uniform process over a large area. In this study, we have used molecular dynamics (MD) simulations for plasma-based ALE processes for SiO₂. Experimental studies of such processes were performed by G. S. Oehrlein *et al.* [1-3] and this study supplements earlier MD study on similar processes by S. Rauf *et al.* [4]

2. Molecular Dynamics (MD) Simulation

2.1 Outline of Simulation

In MD simulation, the equations of motion for each Si, O, C, F, or Ar atom are solved numerically. The interatomic potential functions used in this study are those similar to Stillinger-Weber potential functions [5]. In the simulation, a rectangular box of a SiO₂ crystal (β -cristobalite) is formed with periodic boundary conditions in the horizontal directions. As in the experimental study by Oehrlein *et al.* [2], a fluorocarbon film of a thickness of 7 Å is deposited on the substrate. Then low energy Ar⁺ ions are injected into the substrate, which etch SiO₂ substrate by enhancing chemical reactions between SiO₂ and fluorocarbon molecules. The incident ion energy is set sufficiently low, so that Ar⁺ ions hardly sputter a SiO₂ substrate by physical sputtering only. In our MD simulation, no electrostatic charge effect is taken into account, so incident Ar⁺ ions are modelled by charge-neutral Ar atoms and their role is to

provide sufficient kinetic energy to the surface to cause the chemical reactions mentioned above. In the typical MD simulation in this study, motions of all atoms, except for those of the anchored bottom atoms, are followed under micro canonical conditions for about 300 fs after an ion injection into the surface, and then the system is cooled down gradually to the room temperature over the period of nearly 2.5 ps. Once the substrate temperature reaches the room temperature, a new ion is injected into the substrate at a randomly chosen location. By repeating such injection and cooling cycles, we simulate the ALE of a SiO₂ film with fluorocarbon deposition and low-energy ion impact.

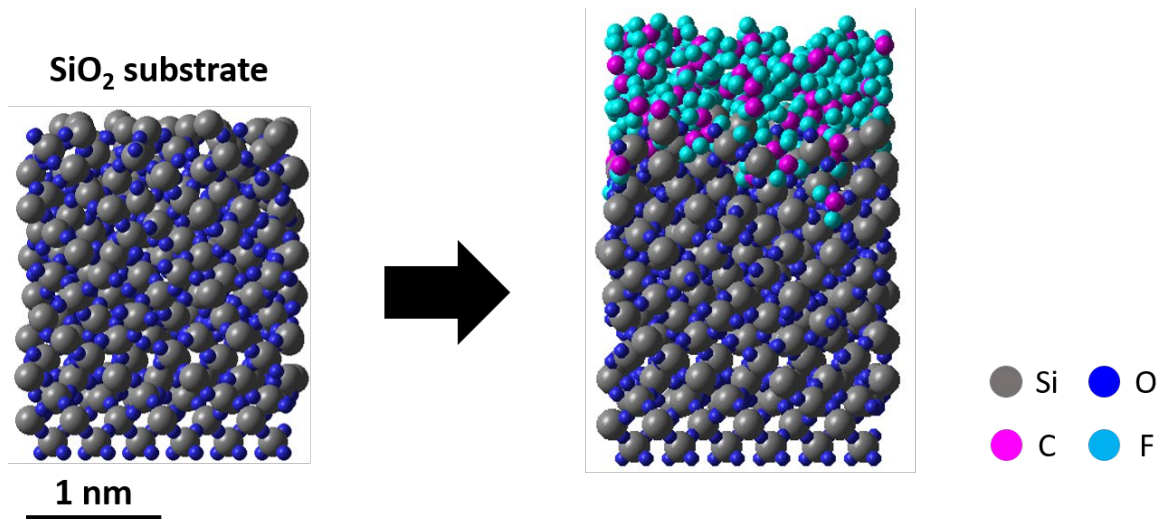


Fig. 1: A side view of a SiO₂ substrate before deposition of a fluorocarbon film (left) and after deposition (right). The film thickness is about 7 Å.

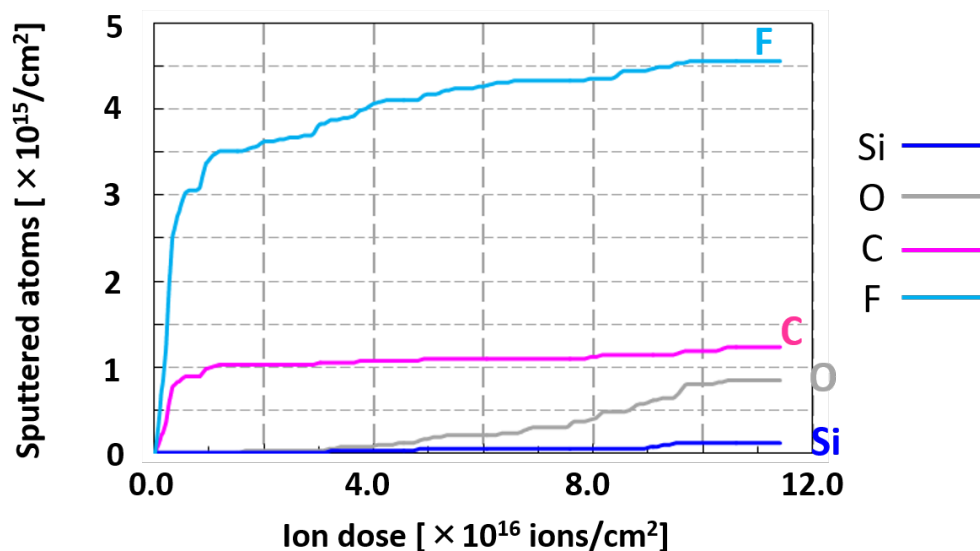


Fig. 2: The total number of atoms removed (sputtered) by Ar⁺ ion impact for each atomic species, i.e., F, C, O, or Si, as a function of the ion dose. The Ar⁺ ion energy is 40 eV. It is seen that O atoms are preferentially sputtered compared with Si atoms.

2.2 Simulation Results

Figure 2 shows the total number of atoms removed by Ar^+ ion impact for each atomic species, i.e., F, C, O, or Si, as a function of the ion dose. The Ar^+ ion energy is 40 eV. It is seen that O atoms are preferentially sputtered compared with Si atoms. The numbers of C and F atoms sputtered from the surface have nearly reached constant values, indicating that the fluorocarbon layer deposited on the SiO_2 surface is nearly run out of, except for C and F atoms strongly bonded with the SiO_2 surface.

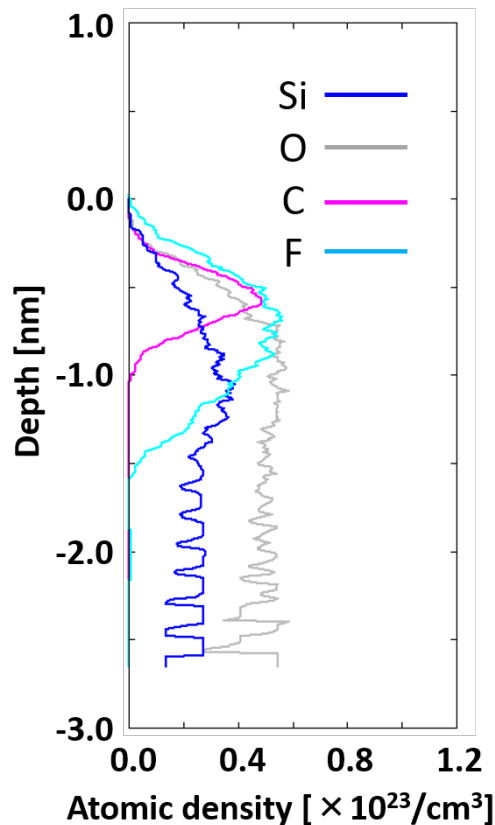


Fig. 3: The depth profiles of atomic species at the ion dose of $11.4 \times 10^{16} \text{ cm}^{-2}$, i.e., at the end of the ion dose of Fig. 2. The depth 0 refers to the location of the initial top surface of the SiO_2 substrate. It is seen that there are a sufficient number of C and F atoms remain on the surface.

Figure 3 shows the depth profiles of atomic species at the ion dose of $11.4 \times 10^{16} \text{ cm}^{-2}$, i.e., at the end of the ion dose of Fig. 2. It is seen that a sufficient number of C and F atoms remain on the surface. Separate analyses show that these C and F atoms are strongly bonded with SiO_2 surface, forming Si-C and Si-F bonds. Such fluorocarbon atoms are difficult to remove by further bombardment of low-energy Ar^+ ions. The remaining carbon on the SiO_2 surface after a single step of the ALE process may serve as a seed layer to enhance fluorocarbon film deposition in the subsequent ALE step, which may eventually lead to thicker fluorocarbon deposition and then end the ALE process.

3. Conclusions

In this study, we have demonstrated how a thin deposited fluorocarbon layer can serve as a source for limited supply of C and F atoms that can react with the SiO₂ substrate surface and form volatile species such as SiF₄ and CO. Our MD simulation shows that low-energy impact by inert gas ions such as Ar⁺ can cause etching reactions as long as the supply of C and F atoms last. However, it is also seen that the remaining C and F atoms are tightly bonded with the SiO₂ surface, which may cause thicker deposition of a fluorocarbon film in the subsequent processes. Although we did not show in this manuscript, our separate simulation results indicate that a small amount of oxygen added to Ar⁺ ion irradiation may contribute to more efficient removal of carbon from the surface and also supplement the deficiency of oxygen caused by the preferential sputtering of oxygen from the surface.

4. References

- [1] G. S. Oehrlein, D. Metzler, and C. Li, ECS J. Solid State Sci. Tech. 4 , N5041 (2015) .
- [2] D. Metzler *et al.*, J. Vac. Sci. Technol. A 32(2), 020603 (2014).
- [3] X. Hua *et al.*, J. Vac. Sci. Technol. A 21(5) (2003).
- [4] S. Rauf *et al.*, J. Appl. Phys. 101, 033308 (2007).
- [5] F. H. Stillinger and T. A. Weber, Phys. Rev. B 31, 5262 (1985).

MASS SPECTROMETRY OF CAPACITIVELY COUPLED PLASMA IGNITED IN CYCLOPROPYLAMINE/ARGON MIXTURE

Miroslav Michlíček^{1,2}, Lenka Zajíčková^{1,2}

¹*Department of Physical Electronics, Faculty of Science, Masaryk University, Brno, Czech Republic*

²*Plasma Technologies, Central European Institute of Technology - CEITEC, Masaryk University, Brno, Czech Republic*

E-mail: michlicekm@mail.muni.cz

In this contribution we report mass spectrometry study of capacitively coupled plasma ignited in cyclopropylamine/argon mixture. We discuss the effect of electron energy used for ionization on fragmentation and overall signal and mass spectra measured for range of conditions relevant for CPA/Ar deposition process. Mass spectrometry of the discharge reveals abundance of fragments, most of which is rapidly consumed when the discharge power is increased. Notable exceptions are fragments at 27 and 28 Th which are rapidly produced from original CPA molecule and probably have a relatively low sticking coefficient.

1. Introduction

Plasma polymerization of amine rich films represent a dry and intrinsically sterile process which is being intensively studied for numerous bio-applications including tissue engineering, protein immobilization, sensors and other applications requiring contact with biological environments.[1] Among possible amine or nitrogen carrying precursors, cyclopropylamine (CPA) has been proposed for preparation of such coating for its nontoxicity and high retention of primary amines.[2,3] Based on the DFT calculated reaction enthalpies, the lowest energy required for CPA radical formation is the ring opening (≈ 2.0 eV). In theory, this reaction should be therefore for low electron temperature plasmas the most probable first step promising fast radical polymerization while maintaining amine functionality.[2]

More recently, the group of Lenka Zajíčková investigated CPA/Ar plasma polymerization in pulsed RF capacitively coupled discharge and showed that the films contain relatively amount of amine groups while being stable in water.[2,3] Furthermore, the coating were shown to promote cell adhesion [4] and were successfully used as mediating layers for biosensors.[5]

Despite of promising properties of the films prepared by plasma polymerization of CPA this process was studied very weakly. Further diagnostics might help in better understanding of the process and further tuning of the deposition conditions beyond simple mechanistic approach.

In this contribution we report mass spectrometry study of typical deposition process in a new experimental PECVD reactor. Mass spectrometry is a powerful diagnostic technique enabling indirect study of the precursor dissociation pattern and can be used for better understanding and optimization of the deposition process.

2. Experiment

The experimental was carried out at a custom-build GEC-like experimental PECVD reactor R4 at CEITEC Nano. The R4 reactor was a stainless steel parallel plate reactor equipped with plasma diagnostics including mass spectrometer (MS) EQP 500 (Hiden), as depicted in Fig. 1. The bottom electrode, 210 mm in diameter, was capacitively coupled to a RF generator working at the frequency of 13.56 MHz. The gases were fed into the chamber through a grounded upper showerhead electrode, 210 mm in diameter. The electrode gap was 55 mm. The bottom, driven electrode was negatively DC self-biased due to an asymmetry of electrode areas, as reactor walls and electrode shielding ring effectively act as grounded electrodes as well. The reactor was pumped down to $< 5 \times 10^{-4}$ Pa by a turbomolecular pump backed by a rotary pump. The leak rate including wall desorption was typically around 0.001 sccm. Working pressure in the chamber was regulated by throttling the pumping speed by a gate valve (VAT). The flow rate of Ar was set to 10 sccm and regulated by an electronic flow controller MKS whereas the flow rate of CPA vapors was set to 1 sccm by a needle valve.

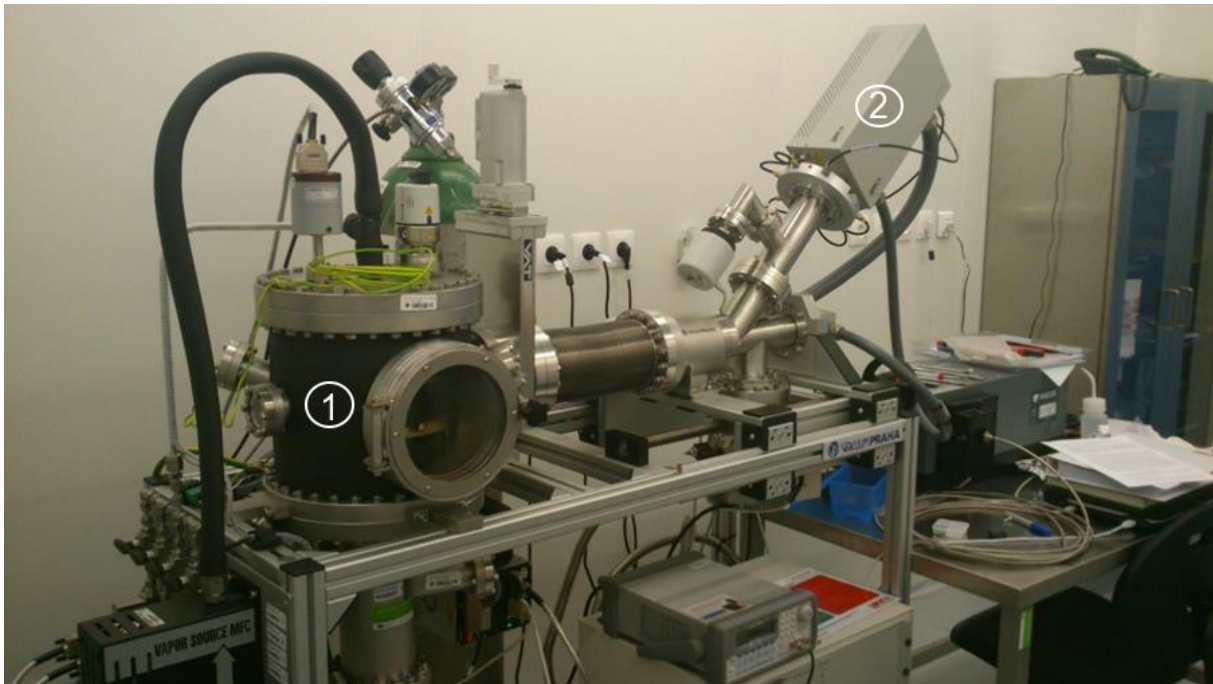


Fig. 1. Experimental PECVD reactor R4 (1) equipped with an EQP 500 mass spectrometer (2).

To obtain mass spectra of species directly in the discharge the EQP 500 mass spectrometer was moved on its supporting rails towards the plasma as depicted in Fig.2. Sampling orifice with a diameter of 300 μm was used. The MS was differentially pumped by a turbomolecular pump backed by a membrane to the pressure of $< 5 \times 10^{-4}$ Pa (depending on pressure in the deposition chamber).

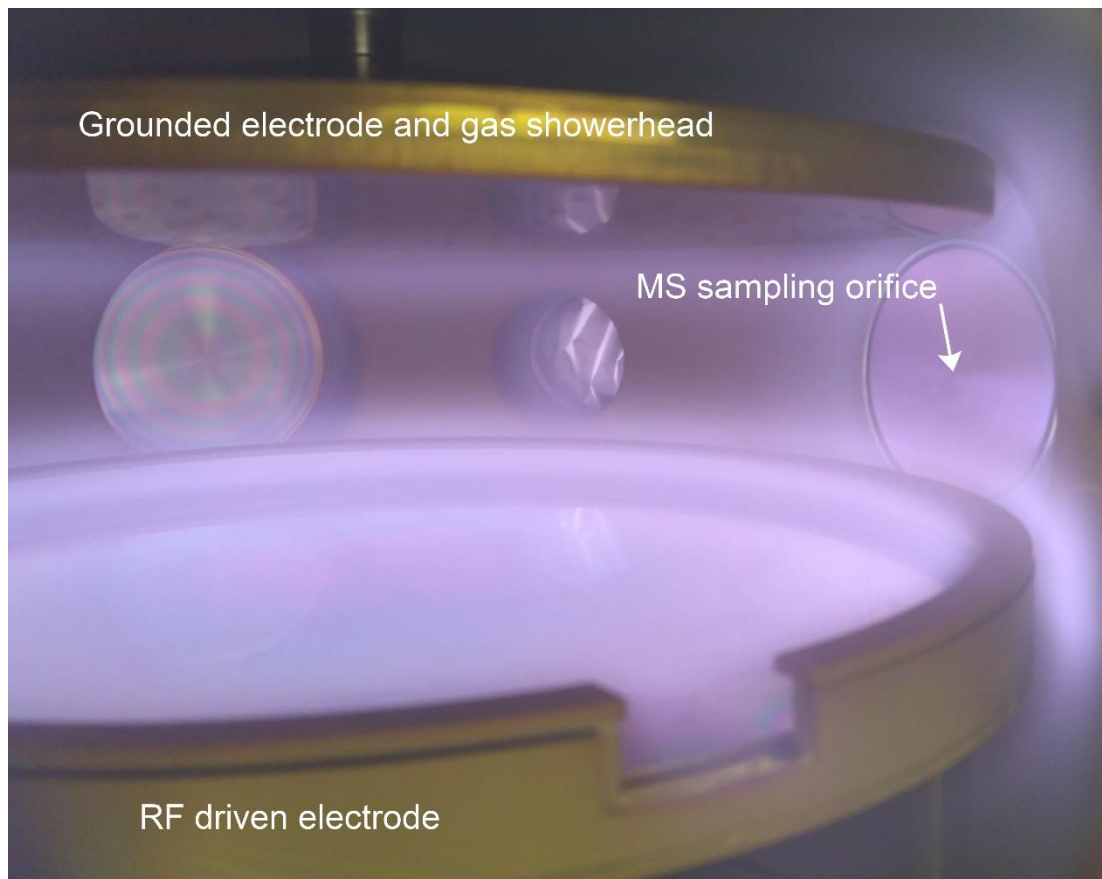


Fig. 2. Detail of the mass spectrometer EQP 500 in proximity of the discharge.

3. Results and Discussion

First, we compare background spectrum and spectrum of CPA without argon in Fig. 3. The background spectrum is dominated by peaks typical for low pressure residual gas – N_2^+ (28 Th), O_2^+ (32 Th), H_2O^+ (18 Th) and CO_2^+ (44 Th). Less prominent peaks can be attributed to smaller fragments such as OH^+ (17 Th) and N^+ (14 Th). Also traces of CPA^+ (55-57 Th) and $(^{14}N^{15}N)^+$ (29 Th) peaks can be clearly identified.

Upon addition of CPA several significant peaks appear. The most probable peaks is not CPA^+ itself (57 Th) but CPA which lost hydrogen atom. Further in the text we will use for this following notation $(CPA-H)^+$. Spectrum contains more dehydrogenated CPA fragments $(CPA-xH)^+$ where $x \in \{0, \dots, 7\}$. The next significant peaks correspond to CPA which after the ring opening lost CH_2 group $(CPA-CH_2)^+$ (42 Th) and some additional hydrogens (41, 40 Th). Strong peak at 39 Th probably correspond to $(CPA-H)$ fragments sustaining additional abstraction of NH_2 group, therefore we note it $(CPA-H-NH_2)^+$. The next peak at 30 Th can be attributed to CPA after ring opening which lost two carbon containing groups $(CPA-CH-CH_2)^+$. Note that this abstraction after the ring opening can happen in a single step even though the notation suggests two step process. The peak at 28 Th which can be attributed to $(CPA-NH_2-CH)^+$ overlaps with N_2^+ . However, assuming the same partial pressure of residual gas as for background (supported by the same O_2^+ and CO_2^+ peak intensity), we can subtract it. Linear intensity is then significantly higher than other organic peaks suggesting that it is the most probable dissociation product caused by MS (intensity is $\approx 65\%$ of $(CPA-H)^+$ peak). Lighter peaks (< 15 Th) can be attributed to CH_x^+ or NH_x^+ fragments.

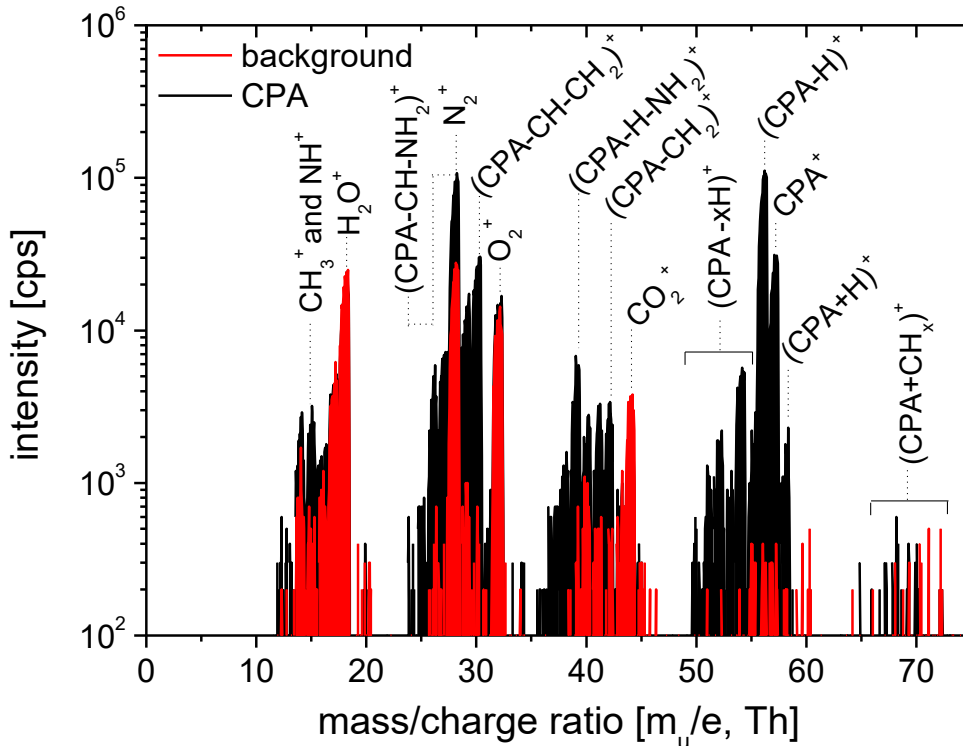


Fig. 3. Mass spectra of background (red) and CPA without argon (black). Spectra were acquired at pressure of 5 Pa in the deposition chamber, while the electron energy for ionization of 70 eV.

Abundance of fragments produced by ionization in the MS spurred us to seek ways to reduce fragmentation. The most obvious one is to reduce electron energy used for ionization. Fig. 4 shows mass spectra of neutrals in the CPA/Ar mixture without plasma, e.g. it shows effect of electron energy in the MS ionizer on dissociation of CPA in the MS. In order to reduce fragmentation by the MS we have tested lower electron energy against the standard of 70 eV, namely 40 eV and 25 eV. This inevitably reduces the signal as clearly visible for strong peaks such as Ar^+ or H_2O^+ , however main peaks of interest

i.e. CPA^+ and $(\text{CPA-H})^+$ are not reduced so strongly ($\approx 70\%$ regardless of peak and a lower electron energy). At the same time however, width of bands (hydrogen abstraction) is reduced significantly and also intensity of main fragment relative to the $(\text{CPA-H})^+$ is decreased. The decrease is $\approx 65\%$ of the original ratio for 70 eV for strong peaks (such as 30 or 28 Th) and even higher for less intensive ones (e.g. 40% for 15 Th or 35% for 54 Th). Overall, this approach increases ratio of primary peak. However, one has keep in mind that weak peaks at lower mass/charge ratios can still be just a product of MS ionization.

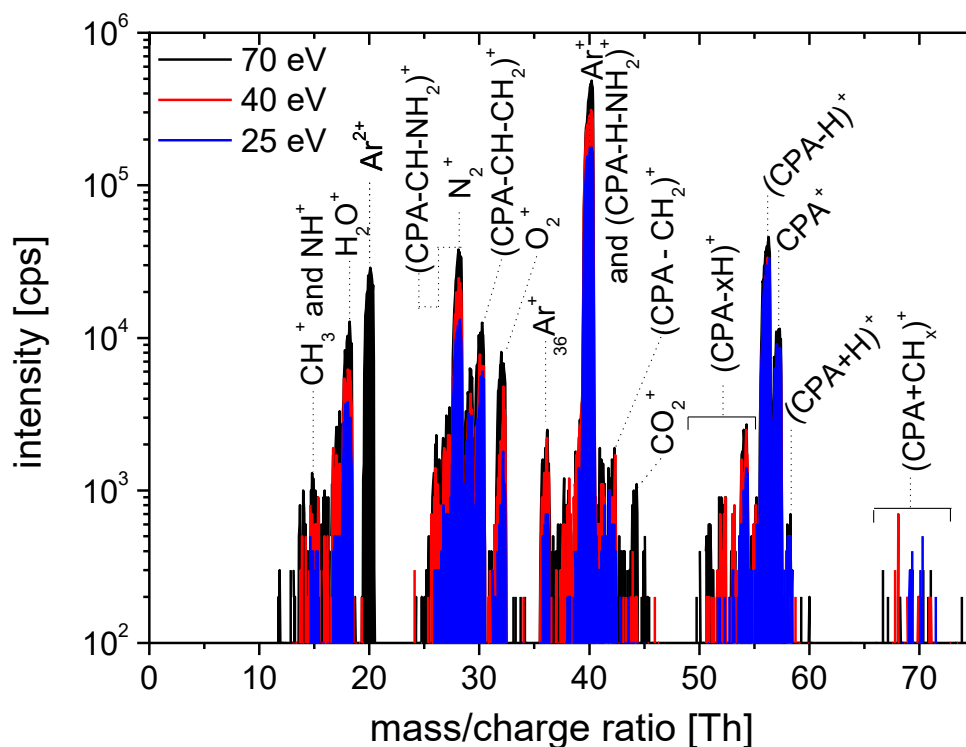


Fig. 4. Mass spectra of neutrals in CPA/Ar mixture without plasma captured with electron energy of 70, 40 and 25 eV. Spectra were acquired at pressure of 5 Pa in the deposition chamber.

In Fig. 5 we show neutral spectra acquired for discharge ignited with varying power. For plotting convenience and to maintain longevity of the MS detector the argon peak (39 - 41 Th) was completely omitted from the measurement. Note that $^{36}\text{Ar}^+$ peak is still present in the spectra for comparison.

Several conclusions can be drawn immediately from assessing the spectra. The spectra consist of few bands belonging to fragments containing integer number of carbon atoms and possibly a nitrogen atom. Breadth of bands is caused by varying number of hydrogen atoms. This effect can be attributed to low energy electrons in plasma. Actually, only the high energy tail of electron energy distribution function (eefd) has sufficient energy for ring opening (≈ 2 eV) and even less for hydrogen abstraction or carbon chain splitting (≈ 4 eV). The most intensive peaks appearing in the spectra are at 27 and 28 Th, therefore containing two carbon or carbon and nitrogen atoms. These peaks remain the most intensive ones even at higher powers which causes quickly decrease of all the peaks. It can be hypothesized that these peaks are rapidly produced from CPA, as it is present already at low power. Furthermore, it appears likely that the peaks have relatively low sticking coefficient as they are present also at high power, when CPA and higher mass fragments are practically consumed. In principle, these fragments could originate also from sputtering of the growing layer. However, in the case, also other lower mass fragments would be present, so we can reject this idea. One can also notice absence of O_2^+ peak, which can be explained by its consumption in the discharge and in turn it explains relatively high amount of oxygen observed in bulk of thin films by XPS with argon sputtering. Also H_2O^+ as source of oxygen should be consumed in the discharge. From this we can hypothesize that peak at 18 Th can be attributed mainly to NH_4^+ which is

readily formed in low pressure plasmas containing hydrogen and nitrogen.[6] Very low signal of hydrogen ions (H^+ , H_2^+ and possibly H_3^+) is probably caused by lot transmission function of the MS, rather than its absence in the discharge, as we observe intensive H_α and also H_β and H_γ lines in optical emission spectra (data not shown).

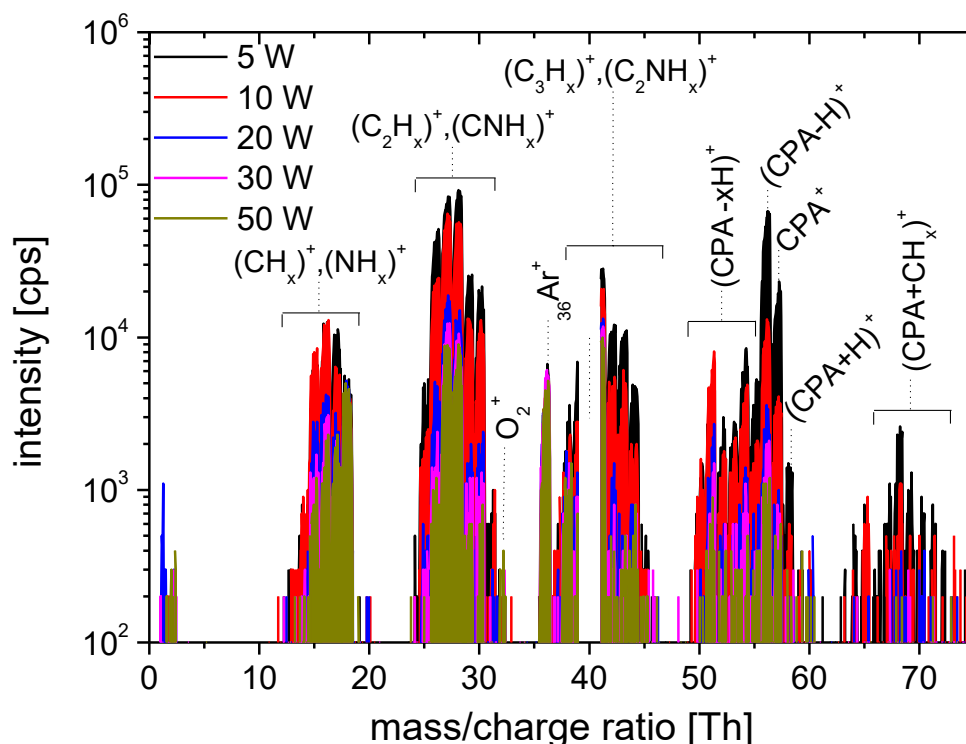


Fig. 5. Mass spectra of neutrals in CPA/Ar mixture with plasma ignited with power 5 – 50 W. Spectra were acquired with electron energy of 25 eV, while pressure in the deposition chamber was 50 Pa.

4. Conclusion

We discussed some effects taking place in CPA plasma polymerization on basis of mass spectrometry diagnostics. It was confirmed that lower electron energy used for ionization reduces also fragmentation in the MS, albeit not completely. Mass spectrometry revealed numerous fragments created in the discharge, most of which is rapidly consumed when the discharge power is increased. Notable exceptions are fragments at 27 and 28 Th which are rapidly produced from original CPA molecule and probably have a relatively low sticking coefficient.

5. Acknowledgment

Authors acknowledge the project CEITEC 2020 (LQ1601) with financial support from the Ministry of Education, Youth and Sports of the Czech Republic (MEYS CR) under the National Sustainability Programme II. Part of the work was carried out with the support of CEITEC Nano Research Infrastructure (ID LM2015041, Ministry of Education, Youth and Sports of Czech Republic, 2016–2019) of CEITEC BUT – Central European Institute of Technology, Brno University of Technology and within the Czech Science Foundation project 18-12774S. M. Michlíček is a Brno PhD Talent scholarship holder – funded by Brno city municipality.

6. References

- [0] Townsend J S and Tiyard H T 1912 *Proc. of the Royal Society of London. Series A* **87** 357.
- [1] Siow K S, Britcher L, Kumar S, Griesser H J. 2006 *Plasma Process Polym* **3** 392–418.
- [2] Denis L, Marsal P, Olivier Y, Godfroid T, Lazzaroni R, Hecq M, Cornil J, Snyders R 2010 *Plasma Process Polym* **7** 172–181.

- [3] Manakhov A, Zajíčková L, Eliáš M, Čechal J, Polčák J, Hnilica J, Bittnerová Š, Nečas D 2014 *Plasma Process Polym* **11** 532–44.
- [4] Manakhov A, Landová M, Medalová J, Michlíček M, Polčák J, Nečas D, Zajíčková L 2017 *Plasma Process Polym* **14** 1600123.
- [5] Makhneva E, Manakhov A, Skládal P, Zajíčková L. 2016 *Surf Coatings Technol* **290** 116–23.
- [6] Carrasco E, Jiménez-Redondo M, Tanarro I, Herrero V J. 2011 *Phys Chem Chem Phys* **13** 19561.

THE EFFECT OF ATTACHMENT ON RF BREAKDOWN

Marija Puač¹, Dragana Marić¹, Zoran Lj. Petrović^{1,2}

¹*Institute of Physics, University of Belgrade, Pregrevica 118, 11080 Zemun, Serbia*

²*Serbian Academy of Science and Arts, Knez Mihailova 35, 11001 Belgrade, Serbia*

E-mail: e-mail address of the corresponding author

This paper investigates influence of attachment on the shape of the RF breakdown voltage curve by Monte Carlo computational code. Space-time evolution of the breakdown process in oxygen and electron energy spectra are analysed and compared with breakdown in argon, as an example of a non-attaching gas with simpler spectrum of energy losses.

1. Breakdown voltage curves in RF fields

Radiofrequency (RF) breakdown has been analysed in our recent papers that explain physical processes leading to the double valued breakdown curves for argon (Savić et al., 2011; Puač et al, 2018). For RF breakdown may be induced by electrons only. Losses were included only as absorption of electrons at electrodes. Apart from surface losses of electrons, there could be losses in the volume of the gas, such as two and three body attachment in case of oxygen. In figure 1 we present breakdown voltage curves for a) argon and b) oxygen at frequency of 13.56 MHz and gaps of 23 mm and 15 mm, respectively. Both breakdown curves exhibit double valued region at lower pressures where a single pressure has two different breakdown voltages.

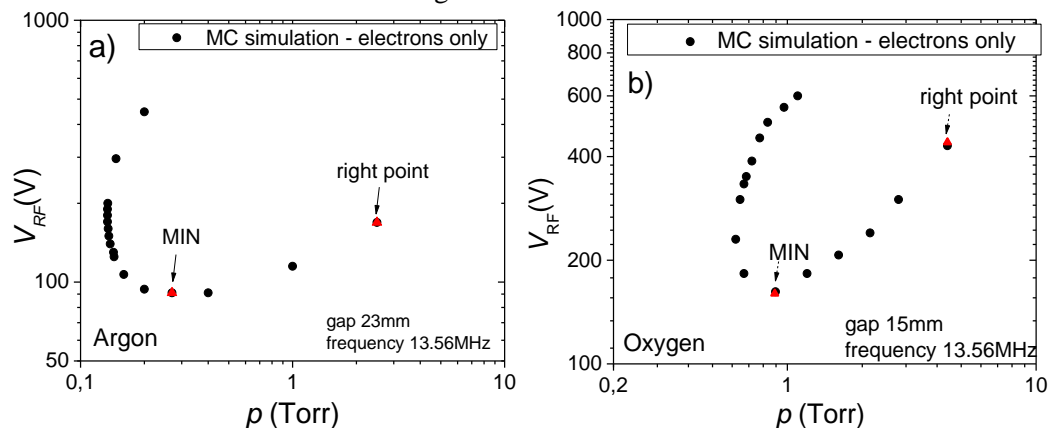


Fig. 1. Breakdown voltage curves for RF breakdown at frequency of 13.56 MHz and different gases: a) argon with distance between electrodes of 23 mm (Puač et al, 2018), b) oxygen with distance between electrodes of 15 mm. In both cases only electrons are included in MC simulation and there are no surface effects at electrodes apart from absorption.

Breakdown voltage depends on balance between electron production in gas by ionizations and their losses. Typically the RF breakdown voltage curve can be divided in two branches: left-hand at lower pressures and high voltages and right-hand branch at higher pressures and lower voltages. Increase of voltage in the left-hand branch is required to overcome losses at electrodes and to enhance multiplication at very low pressures. In the right-hand branch, cloud of electrons does not reach electrodes, but oscillates in the middle of the gap and is spread on both halves. Losses at electrodes are small and increase in voltage is needed for electrons to gain enough energy to perform ionization, when increasing pressure leads to shorter mean free paths.

If we now compare two curves presented in figure 1, we can see that oxygen curve is shifted towards higher pressures and higher voltages, due to great amount of energy losses in electron excitation collisions and electron losses. On the other hand, slopes of the right-hand branches are different. We

know that in this branch losses at electrodes are small, so, in case of oxygen, it is expected that process of attachment will lead to higher required voltages.

2. Spatial profiles of RF breakdown

In figure 2 we can see spatial profiles of electron concentration, mean energy and rate of elastic collisions and ionizations for two points from the figure 1 (indicated by red triangles), which are located at the highest pressures (furthest to the right). In case of argon, cloud of electrons is located in the middle of the gap. For the far right point in oxygen curve, due to a higher voltage required, electrons are being pushed closer to the electrodes. Comparing ionizations for the two points in figure 2, we can see that larger number of ionizations is needed for oxygen breakdown to be maintained. Profiles of mean energy and elastic collisions follow the shape of concentration in both cases. Difference can be seen in oxygen where we have small cut-offs in the moments when field changes its sign due to a more efficient relaxation in molecular gas. In addition the width of the electron ensemble is much smaller and modulation is greater for oxygen. Most importantly visible and more distinct excursions of the electron cloud from one half to the other lead to more asymmetric profile of ionization in case of oxygen

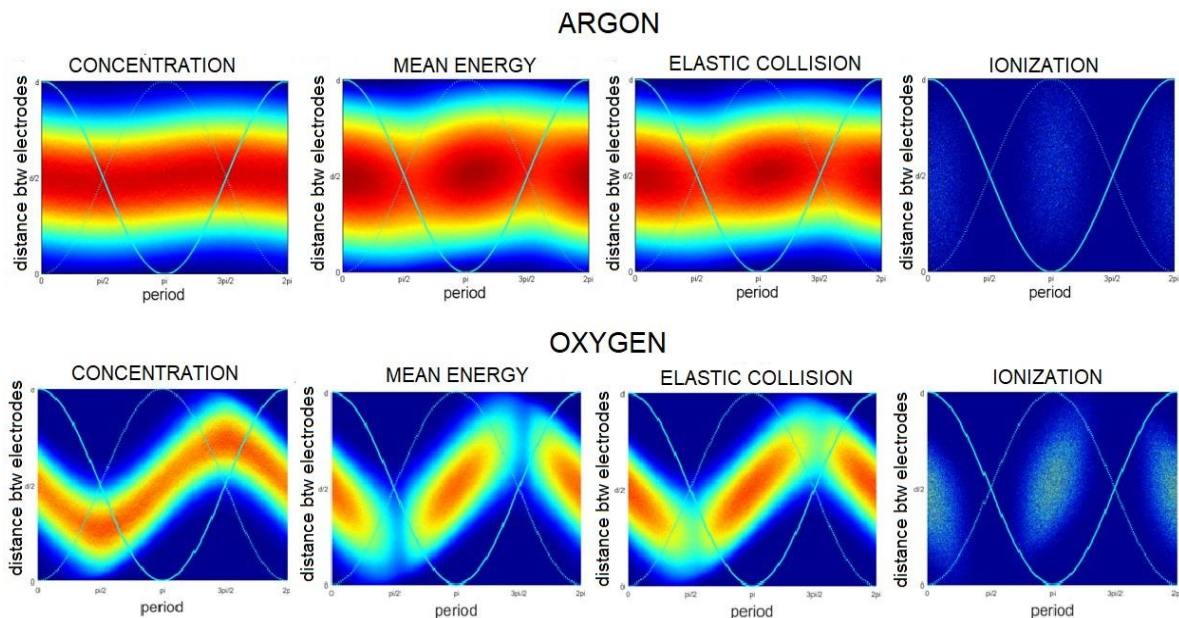


Fig. 2. Comparison of spatial profiles of electron concentration, mean energy and rates of elastic scattering and ionizations for two right points presented in figure 1. Argon: $V=169$ V and $p=2.5$ Torr; oxygen: $V=440$ V and $p=4.4$ Torr.

In figure 3 a comparison of spatial profiles is presented at the two minima: argon and oxygen (indicated by red triangles and letters MIN in figure 1). One can see that there is a more distinctive migration of electron cloud in case of oxygen, as a consequence of a higher voltage. Cloud is narrower and pushed closer to the electrodes. In case of oxygen higher ionizations are still required.

3. Electron Energy Distributions in RF breakdown

Obvious assumption is following: if there is a new loss mechanism in gas, the whole curve should be affected by it. And still that is not a case. Explanation for this can be found in comparison of electron energy distribution functions (EEDF) along the breakdown voltage curves and cross sections for attachment, figures 3 and 4.

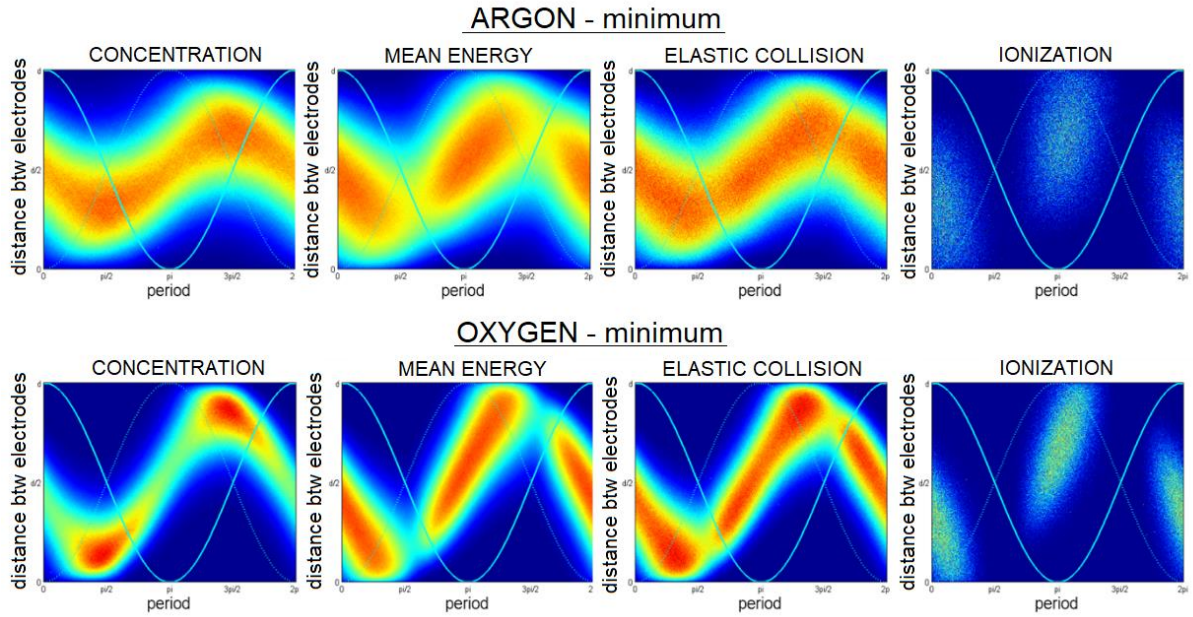


Fig. 3. Comparison of spatial profiles of electron concentration, mean energy and rates of elastic scattering and ionizations for two points that are minima of breakdown voltage curves. Argon minimum: $V=91$ V and $p=0.27$ Torr; oxygen: $V=160$ V and $p=0.89$ Torr.

Electrons in points A and B have larger energies due to high voltages, as expected. Also, EEDFs at different times over one period have greater variation of profiles especially at the highest energies (colours in figure 3A and B). This is because of a smaller number of collisions with the background gas (low pressures), and the fact that electrons can gain large amounts of energy from the field between two collisions, especially when field reaches its maximum. If we now look at the EEDF for points C, D, E and F we can see that energy decreases and EEDFs do not change much over one period of time. Even though points such as E and F have high voltages, due to a large number of collisions with the background gas, portions of energy that electrons may gain from the field between two collisions are uniform and do not depend much on the phase of the field.

Energy span for points labelled by (C) – (F), is around 20 eV, with mean energy of around 10 eV. In figure 4 we can see that at those energies cross sections for attachments are significant. That indicates that process of attachment in the right-hand branch has a large influence on the breakdown conditions. In the left-hand branch we can see that large number of electrons have energies above cross sections for attachments.

4. References

- [1] Savić M, Radmilovic-Radjenovic M., Šuvakov M., Marjanović S., Marić D., Petrović Z. Lj 2011 *IEEE T Plasma Sci.* **39** 2556.
- [2] Puač M., Marić D., Radmilović-Radjenović M., Šuvakova M., Petrović Z LJ 2018 *Plasma Sources Sci. Technol.*, **27**, 075013.
- [3] Itikawa Y 2009 *J. Phys. Chem. Ref. Data* **38** 1.

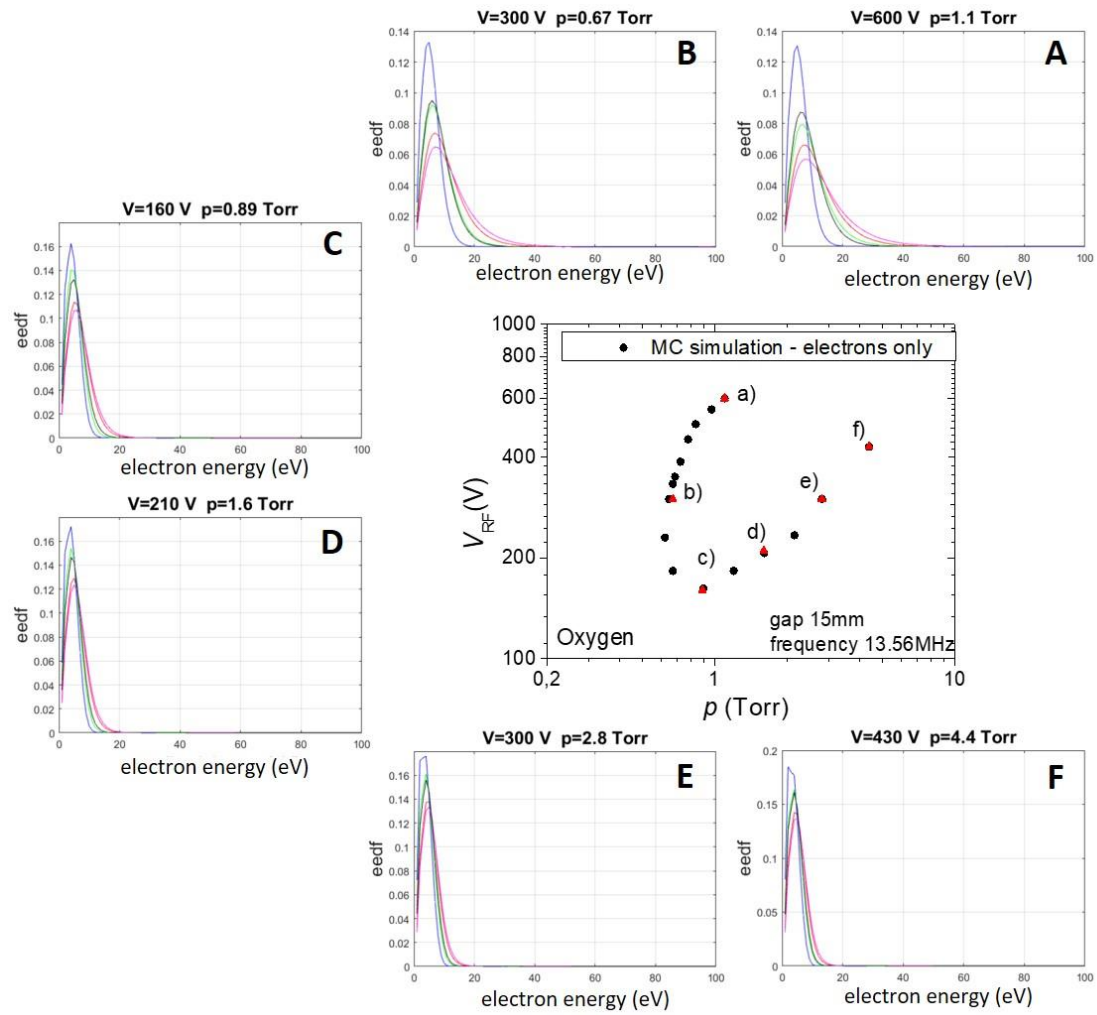


Fig. 3. Electron Energy Distribution Functions along breakdown voltage curve for oxygen as a background gas at frequency of 13.56 MHz and distance between electrodes is 15 mm. Different curves represent different phases of the RF period and their variation indicates modulation in the distribution at different energies.

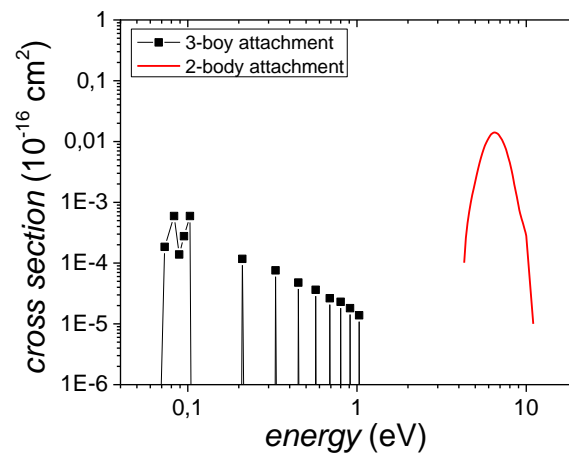


Fig. 4. Cross sections for 3-body and 2-body attachment for oxygen (Itikawa, 2009).

CONSTRUCTION OF A FOURIER TRANSFORM SPECTROMETER FOR THE UV-VIS REGION

Michal Ďurian, Štefan Matejčík

Faculty of Mathematics, Physics and Informatics, Comenius University in Bratislava, Slovakia

E-mail: durian@fmph.uniba.sk

We present the current status of our work in developing a stop-scan Michelson interferometer for low-light optical emission spectroscopy in the UV/VIS spectral region. The current version of the instrument is capable of taking measurements in the 320 nm - 1150 nm spectral range, as demonstrated on a presented spectrum of an HgAr cold-cathode fluorescent lamp. The achieved experimental resolution of 0.21 nm of the 546 nm Hg line matches the expected theoretical value, which gives the resulting spectral resolving power of 2600.

1. Introduction

Fourier transform (FT) spectroscopy is a well-established diagnostic method in multiple scientific fields, especially owing to its performance in the infrared spectral range and a number of inherent advantages when compared to dispersive instruments. First among these is the Jacquinot's throughput advantage, present because an FT spectrometer does not require the use of components such as slits and dispersive elements for its operation, thus allowing more light to reach the detector [1]. Second advantage is the Fellgett's multiplex advantage, which resides in the fact that the signal recorded by the instrument is a superposition of interference contributions of all wavelengths present in the measured spectrum [2]. This is beneficial for the signal-to-noise ratio (SNR), especially when the detector noise is dominant, as is the case in the IR spectrum. It also makes it possible for the measurements taken with an FT instrument to have shorter acquisition time than in the case of a dispersive instrument.

There are many types of interferometer designs, each with their respective features and strengths. The basic distinction among these can be made based on the principle of creation of the interference, either by wavefront splitting or amplitude splitting. One of the most widespread interferometer types is the Michelson interferometer (MI) of the amplitude splitting type. The basic components for the MI are a beamsplitter, a static and a moving mirror. By actuating the moving mirror, the relative optical path difference (OPD) can be changed. Simultaneously, by equidistantly sampling the interference intensity, the interferogram can be obtained and the resulting spectrum calculated using Fourier transformation. Further distinction between various modifications of the MI can be made based upon the type of the mirror motion - continuous or stepping. The continuous motion is more common, is cheaper and allows for quick measurement repetition with subsequent averaging. On the other hand, the stepped mirror motion is well suited for low-intensity applications requiring signal integration at each interferogram position [3]. Finally, there are two important characteristics of an MI that describe its properties. First is the minimum detectable wavelength, which is ruled by the Nyquist sampling theorem and given by the OPD between two adjacent points of the interferogram. For example, if we wish to have a 200 nm wavelength signal in the resulting spectrum, we must sample the interferogram in no more than 50 nm intervals. The second property of an MI is the maximum achievable resolution, which is given by:

$$\Delta\nu = \frac{1}{OPD} = \frac{1}{2L} \quad (1)$$

where L is the total mirror travel, which is equal to half of the total OPD achieved during the interferogram acquisition [4].

In the UV-VIS spectral range, the use of FT spectroscopy is less widespread than in the IR and is mostly reserved to custom made instruments uniquely designed for a particular experiment. There are two major reasons for this [5]. As the wavelength of interest gets shorter, the demands on mechanical precision become much more stringent and eventually become the limiting factor for the performance of the instrument. Also, the construction costs rise significantly. Second reason is, that in

the UV-VIS range the detector noise is no longer a dominant component of the total noise, being replaced by the photon shot noise. Since the latter has different physical principles, we can no longer assume for the multiplex advantage to be valid in all cases. It can be shown that in the case of spectra with low spectral density, as is the typical case of emission spectroscopy, that there is still some multiplex gain for strong spectral lines, although the overall dynamic range decreases [6]. According to [5, 6], the total gain improvement of an FT spectrometer compared to the dispersive instrument can be by a factor up to 1000. For these reasons the application of the FT spectroscopy in the UV-VIS region, while still potentially fruitful, has to be well justified by the needs of a particular experiment.

In our case, we intend to use the developed FT spectrometer at the experiment of Electron Induced Fluorescence (EIF). The EIF experiment is a cross-beam design for the study of interactions of ground-state gas-phase molecules with electrons. The experiment is capable of measuring fluorescence spectra and relative excitation-emission cross-sections. The electron beam is formed by a trochoidal electron monochromator and the electron energy can be set between 0 eV and 100 eV. The experiment uses optical emission spectroscopy (OES) as its diagnostic method and employs a pair of grating monochromators with maximum achieved spectral resolving powers of 1000 and 5000, which are switched depending on the needs of the particular measurement. Detector is a cooled photomultiplier in photon counting mode and spectral sensitivity range from 180 nm to 900 nm. Signal intensities depend strongly on the studied sample gas, the particular line being studied and also on the setting of the monochromator slits. Typical signal levels are $10^{-1} - 10^2$ counts per second with many of the lines often too weak for practical measurement. In order to achieve reasonable SNR, very long acquisition times and averaging are used, which often means that obtaining a single spectrum or cross-section takes multiple days and in extreme cases even a week. More detailed description of the EIF experiment can be found in [7].

Long acquisition times and detection sensitivity are the two pivotal parameters we aim to improve by replacing the grating monochromators with an FT spectrometer. We have opted for the Michelson-type design due to being well documented and used also in the VIS spectral region [8, 3, 9]. We require that the properties of the new FT spectrometer are not limiting the current EIF experiment performance in any aspect. This spawns a number of requirements which subsequently turn into specific design features. First and most notable of these is the capability of stop-scan measurements, in order to be able to integrate weak signals using a photomultiplier. Another requirement is to keep the spectral range of the experiment at least at its current value of 200 nm – 900 nm. These two conditions imply a requirement for the mirror motion mechanism to be able to precisely and reliably perform equidistant steps of 50 nm in length. In terms of spectral resolving power we aim for the value of 4000 - 5000, for which, according to (1), a total mirror travel of 1 mm should be sufficient.

2. Instrumentation Description

The key component of our interferometer is the mirror motion mechanism, which is based on a PI miCos LPS-45 linear translation stage, with 26 mm of total travel capability. For positional feedback it has a built-in linear encoder with 1 nm resolution. The stage motion mechanism is based on PIShift piezo inertia drive, which uses a piezo mechanism and a modified sawtooth-shaped control voltage to actuate a ceramic rod, to which the moving stage is mounted. The linear stage is capable of performing nanometer-scale steps, as is required by our application. However, testing has shown that the inherent accuracy of the motion mechanism coupled with just the internal positional feedback is insufficient to meet the stringent accuracy requirements. This is due to sporadic mechanical backlash of the stepping mechanism, the mechanical setup can skid by up to ± 20 nm, which is a prohibitively large value, detrimental for the quality of the resulting spectrum. This necessitated a significant change in the original optomechanical setup, in form of adding another MI to provide more reliable positional reference, as inspired by [9].

The optomechanical setup of the final instrument consist of two coupled MIs, sharing the linear stage and mostly mirroring each other in their layout and setup. The positional reference provided by the reference interferometer is used to correct any mirror position error, that would affect the equidistantness of data points taken with the measurement interferometer. Schematic layout of the measurement interferometer is in Fig. 1. The two interferometers differ only in configuration of their

inputs. The measurement interferometer uses an optical fiber (F) to bring the light from the source and a lens-aperture-lens setup (C) for spatial filtering and beam collimation. The amount of signal lost at the aperture is negligible compared to losses in dispersive monochromators, so our goal of higher optical throughput is not jeopardized. On the input of the reference interferometer is a 635 nm laser diode with a single collimating lens. The laser diode is thermally and power stabilised in order to keep its radiation properties constant. According to the Nyquist sampling theorem, the current laser diode wavelength implies the lower boundary of the spectral range to be approx. 320 nm. Both interferometers use planar mirrors in tip-tilt mounts (M1, M2) for manipulating their input beam direction. Also, both interferometers use retroreflectors in their arms (R1, R2) for better robustness against external vibrations. Currently, both detectors are based on amplified photodiodes. All optical components are UV-capable, using UV-enhancing coatings and fused silica as substrate.

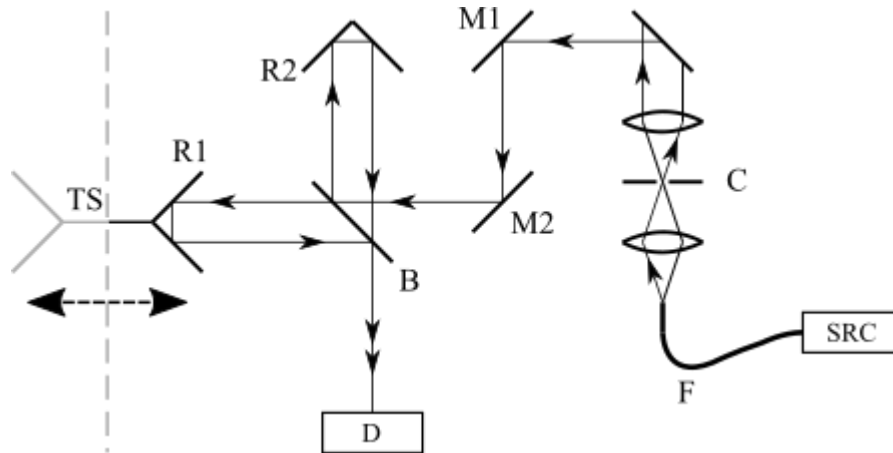


Fig. 1. Schematic of the measurement interferometer.

The reference interferometer is identical, except for the input collimator and light source.

An integral part of the instrumentation is the control software, which collects the data and operates the linear stage. At the start of each measurement, a short calibration measurement with 10 mirror steps is taken. This densely sampled sine-shaped interferogram of the reference laser diode is subsequently evaluated for two parameter values, later used for performing the position reference function. First parameter is the length of mirror step between two adjacent zero-crossings of the measured laser sine interferogram. This value will be used as the base step length of the actual measurement. Second parameter is the signal value at the zero-crossings of the reference laser interferogram, which in turn is used as a reference position in the correction algorithm during the following measurement.

During the actual measurement, the algorithm starts in the corrected zero-crossing mirror position, performs a full step forwards into the next zero-crossing position, performs a correction if necessary and collects data. Then, it performs a half step backwards and again collects the measurement data. The cycle is finished with a one-and-a-half step forward into the next zero-crossing position which is again corrected using the reference interferometer signal. In this manner, we obtain denser sampling of the measurement interferogram and thus shift the lower limit of the spectral range towards shorter wavelengths. It is important to note, that during the interpolating half-steps, the linear stage is required to perform within the reach of the high-precision piezo drive. If a servo-step occurs, potentially causing motion errors, it is detected by a self-built vibration sensor and the software returns to the zero-crossing position before another interpolation attempt.

3. Demonstration Measurement

To demonstrate the current capabilities of our interferometer, we present an emission spectrum of an HgAr cold-cathode fluorescent lamp in Fig. 2. It has been obtained with 1 mm of total mirror travel, which translates to a theoretical resolution of 0.2 nm FWHM and a spectral resolving power of 3500 at 700 nm. The experimentally measured 546 nm mercury line from Fig. 2 has a gaussian-fitted FWHM

of 0.21 nm, which yields 2600 for the experimental spectral resolving power at this wavelength. This good match of the theoretical and experimental values means there were no optical misalignments or other errors during the measurement.

Thanks to using a UV-enhanced silicon photodiode as a detector, the spectral range extends from the lower theoretical limit of 320 nm up to 1150 nm, typical for Si detectors. The line intensities have been calibrated for the Si photodiode spectral sensitivity. It must be noted, that a more thorough spectral calibration is necessary before putting the instrument to use, which can be seen by the significant attenuation of mercury lines below 500 nm, compared to expected table values. This calibration will be performed on the final version of the instrument with a photomultiplier for detector.

Overall, we can conclude that the obtained results are very encouraging towards achieving our goal of applying the interferometer at the EIF experiment, after replacing the current detector with a photomultiplier.

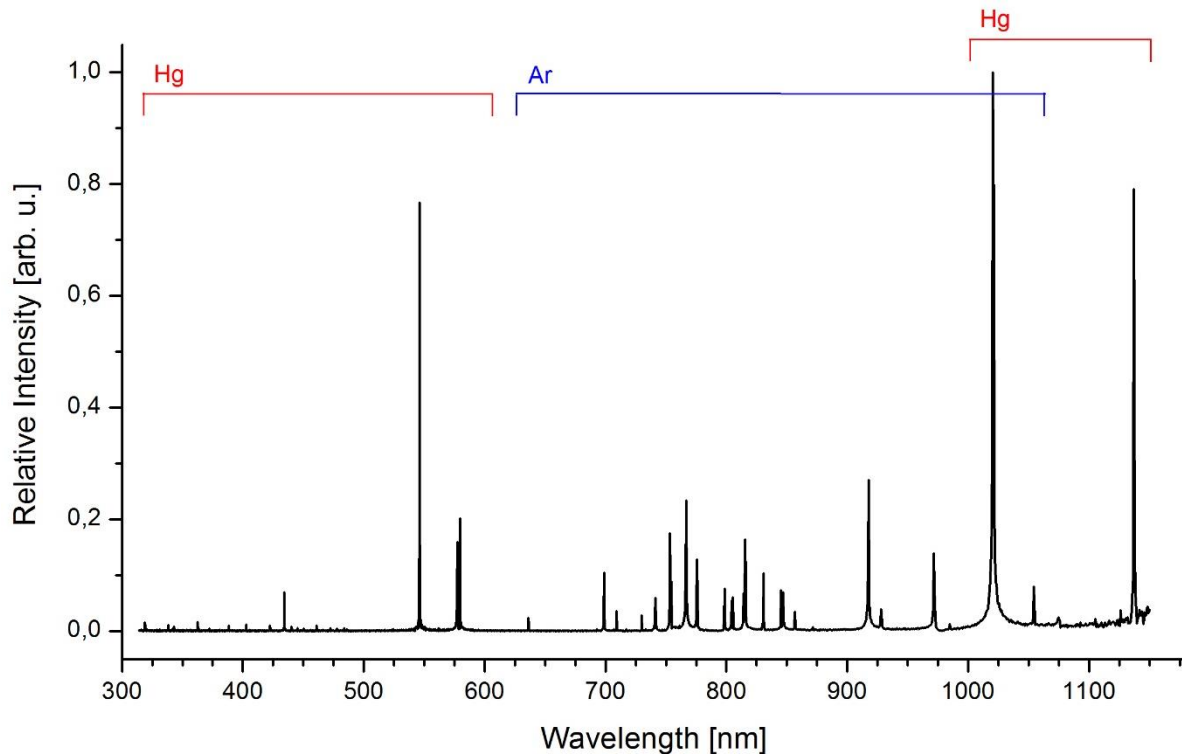


Fig. 2. Obtained demo spectrum of an HgAr CCFL.

4. Acknowledgments

This work was supported by the Slovak Research and Development Agency, project Nr. APVV-15-580 and the grant agency VEGA, project Nr. VEGA-15-089. This project has received funding from the European Union's Horizon 2020 research and innovation programme under grant agreement number 692335.

5. References

- [1] Jacquinot P. 1960 *Rep. Prog. Phys.* **23** 267
- [2] Fellgett P. 1958 *J. Phys. Radium.* **19** 187
- [3] Biggs et al. 1990 *Meas. Sci. Technol.* **1** 630
- [4] Saptari V. 2004 *Fourier-Transform Instrumentation Engineering* ISBN 978-0-8194-5164-4
- [5] Thorne A. 1998 *J. Anal. At. Spectrom.* **13** 407
- [6] Nordstrom R. J. 1982 *Aspects of Fourier Transform Visible/UV Spectroscopy* ISBN 978-1-4899-0336-5 421-452
- [7] Danko M. et al. 2013 *J. Phys. B: At. Mol. Opt. Phys.* **46** 045203
- [8] Biggs P. et al. 1987 *J. Phys. E: Sci. Instrum.* **20** 1005
- [9] Wang X. et al. 2008 *Rev. Sci. Instrum.* **79** 123108

DETERMINATION OF ELECTRIC FIELD IN HUMID AIR PLASMA FROM NITROGEN FNS AND SPS BANDS RATIO

Samuel Omasta¹, Petr Bílek², Zdeněk Bonaventura², Anna Zahoranová¹ and Tomáš Hoder²

¹ Department of Experimental Physics; Faculty of Mathematics, Physics and Informatics, Comenius University in Bratislava, Mlynská Dolina 842 48, Slovakia

² Department of Physical Electronics, Faculty of Science, Masaryk University, Kotlářská 2, 611 37 Brno, Czech Republic

E-mail: samuel.omasta@gmail.com

Spectral band intensities of first negative and second positive system of molecular nitrogen might be used for determination of reduced electric field strength E/n in electrical discharges or even ionizing events in pre-breakdown regime. Theoretical dependence of FNS and SPS intensity ratio $R_{FNS/SPS}$ was verified by many experiments, but there is still absence of agreement, which experimental obtained constants should be used for the most accurate E/n evaluation. The calculations require knowledge of radiative lifetime, $N_2^+(B^2\Sigma_u^+)$ and $N_2(C^3\Pi_u)$ collisional quenching rates, electron energy distribution and electron impact cross-sections. Role of this paper is to evaluate effect of water vapor content in synthetic air on E/n determination. Doing a search on quenching rates and online simulations of EEDF (including evaluation of swarm parameters), we have come to a conclusion, that the outcome of measurement is mainly affected by decrease of $N_2(C^3\Pi_u)$ effective lifetime due to an additional water content. Resulting calibration curve for E/n evaluation was generalized for water fraction up to 10 %.

1. Introduction

First negative (FNS) $N_2^+(B^2\Sigma_u^+) \rightarrow N_2^+(X^2\Sigma_u^+)$ and second positive system (SPS) $N_2(C^3\Pi_u) \rightarrow N_2(B^3\Pi_g)$ of nitrogen is widely used for reduced electric field strength (E/n) determination in nitrogen or air-like discharges[1]–[4]. Method uses band intensity ratio of FNS at 391.5 nm and SPS at 337.1 nm (0-0 vibronic transition) as it is shown in Fig. 1. Number of $N_2^+(B^2\Sigma_u^+)$ and $N_2(C^3\Pi_u)$ states generally depends on their generation and extinction rate. The advantage of this method is fact that both nitrogen systems are excited or ionized from the same ground energy level $N_2(X^1\Sigma_g^+)$, by the same electrons, accelerated by the same electric field (eq. (1,2)).

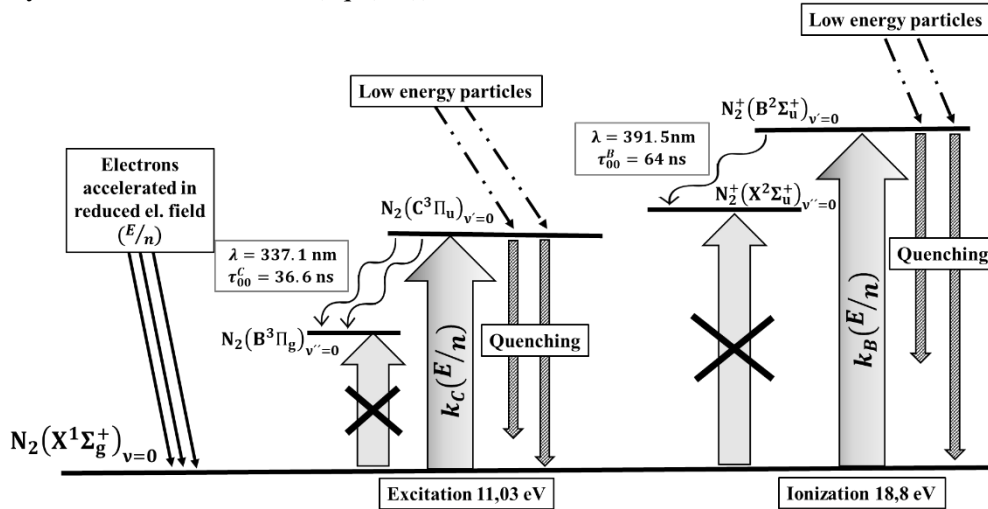


Fig. 1. Illustrative scheme for FNS and SPS. $N_2^+(B^2\Sigma_u^+)$ and $N_2(C^3\Pi_u)$ is generated by accelerated electrons with reaction rates $k_B(E/n)$, $k_C(E/n)$, after that, they are radiated or quenched by low energy (neutral) particles. Lower states of radiative transition should not be populated before deexcitation of upper states.

Consequently, the ratio between number of $N_2^+(B^2\Sigma_u^+)$ and $N_2(C^3\Pi_u)$ states is independent on electron and $N_2(X^1\Sigma_g^+)$ or nitrogen molecule density. Dependence of this ratio on (E/n) is result of different cross-section and energy threshold for $N_2(C^3\Pi_u)$ excitation and $N_2^+(B^2\Sigma_u^+)$ ionization of N_2 by electron impact. Extinction of states $N_2^+(B^2\Sigma_u^+)$ and $N_2(C^3\Pi_u)$ consists of two events: radiative deexcitation (resulting in observable spectral band) and collisional quenching by surrounding particles (decrease intensity of observed spectral band). All those events can be summed up by following differential equations:

$$\frac{dI_B(r,t)}{dt} = k_B(E/n)n_{N_2}n_e(r,t)T_B \frac{1}{\tau_{00}^B} \frac{hc}{\lambda_B} - \frac{I_B(r,t)}{\tau_{eff}^B} \quad (1)$$

$$\frac{dI_C(r,t)}{dt} = k_C(E/n)n_{N_2}n_e(r,t)T_C \frac{1}{\tau_{00}^C} \frac{hc}{\lambda_C} - \frac{I_C(r,t)}{\tau_{eff}^C} \quad (2)$$

where $k_B(E/n)$ and $k_C(E/n)$ are reaction rate constants of $N_2^+(B^2\Sigma_u^+)$ and $N_2(C^3\Pi_u)$ dependent on reduced electric field (E/n) ; n_{N_2} and $n_e(r,t)$ are nitrogen and electron densities; T_B and T_C are transmission coefficients of the detector; λ_B and λ_C are observed wavelength of SPS and FNS (0,0) transition; I_B and I_C are observed intensities of FNS and SPS and τ_{00}^B , τ_{00}^C and τ_{eff}^B , τ_{eff}^C are radiative and effective lifetimes of $N_2^+(B^2\Sigma_u^+)$ and $N_2(C^3\Pi_u)$ states. After dividing eq. (1) by eq. (2) we get FNS and SPS emission ratio (eq. (3)).

$$R_{FNS/SPS}(E/n) = \frac{\left(\frac{dI_B(r,t)}{dt}\right) + \frac{I_B(r,t)}{\tau_{eff}^B}}{\left(\frac{dI_C(r,t)}{dt}\right) + \frac{I_C(r,t)}{\tau_{eff}^C}} \cdot \frac{\tau_{eff}^B}{\tau_{eff}^C} \quad (3)$$

Paris in his work [1] suggested that $R_{FNS/SPS}$ intensity ratio in air can be approximated by following fit:

$$R_{FNS/SPS}(E/n) = 46 \cdot 0.065 \cdot \exp\left[-89 \left(\frac{E}{n}\right)^{-0.5} - 402 \left(\frac{E}{n}\right)^{-1.5}\right] \quad (4)$$

2. Determination of water vapor effect

Electrical discharges in or in contact with water has recently attract much attention. They have been studied due to their behaviour and chemistry differs from those in gases with metal electrodes [5]. Electrical discharges in contact with water generates UV emission and many reactive species, what can leads to e.g. biomedical and environmental applications such as sterilization or decontamination of waste water[6]–[8].

This scientific paper was motivated by effort to realize spatio-temporally measurement of electric field in water barrier discharge. In this section we will discuss how additional water in air affects determination of (E/n) . We assumed that water effective cross-section for inelastic collisions with electrons, can appreciably differ from those of oxygen or nitrogen in air and even small admixture of water vapor can affect electron energy distribution function EEDF. Different EEDF at the same value of (E/n) would also result in diferent rate constants $k_B(E/n)$, $k_C(E/n)$ at this value. The second way the water can affect determination of (E/n) in humid air is through effective lifetimes of $N_2^+(B^2\Sigma_u^+)$ and $N_2(C^3\Pi_u)$.

Effect of water vapor on ratio between $k_B(E/n)$ and $k_C(E/n)$ is shown in fig. 2. Values of $k_B(E/n)$ and $k_C(E/n)$ were calculated online [9], using Phelps database of cross-sections for N_2 and O_2 [10] and Morgan database for H_2O [11]. As we can see, the relative change in ratio of rate constants is nearly constant for $(E/n) > 500$ Td and seems to be proportional to amount of water vapor. On whole (E/n) range it can be approximated by exponential decrease $m\eta \exp\left(-\beta \frac{E}{n}\right) + l\eta$, where η is volumetric fraction of water vapor, m , l and β are constants, while in following calculations only $l = 0.86$ takes place.

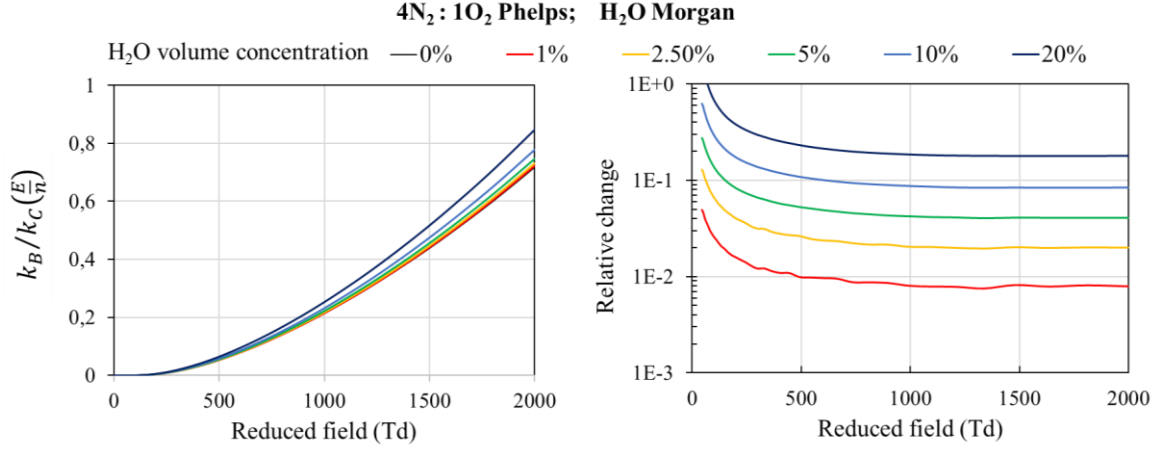


Fig. 2. Rate constant ratio between $k_B(E/n)$ and $k_C(E/n)$ in synthetic air with admixture of H_2O calculated with BOLSIG+. Volumetric fraction of H_2O is given over the graphs. Relative change considering dry synt. air is highlighted on the right. Simulation was calculated for 300 K.

Effective lifetimes are directly dependent on admixture of H_2O as a result of following equations

$$\frac{1}{\tau_{eff}^B} = K_{N_2}^B n_{N_2} + K_{O_2}^B n_{O_2} + K_{H_2O}^B n_{H_2O} + \frac{1}{\tau_{00}^B} \quad (5)$$

$$\frac{1}{\tau_{eff}^C} = K_{N_2}^C n_{N_2} + K_{O_2}^C n_{O_2} + K_{H_2O}^C n_{H_2O} + \frac{1}{\tau_{00}^C} \quad (6)$$

where $K_{N_2}^C, K_{O_2}^C, K_{H_2O}^C, K_{N_2}^B, K_{O_2}^B, K_{H_2O}^B$ are quench rate constants of $N_2^+(B^2\Sigma_u^+)$ and $N_2(C^3\Pi_u)$ by quencher stated as bottom index, $n_{N_2}, n_{O_2}, n_{H_2O}$ are volume densities of these quenchers respectively.

However, accessible data for $K_{H_2O}^C$ and $K_{H_2O}^B$ are rarely measured and there is missing good agreement. As we know from literature, reciprocal lifetimes are also linear to the amount of water present in synthetic air. If we would know exact values $K_{H_2O}^C$ and $K_{H_2O}^B$, we could type following relationship between reciprocal lifetimes and volumetric fraction of water vapor η :

$$\frac{1}{\tau_{eff}^B(\eta)} = \frac{1}{\tau_{eff}^B(0)} \cdot (1 + \psi\eta) \quad (7)$$

$$\frac{1}{\tau_{eff}^C(\eta)} = \frac{1}{\tau_{eff}^C(0)} \cdot (1 + \varphi\eta) \quad (8)$$

As we know from literature, dependence of effective lifetime τ_{eff}^B on η is minor to the dependence of τ_{eff}^C . Values of $\psi = 6.5$ and $\varphi = 0.4$ were established from $1/\langle\tau_{eff}^B(\eta)\rangle$ and $1/\langle\tau_{eff}^C(\eta)\rangle$ (angle brackets indicate mean value), considering the values found in literature [12-14]. Fraction of water vapor η can be real number from interval $(0,1)$, but after consideration of partial pressure of saturated water vapor at 293 K is around 24 mbar ($\eta = 0,024$), we do not expect values of η in ‘‘cold plasma’’ barrier water discharge to overcome 0.1.

3. Conclusion

The reduced electric field strength in air-like discharges can be done by measuring the ratio between spectral band intensities of the first positive and the second negative system of nitrogen. This method has been used over a decade for discharges in synthetic air (or pure nitrogen), but we modified the task and got closer look on additional effect of water. Using online solver BOLSIG+ and accessible rate constants for quenching $N_2^+(B^2\Sigma_u^+)$ and $N_2(C^3\Pi_u)$ states by water, we found out, that 2,5% fraction of H_2O in synthetic air can change outcome of E/n measurement up to 10 % and in 10 % fraction up to 35 %. However, the shape of $R_{FNS/SPS}(E/n)$ does not change significantly due to addition H_2O , so verified or run-in calibration curves for dry air could be used after consideration of a scaling parameter.

4. Acknowledgement

This work has been supported by Slovak Grant Agency for Science VEGA, project 1/0930/17 and by the Czech Science Foundation project under nr. GJ16-09721Y.

5. References

- [1] Paris P et al. 2005 J. Phys. D: Appl. Phys. 38 3894-3899
- [2] Hoder T et al. 2016 Plas. Sour. Sci Technol.25 045021
- [3] Hoder T et al. 2016 Plas. Sour. Sci Technol. 25 025017
- [4] Obrusnik A et al. 2018 Plasma Sour. Sci Technol. 27 085013
- [5] Bruggeman P et al. 2009 J Phys D Appl Phys.;42 053001.
- [6] Vukusic T et al. 2016 Innov Food Sci. Emerg. Technol. 38 407-413.
- [7] Huang Y et al. 2016 IEEE Trans Plasma Sci. 44 938-943.
- [8] Laurita R et al. 2015 Clin Plasma Med. 3 53-61
- [9] Hagelaar G J M and Pitchford L C 2005. Plas. Sour. Sci Technol. 14 722
- [10] Phelps database. www.lxcat.net. Accessed October 11, 2018.
- [11] Morgan database. www.lxcat.net. Accessed October 11, 2018.

THE FIRST PRINCIPLE CALCULATIONS OF THE INTERACTION BETWEEN HEXAFLUOROACETYLACETONE (HFAC) WITH NI AND NIO SURFACES FOR ATOMIC LAYER ETCHING (ALE) APPLICATIONS

Abdulrahman Basher¹, Michiro Isobe¹, Tomoko Ito¹, Masato Kiuchi², Takae Takeuchi³, Kazuhiro Karahashi¹, Satoshi Hamaguchi¹

¹Osaka University, 2-1 Yamadaoka, Suita, Osaka 567-0871, Japan.

²AIST, 1-8-31 Midorigaoka, Ikeda, Osaka 563-8577, Japan.

³Nara Women's University, Kitauoyanishi-machi, Nara 630-8506, Japan.

Email: a.h.basher@ppl.eng.osaka-u.ac.jp

The interactions between hexafluoroacetylacetone (HFAC) with Ni and NiO surfaces have been examined with the use of first principle quantum mechanical (QM) simulation. It is shown that deprotonated HFAC is unlikely to bond with a Ni metal surface as it is. When a Ni or NiO surface is exposed to charge neutral HFAC, its O and C atoms may interact with Ni atoms of the surface, which may lead to the decomposition of HFAC. On a NiO surface, on the other hand, negatively charged O atoms of deprotonated HFAC can be more stably bonded with Ni atoms of a NiO surface than those of enol HFAC (i.e., HFAC whose O atoms are bonded with a single H atom). The highly ionic nature of a NiO surface makes the positively charged Ni atoms of a NiO surface attract the negatively charged oxygen atoms of a deprotonated HFAC. It is surmised that such interaction leads to the formation of highly volatile Ni(HFAC)₂ when HFAC interacts with a NiO surface.

1. Introduction

Organic molecules that can form metal complexes can be ideal etchants for atomic layer etching (ALE) processes for magnetic materials [1]. The use of hexafluoroacetylacetone (HFAC) as an organic etchant, can establish low-damage and highly controlled etching processes on a nickel (Ni) surface [2]. However, HFAC is found experimentally unstable and decomposed on an Ni surface while it can form nickel complex Ni(HFAC)₂ on a NiO surface with an increase of the surface temperature [3]. Moreover, the interaction mechanism of HFAC with Ni and NiO has not been understood well yet [4]. The aim of this work is (1) to explain why HFAC forms Ni complexes – Ni(HFAC)₂ – on a preoxidized Ni surface while no such complexes are formed on a clean Ni surface and (2) to understand why HFAC is decomposed on a clean Ni surface, using first principle simulation.

2. Methodology

In this study, we examine the reaction of a Ni or NiO surface with incident HFAC using the first principle quantum mechanical (QM) simulation. The simulation is performed with GAUSSIAN 09. The B3LYP method is applied as a density functional theory (DFT) model with 6-311G(d) basis set. The structures of a hexafluoroacetylacetone molecule as alkane (HFAC) and enol are optimized using the simulation before they are used whereas the substrate – either Ni or NiO – are fixed as FCC 100.

The single point energy is calculated as a function of the distance between a HFAC molecule and the substrate and the distance is measured from the O atoms of HFAC to the plane. Then, the change in reaction energy ΔE is calculating as shown in eq.1 by subtraction the etchant energy (E_t) and substrate energy (E_2) from the total energy of both of them together (E_t) :

$$\Delta E = E_t - E_1 - E_2 \quad (1)$$

3. Results and discussion

3.1 A Ni surface with enol HFAC

Four different orientations of an enol HFAC molecule (which we denote HFACH) are studied as shown in Fig. 1; an HFACH is (1) perpendicular to the surface and oxygen atoms are close to the

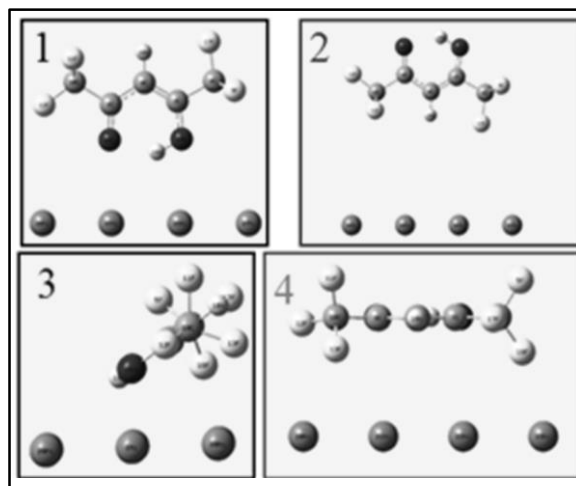


Fig. 1 Different orientations of a HFACH molecule on a Ni surface.

surface ("Ni+HFACH"), (2) perpendicular to the surface but oxygen atoms are far away from the surface ("Ni+ inv. HFACH") (3) tilted at 33° angle toward the surface ("Ni~ 33° HFACH") and (4) parallel to the surface ("Ni//HFACH"). When an HFACH interacts with a Ni metal surface, the O and C atoms of the HFACH may interact with the surface, as shown in Fig. 2, and the HFACH may decompose.

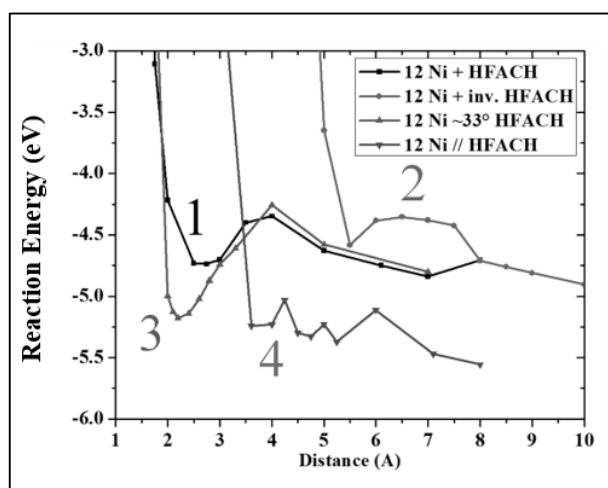


Fig. 2 Change in reaction energy between a Ni surface and HFACH.

3.2 A Ni surface with deprotonated HFAC

The calculation of the interaction between a Ni metal surface and deprotonated HFAC shows that transfer of a H atom from HFAC to form deprotonated HFAC is not likely to occur, Fig. 3.

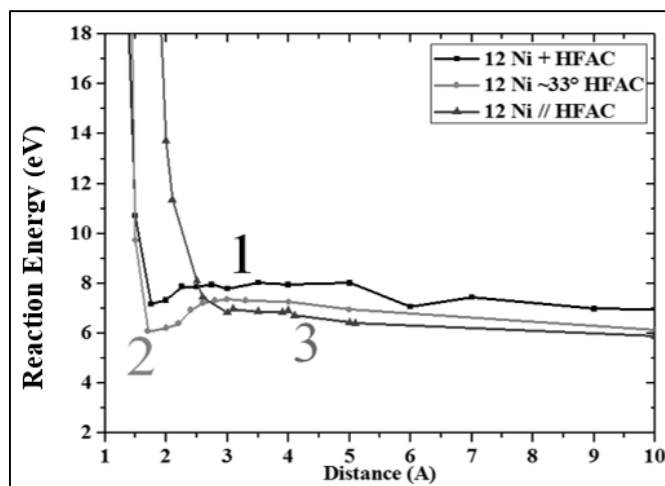


Fig. 3 Change in reaction energy between a Ni surface and a deprotonated HFAC.

3.3 A NiO surface with enol HFAC

The reaction energy curves between a NiO surface and HFACH in Fig. 4 illustrate that the H atom blocks a O atom of the HFACH and the strongest interaction takes place between the other O atom of the HFACH with Ni atoms. However, C atoms of the HFACH may interact with O atoms of the surface, which may also decompose HFACH.

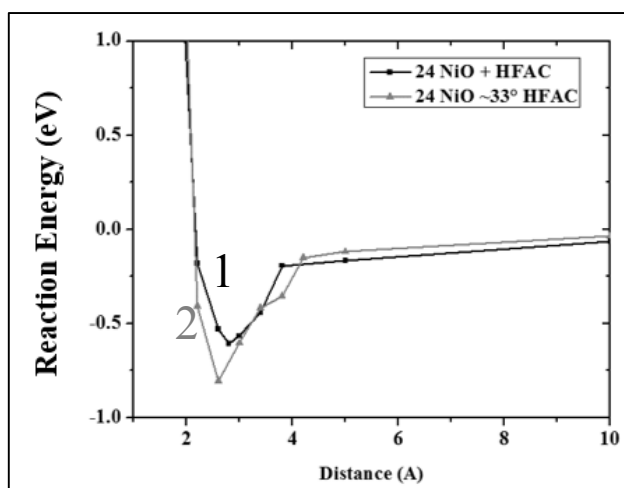


Fig. 4 Change in reaction energy between a NiO surface and a HFAC molecule.

3.4 A NiO surface with deprotonated HFAC

The curves in Fig. 5 indicate deprotonated HFAC can be strongly bonded with Ni on a NiO surface, which may lead to the formation of volatile metal complexes $\text{Ni}(\text{HFAC})_2$.

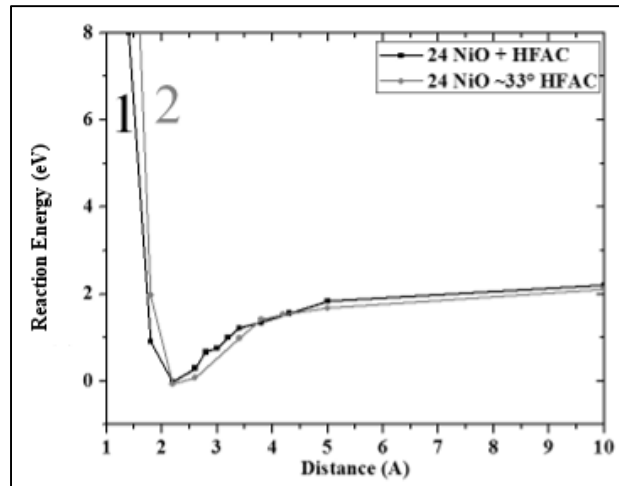


Fig. 5 Change in reaction energy between a NiO surface and a deprotonated HFAC.

4. Conclusions

We have performed QM simulation to examine interactions of HFAC with a Ni or NiO surface. It is found that O atoms of a deprotonated HFAC molecules are attracted to positively charged Ni of a NiO surface.

5. Acknowledgment

We are grateful for Prof. Yoshitada Morikawa and Prof. Ikutaro Hamada for their significant advice to improve this work.

6. References

- [1] Chen J K Kim T Altieri N D Chen E and Chang J P 2017 *J Vac Sci & Tech A* **35** 031304.
- [2] Chen J K Altieri N D Kim T Chen E Lill T Shen M and Chang J P 2017 *J Vac Sci & Tech A* **35** 05C305.
- [3] Ito T Karahashi K and Hamaguchi S 2017 *the 10th EU-Japan Joint Symposium on Plasma Processing JSPP2017 Okinawa Japan*.
- [4] Nigg H L and Masel R I 1999 *J Vac Sci & Tech A* **17** 3477.

FORMATION OF LIFE PRECURSOR MOLECULES IN TITAN RELATED ATMOSPHERE AT RELEVANT TEMPERATURE AND PRESSURE

Stanislav Chudjak, Frantisek Krcma

Brno University of Technology, Faculty of Chemistry, Purkynova 118, 612 00 Brno, Czech Republic

E-mail: xcchudjak@fch.vut.cz

The chemical processes initiated by electrical discharges in prebiotic atmospheres became a hot topic during the last decade because of extensive discovering of exo-planets. The biggest atmospheric data collection is about Saturn's moon Titan atmosphere that is composed mainly from nitrogen and methane at low temperature of about 94 K and pressure about 1.5 atmospheres. The presented contribution gives the first measurement of the main compounds formed in glow discharge in nitrogen-methane gaseous mixture at the liquid nitrogen temperature at pressure of 1.5 atmospheres. The obtained results confirmed formation of many molecules identified at Titan by Huygens landing module. Moreover, the very complex chemistry leading to the formation of currently considered direct life precursors as formamide in significant amount was discovered.

1. Introduction

Laboratory mimic studies of processes running in the exo-planetary atmospheres became a hot topic during the last years because many exo-planets were discovered very recently and their number increases very rapidly. Moreover, the successful space missions like Cassini-Huygens bring a huge number of data from the in situ observations that are impossible using the earth techniques [1-3]. The main interest is focused on the search of life traces or life molecular precursors and consequent discovering the possible ways leading to the life origins formation. The majority of studies were carried out in the Titan's atmosphere up to now because there are many in situ available data and its atmosphere seems to be very similar as Earth's before life creation [3-5]. Besides the exo-planetary atmospheric processes initiated by UV and VUV radiation and particles fluxes coming from the space, the electrical discharge phenomena can play an important role in the planetary atmosphere chemistry [6]. Lightning was confirmed in more planetary atmospheres [7, 8]. The planetary scale processes can be simulated by laboratory experiments using various discharges: corona and DBD conditions are similar as the St. Elmo's fire, spark and arc relates to lightning, and corona and glow conditions are similar to conditions in aurora borealis. Nearly all laboratory studies of Titan atmosphere discharge initiated processes up now were carried out at ambient temperatures and pressure that are not fully reflecting real Titan surface conditions. The presented study gives the first results obtained by glow discharge generated in the Titan like atmosphere (nitrogen-methane mixture) in the flowing regime at the liquid nitrogen temperature [5, 9].

2. Experimental

The experiment was carried out in the simple glass reactor (see Fig. 1) equipped by a pair of tungsten rod electrodes (diameter of 1 mm) in distance of 0.7 mm. The glow discharge was operating at the currents of 10, 20, and 30 mA (corresponding powers of 3.5, 7.0, and 10.5 W). Reactor was placed into Dewar vessel fill able by liquid nitrogen up to level 2 above the electrode system. The nitrogen (99.999%) flow of 200 Sccm and methane (99.95%) flow of 1 Sccm were fixed and controlled by Bronkhorst MCFs. Pressure in the reactor during the experiment was kept at 1.5 atmosphere and was measured by simple membrane based indicator. The exhaust gas analysis was examined by proton transfer reaction time of flight (PTR-TOF) mass spectrometry allowing continual in situ complex analysis of the discharge exhaust gas. Advantage of this technique is immediate response and simultaneous detection of all compounds with proton affinity higher than proton affinity to water molecules. Thus it is not sensitive on any of the gasses in the reaction mixture. Unfortunately, there is impossible to distinguish isomers. Whole line (made of PTFE and stainless steel) to PTR-TOF mass spectrometer was heated up to 80 °C to avoid discharge products condensation. Experiment was completed following the scheme:

- 1) -300 s start of reaction mixture flow
- 2) 0 s start of measurement
- 3) 60 s discharge turn on
- 4) 600 s starting reaction vessel cooling
- 5) 1800 s discharge off
- 6) 2400 s end of vessel cooling
- 7) 3000 s start of reactor heating by hair drier
- 8) 3300 s end of reactor heating by hair drier; nitrogen (99.999%) high flow of 5 Slm purge flow on, opening of exhaust gas valve at the PTR-TOF input
- 9) 4200 s , nitrogen purge flow off; end of experiment

Reactor was not opened or cleaned between experiments, so some contamination (mainly by some deposited material on electrode surfaces) was possible.

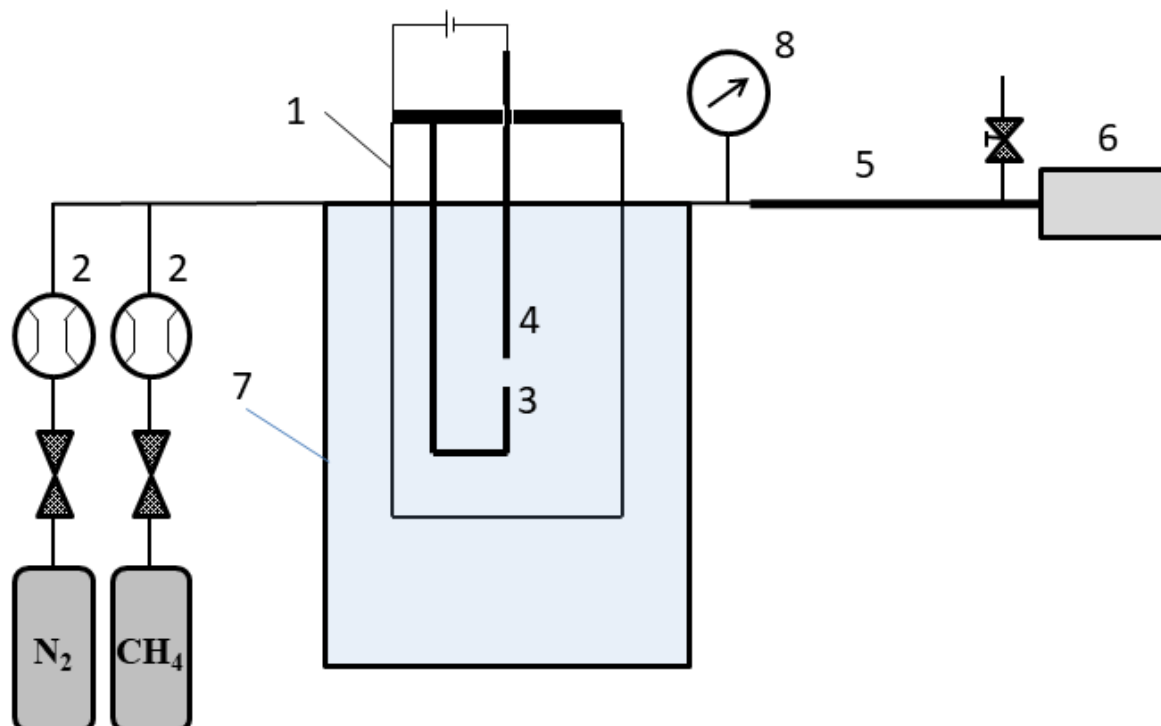


Fig. 1. Scheme of the experimental set up: 1 – Pyrex glass reactor vessel; 2 – mass flow controller; 3 – cathode; 4 – anode; 5 – heated exhaust gas sampling line; 6 – proton transfer reaction time of flight mass spectrometer; 7 – liquid nitrogen vessel; 8 – membrane manometer.

3. Results

The time profiles of concentrations for the selected compounds are given in Figs. 2-5. The hydrogen cyanide (Fig. 2) and acetonitrile (Fig. 3) are the main compounds formed by the discharge in nitrogen-methane mixtures [10, 11]. Both these compounds reach during the discharge operation and later evaporation of condensed discharge products the saturation limit of the current device and thus there are rather complicated to relate them to appropriate kinetic processes. Additionally, the time profile of the HCN shows a strong dependence on the applied power. At the lowest one, the simple production in the discharge is visible followed by concentration decrease during the cooling (due to trapping on the cold reactor walls) followed by the strong concentration increase during the reactor heating. The profile obtained at the medium power of 7 W shows more complicated behaviour. The significant concentration decrease is observed during the discharge operation at the ambient temperature. The additional concentration drop is visible just at the beginning of the discharge cooling and later the concentration reaches nearly the same value as at the lowest power up to the discharge off. The concentration profile after the reactor heating is nearly the same as at the lowest applied power. The most complicated curve was obtained at the highest power. The behaviour up to end of cooling is similar as at the medium power but the first concentration drop starts sooner and it is deeper when

before. Also the concentration during the cooling period is about 30% lower than at the medium power. The dependence after the start of reactor self-heating shows three huge peaks of the HCN presence. There is no reason for this besides the secondary formation of HCN molecules from some bigger clusters deposited (trapped) on the reactor walls.

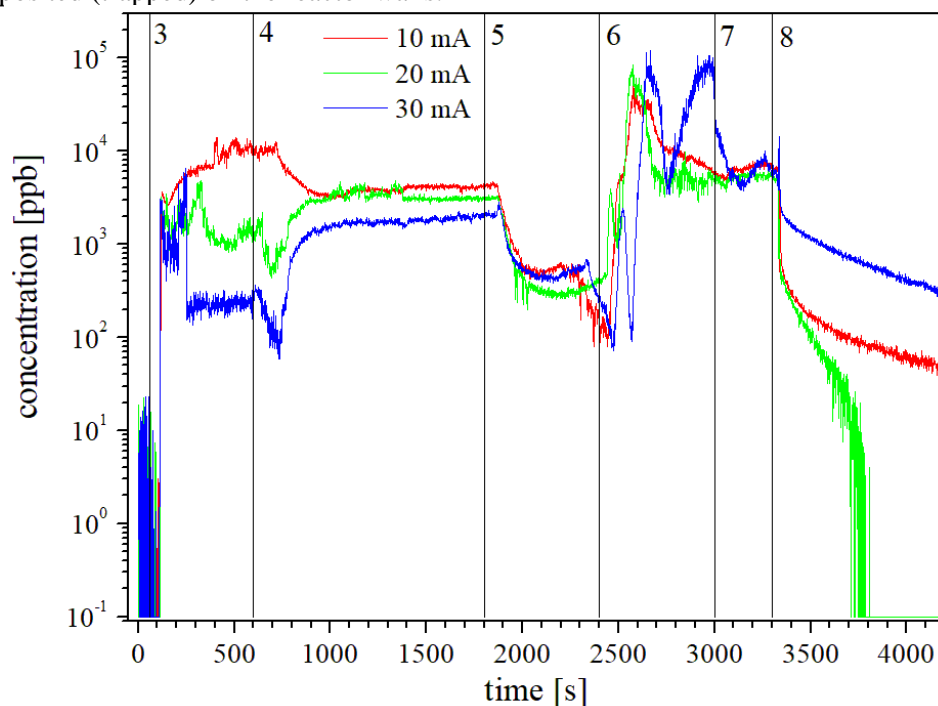


Fig. 2. Concentration of hydrogen cyanide during the experiment. The vertical lines indicate experimental setting points given in experimental section. Note that saturation limit for the used detection technique is about 60 000 ppb for this compound.

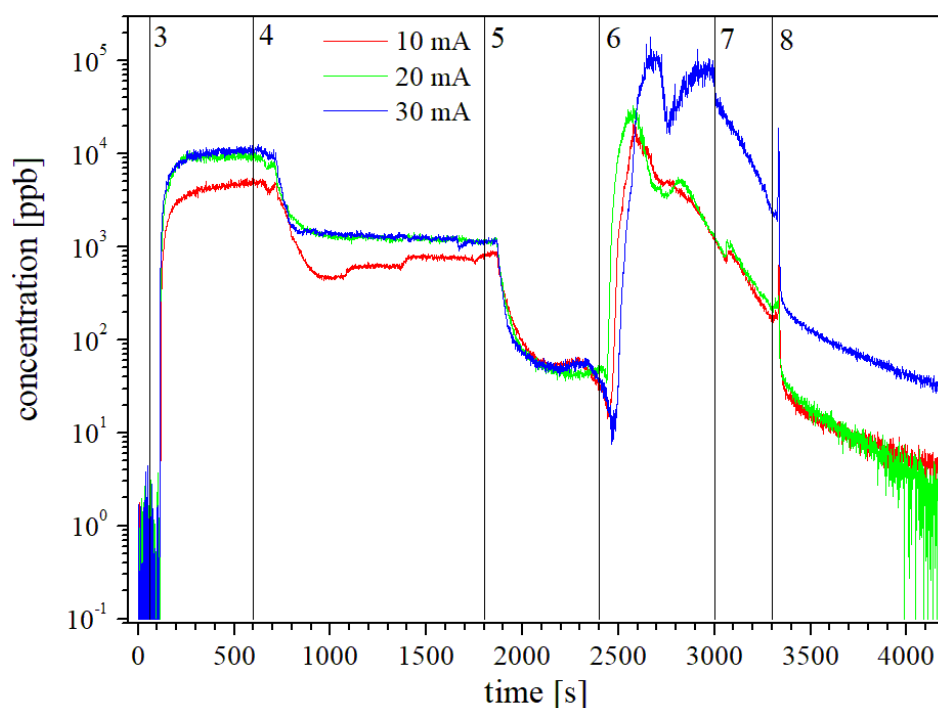


Fig. 3. Concentration of acetonitrile during the experiment. The vertical lines indicate experimental setting points given in experimental section. Note that saturation limit for the used detection technique is about 60 000 ppb for this compound.

The production of acetonitrile (see Fig. 3) in the discharge is increasing with the applied power but it has probably some saturation limit. No unexpected points like in case of HCN were recorded. The concentration time profile during the heating part of experiment shows nearly the same dependences for both the applied powers with faster concentration increase in case of the medium power. The two concentration peaks are visible for the highest applied power, similar like in the case of HCN (the concentration drop is at the same time for the both compounds).

Besides the main formed compounds many tens of other species were successfully identified [10, 11]. The benzene and formamide were selected to present here, only. The first one represents the cyclic hydrocarbons that are important for the synthesis of more complicated organic compounds; formamide is known as the precursor of nuclear acids basis components that can be formed thermally.

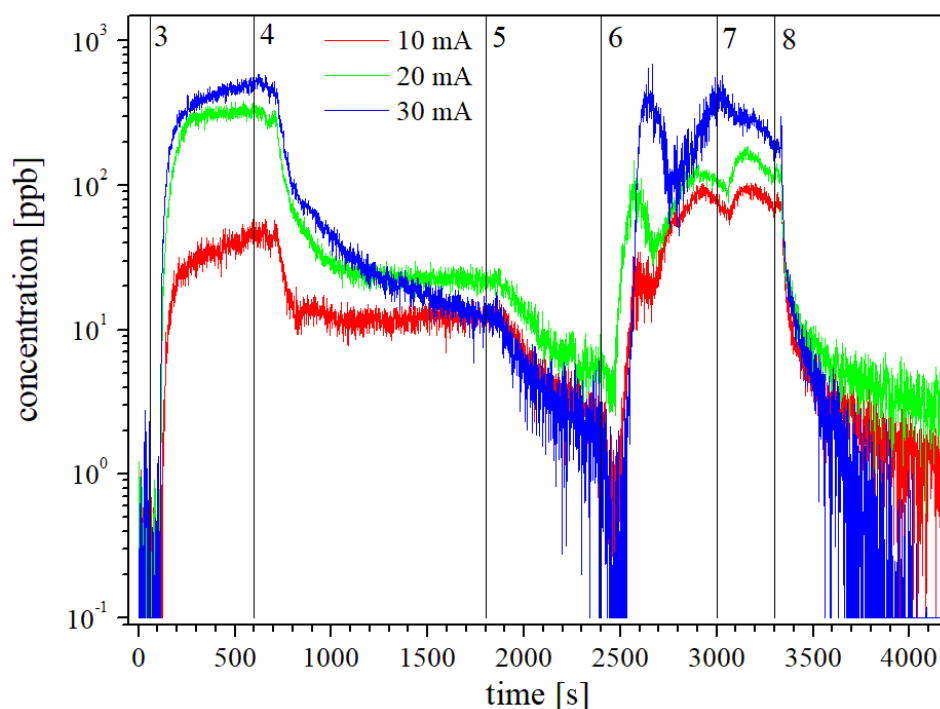


Fig. 4. Concentration of benzene during the experiment. The vertical lines indicate experimental setting points given in experimental section.

Formation of benzene (see Fig. 4) in the discharge at ambient temperature shows strong power dependence. The significant decrease of benzene concentration is visible at the highest applied power during the discharge operating at the liquid nitrogen temperature. We can suppose two effects. The first one is better benzene trapping due to the presence of some other molecules trapped on the glass reactor wall (i.e. surface conditions changes). The second one is formation of some other (probably bigger molecules) at these conditions. This second possibility is more probable because the concentration time dependence during the reactor heating is different from other in the case of highest applied power. The secondary reactions as described in case of HCN are also probable in case of benzene (see curve between point 6 and 7). The final enhancement of benzene concentration after the heating switch on is due to its evaporation from walls.

Concentration time profiles for formamide are shown in Fig. 5. The curves up to the cooling down are similar for all applied power. Concentrations during the cooled period are similar besides the lowest applied power. The high formamide concentrations are detected during the heating period at the highest applied power. This behaviour is very similar as in the case of acetonitrile (see Fig. 3) but without formation of two concentration peaks. This means that reactions of their formation must be different.

The further experiments including analysis of all peaks (even not identified, yet) in the PTR-TOF spectra will be necessary to carry out to be able to understand whole very complex kinetics. Based on the obtained experimental data also the complex kinetic model will be needed to detailed understanding of the possible life precursors synthesis in the Titan atmosphere.

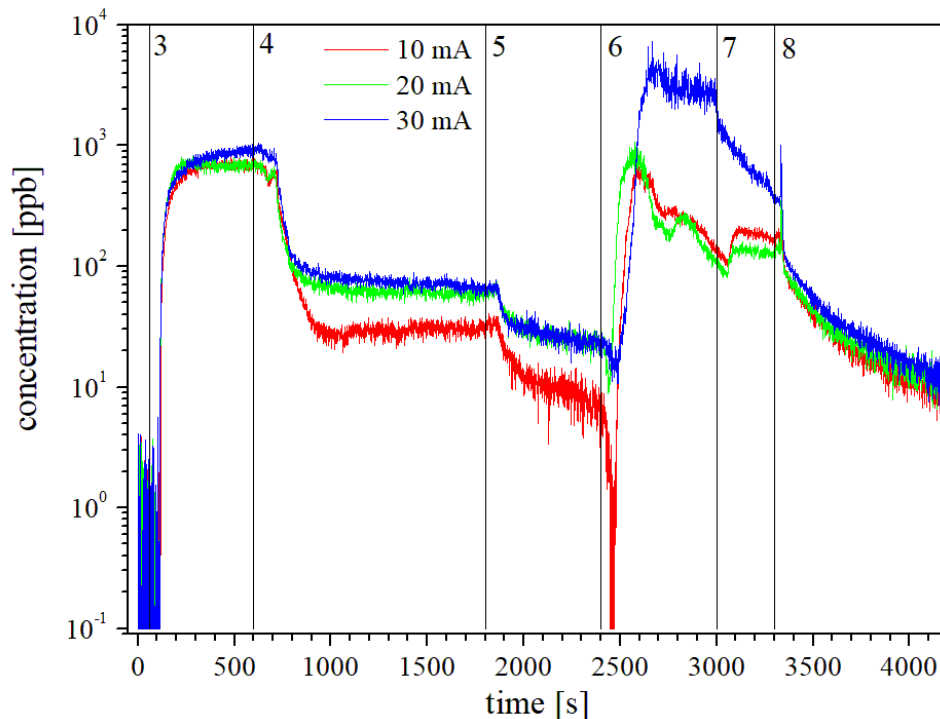


Fig. 5. Concentration of formamide during the experiment. The vertical lines indicate experimental setting points given in experimental section.

4. Conclusion

The presented contribution brings the first experiments obtained in the Titan like atmosphere at relevant temperature and pressure. The shown pilot experimental data demonstrated the important role of temperature for the formation of different molecules that can be the life precursors (like formamide). The detailed further experiments (also done with respect to saturation for some discharge products) will be done to verify the role of discharge operation power and duration as well as role of reaction gas mixture compositions. It will be also necessary to develop complex kinetic model to be able to understand the complex chemistry initiated by electrical discharges in this prebiotic atmosphere.

5. References

- [1] J. M. Bernard et al. *Icarus* 185 (2006) 301
- [2] J. M. Bernard et al. *Proc. Sec. Eur. Workshop on Exo-Astrobiology* (2002) 623
- [3] H. Imanaka et al. *Icarus* 168 (2004) 344
- [4] R.E. Johnson, et al. *Icarus* 271 (2016) 206
- [5] J.A. Kammer, et al. *Planet. Space Sci.* 88 (2013) 92
- [6] A. Ardaseva, et al. *Month. Not. Roy. Astronom. Soc.* 470 (2017) 187
- [7] K. Aplin, G. Fischer *Weather* 72 (2017) 46
- [8] R. D. Lorenz *Progress Earth Planet. Sci.* 5 (2018) 34
- [9] T. Tokano. *Icarus*. 289 (2017) 133
- [10] L. Töröková et al. *Eur. Phys. J. – Appl. Phys.* 71 (2015) Art. No. 20806
- [11] L. Töröková et al. *Contr. Plasma Phys.* 55 (2015) 470

ION MOBILITY SPECTROMETRY MONITORING OF DECOMPOSITION OF DIMETHYL PHTHALATE BY POSITIVE CORONA DISCHARGE

Ladislav Moravský¹, Bartosz Michalczuk¹, Štefan Matejčík¹

¹*Department of Experimental Physics, Comenius University,
Mlynská dolina F-2, Bratislava 842 48, Slovakia
E-mail: ladislav.moravsky@fmph.uniba.sk*

We present new method for monitoring of decomposition of Dimethyl phthalate by corona discharge based on Ion Mobility Spectrometry (IMS). IMS offers detection of low concentration of vapours in air with high sensitivity combined with fast response time and sufficient spectral resolution and therefore is suitable for online monitoring of these compounds. In present work Dimethyl phthalate (DMP) vapours mixed with ambient air at atmospheric pressure were treated by positive corona discharge. Their decomposition was monitored using the IMS technique.

1. Introduction

The problem of fast detection of trace amounts of volatile organic compounds (VOCs) has become an important issue in the last decades. One of the most suitable techniques in this field is Ion Mobility Spectrometry (IMS). Several laboratories have developed IMS or ion mobility-mass spectrometry (IMS-MS) techniques for the analysis of complex chemical compounds [1-6].

Due to its high sensitivity and fast response the CD-IMS technique has been used in present study to detect DMP (Figure 1). Phthalates are VOCs and mainly used as plasticizers, additives to plastics to increase their durability, flexibility, longevity, and transparency. They are used primarily to soften polyvinyl chloride (PVC). In present work DMP has very low vapour pressure of 0.3 Pa at room temperature, thus its relative concentration is only 3.15 ppm. Such low concentration is difficult, or impossible to measure using conventional techniques e.g. infrared (FTIR) spectroscopy. The high sensitivity and fast response of IMS allows to perform online monitoring of DMP and its decomposition.

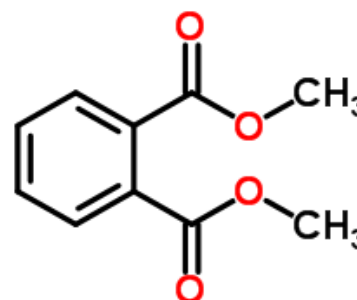


Fig.1: Chemical structure of the investigated molecule.

2. Experimental part

For measuring the mobilities of DMP ions a home-made IMS spectrometer (Figure 2) has been used. It consisted of four major parts which the corona discharge (CD) ion source, the reaction region, drift tube, and a detector which are placed in the end of the drift tube. For detection of VOCs we use Atmospheric Pressure Chemical Ionisation (APCI) technique based on Corona Discharge (CD) ion source. As a drift gas in IMS, we used zero air generated by a zero air generator and an additional moisture trap (Agilent). In case of sample flow, non-purified lab air was constantly sucked in, while the IMS was operated in sub-atmospheric pressure. The sample flow rate was controlled by a micro-splitter valve (Supelco) accompanied by a capillary and a gas flow meter (Platon). The reactant ions (RI) generated in CD were $\text{H}_3\text{O}^+(\text{H}_2\text{O})_n$ ($n=2,3$) and in very low concentration of $\text{NO}^+(\text{H}_2\text{O})_n$ ($n=2,3$). The IMS has been operated in reverse mode. Decomposition of DMP was carried out in corona discharge reactor in wire to cylinder geometry, positive polarity and $U = 3.73\text{-}4.08\text{ kV}$, $I = 10\text{-}40\ \mu\text{A}$. The flow rate of the sample gas was 30 sccm.

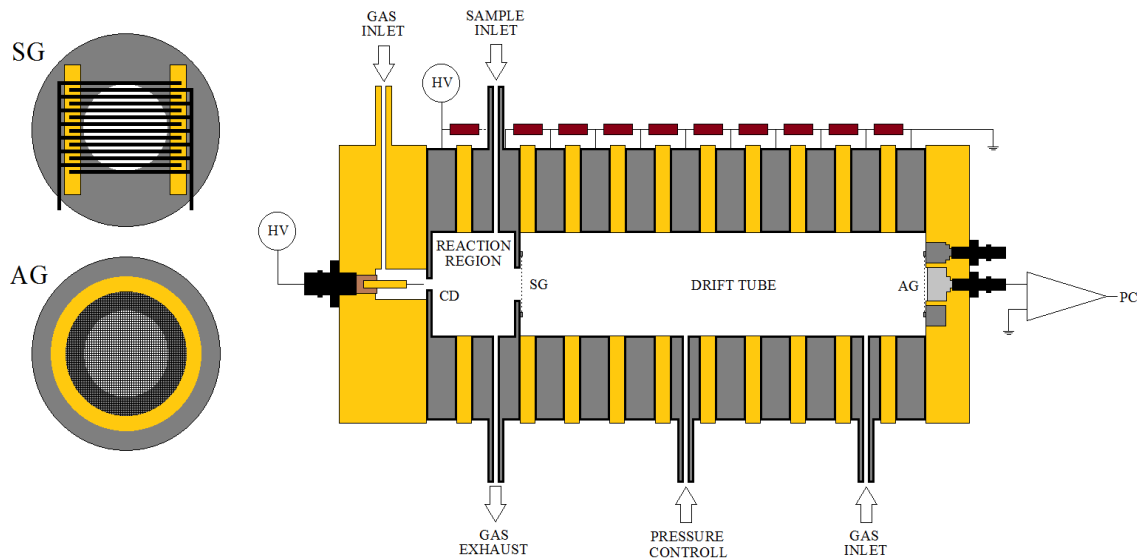


Fig.2: Scheme of the IMS spectrometer : CD – Corona discharge, SG – Shutter grid, AG – Aperture grid, HV – High voltage.

The sample gas has been prepared in a 20 ml glass vial (SUPELCO) with silicone/PTFE screw cap adopted for flow of the air through the vial. The air flow through the glass vial with liquid DMP resulted in preparation of sample gas with DMP concentration of 3.15 ppm. Between the glass vial and an IMS spectrometer the corona discharge reactor have been placed (Figure 3). Introduction of DMP air mixture to IMS without treatment in the corona discharge reactor results in formation of strong peak in mobility spectra shown in Figure 4 related to DMP. With increasing corona discharge power in the reactor the decrease of the intensity of the DMP in the IMS spectrum was observed. This decrease we relate to the decomposition of the DMP molecules in reactor. We were not able to detect in the IMS spectra any new peaks, most probably because the products of the decomposition do not have proton affinity high enough to react with the RI formed in the ion source.

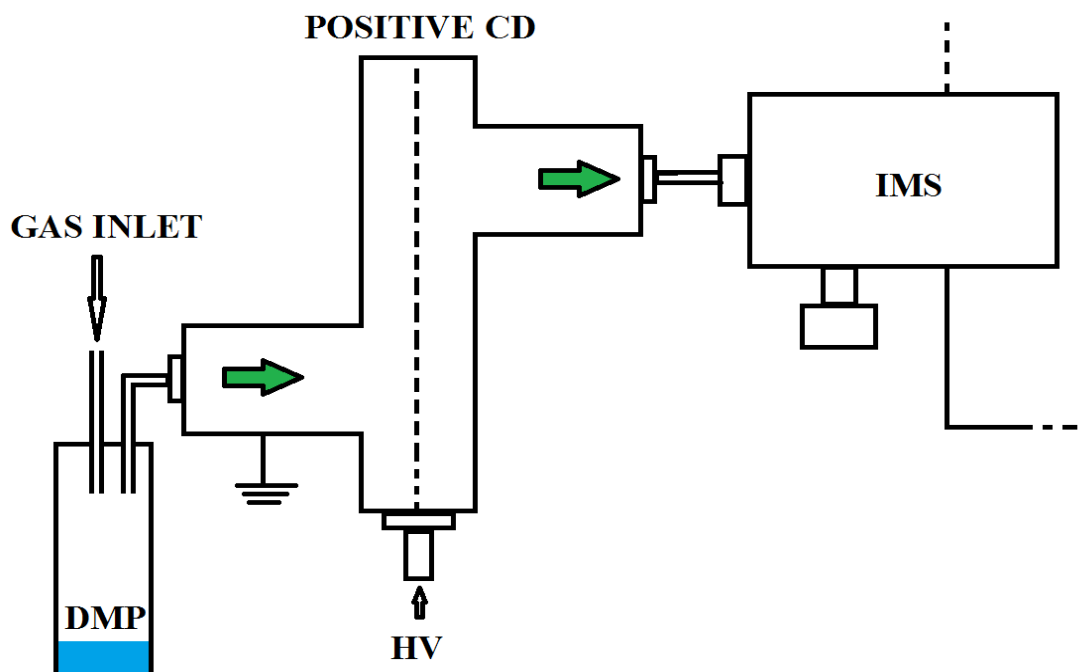


Fig.3: Scheme of the experimental apparatus – glass vial with DMP sample, external corona discharge and the IMS spectrometer

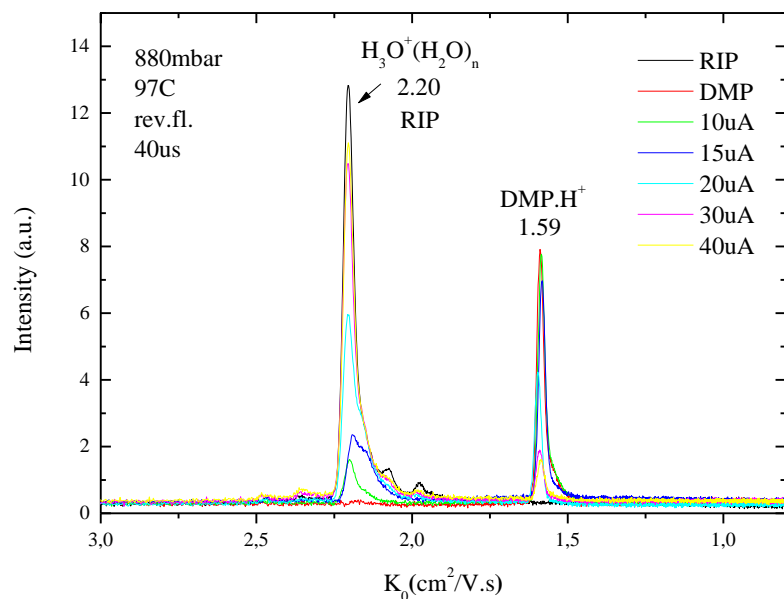


Fig.4: IMS spectra of DMP after degradation by corona discharge at various discharge current.

We compared the intensity of RIP in our case it was $H_3O^+(H_2O)_n$ (with mobility $2.20 \text{ cm}^2 \cdot \text{V}^{-1} \cdot \text{s}^{-1}$) and the $DMP.H^+$ ions (mobility $1.59 \text{ cm}^2 \cdot \text{V}^{-1} \cdot \text{s}^{-1}$) depending on electrical power of external corona discharge (Figure 5). With increasing the discharge power to 80mW the intensity of $DMP.H^+$ peak is decreasing to the half of maximum, while the intensity of RIP increasing. After corona discharge ignition, less DMP molecules from the external corona reactor were penetrate to the IMS spectrometer. Lower concentration of DMP molecules was due to decomposition or capture of the molecules on the reactor wall. We need more experiments to verify our hypothesis.

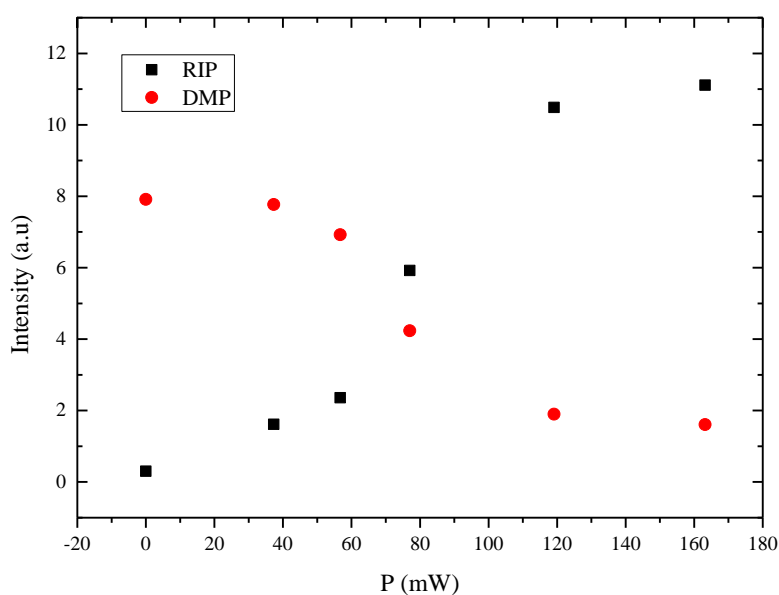


Fig.5: Intensity comparison of the reactant ions and the DMP ion depending on the external corona discharge power.

Acknowledgement:

- European Union's Horizon 2020 research and innovation programme under the Marie Skłodowska-Curie grant agreement No 674911
- Slovak Research and Development Agency Project Nr. APVV-15-0580 and the grant agency VEGA, project Nr. VEGA-15-089.
- European Union's Horizon 2020 research and innovation programme under grant agreement No 692335

References

- [1] S. J. Valentine, X. Y. Liu, M. D. Plasencia, A. E. Hilderbrand, R. T. Kurulugama, S. L. Koeniger, D. E. Clemmer, *Expert Rev. Proteom.* **2** (2005) 553–565.
- [2] S. L. Koeniger, S. J. Valentine, S. Myung, M. Plasencia, Y. J. Lee, D. E. Clemmer, *J. Proteome Res.* **4**, (2005) 25–35.
- [3] R. A. Sowell, S. L. Koeniger, S. J. Valentine, M. H. Moon, D. E. Clemmer, *J. Am. Soc. Mass Spectrom.* **15**, (2004) 1341–1353
- [4] C. Wu, W. F. Siems, J. Klasmeier, H. H. Hill, *Anal. Chem.* **72**, (2000) 391–395
- [5] J. A. McLean, B. T. Ruotolo, K. J. Gillig, D. H. Russell, *Int. J. Mass Spectrom.* **240**, (2005) 301–315
- [6] M.F. Jarrold, *Annu.Rev.Phys. Chem.* **51**, (2000) 179–207

ELECTRON CAPTURE IN IMS DETECTORS – a comparison of ECD, DT IMS and DMS

Jarosław Puton, Edyta Budzyńska, Michał Grabka,

Bartłomiej Fliszkiewicz, Monika Wiśnik-Sawka

Institute of Chemistry, Military University of Technology, Warsaw 00-908, Poland

E-mail: jaroslaw.puton@wat.edu.pl

The electron capture (EC) is an effective method for generation of ionic products which is used in instrumental analysis. The best-known way of taking advantage of this method is to measure electron currents in electron capture detectors (ECDs) applied in gas chromatography. In detectors used in ion mobility spectrometry (IMS), EC can be seen as the one of methods for ionization of sample components in negative mode. If the carrier gas in IMS is nitrogen, EC is the main method for producing negative ions. Our work is devoted to the comparison of detection efficiency of selected analytes in a typical ECD and two different IMS detectors.

1. Introduction

Electron capture detectors (ECDs) have been used in gas chromatography for many years [1]. The construction of these devices is very simple. They are built in the form of small ionization chambers, mostly of cylindrical geometry, with an internal radioactive source. The carrier gases used in the ECD are pure nitrogen or argon with an admixture of hydrocarbons. As a result of the ionization of these gases, positive ions and electrons are produced. Electrons can be captured by the molecules of the sample components with high electron affinity. Negative ions produced in such way move in the electric field much slower than electrons. Under ECD conditions, ion-ion recombination occurs much more efficiently than electron-ion recombination and therefore the introduction of an electrophilic compound to the detector results in a reduction of the ionic current. Electron capture (EC) is a process whose efficiency depends on the energy of electrons [2]. Very often, the highest values of the capture cross-section are obtained for thermal electrons. For this reason, the ECDs are supplied with short voltage pulses that allow for collecting of all electrons that have not been captured by the analyte molecules. In the intervals between pulses, the value of the electric field is close to zero. This prevents the "heating" of electrons, which lowers the cross-section for the capture. The detection limits obtained with the use of ECD in the analysis of compounds with high electron affinity are very low. For some substances it is possible to obtain a coulometric effect. It consists in the fact that virtually every analyte molecule introduced into the detector is ionized, and the electric charge transferred to the molecule changes the value of the ionic current [3]. A comprehensive review of ECD research is contained in the monograph by Zlatkis and Pool [4].

Ion mobility spectrometry (IMS) is an analytical technique based on the measurements of ionic motion in an electric field in the gas phase [5]. In contrast to ECD, IMS detectors enable the identification of ionic products. There are several IMS variants that differ in the ion-separation method [6]. The classic variant uses spectrometers with a drift tube (DT IMS), whose operation is based on the measurement of ions' drift times. Another kind of IMS detectors - differential mobility spectrometers (DMSs) have been known for about 25 years [7]. In these instruments, the separation of ions takes place on the basis of non-linear effects occurring during their movement in the electric fields of high intensity. If the carrier gas in the IMS detectors is nitrogen, the ionization of the sample components in the negative mode occurs as a result of the EC. Studies on such processes was carried out by Karasek [8] and Spangler [9]. They found that the conditions occurring in IMS detectors are definitely different from those that are present in ECDs. The electric field in ionic reactors of IMS detectors has a value of the order of 200 V / cm. Under such conditions, the average electron energy in nitrogen reaches about 0.5 eV, which is significantly higher than thermal energy. This has a significant impact on the ionization efficiency of the sample components in EC mode. DT IMS can also be used to study the kinetics of the electron capture process [10,11].

The main purpose of our research was to compare the analytical properties of ECD and two types of IMS detectors working in the electron capture mode for several characteristic analytes. The principle of operation of detectors used in research is shown in Fig. 1. All detectors were equipped with ^{63}Ni radioactive sources emitting beta radiation.

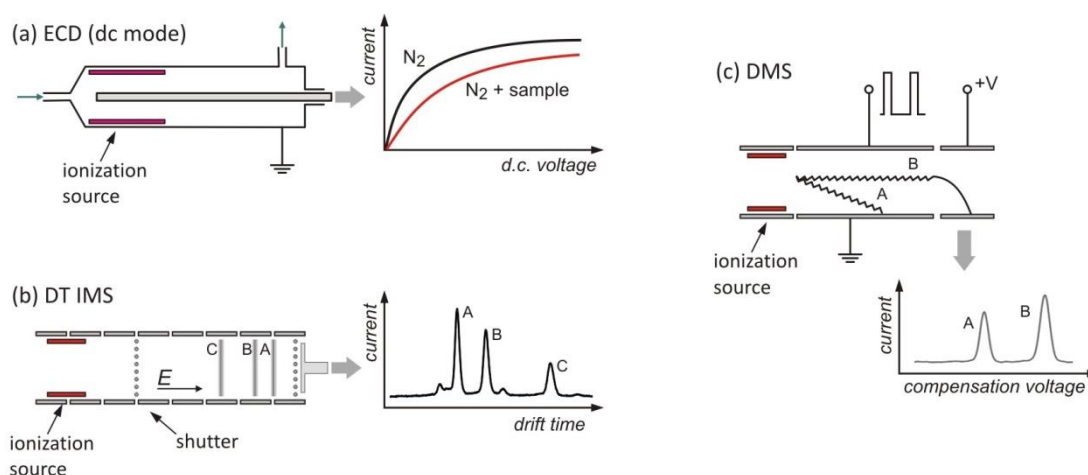


Fig. 1. Schemes of construction and the principle of operation for electron capture detector (a), drift tube ion mobility spectrometer (b) and differential mobility spectrometer (c).

2. Results and discussion

Three detectors were used in our research: ECD DNW 600 detector (Department of Nuclear Physics, Kraków), DT IMS detector (own construction built at the Military University of Technology, Institute of Chemistry, Warsaw) and DMS detector (prototype device developed at the Military Institute of Chemistry and Radiometry, Warsaw). The research was carried out for organic compounds that contain chlorine atoms in their molecules: carbon tetrachloride (CCl_4), chloroform (CHCl_3) and benzyl chloride ($\text{C}_7\text{H}_7\text{Cl}$) (Sigma Aldrich) with purity $\geq 99\%$, as well as 2-chloroethyl ethyl sulphide (CEES) (Sigma Aldrich) with purity of 97%.

Comparison of the properties of different detectors required the use of the relative signal S_{rel} . It was calculated using the formula:

$$S_{rel} = \frac{S(C_x) - S(0)}{S(C_{sat}) - S(0)} \quad (1)$$

where $S(C_x)$ is the absolute signal measured at analyte concentration C_x , $S(0)$ the signal measured at the analyte concentration equal to zero and $S(C_{sat})$ is the signal measured at the analyte concentration causing saturation of detector's response.

All chemical compounds selected for analysis were ionized in dissociative electron capture process. Its result is the generation of chloride ions (Cl^-) in the reaction described by the equation:



Analyte vapors were introduced into the detector from a gas generator containing permeation standards and a dilution system with mass flow controllers. Measurements of the detector signal allowed to determine the calibration curves. Their course is shown in Fig. 2. For all detectors, the highest sensitivity is observed for CCl_4 . The ionization efficiency for other analytes is smaller and different for particular detectors.

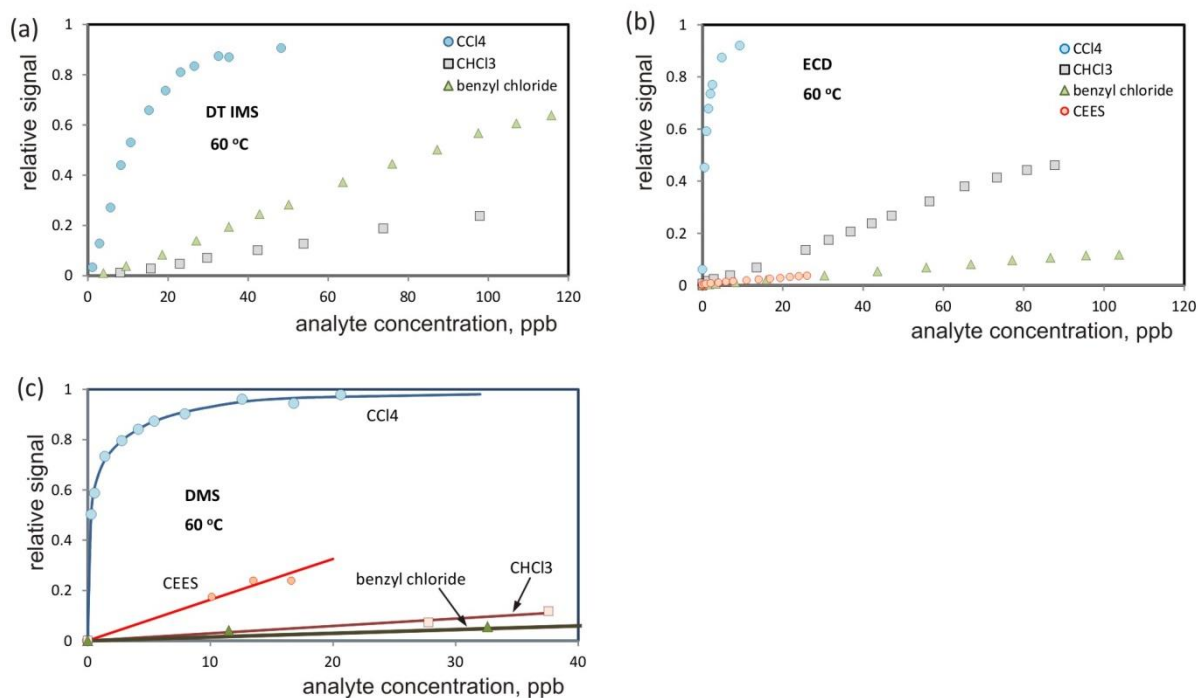


Fig. 2. Calibration curves for test analytes measured with three different detectors.

Based on the initial slope of the calibration curves, detection sensitivity was determined for individual detectors and analytes. The maximum value of sensitivity (175 % / ppb) was achieved for CCl_4 in ECD operating in the pulse mode. When comparing graphs, it can be seen that the sequences of curves in the graphs for different analytes depend on the type of detector. For example, in DT IMS the sensitivity for benzyl chloride is 2.4 times higher than for chloroform. The contrary regularity is observed in the case of ECD, where the sensitivity for benzyl chloride is almost 5 times lower than for chloroform. It is also interesting to compare the signal intensities for CCl_4 and chloroform. In the case of DT IMS, the proportion of sensitivities for both compounds is 24, whereas for ECD it is equal to 158. The explanation of this effect may be based on the dependence of the electron capture rate for CCl_4 and chloroform on electron energy [12,13]. The rate constant for CCl_4 decreases monotonically with the increase in electron energy, while the capture efficiency for chloroform reaches a maximum for energy equal to approx. 0.2 eV (Fig. 3). The measurements we made using the electron capture chamber (BEAM experiment), showed that the maximum EC cross-section for benzyl chloride is observed at 0.5 eV. Such energies are reached by electrons in DT IMS. Therefore, it can be concluded that better conditions for CCl_4 detection occur in DMS or ECD, and DT IMS is better for measuring low concentrations of chloroform or benzyl chloride. CEES is ionized effectively at lower electron energies. The largest signal for this compound is obtained in DMS.

3. Conclusion

Chemical ionization in the negative mode is used much less frequently in chemical analysis than the ionic-molecular reactions leading to the formation of positive ions. However, there is a large group of chemicals that are interesting in terms of safety or environmental protection, which can be effectively detected mainly in the negative mode. In the case when the nitrogen is used as a carrier gas, ionization of the analyte occurs by electron capture. This process can be observed both in ECDs and ion mobility spectrometers. Our studies have shown that the achieved sensitivity is very different for different compounds. It was also demonstrated that the effectiveness of detection depends on the type of detector. This is due to the fact that capture cross section of molecules strongly depends on average energy of electrons. Compounds with high cross-sections for thermal electrons capture are effectively ionized in ECD (pulse mode) and DMS. If the optimal electron energy is more than 0.1 eV, effective ionization is possible in DT IMS.

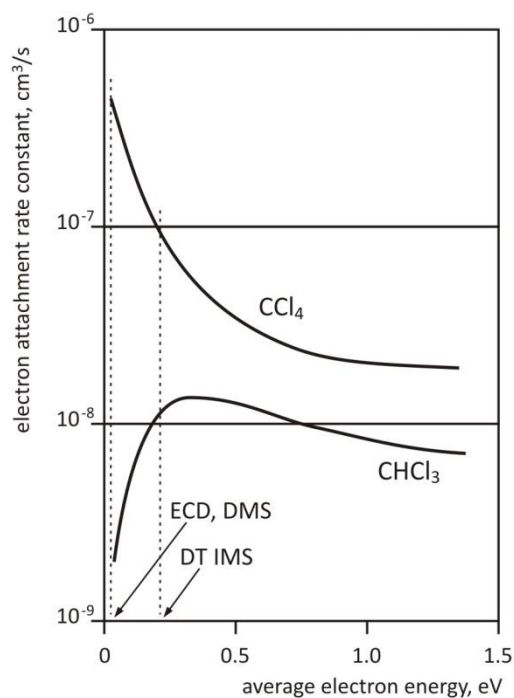


Fig. 3. Electron attachment rate constant as function of average electron energy for CCl_4 and chloroform (based on [12] and [13]).

4. Acknowledgements

This work has been supported by the project Research Grant funded by Polish Ministry of National Defence (GB MON/13-994/2018/WAT) (Poland).

5. References

- [1] J.E. Lovelock, S.R. Lipsky, *J. Amer. Chem. Soc.* **82** (1960) 43.
- [2] L. G. Christophorou, R. N. Compton, G.S. Hurst, P.W. Reinhardt, *J. Chem. Phys.* **43** (1965) 4273.
- [3] J. E. Lovelock, *Anal. Chem.* **33** (1961) 162.
- [4] A. Zlatkis, C.F. Poole, *Electron Capture Theory and Practice in Chromatography*, *J. Chrom.* **20** (1981) 1-429.
- [5] G.A. Eiceman, Z. Karpas, H.H. Hill Jr., *Ion Mobility Spectrometry*, 3rd ed., CRC/Taylor & Francis, Boca Raton, 2013.
- [6] R. Cumeras, E. Figueras, C.E. Davis, J. I. Baumbach I. Gràcia, *Analyst* **140** (2015) 1376.
- [7] I. A. Buryakov, E. V. Krylov, E. G. Nazarov, U. K. Rasulev, *Int. J. Mass Spec. Ion Process.* **128** (1993) 143.
- [8] F.W. Karasek, O.S. Tatone, D.M. Kane, *Anal. Chem.* **45** (1973) 1210.
- [9] G.E. Spangler, P.A. Lawless, *Anal. Chem.* **52** (1980) 193.
- [10] M. Tabrizchi, A. Abedi, *J. Phys. Chem. A* **108** (2004) 6319.
- [11] Ch. Huang, B. Xu, W. Niu, H. Gao, Y. Hong, L. Xia, Y. Lu, Ch. Shen, Y. Chu, *Int. J. Mass Spectrom.* **402** (2016) 29.
- [12] A.A. Christodoulides, L.G. Christophorou, *J. Chem. Phys.* **54** (1971) 4691.
- [13] T. Sunagawa, H. Shimamori, *Int. J. Mass Spectrom.* **205** (2001) 285.

SMALL MOLECULE ANALYTICS TO ELUCIDATE PLASMA – LIQUID INTERACTIONS

Kristian Wende¹, Giuliana Bruno¹, Thomas von Woedtke², Klaus-Dieter
Weltmann², Jan-Wilm Lackmann¹

¹ZIK *plasmatis*, Leibniz Institute for Plasma Science and Technology (INP), Greifswald, Germany

²Leibniz Institute for Plasma Science and Technology (INP), Greifswald, Germany

E-mail: kristian.wende@inp-greifswald.de

In plasma medicine, cancer and chronic wounds patient benefit from cold atmospheric plasma treatments. However, the biochemical mechanisms are still underexplored. In this study, the interaction of plasma jets with dissolved small molecule tracer compounds was investigated. Via high-resolution mass spectrometry, covalent modifications resulting from the impact of plasma derived gas phase and liquid phase species were identified and a dynamic model relating the different discharge parameters with the deposited and effective reactive was built. In particular, the roles of the short-lived species atomic oxygen and singlet oxygen compared to OH radicals and the long-lived species hydrogen peroxide were addressed. It seems that a considerable amount of the species interacting with the tracer molecules derives from the liquid phase, suggesting that the composition of the treated system significantly modulates the (bio) chemical impact of a plasma source.

1. Introduction

The effectiveness of cold atmospheric plasma (CAP) in various applications, such as microbial inactivation, plant seed germination, cancer treatment, and healing of chronic or acute wounds, is predominantly addressed to the action of reactive species¹⁻⁴. In the core region of noble gas jet plasmas and especially in the effluent, a high number of reactive oxygen and reactive nitrogen species have been detected, alongside with electrons and noble gas ions or metastables. The specific composition is determined by the working gas composition and plasma source design including the characteristics of the high frequency voltage waveform and further modulated by distance from the active plasma zone or ambient conditions. Significant input from the plasma physics community seeks to describe and understand the resulting multi-dimensional dynamics of the active species composition.

From the biochemical point of view only species transferred into (or onto) the aqueous cell environment or tissue (skin, wounds, cancer nodules) are relevant. After entering the biological system, plasma-derived species interact with signalling protocols of human or animal cells, compromise cellular integrity, or trigger downstream reactions that relay the impact of the plasma source from the point of entrance to other parts of the model or body. Which reaction of the biological system follows the treatment depends in large parts on the number and chemical properties of the species hitting the target (“plasma dose”). Therefore, a thorough understanding of the plasma derived species trajectories is desired in order to broaden CAP treatment options in plasma medicine, foster plasma source design for medical applications, and increase safety.

So far, a wealth of studies shows either clinical impact of CAP, with chronic or acute wounds as the major topic, or in vitro results using different primary or – more often – immortalized cell lines⁵⁻¹⁰. The latter range from simple killing, over detection of cell death mechanisms, to metabolic activity, cell cycle analysis or secretion of signal molecules. Such, while we have good knowledge on the functional outcomes resulting from a given plasma treatment, we lack a connection between the gas phase species generated by the plasma, their path into the biological system, and their primary targets. Starting early on, labs within the plasma community investigated liquids, most often water, for the presence of detectable reactive species. The long lived species hydrogen peroxide (H₂O₂), protons (H₃O⁺), nitrite (NO₂⁻), and nitrate (NO₃⁻) were found frequently and could be quantified with a number of methods. Short lived species, such as peroxyxynitrite (ONOO⁻) was determined to be present by following decay processes of the precursors nitrite and hydrogen peroxide in acidic solutions, but direct detection of ONOO⁻ remains elusive. Using electron paramagnetic resonance spectroscopy, hydroxyl radicals (OH), superoxide anion radical (O₂⁻) and nitric oxide (NO) were detected, but could not be quantified due to unknown reaction probabilities of the used spin traps with the respective radicals^{11, 12}. With that, an

unsatisfying picture of plasma – liquid interaction emerges as the community is frequently challenged for just creating hydrogen peroxide.

While H₂O₂ is clearly a major product of some plasma discharges especially when working gases are not absolutely dry, other do not produce it (or do so only transiently) and nonetheless have a massive impact on biological systems^{13, 14}. Here, experimental proof is presented that for plasma discharges in direct proximity to aqueous systems containing organic compounds short lived species dominate the long lived hydrogen peroxide. Using cysteine as small organic tracer compound and the peptide bradykinin as biological macromolecule prototype the chemical impact of the argon jet kINPen and the helium jet COST jet was evaluated using high resolution mass spectrometry as tool to elucidate plasma derived covalent modifications. While in the case of cysteine the thiol group is the preferred target of plasma derived reactive oxygen species, peptides such as bradykinin are targeted by both ROS and RNS. These results clarify the role of plasma derived species and allow the conclusion, that in the clinical setting a large proportion of the chemical energy applied is scavenged by the organic molecules outside the cells. Future work must seek to understand the further fate of the newly generated chemical groups and their biological impact.

2. Methods

Plasma treatments: The argon-driven plasma jet kINPen09 or the helium driven COST jet was used in these experiments^{15, 16}. The working gas flow (3 or 1 slm, respectively) was in part enriched with 0.5 or 1 % molecular gas (oxygen, nitrogen, or a 1:1 mixture of both). In some of the experiments, heavy molecular oxygen (¹⁸O₂) was introduced in the working gas. The distance between jet-nozzle and liquid surface was constant at 9 mm (kINPen) and 4 mm (COST jet), as well as the treated volume (750 µL) in 24 well plates. Treatment times between 30 s and 600 s were used. Aqueous solutions of cysteine at different concentrations were treated, but in the present study 300 µM cysteine were predominantly used. Direct and indirect treatments of cysteine solutions were performed; while in the first case the plasma impacts directly on the liquid, in the second case aqueous solutions were treated in absence of cysteine. Immediately after the treatment, cysteine was added to the plasma treated liquid and allowed to react for 1 minute.

Cysteine derivative elucidation: cysteine-derived structures after plasma impact were characterized via high resolution mass spectrometry (Sciex TripleTOF 5600) via direct infusion. A negative polarity of 4000V on a Turbo V ion source, -10 V collision energy and -10 V declustering potential was used, and a mass range from 50 to 400 m/z at a scan rate of 3 Hz was scanned. If desired, MS2 experiments were performed to achieve substructure information. For the quantification, Hydrophilic interaction liquid chromatography (HILIC) was coupled to a mass spectrometric detection (Sciex QTrap5500). A Multiple Reaction Monitoring modality was set, leading to a more accurate quantification based on MS2 transitions specific for each derivative. The hydrogen peroxide (H₂O₂) was quantified via ferrous oxidation-xylenol orange (FOX) assay.

3. Results and discussion

A number of plasma-induced cysteine derivatives were observed via high resolution mass spectrometry. Information about the structures were obtained by the MS/MS analysis and fine mass, and the identified compounds are shown in Figure 1.

and is oxygen-driven. The concentration and composition of the detected cysteine derivatives are highly dynamic and allow conclusions on the plasma source and discharge parameters. A clear distinction between kINPen and COST jet could be detected by the model system, further modulated by the composition of the working gas (Fig 3).

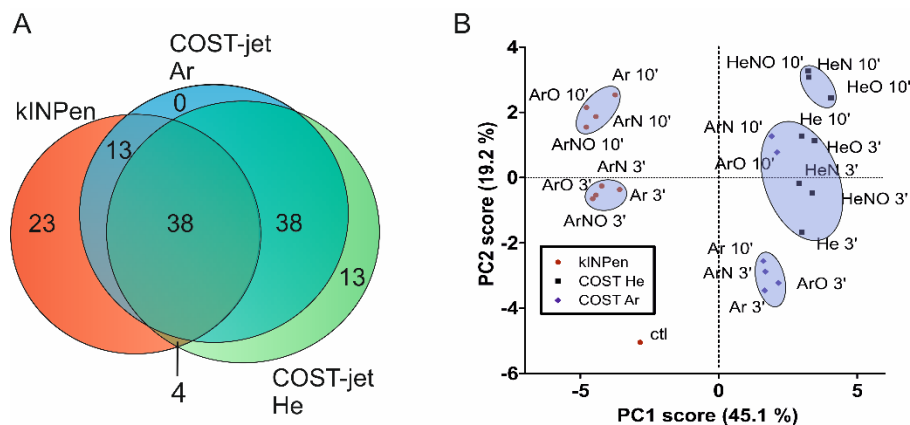


Fig. 3: Venn diagram of all detected cysteine modifications (A) and corresponding PCA (B). Overall, 129 significant products were detected specific to the shown conditions (A). The percentages for the principal components (PC) indicate how much spectral differences can be described with PC1 or PC2, respectively¹⁷.

To confirm the predominant action of short lived reactive species in the oxidation of cysteine, direct treatments were compared with indirect treatments. Indeed, while in the first case the liquid receives the direct effect of all the plasma components (e.g. reactive species, radiation), in indirect treatments the liquid interacts mostly with long-lived species. Figure 4 shows experiments performed via HILIC-MRM separation and quantification of the cysteine derivatives.

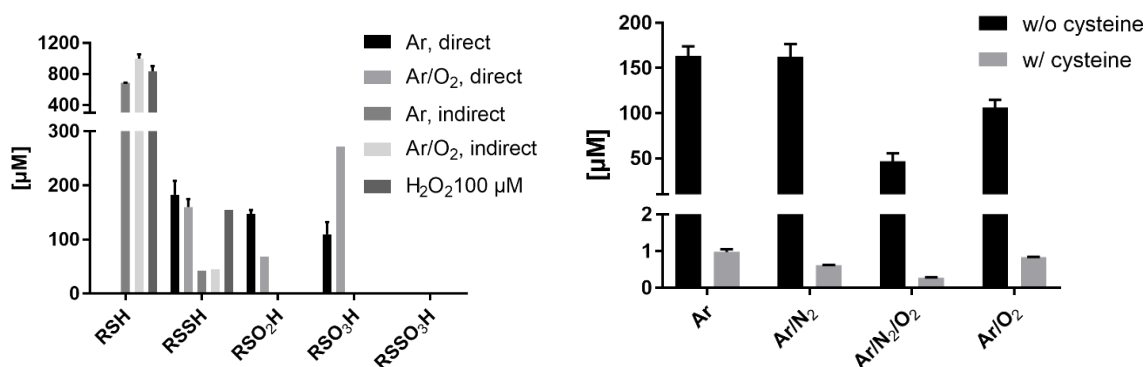


Fig. 4. Impact of direct vs indirect treatments on the cysteine thiol moiety (cysteine 1 mM, 10 min, left). RSH = cysteine, RSSR = cystine, RSO₂H = Cysteine sulfinic acid, RSO₃H = cysteine sulfonic acid, RSSO₃H = cysteine-S-sulfonate. Hydrogen peroxide deposition under different working gases w/ or w/o the presence of cysteine (0.3 mM, 3 min, right).

In this case, the attention was given mostly for the production of cystine (RSSR, primary product) and cysteine sulfinic (RSO₂H) or sulfonic acid (RSO₃H, secondary/tertiary products). The results clearly show that in case of direct treatments a strong oxidation on the thiol occurs, leading to the presence of both cysteine sulfinic and cysteine sulfonic acid. In case of the indirect treatment, no oxidized compounds except cystine are produced. Cystine is also the product that occurs when only hydrogen peroxide is used as control experiment, indicating that in the indirect treatment H₂O₂ is the dominant active species. In contrast, recent publications indicate that singlet oxygen (¹O₂) as well as atomic oxygen (O) may be the relevant reactive species in the case of the direct treatment. Ozone (O₃) might be excluded, as it is generated by three body collisions, that occur predominantly in the far regions of the effluent (>20 mm from nozzle).

To test the penetration of plasma generated species into aqueous liquids, $^{18}\text{O}_2$ was used as an admixture to the working gas (Fig. 5). Among all derivatives, cysteine sulfonic acid was chosen as representative compound, since many of the derivatives follow the same behaviour. The incorporation of zero, one, two (dominant) or three heavy oxygen atoms was observed. These data suggest the diffusion of gas phase reactive species into the bulk liquid, leading to the direct oxidation of the cysteine without interaction with water. Mainly two gas phase ^{18}O atoms were incorporated, hinting at singlet oxygen as a major contributor. Using EPR, significant amounts could be detected in the gas phase and indications were found in the liquid phase¹⁸. Interestingly, some ^{16}O atoms were incorporated into the compound, indicating that either the solvent (H_2^{16}O based) entered the active parts of the effluent and was cleaved there, or that gas phase species were able to lyse the water at the interphase to generate ^{16}OH radicals or similar reactive species.

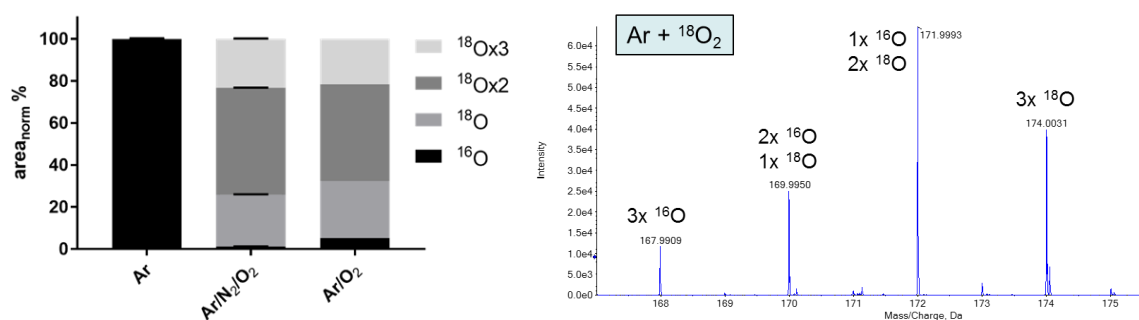


Fig. 5. Incorporation of gas phase oxygen species in the cysteine sulfonic acid (cysteine 0.3 mM, 1 min, left). High resolution mass spectrum showing the incorporation of 1, 2, or 3 ^{18}O atoms into cysteine sulfonic acid (right).

4. Conclusions

Using cysteine as a model substance, its derivatives generated by the plasma treatment form distinctive patterns enabling description and standardization of the chemical potential of different plasma source and discharge parameters in liquids. It is suitable as a tool to understand the liquid chemistry of the chosen treatment conditions. For the plasma sources tested here, a strong impact of short-lived oxygen species produced in the gas phase and that are directly deposited in the aqueous liquid or at its surface and directly acting on the cysteine thiol moiety, was shown. In contrast, hydrogen peroxide dominated liquid chemistry produced by indirect plasma treatment failed to return strongly oxidized cysteine derivatives and it must be assumed that the direct plasma treatment performed in the clinical applications of CAPs are not well described by many (cell) models using plasma treated liquids (“plasma activated medium, PAM”). By using isotope pattern, the transition of gas phase species into bulk liquid residing cysteine molecules was determined, yet a small amount of liquid phase oxygen was also detected in the oxidized cysteine derivative. The origin of this needs to be clarified in future experiments.

5. References

1. Reuter, S.; von Woedtke, T.; Weltmann, K.-D., The kINPen—a review on physics and chemistry of the atmospheric pressure plasma jet and its applications. *J. Phys. D: Appl. Phys.* **2018**, *51* (23), 233001.
2. Schmidt-Bleker, A.; Winter, J.; Bösel, A.; Reuter, S.; Weltmann, K.-D., On the plasma chemistry of a cold atmospheric argon plasma jet with shielding gas device. *Plasma Sources Sci. Technol.* **2015**, *25* (1), 015005.
3. B. Graves, D., Mechanisms of Plasma Medicine: Coupling Plasma Physics, Biochemistry and Biology. **2017**, *PP*, 1-1.
4. Graves, D. B., Oxy-nitroso shielding burst model of cold atmospheric plasma therapeutics. *Clinical Plasma Medicine* **2014**, *2* (2), 38-49.

5. Schmidt, A.; Dietrich, S.; Steuer, A.; Weltmann, K.-D.; von Woedtke, T.; Masur, K.; Wende, K., Non-thermal plasma activates human keratinocytes by stimulation of antioxidant and phase II pathways. *J. Biol. Chem.* **2015**, *290* (11), 6731-6750.
6. Keidar, M.; Yan, D.; Beilis, I.; Trink, B.; Sherman, J. H., Plasmas for Treating Cancer: Opportunities for Adaptive and Self-Adaptive Approaches. *Trends Biotechnol.* **2018**, *36* (6), 586-593.
7. Schmidt, A.; Bekeschus, S.; Wende, K.; Vollmar, B.; von Woedtke, T., A cold plasma jet accelerates wound healing in a murine model of full-thickness skin wounds. *Exp. Dermatol.* **2017**, *26* (2), 156-162.
8. Schmidt, A.; Bekeschus, S.; Jablonowski, H.; Barton, A.; Weltmann, K.-D.; Wende, K., Role of ambient gas composition on cold physical plasma-elicited cell signaling in keratinocytes. *Biophys. J.* **2017**, *112* (11), 2397-2407.
9. Metelmann, H.-R.; Seebauer, C.; Müller, V.; Fridman, A.; Bauer, G.; Graves, D. B.; Povesle, J.-M.; Rutkowski, R.; Schuster, M.; Bekeschus, S., Clinical experience with cold plasma in the treatment of locally advanced head and neck cancer. *Clinical Plasma Medicine* **2017**.
10. Liedtke, K. R.; Bekeschus, S.; Kaeding, A.; Hackbarth, C.; Kuehn, J. P.; Heidecke, C. D.; von Bernstorff, W.; von Woedtke, T.; Partecke, L. I., Non-thermal plasma-treated solution demonstrates antitumor activity against pancreatic cancer cells in vitro and in vivo. *Sci. Rep.* **2017**, *7* (1), 8319.
11. Reuter, S.; Schmidt-Bleker, A.; Tresp, H.; Winter, J.; Iseni, S.; Hammer, M.; Duennbier, M.; Weltmann, K. D., Interaction of Atmospheric Pressure Plasma Jets with Liquids. *Plasma Physics and Technology* **2014**, *1* (2), 55-57.
12. Gorbanev, Y.; O'Connell, D.; Chechik, V., Non-Thermal Plasma in Contact with Water: The Origin of Species. *Chemistry (Easton)* **2016**, *22* (10), 3496-3505.
13. Bekeschus, S.; Wende, K.; Hefny, M. M.; Rodder, K.; Jablonowski, H.; Schmidt, A.; Woedtke, T. V.; Weltmann, K. D.; Benedikt, J., Oxygen atoms are critical in rendering THP-1 leukaemia cells susceptible to cold physical plasma-induced apoptosis. *Sci. Rep.* **2017**, *7* (1), 2791.
14. Wende, K.; Williams, P.; Dalluge, J.; Van Gaens, W.; Aboubakr, H.; Bischof, J.; von Woedtke, T.; Goyal, S. M.; Weltmann, K.-D.; Bogaerts, A.; Bruggeman, P., Identification of the biologically active liquid chemistry induced by a nonthermal atmospheric pressure plasma jet. *Biointerphases* **2015**, *10* (2), 029518.
15. Weltmann, K. D.; Kindel, E.; Brandenburg, R.; Meyer, C.; Bussiahn, R.; Wilke, C.; Von Woedtke, T., Atmospheric pressure plasma jet for medical therapy: plasma parameters and risk estimation. *Contributions to Plasma Physics* **2009**, *49* (9), 631-640.
16. Kelly, S.; Golda, J.; Turner, M. M.; Schulz-von der Gathen, V., Gas and heat dynamics of a micro-scaled atmospheric pressure plasma reference jet. *Journal of Physics D-Applied Physics* **2015**, *48* (44).
17. Lackmann, J. W.; Wende, K.; Verlackt, C.; Golda, J.; Volzke, J.; Kogelheide, F.; Held, J.; Bekeschus, S.; Bogaerts, A.; Schulz-von der Gathen, V.; Stapelmann, K., Chemical fingerprints of cold physical plasmas - an experimental and computational study using cysteine as tracer compound. *Sci. Rep.* **2018**, *8* (1), 7736.
18. Jablonowski, H.; Sousa, J. S.; Weltmann, K.-D.; Wende, K.; Reuter, S. J. S. r., Quantification of the ozone and singlet delta oxygen produced in gas and liquid phases by a non-thermal atmospheric plasma with relevance for medical treatment. *Sci. Rep.* **2018**, *8* (1), 12195.

INACTIVATION OF INDOOR AIRBORNE BACTERIA BY DBD

Ju Young Park^{1,2} and Jun Choi^{1*}

¹ Advanced Forming Process R&D Group, Korea Institute of Industrial Technology, Korea

² Department of Electrical Engineering, Pusan National University, Korea

E-mail: junchoi@kitech.re.kr

This paper describes the analysis of removal efficiency of indoor airborne bacteria by dielectric barrier discharge (DBD). An in-house system composed of DBD device, air sampler, nebulizer and circulating pan was set up to evaluate the antibacterial effect of the airborne bio-aerosol. In this work, two groups of samples were separately used and each sample was exposed to the DBD for 5 minutes and 10 minutes, respectively. The removal rate increased from $57 \pm 9 \%$, $74 \pm 11 \%$ as the treatment time increased from 5 minutes and 10 minutes. The removal efficiency increased with increasing treatment time. The experimental results demonstrated the DBD can be effective for the removal of airborne bacteria. Therefore, it is noted that the DBD can be applied to enclosed spaces such as vehicles, ships and indoors to improve the air quality.

1. Introduction

Bio-aerosols have plants, microorganisms, viruses, airborne bacteria, mites and fungi. They are harmful substances that can cause serious diseases to the human. Therefore, the airborne bacteria with pathogenicity should be removed to improve indoor air quality. In general, high efficiency specific air filter and ultraviolet-C (UV-C) are used to remove airborne bacteria. Although these methods can provide high removal rate of airborne bacteria, they have limitations due to regular filter replacement and UV-C exposure [1]. The DBD has the highest removal efficiency, even though the complexity and manufacturing costs are higher than the air filter and UV-C [2]. The airborne bacteria are removed or inhibited by the reactive species such as nitric oxide, atomic oxygen and hydroxyl generated by DBD. Many studies on the bacteria removal with DBD have been reported for the last decades. However, most of studies focused on stationary bacteria captured on the surfaces like agar plate. In this study, the removal rate of indoor airborne bacteria was directly analyzed by sampling the air treated by DBD with time.

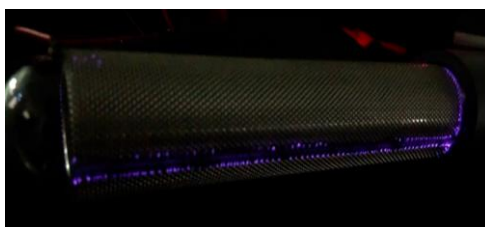


Fig. 1. Photograph of the DBD device during the plasma generation.

2. Experimental setup and results

The DBD device, air sampler, nebulizer and circulating pan were used to measure the bactericidal performance. The DBD device was composed of a quartz tube as a dielectric and aluminum and stainless mesh as two electrodes respectively. For the plasma generation with DBD, 6 kV peak-peak and 11 kHz sinusoidal wave was applied to the plasma device. The initial number of bacteria was set to zero through the UV-lamp and the sprayed solution sterilized with an autoclave contains the bacteria. The *Staphylococcus epidermidis* (*S. epidermidis*) were used as a sampled bacteria. The sprayed solution was vortexed for about 15 to 20 seconds to prevent precipitation. The airborne bacteria were sampled for 5 minutes at a flow rate of $20 \text{ L} \cdot \text{min}^{-1}$ through air sampler using the Anderson impact method and the sampling was about 10 % of the chamber volume. The air with the bacteria was exposed to DBD for 5 minutes and 10 minutes. Then the samples were incubated at $37 \text{ }^\circ\text{C}$ for 24 hours. The colony forming unit method was used to measure the removal efficiency of airborne bacteria after incubation. The experimental results have error range. The error was due to the fact that not all airborne bacteria respond perfectly to the

DBD despite the use of circulating fans. The removal rate was $57 \pm 9 \%$ at 5 minutes and $74 \pm 11 \%$ at 10 minutes depending on the exposure time to the DBD. As a result, the removal efficiency of airborne bacteria increased with increasing exposure time.

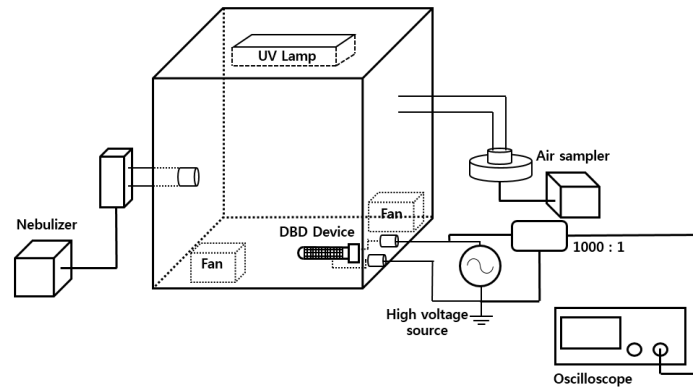


Fig. 2. Schematic of the experimental setup for inactivation of airborne bacteria using DBD.

3. CONCLUSION

In summary, the removal efficiency of airborne bacteria by DBD was analyzed to confirm the effect of treatment time on the inactivation of bacteria in air. The *S. epidermidis* showed high reactivity to DBD and the removal efficiency of airborne bacteria increased with increasing exposure time. The removal rate of airborne bacteria was calculated by comparing the number of colony forming populations before and after treatment. The airborne bacteria were removed $57 \pm 9 \%$ for 5 minutes and $74 \pm 11 \%$ for 10 minutes. These results show that the DBD is capable of removing the airborne bacteria and affects in improving the quality of indoor air.

Tab. 1. The experimental conditions.

Parameter	Value
Temperature (°C)	24 ± 2
Humidity (%)	55 ± 5
Volume of spray (ml)	7
Chamber volume (m ³)	1

4. References

- [1] Gallagher M J et al., 2007 *IEEE Transactions on Plasma Science*, **35** 5.
- [2] Park C W and Hwang J H, 2013 *Journal of Hazardous Materials*, **244-245** 421.

TUNNING THE PAW COMPOSITION BY A SURFACE-WAVE MICROWAVE DISCHARGE

Kinga Kutasi¹, Slobodan Milošević²

¹Wigner Research Centre for Physics of Hungarian Academy of Sciences, Konkoly-Thege Miklos str. 29-33, H-1121 Budapest, Hungary

²Institute of Physics, Bijenička cesta 46, Zagreb, Croatia
E-mail: kutasi.kinga@wigner.mta.hu

It is shown the possibility of tuning the ratio of active species concentrations over three orders of magnitude in deionized water activated with a surface-wave microwave discharge.

1. Introduction

In the last decade plasma-activated water (PAW) has received a lot of attention from the plasma medicine and plasma agriculture community due to its potential to induce oxidative stress to cells. PAW has been found to have antimicrobial and antibacterial effects [1-3], while in the field of agriculture with PAW the improvement of seeds germination and plant growth have been targeted [4-6].

By PAW it is meant the water, which contains reactive species, mostly reactive oxygen and nitrogen species (RONS), generated by the interaction of active or afterglow plasma with water. The main long-lived RONS produced in PAW have been identified to be the H_2O_2 , NO_2^- and NO_3^- , whose lifetime has been defined to vary from couple of days to weeks. PAWs have been created typically in the amount of 0.1-30 ml, with the concentration of generated species decreasing with the volume of the treated water [7-9]. For example, by treating 60 ml of deionized water (DIW) for 5 min with a ns air DBD it has been obtained PAW with pH 2.7, and concentration of H_2O_2 8.5 mg/l, of NO_2^- 7mg/l and NO_3^- 93 mg/l [9].

Usually the studies report one or two PAW conditions and do not give suggestions for the tuning of the PAW composition, which would be welcomed in order to be able to define the role of different species acting in synergy in the biological applications. For tuning the PAW composition an attempt has been done by Ito *et al.* [10] by using a He DBD jet with different shielding gases obtaining ratios of $[\text{NO}_2^-]/[\text{H}_2\text{O}_2]$ ranging between 0 to 0.18. However, here no information is given about the density of NO_3^- molecules, which can be also formed during storage from the reaction of NO_2^- with H_2O_2 .

In the present work we study the possibility of tuning the composition of PAW through the activation of DIW with a surface-wave microwave discharge by varying the discharge and treatment conditions.

2. Experimental

The surface-wave microwave discharge [11] is generated with the help of a surfatron launcher (Sairem, Surfatron 80) in a quartz tube of outer diameter 6 mm and inner diameter 4 mm using as a main gas Ar at gas flow rates of 1500-2000 sccm. During experiments Ar- N_2/O_2 binary and ternary mixtures are also used with the O_2 and N_2 gas flow rates ranging between 10-100 sccm. The input power is varied between 25 and 30 W. The quartz tube is fixed inside the surfatron in such a way that downstream the edge of the quartz tube is at 14.5 mm distance from the closing plate of the surfatron. This insures that at the powers and gas flow rates used the plasma plume outside the tube is long enough to allow different contact points with the water surface. A Berzelius beaker of 35 ml filled with 32 ml of DIW is positioned below the plasma plume with the water surface being at $d = 5.5$ mm, 8.5 mm or 10.5 mm distance from the edge of the quartz tube. In order to avoid the overheating of the quartz tube during treatments compressed air is applied along the quartz tube with a gas flow rate of 8 slm. This air flow shields the plasma plume, while also results in about a 1 mm dislocation of the water surface.

3. Results

Table 1 shows the different treatment conditions applied and the characteristics of the generated plasma activated water. The concentration of H₂O₂, NO₂⁻ and NO₃⁻, and the pH of samples have been measured with QUANTOFIX test strips and evaluated with the QUANTOFIX Relax unit (by Macherey-Nagel, GmbH). The samples have been analyzed immediately after the treatment, as well as the ageing in closed containers at room temperature has been followed.

Ar_1. 2000 sccm Ar, 25 W, 5.5mm					ArN₂_1. 2000 sccm Ar-40 sccm N₂, 27 W, 5.5mm				
t [min]	[H ₂ O ₂] [mg/L]	[NO ₂ ⁻] [mg/L]	[NO ₃ ⁻] [mg/L]	pH	t [min]	[H ₂ O ₂] [mg/L]	[NO ₂ ⁻] [mg/L]	[NO ₃ ⁻] [mg/L]	pH
0	84	6.8	92	5.7	0	40	12	136	5.3
95	63	0.5	49	4.6	82	36	1.3	63	4.3
83567	50	<0.5	40	6.6	83535	23	<0.5	56	6.3
Ar_2. 2000 sccm Ar, 25 W, 10.5mm					ArN₂_2. 1500 sccm Ar-40 sccm N₂, 27W, 5.5mm				
0	4	6.4	74	5.9	0	9	9.6	104	5.6
93	7	5.4	79	5.5	86	9	5.6	80	5.5
83559	0.6	<0.5	39	6.5	83540	2.4	0.5	40	6.6
Ar_3. 1500 sccm Ar, 25W, 5.5mm					ArN₂_3. 2000sccm Ar-40sccm N₂, 27W, 10.5mm				
0	46	12	123	5.4	0	2	6.6	73	5.8
93	25	1.6	61	5.1	81	2	5.9	79	5.4
83554	21	<0.5	55	6.2	83529	<0.5	1.6	36	6.5
Ar_4. 2500 sccm Ar, 26 W, 5.5mm					ArN₂_4. 2000sccm Ar-40sccm N₂, 27W, 10.5mm, 10min				
0	85	6.2	89	5.5	0	4	14	141	5
90	56	0.5	47	4.5	92	3	6.3	101	5.3
83419	65	<0.5	49	6.2	83488	<0.5	<0.5	61	5.8
ArN₂O₂_1. 2000sccmAr-40sccmN₂-10sccmO₂, 25W, 5.5mm					ArN₂_5. 2000sccm Ar-60sccm N₂, 27 W, 5.5mm				
0	20	8.8	104	5.4	0	17	8.7	128	5.5
76	19	1.8	59	5.5	68	25	2.8	68	4.8
83486	16.6	<0.5	53	5.8	83508	15	0.5	51	6.3
ArN₂O₂_2. 2000sccmAr-40sccmN₂-20sccmO₂, 25W, 5.5mm					ArN₂_6. 2000sccm Ar-60sccm N₂, 27 W, 8.5mm				
0	37	12	128	5.3	0	3	4.9	62	5.8
74	14	2.7	64	4.9	79	4	4	55	5.8
83484	8.5	<0.5	43	5.9	83520	<0.5	<0.5	24	6.6
ArO₂_1. 2000sccm Ar-20sccm O₂, 25W, 5.5mm					ArN₂_7. 1500 sccm Ar-60 sccm N₂, 27 W, 5.5mm				
0	80	9.3	113	5.5	0	3	4.5	59	6
73	37	0.5	50	4.9	66	3	3.4	52	6
83451	43	<0.5	45	5.8	83503	<0.5	<0.5	22	6.7
ArO₂_2. 2000sccm Ar-40sccm O₂, 25W, 5.5mm					ArN₂_8. 2000sccm Ar-100sccm N₂, 30W, 5.5mm				
0	75	13	122	5	0	11	6.5	73	5.8
84	41	1	66	4.4	84	11	3.8	52	5.5
83388	35	<0.5	57	5.9	83484	5	<0.5	29	6.4

Table 1. The treatment conditions: gas flow rates, input power and quartz tube-water surface distance, and the concentration of active radicals created in PAW at different ageing moments.

First of all different Ar discharge conditions have been tested by changing the gas flow rate and the treatment distance. The plasma plume is characterized by a decreasing electron density profile, thus by changing the treatment distance it is changed the electron density at the plume - water surface interaction point. The electrons by interacting with the water surface can create OH radicals, which afterwards through the recombination reaction form H₂O₂. This is well illustrated by the obtained

results, namely at lower treatment distance, where higher electron density occurs at the water surface higher H_2O_2 concentration is obtained. By decreasing the gas flow rate (Ar_3) condition, the plasma plume is slightly shorter, and meanwhile more air is also able to diffuse into the plume, which favours the formation of nitrate and nitrite radicals. Fig. 1. shows the spectra of the plume close to the water surface. Optical emission spectra have been measured using an AvaSpec-3648 type spectrometer with 0.2 nm resolution and covering a spectral range of 250–800 nm. The spectra indicate the absence of OH molecules (308 nm) in the plume, which suggests, that the OH radicals are created directly in the liquid phase. The spectra also show, that at the lower treatment distance the emission intensity of the Ar lines (602-830 nm), which results from the electron excited Ar atoms, are higher. This is a good indication of the higher electron density at the interaction point.

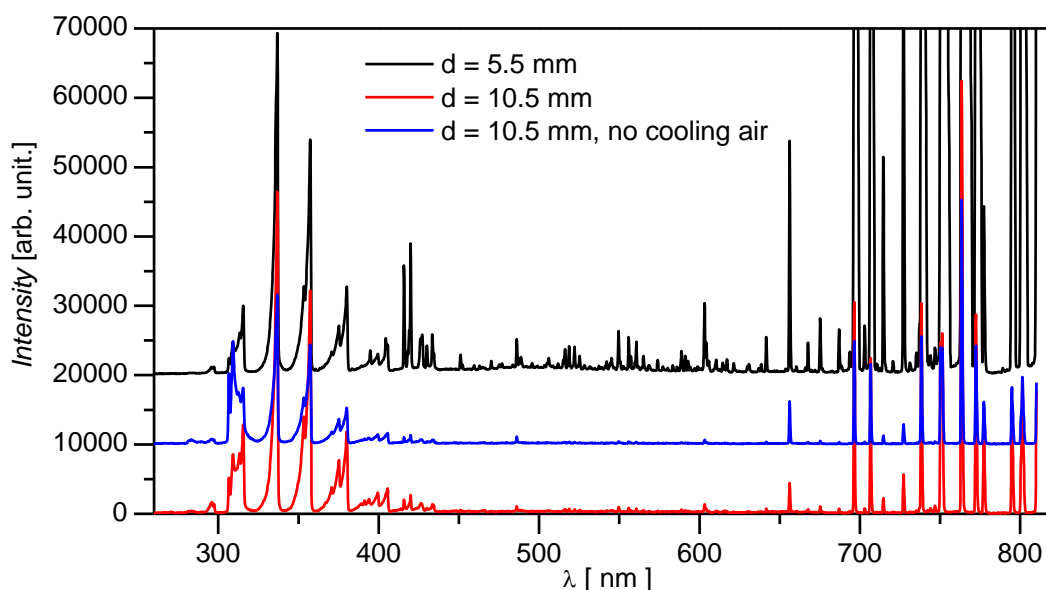


Fig. 1. Spectra of plasma plume close to the water surface for different quartz tube-water distances in the case of the 2000 sccm Ar, 25 W discharge. The spectra are shifted in intensity for clarity.

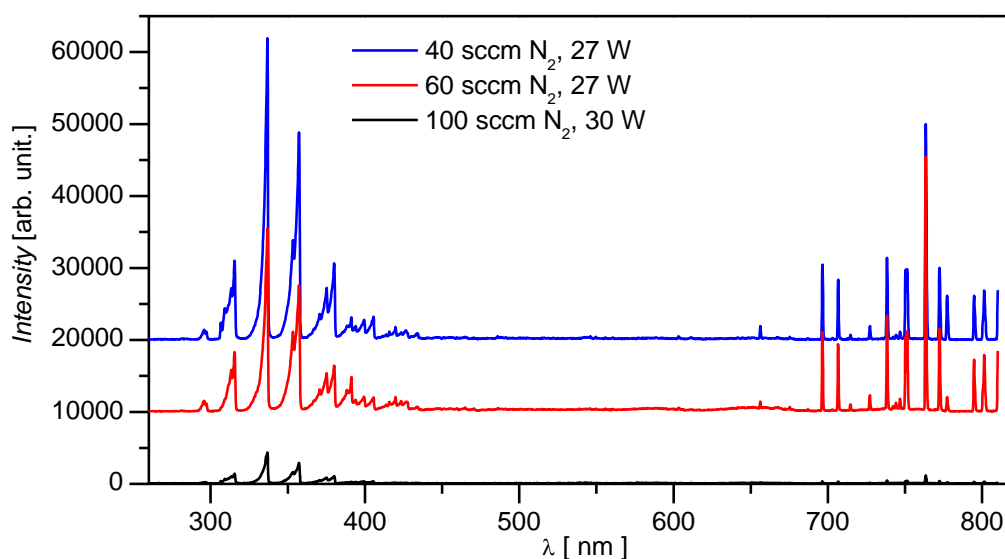


Fig. 2. Spectra of plasma plume close to the water surface for different N_2 content discharges in the case of $d = 5.5$ mm.

By adding N₂ to Ar (conditions Ar_N₂ in Table 1.) the length of the plasma plume decreases, while the plasma becomes stable only at the higher 27 W power. This effect is well reflected by the much lower H₂O₂ concentrations obtained with the N₂ content initial gas mixture discharges. Meanwhile, higher nitrite and nitrate concentrations are obtained due to the more pronounced presence of NO and NO₂ radicals in the gas and consequently in the liquid phase, through the following reactions: NO_{2(aq)}+NO_{2(aq)}+H₂O_l → NO₂⁻ + NO₃⁻ + 2H⁺ and NO_(aq)+NO_{2(aq)}+H₂O_l → 2NO₂⁻ + 2H⁺.

Fig.2. shows the spectra of different N₂ content discharges for the d = 5.5 mm case, close to the water surface. With the addition of 100 sccm of N₂ the emission intensity decreases considerably low. This indicates, that in this case the plasma plume becomes so short, that it is already the afterglow plasma, which interacts with the water surface. This results, as expected, in a lower H₂O₂ concentration. The active species concentrations of the ArN₂_1. versus ArN₂_3. conditions indicate, that along the plasma plume the density of NO and NO₂ radicals also decreases, as well as along the afterglow, thus with higher treatment distance lower nitrite and nitrate concentrations are obtained in PAW. This is also reconfirmed by the ArN₂_5. and ArN₂_6 conditions where the discharge with 60 sccm N₂ in the initial gas mixture has been used. It is further found, that by doubling the treatment time - ArN₂_3. versus ArN₂_4. condition – practically the doubling of the active species concentration in PAW is obtained.

Concerning the ageing of the PAW, it is found that at room temperature the concentration of the peroxide and nitrate decrease by a factor of 2 during 2 months of storage. In fact, a very fast recombination phase is observed during the first hour, which is followed by a much slower one. In what concerns the nitrite, it recombines very fast with the peroxide, resulting in nitrate. The weakening of this effect is shown by the ArN₂_3. condition, where very low peroxide concentration is measured right after the treatment, which has resulted in a much slower decrease of nitrite concentration, i.e. the nitrite does not disappear totally after two months, contrary to the other conditions where the starting concentrations of peroxide are considerably higher.

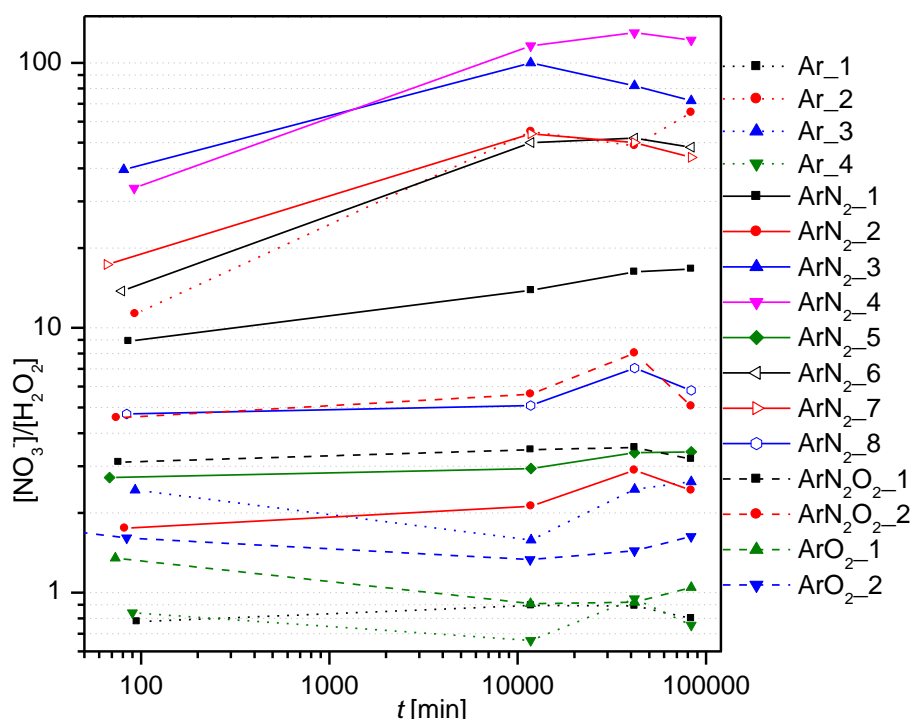


Fig. 3. Ratio of concentrations as a function of ageing time for the different treatment conditions.

Finally, Fig. 3. shows the ratio of the nitrate to peroxide concentration as a function of ageing for the different treatment conditions as listed in Table 1. By changing the treatment distance and the initial gas mixture composition of the discharge, the [NO₃⁻]/[H₂O₂] concentration ratio can be varied over three orders of magnitude from about 0.5 to 150 (we note that the lowest detection limit of H₂O₂ is 0.5 mg/l, and in the ratio calculations the concentrations that are lower than that value are taken as 0.5). In the case of the treatment conditions where initially (t = 0.5 min) low H₂O₂ concentrations are

obtained, the ageing has a more pronounced effect on the concentrations ratio, due to the strong recombination of H₂O₂.

Acknowledgement

This work has been financially supported by the Croatian Science Foundation through projects IP-2013-11-2753 and by the Croatian - Hungarian bilateral project TÉT_16-1-2016-0014.

4. References

- [1] Kamgang-Youbi G, Herry J-M, Bellon-Fontaine M-N, Brisset J-L, Doubla A and Naïtali M 2007 *Appl. Environ. Microbiol.* **73** 4791.
- [2] Ikawa S, Kitano K, Hamaguchi S 2010 *Plasma Processes Polym.* **7** 33.
- [3] Kobayashi T, Iwata N, Oh J-S, Hashizume H, Ohta T, Takeda K, Ishikawa K, Hori M, Ito M 2017 *J. Phys. D: Appl. Phys.* **50** 155208.
- [4] Puač N, Škoro N, Spasić K, Živković S, Milutinović M, Malović G and Petrović Z Lj 2017 *Plasma Processes and Polymers* **15** e1700082.
- [5] Sivachandiran L, Khacef A 2017 *RSC Adv.* **7(4)** 1822.
- [6] Thirumdas R, Kothakota A, Annapure U, Siliveru K, Blundell R, Gatt R, Valdramidis V P 2018 *Trends in Food Science and Technology* **77** 21.
- [7] Oehmigen K, Ha'hnel M, Brandenburg R, Wilke Ch, Weltmann K-D, von Woedtke Th 2010 *Plasma Processes Polym.* **7** 250.
- [8] Pavlovich M J, Chang H-W, Sakiyama Y, Clark D S, Grave D B 2013 *J. Phys. D: Appl. Phys.* **46** 145202.
- [9] Laurita R, Barbieri D, Gherardi M, Colombo V, Lukes P 2015 *Clin. Plasma Med.* **3** 53.
- [10] Ito T, Uchida G, Nakajima A, Takenaka K, Setsuhara Y 2017 *Jpn. J. of Appl. Phys.* **56** 01AC06.
- [11] Castanos-Martinez E, Moisan M and Kabouzi Y 2009 *J. Phys. D: Appl. Phys.* **42** 012003.

ATMOSPHERIC PLASMAS FOR GENERATION OF NANOSTRUCTURED MATERIALS

Jan Benedikt¹, Ove Hansen¹, Oleksander Polonskyi¹, Mohamed Mokhtar Hefny², David Necas³, Lenka Zajickova³, Judith Golda¹

¹Kiel University, Kiel, Germany

²Ruhr-Universitry Bochum, Bochum, Germany

³CEITEC and Masaryk University, Brno, Czech Republic

E-mail: benedikt@physik.uni-kiel.de

The transport of reactive species to the substrate, the effect of recombination reactions of reactive species in the gas phase, and the substrate reaction probability play a crucial role in the efficiency of the surface treatment or the growth of thin films. We will demonstrate that the highly collisional conditions result in high surface treatment efficiency even for species with low surface reaction probability. Additionally, we will report on the use of He/O₂ plasma for the treatment of Cu films at well-defined surface temperature to generate nanostructured copper oxide layers.

1. Introduction

Atmospheric non-equilibrium plasmas can generate high densities of reactive species or dissociate effectively precursor gases. Contrary to low-pressure plasmas, the collisions prevent ion bombardment and the diffusion is slow as transport mechanism. On the other hand, energy can be effectively stored in form of excitation energy (metastable atoms, excimers, metastable molecules such as N₂(A)) and a convection can be used as an effective transport of reactive species in atmospheric plasma jets. However, the main application of atmospheric plasmas is mainly in surface treatment applications, they are not widely used in applications for thin film generation or etching due to the limited quality of the deposited material, missing ion bombardment and only localized treatment. Their potentials material synthesis are mainly demonstrated in proof of principle experiments [1], where especially interesting is the formation of nanostructured materials [2,3] or nanoparticles [4].

2. Experimental setup

The experiments are performed with two atmospheric plasma sources: i) a so-called COST reference jet [5] with two metal electrode at the distance of 1 mm and with capacitive coupling of the rf-power, which generates cold plasma in He with small admixture of reactive gas, and ii) a similar jet with a glass capillary with rectangular profile in between the electrodes (see Fig. 1). The capillary as dielectrics in the latter case allows much larger power being applied to the plasma without development of electric arc and electrode damage.

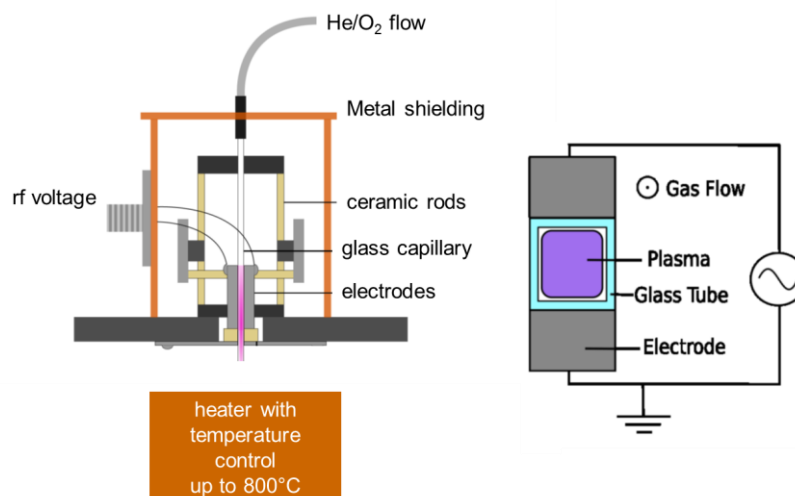


Fig. 1. Scheme of the experimental setup. The inner cross-section of the glass capillary is 1x1 mm².

3. Results and Discussion

The cold plasma generated in the COST reference jet has been used to etch hydrogenated amorphous carbon films. The comparison of the etch profile with the simulation of the species transport in the gas phase to the surface have revealed, that the surface reactivity of the O atom is below 1% (data not shown, for details see [6]). Additionally, the highly collisional environment with very slow diffusion provides high reaction rate at the surface even for species with low surface reaction probability. The simulations indicate that the overall reaction rate at the surface drops just with factor two when the O reactivity is changed in the model from 100% to 1%.

The oxidation of the surface is utilised in the experiment with the second jet, where much higher power is applied and thin copper film on silicon wafer is treated at variety of substrate temperatures (100°C – 800°C). The absorbed power in the plasma as obtained from the measurements of calibrated volt and current probes. Fig. 2 clearly demonstrate the transition from the volumetric (α mode) discharge to contracted discharge (sometimes called γ mode discharge) at transition voltage around 450 V. The plasma is in this case located in two 100 μm thin layers in front of the both electrodes.

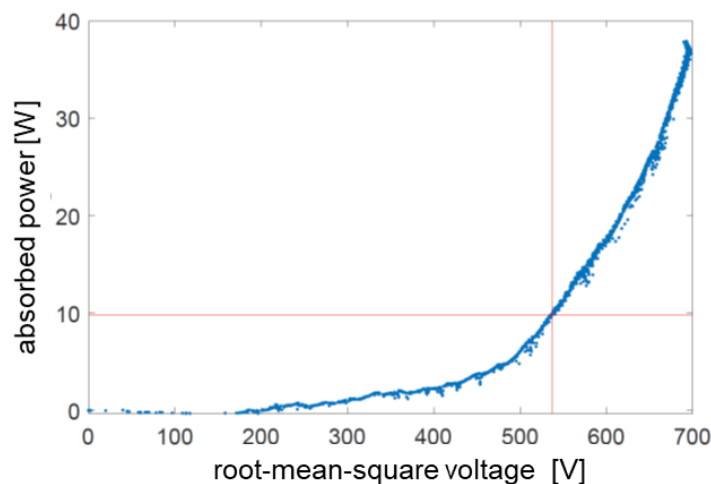


Fig. 2. Measured absorbed power as a function of applied root-mean-square voltage.

The contracted mode can be operated for long time (no damage or change observed after 20 hour of operation). The gas temperature, which is around 40 °C in the α mode, rises to 400 °C in the contracted mode as measured with a thermocouple at the capillary exit. The O_2 dissociation degree is around 10% in the α mode and it is expected that this value will be closed to 100% in the contracted mode due to higher plasma density, promoting electron impact dissociation, and higher gas temperature, which slows down or even prevents recombination reactions. Mass spectrometry measurements are being prepared to measure the O_2 dissociation degree and O atom density.

The morphology of treated copper film has been analysed with scanning electron microscopy (SEM) as function of surface temperature, time, and O_2 concentration in the gas mixture at absorbed power of around 10 W. Figure 3 shows an example of the surface morphology under the running jet with O atoms being involved in the treatment and at the region far away from the jet axis, where the thermal oxidation at the same temperature took place. It is clearly visible that the treatment with O atoms leads to formation of vertical nano walls, which are not observed in the thermal treatment. The non equilibrium conditions resulting from the enhanced O_2 dissociation and presence of O atoms result very probably in enhanced mobility of oxygen along the surface providing conditions for formation of unique nanostructures. It should be noted that similar structures are observed at 100°C (no oxidation) and at 800°C (the similar structure of large oxide grains). The XPS measurement revealed in both cases the presence of more stable cupric oxide CuO . Similar observations have been obtained previously by Altaweel *et al.* [2] under microwave atmospheric plasma jet without the control of the surface temperature.

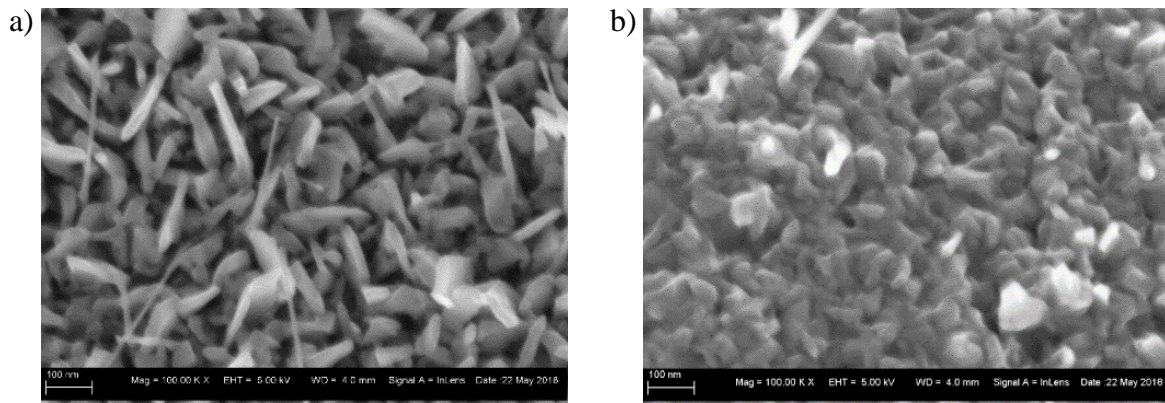


Fig. 3. SEM image of the surface of copper oxide after 60 minutes of treatment with a) plasma afterglow with O atoms and b) with He/O₂ gas. Conditions: He flow 1 slm, O₂ flow 5 sccm, applied rf-power 50 W, absorbed plasma power 10 W.

4. Conclusions

The surface treatment of metallic layers leads to nanostructured oxidation with different morphology compared to thermal oxidation. The aim of this and following study is to provide fundamental understanding of surface reactions involved in the oxidation process.

5. References

- [1] Mariotti D, Belmonte T, Benedikt J, Velusamy T, Jain G and Švrček V 2016 *Plasma Process Polym* **13** 70–90
- [2] Altaweel A, Filipič G, Gries T and Belmonte T 2014 *J Cryst Growth* **407** 17
- [3] Mariotti D and Ostrikov K 2009 *J. Phys. D: Appl. Phys.* **42** 092002
- [4] Askari S, Svrcek V, Maguire P and Mariotti D 2015 *Adv. Mater.* **27** 8011
- [5] Golda J *et al.*, 2016 *Journal of Physics D: Applied Physics* **49** 084003
- [6] Mokhtar Hefny M, Nečas D, Zajíčková L, Benedikt J, 2018 submitted to *Plasma Sources Sci. Technol.*

PLASMA FORMATION IN CONDUCTING LIQUIDS: GROWTH AND NATURE OF THE VAPOUR LAYER

Leonidas Asimakoulas¹, WG (Bill) Graham¹, Frantisek Krcma², Tom A. Field¹

¹*Centre for Plasma Physics, Queen's University Belfast, BT7 1NN, N. Ireland, U.K.*

²*Faculty of Chemistry, Brno University of Technology, Purkynova 118, 61200 Brno, Czech Republic*
E-mail: t.field@qub.ac.uk

Plasma generation inside conducting liquids is frequently preceded by the growth of a vapour layer. The growth of vapour layers has been observed with a fast framing camera. The images have been analysed to estimate the conductivity of this vapour layer. Surprisingly high values of vapour conductivity are estimated which raise questions about the nature of the vapour layer.

1. Introduction

Plasmas in liquids have been studied for some time and various reviews have been made, e.g. [1]. When electrodes are submerged in the liquid there are generally two types of behaviour. At high voltages (>1 kV), over short timescales ($< \mu$ s) and with low conductivity liquids (e.g. oil, distilled water) the discharges tend to be formed by direct breakdown in the liquid itself. By contrast with lower voltages (~ 100 V), longer pulses ($> \mu$ s) and more conducting liquids (e.g. electrolyte solutions, sea water) a vapour layer tends to form prior to breakdown around a powered electrode, or wherever the current density is highest. Breakdown then occurs in this vapour layer. In this work the vapour layer has been investigated.

2. Experiments, Results, Analysis and Conclusions

Breakdown has been observed with a Photron fast framing camera (SA-X2) in 0.9% g/l saline solutions excited by 1 ms 300 V pulses with typical pulse repetition frequencies of 1 Hz. The vapour layer that forms prior to breakdown has been imaged by shadowgraphy with the fast framing camera. A vapour layer grows around the powered electrode. A clear boundary is observed between the vapour layer and the surrounding liquid. The images are analysed to determine the shape of the vapour layer around the electrode. The shapes are then imported into finite element modelling software. The average conductivity of the vapour layer is estimated by comparison of the experimentally measured electrical characteristics of the discharge and the finite element model. Normally it would be expected that vapour would have a lower conductivity than an electrolyte solution, however, here vapour conductivities approaching the conductivity of the saline solution itself are estimated. Thus, we have to conclude that there are charge carriers in the vapour that enable this conductivity. The exact nature of the vapour layer is not clear. For example, it is not clear what the charge carriers may be; different possibilities will be considered in the talk

3. References

[1] P.J. Bruggeman *et al.* 2016 *Plasma Sources Science and Technology* **25** 053002.

EMISION CHARACTERISTICS OF GAS-DISCHARGE PLASMA OF ATMOSPHERIC PRESSURE DIELECTRIC BARRIER DISCHARGE ON ZINC DIODIDE VAPOR WITH NEON AND XENON MIXTURES

Antonina Malinina, Alexander Malinin, Alexander Shuaibov

Uzhhorod National University, Ukraine

E-mail:antonina.malinina@uzhnu.edu.ua

Studies are presented on the emission characteristics of a gas-discharge plasma of atmospheric pressure dielectric barrier discharge on mixtures of zinc diiodide vapor with neon and xenon. The repetition rate of plasma pump pulses was 130 kHz. The following regularities were established: in the emission spectra of the plasma of the barrier discharge in the range of 200 - 750 nm with a resolution of 0.05 nm, the temporal characteristics of voltage and current, the dependences of the radiation brightness on the partial pressure of neon and xenon. Radiation was detected: exciplex molecules ZnI^* and XeI^* , excimer molecules I_2^* , lines of zinc and neon atoms. The specific average radiation power in the spectral range $\Delta\lambda = 550\text{-}650$ nm, which had a value of 54.4 mW/cm^3 , was determined.

1. Introduction

Data on the emission characteristics of a gas-discharge plasma in mixtures of zinc diiodide vapor with neon and xenon are important for the diagnostics and optimization of the spectral and energy characteristics of spontaneous (excilamps) and coherent radiation sources (lasers). Such mixtures under gas-discharge plasma conditions can be promising working media for creating ecologically clean spectral radiators in the orange - red and ultraviolet spectral ranges. Studies of the emission characteristics of lasers and spontaneous emission sources on mixtures of zinc diiodide vapor and inert gases when optically pumped by an ArF-exciplex laser (193nm) and under conditions of a gas-discharge plasma of a pulsed periodic discharge, as well as a barrier discharge with a sinusoidal pumping pulse, were represented in [1-6]. The authors of the paper [1] present the results on the creation of a laser at a wavelength of 600–604 nm on electron-vibrational transitions $B^2\Sigma^+_{1/2} \rightarrow X^2\Sigma^+_{1/2}$ of zinc monoiodide molecules (ZnI) in a mixture of zinc diiodide vapor (ZnI_2) with inert gases argon and neon. The energy states of ZnI molecules were excited under the dissociative excitation of ZnI_2 molecules by radiation from an ArF exciplex laser (193 nm). The authors of [2] studied the quenching of the energy states of a ZnI molecule in a collision with ZnI_2 molecules, and also determined the amplification factor of a small signal from a ZnI laser. The results of studies [1,2] allowed the authors to make a conclusion about the prospects of creating a compact, tunable orange-red laser. In [3], the optical characteristics of the source of spontaneous emission of a repetitively pulsed barrier discharge were studied at pulse repetition rates of 0.1–1 kHz in mixtures of ZnI_2 vapor with helium and neon. They observed spontaneous emission in the spectral region of 450–620 nm (the spectral band of ZnI molecules (614.0 nm) and atomic zinc lines (468.0, 472.2, and 481.1 nm)). The authors concluded that the emission of ZnI molecules occurs as a result of their excitation during the dissociative excitation of ZnI_2 molecules by electron impact. In [4–6], data are presented on the optical and electrical characteristics of radiation from a gas-discharge plasma of a barrier discharge on two and three component mixtures of zinc diiodide vapor with inert gases helium, neon, xenon and krypton with a sinusoidal pump pulse of working mixtures with frequencies up to 130 kHz. In these studies, regularities were found in the spectral composition of the mixtures, and the emission brightness of the exciplex zinc monoiodide molecules (ZnI^*) was determined in relative units for each mixture. It was found that for a mixture of ZnI_2 vapor with helium, the maximum brightness of ZnI^* radiation is observed at partial pressures of the components of the mixture of 0.5 Pa and 100 kPa, respectively. In

addition, the spectral bands of molecular iodine were detected, the most intense of which was the I_2 ($D' \rightarrow A'$) band with a maximum at $\lambda = 342$ nm and spectral bands of the electron-vibrational transition $B \rightarrow X$ in the wavelength range 420 - 480 nm, as well as zinc lines -triplet $5s \rightarrow 4p$ (468.0, 472.2, and 481.0 nm) and $4d \rightarrow 4p$ line (636.2 nm). The average radiation power per unit volume was 34 mW/cm³ in the wavelength range $\Delta\lambda = 550$ -650 nm, the efficiency relative to the power input into the discharge was ~ 8% [6].

The present work is devoted to a comprehensive study of the emission characteristics of a gas discharge plasma of atmospheric pressure dielectric barrier discharge (DBD) in mixtures of zinc diiodide vapor and neon with a small addition of xenon at a pump pulse repetition rate of 130 kHz.

2. Technique and methods of experiment

Fig. 1 shows the main components of the experimental setup for studying the optical characteristics of a gas-discharge plasma in mixtures of zinc diiodide vapor, neon and xenon. Gas-discharge plasma was excited by a dielectric barrier discharge (DBD) in a compact cylindrical emitter with one dielectric barrier with a capacity of $C_d = 40$ pF, made of a quartz tube. The outer diameter of the tube 5 with a wall thickness of 1 mm was equal to 8.8 mm. Inside along the axis molybdenum electrode 4 with a diameter of 1 mm was located.

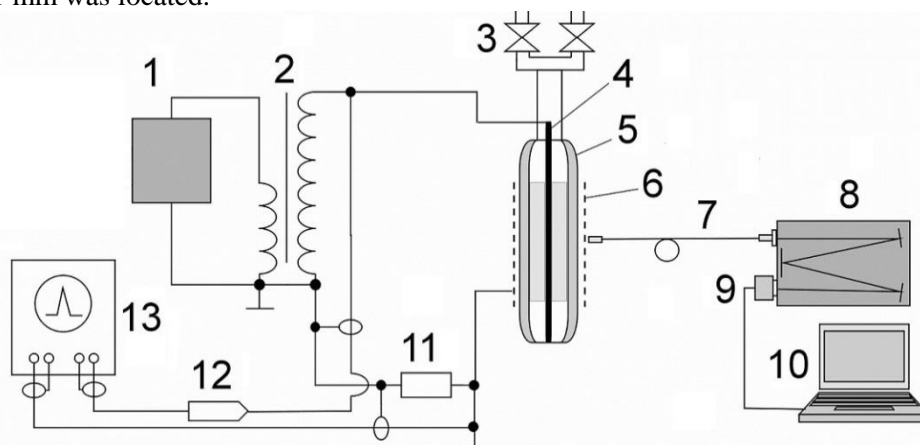


Fig.1. The schema of the experimental setup: 1–pulsed generator, 2 – high-voltage transformer, 3 – system for pumping and injecting gases, 4 – an electrode, 5–a quartz tube, 6 – a mesh (outer electrode), 7 – optical fiber, 8 – monochromator, 9 – CCD detector, 10 – personal computer, 11 – shunt, 12 –voltage divider, 13 – digital oscilloscope.

The discharge gap was 2.9 mm. The outer electrode 6 was made of a grid (transmittance of radiation $T = 50\%$) and had a length of 30 mm.

The barrier discharge was excited at a total pressure of the mixture 102 -200 kPa. A high-voltage generator with an average power of up to 100 W made it possible to vary the amplitude and frequency of a sinusoidal voltage applied to the electrodes to 7 kV and 130 kHz, respectively. The temporal dependences of the voltage on the source electrodes and the discharge current were recorded by a HP 54820A Infinium dual-beam digital oscilloscope. The signals to the oscilloscope came from a Tektronix P6015A 12 voltage divider and a shunt 11, respectively.

The discharge radiation was recorded in the direction perpendicular to the lateral surface of the quartz tube and analyzed in the spectral range 400 - 750 nm. The radiation spectra were studied using a Jobin Yvon TRIAX 550 spectrometer (1200 lines / mm grating, 0.02 mm slit, quartz optical fiber, Spectrum ONE CCD detector cooled with liquid nitrogen). The spectral resolution of the recording system was 0.05 nm. The registration system was calibrated by relative intensity using a reference tungsten lamp.

The average discharge radiation power was measured with a LabMaster Ultima instrument using a measuring head for the range 400 - 1100 nm. The total radiation power of the source was determined taking into account the geometrical factor by isolating a small area of diameter D located at a distance L from the emitter to the photodetector on the working surface of the discharge tube. When $L > 10D$, this area can be considered as a point source of radiation. The calculation assumed a uniform spatial

distribution of the radiation intensity in the total solid angle 4π . The geometrical factor was calculated as $k_1 = 4\pi / \Omega_2$, where $\Omega_2 = \pi r^2 / L^2$ is the solid angle of the photodetector, r is the radius of the photoreceiver aperture, $r = 3$ mm. A ZhS-18 light filter with a transmittance of $k_2 = 0.97$ in the range $\Delta\lambda = 550\text{-}650$ nm was installed between the diaphragm and photoreceiver. Thus, the radiation power per unit area was determined from the expression $W = W_0 k_1/k_2$, where W_0 is the power measured by the device.

Working mixtures were prepared directly in the radiator. Salt ZnI_2 in the amount of 100 mg is pre-poured into the discharge cuvette. After salt was loaded, it was dehydrated by heating the radiator at a temperature of $70\text{-}100^\circ\text{C}$ and pumping out for 2 hours. The partial pressure of ZnI_2 vapor was determined from the temperature of the cooler point of the radiator based on the interpolation of reference data from [7] and in our conditions was 0.03 - 12 Pa. The partial pressure of neon and xenon gases was measured with an accuracy of 10 Pa.

The measurement error of the discharge current and voltage on the electrodes was 10%, and the absolute value of the total radiation power of the source - 25%.

3. Results and their discussion

Immediately after the initiation of the atmospheric pressure barrier discharge in mixtures of zinc diiodide vapor with inert gases, the DBD filament regime was observed, typical for frequencies ~ 100 kHz - a set of cone-shaped microdischarges with a top on a metal electrode and a base on the inner surface of a quartz tube. The color of the discharge in the initial stage of the first 30 s was red. The next 30-60 s discharge burned in blue-green. As the mixture self-heated, the discharge color turned orange. At the same time, a more diffuse and uniform discharge pattern was observed, the brightness contrast in the volume discharge and filaments was noticeably smoothed.

Typical oscillograms of current and voltage are shown in Fig. 2 and 3. In each

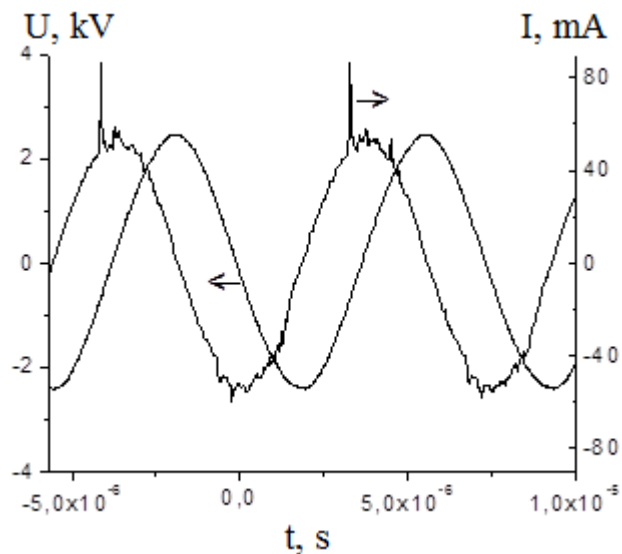


Fig. 2. Oscillograms of voltage and current pulses of a DBD in a mixture $\text{ZnI}_2 / \text{Ne} = 0.5 \text{ Pa} / 200 \text{ kPa}$, $f = 130 \text{ kHz}$.

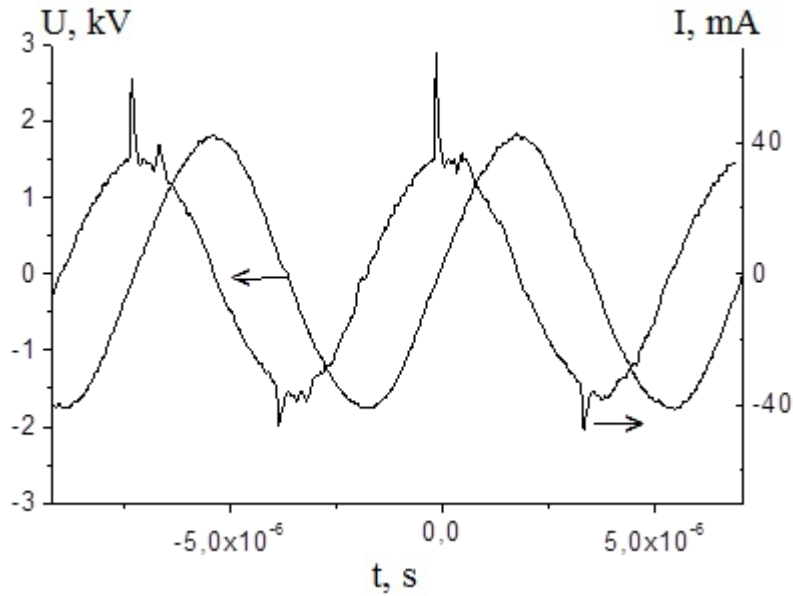


Fig. 3. Oscillograms of voltage and current pulses of a DBD in a mixture $\text{ZnI}_2 / \text{Xe} / \text{Ne} = 0.5 \text{ Pa} / 2 \text{ kPa} / 200 \text{ kPa}$, $f = 130 \text{ kHz}$.

half-period of the applied voltage on the oscillogram of the recorded current on the bias current curve, a series of sharp picks of different amplitude and of approximately the same duration were observed. Each pick of current is caused by a set of filamentary microdischarges — filaments that occur in the discharge gap and are statistically distributed in time. The oscillogram of current pulses is asymmetric — in the positive half-period, the first pick had a much larger amplitude than the others, and in the negative half-period the amplitude of all the picks was approximately the same. Adding Xe to the ZnI_2 / Ne mixture led to an increase in the amplitude of the first current pick in the negative half-period (Fig. 3).

Typical survey radiation spectra of the DBD plasma on a binary mixture of zinc diiodide vapor with neon and a ternary mixture of $\text{ZnI}_2 / \text{Xe} / \text{Ne}$ are shown in Fig. 4 and 5.

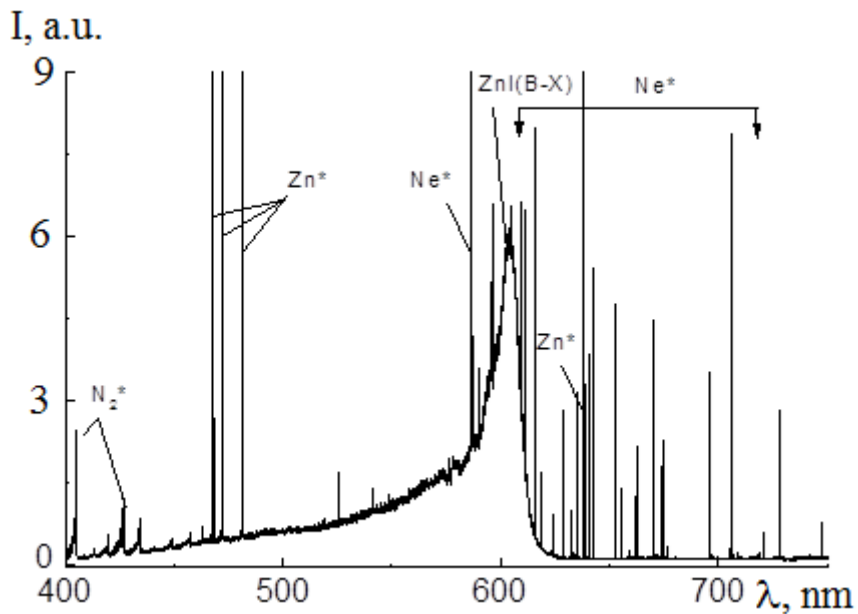


Fig.4. The survey emission spectrum of the DBD on a mixture of $\text{ZnI}_2 / \text{Ne} = 0.5 \text{ Pa} / 200 \text{ kPa}$.

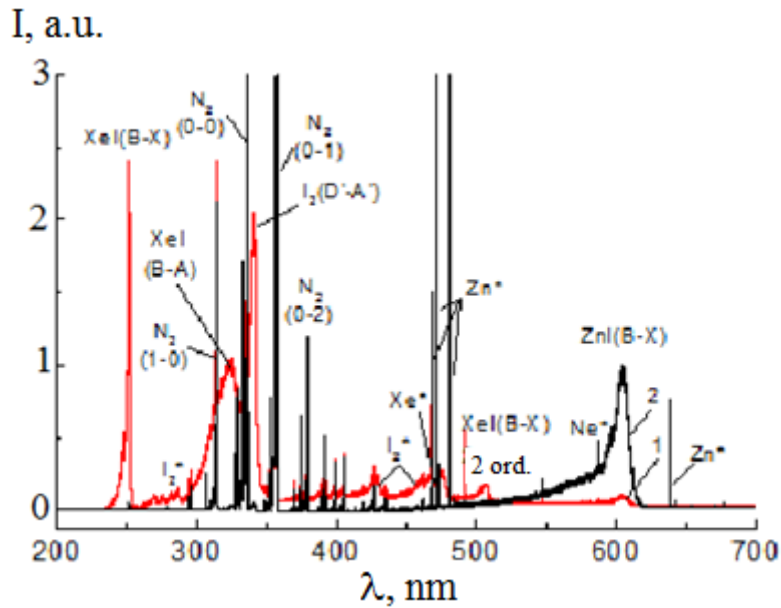


Fig.5. The survey emission spectrum of the DBD in mixtures: 1 - $\text{ZnI}_2 / \text{Xe} / \text{Ne} = 0.001 \text{ Pa} / 30 \text{ kPa} / 170 \text{ kPa}$; 2 - $\text{ZnI}_2 / \text{Xe} / \text{Ne} = 0.5 \text{ Pa} / 30 \text{ kPa} / 170 \text{ kPa}$.

In the spectra in the visible range, the spectral band with a maximum at $\lambda = 602 \text{ nm}$, which had a weakly resolved vibrational structure and corresponded to the electronic vibrational transition $\text{B}^2\Sigma^+_{1/2} \rightarrow \text{X}^2\Sigma^+_{1/2}$ of ZnI molecule was significantly distinguished [8]. $\text{ZnI} (\text{B} \rightarrow \text{X})$ radiation appears with $\lambda \sim 400 \text{ nm}$, and its main part is concentrated in the range of $590 - 608 \text{ nm}$. The shape of $\text{ZnI} (\text{B} \rightarrow \text{X})$ spectral band has a steeper increase in intensity from the long-wavelength region and a slow decline in the short-wavelength region. At atmospheric pressure of the mixture, due to the completion of the vibrational relaxation, transitions occur mainly from the lower vibrational levels of the excited electronic state [9].

The FWHM for $\text{ZnI} (\text{B} \rightarrow \text{X})$ was $15\text{--}16 \text{ nm}$, which is consistent with the results of work [1], where optical pumping of the ZnI_2 / Ar mixture by ArF laser radiation was used. The spectra also contained atomic zinc lines - a triplet $5s \rightarrow 4p$ ($468.0, 472.2$ and 481.0 nm), a $4d \rightarrow 4p$ line (636.2 nm) [10] and spectral bands of molecular iodine, the most intense of which was the spectral band $\text{I}_2 (\text{D}' \rightarrow \text{A}')$ with a maximum at $\lambda = 342 \text{ nm}$ [8]. The intensity of the atomic lines and the brightness of the molecular bands strongly depended on the temperature of the working mixture. The intensity of zinc lines increased with increasing temperature, while the brightness of the bands of molecular iodine fell (Fig. 3). Under the brightness of the molecular band was understood the area under the curve in the spectrum. In the spectral region of $315\text{--}425 \text{ nm}$, bands of molecular nitrogen were also observed, corresponding to the transition of the second positive N_2 system. They manifested themselves in the spectrum due to the discharge (parasitic) burning in the air between the outer surface of the quartz tube and the mesh. At a temperature of $<100\text{--}120^\circ \text{C}$, spectral bands were observed in the studied mixtures in the range of $420\text{--}480 \text{ nm}$, which were identified with the emission of $\text{I}_2 (\text{B} \rightarrow \text{X})$ molecules (Fig. 3). In the DBD emission spectra of ZnI_2 / Ne (Fig. 2), the intensity of atomic neon lines noticeably decreased as the working medium warmed up and was due to a decrease in the electron temperature in the discharge with an increase in the concentration of easily ionized particles, namely zinc diiodide molecules and zinc atoms [11].

In the emission spectrum of the ternary mixture $\text{ZnI}_2 / \text{Xe} / \text{Ne}$, in addition to the radiation $\text{ZnI} (\text{B} \rightarrow \text{X})$, Xe^* and Ne^* , at a mixture temperature of up to $\sim 150^\circ \text{C}$, spectral emission bands of the exciplex

molecules $\text{XeI(B}\rightarrow\text{X)}$ and $\text{XeI(B}\rightarrow\text{A)}$ with maxima at 253 and 325 nm were observed (Fig. 5). In this case, the radiation of exciplex $\text{XeI(C}\rightarrow\text{A)}$ molecules was clearly not manifested. A regularity was observed with the addition of xenon in the spectrum, the number of neon lines sharply decreased, the absence of Ne^* lines in the region of 600–750 nm, which is explained by the Penning ionization of Xe atoms by excited neon atoms [11].

With an increase in the partial pressure of neon in the ZnI_2/Ne mixture within 102–200 kPa, the emission brightness of the exciplex $\text{ZnI(B}\rightarrow\text{X)}$ molecules increased by about three times without signs of saturation (Fig. 6).

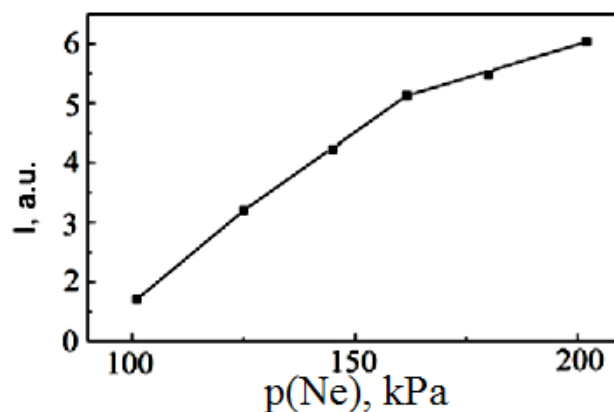


Fig. 6. The dependence of the emission brightness of the ZnI(B-X) spectral band on the value of the neon partial pressure in the ZnI_2 / Ne mixture.

When adding xenon (Fig. 7), a maximum is observed in the dependence of the emission brightness of the ZnI(B-X) band on the xenon partial pressure in the region of $p(\text{Xe}) = 8\text{--}10 \text{ kPa}$. In these experiments, the total pressure of $\text{ZnI}_2 / \text{Xe} / \text{Ne}$ mixtures was 200 kPa and the same energy input to the discharge was provided.

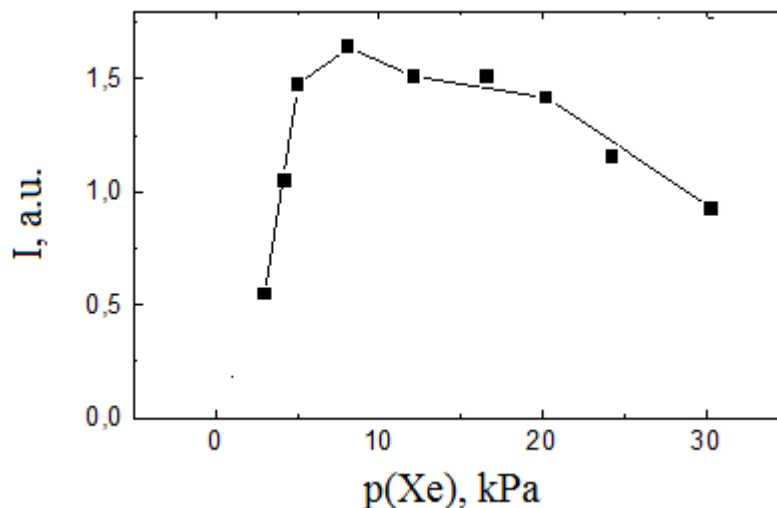


Fig.7. The dependence of the emission brightness of the ZnI(B-X) band on the xenon partial pressure. The partial pressure of ZnI_2 neon is 200 kPa, $f = 130 \text{ kHz}$.

Measurement of the average radiation power of the radiator was carried out at a total pressure of 200,5 kPa (Fig. 8). After switching on the discharge, with an increase in temperature, the average power firstly grew within 18 minutes, after which a slight decrease in it over 8 minutes. Then the emitter entered the mode for 10 minutes and stabilization of power was observed. The maximum value of the average radiation power per unit volume in the visible range was 54.4 mW/cm^3 (Fig. 8), the efficiency relative to the power input in the discharge was $\sim 12.8\%$.

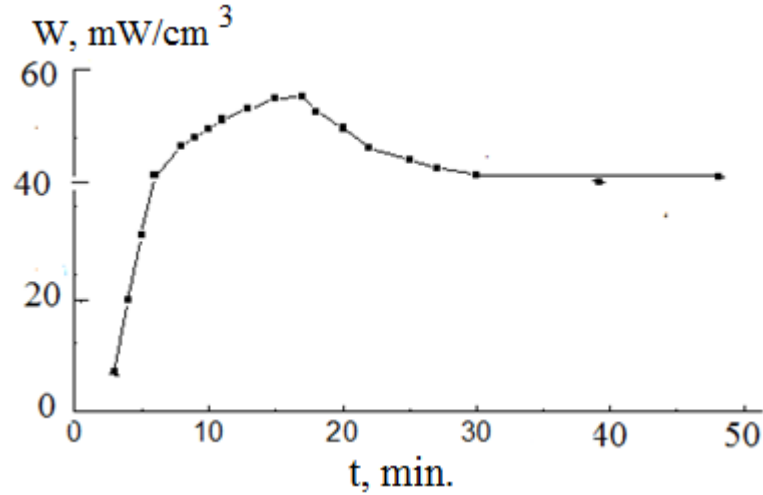
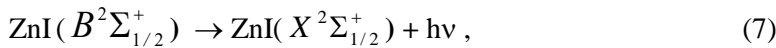
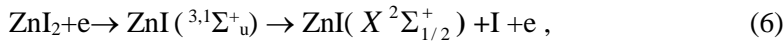
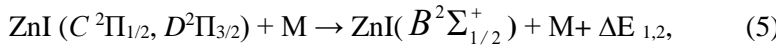
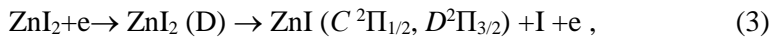
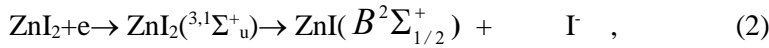
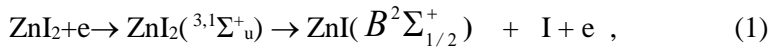
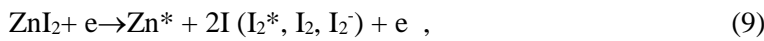
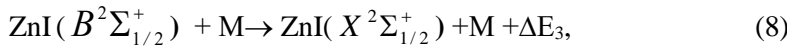


Fig. 8. The dependence of the radiation power of the gas-discharge plasma of the barrier discharge on the $\text{ZnI}_2 / \text{Xe} / \text{Ne}$ mixture = 0.5 Pa / 10kPa/ 190 kPa on the discharge burning time in the range $\Delta\lambda = 550\text{-}650$ nm.

The emission of spectral bands and plasma lines of a DBD on a mixture of zinc diiodide vapors with neon and xenon is probably observed as a result of the following reactions [12,13]:



$$\lambda_{\text{max.}} = 602 \text{ nm},$$



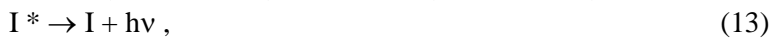
$$\lambda_{\text{max.}} = 342 \text{ nm}$$



$$\lambda = 420 - 480 \text{ nm}$$



$$\lambda = 468.0, \lambda = 472.2 \text{ nm}, \lambda = 481.0 \text{ nm}, \lambda = 636.2 \text{ nm},$$



$$\lambda = 589,4 \text{ nm}$$



$$\lambda = 587,2 \text{ nm},$$



$$\lambda = 823 \text{ nm},$$



where M is the concentration of quenching molecules and atoms (ZnI_2 , Ne), respectively, $\Delta E_{1,2}$ - is the energy difference in the reactions (5), ΔE_3 , ΔE_4 , ΔE_5 - the energy difference in the reactions (8), (16) and (19).

In addition, the formation of ZnI (B) molecules can also occur in electron-ion and ion-ion recombination reactions. But the contribution of such processes is insignificant due to lower concentrations of the initial components [12].

Reactions (1) and (2) are known as the main sources of exciplex molecules of zinc monoiodide (ZnI^*), which rate constants are not currently known. It can be assumed that they are within the range of 10^{-15} m^3/s and 10^{-17} m^3/s , respectively, since the specific radiation power in the spectral band of the exciplex ZnI^* molecule (Fig. 5) is close to the specific radiation power in the spectral bands of the exciplex molecules mercury monoiodide and mercury monobromide [14]. In addition, zinc monoiodide molecules can be formed in reactions (3) due to the excitation of zinc diiodide molecules to state D in collisions with electrons (D is a state that is the sum of several states that are between 7 and 13 eV (ionization threshold ZnI_2)) [2, 12].

Emission from the D - state of ZnI_2 is not observed, since this state quickly predissociates with the formation of electronically excited ZnI^* molecules in C and D - states [12]. The excitation of ZnI^* molecules in the C and D states is also possible when xenon atoms collide in the metastable $^3\text{P}_2$ state with ZnI_2 molecules (reaction (4) [2]. These states are quenched in reaction (5) leading to a high population $B^2\Sigma_{1/2}^+$ - state of zinc monoiodide [12]. The reaction of the collision of zinc diiodide molecules with electrons (6) is a channel for the formation of zinc monoiodide molecules in the ground state, the rate constant of which, according to our estimate, is $\sim 10^{-15}$ m^3/s . Electron-vibrational transition $B^2\Sigma_{1/2}^+ \rightarrow (X^2\Sigma_{1/2}^+)$ lead to emissions of spectral bands with a maximum intensity at a wavelength of $\lambda_{\text{max.}} = 602$ nm (reaction (7)) [8]. The emission of spectral bands with a maximum intensity at a wavelength of $\lambda_{\text{max.}} = 342$ nm is caused by the $D' \rightarrow A'$ vibrational transition of iodine molecules (reaction 10), and the emission of spectral bands at $\lambda = 420 - 480$ nm is caused by the electron-vibrational transition $B \rightarrow X$ of iodine molecules (reaction 11) [8]. Excited iodine molecules are formed in reaction (9). Excited zinc atoms are formed due to the passage of reactions (9) due to the large effective cross section for the dissociative excitation of zinc diiodide molecules by electrons \sim [13]. Reaction (14) is responsible for the excitation of atoms of the neon buffer gas. An important role in the emission of spectral bands and lines belongs to the processes of quenching states, from which emission occurs, both by zinc diiodide molecules (reaction 8) and by atoms of the neon buffer gas (reaction 16) due to which the radiation intensity decreases, the rate constants have a value of $1.7 \cdot 10^{-9}$ m^3/s and $\sim 1.5 \cdot 10^{-11}$ m^3/s [2].

The difference in oscillograms of current for zinc diiodide vapor with neon and xenon mixtures (Fig. 2 and Fig. 3) is due to the fact that the discharge occurs in the "cylinder-wire" system, only one electrode is covered with a dielectric, and in one case charge transfer occurs first through the dielectric barrier, and then through the plasma, and in the other way around, first through the plasma and then through the dielectric. The effect of xenon on the oscillogram of the current (Fig. 3) is associated with the change in plasma parameters and is due to the greater role of the stepwise ionization processes in the generation of electrons at the initial stage of discharge in this mixture [11]. In addition, Penning ionization of Xe effectively proceeds with Ne (reaction (19)).

The nature of the dependence of the emission brightness of the ZnI spectral band (B-X) on the value of the neon partial pressure in the ZnI_2 / Ne mixture (Fig. 6) can be caused by an increase in the temperature of the working mixture and, in turn, by an increase in the partial vapor pressure of ZnI_2 [11]. An increase in the intensity of radiation in mixtures with xenon (Fig. 7) can be the transfer of energy from xenon atoms in the metastable $^3\text{P}_2$ state to ZnI_2 molecules (reaction 4) and the quenching of the $C^2\Pi_{1/2}$, $D^2\Pi_{3/2}$ states of the ZnI molecule [2,12].

The reduction of radiation power (Fig. 8) is due to a decrease in the intensity of the emission of neon, xenon and spectral bands of molecular iodine (Fig. 3) due to absorption of their emission by zinc diiodide in the region in the range $\Delta\lambda = 550-650$ nm, which passes the ZhS-18 light filter used by us when measuring radiation power.

4. Conclusion

Thus, as a result of complex studies of the optical characteristics of a gas-discharge plasma of the atmospheric-pressure DBD on mixtures of zinc diiodide vapor with neon, intense emission from the spectral band with a maximum at $\lambda = 602$ nm of exciplex zinc monoiodide molecules was detected, most of which is concentrated in the wavelength range 590-608 nm. In addition, the spectral bands of molecular iodine were detected, the most intense of which was the $I_2(D' \rightarrow A')$ band with a maximum at $\lambda = 342$ nm and the spectral bands of the electron-vibrational transition $B \rightarrow X$ in the wavelength range 420 - 480 nm, and the zinc lines represent the $5s \rightarrow 4p$ triplet (468.0, 472.2, and 481.0 nm) and the $4d \rightarrow 4p$ line (636.2 nm). In the emission spectrum of the ternary mixture $ZnI_2 / Xe / Ne$, in addition to the radiation $ZnI (B \rightarrow X)$, Xe^* and Ne^* , at the mixture temperature up to $\sim 160^\circ C$, the emission bands of the exciplex molecules $XeI (B \rightarrow X)$ and $XeI (B \rightarrow A)$ with maxima at 253 and 325 nm were observed, 80% of the radiation power of the source falls on the spectral band $B \rightarrow X$ of zinc iodide molecule ($\lambda_{max} = 602$ nm) with a width of 15–16 nm.

The average radiation power from a unit of volume reached a value of $54.4 \text{ mW} / \text{cm}^3$ in the wavelength range $\Delta\lambda = 550\text{-}650$ nm, the efficiency relative to the power applied to the discharge was $\sim 13\%$.

A radiator based on a gas discharge plasma of atmospheric pressure with high-frequency pumping of a working mixture of zinc diiodide vapor with neon and xenon can be the basis for creating a self-heating excilamp that emits in the orange spectral range. The scaling of the working area of the barrier discharge will make it possible to use the radiator in biotechnology, medicine, etc.

5. References

1. McCown A W and Eden J G 1981 *Appl. Phys. Lett.* **39**(5) 371.
2. McCown A W, Ediger M N and Eden J G 1982 *Optics Communications* **40**(3) 190.
3. Konoplev A N, Kelman V A, Shevera V S 1983 *Journal of Applied Spectroscopy* **34** 315.
4. Guivan N N, Malinin A N 2005 *Optics and Spectroscopy* **99**(5) 703.
5. Guivan N N, Malinin A N 2006 *High Temperature* **44**(3) 356.
6. Malinina A A, Malinin A N, Shuaibov O K 2018 *Problems of Atomic Science and Technology* **6** (to be published).
7. Efimov A E, Belorukova L P, Vasilkova I V, Chechev VP 1983 *Properties of inorganic compounds. Reference book* (L.: Chemistry) 392.
8. Pearse R W, Gaydon A G 1963 *The identification of molecular spectra. Third edition.* (L.: Chapman Holl LTD) 347.
9. Datsyuk V V, Izmailov I A and Kochelap V A 1998, *Physics Uspekhi* **41** 379.
10. Zaydel A N, Prokofiev V K, Raysky S M, Slavny VA. and Shreider E Ya 1977 *Tables of spectral lines* (M.: Nauka) 800.
11. Raizer Yu P. 1991 *Gas Discharge Physics* (Nauka: Moscow) 449.
12. McDaniel E W and Nighan W L 1982 *Gas Lasers* (New York: Academic Press) 486.
13. Smirnov Yu M 2002 *High Energy Chemistry* **36**(1) 1.
14. Malinina A A, Malinin A N 2016 *American Journal of Optics and Photonics* **4** 14.

NEW AND VERSATILE MINATURE MICROWAVE PLASMA SOURCE

Ilija Stefanović^{1,4}, Nikita Bibinov¹, Horia- Eugen Porteanu², Michael Klute³,
Ralf-Peter Brinkmann³ and Peter Awakovicz¹

¹ Ruhr-University Bochum, Faculty of Electrical Engineering and Information Technology, Institute for Electrical Engineering and Plasma Technology, Bochum, Germany

² Microwave Department, Ferdinand-Braun-Institute, Leibniz-Institute for High-Frequency Technic, Berlin, Germany

³ Ruhr-University Bochum, Faculty of Electrical Engineering and Information Technology, Institute for Theoretical Electrical Engineering, Germany

⁴ Serbian Academy of Sciences and Arts, Institute of Technical Sciences, Belgrade, Serbia

E-mail: ilija.stefanovic@rub.de

Miniature Microwave Inductively Coupled Plasma (MMWICP) source is characterized by means of Optical Emission Spectroscopy (OES) in nitrogen gas flow, which gives the information on basic plasma properties. Depending on the incident power the discharge runs in E-mode or in more efficient H-mode. The high resolution radial images of the source reveal different morphologies of different discharge modes. The measurements show an unexpected limitation in dissipated power, accompanied by spontaneous transition from H- to E-mode. The efficiency of the source is high: about 67% of incident power (P_0) is deposited in the discharge, which is estimated from OES.

1. Experimental set-up

MMWICP source consist of a quartz tube with the outer diameter of 7 mm and 1 mm thick walls (see figure 1). Through the quartz tube a continuous flow of 150 sccm (standard cubic centimetre per minute) of N_2 is running. While the source operates in the wide range from few tenths of Pa to atmospheric pressure, during the reported experiment the gas pressure is kept at 1000 Pa. The microwave power is coupled through a copper resonator, which combine an inductive loop and a gap capacitor unified in a single copper block. The resonator is tuned to the resonance frequency of 2.6 GHz. The MW power is provided by a signal generator with the maximum delivered power of 250 W. The generator is equipped with an integrated directional coupler and two power meters, measuring the forwarded and reflected powers. The further details are provided in [1].

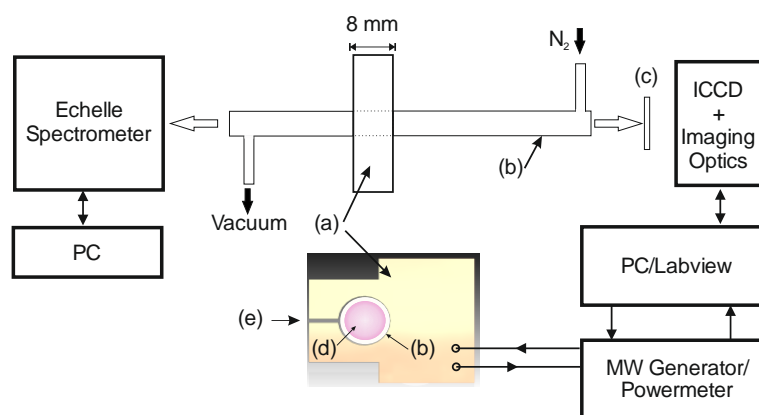


Fig. 1. Schematic of the experimental set-up for characterization of MMW plasma source. Top: optical arrangement; bottom: copper resonator cross section perpendicular to the optical axis. (a) copper resonator, (b) quartz tube, (c) interference filter (d) plasma and (e) gap capacitor.

The OES is conducted by collecting light emission perpendicular to the discharge cross-section. A calibrated Echelle spectrometer measures absolute intensity of two nitrogen

emission lines: $N_2(C,0-0)$ and $N_2^+(B,0-0)$. The population/depopulation of N_2 (C) and N_2^+ (B) states is well described and previously used to determine the plasma conditions in different sources [2, 3]. In the combination with a simple collision- radiative model, the outcome of OES is line integrated plasma density n_e , electron velocity distribution function (EVDF) and normalized electrical field strength E/N . The analysis of the vibrational spectra gives rotational temperatures of N_2 and N_2^+ , respectively. Since the electronic impact excitation of diatomic molecules is limited by the selection rule $\Delta J = 0, \pm 1$, the rotational distribution in the excited molecular state is approximately equal to the rotational distribution in the ground state of the molecule. This allows to determine a gas temperature T_g in the plasma by using the rotational distribution in the emission spectrum of the $N_2(C-B,0-0)$ vibrational band. Simultaneously to OES, a calibrated Intensified Charge-Coupled Device (ICCD) camera is recording the radial distribution of plasma emission. Two narrow band-pass interference filters can be used to separate two different emission lines: $N_2(C,0-0)$ and $N_2^+(B,0-0)$. By using the same analysis as by space averaged OES, the radially resolved line integrated n_e and E/N are determined.

2. Results

The MMWICP characteristics depend strongly on the absorbed power P_a . For the sake of comparison two different absorbed powers are chosen, corresponding to the different discharge modes: hybrid mode (E/H) at $P_a = 12$ W and H-mode at $P_a = 80$ W. The OES reveals different plasma densities and gas temperatures of both modes. The H-mode has $n_e = 3.5 \times 10^{19} \text{ m}^{-3}$ and $T_g = 1600$ K, which is expected by high efficient inductive coupling. At low powers the discharge still reaches relatively high plasma density of $n_e = 6.8 \times 10^{18} \text{ m}^{-3}$.

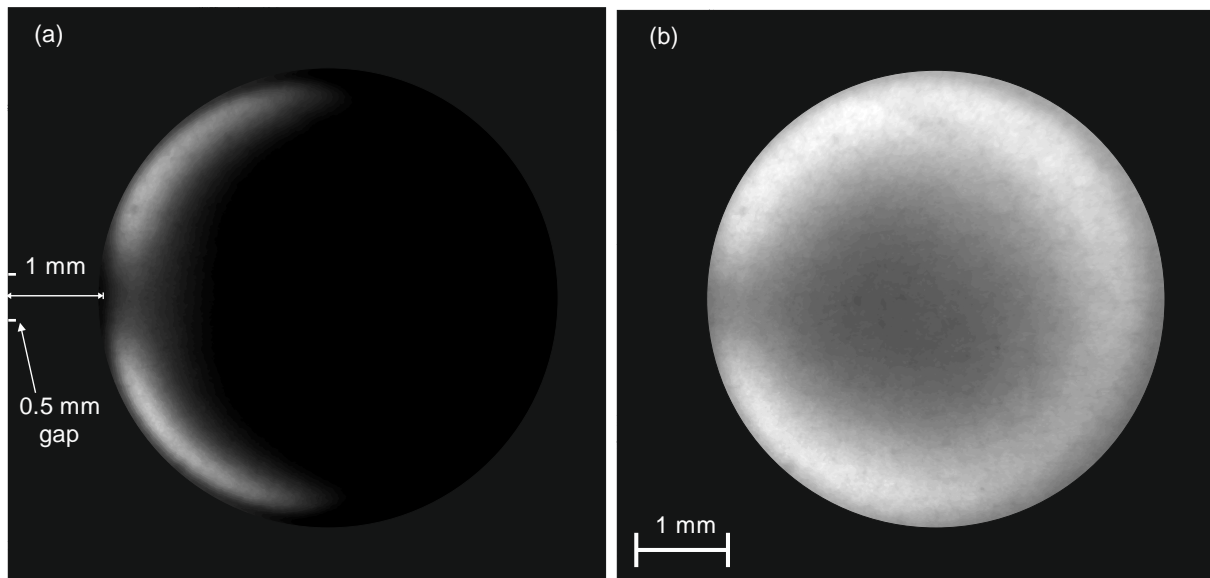


Fig. 2. Radial images of the MW plasma: (a) hybrid E/H mode, absorbed power $P_{\text{abs}} = 12$ W and (b) H - mode, $P_{\text{abs}} = 78$ W. Two horizontal bars on (a) indicate the approximate position of the 0.5 mm gap capacitor, situated closely to the outer quartz tube wall, e.g. 1 mm away from the plasma to the left. Light reflection by the tube wall is suppressed. (Reproduced from [1]).

Fig. 2 presents two high-resolution images of a discharge cross-section at two different absorbed powers: (a) 12 W and (b) 78 W. These conditions corroborate with two different discharge modes. At low powers the discharge is concentrated in the vicinity of the gap capacitor, indicating strong capacitive coupling, which is characteristic for the E-mode. Nevertheless, the high plasma density and the discharge morphology suggests the existence of

hybrid E/H mode rather than pure E-mode. The gas temperature in this hybrid mode is about 650 K. The H-mode morphology reassembles a “donut” shape. The discharge emission peaks at the vicinity of the tube wall and have a ring form according to the circular pattern of the current flow by inductive power coupling.

The narrow band interference filters in front of the camera objective isolate the spatially resolved absolute light intensities either of $N_2(C,0-0)$ or $N_2^+(B,0-0)$ over the discharge cross-section. By using the same analysis as by OES the spatially resolved n_e and E/N are recorded. The dissipated power P_{diss} density in the plasma can be estimated by

$$\frac{P_{diss}}{V} = n_e e v_d \left(\frac{E}{N} \right) N. \quad (1)$$

V is the plasma volume, e – the elementary charge, v_d – the electron drift velocity and N the gas density. The integration over the plasma volume gives a value of dissipated power in the H – mode about $P_{diss} = 52$ W. The comparison with P_a by electrical measurements, which include the power absorbed in connectors, cables, copper resonator and plasma, gives relative good agreement.

One of the intriguing characteristics of the MMWICP source is the *limitation in the absorbed power*. We have to note that, by increasing the incident power for given pressure and reactor radius there is a limitation at 158 W. By further increase, the plasma cannot support the H-mode and switch to the E-mode or the hybrid mode. The reason for this behavior is still not clearly understood and needs further experimental and theoretical studies. Nevertheless, some preliminary results on the spontaneous transition from H- to E-mode for the pressure of $p = 470$ Pa in nitrogen are shown on Fig. 3.

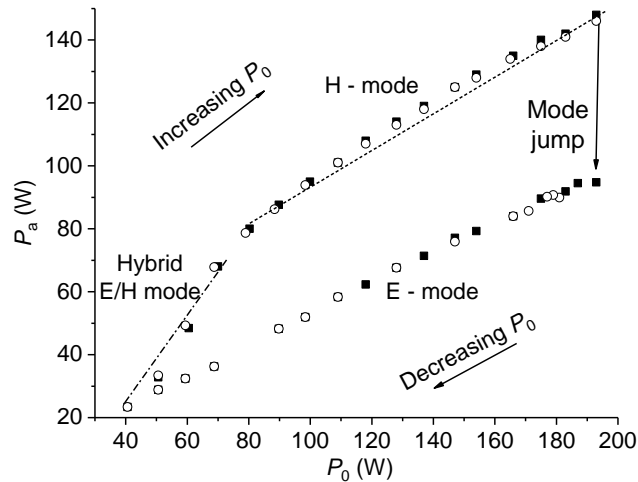


Fig. 3. Absorbed MW power P_a vs. incident power P_0 . Different points indicate two cycles of power variation. Different discharge modi are indicated: H-mode, E-mode and hybrid (E/H) mode. For the given pressure of 470 Pa the maximum absorbed power is $P_a = 148$ W. The MW frequency is $f = 2.465$ GHz and is kept constant during the measurements. The straight lines are arbitrary and are used to indicate different slopes of power change in hybrid- and H- mode.

The discharge is ignited in hybrid (E/H) mode at incident power $P_0 = 40$ W. By increasing the incident power, the absorbed power follows and from $P_0 > 80$ W the discharge is running in H- mode. By reaching some critical value (about $P_a = 148$ W for 470 Pa and $P_a = 158$ W for 1000 Pa) the discharge switch to E- mode spontaneously (indicated as a “Mode jump” at Fig. 3). By decreasing P_0 the discharge runs through the lower branch of the hysteresis. Only at low incident powers it is than possible to run the discharge through upper hysteresis’s

branch again. Two consecutive cycles of measurements (solid and opened symbols in figure 3) show high degree of reproducibility.

The novel MMWICP source operated in nitrogen flow at 1000 Pa is characterized by optical emission spectroscopy and optical imaging. The absolute intensities of the second positive and the first negative emission systems of molecular nitrogen are measured. The careful analysis of the rotational distributions of $N_2(C-B,0-0)$ and of $N_2^+(B-X,0-0)$ vibrational bands helps to rule out the stepwise excitation as the dominate excitation mechanism for the $N_2^+(B-X)$ state. The absolute intensity measurements detect the high electron density ($3.5 \times 10^{19} \text{ m}^{-3}$) and high gas temperature (1600 K). Optical imaging reveals different emission patterns for H – mode and hybrid – mode. Additionally, the spatially resolved optical emission is used to obtain the distributions of electron density and electric field over the discharge cross-section. The relative high discharge efficiency is measured: about 67% of the incident power is consumed in the H-mode. Some limitations in the maximum of the absorbed power is detected and deserve further analysis. The preliminary measurements on atmospheric pressure discharge in argon indicates that the MMWICP source can be widely used for industrial and other applications such as plasma medicine and biotechnologies.

3. References

- [1] Stefanović I, Bibinov N, Porteanu H- E, Klute M, Brinkmann R- P and Awakowitz P 2018 *Plasma Sources Sci. Technol.* in press <https://doi.org/10.1088/1361-6595/aaefcc>
- [2] Steves S, Styrnoll T, Mitschker F, Bienholz S, Bibinov N and Awakowicz P 2013, *J. Phys. D: Appl. Phys.* **46**, 445201
- [3] Pothiraja R, Ruhrmann C, Engelhardt M, Bibinov N and Awakowicz P 2013 *J.Phys.D:Appl.Phys*, **46**, 464012

HYDROPHILICITY OF PLASMA-TREATED POLYMERS AS A RESULT OF SURFACE CHARGING

M. Yablokov¹, R. Gainutdinov², A. Tolstikhina², D. Temnov^{3,4}, S. Kulemina^{3,4},
A. Kuznetsov¹

¹*Enikolopov Institute of Synthetic Polymer Materials, Russian Academy of Sciences,
Profsoyuznaya Str. 70, 117393 Moscow, Russia*

²*Shubnikov Institute of Crystallography of FSRC "Crystallography and Photonics"
Russian Academy of Sciences, Leninskii pr. 59, 119333 Moscow, Russia*

³*Herzen State Pedagogical University of Russia, 6 Kazanskaya st., 191186, St. Petersburg,
Russia*

⁴*Saint Petersburg National Research University of Information Technologies, Mechanics and
Optics, Kronverkskiy prospekt, 49, 197101, St. Petersburg, Russia*

E-mail: yabl1@yandex.ru

It was shown that direct current glow discharge treatment of fluorocarbon polymer films leads to their significant hydrophilization and formation of electret state. The relationship of electret charge and hydrophilicity of fluorocarbon polymers was studied. Hydrophobic recovery up to the initial value of contact angle was observed after thermal depolarization of plasma-treated polymer films. The process of hydrophobic recovery with time in ambient conditions of polymer films treated by direct current glow discharge was considered as a consequence of relaxation of electret charge, acquired by plasma-treated polymer films.

1. Introduction

Modification of polymers by low-temperature plasma is as a very effective method for enhancement of the films wettability and adhesive strength [1,2]. The changes in plasma-modified polymers take place within a surface layer with thickness 50 nm [3]. We have shown earlier that the direct current glow discharge treatment of fluorine-containing polymers leads to the significant hydrophilization and improvement of adhesion properties and also to appearance of stable surface charges [4,5]. Recently we showed the existence of correlation of wetting, adhesion and electret properties of PTFE films, modified by direct current glow discharge [6].

Stability of properties of plasma-modified polymer films is very important question for their practical usage. One of the most significant problems is the stability of wetting. Hydrophobic polymer surfaces after plasma treatment become hydrophilic, and this hydrophilicity is lost with time. This process is called "hydrophobic recovery", and the nature of this process is not yet well established. We report in this work on the investigations of the hydrophilization and electric charging of plasma-modified polymer films, and treat hydrophobic recovery as the result of relaxation of surface charges on polymer surface.

Important question is the evolution of surface morphology and distribution of surface charges of polymer film after plasma treatment. Kelvin probe force microscopy [7,8] gives the possibility measure the distribution of surface potential and surface charges. AFM and Kelvin probe force microscopy was used in this work for surface characterization of glow-discharge treated polymer films.

2. Experimental

The procedure for film modification by DC discharge is detailed in [9]. Two symmetrical parallel plate aluminum electrodes of 13,5 cm in diameter with 4 cm distance between electrodes – cathode and anode, were used. Samples of the polytetrafluoroethylene (PTFE) and poly(ethene-co-

tetrafluoroethene) (ETFE) films of 40 μm thickness (“Plastpolymer”, St. Petersburg, Russia) were used in the study. Polymer samples were placed on the bottom electrode of the two electrode system. Working plasma gas was air, pressure of 10 Pa and a discharge current of 50 mA, treatment time 40 s. Surface properties were characterized by values of the contact angle measured with an Easy Drop DSA100 instrument (KRUSS, Germany) using deionized water as a test liquid. The electret potential was measured by the compensation technique using a dynamic capacitor.

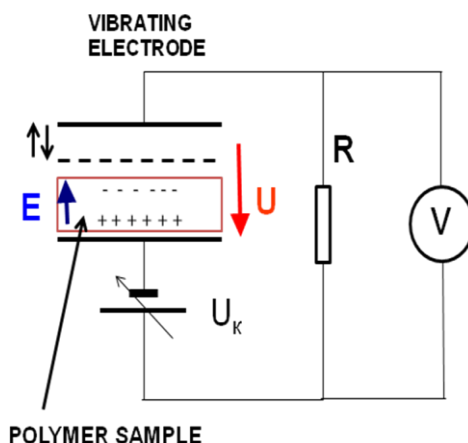


Fig.1 Schematics of experimental setup for the effective surface charge measurements by the dynamic capacitor method: E – electric field, induced by surface charges, U – compensating constant electric field, produced by power supply (U_k), R- resistor for measurement of voltage drop (V).

Alternating current nanovoltmeter operates as “zero-indicator”. The method of dynamic capacitor is based on the effect of electrostatic induction arising in the electric contour with vibrating electrode of electric capacitor. From the measured value of electret potential (U), the effective density of the surface charge (σ) was calculated by the equation $\sigma = \epsilon_0 \epsilon U/L$. In this equation, ϵ_0 is the electric constant and L is the thickness of the polymer film. Dielectric permittivity of the samples was taken to be $\epsilon = 2$. The experimental setup and the procedure of measurement are detailed in [10]. The spectra of thermostimulated depolarization (TSD) of PTFE films were obtained on a TSCII device (Setaram, France) in helium atmosphere with heating rate of 9 K/min. The currents were measured by a Keithley electrometer 6517E. Surface topography of plasma-treated polymer films was studied using a NTEGRA Prima (NT-MDT Spectrum Instruments, Russia) atomic force microscope (AFM). Measurements were carried out in the semicontact (tapping) mode to obtain a three-dimensional image. The spatial distribution of potential was investigated with the method of Kelvin probe force microscopy. All experiments on the preparation and precision study of the samples surface were carried out under controlled conditions of the TRACKPORE ROOM-05 measuring complex.

3. Results and Discussion

Wettability and electret properties of polymer films were measured simultaneously. The experimental data on changes in contact angle of water (θ) and effective surface charge density (σ) for the PTFE films are shown on Fig.1, and for ETFE film are shown on Fig.2 It can be seen that the plasma treatment of PTFE films at the anode is more effective for wettability enhancement, than at the cathode. For ETFE films cathode-treatment is more effective, than anode treatment. Heating of polymer films to the temperature of full relaxation of electret charges, determined from thermostimulated depolarization currents measurements, leads to complete loss of hydrophilicity of plasma-treated films and hydrophobic recovery. Contact angles of plasma treated and heated films return to the value of contact angles, relevant to pristine samples. After modifying PTFE film at the anode, the effective density of negative charge increases to $-36 \mu\text{C}/\text{m}^2$, whereas the film treated at the cathode acquires a positive surface potential, equal to $140 \mu\text{C}/\text{m}^2$. Pristine PTFE film had a small negative surface potential and the effective charge density $\sigma = -15 \mu\text{C}/\text{m}^2$.

Thermostimulated depolarization (TSD) currents of glow-discharge treated PTFE films are shown on Fig.3.

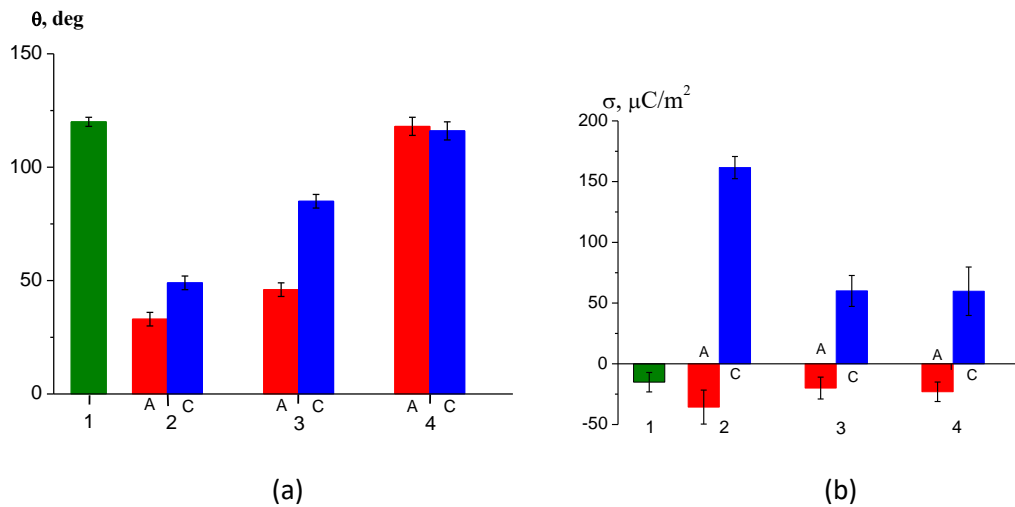


Fig. 1. Wettability and charging induced by DC discharge treatment of PTFE films: (a) values of contact angle of water θ , (b) effective surface charge density σ , for (1) the pristine film, (2) the film modified by plasma at the anode (A) and the cathode (C), (3) the plasma-modified film immersed in distilled water for 1 minute and dried, and (4) the plasma-modified film treated at 300°C for 20 min.

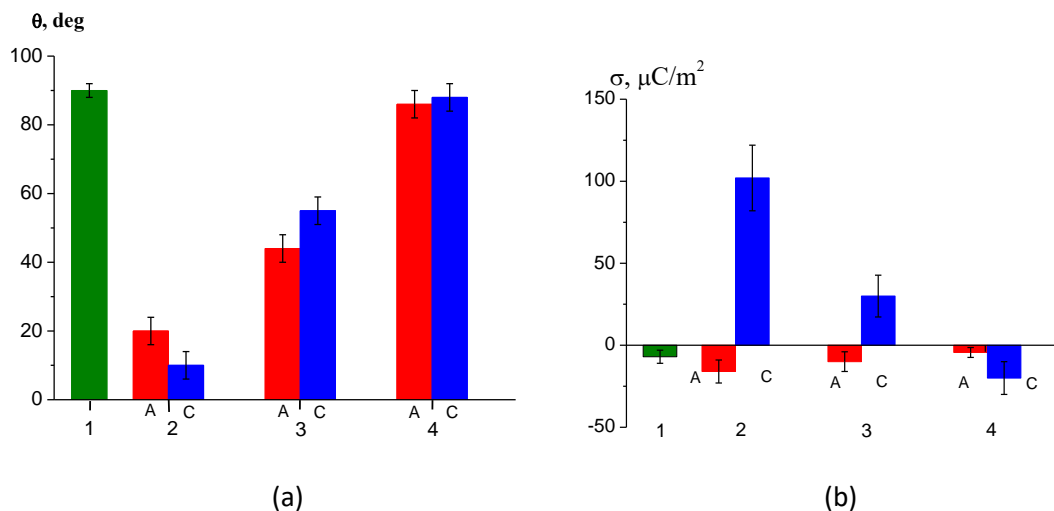
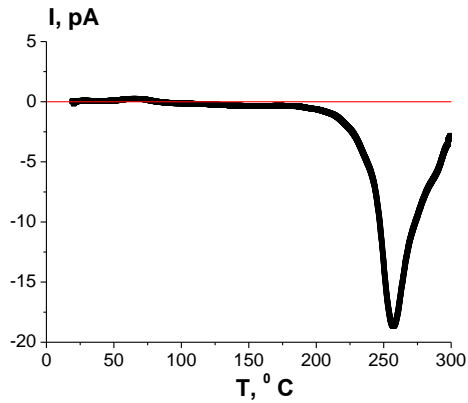


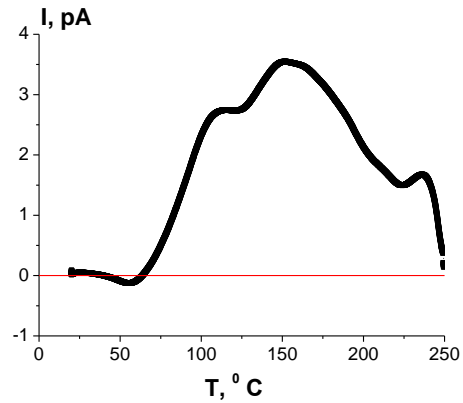
Fig. 2. Wettability and charging induced by DC discharge treatment of ETFE films: (a) values of contact angle of water θ , (b) effective surface charge density σ , for (1) the pristine film, (2) the film modified by plasma at the anode (A) and the cathode (C), (3) the plasma-modified film immersed in distilled water for 1 minute and dried, and (4) the plasma-modified film treated at 250°C for 20 min.

It is known that the experimentally determined value of the effective surface charge density is an integral characteristic of the electret state and is the sum of homo- and heterocharges. For both TSD curves maximums of currents with different polarity are observed. Major high-temperature peaks on the curves obviously belong to relaxation of homocharges, which are injected into the polymer surface during DC discharge treatment. Low-temperature minor peaks may be attributed to heterocharge, connected with orientation of polar groups during plasma treatment of polymer film. These polar groups are formed during oxidation reactions and oriented in electric field in the surface layer during polymer plasma modification. So, the nature of the DC discharge-induced electret state in the polymer film may be associated not only with the charges, but also with oriented dipoles on the surface.

Direct current glow discharge treatment leads to dramatic changes in polymer film morphology. Surface topography and Kelvin probe potential relief of PTFE films, treated at the cathode is shown on Fig.4, treated at the anode is shown on Fig.5.

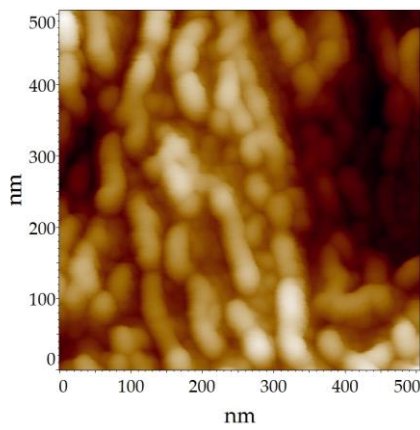


(a)

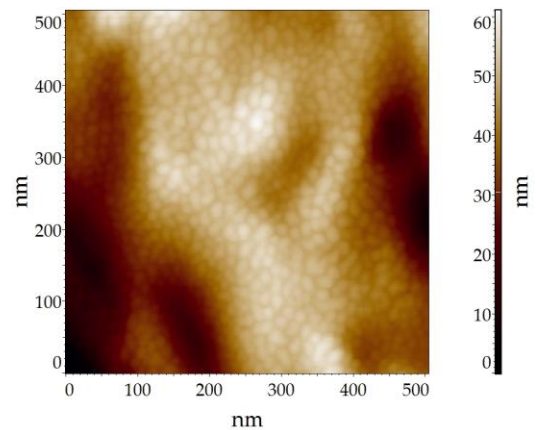


(b)

Fig. 3. Temperature dependence of depolarization currents glow-discharge treated PTFE films (a) at the anode (b) at the cathode

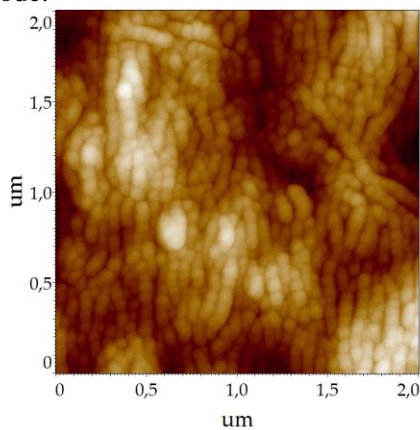


(a)

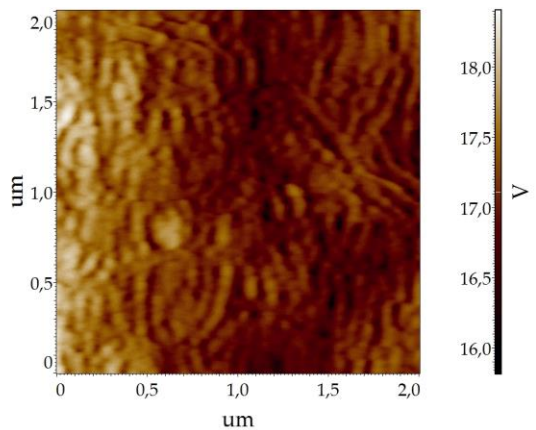


(b)

Fig.4. AFM images of plasma-treated PTFE films: (a) modified at the cathode and (b) at the anode.



(a)



(b)

Fig. 5. AFM image of cathode-treated PTFE films: (a) surface topography (b) Kelvin mode.

As can be seen from Fig.4, the characteristic dimensions of the morphological features of the PTFE film treated at the anode and cathode differ significantly. For the film processed at the anode is characteristic a relatively flat relief with pronounced nanosized cracks forming many-sided, relatively flat fragments with a characteristic size of 15-20 nm. For the film treated at the cathode, the characteristic elements of the relief are cylindrical elongated formations with a diameter of about 30 nm and a length of up to 100 nm, oriented coaxially. Correlation of electric potential contrast with

topography is observed on Fig.4 and Fig.5 for PTFE films. This effect is especially pronounced for the images shown on Fig.4.

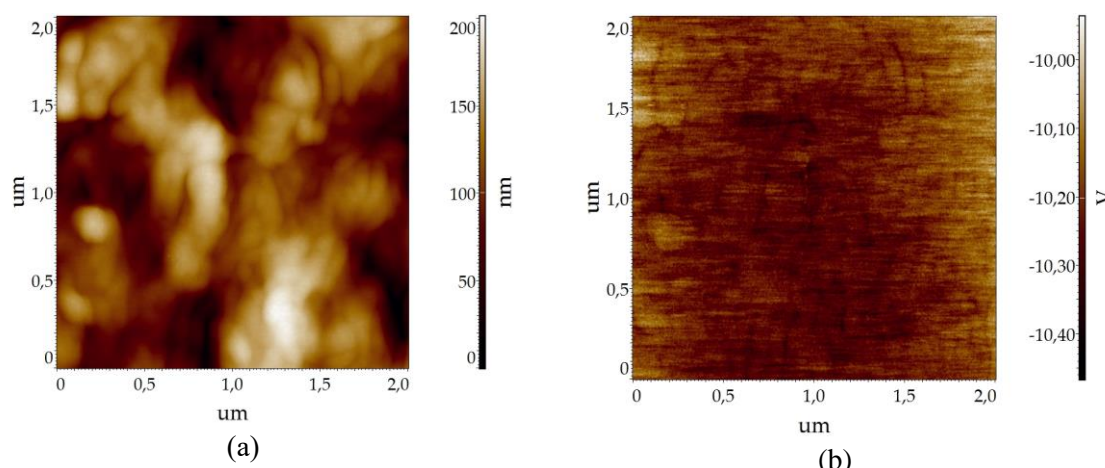


Fig.5. AFM image of anode-treated PTFE films: (a) surface topography (b) Kelvin mode

A serious problem in the study of the surface of dielectrics by the method of AFM is the effect of surface charge on the mapping of the surface topography [11]. Since the electrostatic interaction is more long-range compared to Van der Waals forces, the study of the surface relief in semi-contact mode does not reflect the surface relief, but the space charge distribution. This leads to the fact that the image is blurred, small relief elements are not displayed at all. To correctly display the surface relief, it is necessary to get rid of the charge induced on it. This can be achieved, for example, by increasing the relative humidity to 40–60%, depending on the sample under study. A clean climate controlled box is best suited for this task [12].

It was shown that the experimental dependences of the magnitude of contact angles and the surface charge density of PTFE films treated in glow discharge from the storage time in air correspond to the theoretical model of wetting of charged polymer films, which is based on considering the interfacial surface energy as a function of surface charge density [13].

Experimental results obtained in our work shows that hydrophilicity of plasma-treated polymers can be controlled via regulation of surface charging.

4. References

- [1] Cvelbar U Walsh J Černák M et al. 2018 *Plasma Process Polym* e1700228.
- [2] Hegemann D Brunner H Oehr C 2003 *Nucl. Instrum. Methods Phys. Res. Sect. B.* **208** 281.
- [3] Yablokov M Sokolov I Malinovskaya O Gilman A Kuznetsov A 2013 *High Energy Chem.* **47** 32.
- [4] Gilman A Piskarev M Yablokov M Kuznetsov A 2015 *Russ. J. General Chem.* **85** 1302–1310.
- [5] Richkov A Yablokov M Kuznetsov AE, Gilman A Kuznetsov AA 2010 *High Energy Chem.* **44** 347.
- [6] Yablokov M Piskarev M Gilman A Kechekyan A Kuznetsov A *High Energy Chem.* 2015 **49** 207-210.
- [7] Nonnenmacher M Oboyle M P Wickramasinghe H K 1991 *Applied Physics Letters* **58** 2921.
- [8] Sorokina K L Tolstikhina A L 2004 *Crystallography Reports* **49** 476.
- [9] Richkov D Yablokov M Richkov A 2012 *Appl. Phys. A, Mater. Sci. Process.* **107** 589.
- [10] Yablokov M Kechekyan A Gilman A Ozerin A 2011 *Nanotechnics* **2** (26) 86.
- [11] Tolstikhina A L Gainutdinov R V Zhanavskiy M L Sorokina K L Belugina N V Grishchenko Yu V 2008 *Journal of Surface Investigation-X-Ray Synchrotron and Neutron Techniques* **2** 722.
- [12] Tolstikhina A L Gainutdinov R V Zhanavskiy M L Sorokina K L Belugina N V Grishchenko Yu V Shestakov V D 2009 *Russian Microelectronics* **38** 110.
- [13] Bormashenko E Multanen V Chaniel G Grynyov R Shulzinger E Pogreb R Whyman G *Colloids & Surf. A* 2015 **487** 162-168.

INCREASING THE EFFICIENCY OF PLASMA JET TREATMENT BY THE PRECURSOR ADDITION

Zbyněk Voráč, Maja Korous, Barbora Pijáková, Jozef Ráhel'

*Department of Physical Electronics, Faculty of Science, Masaryk University, Kotlarska 267/2, 611 37
Brno, Czech Republic*

E-mail: zbynda@mail.muni.cz

Radiofrequency plasma jet was used for plasma-chemical modification of plastics surfaces. Chemical precursor passing through the active zone of the plasma was employed to improve the treatment efficiency. The purpose of these modifications was to connect reactive groups to the surface of the materials. Improved plastic wettability and increased adhesion of paints were obtained. The effect of plasma-chemical modification of the surface with plasma in the presence of the precursor was higher than that of plasma alone.

1. Introduction

Plastics have good mechanical properties, can be molded easily and are cheap. For these reasons, they represent one of the most used materials. In order to increase the lifetime and in particular to improve the aesthetic properties, the surface of the plastic products is painted. Plastics' low surface energy and inertness often lead to a low adhesion of the coatings. Therefore, the surface of plastics is often pretreated chemically or by discharge plasma before the coating.

In the industrial practice the surface plasma-chemical modifications are most often carried out by a corona discharge or ionization. The main advantages of these methods lay in their low acquisition and operating costs and considerable robustness. Further experimental studies in this field are focused on the use of an atmospheric pressure plasma jet (APPJ), and the dielectric barrier discharge (DBD). [1] The discharges are typically operated in air, nitrogen or argon. Sometimes, when a hydrophobic character of treated surface is desired, a suitable (mostly organosilicone) precursor is added to the working gas [2]. The use of organic precursor additive to achieve the opposite effect (i.e. wettability or adhesion improvement) is surprisingly rare [3].

In recent years, we have been working on the use of radio frequency plasma nozzles to improve the adhesion of coatings and adhesives for plastics and some other materials. We studied the effect of processing conditions, plastic, and the type of paint to pull-off test for adhesion according to ISO 4624. It was found that one of the promising possibilities of further increasing the efficiency of the plasma treatment is addition other chemicals to the working gas.

The construction of plasma nozzles [4] allows the addition of volatile precursors to the working gas while maintaining a homogeneous discharge and long lifetime. Passage of the precursor through the core of the plasma allows its decomposition into reactive fragments while blowing in the direction of the substrate. This provides optimal conditions for the simultaneous action of plasma and reactive ions and fragments or radicals.

2. Experimental

Tests were carried out on plastic car parts. For the experiments, parts made from acrylonitrile butadiene styrene (ABS) copolymer were selected. ABS is the world's most popular thermoplastic. It is health harmless and has good mechanical properties. The surface was first cleaned with detergent and isopropyl alcohol. Subsequently, samples were processed by plasma. Samples were then sprayed with 2K-PUR acrylic paint LV AKZ 421 RAL 2009 (Synpo, Czech Republic) designed for single-layer coating of plastics. After 21 days of drying and aging, the pull-off test for adhesion according to ISO 4624 was tested.

Plasma jet was powered by Cesar 136 (Advanced Energy) working on frequency 13.56 MHz. The nozzle was connected to a generator through a matching LC network comprising a capacitor with variable capacity and a coil with adjustable impedance. Electromechanical scheme of the matching network is shown in Figure 1. Commercial matching networks most often use approximate impedance settings via wiring to some coil thread. Fine tuning (often automatic) is done using capacitors with adjustable capacity. This solution is easier to modify for electronically controlled operation, but phase

matching with the continuously adjustable coil impedance allows us to adapt to a wider range of operating parameters.

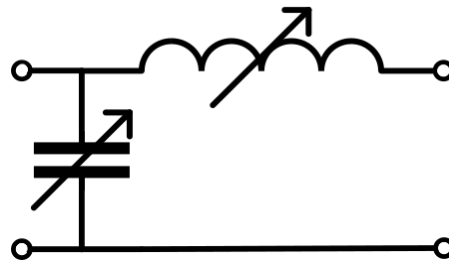


Fig. 1. Electrical scheme of the matching network. The capacity can be set in the range of 200–1200 pF and the coil impedance 0–8 μ H.

The slit nozzle design [5] consisted of PTFE frame that joined the individual nozzle functional parts (Figure 2). The frame also includes a built-in working gas distributor and homogenizer. This ensures laminar flow eliminating the parasitic processes in plasma. To the frame are inserted two parallel corundum plates with dimensions of 11×13×1 mm. These form the nozzle walls and the dielectric necessary for the discharge. Mutual plates distance was defined by 2 mm thick strips of borosilicate glass. Leakage of gas from the nozzle between the corundum electrodes and the Teflon frame was prevented by the rubber seal. The mounting of the plates to the frame was made by plastic fixing screws. The powered and grounded silver electrode is formed directly on the wall of the dielectric plate. The distance and geometry of the electrodes have been optimized for maximum field strength and homogeneity. By finding a suitable shape of the electrodes, the otherwise preferred burning of the discharge at the corners of the electrodes was limited.

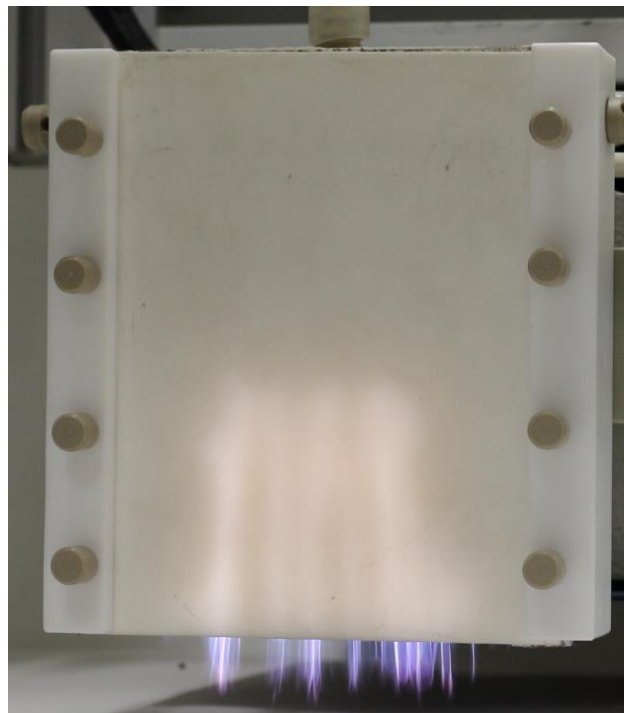


Fig. 2. Atmospheric pressure plasma jet. Due to the short exposure time, inhomogeneity and the filamentary nature of the discharge can be observed.

The addition of the precursor to the discharge was accomplished by dividing the working gas (argon) flow into two parts. The first part went through the flow regulator directly to the nozzle. The second, usually significantly smaller, was led through the flow regulator into the container, where it bubbled through the liquid precursor. Prior to entering the plasma nozzle, both branches were joined to pass together through the jet homogenizer.

Generator output was set to 180 W. The width of the nozzle slot, which simultaneously determined the discharge width was 10 cm. Argon flow through the nozzle was 50 l/min and flow through the precursor vessel was 2 l/min. The workpiece was moved beneath the nozzle at a speed of 60 mm/min and the passage was repeated 6 times. Precursor tested for improving the adhesion was water.

3. Results

Surface treatment of ABS by plasma jet resulted in improved adhesion of the coating. When water vapor was added to the working gas, the adhesion increased even more. Measured pull out force values are summarized in Table 1. In addition, it was also possible to observe higher variability of individual measurements. This was probably due to the inhomogeneity of the plasma resulting in uneven surface treatment.

Tab. 1. Pull out force on samples of ABS and ABS with 5% polycarbonate.

Substrate	Treatment	Pull out force [MPa]
ABS	Reference	2,1 ± 0,3
ABS	Plasma	3,4 ± 0,4
ABS	Plasma + H2O	3,5 ± 0,4
ABS+PC	Reference	2,4 ± 0,1
ABS+PC	Plasma	2,6 ± 0,5
ABS+PC	Plasma + H2O	2,9 ± 0,4

Measured data shows a significant impact of the plastic composition on the effectiveness of plasma treatment. The 5% addition of polycarbonate (PC) used to reduce the water absorption of ABS markedly influenced the adhesion of the coating.

4. Conclusion

Plasma nozzles can be used to increase the adhesion of paint to plastics. By adding the precursor to the working gas, the processing efficiency increases. Precursors can also be used to enrich plasma with active substances acting on the surface of the material. The advantage of this arrangement is the possibility of passing the precursor through the active plasma zone and its drift toward the processed material, which ensures the interaction of the effects of the chemicals and the plasma. Another advantage is the relatively low thermal load of the treated surface. This technology enables the machining of complex shapes and structured surfaces. The slit width and hence the width of the plasma can be scaled.

5. Acknowledgement

This work was supported by the Technology Agency of the Czech Republic, project TE02000011.

6. References

- [1] Kostov, K.G., Nishime, T.M.C., Castro, A.H.R., Toth, A., Hein, L.R.O. 2014 *Applied Surface Science* **314**, 367.
- [2] Laroussi, M, Akan, T 2007 *Plasma Processes and Polymers* **4**,777.
- [3] Odrášková, M., Szalay, Z., Ráhel', J., Zahoranová, A., Černák, M. 2008 *AIP Conference Proceedings* **993**, 391.
- [4] Dugáček, J., Dvořáková, H., Sťahel, P. 2017 *Conference Proceedings, 9th International Conference on Nanomaterials - Research and Application*, 260.
- [5] Masarykova univerzita, Brno. Štěrbinová plazmová tryska se zlepšenou energetickou účinností. Původci: Ráhel', J., Pijáková, B., Korous, M., Dvořáková, E., Voráč, Z. Česká republika. Užiténý vzor CZ 30999 U1 03.08.2017.

μPlasmaPrint: digital on-demand surface engineering

B. Rais^{1*}, H. De Haan¹

¹ *InnoPhysics B.V., Fransebaan 592a, 5627 JM Eindhoven, The Netherlands*

* *bilel.rais@innophysics.nl*

Abstract

InnoPhysics has developed and commercializes the μPlasmaPrint technology, an atmospheric pressure micro-plasma system which enables area-selective functionalization by means of a dot-wise patterning of the plasma treatment/deposition with resolutions from millimeters down to 150 μm. In order to improve the μPlasmaPrint resolution and to improve the processing and substrates flexibility, InnoPhysics has developed new hardware and process options. Recent developments will be shown related to process feedback through surface wettability mapping and the development of a stand-alone μPlasmaPrint head with integrated electrode to enable the application of μPlasmaPrint on not only 2D, flat substrates, but also more complex, 3D workpieces. On the process side, developments will be presented to enable non-fouling hydrophilic coatings in plastic biomedical devices by combining μPlasmaPrint with liquid coating dispensing.

Introduction

Plasma treatment of surfaces is a well-known technique to modify properties of surfaces, for example to decrease the hydrophobicity of plastics. It is common for surfaces to be treated integrally, however, this might be unnecessary or even undesirable: in many cases one would like to treat surfaces locally and in a patterned manner. One way of doing this would be to use a mask that shields certain parts of the surface from the plasma. InnoPhysics' way of doing this is more flexible and versatile: small individual plasmas are created only there where desired (on demand) while the plasma print head scans across the surface.

Using the digital and on demand paradigms known from inkjet printing, surfaces can be plasma treated directly from an electronic image (no mask), which allows for efficient process development and short, customized production runs with a fast turnaround time and minimal consumable usage.

InnoPhysics has made its plasma printing technology available in the form of a Modkit, which is a kit specifically designed such that it can be integrated into different motion platforms. Once installed, the PlasmaPrint hardware can be exchanged back for the original hardware and vice versa. The control settings for the PlasmaPrint process can be integrated into an existing graphical user interface, or it can be supplied with its own user interface.

When integrated into an XYZ-motion platform, such as the Roth&Rau LP50 inkjet printer or the Roland platform, PlasmaPrint processes can be developed efficiently, allowing for effective proof-of-principle and prototype developments.

Experimental

The principle of μPlasma patterning [1] is shown in Figure 1. A print head consisting of two rows of twelve needles is positioned above a substrate table. The needles on the print head act as ground electrodes, whilst the substrate table is kept at high voltage to complete the electrical circuit. The substrate located on the substrate table acts as the dielectric barrier. The needles in the print head can individually, move up and down

mechanically. As the needle moves closer to the substrate table at a pre-set applied voltage and chosen gas composition, the electrical breakdown is achieved and plasma ignites.

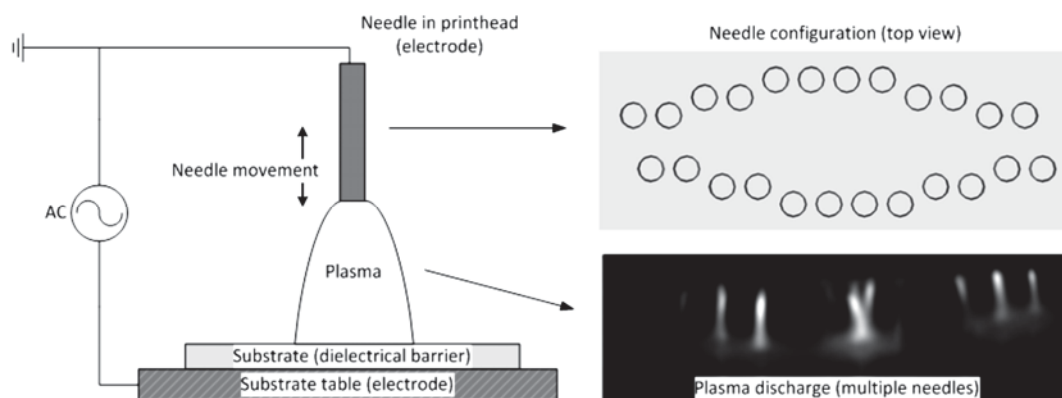


Fig. 1. Schematic drawing of μ Plasma printer setup.

The μ Plasma setup works at ambient pressure and temperature in an open system with direct contact to the external environment. In normal operation mode, this means that the plasma will be generated in air at room temperature (22-24°C) and with a relative humidity present at that moment in time. The μ Plasma setup also accommodates throughput of different gas (mixtures) like dry (compressed) air, nitrogen, argon or precursor materials to influence the reactivity of the plasma gas or to be able to deposit layers on top of the substrate. For this, gas is led through a mass flow controller, and in case of a mixture with a precursor material through a wash bottle with bubbler. Approx. 200 ml/min of gas (mixture) is needed to create a small overpressure of approx. 5 Pa in between the print head and substrate to expel (most) of the air during the μ Plasma patterning.

For the construction of the Lab-on-a-chip capillaries, standard microscopic glass slides (76x26 mm²) were used. Because of the small contact angle of water on glass, i.e. less than 5 degrees, the glass slides were pre-treated with dodecyl-thioclorsilane (Sigma Aldrich), in order to make the glass hydrophobic. First, the glass was thoroughly cleaned by rinsing with deionised water, and n-propanol before being dried in air. Next, the glass slides were placed in a solution of 0.001 M dodecyl-thioclorsilane in toluene at 3°C for 30 minutes under a nitrogen atmosphere to deposit a monolayer of dodecyl-thioclorsilane (DTS) on the glass slide. After coating, the glass slides were sequentially rinsed with toluene, ethanol and deionized water and dried with nitrogen. The hydrophobic nature of the glass slides was checked by measuring the water contact angle measurement using a Dataphysics OCA-30 contact angle measurement device. Contact angles over 100° were measured for the treated glass slides. The plasma from the μ Plasma printer selectively removes the DTS, exposing the original glass surface.

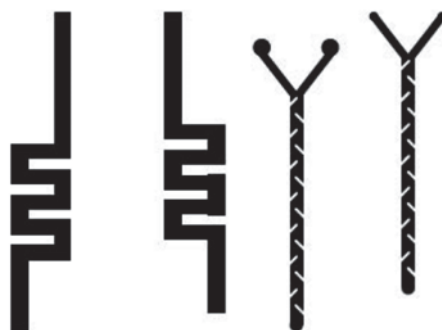


Fig. 2. Two examples of μ Plasma printed structures.

Even though multiple structures were printed, in Figure 2 two examples of printed structures are shown. The structures were printed at 20 mm/s at 4.5 kV and 50 μm print height between print head and glass substrate with 90 dpi. A nitrogen flow of 200 ml/min at ambient pressure (99.999% Praxair) was used as plasma gas. To create the hydrophilic capillaries, two glass slides were μPlasma patterned upon using, among others the mirror image structures from Figure 2. After printing, the capillaries were formed by placing the glass slides on top of each other. In between the glass slides, adhesive tape (3M Scotch tape, thickness 0.10 mm) is placed to create a space between the slides. To test the functionality of the capillary design, water coloured with a dye for better visual contrast was positioned at the opening of the design. Under capillary force the water enters the reactor and fills the channel. The progress of the liquid flow through the capillary is filmed and analysed.

Results

Figure 3 shows the top and bottom glass slides for the two designs presented above. For clarity the hydrophilic tracks are visualized with steam after μPlasma patterning. Water droplets form on the hydrophobic area of the glass slides, while on the plasma printed reactor design the water droplets fully wet leaving a clear surface, thus showing the printed design. On the design of Figure 3b, the hydrophobic obstructions are clearly visible. This shows that narrow tracks with high difference in wettability are obtainable through μPlasma patterning.

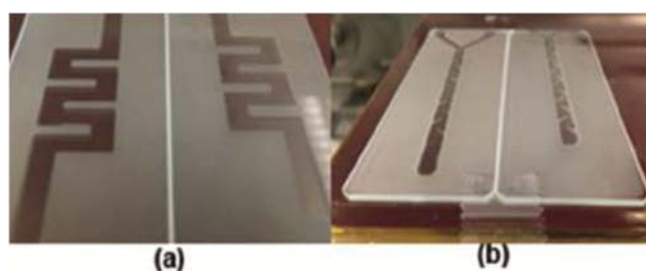


Fig. 3. Top and bottom of the two designs from Figure 2. For clarity the hydrophilic tracks are visualized with steam.

After μPlasma patterning the glass slides with the two designs were placed on top of each other, 0.1 mm thick scotch tape was used as spacer between the slides to create a gap. Droplets of coloured water, for better visual contrast, were placed at the entrance of the designs. Under capillary pressure, the water is transported through the hydrophilic channel. The large difference in surface energy between the DTS-layer and the μPlasma treated channel prevents the water to exit the channel. In Figure 4, the coloured water flowing through the printed channels can be seen. In Figure 4b, Water with two differently coloured dyes was used to show the mixing along the length of the design from Figure 2b. Due to the hydrophobic obstructions on the top and bottom of the capillary, the flow of the water is slightly restricted and mixing along the length is enhanced.

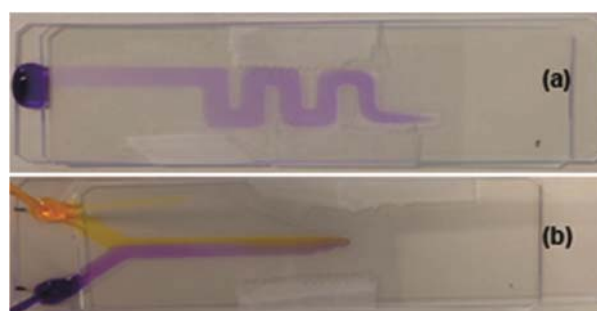


Fig. 4. Droplets of coloured water entering the two closed designs from Figure 2 (a) line structure, (b) mixer with dual inlet and hydrophobic obstructions.

To investigate the quality of the capillary, the filling of the line design from Figure 4 was used to analyse the velocity of the water within the capillary and compared to the Lucas -Washburn equation [2]:

$$x^2 = \frac{\gamma \cdot D_H}{4 \cdot \eta} \cdot t$$

In the equation, x is the distance the water has entered the capillary (m), γ the surface tension of water (72.8 mN/m), η the viscosity of water (1 mPa·s) and t the time (s). For the hydraulic diameter D_H , the dimensions of $3 \times 0.10 \text{ mm}^2$ for the capillary are used, making $D_H=0.192 \text{ mm}$ and the constant $\frac{\gamma \cdot D_H}{4 \cdot \eta} = 35 \text{ cm}^2/\text{s}$. Figure 4 shows the result of the video analysis (filmed at 25 fps). Each measurement represents a single frame. After 2.2 seconds the capillary is completely filled. Fitting the experimental results according to the equation results in a constant of $a=38 \text{ cm}^2/\text{s}$ and an adjusted R-square of 0.9975. From the Lucas-Washburn equation, the constant was calculated at $a=35 \text{ cm}^2/\text{s}$. As the μ Plasma patterning setup in reality produces wider tracks than defined by the bitmap, the hydraulic diameter in the Lucas-Washburn equation is underestimated. Taking this into account, the experiments show good agreement with the previous equation.

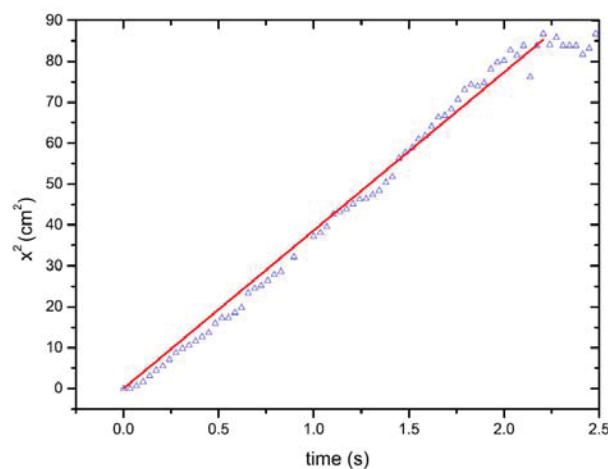


Fig. 5. Squared penetrated distance of liquid versus time for the meandering line. (Δ) experimental data, linear fit equals: $x^2=38 \cdot t \text{ cm}^2$ with $R^2=0.9975$.

Conclusions

Overall, this shows that μ Plasma patterning can be used to create hydrophilic tracks in between two hydrophobic surfaces. To work as capillary, the plasma printed tracks do not have to be closed on all sides, as the steep gradient in wetting between the printed track and surrounding area prevents leakage out of the printed tracks.

References

- [1] T. Huiskamp et al. "Maskless Patterning by Pulsed-Power Plasma Printing." IEEE Transactions on Plasma Science 40 (2012): 1913-1925.
- [2] Washburn, E.W., The Dynamics of Capillary Flow. Physical Review, 1921. 17(3): p. 273-283.

MANIPULATION OF POWDERY MATERIALS BY A SEQUENTIALLY PULSED COPLANAR BARRIER DISCHARGE

Jozef Ráhel', Miroslav Zemánek, Martina Ilčíková, Radek Zischka,
Jaromír Hašana

Masaryk University, Department of Physical Electronics, Kotlářská 2, 611 37 Brno, Czech Republic
E-mail: rahel@mail.muni.cz

Practical implementation of dielectric barrier discharge (DBD) plasma activation of fine powders requires a proper management of their transport through the active discharge zone. We present results of a new method for the powder transport, which takes benefit from the natural tendency of powders to concentrate outside the DBD's microfilament plasma channel. We have extended the number of DBD high voltage electrodes to 3 and 4 and started to sequentially energize only a chosen electrode pair. Locally fired plasma caused powders to pile up outside the formed discharge zone. Switching to another electrode pair shifted the place where powders pile up to a neighbouring area. At optimized conditions, the repetitive shift of piling area was sufficient to initiate the directional drift of treated powders.

1. Introduction

Our recent work on the activation of fine ceramic powders by atmospheric pressure DBD (dielectric barrier discharge) revealed a significant potential for its further deployments in the field of advanced ceramic engineering. The need of dispersant additives for preparing stable water-based ceramic suspensions can be reduced or even completely removed [1]. Slip casted Al_2O_3 samples from DBD activated powders exhibited finer pore size distribution and higher sinterability. Final microstructure of sintered samples had the grain size reduced by a factor of 1.7 [2]. DBD activated powders had a beneficial effect on the performance of electrophoretic deposition (EPD) of ceramic layers. It altered the deposition rate, reversed the deposition polarity from cathodic to anodic, and reduced significantly the deposit surface roughness [3, 4]. Depending on the type of DBD working gas, the dielectric impedance characteristics of nanoparticle-based nanofluids could be affected and tuned [5].

All these promising findings gave rise to new set of practical problems associated with the controlled transport of treated powders through the active plasma zone. We have learnt that effective plasma treatment of sub-micron sized Al_2O_3 or ZrO_2 powders requires rather long (~30-60 sec) dwell time of powders within the active plasma zone. This complicates considerably the use of strong air flow to carry the treated powders through the zone. To make the things even more complicated, during the plasma treatment, powder particles are electrically charged and attracted to the discharge electrode. The particles become stucked to the surface of electrode. The formed powder layer has a detrimental effect on the density and onset voltage of DBD plasma microchannels. Powder layer represents the path of higher electrical resistivity for DBD microfilaments. These begin to form outside the area occupied by the piles of adhered powder, and the necessary contact of plasma with to-be-treated powder is lost.

A distinctive phenomenon associated with the use of coplanar geometry of DBD is that powder piles are formed preferentially in the area above the inter-electrode space. The effect is illustrated in Fig. 1. We suppose that the 'piling effect' can be explained by the interplay of: (1) specific arching shape of coplanar DBD plasma microchannels; (2) creation of stationary vertex by plasma microchannels induced ionic wind from opposite directions; (3) ponderomotive force attracting the charged particles to the highest gradient of electric field situated above the electrode edges; and (4) piezoelectric vibrations of HV powered DBD electrode dielectrics. The relative importance of the listed factors has not been studied in detail yet. But we expect that their relative importance corresponds well to the respective number of the listing above.

Despite the lack of deeper understanding of the principal mechanism behind, the piling effect seems to be a general phenomenon. It was observed on all types of tested inorganic and organic powder materials e.g. Al_2O_3 , TiO_2 , ZrO_2 , SiO_2 , $\text{Na}_2\text{O}_{13}\text{Ti}_6$ or paint pigments. Based on this, we have decided to use the observed phenomenon to our benefit and use it to induce a lateral drift of piled powders along the surface

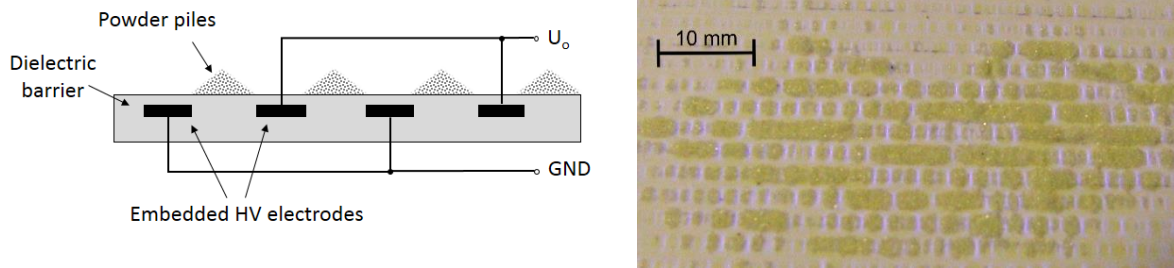


Fig. 1. Schematic cross-section and actual view (Al_2O_3 powder) documenting the piling effect on the surface of coplanar DBD.

of dielectric electrode. For this sake, we have extended the number of HV power electrodes and started to sequentially energize only a given electrode pair. By doing so, plasma was incited only at a specific place of discharge area, causing powders to pile up at the corresponding location. By switching to another electrode pair, the place of powder piling should be moved. At optimized conditions, the repetitive shift of piling area should be sufficient to introduce a native unidirectional drift of treated powder material.

2. Experimental

Two distinct designs of coplanar multiple electrodes were tested. The first one (Fig. 2a) consisted of three isolated electrodes arranged in the pattern of 1-2-3-1-2-3- etc. We termed this design as ‘3-phase electrode’. The second system (Fig. 2b,c) had an additional grounded electrode (0 or GND) inserted between each pair of the HV powered electrodes. This design allowed construction of faster and more reliable HV power supply. The electrode pattern can be depicted as 1-0-2-0-3-0-1-0- etc. We termed this design as ‘4-phase electrode’.

Discharge plasma between the neighbouring electrode pair is incited when (and only when) one of the electrode is connected to HV side of power supply, and the neighbouring one is grounded. Hence, in order to incite a traveling plasma wave in the 3-phase electrode of Fig. 2a, we had to sequentially ground one of the electrodes U_1 , U_2 , U_3 , while keeping the remaining electrodes at HV (or vice versa).

Resulting sequence of areas covered by the discharge plasma (pink colour) is schematically shown in Fig. 2a. The 4-phase electrode system allows two distinct powering regimes (patterns). Fig. 2b depicts sequential grounding of only one from the trio of HV electrodes. Fig. 2c shows the situation when two of HV electrodes tripled are grounded simultaneously.

The sequential grounding of 3-phase electrode design was realized by a rotating switch shown in Fig. 3. Its main benefit lays in relatively simple and affordable construction. Its main drawback is relatively low modulation frequency. The switch’s stator had three mechanical contacts with the same polar distance from the rotation axis. These were connected to the discharge electrodes U_1 , U_2 , U_3 . Along the rotor circumference two electrically non-interconnected metallic pads were mounted. The first pad was connected to the HV output of power supply (Lifotech, 20 kHz, 15 kV_{rms}), the second was grounded. Actual position and size of metallic pads was chosen so that the rotation would cause periodical grounding of respective stator contact, while interconnecting (shortcutting) the remaining two.

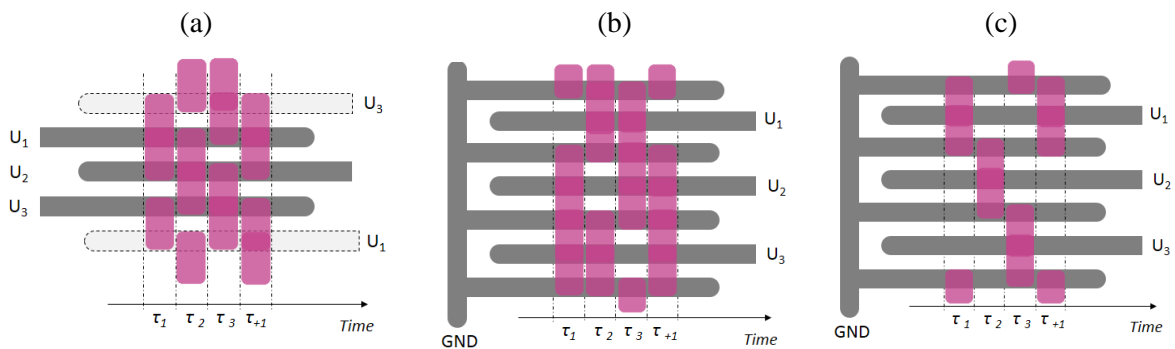


Fig. 2. Schematic of tested electrode designs and electrode energizing pattern. The pink colour denotes the space occupied by discharge plasma at respective time of τ_i .

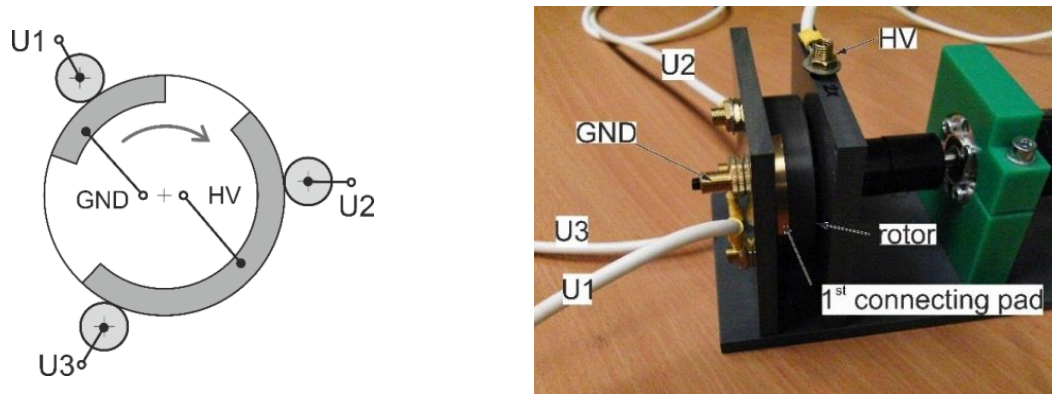


Fig. 3. Schematic wiring and actual view of the rotating switch

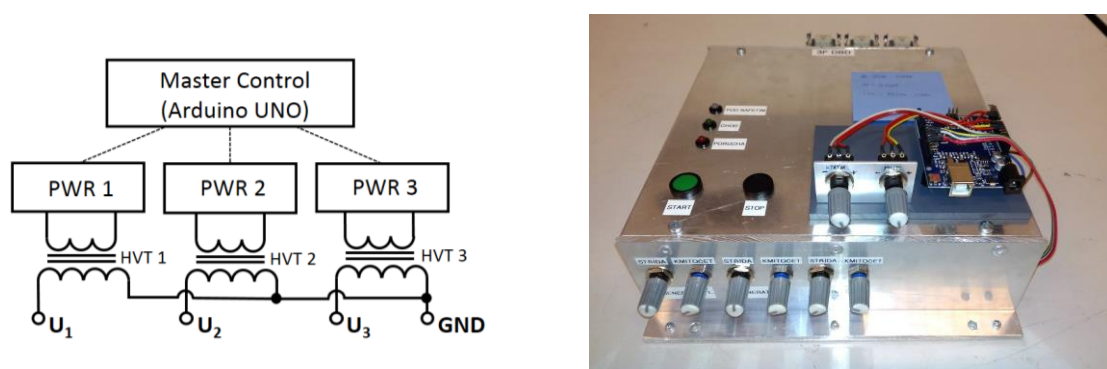


Fig. 4. Block diagram and actual view of our in house built power supply (three HV transformers not shown here).

An uncontrolled disconnection of rotating switch (i.e. while the electrical current still flows through closed switch) would cause an arc breakdown and the HV power supply malfunction. Therefore, the amplitude of HV voltage had to be always reduced before the rotating switch turned off. For this sake, angular position of stator was monitored by the photodiode sensor, connected to the driving circuit of power supply. Reduction of applied voltage was achieved by switching off the driving frequency. Electrical measurements confirmed that the resulting damped oscillation in the discharge system was sufficiently fast to provide the required reduction of HV amplitude.

To achieve higher modulation frequency the rotating switch has to be replaced e.g. by faster HV transistors switches (three of them). This option turned out to be price prohibitive. However the 4-phase electrode design with inserted grounded electrode allowed us to construct a fully electronically driven sequenced HV power supply, without any HV transistor switches (although three instead of single HV transformers had to be used now - Fig. 4). The presence of GND electrode provided a necessary return path for discharge current (outside the HV transformer secondary winding), so it did not cause any backward induction in the power supply driving electronics.

3. Results

Figure 5 displays the discharge appearance for all Fig. 2 setups respectively. The topology of spiral electrodes was used to prevent powering electrodes to cross-over each other. As can be seen the 3-phase electrode offered the best coverage of surface by discharge plasma. Using the 4-phase electrode energized according by Fig. 2c pattern resulted in least surface coverage by discharge plasma. Operation of 4-phase electrode energized by Fig. 2b pattern showed two distinct intensities of generated plasma; borderline plasma was more intense than the plasma in the centre.

The presence of transport effect was tested using coloured glass microbeads (*ballotini*) of 100-200 μm average diameter. The 3-phase electrode design provided an excellent lateral transport of uniformly dispersed glass beads. Right after the start a narrow microbeads pile was formed at the outer edge plasma formed region. Afterwards, upon switching to further electrode pair the pile changed rapidly its position to the new freshly formed region. It was found experimentally, that two conditions had to be met in order to observe strong particles drift. First, the density of dispersed particles has to be less than some

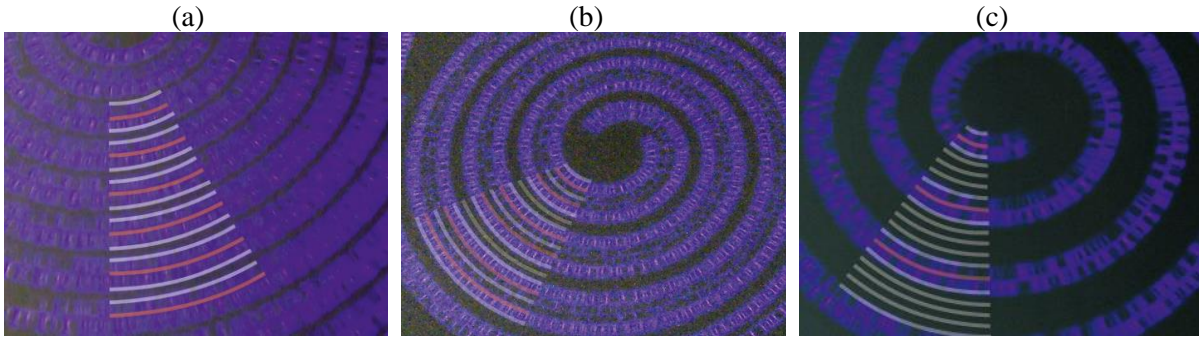


Fig. 5. Actual appearance of multi electrode systems corresponding to Fig 2 respectively. The grey auxiliary lines denote the position of grounded electrodes (at given time instant). Pink lines indicate the position of powered electrodes.

critical value. If not, too massive pile is formed, which would prevent further discharge formation. The transport effect was ceased. Second, the frequency of rotation switch has to be adjusted to some resonance one. Experiments with different particles sizes revealed, that the light particles (such as fine ceramic powders) require higher driving frequency. This is due to their higher acceleration obtained by the given plasma impulse. To transport fine powders faster switching unit was therefore needed. This led to the construction of 4-phase electrode and its HV power unit.

Performed experiments showed that the energizing pattern of Fig. 2c is better suited for unidirectional transport of glass microbeads (Fig. 6). The configuration of Fig. 2b failed to render the unidirectional drift of glass medium. Instead the power piles oscillated around the stable central position. Our analysis led to the conclusion, that it is due to different intensity of plasma generated above the border and the central electrodes sustain the plasma (Fig. 5b). Still, the oscillating behaviour of the powders can be beneficial by introducing a native mixing of plasma treated particles. The construction of our devised power supply allows an instantaneous mutual transition between both energizing regimes. It should be noted however, that lower area of plasma generated by the 4-phase electrode system in Fig. 2c powering pattern causes less intensive mass transport when compared to the 3-phase electrode. The 4-phase system required almost two-times more time to fully clear the electrode surface covered by uniformly dispersed glass beads than the 3-phase system.

4. Conclusion

Sequentially pulsed coplanar DBD is able to provide a considerable unidirectional drift to plasma treated powders. Two important constrains were identified: (1) only a thin powder layer can be manipulated; (2) driving frequency has to be matched to the mass of transported powders. The 3-phase electrode system exhibited the strongest transport properties for the tested material. However, its up-scaling to higher speeds is a challenging HV engineering task. Alternative 4-phase system simplifies the design requirements on multiphase HV power supply, while offering still a reasonably strong powder transport. In the tested electrode system sequential powering of only one at the time from the three energizing electrodes resulted in intended unidirectional drift. Sequential powering of two energizing electrodes at once renders oscillation movement of powder medium.

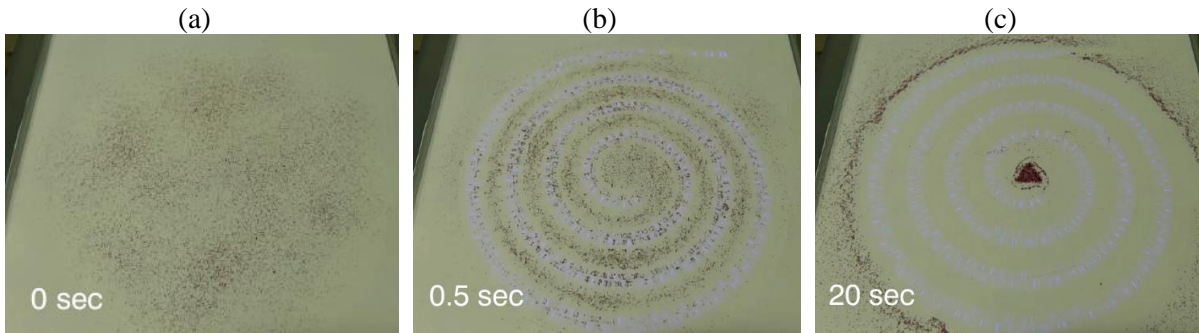


Fig. 6. Demonstration of lateral transport of 200 µm glass beads. The 4-phase electrode with Fig 2c energizing pattern.

5. Acknowledgement

This work was funded by the Czech Science Foundation project No. 17-05620S and by the Technology Agency of Czech Republic, project no. TACR TE02000011. The work was supported by project LO1411 (NPU I) funded by the Ministry of Education, Youth and Sports of Czech Republic.

6. References

- [1] Szalay Zs, Bodišová K, Pálková H *et al.* 2014 *Ceramics International*, **40** (8B) 12737.
- [2] Pouchlý V, Ráhel' J, Spusta T *et al.* accepted in *J. Eur. Ceram. Soc.* doi: 10.1016/j.jeurceramsoc.2018.11.022
- [3] Drdlik D, Moravek T, Ráhel J *et al.* 2018 *Ceramics International*, **44** (8) 9787.
- [4] Ilčíková M, Ráhel' J 2019, Proc of XXII SAPP (this symposium) Štrbské Pleso, Slovakia.
- [5] Ambrico M, Morávek T, Ambrico PF, Ráhel J. 2018 *Powder Technology* **340**, 570.

GASEOUS AND AQUEOUS REACTIVE OXYGEN AND NITROGEN SPECIES OF AIR PLASMAS WITH WATER

Zdenko Machala, Barbora Tarabová, Dominika Sersenová, Mário Janda,
Karol Hensel

Faculty of Mathematics, Physics and Informatics, Comenius University, Bratislava, Slovakia
E-mail: machala@fmph.uniba.sk

The need of control and tunability of the chemical composition and biomedical effects of plasma activated water/media (PAW/PAM) is emerging for applications in biomedicine and agriculture. We compare two non-thermal air plasma sources: streamer corona and transient spark, interacting with water in open and closed reactors and enhance the plasma-liquid interaction by water electro-spray through these discharges. We demonstrate that the plasma gaseous products strongly depend on the discharge regime, its deposited power and gas flow conditions. The gaseous products then determine the chemical properties of the PAW and the dominant aqueous reactive oxygen and nitrogen species (RONS). Transient spark produces higher concentrations of gaseous and aqueous RONS and induces stronger antibacterial effects than streamer corona.

1. Introduction

Non-thermal plasmas generated by electrical discharges in atmospheric pressure air are sources of various reactive species. When generated in contact with water, they enable the transfer of reactive oxygen and nitrogen species (RONS) formed in the gas-phase plasma into the water or aqueous solutions and so generate the *plasma activated water* (PAW). PAW is typically a strong antibacterial agent and besides multiple uses in medicine for disinfection it has the potential for food processing or agriculture applications. [1-6]

We prepare PAW by a DC-driven streamer corona (SC) and transient spark (TS) discharges operated in air with water electro-spray. The production of active species (e.g. O_3 , NO, NO_2 and OH) in the gas and consequently the PAW properties can be controlled by the discharge regime and gas-flow and liquid-flow parameters. In low power air corona discharge, water electro-spray increased O_3 production, which enhanced the biocidal effects. In the higher power TS, dominant gaseous products are NO_x that lead to significant NO_2^- and NO_3^- in the PAW and practically no O_3 . The bactericidal action is then mainly due to the synergy of H_2O_2 , NO_2^- and acidic milieu (via ONOOH formation) and typically decays in time within several hours post plasma activation, depending on temperature and pH [4,7]. The controlled and selective generation of RONS using air plasmas with water will facilitate targeted applications of cold plasmas and PAW to various fields including disinfection and antimicrobial applications, food processing, agriculture, and even cancer therapies, where the roles of different key reactive species on cancer cell biochemistry is particularly delicate [6,8].

2. Experiment

DC-driven streamer corona and transient spark discharges in positive polarity were generated in point-to-plane configuration in ambient air at atmospheric pressure. Positive streamer corona and transient spark discharge regimes used here has been described in more details in [9-10]. Figure 1 shows a schematic of the set-up used for water electro-spray through SC or TS discharge.

We used a high voltage (HV) hollow needle anode opposite to the metallic (stainless steel) grounded mesh cathode. The inter-electrode spacing between the needle and the mesh was kept at 10 mm. A positive high voltage was applied from the power supply *Technix SR20-R-1200* through the ballast resistor R (20 M Ω for SC or 10 M Ω for TS). The discharge voltage was measured by the HV probe *Tektronix P6015A* and the discharge current was measured as a voltage drop across 50 or 1.2 Ω resistors for SC and TS, respectively. The electrical parameters were processed and recorded during the experiments by a 200 MHz oscilloscope *Tektronix TDS 2024C*. Typical current and voltage waveforms and other discharge characteristics of SC and TS discharge with water electro-spray or water cathode, were documented in detail in our previous publications [3,4,9,10]. Both TS and SC can be operated in the same versatile setup with the same HV power supply, which represents an advantage for practical applications. Both discharges were combined with water electro-spray that enabled the

water flow with various flow rates in the range 0.01-1 mL/min by the syringe pump *New Era Pump Systems NE-300* directly through the high-voltage needle electrode into the active discharge region, where it was sprayed to micrometric droplets. The interaction of plasma with water droplets allows for very efficient mass transfer of plasma-generated active species into water [3-4].

Besides operating in the open ambient air reactor, we operated the same plasma discharges in a closed reactor (50 mL volume) with a defined low air flow rate (0.5 L/min). This air flow rate determines the gas mixing and accumulation of species produced by the plasma.

Gaseous NO and NO₂ concentrations were measured online by electrochemical gas sensors *Membrapor NO2/S-1000* and *NO/SF-1000* (resolution 5 ppm, 0-1000 ppm). Fourier transform infrared (FTIR) absorption spectrophotometer *Shimadzu IRAffinity-1S* was used for the detection of gaseous nitrogen oxides NO, NO₂ and N₂O; nitric and nitrous acids HNO₃, HNO₂, and ozone O₃ with the resolution 1 cm⁻¹ inside a 10 cm long gas cell. Ozone concentrations were measured by UV absorption using 253.8 nm mercury lamp and the compact fiber optic spectrometer *OceanOptics SD2000*, employing the Lambert-Beer law with the absorption cross section $1.14 \times 10^{-21} \text{ m}^2$ [11] in a 12.5 cm gas cell.

The detection of aqueous RONS in the PAW is challenging due to the chemical instability of the detected RONS and possible cross-reactivities of the used analytical methods. We tested and adapted colorimetric methods for special PAW conditions, such as colorimetric detection of H₂O₂ by TiOSO₄ reagent, NO₂⁻ and NO₃⁻ by Griess reagents, and O₃ by indigo blue dye [12]. Here we focus on the detection of RONS formation induced by air plasma gas-liquid chemistry in PAW, namely to H₂O₂, NO₂⁻ and NO₃⁻, and dissolved O₃ produced in PAW by the two discharges.

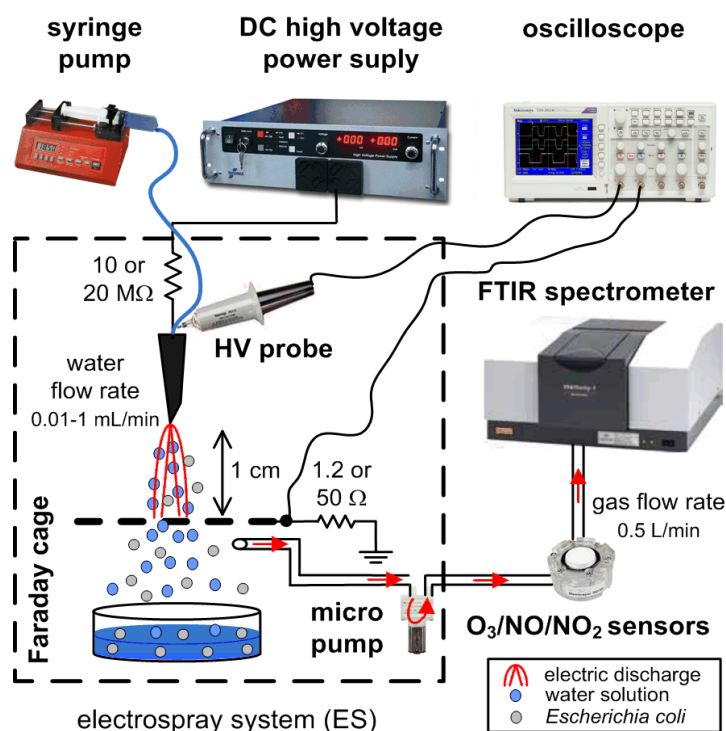


Fig. 1. Schematic of the set-up used for water activation by electro spray through streamer corona or transient spark discharges and gas diagnostics.

3. Results and discussion

Both discharges used in this study are driven by DC high voltage but are self-pulsing. Their typical characteristics are:

Streamer corona (SC): the mean power 0.2-0.4 W, the pulse repetition frequency ~10 kHz, operated with water electro spray (ES) flow rates 0.01-0.5 mL/min. The typical voltage and current pulse waveforms of SC-ES are depicted in Fig. 2a.

Transient spark (TS): the mean power 1.5-2.3 W, the typical pulse repetition frequency ~ 1 kHz, the typical pulse duration ~ 25 ns. TS was operated with water electro spray flow rates 0.5-1 mL/min. The typical voltage and current pulse waveforms of TS-ES are depicted in Fig. 2b.

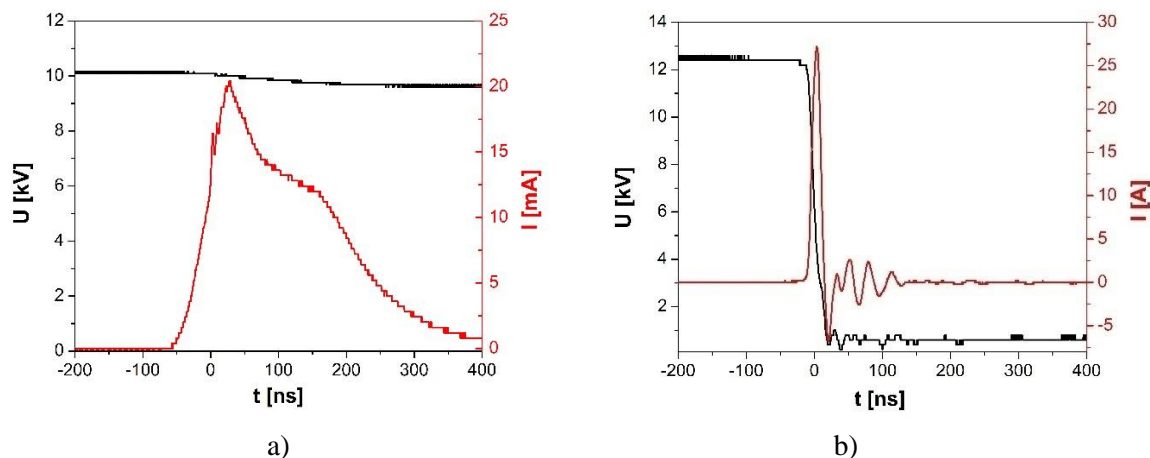


Fig. 2. The typical voltage and current pulse waveforms of SC (a) and TS (b) with water electro spray.

In air SC, both O_3 and NO_x are produced [13]. Similar to air surface DBDs, low power discharge leads dominantly to O_3 production, while higher power discharges increase the gas temperature which promotes NO_x production and the thermal depletion of O_3 combined with the chemical decay of O_3 by fast reaction with NO . In addition to O_3 and NO_x gaseous products, water vapors in air significantly influence the plasma induced gas-phase chemistry, especially thanks to highly reactive hydroxyl ($\cdot OH$) radicals. We detected lower concentrations of the gas phase NO , NO_2 and O_3 in humid air compared to the dry air. When the discharges are operated with water electro spray, there is a strong water evaporation and humidification of the air, which enhanced the $\cdot OH$ formation. Moreover, the transport of NO , NO_2 , O_3 , and other species such as HNO_2 into the bulk water, i.e. their solvation driven by the Henry's law equilibria, also decrease NO , NO_2 and O_3 concentrations in the gas phase.

The water electro spray improves the gas-liquid transport of the gaseous NO_x into the liquid resulting in NO_x dissolution in the water. NO formation in SC-ES was considerably lower compared to TS-ES due to the much lower power. NO_2 formation in general increased with the discharge power in all systems and SC generated considerably lower NO_2 due to the lower discharge power.

Comparison of the NO , NO_2 and gaseous O_3 concentrations produced by TS and SC, without and with ES, in open and closed systems together is shown in fig. 3. Apparently, the closed reactor resulted in considerably higher (~ 1 order of magnitude) concentrations of all measured species for both TS and SC. The closed reactor with a slow air flow rate enables accumulation of species, whereas immediate dilution of species with the surrounding ambient air occurs in the open reactor.

It is clear that SC in all systems generated lower NO and NO_2 (due to its lower power) but higher O_3 concentrations than TS. SC corresponds well to the low power ozone mode and TS to the high power NO_x mode of the surface air DBD described by [14]. O_3 was completely absent in our NO_x -dominated TS without water and in TS or TS-ES in the closed reactor.

SC in the closed reactor produced negligible NO concentrations, lower than in the open reactor. At the same time, there was considerably more O_3 produced by SC in the closed reactor. The reaction of NO oxidation by O_3 probably depleted most of the generated NO that was oxidized to NO_2 , while the excess O_3 remained in the gas. Detailed gas-phase air plasma chemistry is described in [9].

Both air discharges, SC and TS, with water electro spray treatment in both open and closed reactors were tested and by this way prepared the plasma activated water (PAW). We focused on the detection of long-lived aqueous RONS produced in PAW, namely H_2O_2 , NO_2^- and NO_3^- , and dissolved O_3 . Clearly, the aqueous RONS concentrations are related to the plasma formed gaseous RONS.

Aqueous $H_2O_2(aq)$ is produced by extremely fast dissolution of gaseous $H_2O_2(g)$ formed in the gas. The Henry's law solubility coefficient of H_2O_2 ($k_H \approx 9 \times 10^2 \text{ mol} \cdot \text{m}^{-3} \cdot \text{Pa}^{-1}$) is about 7 orders of magnitude larger than that of NO or NO_2 or O_3 [46], thus all $H_2O_2(g)$ readily transfers into $H_2O_2(aq)$ through the gas-liquid interface. Nitrites NO_2^- and nitrates NO_3^- are generated in the PAW from the dissolved gas-

eous NO and NO₂ [10,24,62]. The solubility coefficients of NO or NO₂ are much smaller than that of H₂O₂ [15], thus NO(g) and NO₂(g) would not readily transfer into water to form NO₂⁻(aq) and NO₃⁻(aq). Enhancement of NO_x dissolution by increasing the surface area of the plasma-liquid interface by spraying water into fine droplets in the ES system is helpful. Since protons H⁺ are released in the PAW by the above reactions, acidic pH is typical for PAW prepared by air plasmas.

The reaction between H₂O₂ and NO₂⁻ occurs under acidic PAW conditions and leads to the formation of peroxyxynitrites (peroxyxynitrous acid) [4,7,12]:



ONOOH then decomposes at acidic pH to [•]OH and [•]NO₂ radicals [7,12]:



Fig. 4 shows the measured concentrations of H₂O₂, NO₂⁻, NO₃⁻ in PAW and corresponding pH for TS and SC with water ES in the open and closed reactor. The low power SC generates less H₂O₂ and much less NO₂⁻ + NO₃⁻. The higher power TS generates both H₂O₂ and NO₂⁻ + NO₃⁻, with the ratio of H₂O₂/NO₂⁻ approximately 2 in the open system. On the other hand, after TS water activation in the closed system, much less H₂O₂ and much more NO₂⁻ and particularly high NO₃⁻ were detected, which resulted in very acidic pH (2.4). In such case, the antibacterial effects might have been enhanced. NO₂⁻ was higher in TS than SC, and mostly increased with energy density per water volume. Closed TS resulted in very high NO₂⁻ and NO₃⁻. SC in the closed reactor also generated high NO₃⁻ (yet lower than TS-ES closed) at pH 3.1, while very low NO₂⁻. This might be possibly due to the NO₂⁻ depletion with ozone.

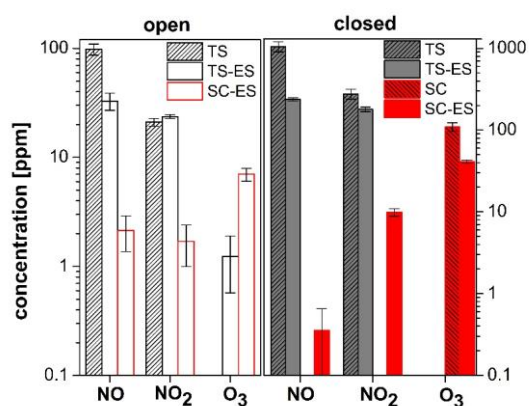


Fig. 3. Gaseous NO, NO₂ and O₃ concentrations generated by TS and SC discharges, without and with water ES, in the open and closed (50 mL, 0.5 L/min air flow) reactors. Logarithmic scale. Statistical mean values with standard error of the mean.

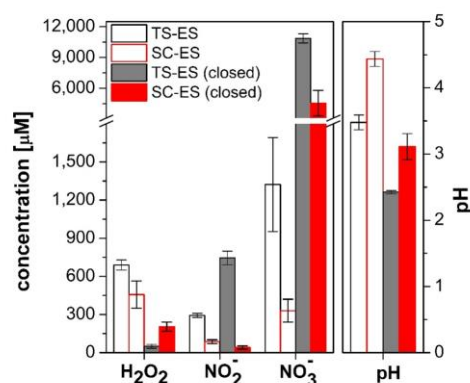


Fig. 4. Concentrations of aqueous H₂O₂, NO₂⁻, NO₃⁻ in PAW and corresponding pH for TS and SC with water ES, in the open and closed reactor. Statistical mean values with standard error of the mean.

H₂O₂ is dominantly formed from [•]OH radicals in the gas and solvates extremely. We should note that in the ES, there is a good gas-liquid mixing that might enhance the aqueous peroxyxynitrite chemistry (Equations 1 and 2), which would then faster deplete the produced H₂O₂(aq). The measured H₂O₂(aq) concentrations after treatment may be then lower with respect to the H₂O₂(aq) really produced during the plasma-water interaction. NO₃⁻ were higher for TS than SC, which can be certainly related with considerably higher gaseous NO and NO₂ production in the TS (Fig. 5).

O₃(aq) concentrations in PAW increased as a function of energy density in the open reactor with SC-ES. Dissolved ozone concentrations O₃(aq) in PAW were detected with at least some degree of reliability in SC. There was almost negligible gaseous O₃ detected in TS, and consequently undetectable O₃ dissolved in PAW either.

4. Conclusions

The potential use of plasma activated water and liquids is constantly growing in various biomedical and agriculture applications. The PAW chemical properties and effects strongly depend on the plasma sources and discharge regimes used and their interaction with water. We compared two non-thermal atmospheric plasma sources operating in air and interacting with water: a lower power streamer corona (SC, 0.4 W) and a higher power transient spark (TS, 2 W). We analyzed their gaseous and aqueous RONS in the air and the PAW. Water was activated in the electrospray system (ES) with fine aerosol droplets sprayed through the plasma zone. We also compared the open air and closed small volume reactor at different air flow rates to understand the effects of reactor volume and air flow rate on the gaseous and aqueous chemistry.

Both SC and TS represent inexpensive and easy to operate nonequilibrium air plasma sources that can be run in the same versatile setup. Switching between them can be easily managed by changing the resistor in the circuit. Each of these discharge regimes generates air plasma of different properties that results in different gaseous products: dominated by O₃ in lower power SC and NO_x in higher power TS. The gaseous products, their production rates and solvation determine the aqueous RONS in the activated water, which then control the antibacterial effects of such PAW. Gas flow conditions in the reactor strongly influence gaseous and aqueous RONS production. We applied water electrospray through the discharges as the efficient method of the transfer of the plasma gaseous species into the PAW. Other ways of water interaction with air plasmas can lead to different transfer mechanisms of some species (especially those with low solubility), which may influence the aqueous chemistry and antibacterial effects and will be a subject of our future study.

Acknowledgement: This work was supported by Slovak Research and Development Agency APVV-0134-12, APVV-17-0382, and Slovak Grant Agency VEGA 1/0419/18.

5. References

- [1] Bruggeman P J, Kushner M J, Locke B R, et al. 2016 Plasma-liquid interactions: a review and roadmap *Plasma Sources Sci. Technol.* **25** 053002
- [2] Lu X, Naidis G V., Laroussi M, Reuter S, Graves D B and Ostrikov K 2016 *Phys. Rep.* **630** 1–84
- [3] Machala Z, Chládeková L and Pelach M 2010 *J Phys D Appl Phys* **43** 222001
- [4] Machala Z, Tarabová B, Hensel K, Spletlikova E, Sikurova L and Lukeš P 2013 *Plasma Process. Polym.* **10** 649–659
- [5] Pawlat J 2013 *Eur. Phys. J. Appl. Phys.* **61** 24323
- [6] Lu P, Boehm D, Bourke P and Cullen P J 2017 *Plasma Process. Polym.* **14** e1600207
- [7] Lukeš P, Dolezalova E, Sisrova I and Clupek M 2014 *Plasma Sources Sci. Technol.* **23** 015019
- [8] Bauer G and Graves D B 2016 *Plasma Process. Polym.* **13** 1157–1178
- [9] Machala Z, Tarabová B, Sersenová D, Janda M, Hensel K 2018, *J Phys D: Appl Phys* **52** 034002
- [10] Kovalova Z, Leroy M, Kirkpatrick M J, Odic E and Machala Z 2016 *Bioelectrochemistry* **112** 91–99
- [11] Smith M A H, Devi V M, Benner D C and Rinsland C P 2001 *J. Geophys. Res.* **106** 9909–9921
- [12] Tarabová B, Lukeš P, Janda M, Hensel K, Šikurová L and Machala Z 2018 *Plasma Process. Polym.* **15** e1800030
- [13] Janda M, Martišovitéš V, Hensel K and Machala Z 2016 *Plasma Chem. Plasma Process.* **36** 767–781
- [14] Pavlovich M J, Clark D S and Graves D B 2014 *Plasma Sources Sci. Technol.* **23** 065036
- [15] Sander R 2015 Compilation of Henry's law constants (version 4.0) for water as solvent *Atmos. Chem. Phys.* **15** 4399–4981

Poster Presentations

DC VACUUM BREAKDOWN AT MICRO-METER SEPARATIONS

Arian Fateh Borkhari¹, Matej Klas¹, Štefan Matejčík¹

¹ *Department of Experimental Physics, Comenius University
Mlynska dolina F2, 842 48 Bratislava, Slovakia*

We have carried out an experimental study to determine the DC vacuum breakdown at micro meter separation of stainless steel electrodes. The voltage-current characteristics have been measured between sphere to plane electrodes configuration and with electrode separation from 2.5 to 20 μ m. In addition, the changes of the effective area were investigated based on various distance gap. We have applied Fowler-Nordheim theory (F-N) of field emission to determine the enhancement factor β .

1. Introduction

Micro-discharge plasmas have been widely applied in many different industries, such as materials processing, medical technology, gas and water treatment and so forth in various range of pressure value [1]. At micro-meter separation and low pressure, the comparison of discharge breakdown voltage with vacuum breakdown is important. The vacuum breakdown does not depend on the gas pressure as the dominant effect is the field emission of the electrons from the electrodes under action of high electric fields. For the field emission high electric fields (above 10⁷ V/M) are necessary for this reason high vacuum is a good insulator [2,3].

In the case of vacuum breakdown, the shape of the electrodes and the finishing of the electrode surfaces play an important role. In general, the quality of the surfaces (removal of scratches, points and craters, polishing) appears to be an essential [4] and the current threshold value could depend on such specific details as the shape, size and material of the electrode. Besides mechanical polishing, chemical techniques of cleaning and polishing of electrodes are of great importance, because contaminations of surfaces and the oxide layers may influence the field emission [5].

If the electric fields are strong enough, the electrons from metal can tunnel through the work function barrier into vacuum [6,7]. The field emission is described by Fowler-Noerdheim equation [8]:

$$I_{FE} = J_0 S \frac{(\beta E)^2}{E_0} \exp\left(-\frac{E_0}{\beta E}\right) \quad (1)$$

$$E_0 = 6.83 \times 10^9 \phi^{3/2} \text{ V/m}, \quad J_0 = 1.54 \times 10^{-6} \frac{E_0^2}{\phi} \text{ A/m}^2 \quad (2)$$

where J_0 and E_0 are constants that depend on the material of the electrode. The work function ϕ is an important characteristic of the material for field emission and for stainless steel has value of 4.4 eV [9].

We have used scanning electron microscopy (SEM) to visualize and characterise the electrode surface. The SEM has an extreme depth of field to measure the surface structure and elemental composition of the surface. Scanning electron microscopy of the electrode can detect field emission sites that are subjected to the highest electric fields (sharp points with) [10]. The enhancement factor changes with electrode separation and ratio of the local electric field to applied electric field E [11,12].

2. Experimental Setup & Results

The electrodes are located in the vacuum chamber pumped by turbo-molecular pump (approximately 2×10^{-6} mbar). In Figure 1, we present a simplified schematic view of the electrode system and a schematic view of the electric circuit for the breakdown measurement. The circuit consisted of high voltage power supply (DC voltage up to 10kV), resistors to limit the DC current ($3.1\text{M}\Omega$), high voltage probe and a circuit for current measurement. We have applied back-to-back diodes allows positive and negative current to flow and be measured. In this study we have used electrodes (anode and cathode) of different shapes (plane to sphere 5mm diameter). The electrodes can be spatially adjusted in three directions and the electrode separation can be controlled to about $1\mu\text{m}$.

The surfaces of the electrodes were prepared by polishing by diamond polishing compound (lapping paste) with 3.5, 2.5, 1 and 0.25-micron grades. The final cleaning of electrodes was done by deionized water in ultrasonic bath.

The effective area of the cathode S , was calculated taking into account its spherical shape. The effective area S for field emission depends on the electrode gap distance d and voltage. The D parameter is assumed to be 0.1 (10 percent) of the d value (for instance; if $d=5\mu\text{m}$ so $D=0.5\mu\text{m}$). Thus, the effective cathode area S was increasing with the increasing electrode distance from 3.9×10^{-9} to $3.14 \times 10^{-8} \text{ m}^2$ (respectively for 2.5 to $20\mu\text{m}$).

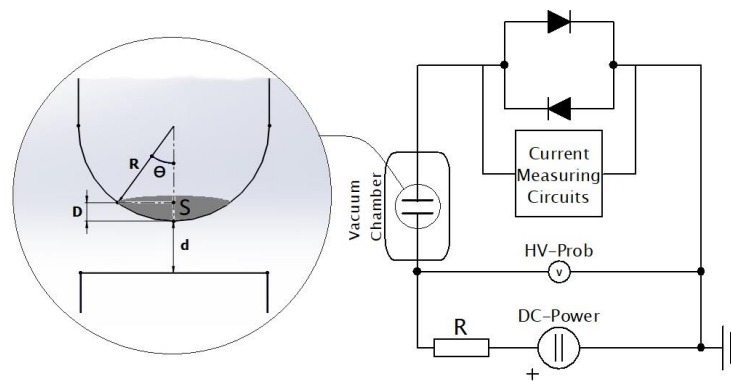


Fig. 1. The schematic of the electric circuit is illustrated containing the exaggerated effective area S , gap distance d , the departure distance D

The electron current measurements have been done in the range between 40nA to 300nA just as a criterion of dark currents. In the vacuum, we define vacuum breakdown potential, if the emission current exceeds a critical value of the current (dark current of 40nA). The experimental breakdown voltage as a function of electrode separation and its standard deviation is presented in Fig. 2. We have set 40nA current as a breakdown limit. In addition, the experimental voltages are compared with theoretical F-N values calculated for different enhancement factors β .

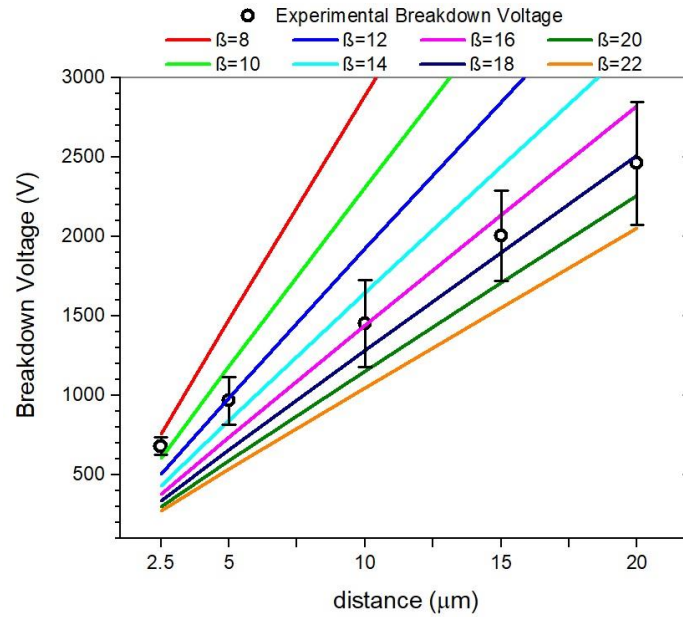


Fig. 2. The experimental vacuum breakdown voltage curve (open circles) and their standard deviation measured for dark current value 40nA and electrode gaps from 2.5 to 20 μ m. F-N breakdown voltages for different values of β .

The vacuum breakdown electric field as function of electrode separation measured for 40nA breakdown current is displayed in Fig. 3. The breakdown electric field was decreasing with expanding electrodes gap. The breakdown electric field values span from 300 to 100 MV/m for 2.5 to 20 μ m electrode separations. Standard deviation was calculated from the standard deviation of the measured quantities. The measured electric current was generated by field emission, i.e., the free generated by tunnelling through the work function barrier of the electrodes, which was lowered by high electric field. The field emission can be effected by the surface defects such as melted spots, oxide layer and craters on the surface. These defects are created on the surface during experiments. The presence of these defects is illustrated by the deviation in the values of breakdown electric fields in figure 3.

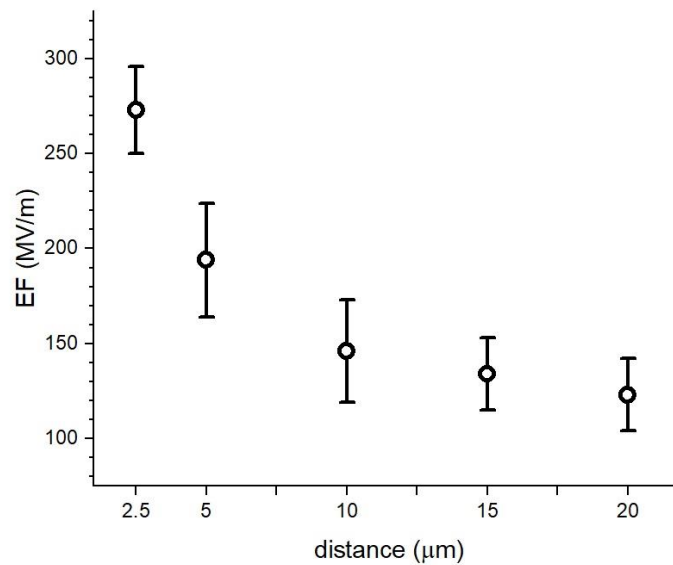


Fig. 3. The experimental values of the vacuum breakdown electric fields for 40nA dark current value based an electrode separation from 2.5 to 20 μ m.

The Figure 4 shows the experimental volt current characteristic of the vacuum field emission measured for electrode separation of 5 μ m. The experimental curve is compared with theoretical

Fowler-Nordheim plots for different values of the enhancement factor. The enhancement factor β was continuously varied with the increasing emission field and of course the current.

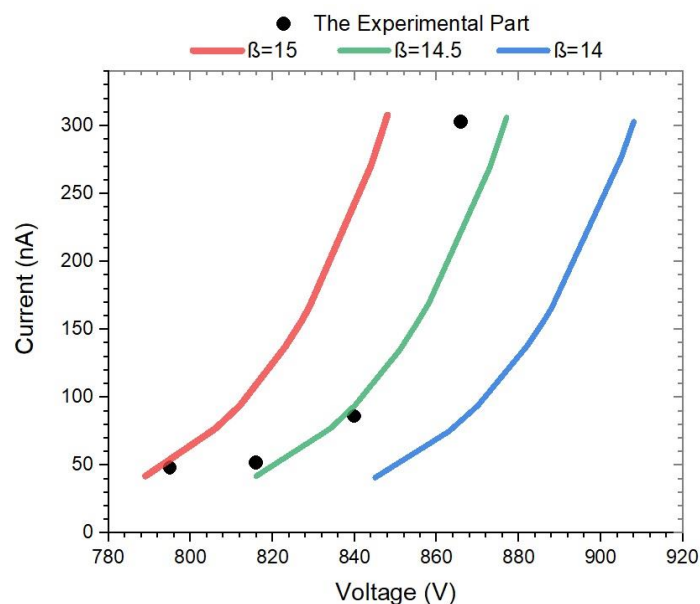


Fig. 4. The experimental voltage-current characteristics at $d=5 \mu\text{m}$ gap and calculated from F-N Equation V-A characteristics for different enhancement factor β values.

3. Conclusion

In this study we present experimental study of DC vacuum electric breakdown including the volt-ampere characteristics and F-N plots for electrode gaps ranging from 2.5 to 20 μm . The breakdown voltages were measured for 40nA dark current. The Fowler-Nordheim parameters such as field enhancement factor, emitter area and the DC breakdown electric field were determined for given electrodes. The high quality electrode surface polishing and its purity effects substantially the electric breakdown in vacuum, for this reason the preparation of the electrodes is an important condition for the accuracy of measurement.

Acknowledgements:

This project has received funding from the European Union's Horizon 2020 research and innovation programme under grant agreement No. 692335. This work has been supported by Development Agency Projects Nr. APVV-15-580, VEGA 1/0733/17 and SK-SRB-2016-0035.

4. References

- [1] L Lin and Qi Wang. 2015. *Plasma Chemistry and Plasma Processing. Volume 35, Issue 6, pp 925–962.*
- [2] D. Alpert, D. A. Lee, E. M. Lyman, and H. E. Tomaschke. 1964. *Journal of Vacuum Science and Technology.1:35 50.*
- [3] R. A. Millikan and R. A. Sawyer. 1918. *Physical Review. 12:167 170.*
- [4] Robert Sherman, John Grob, and Walter Whitlock. 1991. *Journal of Vacuum Science and Technology B. 9(4):1970-1977.*
- [5] Robert Sherman, Drew Hirt, and Ronald Vane. 1994. *Journal of Vacuum Science and Technology A, 12(4):1876-1881.*
- [6] R. J. Noer. 1982. *Applied Physics A. 28:1 24.*
- [7] I. Brodie and I. Weissman. 1964. *Vacuum. 14(8):299 301.*
- [8] R. H. Fowler and L. Nordheim. 1928. *Proceedings of the Royal Society (London). 119:173 181.*
- [9] D. Baikie, U. Peterman and B. Lagel. 2001. *Journal of Vacuum Science & Technology A. 19.4.*
- [10] Gerrard Eddy Jai Poinern. 2015. *CRC Press. Taylor & Francis Group 3.4.*
- [11] Ph. Niedermann et al. 1990. *Journal of Vacuum Science and Technology A, 8(1):594-597.*
- [12] M. Radmilovic-Radjenovic, B. Radjenovi, S. Matjecik and M. Klas. 2013. *EPL Journal, 103 45002.*

DISCHARGE FORMATION INSIDE THE HONEYCOMB STRUCTURES ASSISTED BY SURFACE BARRIER DISCHARGE

Richard Cimerman, Emanuel Mat'áš, Karol Hensel

*Faculty of Mathematics, Physics and Informatics, Comenius University,
Mlynská Dolina F2, 842 48, Bratislava, Slovakia
E-mail: cimerman@fmph.uniba.sk*

In this paper, we experimentally investigated discharge formation inside the honeycomb catalysts. Honeycomb structure of the catalyst was simulated by a bundle of glass capillary tubes. The discharge inside the capillary tubes was formed with the assistance of surface barrier discharge generated by a perforated ceramic substrate and by applying DC high voltage across the capillaries. We evaluated basic electrical and optical characteristics of the discharge using ambient or synthetic air as carrier gases with various flow rates. The effect of polarity of the applied DC high voltage was also studied. The results showed the positive effects of air humidity and air flow rate on stability and quality of the discharge inside capillary tubes. With negative DC high voltage, the highest emission intensity of the capillary discharge was observed for air flow rate of 0.5 L/min, while with positive DC high voltage, it was for air flow rates of 1.0 and 2.4 L/min. These results and the other details related to properties of the surface barrier discharge will be presented during the conference.

1. Introduction

Plasma catalysis is gaining an increasing interest in many environmental applications, e.g. air and water pollution control. It is characterised by high catalyst selectivity as well as high plasma reactivity which can lead to higher pollutant removal efficiencies with lower energy consumption when compared to individual catalytic or plasma processes [1, 2]. In the catalytic processes, besides the catalyst composition also its shape and structure play a crucial role [3]. In plasma catalytic systems, the catalyst can be present as a coating or as a layer on the plasma reactor walls or electrodes, or it can take the form of powder, beads or pellets packed in the reactor volume. In addition to these packed bed reactors, also honeycomb catalysts are sometimes used as they have an advantage of low pressure drop and high surface-to-volume ratio. However, generation of stable and homogeneous non-thermal streamer discharge plasma inside thin and long channels of the honeycomb is relatively difficult. Formation of plasma requires high onset voltages due to losses of charged particles by interaction with the channel walls [4] and it is often unstable and associated with frequent sparking that is undesirable due to possible mechanical damage of ceramics and even with a respect to some applications.

In order to understand plasma discharge generation and propagation inside the honeycomb structures, the processes have been studied by numerical modelling by various research groups [5–7]. *Zhang et al.* found, that in the case when streamer is initiated along the dielectric surface (i.e. wall of honeycomb channel), the discharge will be further enhanced due to surface charging along the dielectric surface [5]. *Jánsky et al.* found, that discharge propagation velocity inside the thin tube increases with the increase of the applied voltage and with the decrease in both the tube radius and relative permittivity [6, 7]. In addition to modelling, experimental investigations of plasma discharge formation in honeycomb catalyst have been also studied [8–12]. In these works, the honeycomb structure was simulated by a bundle of glass capillary tubes. The discharge inside capillaries (also called honeycomb or capillary discharge) was generated by a three-electrode geometry. Firstly, discharge plasma was formed by auxiliary pellet bed discharge [8–10] or surface barrier discharge [11, 12]. Secondly, the plasma of auxiliary discharge was extended into the honeycomb structure upon the application of DC high voltage (HV) across the capillaries. *Hensel et al.* and *Sato et al.* found, that onset DC HV amplitude increases with the length and decreases with the diameter of capillaries. Further, with extending the length of capillaries at a given DC voltage, the discharge current and power decreases. In contrast, the diameter of the capillaries (1-2 mm) showed marginal effect on the discharge power [8, 9]. The average electric field strength for the onset of the capillary discharge was about 10 kV/cm for capillaries with 2.0 mm in inner diameter and 20 mm in length [10]. In addition to

investigation of basic discharge properties, experiments focused on regeneration of diesel particulate filter [13] or removal of NO_x from simulated diesel exhaust gas [14, 15] have been also performed.

The objective of this work was to study electrical and optical characteristics of the discharge formed inside honeycomb structure which was simulated by a bundle of glass capillaries. In the past, we investigated the discharge generation assisted by a packed bed discharge [8, 9] or a diffuse coplanar surface barrier discharge (DCSBD) [12]. Here, the capillary discharge was formed with the assistance of surface barrier discharge (SBD) generated by a perforated ceramic substrate (also called as a plasma actuator). The effects of air humidity, air flow rate and polarity of DC HV applied across the capillaries were investigated on quality (stability) and homogeneity of the capillary discharge.

2. Experimental setup and methods

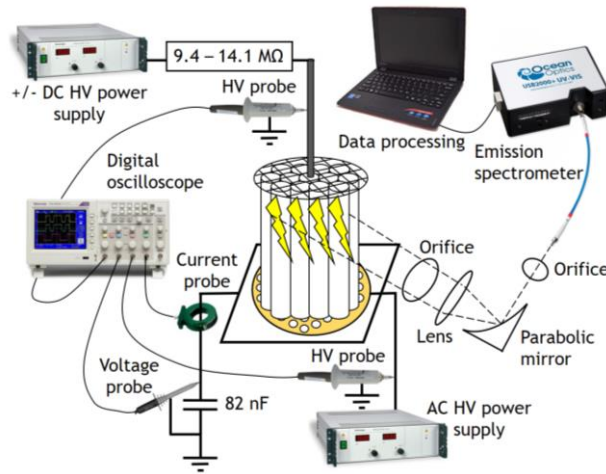


Fig. 1. Experimental setup.

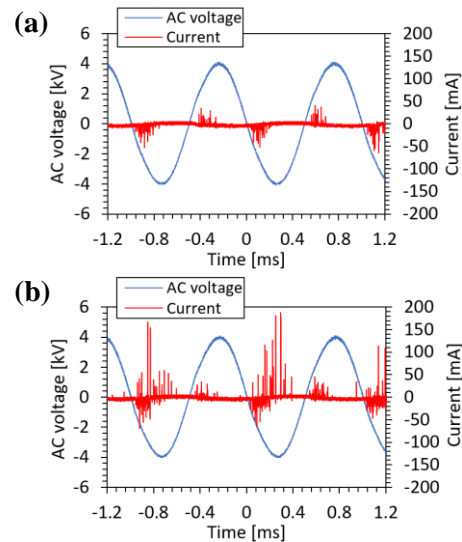


Fig. 2. Voltage and current waveforms of (a) surface barrier discharge (AC HV 4 kV @ 1 kHz) and (b) capillary discharge (AC HV 4 kV @ 1 kHz; DC HV +16 kV; R 9.4 MΩ).

The experimental setup is depicted in the Fig. 1. The ceramic substrate (*Kyocera*) with the dimensions of 50 x 50 x 1 mm and perforated by 170 holes with an inner diameter of 1.5 mm, consisted of one Ni/Au electrode embedded within the ceramic and the other one printed on the ceramic surface. The substrate was powered by AC HV power supply consisting of function generator (*Gwinstek SFG-1013*), signal amplifier (*Omnitronic PAP-350*) and high voltage transformer. The SBD was formed by applying AC HV to the air-exposed electrode (3–7 kV at 1 kHz) while the embedded electrode was grounded. The bundle of glass capillaries was placed perpendicularly on the ceramic substrate, while a metal mesh serving as a third electrode was placed on the top of them and was powered by DC HV power supply (*Technix SR20-R-1200*). The waveforms of the applied AC and DC voltages were measured by HV probes (*Tektronix P6015A*) and the discharge current pulses were measured by a current probe (*Pearson Electronics 2877*) connected to a digital oscilloscope (*Tektronix TDS2024C*). The power consumption of the SBD was evaluated using the Lissajous figure method [16] with an 82 nF capacitor and a voltage probe (*Tektronix P2220*). An optical emission spectroscopy system consisted of dual-fibre optic spectrometer (*Ocean Optics SD2000*), optic fibre, two orifices, parabolic mirror and lens. Photographs of the discharge were taken with a digital camera (*Sony Alpha DSLR-A230*) with manually adjustable aperture and exposure. Ambient and synthetic air were used as the carrier gases and their flow rate (0.5, 1.0 and 2.4 L/min) was controlled by flow meters. A relative humidity of the ambient air was approx. 60%.

3. Results and discussion

The Fig. 2. (a) shows typical voltage and current waveform of the SBD while the Fig. 2. (b) shows the waveform recorded during the operation of both SBD and the capillary discharge. In contrast to the

waveform of SBD, formation of capillary discharge can be recognized by the presence of current pulses of much bigger amplitude during the maximum amplitude of the AC applied voltage (Fig. 2. (b)) that occurred only when both AC and DC HV were applied. When positive DC HV was used, capillary discharge formed only during the negative half-period of the applied AC voltage and vice-versa, because of the biggest potential difference (approx. 20 kV) across the capillaries.

The Fig. 3. shows the plasma ceramic substrate with glass capillaries in different conditions: (a) without applied HV; (b) with applied only AC HV and (c) with applied both AC and DC HV. The photographs in the Figs. 3. (b) and (c) correspond to voltage and current waveforms in the Figs. 2. (a) and (b), respectively. In the Fig. 3. (b), light was emitted by the SBD only, while upon application of DC HV across the capillaries, the streamer propagation formed the homogeneous capillary discharge inside them (Fig. 3. (c)). On the other hand, upon application of only DC HV without the assistance of SBD, the discharge in capillaries had significantly lower emission intensity and was localised only inside one or two capillaries. The mechanism of capillary discharge formation can be explained by a superposition of the AC powered surface barrier discharge and the DC powered streamer corona discharge. The first one serves as an ionizer producing charged particles while the latter one produces and maintains ionic wind toward the DC electrode [9].

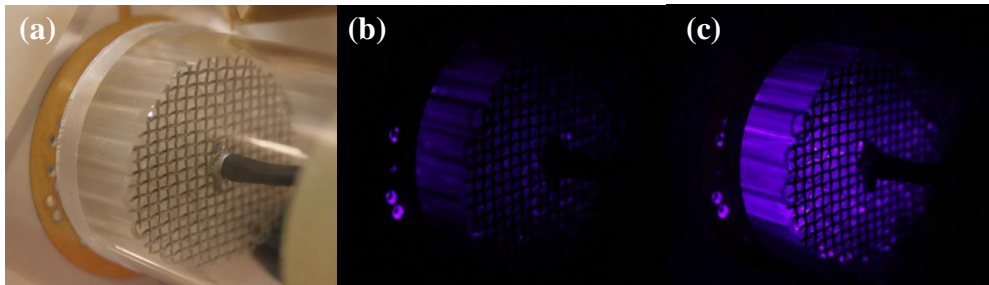


Fig. 3. The ceramic substrate with glass capillaries: (a) without discharge; (b) with applied AC HV (4 kV @ 1 kHz); (c) with applied both AC and DC HV (4 kV @ 1 kHz; +16 kV, respectively) (ambient air, 2.4 L/min) (Exposure time 4 s, f/5.6, ISO 400).

We evaluated the quality (stability, activity) of the capillary discharge by measuring its light emission intensity. Higher emission intensity reflects higher number of stable discharges maintained in the streamer discharge regime. The emission intensity is also a measure of discharge activity, i.e. concentration of active species generated by the discharge. Possible instability of the discharge is associated with its transition from the streamer to the spark regime, what is usually undesirable in practical applications. The discharge emission intensity was evaluated based on the 0–1 spectral band (357 nm) of 2nd positive system of N₂ instead of 0–0 spectral band because of strong attenuation of the intensity of this spectral band occurred when light passed through the glass capillaries.

The Fig. 4. shows the comparison of emission intensity of the capillary discharge in ambient and synthetic air with various air flow rates in the case of negative (Fig. 4. (a)) and positive DC HV (Fig. 4. (b)). The positive effect on the discharge quality was observed with the increasing of the air humidity. When dry synthetic air was used as a carrier gas, the capillary discharge did not form, regardless of air flow rate and the polarity of the DC HV. On the other hand, when humid ambient air was used, a stable discharge dominant in terms of emission intensity was observed – for negative DC HV with flow rate of 0.5 L/min (Fig. 4 (a)) and for positive DC HV with flow rates of 1.0 and 2.4 L/min (Fig. 4 (b)). The positive effect of the air humidity on the capillary discharge quality and stability was also reported in [9, 15].

We also studied the effect of air flow direction on quality (stability) of the capillary discharge. The best result was obtained in case when the air passed firstly through the ceramic substrate and then through the bundle of capillaries. In such case, the air was preionised by the SBD and discharge inside the capillaries was ignited with lower DC HV amplitudes. When air flow direction was reversed, the discharge remained localised especially near to the mesh electrode, its emission intensity was lower and was quite unstable with occasional sparking.

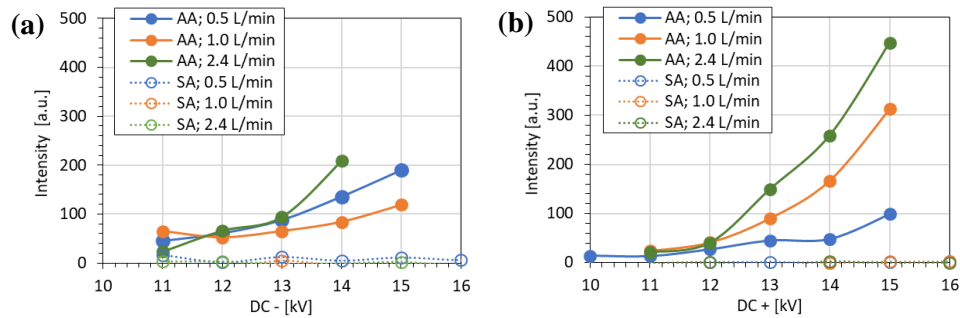


Fig. 4. Emission intensity of the capillary discharge as a function of amplitude of the applied (a) negative or (b) positive DC HV in ambient air (AA) and synthetic air (SA) with various flow rates (0.5; 1.0 and 2.4 L/min).

4. Conclusion

In this paper, we experimentally studied formation of plasma discharge inside the honeycomb structure simulated by a bundle of glass capillary tubes. The discharge inside the capillaries was formed by a superposition of AC powered surface barrier discharge coupled in series with DC high voltage applied across the capillaries. The capillary discharge was maintained in the streamer discharge regime and positively supported and stabilised by increasing the air humidity. The effect of polarity of the DC high voltage, air flow rate and its direction were also studied. With negative DC high voltage, the highest emission intensity of the capillary discharge was observed for air flow rate of 0.5 L/min, while with positive DC HV, it was for air flow rate of 1.0 and 2.4 L/min. In general, we found that air humidity and air flow rate have positive effect on homogeneity, quality and stability of the capillary discharge. Further investigation focused on long-term stability and chemical activity of the capillary discharge is needed in order to determine the optimal conditions of the capillary discharge operation with the respect to eventual applications.

5. Acknowledgements

This work was supported by Slovak Research and Development Agency grants APVV-0134-12 and APVV-17-0382, Comenius University Grants UK/319/2017, UK/373/2018 and by Special Grant of Faculty of Mathematics, Physics and Informatics.

6. References

- [1] Whitehead J C 2016 *J. Phys. D: Appl. Phys.* **49** 243001
- [2] Neyts E C, Ostrikov K K, Sunkara M K and Bogaerts A 2015 *Chem. Rev.* **115** 13408–46
- [3] Kim H H and Ogata A 2011 *Eur. Phys. J. Appl. Phys.* **55** 13806
- [4] Cheng H, Lu X and Liu D 2015 *Plasma Process. Polym.* **12** 1343–1347
- [5] Zhang Q-Z and Bogaerts A 2018 *Plasma Sources Sci. Technol.* **27** 105013
- [6] Jansky J, Tholin F, Bonaventura Z and Bourdon A 2010 *J. Phys. D: Appl. Phys.* **43** 395201
- [7] Jansky J, Le Delliou P, Tholin F, Tardiveau P, Bourdon A and Pasquiers S 2011 *J. Phys. D: Appl. Phys.* **44** 335201
- [8] Hensel K, Sato S and Mizuno A 2008 *IEEE Trans. Plasma Sci.* **36** 1282–1283
- [9] Hensel K 2009 *Eur. Phys. J. D.* **54** 141–148
- [10] Sato S, Hensel K, Hayashi H, Takashima K and Mizuno A 2009 *J. Electrostat.* **67** 77–83
- [11] Mizuno A 2013 *Catal. Today* **211** 2-8
- [12] Hensel K, Janda M and Ráhel J 2009 *ISPC 19 Ruhr-University Bochum Germany*
- [13] Hayashi H, Sakiyama D, Takashima K and Mizuno A 2012 *Int. J. Plasma Environ. Sci. Technol.* **6** 160–165
- [14] Sato S and Mizuno A 2010 *Int. J. Plasma Environ. Sci. Technol.* **4** 18–23
- [15] Takashima K, Suzuki T, Nomura Y, Hinata Y, Hayashi H, Kurita H and Mizuno A 2013 *Int. J. Plasma Environ. Sci. Technol.* **7** 142–147
- [16] Kogelschatz U 2003 *Plasma Chem. Plasma Process.* **23** 1–46

HEAVY-PARTICLE INDUCED SURFACE PROCESSES IN CAPACITIVE RADIO FREQUENCY DISCHARGES DRIVEN BY TAILORED VOLTAGE WAVEFORMS

Aranka Derzsi^{1,2}, Julian Schulze^{2,3}

¹*Institute for Solid State Physics and Optics, Wigner Research Centre for Physics, Hungarian Academy of Sciences, 1121 Budapest, Hungary*

²*Department of Physics, West Virginia University, Morgantown, WV 26506, USA*

³*Institute of Electrical Engineering and Plasma Technology, Ruhr-University Bochum, 44780 Bochum, Germany*

E-mail: derzsiaranka@gmail.com

We study the characteristics of low-pressure Ar discharges with Cu electrodes, driven by tailored voltage waveforms, comprising a maximum of four harmonics of the 13.56 MHz base frequency via kinetic Particle-in-Cell/Monte Carlo Collisions simulations. We discuss the effects of modifying the driving voltage waveform on the plasma parameters and particle properties at the electrodes, as well as on the heavy-particle induced secondary electron emission and sputtering of the surface material.

1. Introduction

Low-pressure capacitively coupled plasmas (CCPs) are basic tools for a variety of plasma processing applications [1-3]. In such applications, which are based on the interactions of plasma particles with the boundary surfaces, the control of particle properties at the surfaces is of key importance. The application of tailored voltage waveforms to excite CCPs offers advanced control of various particle flux-energy distribution functions in technological plasmas. Such waveforms have a non-sinusoidal shape and can be generated as the sum of signals with a fundamental frequency and a number of its higher harmonics with defined phase shifts between them. The waveform shape can be changed by individually varying the harmonics' amplitudes and phases. This affects the division of the sheath voltages and, therefore, the energy of ions arriving at the two electrodes. This type of excitation allows the ion energy to be tuned by the phase angle between the driving harmonics based on the electrical asymmetry effect (EAE) [4-5], due to the varying DC self-bias that is caused by the electrically asymmetric excitation waveform [6-12].

Here, we investigate CCPs excited by tailored voltage waveforms via kinetic Particle-in-Cell/Monte Carlo Collisions (PIC/MCC) simulations. We focus on the domain of low-pressures (0.5 Pa), where at high voltages the plasma particles can reach the electrodes at high energies and can induce significant secondary electron emission (SEE), as well as sputtering of the surface material. Such discharge conditions are typical in industrial applications such as etching, plasma sputtering, and plasma immersed ion implantation. We discuss the characteristics of Ar discharges with Cu electrodes, driven by a maximum of four harmonics of 13.56 MHz, as a function of the driving voltage waveform, including the study of surface processes involving heavy particles, such as the SEE and surface sputtering.

2. The simulation method

The calculations are based on our electrostatic 1d3v bounded plasma PIC/MCC code. We investigate geometrically symmetric discharges in argon. The distance between the plane, parallel, and infinite electrodes is 6.7 cm. One electrode is grounded, while the other electrode is driven by the following voltage waveform:

$$\phi(t) = \sum_{k=1}^N \phi_k \cos(2\pi k f_1 t + \theta_k) \quad \text{with} \quad \phi_{tot} = \sum_{k=1}^N \phi_k, \quad (1)$$

where N is the total number of consecutive harmonics, k is an integer number and f_1 is the fundamental frequency. ϕ_k and θ_k are the amplitude and the fixed, but adjustable phase, respectively, of the k th harmonic. ϕ_{tot} is the total applied voltage amplitude. "Peaks"-type voltage waveforms are generated by setting all phase angles to zero, while "valleys"-type waveforms are obtained by changing the phase

angles of all the even harmonics to $\theta_k = 180^\circ$. Fig. 1 shows examples of the normalized driving voltage waveform, $\phi(t)/\phi_{tot}$, for specific values of N and θ_k .

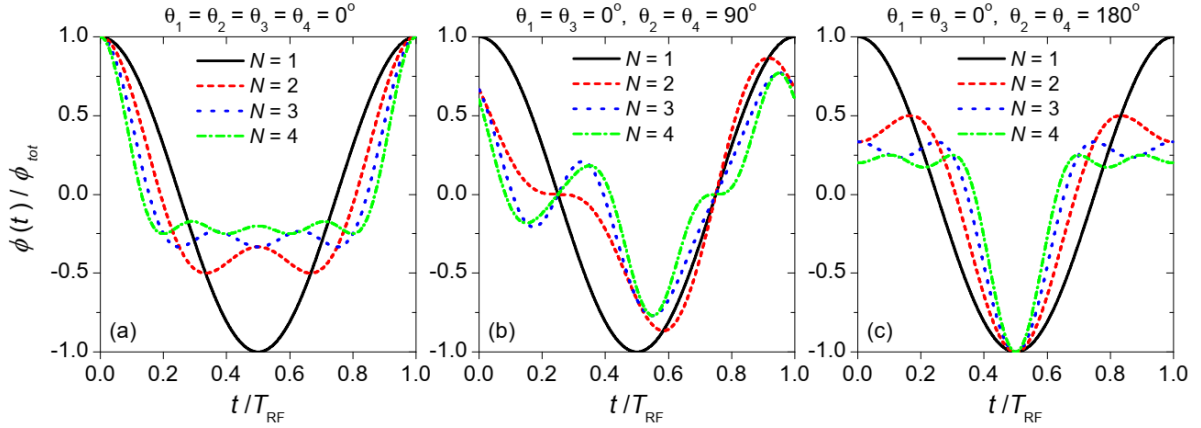


Fig. 1. Normalized driving voltage waveforms, $\phi(t)/\phi_{tot}$, for specific values of values of N and θ_k . The time axis covers one period of the fundamental frequency, f_1 . $T_{RF} = 1/f_1$.

In this study $f_1=13.56$ MHz and ϕ_{tot} takes values between 250 V and 2000 V. The amplitudes of the individual harmonics are set according to the following equations:

$$\phi_k = \phi_0 \frac{N-k+1}{N} \quad \text{with} \quad \phi_0 = \frac{2\phi_{tot}}{N+1}. \quad (2)$$

We assume that the electrodes are made of Cu and the surface conditions of both electrodes are identical. The plasma particles traced in the simulations are electrons, Ar^+ ions, fast Ar neutrals (Ar^f), sputtered Cu atoms and Cu^+ ions. At the electrodes, electrons are reflected with a probability of 0.2, independently of their energy and angle of incidence [13]. SEE due to electron impact is neglected, which is clearly a simplification - recent studies show considerable effect of electron induced SEEs on the discharge characteristics at low pressures and high voltage amplitudes [14,15]. SEE induced by Ar^+ ions and fast Ar atoms are taken into account in the simulations. The effective secondary electron emission coefficient (SEEC), γ^* , which characterizes the heavy-particle induced SEE, is calculated self-consistently based on the energies and corresponding yields of the individual Ar^+ and Ar^f particles impacting the electrodes [16]. The energy-dependent SE yields for these particles are calculated according to formulas provided in [17,18] for “dirty” surfaces (typical for laboratory conditions). Sputtering of the electrodes by Ar^+ ions, Ar^f neutrals and Cu^+ ions are implemented in the simulations – the sputtering yields as a function of the energy of the bombarding particles, calculated based on [19], are shown in Fig. 2. The depletion of the Ar neutral density due to the sputtered Cu atoms is small ($n_{Cu}/n_{Ar} < 5 \times 10^{-4}$) and, therefore, neglected in the simulations.

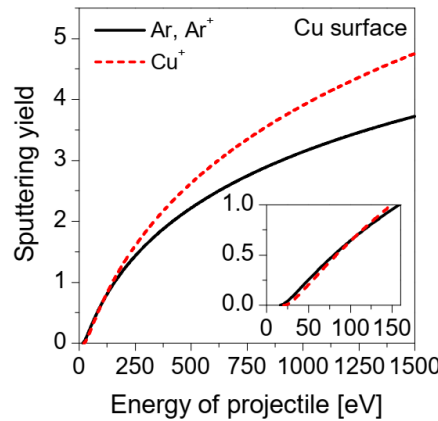


Fig. 2. The sputtering yield [atoms/projectile] for Ar^+ ions, fast Ar neutrals (Ar^f), and Cu^+ ions on Cu surfaces as a function of the energy of the bombarding particle [19]. The threshold energy for sputtering is 16 eV for Ar species and 20.4 eV for Cu^+ ions.

The neutral gas pressure is 0.5 Pa in all simulations. The gas temperature is constant, taken to be 400 K.

3. Results

Fig. 3 presents discharge characteristics obtained for $N=1$ (single-frequency excitation) for varying ϕ_1 ($\phi_1 = \phi_{tot}$). By increasing ϕ_1 from 250 V to 2000 V the mean energy of Ar^+ ions and fast Ar neutrals at the electrodes increases from about 95 eV to 270 eV for Ar^f , and from 110 eV to 660 eV for Ar^+ (panel (a)). Under such conditions, significant sputtering of the electrodes is generated by these particles (see Fig. 2, the sputtering yield is higher than 1 for particle energies above 160 eV and increases with increasing particle energies). The high sputtering yields at high particle energies lead to a strong increase of the peak Cu density as ϕ_1 is increased (panel (c)): at 2000 V the Cu density is about 5 times higher than the plasma density. This is illustrated also in Fig. 4, which shows the time-averaged density distributions of particles in the discharge gap for different values of ϕ_1 . Most sputtering is caused by Ar^+ ions – their contribution to the sputtering is about 80 % for all ϕ_1 , while that of fast Ar atoms is about 20 % (panel (b)). The contribution of Cu^+ ions to the sputtering is less than 1 % for all conditions investigated here. The effective SEEC, γ^* , shown in the right scale of panel (b), changes as a function of ϕ_1 , reaching the highest value of 0.33 at the highest ϕ_1 of 2000 V.

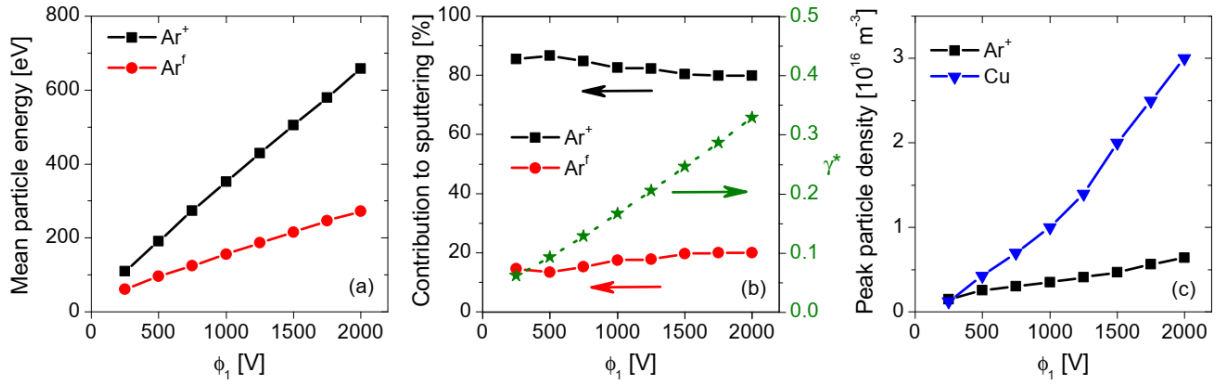


Fig. 3. The mean energy of Ar^+ ions and fast Ar neutrals at the electrodes (a), their contribution to the sputtering of the Cu electrodes (b, left scale), the self-consistently calculated SEEC, γ^* (b, right scale), and the density of Ar^+ ions and Cu neutrals at the centre of the discharge (c) as a function of the driving voltage amplitude.

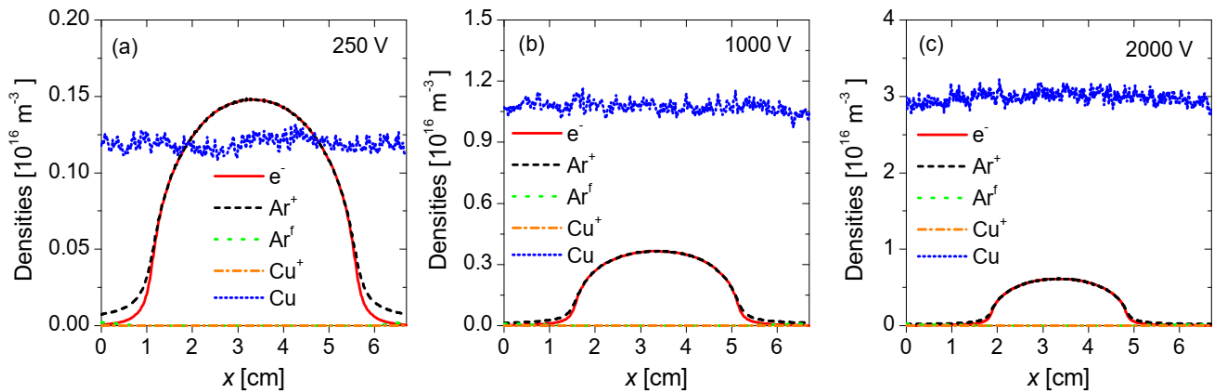


Fig. 4. Time-averaged density distributions of particles in the discharge gap for different values of ϕ_1 : (a) 250 V, (b) 1000 V, and (c) 2000 V.

Fig. 5(a) shows the dc self-bias, η , as a function of the identical phase angle of the even harmonics ($\theta = \theta_2 = \theta_4$, $\theta_1 = \theta_3 = 0^\circ$) for different numbers of applied harmonics, N . The harmonics' amplitudes are chosen according to equation (2) with $\phi_{tot} = 1000$ V. The self-consistently calculated SEEC, γ^* , and the (outgoing) flux of sputtered Cu atoms at both electrodes are shown in panels (b) and (c) of Fig. 5, respectively, as a function of θ . By adjusting θ , the dc self-bias can be tuned effectively, and adding

more consecutive harmonics (increasing N), significantly enhances the control interval of η . As a result, the mean Ar^+ ion energy at the electrodes can be controlled by adjusting θ (Fig. 5(a)): by varying θ from 0° to 180° , the mean Ar^+ energy increases at the grounded electrode and decreases at the powered electrode. Similar trends can be observed for the mean energy of Ar^f particles (Fig. 5(d)), as these fast neutrals are mainly created by charge exchange collisions between Ar^+ ions and atoms of the background Ar gas in the sheath.

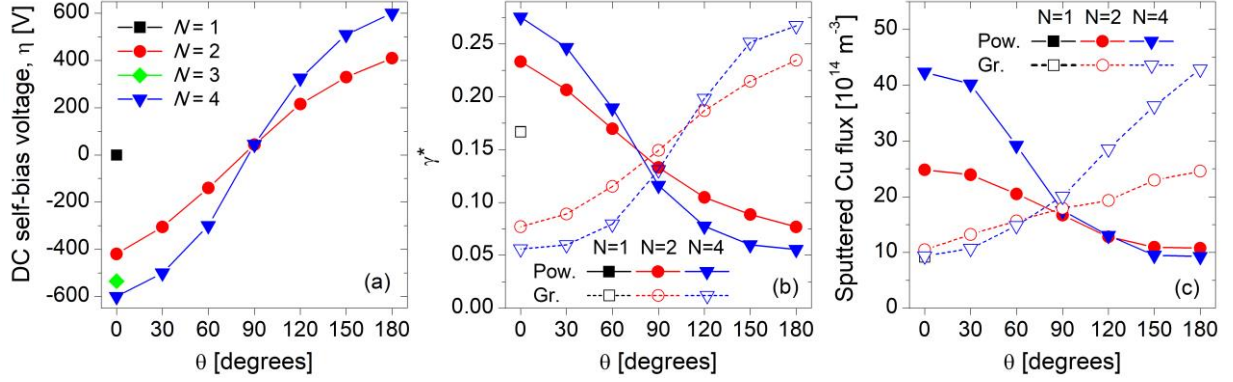


Fig. 5. (a) Dependence of the self-bias voltage, η , on the identical phase angle of the even harmonics ($\theta = \theta_2 = \theta_4, \theta_1 = \theta_3 = 0^\circ$) for different N . The self-consistently calculated SEEC, γ^* (b) and the (outgoing) flux of sputtered Cu atoms (c) at both electrodes for different N as a function of θ . $\phi_{tot} = 1000 \text{ V}$.

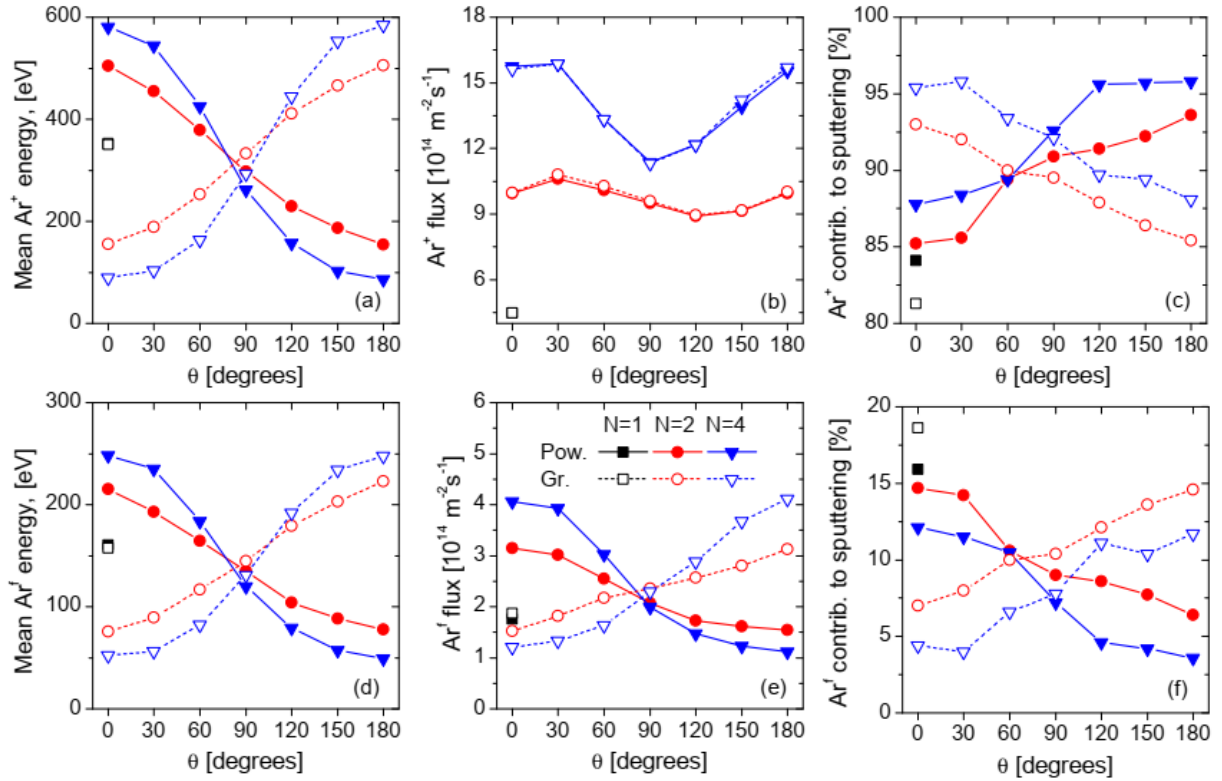


Fig. 6. The mean energy (a and d) and flux (b and e) of Ar ions and fast Ar neutrals at the electrodes, respectively, as well as their contribution to the sputtering of the Cu electrodes (c and f) for different N as a function of θ . $\phi_{tot} = 1000 \text{ V}$.

The variation of the energy of the Ar ions and fast neutrals at the electrodes with θ influences the surface processes involving these particles, such as the SEE and sputtering induced by heavy particles. As the SEE yields, as well as the sputtering yields are functions of the bombarding heavy-particle energies,

tuning the control parameter for the particle energies (θ) leads to changes of the SEECs (Fig. 5(b)), as well as changes of the flux of sputtered atoms (Fig. 5(c)) at both electrodes. The variation of the time-averaged density distributions of particles, including Cu atoms, for different values of the phase angle of the even harmonics, θ , is illustrated in Fig. 7 for $N = 4$ harmonics.

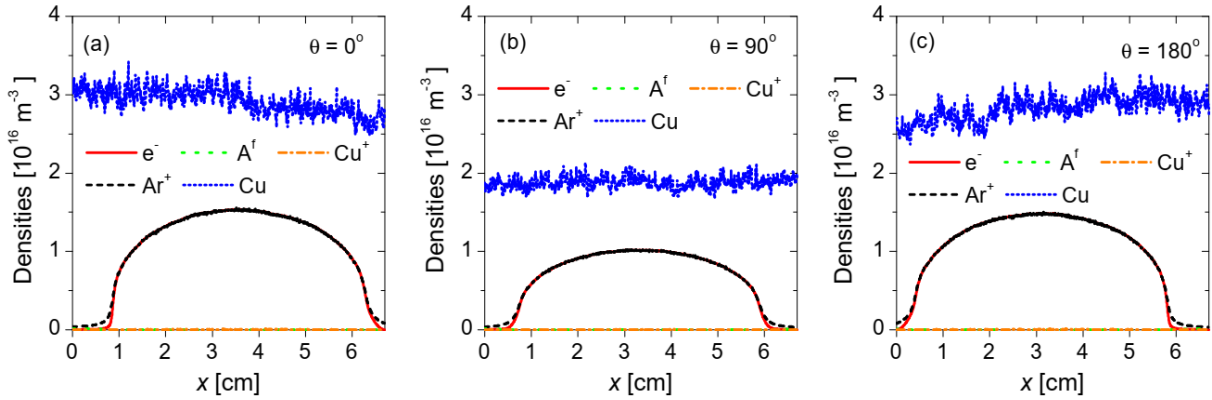


Fig. 7. Time-averaged density distributions of particles in the discharge gap for $N = 4$ harmonics, for different values of θ : (a) 0° , (b) 90° , and (c) 180° . $\phi_{tot} = 1000$ V.

Acknowledgments

This work was supported by the US NSF grant No. PHY.1601080, by the German Research Foundation (DFG) within the frame of the collaborative research centre SFB-TR 87, by the Hungarian National Research, Development and Innovation Office via grants K-119357, PD-121033 and FK-128924, and by the J Bolyai Research Fellowship of the Hungarian Academy of Sciences.

4. References

- [1] Lieberman M A and Lichtenberg A J 2005 Principles of Plasma Discharges and Materials Processing 2nd edn (Hoboken, NJ: Wiley)
- [2] Makabe T and Petrović Z 2006 Plasma Electronics: Applications in Microelectronic Device Fabrication (London: Taylor and Francis)
- [3] Chabert P and Braithwaite N 2011 Physics of Radio-Frequency Plasmas (Cambridge: Cambridge University Press)
- [4] Heil B G, Czarnetzki U, Brinkmann R P and Mussenbrock T 2008 *J. Phys. D: Appl. Phys.* **41** 165202
- [5] Schulze J, Schuengel E, Donkó Z and Czarnetzki U 2011 *Plasma Sources Sci. Technol.* **20** 015017
- [6] Lafleur T, Boswell R W and Booth J P 2012 *Appl. Phys. Lett.* **100** 194101
- [7] Donkó Z, Schulze J, Czarnetzki U, Derzsi A, Hartmann P, Korolov I and Schuengel E 2012 *Plasma Phys. Control. Fusion* **54** 124003
- [8] Johnson E V, Delattre P A and Booth J P 2012 *Appl. Phys. Lett.* **100** 133504
- [9] Bienholz S, Styrnoll T and Awakowicz P 2014 *J. Phys. D: Appl. Phys.* **47** 065201
- [10] Diomede P, Economou D J, Lafleur T, Booth J P and Longo S 2014 *Plasma Sources Sci. Technol.* **23** 065049
- [11] Bruneau B, Gans T, O'Connell D, Greb A, Johnson E V and Booth J P 2015 *Phys. Rev. Lett.* **114** 125002
- [12] Lafleur T 2016 *Plasma Sources Sci. Technol.* **25** 013001
- [13] Kollath R 1956 *Encyclopedia of Physics* vol 21, Flügge S (Berlin: Springer) p 264
- [14] Horváth B, Daksha M, Korolov I, Derzsi A and Schulze J 2017 *Plasma Sources Sci. Technol.* **26** (2017) 124001
- [15] Horváth B, Schulze J, Donkó Z and Derzsi A and *J. Phys. D: Appl. Phys.* **51** (2018) 355204
- [16] Donkó Z 2000 *J. Appl. Phys.* **88** 2226
- [17] Phelps A V and Petrović Z Lj 1999 *Plasma Sources Sci. Technol.* **8** R21
- [18] Phelps A V, Pitchford L C, Pédoussat C and Donkó Z 1999 *Plasma Sources Sci. Technol.* **8** B1–2
- [19] Matsunami N et al. 1984 *Atom. Data and Nucl. Data Tables* **31** 1

ACCELERATING MONTE CARLO PARTICLE-IN-CELL (MCC-PIC) SIMULATIONS OF DISCHARGES

Ján Ďurian¹, Štefan Matejčík¹, Zoltán Donkó²

¹*Department of Experimental Physics, Faculty of mathematics, physics and informatics, Comenius University in Bratislava*

²*Wigner Research Centre for Physics, Hungarian Academy of Sciences, Budapest, Hungary*

E-mail: durian5@uniba.sk

We present a newly developed Particle-in-Cell code for simulations of discharges in gases. We have used two numerical methods in our code, the Box-Muller Transforms and a fast implementation of the exponential function, both of which proved to be over twice as fast as numerical methods usually found to be used in plasma simulations, while still providing excellent accuracy. We also tested these numerical methods in a simulation of a standard RF discharge. We have found the results to be in excellent agreement with the benchmarking calculations, showing that our code is stable and accurate, and ready to be developed further.

1. Introduction

In this paper we present a Monte Carlo Particle-in-Cell (MCC-PIC) code capable of simulating electrical discharges in gases, as well as the application of some optimized numerical methods.

Particle-in-Cell (PIC) are a family of numerical methods which separate the evolution of the continuum into two steps: the so-called Eulerian step (calculations performed on a static, Eulerian grid) and the Lagrangian step (calculations performed on moving particles) [1].

A standard electrostatic PIC code consists of four main components in this order: weighting (particles to grid), the field solver, weighting (grid to particles) and the particle mover. Weighting serves as a translation between the continuous space of particles and the discrete space of the points of the simulation grid, utilizing interpolations to provide the translation. The field solver uses the charge density outputted by the particles-to-grid weighting to obtain the electric field in each point of the simulation grid. Then follows the grid-to-particle weighting which interpolates the electric field from the positions of the grid points to the particle positions. Finally, the particle mover converts the interpolated electric field into particle accelerations, and pushes the particles in space, modifying their velocities and positions [2]. Some particles may cross the boundaries of the simulation space. In that case, they're removed from the simulation. However, particles can also be created at the boundaries through effects of, for instance, secondary emission.

In MCC-PIC, a fifth component – Monte Carlo Collisions – is inserted in between the particle mover and the particles-to-grid weighting. This component takes care of evaluating all particle reactions in plasma: scattering, excitation, ionization, recombination, etc. The first step is to evaluate the probability of a collision between the incident and the target particle species using the equation [3]

$$P = 1 - e^{-n_g \sigma_T g \Delta t} \quad (1)$$

where P is the collision probability, n_g is the target species density obtained via the law for the ideal gas, σ_T is the total cross section of the incident particle, g is the relative velocity between the incident and the target particle in the center-of-mass frame, and Δt is the simulation time step.

Once the collision probability is calculated, the algorithm proceeds to generate a random number between 0 and 1, R_{01} . A reaction happens, if

$$R_{01} < P \quad (2)$$

The following step involves determining the type of the reaction (scattering, excitation, ionization, etc.), and executing the reaction. [3]

Our code, follows the same structure as outlined in this chapter. We use linear interpolations for the particle-to-grid and grid-to-particle weighting, the Thomas algorithm for solving the field equations¹, and we use a standard Euler integrator for the particle mover, with the intention of upgrading it to Leapfrog in the future. For MCC, we use two methods which differ from what is normally used in the scientific community, which we will describe in the following chapters.

2. Box-Muller Transforms

In order to evaluate the collision probability according to equation (1), we must first sample the velocities of neutral particles. The principal issue with this is that Random Number Generators (RNGs) only output sets of numbers with a uniform distribution [5], whereas we need velocity vectors whose x, y and z components follow the Gaussian distribution².

This problem can be solved by transforming a set of numbers with the uniform distribution into a set of numbers with a different distribution. The standard way of achieving this is using the Inverse CDF³ (ICDF) method, also known as the Inverse Sampling Method. While this method is robust, it is also computationally expensive (in our plasma simulations, the sampling of the Gaussian distribution proved to actually be the most computationally expensive part of the MCC algorithm), which is why we looked for a more optimal solution.

In our case, a more optimal solution to this problem are the Box-Muller Transforms (BMT). BMT is an operation which transforms a set of numbers with the uniform distribution (such as the output of RNGs) directly into a set of numbers with the Gaussian distribution (such as the x, y and z components of the particle velocities) in a fast, efficient way. [4]

To test the accuracy and speed of the BMT and how it compares to ICDF, we've set up a short test in which we sampled the x, y and z components of a vector with the Gaussian distribution with both methods. We then combined these components into the length of the vector, which we plotted onto a graph (Figure 1), expecting to obtain the Maxwell-Boltzmann distribution.

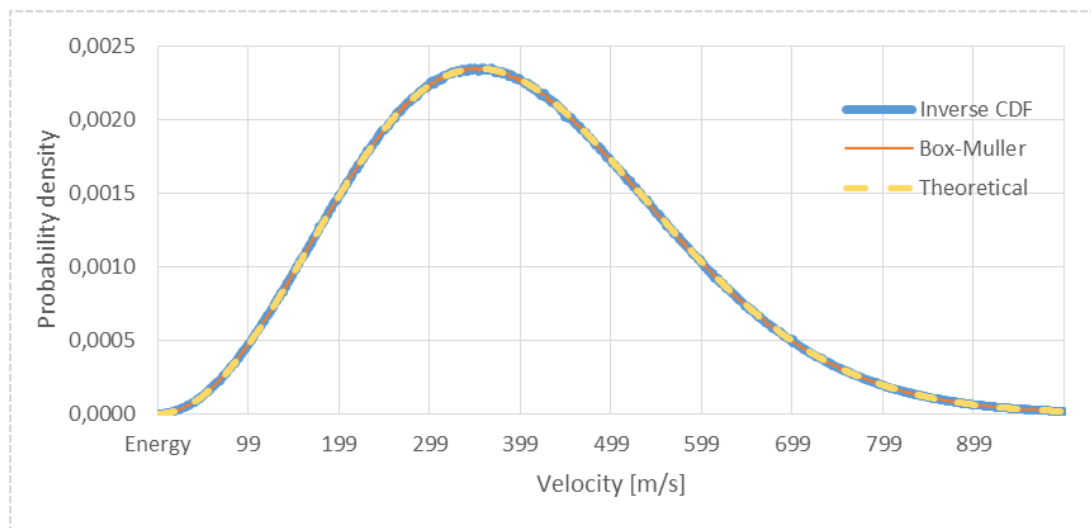


Fig. 1: Results comparison for both the ICDF and BMT methods for sampling the velocity of neutral atoms.

¹ Our code is a 1D electrostatic one, the Discrete Poisson Equation gets transformed into a tridiagonal system, prompting the use of the Thomas algorithm as a fast and accurate solution.

² The size of such vectors will follow the Maxwell-Boltzmann distribution.

³ CDF – Cumulative Distribution Function

We generated 50 million velocity samples (150 million random numbers in total) using both methods, for Argon ions at the temperature of 300 K. From Figure 1 we can observe a total match of the results of the two methods, in both cases we obtained a prime example of a Maxwell-Boltzmann distribution.

The biggest difference in the results is that while the ICDF method took 18.847 seconds to finish generating 50 million velocities, the BMT method took only 8.133 seconds to finish the same workload, which is a 57% improvement in speed. The average deviation in the resulting probability density between the two methods was determined to be $4.40 \cdot 10^{-6}$, most of which is caused by the noise commonly present in algorithms involving RNGs (Monte Carlo methods).

The test program was run on an Intel Xeon E5-1660 v2 CPU, utilizing only one of its cores.

3. A fast exponential function - FastExp

After implementing the BMTs for velocity sampling in our code, we have found that the standard method available for computing the exponential function was taking most of the computational run time of the whole program. We have tried to find a more optimal solution.

One such method is based on directly implementing the Euler's representation of the exponential function, shown in equation (3).

$$e^x = \lim_{n \rightarrow \infty} \left(1 + \frac{x}{n}\right)^n \quad (3)$$

If we choose a reasonably big n , we can quickly achieve sufficiently accurate results by directly implementing the formula in our code. Moreover, if we choose n to be a power of two (for instance 256), we can simply multiply the $1 + x/n$ expression by itself 8 times to obtain the approximation of the exponential function at the given point x . In our code, we have chosen x to be 1024, and we multiplied the mentioned expression 10 times to achieve higher accuracy. For better clarification, we have branded this method as FastExp.

To verify the reliability of this solution, we have written another test to measure the accuracy and the speed improvement of this method. We have computed the exponential function for 100 million numbers ranging from -10 to 10, using both the standard implementation of the exponential function, and our FastExp method. We have determined the error of the FastExp method by subtracting the curve produced by the FastExp from the curve produced by the standard method.

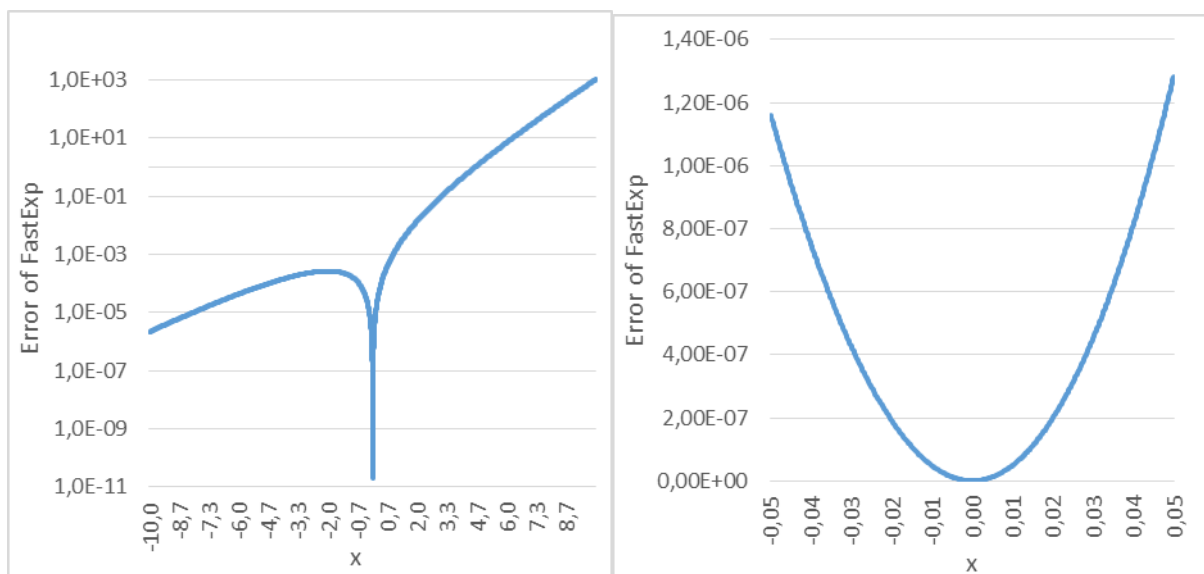


Figure 2: Left – the error of FastExp on the interval from -10 to 10, Right – the error of FastExp around the values of x close to 0.

In the Figure 2 we have displayed the error as a function of x . We can see a massive increase in the error of the FastExp method for inputs above 4, which raises the question of the reliability of this method. However, if we take a closer look at the exponential function used in the PIC code as given in the equation (1), we can notice that the input of the exponential function is always a negative number. The maximum error of the FastExp method in the input interval from -10 to 0 was found to be $2.64 \cdot 10^{-4}$.

Analyzing this deeper, a quick test showed that during a simulation of a standard RF discharge, our PIC code only ever produced inputs ranging from -0.03 to 0 for the exponential function. The error of the FastExp method in this interval ranges from $4.26 \cdot 10^{-7}$ to 0 respectively (as seen on Figure 2, right), which is sufficiently accurate for the needs of our code.

Another huge advantage of the FastExp method is the superior speed compared to the standard implementation of the exponential function. The standard method took 1.443 seconds to finish, while FastExp only needed 0.710 seconds to complete the same work, which is 51% faster.

That makes FastExp a good alternative and a fast implementation of the exponential function. The test program was again run on an Intel Xeon E5-1660 v2 CPU, utilizing only one of its cores.

4. A test simulation

Having implemented the all of the basic components of the PIC code, we ran a test simulation to verify the stability and accuracy of the code and to see how the above-mentioned BMT method and the FastExp perform in an actual application.

We have simulated a low-pressure RF discharge in a pure Argon gas. The parameters of the discharge were as follows: the distance of the electrodes was set to be 2,5 cm, and the voltage between the electrodes was 250 V, with a frequency of 13.56 MHz. The Argon gas pressure was 10 Pa, and its temperature was set to 300 K. From the simulation parameters, we chose the number of grid points to be 400, and the time step was set to have the code perform 2000 time steps per one period of the AC voltage. Ion sub-stepping was enabled, and was set to 20. The weight of both electron and Argon ion superparticles was set to $1.5 \cdot 10^5$, and their initial count was 1000, uniformly distributed across the electrode gap.

In the kinetic model we have assumed 5 types of reactions in this simulation, including 3 electron-neutral reactions (elastic scattering, excitation and ionization). We have included only one excited state of Argon (excitation energy of 11.5 eV) and only a single ionization of Argon ions. For ion-neutral interactions we have taken isoscattering and backscattering into account. We have not included recombination reactions in the model. The simulation ran for 2.4 million time steps, which represent about $8.85 \cdot 10^{-5}$ s of the discharge.

In Figures 3 and 4 we present the results of the simulation. The data in Figure 3 are in agreement with reference studies [6] for this type of discharges. We have observed the quasi-neutrality of the plasma for most of the inter-electrodes space. Near the electrodes, we have seen the perturbation of the quasi-neutrality due to a faster drop of electron density compared to the density of ions. This is an expected behavior in an RF discharge, as electrons have a much higher mobility, and respond to changes in the outer electric field much faster than the ions, prompting them to escape the electrode gap more easily, depending on the phase of the excitation voltage.

In Figure 4 we show the time evolution of the number of the electron and ion superparticles, and therefore the time evolution of their density. We see that it took 50 microseconds for the system to achieve a state of equilibrium, where the time evolution of the electron and ion count levelled out.

These results show that our code is stable with the methods we used: BMT for sampling the neutral atom velocities and the FastExp method for computing the exponential function when determining collision probability. That allows us to progress further with the development of this code in order to handle more complex simulations more efficiently.

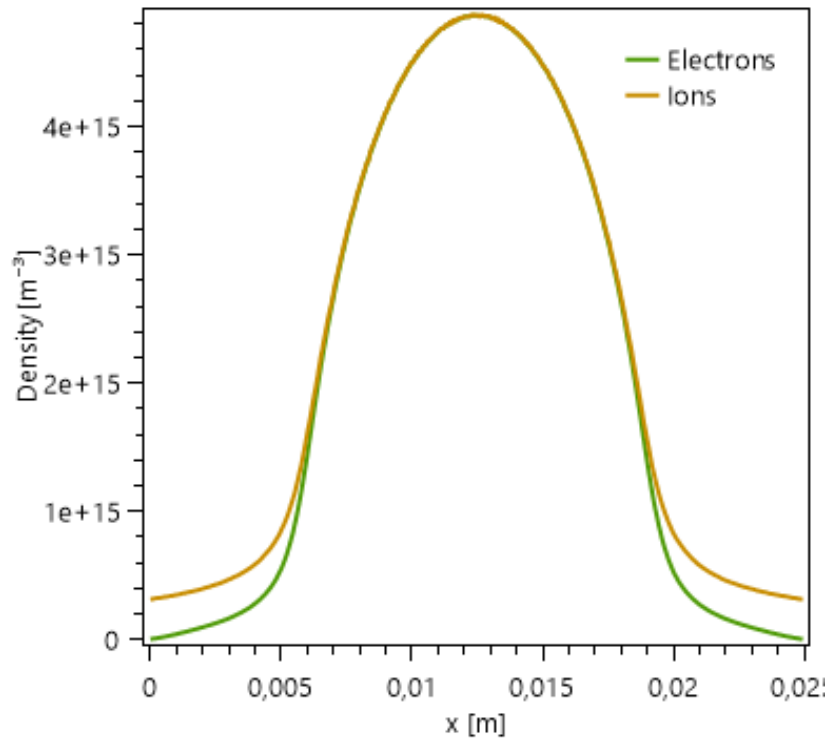


Figure 3: The time-averaged density distribution of electrons and ions at the end of the simulation.

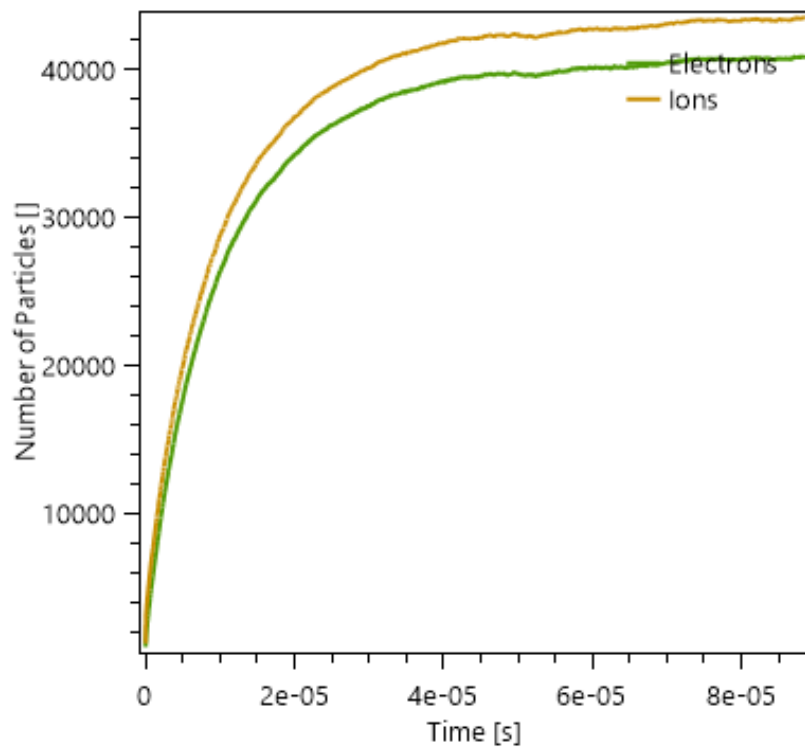


Figure 4: Time evolution of the count of the electron and ion superparticles during the simulation.

5. Conclusion

In this paper, we presented an implementation of two numerical methods which are faster than methods usually used in the MCC-PIC simulations. We have described both the BMT and FastExp methods and compared their performance and accuracy with the standard methods (ICDF and the implementation of the exponential function in the standard math libraries). We have found that both methods were more than two times faster as the standard methods, while still providing a very good accuracy in their outputs.

We also tested the stability of our code by running a simulation of a standard RF discharge. We observed results in good agreement with the reference simulations, which showed that our code is stable, and can be further developed to include more reactions between the charged the neutral particles and improve the accuracy of the code, with the goal of being able to simulate high-pressure discharges in microgaps.

Acknowledgments

This work was supported by grant agency VEGA project nr. 1/0733/17; Slovak research and development agency project nr. APVV-15-0580.

This project has received funding from the European Union's Horizon 2020 research and innovation programme under grant agreement No 692335.

6. References

- [1] Grigoryev Yu. N., Vshivkov V. A. and Fedoruk M. P., *Numerical "Particle-in-Cell" Methods*, VSP BV, Utrecht, 2002
- [2] Birdsall C. K. and Langdon B. A., *Plasma Physics via Computer Simulation*, Taylor & Francis, New York, London, 2004
- [3] Verboncoeur J. P., *Particle simulation of plasmas: review and advances*, Plasma physics and controlled fusion 47, 2005
- [4] Shinzato T., *Box Muller Method*, 2007: http://www.lmpt.univ-tours.fr/~nicolis/Licence_NEW/08-09/boxmuller.pdf
- [5] DiCarlo D., *Random Number Generation: Types and Techniques*, Liberty University, 2012
- [6] Donkó, Z.: unpublished

PLASMA FORMATION IN CONDUCTING LIQUIDS: TIME TO BREAKDOWN

Mohammad Karim¹, Leonidas Asimakoulas¹, WG (Bill) Graham¹, Tom A. Field¹

¹*Centre for Plasma Physics, Queen's University Belfast, BT7 1NN, N. Ireland, U.K.
E-mail: t.field@qub.ac.uk*

Plasma generation inside conducting liquids is frequently preceded by the growth of a vapour layer. A simple rule of thumb is presented to estimate the time to breakdown by calculating the time it takes to develop a vapour. The accuracy of this method is evaluated in combination with a number of experimental measurements.

1. Introduction

Plasmas in liquids have been studied for some time and various reviews have been made, e.g. [1]. When electrodes are submerged in the liquid there are generally two types of behaviour. At high voltages (>1 kV), over short timescales ($< \mu$ s) and with low conductivity liquids (e.g. oil, distilled water) the discharges tend to be formed by direct breakdown in the liquid itself. By contrast with lower voltages (~ 100 V), longer pulses ($> \mu$ s) and more conducting liquids (e.g. electrolyte solutions, sea water) a vapour layer tends to form prior to breakdown around a powered electrode, or wherever the current density is highest. Breakdown then occurs in this vapour layer. In this work the time to form a vapour layer has been investigated.

2. Experiments, Results, Analysis and Conclusions

A simple model will be presented, which can be used as a rule of thumb to predict the time it takes to grow a vapour layer prior to electrical breakdown in a conducting liquid. If it is assumed that breakdown happens immediately after the vapour layer is established then the time to breakdown is estimate with this method. The reliability/usefulness of this model has been tested with experimental measurements of time to breakdown, for example, in solutions with different salinities.

3. References

[1] P.J. Bruggeman *et al.* 2016 *Plasma Sources Science and Technology* **25** 053002.

ELECTRON INDUCED FRAGMENTATION OF 2,6 - DICHLOROANISOLE

Ján Blaško¹, Marián Danko¹, Beáta Feilhauerová¹, Peter Papp¹, Štefan Matejčík¹

¹ *Department of Experimental Physic, Faculty of Mathematic, Physics and Informatics, Comenius University, Mlynská dolina, 842 48 Bratislava, Slovakia*
E-mail: blasko27@uniba.sk

In this paper, we studied the formation of positive ions of the molecule 2,6 – dichloroanisole (DCA) by mass spectrometry (MS). By using the monochromatic electron beam and the quadrupole mass spectrometer, we were able to measure and describe the processes of electron ionisation and electron dissociation. Fragmentation of the molecule is characterized by sequential dissociation of benzene carbon atoms. The ionisation energy of the molecule was determined to be 9.32 eV. Dissociative threshold energies were also determined for other ionised fragments.

1. Introduction

An unpleasant odour worldwide known as cork taint, is a serious problem for both wine and cork industries. Several compounds have been identified by researches as potential contributors, which cause the musty odour of wines. These compounds include mainly chloroanisoles, in particular 2,4,6-trichloroanisole (TCA); 2,6-dichloroanisole (DCA); 2,3,4,6-tetrachloroanisole (TeCA); pentachloroanisole (PCA), bromoanisols such as 2,4,6-tribromoanisole (TBA), etc. We have measured and evaluated TCA and TBA in the past [1], now this paper deals with DCA.

Chloroanisoles are probably formed by microbiological methylation of halogen phenols in the presence of various microorganisms, especially bacteria or fungicides. This formation of chloroanisoles occurs under specific conditions of temperature and humidity [2]. The source of cork taint according to Chatonnet et al. [3] comes from halogen phenols used as fertilizers in the technical industries. In the experimental work [4], the authors point to influencing the taste of European bottled wines with cork taint between 0.1 and 10 % of their production volume. There are studies confirming the migration of chloroanisoles from cork to wine, but they also demonstrate that this migration is not so significant [5-6]. However, the fact is that a very small migration is sufficient to reduce the quality of the wine. In experimental work [7], authors points to possibility of causing an unpleasant odour or taste at concentrations of 1 – 50 ng l⁻¹. Several authors analysed the content of chloroanisoles in contaminated wines and subsequently in contaminated cork stoppers [8-9]. Different values of concentrations of chloroanisoles in wines and in its cork stoppers were found. Concentrations in wines were ranged from 0.2 to 41 ng l⁻¹, while in cork stoppers were ranged from 1 to 125 ng cork⁻¹. Tanner et al. [10] reported that up to 50 % of the chloroanisoles present in cork stoppers can be migrated to wine. On the other hand, Chatonned et al. [11] stated that this value in their observations was less than 6 %. Therefore, there are no compelling results regarding the relationship between the total content of chloroanisoles in the wine and in its cork stoppers.

There are several technologies for eliminating undesirable cork material impurities. The most advanced process is ozonisation so far. However, this method is not sufficient, because the ozonisation method penetrates only to 5 mm thickness of cork stoppers. In addition to the elimination of chloroanisoles from material, it is also necessary to quantify it. Currently, the most advanced method for determining concentration is laser desorption and subsequent analysis using ion mobility spectrometry (IMS) [12].

2. Experiment

We use the mass spectrometry analysis (MS). Electron and molecular cross beam are used to investigate electron – molecular reactions (Fig.1). The electron beam is formed with the help of a trochoidal electron monochromator (TEM), which forms a beam of monochromatic electrons in the energy range from 0 eV to 120 eV. Subsequently, the electrons are transported to the Faraday Cup where we can determine the electron current by connecting picoamper meter (Keithley 485 pA). The principal part of the apparatus consists of a heated vacuum chamber. A narrow capillary is inserted into the vacuum chamber through which the molecular beam is brought to collision region with

electron beam in TEM. Samples in liquid and gaseous form are placed in an external infiltration system. In a study of solid state, the solid material is placed directly in the vacuum chamber where it is sublimed to the vacuum. The ions generated by the interaction of the molecular and electron beam are carried by weak electric field on ions optics. The ion optics directs the ions to the principal axis of the quadrupole mass spectrometer (QMS). In this analysis the ions are separated in a mass spectrometer. After that the separated ions are directed by deflectors to the electron multiplier. Then, the signal enters the measuring card that is controlled by the measuring software. The QMS is controlled by a control unit which controls the QMS parameters. It is possible to vary the m/z ratio (m – mass of the molecule, z – charge of the molecule) and the resolution of the mass spectrometer. This will ensure the passage of only a certain group of particles.

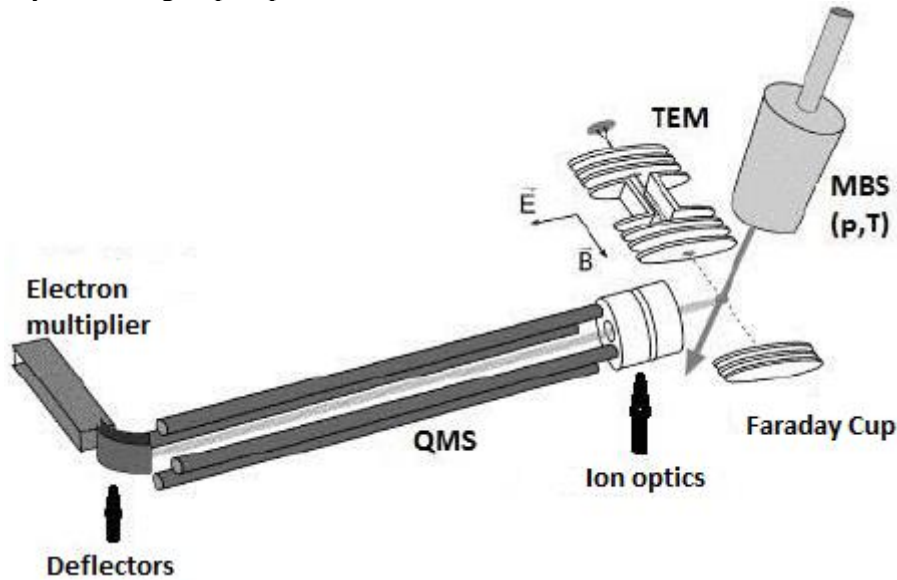


Fig.1. The experimental apparatus; (TEM) – Trochoidal electron monochromator; (QMS) – Quadrupole mass spectrometer; (MBS) – Molecular beam source [13].

Measurement of electron induced processes consists of two standard modes. The first mode takes place at the constant energy of the interacting electrons and the m/z ratio changes on QMS. In this way a mass spectrum consisting of ionised products is formed by electron induced processes. In the case of the present study, the mass spectrum was obtained with electron energy 70 eV. In the second mode is set up a constant value of m/z ratio on QMS and there is a linear change of the acceleration voltage for the electrons. For ions with particular mass and charge ratio the dependence on their formation according to the energy of the interacting electrons is determined, also called relative effective - cross section.

We have measured such dependencies for positive ions detected in the mass spectrum. During the evaluation of the measurements we were focused mainly on the rise edge area of the effective cross section, where we were looking for the start edge value. This defines the value of the threshold energy (AE – appearance energy) for a particular reaction. For this we use the special form of the Wannier formula [14]. The single threshold transition of the molecule to the ionised state is represented by the equation:

$$S(\varepsilon) = b ; \varepsilon < A \quad (1)$$

$$S(\varepsilon) = b + a(\varepsilon - AE)^d ; \varepsilon > AE \quad (2)$$

where ε is the energy of interacting electrons, AE is threshold energy and a, b, d are independent parameters. The double threshold transition of the molecule to the ionized state is represented by the equation:

$$S(\varepsilon) = b ; \varepsilon < AE \quad (3)$$

$$S(\varepsilon) = b + a_1(\varepsilon - AE_1)^{d_1} ; \varepsilon > AE_1 \quad (4)$$

$$S(\varepsilon) = b + a_1(\varepsilon - AE_1)^{d_1} + a_2(\varepsilon - AE_2)^{d_2} ; \varepsilon > AE_2 \quad (5)$$

In the process of examining effective cross sections, it is important to calibrate the energy scale. Calibration was performed by measuring the ionisation energy of argon atoms. The value of ionisation

energy of Ar atoms is 15.759 eV. Each of the noble gases can be used as a calibration gas, thanks to their steep starting edge in effective cross section and well known values. To improve the signal to noise ratio, the measurements of the effective cross section were periodically repeated and then averaged. We used energy range 5 eV for 200 steps. It is 0.025 eV for one step. The pressure in the vacuum chamber was 10^{-7} mbar while measuring.

Analysed solid sample 2,6 – dichloroanisole with 97% purity (Sample No. 157325) was ordered from Sigma – Aldrich Company. We did not place the sample in the vacuum chamber, but in an external impregnation system, due to the too extensive evaporation of DCA and its deposition on the monochromator. In the external impregnation system, the sample was heated and evaporated into the vacuum chamber through a capillary forming a molecular beam. The formed molecular beam collided with a beam of electrons under single – collision conditions.

3. Results and discussion

On the Figure 2 we present the mass spectrum of the positive ions of the 2,6 – dichloroanisole (DCA) molecule. The mass spectrum of the DCA molecule ranging from 10 to 200 Th was recorded with energy of interacting electrons 70 eV. For some selected processes, we investigated the effective cross section in the area of starting edge and determined the threshold energy values. The threshold energies of the selected fragments are shown in Figure 3.

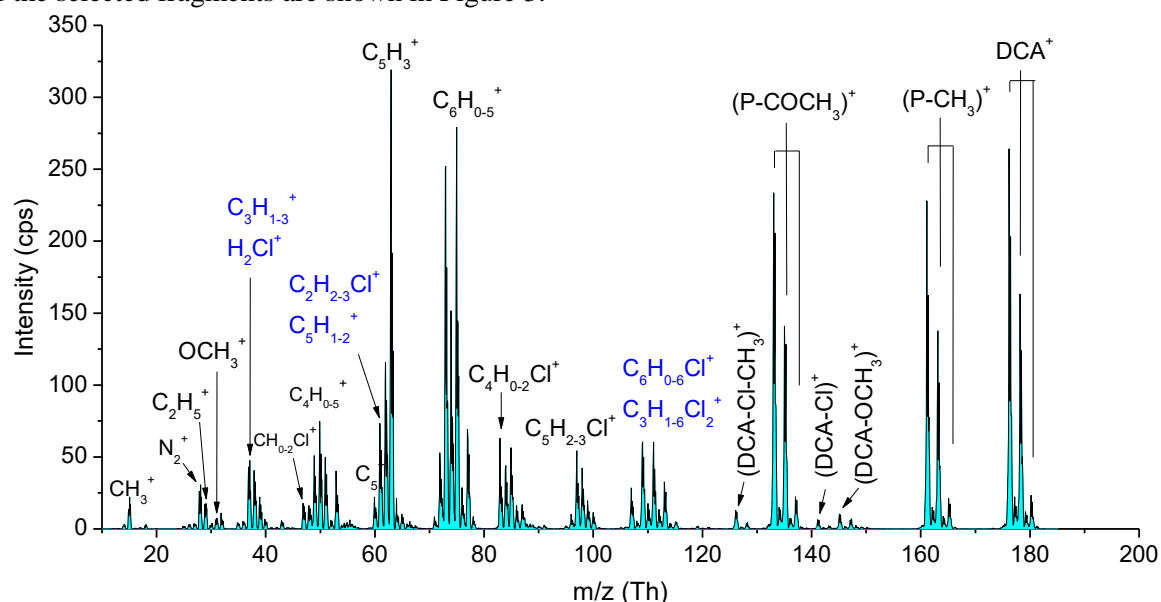


Fig. 2. Mass spectrum of DCA molecule, energy of electrons 70 eV.

In mass spectrum we can observe the significant isotopic character of the molecule, which is due to the presence of chlorine atoms. The fact that we know the isotopic ratios, allows us to significantly better characterization of the individual products that were formed in the processes of the electron ionisation and electron dissociation. Several characteristic sequences can be observed in the spectrum. Such sequences are represented by sequential dissociation of benzene carbon atoms. These sequences occur after partial dissociation of some parts of the molecule. The design of the individual sequences are illustrated in Fig. 2. In the mass spectrum, for the sake of clarity, we have listed the products of the individual positive ions, which differ by one or more hydrogen atoms by the symbol e.g. $H_{0.2}$.

When we progress in the mass spectrum from the largest weight of products we can see the formation of DCA^+ in the mass m/z 176. This product can also be referred as P^+ (Parent) with ionisation energy of 9.32 eV. Subsequently we can see the formation of $(DCA - CH_3)^+$ in the mass m/z 161. The threshold energy was set at 11.55 eV. From the energy difference of the given products we can estimate the dissociation energy value (DE). For the dissociation of CH_3 from the positive molecular ion DCA^+ , $DE(DCA^+ - CH_3) = 2.23$ eV. Interesting is the formation of a positive ion with mass m/z 133 $(DCA - COCH_3)^+$. This process is much more intense than the formation of ions $(DCA - Cl)^+$ and $(DCA - OCH_3)^+$ that can be expected to occur during ionisation. The dissociation energy for the process is about 3.88 eV.

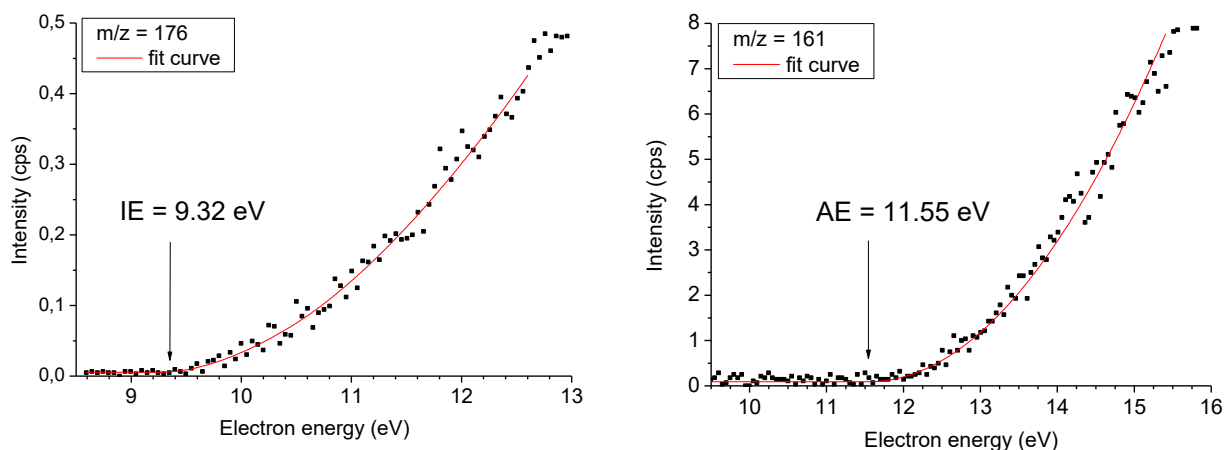


Fig. 3. Area of starting edge of effective cross section for selected processes of the DCA molecule.

Another set of peaks is about the mass m/z 110. From the ratio of intensities is determined that these peaks represent $C_6H_{0.4}Cl^+$ fragments or a combination of $C_6H_{0.4}Cl^+$ and $C_3H_{1.5}Cl_2^+$ fragments. Afterwards we can see the first beginning characteristic sequence with a difference of approximately 12 Th. The peaks represent fragments $C_6H_2Cl^+$, $C_5H_2Cl^+$, $C_4H_2Cl^+$, respectively. This characteristic sequence is immediately followed by another characteristic sequence represented by the products $C_6H_2^+$, $C_5H_2^+$, $C_4H_2^+$. In the mass m/z 61 and 62 is likelihood of formation of four products $C_2H_2.3Cl^+$, $C_5H_{1.2}^+$. Subsequently, on a mass from m/z 37 to m/z 39, there is a set of peaks having a similar property to blue colour labelled products at higher masses represented by $C_3H_{1.3}^+$ products. However, the products at m/z 37 can be assigned not only to C_3H^+ , but also to H_2Cl^+ . The lightest fragment in the mass spectrum is m/z 15, which is CH_3^+ . The most intense peak in the mass spectrum was detected at m/z 63 and it represents fragment $C_5H_3^+$. We claim that we had a well-drained apparatus, as the residual air peaks in mass m/z 28 and 32 have from small to negligibly small intensity.

Tab. 1. Resulting threshold energy values for a specific mass and products of DCA molecule dissociation

m/z (Th)	Product	Threshold	m/z (Th)	Product	Threshold
176	DCA ⁺	9.32	76	C ₆ H ₄ ⁺	12.94
161	(DCA – CH ₃) ⁺	11.55	75	C ₆ H ₃ ⁺	15.25
133	(DCA – COCH ₃) ⁺	13.2	74	C ₆ H ₂ ⁺	16.95
111	C ₆ H ₄ Cl ⁺	14.42	73	C ₆ H ⁺	17.63
	C ₃ H ₅ Cl ₂ ⁺		72	C ₆ ⁺	16.82
110	C ₆ H ₃ Cl ⁺	14.88	63	C ₅ H ₃ ⁺	14.8
	C ₃ H ₄ Cl ₂ ⁺		62	C ₅ H ₂ ⁺	20.06
109	C ₆ H ₂ Cl ⁺	17.00		C ₂ H ₃ Cl ⁺	
	C ₃ H ₃ Cl ₂ ⁺		61	C ₅ H ⁺	19.84
107	C ₆ Cl ⁺	16.5		C ₂ H ₂ Cl ⁺	
	C ₃ HCl ₂ ⁺		48	C ₄ ⁺	17.22
98	C ₅ H ₃ Cl ⁺	13.44		CHCl ⁺	
97	C ₅ H ₂ Cl ⁺	15.3	47	CCl ⁺	21.41
85	C ₄ H ₂ Cl ⁺	15.9	38	C ₃ H ₂ ⁺	22.2
84	C ₄ HCl ⁺	16.81	37	C ₃ H ⁺	23.55
83	C ₄ Cl ⁺	16.45		H ₂ Cl ⁺	

In the Tab. 1. we have demonstrated the resulting threshold energy values of selected DCA dissociation products. In the table, it is interesting to note the products at m/z 63 and at m/z 62 which represents $C_5H_3^+$ and $C_5H_2^+$, respectively. $C_5H_3^+$ is dissociated one hydrogen less than $C_5H_2^+$. Product

$C_5H_3^+$ has lower threshold energy, but the difference between these two threshold energy values is 5.26 eV. This could mean that at m/z 62 may be formed two different fragments, not only $C_5H_2^+$ but also $C_2H_3Cl^+$. At m/z 61 fragment $C_2H_2Cl^+$ could be formed in a similar way. We also used these possibilities in the mass spectrum to determine the probabilities of chemical formulas.

4. Conclusion

In this paper, we have measured the mass spectrum of the 2,6-dichloroanisole molecule and the particular threshold energies for the start edges of the products produced in the electron ionisation and electron dissociation ionisation processes. Subsequently, we have determined what fragment of the DCA molecule is present with the highest probability at given threshold energies and masses. We determined the ionisation energy of the DCA molecule, whose value was set at 9.32 eV.

Acknowledgments: This work was supported by the Slovak Research and Development Agency. Project No. APVV-15-0580 and VEGA project VEGA 1/0417/15. This project has received funding from the European Union's Horizon 2020 research and innovation programme under grant agreement No 692335.

5. References

- [1] Asfandiarov N L, Muftakhov M V, Pshenichnyuk S A, Papp P, Danko M, Lacko M, Blaško J, Matejčík Š and Modelli A 2017 *The Journal of Chemical Physics* **147** 234302.
- [2] Fontana A R and Altamirano C J 2010 *Talanta* **81** 1536–1541.
- [3] Chatonnet P, Bonnet S, Boutou S and Labadie M. D. J. 2004 *Agric. Food Chem.* **52** 1255–1262.
- [4] Juanola R and Subira D 2002 *Journal of Chromatography A* **953** 207.
- [5] Capone D L, Skouroumounis G K and Sefton M A 2002 *Australian J. Grape Wine* **8** 196.
- [6] Juanola R and Subira D 2005 *Eur. Food Res. Technol.* **220** 347.
- [7] Gayon P R, Glories Y, Maujean Y and Dubordieu D 2000 *Handbook of Enology: The Chemistry of Wine and Stabilisation and Treatments* **2** 209.
- [8] Pollnitz A P, Pardon K H, Liacopoulos D and Sefton M A 1996 *Austr. J. Grape Wine Res.* **2** 184.
- [9] Howland P R, Pollnitz A P, Liacopoulos D and Sefton M A 1997 *Austr. J. Grape Wine Res.* **3** 141.
- [10] Tanner H and Zannier C 1983 *Schweiz. Z. Obst-Weinbau* **117** 468.
- [11] Chatonnet P, Guimberteau G, Dubordieu D and Boidron J N 1994 *J. Int. Sci. Vigne Vin.* **28** 131.
- [12] Lichvanová Z, Ilbeigi V, Sabo M, Tabrizchi M and Matejčík S 2014 *Talanta* **127** 239-243.
- [13] Stano M, Matejčík S, Skalný J D and Märk T D 2003 *Journal of Physics B: Atomic, Molecular and Optical Physics* **36** 261.
- [14] WANNIER G. H. 1953 *Phys. Rev.* **90** 817.

DISSOCIATION OF DIMETHYL PHTHALATE MOLECULE INDUCED BY LOW-ENERGY ELECTRON IMPACT

Beáta Feilhauerová¹, Ján Blaško¹, Peter Papp¹, Štefan Matejčík¹

¹FMFI, Comenius University, Bratislava

E-mail: beata.hergelova@fmph.uniba.sk

Experimental investigation of electron ionization of dimethyl phthalate was carried out using crossed electron beam and molecular beam method. We have recorded the mass spectra of positive ions at ~70 eV and ~20 eV and assigned them to possible fragments. For more precise assignment of fragments, calculations of chemical structure are planned. The ionization energy of the parent was estimated to be 9.3 eV, which is lower value than the value of Kuhn 1968 [1] (9.64 ± 0.07 eV) presented on NIST. Appearance energies for some DMP fragments were estimated, too.

1. Introduction

Phthalates are widely used as plasticizers in plastics to provide better flexibility of the material. However, in general phthalates present significant risk for the human health, when they get into human body after they get released from the material and enter human body in higher concentrations (toys for children; drinking water) or in smaller concentration in long term (everyday use of hemodialysis bags) [2]. In order to restrict phthalate release from the material it is necessary to promote the cross-linking process between plastic and the phthalate. It is also difficult to remove phthalates from drinking water [3].

Dimethyl phthalate (DMP) has chemical structure $C_{10}H_{10}O_4$. It has relatively high vapour pressure (4.19×10^{-3} mm Hg at 20 °C) in comparison to other phthalates. DMP is readily absorbed from the skin, intestinal tract, the peritoneal cavity, and lung [4]. Dimethyl phthalate is used as corrosion inhibitor, anti-scaling agents or plasticizer in solid rocket propellants, lacquers, plastics, safety glasses, rubber coating agents, molding powders, insect repellents, and pesticides [2].

Due to health hazard caused by phthalates, there is a need for better understanding of fragmentation processes in various environments. DMP has the most basic structure of all phthalates, therefore it is essential to understand and properly assign the fragments formed after dissociative electron ionization of DMP. Fragmentation of DMP to 5 major fragments was described in [5] and using a tandem mass spectrometry they pointed out it undergoes simpler fragmentation mechanism than other more complex phthalates. Ionization potential of DMP was estimated by Kuhn in 1968 [1] by the thermal electron-capture technique, which might not be sufficiently precise. However, the electron affinities of DMP fragments were not measured yet. Fragmentation of more complex phthalate, such as dicyclohexyl phthalate, was recently studied in our group [6].

2. Experimental setup

For investigation of electron induced processes in DMP an experiment with crossed electron and molecular beam was used (see scheme in Fig.1). The molecular beam source (MBS) was filled with DMP (CAS: 131-11-3, purity > 99%, Sigma Aldrich), where it was evaporated at 45 °C and effused into vacuum by a capillary system. The electrons were produced by a wolfram filament and by means of trochoidal electron monochromator (TEM) only electrons with certain energy were lead into collisional region with the molecular beam from MBS. The positive ions were extracted by a weak electric field from the collisional region into the quadrupole mass spectrometer (QMS), where ions with selected m/z passed through QMS into the channeltron electron multiplier (CEM) detector.

The pressure in the vacuum chamber was during the measurements in range 8×10^{-8} mbar to 1.5×10^{-7} mbar. The apparatus was operated in two different modes. In the first one the mas spectrum was collected at a constant electron energy of ~70 eV and ~20 eV in range from m/z 10 Th to 200 Th. In the second mode, the ion efficiency curves for particular ions with given m/z were measured as a

function of incident electron energy (with a step of ~ 0.03 eV) around the threshold energy of selected ion fragment. The appearance energy (AE) of the selected process after electron ionization was estimated based on the Wannier law [7] with an estimated error of 0.1 eV. For calibration of the kinetic energy of the electrons we used Ar as well-established calibration gas with threshold energy of first ionization energy of 15.76 eV.

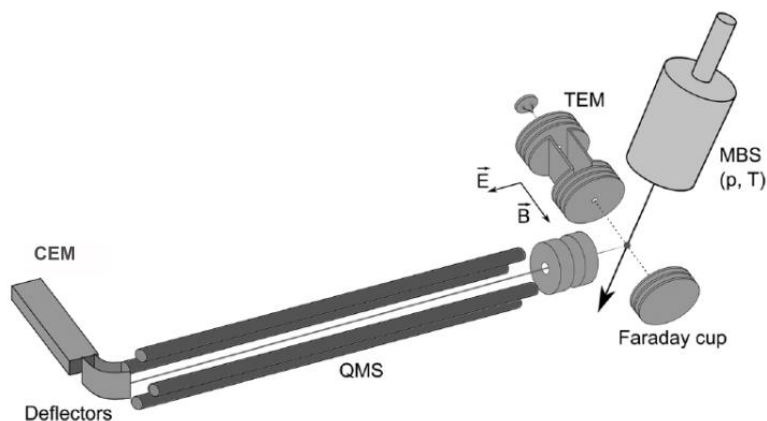


Fig.1. The schema of the electron and molecular cross-beam experiment based on [6].

3. Results

The positive ion mass spectrum of DMP recorded at ~ 20 eV is shown in Fig.2 and at ~ 70 eV in Fig.3. The parent molecular ion (P) with m/z 194 was detected, as well as other fragments identified by Yin [5] with m/z 163, m/z 133, m/z 104 and m/z 77. The DMP ionization energy was estimated to be $9.3 \text{ eV} \pm 0.1 \text{ eV}$ (Fig. 4 - left), which is a lower value than available in NIST database (9.64 eV [1]). This discrepancy is probably due to cut-off of weak signals in case of Kuhn et al. [1]. The fragment with m/z 163 represents the P-OCH₃ fragment of DMP molecule with cleavage of the methoxyl group. The fragment with m/z 164 represents its isotope. Its appearance energy was estimated to be at 10.1 eV. The second fragment with m/z 133 represents P-OCH₃-OCH₂ (removal of two methoxyl groups OCH₂) and hydrogen migration from methoxyl group to the ion. The third fragment with m/z 104 represent dissociation of the ester and the methoxyl group of the DMP molecule P-COOCH₃-OCH₃. The ions with m/z 77 represent the benzene ring (after cleavage of both ester groups of the phthalate) and one hydrogen migration form the ester group to bond with benzene ring. Its threshold appearance energy was estimated to be at 15.8 eV (Fig. 4 - right).

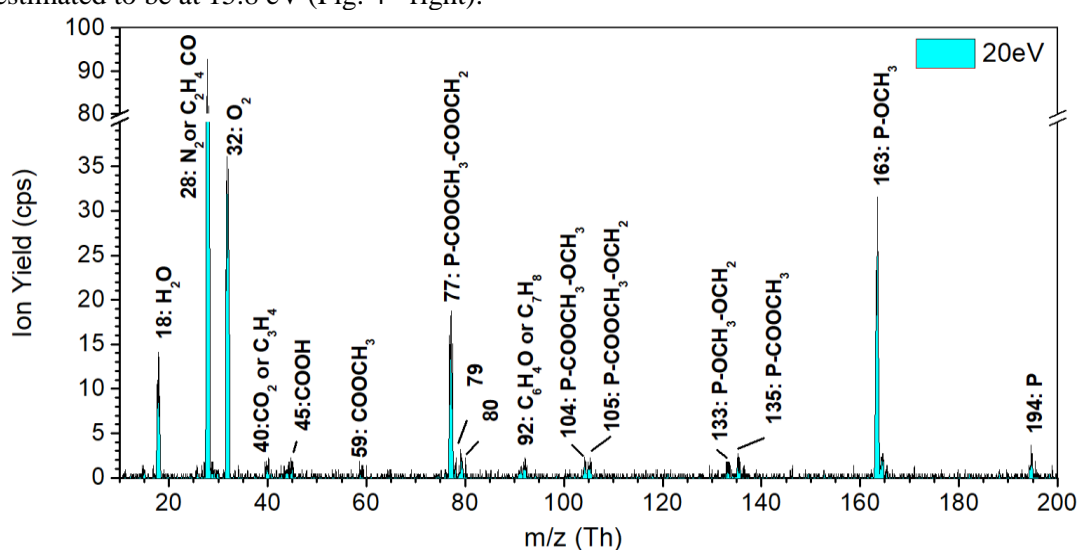


Fig. 2. Mass spectra of DMP molecule at ~ 20 eV.

In the mass spectrum at 20 eV we have observed additional peaks. The peak with m/z 135 should represent the loss of one complete ester side-chain COOCH_3 from DMP molecule. Peak at m/z 105 is formed by hydrogen transfer from neutral fragments to m/z 104 ion ($\text{P-COOCH}_3\text{-OCH}_3$). The peak with m/z 92 is most probably formed by cleavage of hydrogen from $\text{C}_6\text{H}_4\text{O}$ comparable with the fragment with m/z 93 ($\text{C}_6\text{H}_4\text{OH}$) [5]. However, for more precise identification of ions the quantum chemical calculations are planned in the future. This is valid as well for the peaks with m/z 79 and m/z 80, which could be assigned to m/z 77 $\text{P-(COOCH}_3)_2$ after hydrogen transfer or to the ions formed via benzene ring break into compounds like $\text{C}_5\text{H}_3\text{O}$ and $\text{C}_5\text{H}_4\text{O}$, respectively. The fragment with m/z 59 is the positive ion of the ester group COOCH_3 and the fragment at m/z 45 can be assigned to HCO_2^+ ions.

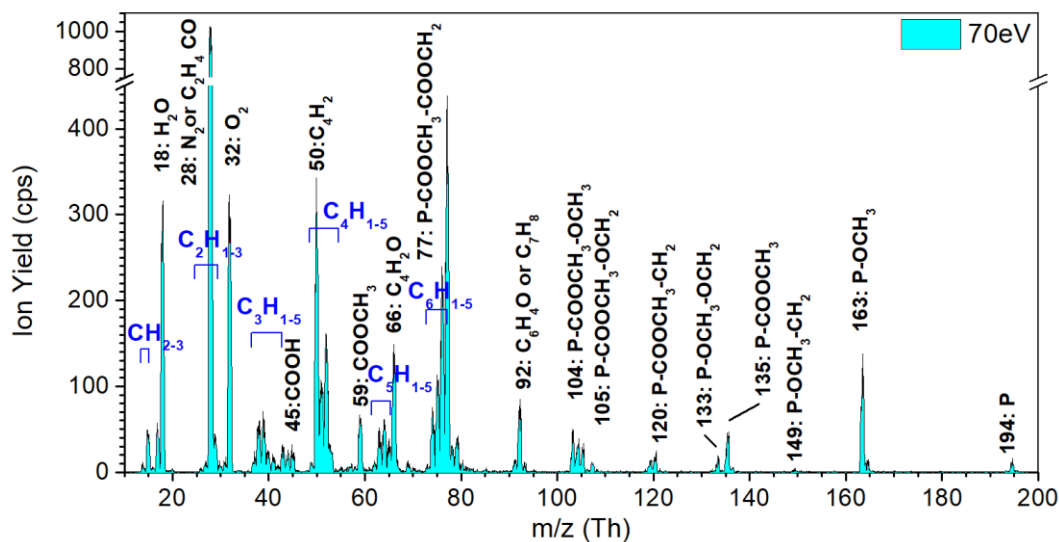


Fig. 3. Mass spectra of DMP molecule at ~ 70 eV.

The spectrum at 70 eV (Fig. 3) is in good agreement with the NIST spectrum. There are new sequences of peaks in the spectrum in comparison to the mass spectrum at 20 eV, these ions required energies above 20 eV for their formation. The peak at m/z 149 should, according to Yin [5], correspond to a DMP molecule without a methoxyl and a methyl group associated by H atom transfer from these neutral fragments to form a hydroxyl group $\text{P-OCH}_3\text{-CH}_2$. Albeit, according to Yin [5] the fragment with m/z 149 should not be present during DMP, we have proven its formation during DMP fragmentation.

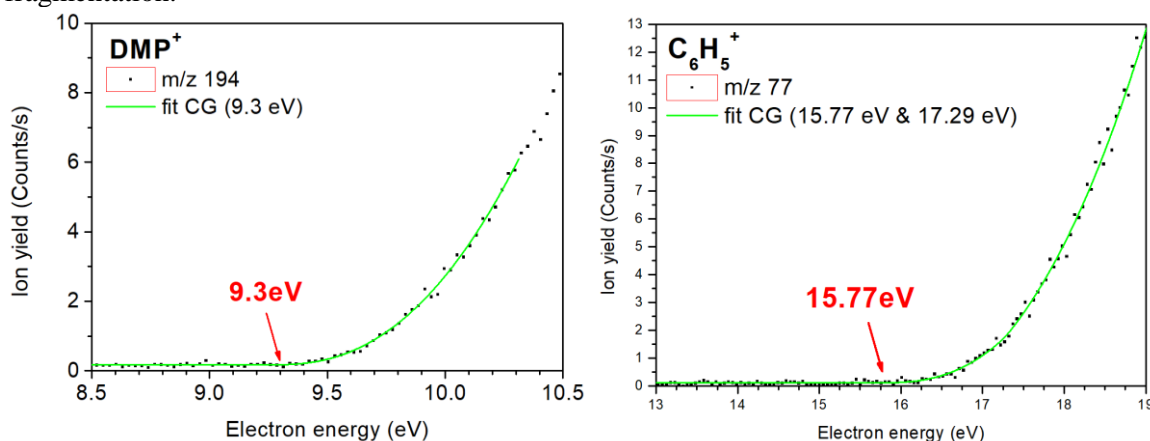


Fig. 4. Region of starting edge of effective cross section of DMP molecule ionization (left) and the process representing loss of both ester groups COOCH_3 (right).

The intensive peak at m/z 77 is part of a sequence of peaks from m/z 73 to 77 corresponding to fragments of benzene ring C_6H_{1-5} (blue in Fig. 3) by the hydrogenation. The ions originating from benzene ring break to smaller fragments (C_5H_{2-5} (m/z 62-65), C_4H_{1-5} (m/z 49-53), and C_3H_{1-5} (m/z 37-41), C_2H_{1-3} (m/z 25-27) and CH_{2-3} (m/z 14-15)), indicated by blue labels (Fig. 3). The new strong ions

m/z 66 we associate to DMP fragment that contains an oxygen atom C_4H_2O , the ion C_5H_6 would need two hydrogen atoms to migrate from side chains what we consider as less probable.

From the ion efficiency curves of the most prominent fragment ions we have estimated the appearance energies (AE) of the ions. The estimated values AE are listed in the Tab. 1.

Tab. 1. Main products of DMP fragmentation and appearance energies of some ions as determined in the present work.

m/z	Product	AE (eV)
194	P	9.3
163	P - OCH_3	10.1
77	P - $COOCH_3$ - $COOCH_2$	15.8
50	C_4H_2	22.2

Acknowledgments: This work was supported by the Slovak Research and Development Agency. Project No. APVV-15-0580. Financing of this work was by the Slovak Grant Agency VEGA 1/0733/17. This project has received funding from the European Union's Horizon 2020 research and innovation programme under grant agreement No 692335.

4. Conclusion

We have studied formation of the positive ions formed by electron ionization of DMP by means of crossed electron and molecular beam experiment. We have measured the mass spectra of the molecule at different electron energies (20 and 70 eV). The measurements at ~ 20 eV already showed most prominent products of DMP fragmentation according to Yin [5]. We recorded the ion efficiency curves in the threshold region of the most dominant fragments and estimated the appearance energies of the ions. The ionization energy of the parent was estimated to be lower (9.3 eV) than the value given by Kuhn [1] in NIST (9.64 eV). DMP shows similar fragmentation paths as other more complicated phthalates. The electron energies above 20 eV were to break down the benzene ring to smaller fragments.

5. References

- [1] Kuhn WW F, Levins R J and Lilly Jr. A C 1968 *Journal of Chemical Physics* **49** 5550.
- [2] <https://www.epa.gov/sites/production/files/2016-09/documents/dimethyl-phthalate.pdf>
- [3] <https://pubchem.ncbi.nlm.nih.gov/compound/8554#section=Cleanup-Methods>
- [4] Bingham E, Cohrssen B and Powell CH 2001 *Patty's Toxicology* Volumes 1-9 5th ed. John Wiley & Sons. New York, N.Y., V6 819.
- [5] Yin P, Chen H, Liu X, Wang Q, Jiang Y and Pan R. 2014 *Analytical Letters* **47**(9) 1579.
- [6] Lacko M, Papp P and Matejčík Š 2018 *The Journal of Chemical Physics* **148** 214305.
- [7] Wannier G H 1953 *Physics Review* **90** 817.

INFLUENCE OF ELECTRIC FIELD ON ION CHEMISTRY OF GLYOXAL

Michal Lacko¹, Felix Piel^{2,3}, Michaela Malásková^{3,4}, Patrik Španěl¹

¹*The Czech Academy of Science, J. Heyrovský Institute of Physical Chemistry, Dolejškova 2155/3, 182 23 Prague, Czech Republic*

²*IONICON Analytik GmbH, Eduard-Bodem-Gasse 3, Innsbruck, Austria*

³*Institute für Ionenphysik und Angewandte Physik, Leopold-Franzens-Universität Innsbruck, Innsbruck, Austria*

³*Institute for Breath Research, University of Innsbruck, Rathausplatz 4, Dornbirn, Austria*

E-mail: michal.lacko@jh-inst.cas.cz

We present an experimental investigation of glyoxal ion chemistry with H_3O^+ reagent ion. Glyoxal represent interesting group of volatiles organic compounds with its proton affinity close to proton affinity of water. Experiments were provided using three different experimental techniques: selected ion flow tube mass spectrometry (SIFT-MS), proton transfer reaction mass spectrometry (PTR-MS) and selected ion flow-drift tube mass spectrometry (SIFDT-MS). The aim of the work is to describe an effect of humidity and electric field on the mentioned ion molecular interaction. In the study we presented influence of high electric field on ion chemistry as well as the importance of the secondary process.

1. Introduction

Glyoxal (OC(H)C(H)O) is in humid environments highly reactive and is presented in many basic biological processes. Glyoxal was associated as a source of oxidation stress [1] or as a part of catalytic reaction formed basic organic molecules in inorganic environment [2]. Moreover, complex organic molecules in the earth atmosphere can be reduced into glyoxal [3].

For experimental investigation using a SCI-MS (Soft Chemical Ionization Mass Spectrometry) is glyoxal interesting type of molecule due to its proton affinity ($\text{PA}(\text{glyoxal}) = 161.41 \text{ kcal/mol}$ to 165.06 kcal/mol) [4] close to PA of water ($\text{PA}(\text{H}_2\text{O}) = 165.15 \text{ kcal/mol}$) [5]. Interaction of glyoxal within SCI-MS widely used H_3O^+ reagent ions is therefore a reversible reaction, strongly dependent on temperature of external electric field. Interaction with H_3O^+ reagent ion should produce protonated glyoxal with m/z 59 [6,7], which can be used for evaluation of glyoxal presence in an environment.

The pilot study of Stöninger et al. [8] provided on proton transfer reaction mass spectrometry (PTR-MS) showed dependence of the with m/z 59 product abundance on humidity and formation of a product with m/z 31 (probably CH_2OH^+).

In the present study we investigated interaction of glyoxal molecule with H_3O^+ using SIFT-MS, PTR-MS and SIFDT-MS experiments at variable humidity conditions. The aim of the work is to fully understand the ion chemistry in the presence of electric field.

2. Methods

The experimental investigation of H_3O^+ reagent ions interaction with glyoxal molecule was carried out using three SCI-MS experiments: selected ion flow tube mass spectrometry (SIFT-MS), proton transfer reaction mass spectrometry (PTR-MS) and selected ion flow drift tube mass spectrometry (SIFDT-MS).

- The SIFT-MS experiments [9,10] were carried out using Profile 3 (Instrument Science, Crewe, UK) instrument. Reagent ions (H_3O^+) generated in microwave discharge in water vapour are selected according to their m/z ratio in the first quadrupole system. The selected ions are then focused into a 5 cm long flow tube and injected into a helium carrier gas (pressure $p = 1.4 \text{ mbar}$, temperature $T = 293 \text{ K}$) where they are thermalized. The diluted glyoxal sample is then introduced at a known flow rate into carrier gas to interact with precursor ions. Formed ion products are then analysed at the end of the flow tube by second quadrupole mass spectrometer.

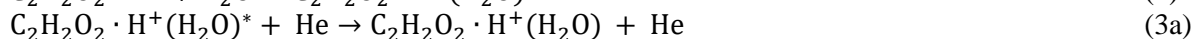
- The PTR experiment is essentially a flow-drift tube CI analytical technique [11,12,13], where ions are generated in a hollow cathode discharge and injected into a flow/drift tube buffered with the sample gas to be analysed, usually air. The ions experience an electric field coaxial with the flow tube and gain energy reaching a drift speed in the field direction and arrive at a downstream orifice where they are sampled into a differentially pumped mass spectrometer system and analysed in an analogous way to that in SIFT-MS.
- The SIFDT-MS experiment extends the selected ion flow tube mass spectrometry, SIFT-MS, by the inclusion of a static but variable E -field along the axis of the flow tube reactor in which the analytical ion-molecule chemistry occurs [14,15,16]. The ion axial speed is increased in proportion to the reduced field strength E/N (N is the carrier gas number density) and the residence/reaction time, t , which is measured by Hadamard transform multiplexing, is correspondingly reduced.

Glyoxal was prepared from 40% glyoxal solution obtained from Sigma-Aldrich Co. Synthesis was based on thermal decomposition of higher glyoxal oligomers used previously [17]. The humidity changes in experiments were provided by controlled injection of water into the sample solution or carrier gas.

3. Results and Discussion

The ion chemistry of main ion products of glyoxal interaction with H_3O^+ reagent ion in field free SIFT-MS experiment is presented in Fig. 1. At low humidity (left part of the Fig. 1 top) we may have observed primary formation of protonated glyoxal ($\text{C}_2\text{H}_3\text{O}_2^+$) with m/z 59 as was predicted by previous publications [6,7]. Increase of humidity however lead to formation of fragment with m/z 31, probably representing protonated formaldehyde (H_2COH^+). The formation become dominant at high humidity levels.

Using a basic modelling of ion molecular kinetics, and following analysis uncovered two-step process leading to formation of protonated formaldehyde (Eq. 1-3). The process requires formation of glyoxal water cluster, which has excess of Gibbs free energy and its unstable. Collision with carrier gas may stabilize the molecule into a stable protonated glyoxal water cluster. Otherwise system dissociates into the protonated formaldehyde and formic acid.



In PTR-MS experiment, homogenous electric field provided additional collisional energy to reagent. This is mainly used to reduce the hydronium cluster formation and thus enhanced sensitivity of the instrument. Additional reaction energy accelerating proton transfer from H_3O^+ to glyoxal according to Arrhenius equation. Ion chemistry at 130 Td showed in Fig. 1 bottom however differ from field free interaction observed in SIFT-MS experiment. At low humidity, formation of protonated formaldehyde is dominant. For increasing humidity, fragmentation becoming suppressed and formation of protonated glyoxal is increasing.

The observation shows that secondary dissociation observed for field free SIFT-MS conditions is not important. Dominant are probably primary processes forming protonated formaldehyde by direct collisional induced dissociation (assisted with proton transfer reaction) of H_3O^+ reagent ion on neutral glyoxal.

The decrease of the fragmentation with humidity is however interesting. This effect may be caused for example by reduction of the ion velocity traveling in the drift tube by collisions with water molecules. The SIFDT-MS experiment provided insight to the energetics of the interaction, using Hadamard modulation to estimate ion velocity, from where the interaction energy between reagent ion and neutral can be calculated as

$$E_r = \frac{m_r}{m_r+m_i} \left(\frac{1}{2} m_i v_d^2 + \frac{1}{2} m_c v_d^2 \right) + \frac{3}{2} kT, \quad (4)$$

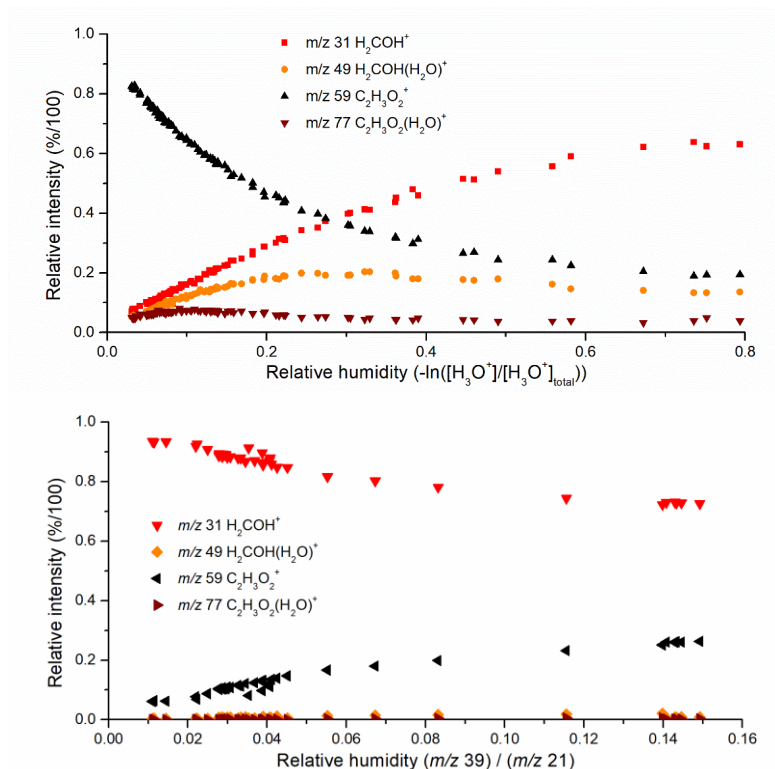


Fig. 1. Relative intensities of glyoxal product ions obtained using H_3O^+ reagent ion, provided by two different experiments as a function of humidity. The top graph represents the field free experiment provided by SIFT-MS, while the bottom graph was provided by PTR-MS at $E/N = 130$ Td. The x-axis in both graphs represents changes of the humidity in the system, growing from left to right. Calculation of humidity differ between experiments, but still representing ratio of primary H_3O^+ ions to its higher water clusters, which are formed as second order reactions with water molecules. The opposite trend in the formation of m/z 31 and m/z 59 between two experiments is clearly visible.

where m_i is mass of a reagent ion, m_r is mass of a reagent neutral, m_c is mass of carrier gas, v_d is ion drift velocity, k is Boltzman constant and T is temperature [14]. The equation can be modified to provide calculation of interaction energy between ions and carrier gas molecules as

$$E_r = \frac{m_c}{m_c + m_i} \left(\frac{1}{2} m_i v_d^2 + \frac{1}{2} m_c v_d^2 \right) + \frac{3}{2} kT. \quad (5)$$

Study of ion kinetic between H_3O^+ reagent ion and glyoxal is presented on Fig. 2. Here, the product ion ratio is presented as function of reaction energy calculated according to Eq. 4. The graphs in the Fig. 2 shows increasing level of humidity. For low energy conditions results agree with observations provided by SIFT-MS, while for high interaction energy results agree with observations provided by PTR-MS.

Fig. 3 then shows difference in reaction energy of H_3O^+ reagent ion interacting with neutral glyoxal between dry and very wet humidity levels. The energy difference is comparable with thermal energy of ions, becoming more important for high field conditions.

Finally, we provided investigation of possibility of eventual secondary processes in PTR-MS. Here, protonated glyoxal dissociating on carrier gas. For this experiment we injected glyoxal into the plasma source of SIFT-MS and we measured the ion velocity of formed ion. Results are presented on Fig. 4 left, where we can compare the reaction energy between ions with He carrier gas. Data shows, the interaction energy of protonated glyoxal with the carrier gas (app. 0.14 eV at 90 Td) to be lower than interaction energy of H_3O^+ ions interacting with neutral glyoxal (app. 0.88 eV at 90 Td). The effect of

humidity on ion velocity of protonated glyoxal is showed on Fig. 4 right. The energy shift is comparable with the one observed for H_3O^+ ions presented in Fig. 3.

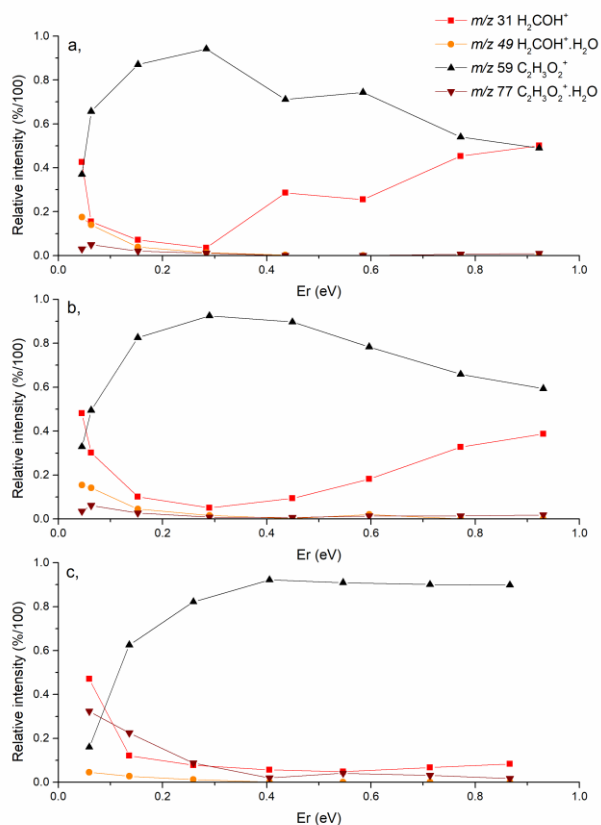


Fig. 2. Product branching ratios of glyoxal interacting with H_3O^+ reagent ion provided by the SIFDT-MS in He carrier gas. The x-axis represents the interaction energy of the H_3O^+ reagent ion with neutral glyoxal during the primary reaction calculated according to the Eq. 4. The top figure (a) represents dry conditions, the middle figure (b) represents wet (0.5 ml of liquid water diluted in 10 l of He) and the bottom figure (c) stands for very wet conditions (5 ml of liquid water diluted in 10 l of He).

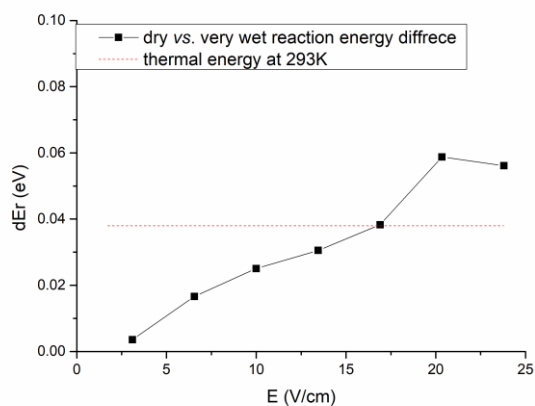


Fig. 3. The difference in reaction energy of the H_3O^+ reagent ion interacting with glyoxal in He between dry and very wet conditions (5 ml of liquid water diluted in 10 l of He). The energy change is compared with thermal energy at 293 K.

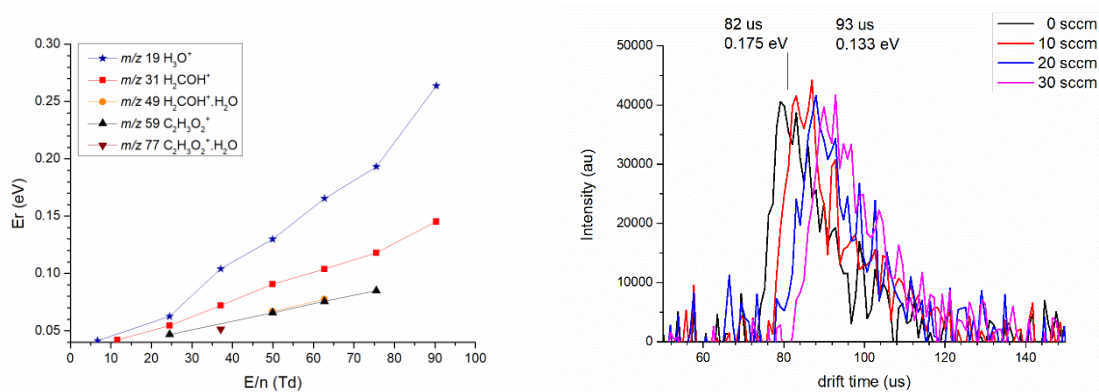


Fig. 4. Left – evolution of ions collisional energy with dry He carrier gas provided at 293 K and 1.1 Torr calculated according to the Eq. 5. Right – effect of humidity in the drift-flow tube on the time profile of the protonated glyoxal ion drift velocity and the collisional energy at ~ 63 Td. The humidity was changed by injecting defined amount of humid He (5 ml of liquid water diluted in 10 l of He) into the flow drift tube.

4. Conclusion

In the study we investigated the ion chemistry of glyoxal with H_3O^+ reagent ion at variable electric field and variable humidity. The experiments were carried out using three different experimental techniques: SIFT-MS, PTR-MS and SIFDT-MS. Results showed significance of secondary processes on glyoxal ion chemistry for field free conditions. For experiments containing homogeneous electric field we observed opposite effect, probably caused by combination of collisional induced dissociation and proton transfer reaction of reagent H_3O^+ ion with neutral glyoxal molecule. To complete the understanding of ion chemistry, we estimated ion drift velocities and calculated reaction energies between ions and neutrals presented in the drift tube for He carrier gas. The results show that primary reaction of H_3O^+ reagent ion with neutral glyoxal carrying more energy than protonated glyoxal interacting with He carrier gas.

5. Acknowledgment

This project has received funding from the European Union's Horizon 2020 research and innovation programme under the Marie Skłodowska-Curie grant agreement No 674911.

6. References

- [1] Manini P, d'Ischia, M 2015 *Aldehydes As Markers of Redox Imbalance in Fanconi Anemia and in Other Oxidative Stress-Related Disorders*. *FANCONI ANEMIA AND OXIDATIVE STRESS*, Nova Science Publishers, New York, p. 69.
- [2] Shkrob I. A, Marin T W, He H, Zapol P *Jour. Phys. Chem. C* **116** 9450-9460.
- [3] Volkamer R., Platt U, Wirtz K, 2001 *J. Phys. Chem. A* **105**, 7865–7874.
- [4] Wróblewski T, Ziemczonek L, et al. 2007 *Europ Phys J Spec Topics*, **144** 191-195.
- [5] NIST WebBook Chemie, Standard referenjcce database number 69, cited in January 2018. <http://webbook.nist.gov/chemistry/>
- [6] Williams J, Pöschl U, et al. 2001 *J Atm Chem*, **38** 133-166.
- [7] Knighton W B, Rogers T M, et al. 2007 *J Prop Power*, **23**(5), 949-958.
- [8] Stöninger C, Derstroff B, et al. 2017 *J. Mass Spec.*, **52** 30-35.
- [9] Španěl P, Smith D 1996 *Med Biol Eng Comput* **34** 409.
- [10] Španěl P, Dryahina K, Smith D 2006 *Int J Mass Spectrom* **249** 230.
- [11] Lindinger W, Hansel A, Jordan A 1998 *Int J Mass Spectrom Ion Process* **173** 191.
- [12] Blake R S, Monks P S, Ellis A M 2009 *Chem Rev* **109** 861.
- [13] de Gouw J, Warneke C 2007 *Mass Spectrom Rev* **26** 223.
- [14] Spesyvyi A, Smith D, Spanel P 2017 *Phys Chem Chem Phys* **19** 31714.
- [15] Spesyvyi A, Sovova K, Spanel P 2016 *Rapid Commun Mass Spectrom* **30** 2009.
- [16] Spesyvyi A, Smith D, Spanel P 2015 *Anal Chem* **87** 12151.
- [17] Guimbaud C, Catoire V, et al. 2017 *Int J Mass Spectrom* **263** 276-288.

LOW ENERGY ELECTRON ATTACHMENT TO OCTAFLUOROCYCLOBUTANE MOLECULES AND CLUSTERS

Dušan Mészáros, Peter Papp, Štefan Matejčík

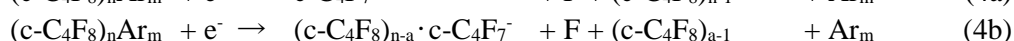
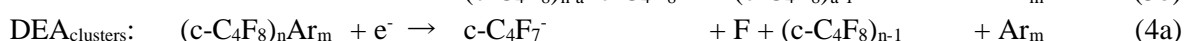
Department of Experimental Physics, Faculty of Mathematics, Physics and Informatics, Comenius University in Bratislava, Mlynská dolina, 842 48 Bratislava, Slovakia

E-mail: peter.papp@uniba.sk

We present low energy electron interaction studies of a precursor $c\text{-C}_4\text{F}_8$ in Plasma Enhanced Chemical Vapour Deposition (PECVD) and in the alternative Deep Reactive-Ion Etching (DRIE) spraying technology. The electron attachment (EA) and dissociative electron attachment (DEA) will be compared in the gas phase and in the molecular clusters measured with the CLUSTER-ILN experiment. The cluster experiment of that molecule was performed for the first time. EA and DEA resonances were measured at energy ranges ~ 0 eV, ~ 4 eV, ~ 8 eV and ~ 11 eV, most of these channels acting as core excited processes for formation of DEA products. The 0 eV resonance is open exclusively for the molecular ion only, but in the clusters the higher energy resonances are accessible as well. A two-step process of formation of the molecular ion via electron self-scavenging and ring opening will be described.

1. Introduction

Interaction of low energy electrons with molecules and molecular clusters is one of the elemental processes in plasma and plasma technologies. In our study we are focusing on electron attachment (EA) and dissociative electron attachment (DEA) on octafluorocyclobutane ($c\text{-C}_4\text{F}_8$). $c\text{-C}_4\text{F}_8$ is used as precursor gas in Plasma Enhanced Chemical Vapour Deposition (PECVD) and Deep Reactive-Ion Etching (DRIE). It's well known about $c\text{-C}_4\text{F}_8$ that it has strong EA on parent molecule at electron energy 0 eV, which can be used for calibration of electron energies in electron beam experiments. The CLUSTER-ILN experiment [1] (Fig. 1) was used to measure the electron molecular and cluster interactions, with a trochoidal electron monochromator ($\sim 150\text{-}300$ meV measured at FWHM of the SF_6^- peak) and quadrupole mass analyser for identifying the charged products of electron impact, both in a perpendicular orientation. We use an external bottles to prepare the mixture of $c\text{-C}_4\text{F}_8$ and Ar gas, in this experiment ~ 500 mbars of $c\text{-C}_4\text{F}_8$ and ~ 5 bars of Ar, which is then introduced into the vacuum via $80\ \mu\text{m}$ nozzle placed in the expansion chamber, where the cooling of the gas via supersonic expansion performs and a beam of molecular clusters is separated with the skimmer (0.8 mm) into the reaction chamber. The gas phase results reported in this paper were obtained from electron molecular interactions directly in the reaction part of the electron monochromator. EA and DEA were measured on $c\text{-C}_4\text{F}_8$ in gas phase and on $(c\text{-C}_4\text{F}_8)_n\text{Ar}_m$ clusters. Only the most intensive cluster products such as F^- , $c\text{-C}_4\text{F}_7^-$ and $c\text{-C}_4\text{F}_8^-$ were studied both in gas phase as well as in clusters. These processes are listed below.



Low energy electron (0-20 eV) reactions with molecules and clusters may perform scattering, attachment, excitation and ionization reactions. From all of those possibilities we are studying at the Comenius University in Bratislava ionisation reactions, specifically the formation of negative ions. In

this work we have performed measurements of electron attachment to molecules (1), clusters (3a) and (3b) and corresponding dissociative electron attachment (reactions (2), (4) and (5)). Although we can see some products in the gas phase and cluster (like (1) and (3a)), the process formation of these products can differ significantly, which will be discussed in this work as well.

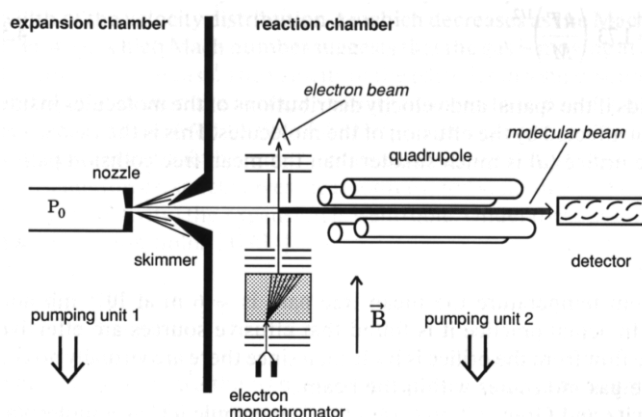


Fig. 1. The schema of CLUSTER-ILN experiment [1] experiment built at the Freie Universität Berlin and recently moved to the Comenius University in Bratislava.

2. Dissociative electron attachment to *c*-C₄F₈ in gas phase

At the beginning of the presented studies we have performed the measurements of electron attachment to *c*-C₄F₈ in the gas phase only and compared these results with the previously published [2-4], they are summarized in Table 1. All reported fragments are in good agreement with works of Harland [2] and Feil [3] and energy positions of negative ion states given by Christophorou [4]. All fragments have in common the strongest resonance from 3 eV to 5 eV. F⁻, CF₃⁻, C₂F₃⁻, F₂⁻, CF₂⁻, C₃F₅⁻ have the main resonance followed by two high energy resonances around 8.5 eV and around 11 eV. Electron affinities for all fragments and parent ion are listed in Tab. 1.

Tab 1. The gas phase DEA products of *c*-C₄F₈, peak positions of the resonances, electron affinities EA of the neutral counterparts.

Ion	Neutrals	Peak Position [eV]		Gas ph.	EA of neutrals [eV]
		[2]	[3]		
F ₂ ⁻				0.42	3.0 [5]
	+ <i>c</i> -C ₄ F ₆	4.95		4.79	
	+ C ₂ F ₂ + C ₂ F ₄	8.50		8.38	
	+ C ₂ F ₂ + 2CF ₂	10.40		10.84	
CF ₂ ⁻	+ CF ₂ + C ₂ F ₄	4.95		4.59	0.18 [6]
	+ 3CF ₂	8.80		8.38	1.30 [2]
	+ C ₂ F ₄ + CF + F	11.20		11.23	
CF ₃ ⁻	+ C ₃ F ₅	4.95	4.8 9.5, 12.0	4.64 8.43, 11.08	2.1 [7]
C ₂ F ₃ ⁻			4.9, 7.9, 9.3, 12.3	4.74, 8.58, 11.13	2.0 [7]
C ₂ F ₅ ⁻				0.63, 2.89	
C ₃ F ₅ ⁻	+ CF ₃		2	1.84	2.99 [8]
	+ CF ₂ + F	4.35	4.1	3.95 7.94	

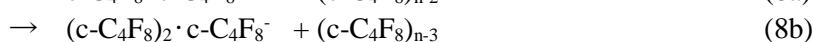
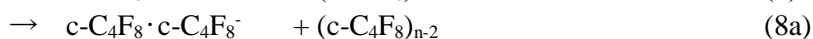
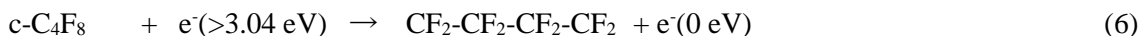
3. Dissociative electron attachment to c-C₄F₈ clusters

In this chapter we will discuss the common features and main differences of our gas phase and cluster measurements of the formation of molecular ion c-C₄F₈⁻ and its main cluster products c-C₄F₇⁻ and F⁻. As the common feature, the formation of molecular ion and its dimer or trimer clusters is dominantly a low energy process with a strong resonance ~0 eV. The higher energy resonances 4.4 eV, 8.6 eV, 11.9 eV or 15.5 eV (Tab. 2) identified for the gas phase DEA products remain opened in the clusters as well. However these higher energy resonances were not seen in the gas phase measurement of molecular ion. Moreover, the 0 eV resonance is decreasing in favour of the resonance at 0.45 eV in the cluster measurements (Fig. 2). The most of these higher energy resonances of the parent ion and its fragments have origin in core excited processes, they can be associated with the excited states of neutral c-C₄F₈ [11]. Except the resonance at 4.4 eV which has no explanation via an excitation process of c-C₄F₈ as its first excited states lies above 8 eV [11]. Only higher energy resonances were measured for c-C₄F₇⁻ and its clusters unlike at gas phase (Tab. 2) where only one resonance at 3.46 eV has been measured. Higher energy resonances were more propagated with increasing number of molecules in the cluster with F⁻ fragment (Fig. 2). The ratio of ion yields between 4.6 eV and 8.2 eV has changed with the increasing size of cluster significantly. Formation of fragments F⁻ and c-C₄F₇⁻ is a competitive process, its efficiency should depend on the electron affinities of the corresponding fragment products, which are listed in Tables 1 and 2.

Tab 2. The gas phase and cluster EA to c-C₄F₈ and DEA to c-C₄F₇⁻ and F⁻, peak positions of the resonances, electron affinities EA of the neutral counterparts.

Ion	Neutrals	Peak Position [eV]				EA of neutrals [eV]
		[2]	[3]	Gas ph.	Clusters	
F ⁻	+ c-C ₄ F ₇			2.53		3.4 [9]
	+ F + c-C ₄ F ₆	4.95	4.7	4.40	4.6	
	+ CF ₂ + C ₃ F ₅	7.40	6.9	7.03	8.2	
	+ C ₂ F ₃ + 2CF ₂	8.60	8.2	8.04	10.9	
	+ CF + 3CF ₂	10.80	10.6	10.48		
c-C ₄ F ₇ ⁻	+ F			3.46	8.5, 11.7, 15.0	
c-C ₄ F ₈ ⁻			0.0	0.0	0.5, 4.4, 8.6,	0.63 [10]
		0.45		0.45	11.9, 15.5	

Resonance at 4.4 eV occurring in the cluster measurements of molecular ion and its dimer and trimer remains unexplained as it has no background from any excitation process. We have found an explanation via ring opening of the neutral c-C₄F₈ Initiated with electron of kinetic energy higher than 3 eV (6). A neutral biradical and an electron with kinetic energy ~0 eV are formed then. Only in the cluster environment this electron can be attached with a neighbouring c-C₄F₈ molecule(s) and form the molecular negative ion (7) or its dimer and trimer (8a and 8b). This process is called self-scavenging of electrons. Threshold energy was calculated via MP2/def2-TZVP and result was 3.04 eV. Which agrees with experimental data.



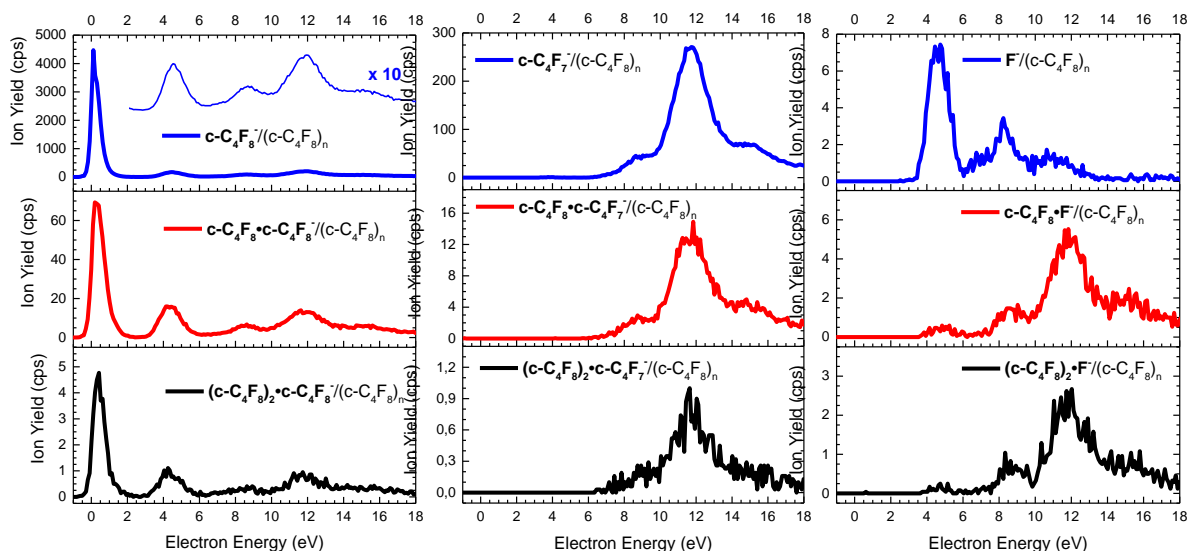


Fig. 2. Energy dependence spectra of the ions $c\text{-C}_4\text{F}_8^-$, $c\text{-C}_4\text{F}_7^-$ and F^- formed via EA to $c\text{-C}_4\text{F}_8$ clusters (top), with one (middle) and two (bottom) parent molecules in a cluster.

4. Conclusion

The electron attachment and dissociative electron attachment to gas phase octafluorocyclobutene molecule and its clusters were performed. The energetical profile of formation of the gas phase DEA products, the electron affinities of most of the neutral fragments and the neutral $c\text{-C}_4\text{F}_8$ were already known. We have found a good agreement of the gas phase results with those previously published data. From the point of view of larger environments like higher pressure plasmas or aggregates the cluster measurements bring new previously not published data. We have performed a comparison of gas phase and cluster ion yields of the molecular ion and its dimer and trimer clusters and the same for the most abundant products coupled with ions $c\text{-C}_4\text{F}_7^-$ and F^- . We have described the possibility of formation of the molecular ion and its cluster via higher energy resonances and especially the resonance at ~ 4 eV via a two-step reaction associated with a ring opening in neutral molecule and EA of electron with lost energy to a neighbouring molecule.

5. Acknowledgments

This project has received funding from the European Union's Horizon 2020 research and innovation programme under grant agreement No 692335. This work was supported by the Slovak Research and Development Agency contract no. APVV-15-0580 and the Slovak Grant Agency for Science contract no. VEGA 1/0733/17.

6. References

- [1] Ingolfsson O., Weik F., Illenberger E., *Int. J. Mass. Spec.*, **155**, (1996), 1.
- [2] P. W. Harland, et al., *Int. J. of Mass Spectrom. Ion Phys.*, **10**, (1972), 11.
- [3] S. Feil, et al., *Int. J. Mass. Spectrom.*, **277**, (2008), 41.
- [4] L. G. Christophorou, et al., *J. Phys. Chem. Ref. Data*, **30**, (2001), 449.
- [5] P. G. Wenthold, et al., *J. Phys. Chem.*, **99**, (1995), 2002.
- [6] R. L. Schwartz, et al., *J. Phys. Chem. A*, **103**, (1999), 8213.
- [7] J. C. J. Thynne, et al., *Int. J. Mass. Spectrom. Ion Phys.*, **5**, (1970), 329.
- [8] I. Sauers, et al., *J. Chem. Phys.*, **71**, (1979), 3016.
- [9] C. Blondel, C., *J. Phys. B: Atom. Mol. Opt. Phys.*, **34**, (2001), L281.
- [10] T. M. Miller, et al., *J. Chem. Phys.*, **120**, (2004), 7024.
- [11] T. Nakamura, et al., *Jpn. J. Appl. Phys.*, **40** (2A), (2001), 847.

EXCITATION OF WATER INDUCED BY ELECTRON IMPACT

Juraj Országh¹, Dennis Bodewits², Barbora Stachová¹, Štefan Matejčík¹

¹*Department of Experimental Physics, Comenius University in Bratislava, Slovakia*

²*Department of Physics, Auburn University, Alabama, USA*

E-mail: juraj.orszagh@uniba.sk

Electron induced excitation reactions of water were studied by means of optical emission spectroscopy in the spectral range between 200 nm and 800 nm in crossed beams experiment. Excited water cation H_2O^+ , fragments OH, OH^+ and H and O were identified in the spectrum. For most intensive transition the cross sections and threshold energies were determined.

1. Introduction

Electron induced processes are abundant in various environments from space, planetary atmospheres through industry to laboratory. In astrophysics using the optical emission spectroscopic methods they can act as remote probe of physical properties of environments since every molecule or atom has a unique spectrum.

Analysis of the data from the Rosetta mission to comet 67P/Churyumov-Gerasimenko shown that the emission from the comet coma is induced mostly by electron impact outside the 2 AU pre-perihelion [1]. The emission fades if the comet is within 2 AU of the Sun. The effect can be caused by increased concentration of water in the coma leading to different energy distribution of electrons [2]. To assess such effect, it is necessary to thoroughly study the electron impact fluorescence of water including the cross sections in laboratory conditions as current data are incomplete or insufficient.

2. Experiment

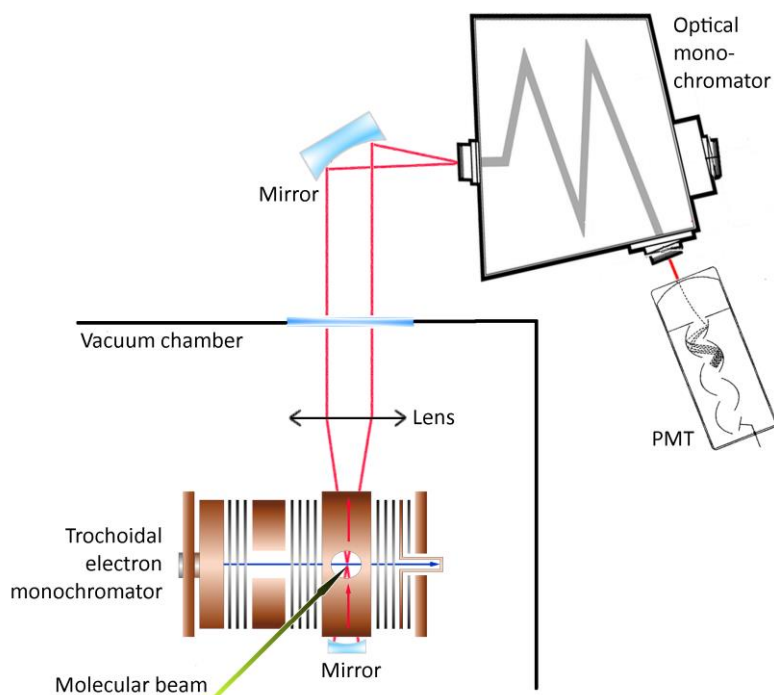


Fig. 1. Experimental apparatus

The apparatus used for the experiment was described in detail in previous publication [3] and is schematically depicted in figure 1. It utilized crossed beams configuration. The sources of electron (trochoidal electron monochromator) and molecular beams (effusive capillary) are in a vacuum chamber with background pressure of $\sim 10^{-8}$ mbar. The experiments were carried

out at $\sim 1.5 \times 10^{-4}$ mbar. We have checked the linearity of the spectral line intensities on the pressure so that the single collision conditions were maintained [4]. The fluorescence radiation was collected by an optical system located perpendicularly to the crossing beams which focused the fluorescence signal onto the entrance slit of the Oriel Cornerstone 260 Czerny-Turner $\frac{1}{4}$ m optical monochromator. After passing through the optical monochromator, the signal was detected by a low-noise, Peltier-cooled photomultiplier working in the photon counting regime. The measurement was done in two modes: spectral measurement at constant electron energy or cross section measurement at specific wavelength corresponding to one deexcitation. The energy of the electron beam was absolutely calibrated by introducing a mixture of N_2 and H_2O into the apparatus and by measuring the intensity profile of the N_2 ($C^3\Pi_u-B^3\Pi_g$)(0-0) band at 337 nm which exhibits relatively sharp maximum at 14.1 eV [5] and intensity profile of H_β line. Subsequently the profile of H_β line was aligned with the same measurement in pure water vapours to calibrate the electron energy.

3. Results and discussion

The spectral region between 200 nm and 900 nm has been studied. The spectrum shown in the figure 2 is corrected for the spectral sensitivity of the experimental device. In the spectrum measured at electron energy 50eV the emission corresponding to deexcitation of atomic hydrogen (Balmer series), OH ($A^2\Sigma^+-X^2\Pi$), OH⁺ ($A^3\Pi-X^3\Sigma^-$) and H₂O⁺ ($\bar{A}^2A_1-X^2B_1$) have been detected. The spectral bands corresponding to OH, OH⁺ and H₂O⁺ were identified according to the [6] and [7].

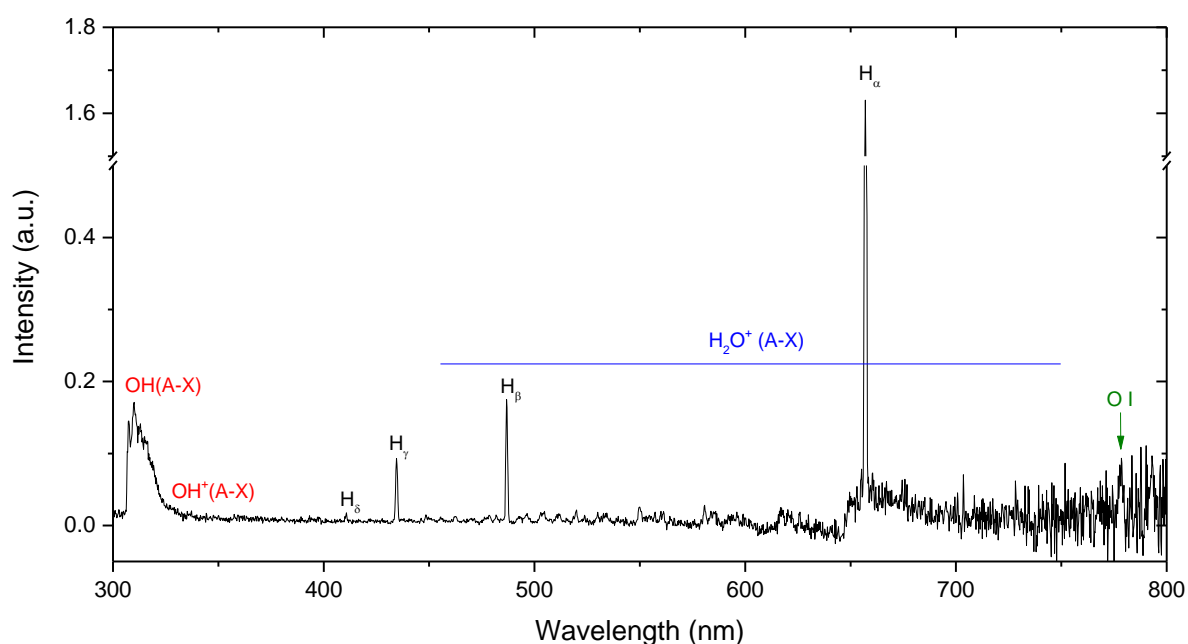


Fig. 2. Emission spectrum of water induced by 50 eV electrons impact.

In the spectral region above 800 nm no line nor band has been identified. One of the reasons can also be relatively low detector sensitivity. The O I ($3s^5S^0 - 3p^5P$) at 777 nm line is very faint, almost hidden within the detector noise. The detail of the OH (A-X) transition is shown in the figure 3 including the region below 300 nm. All the detected water cation band correspond to the various vibrational transitions of H₂O⁺ (A-X) and are present between 450 nm and 750 nm.

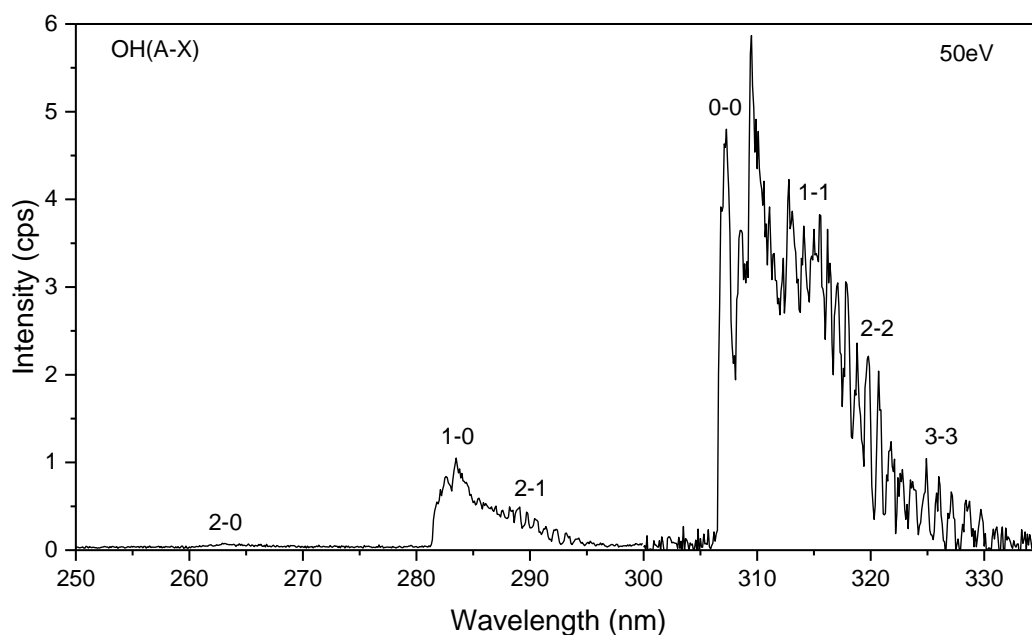


Fig. 3. Emission spectrum showing the detail of OH (A-X) transition measured at 50 eV electrons impact.

Apart from the spectral measurement the cross sections for the most intensive transitions were determined as well. The curves for Balmer's series were measured for transition H (3-2) to H (7-2). For each cross section the threshold energy was determined by simple fitting procedure. These values were compared to theoretical thresholds based on enthalpy of formation. The cross section curve for H (4-2) transition is shown in the figure 4.

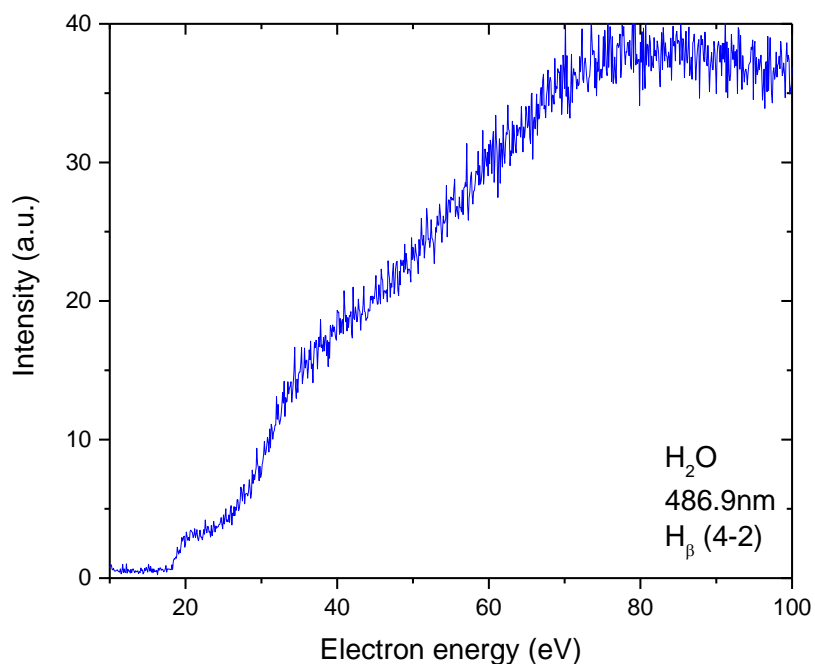


Fig. 4. Cross section curves of OH (A-X), OH+ (A-X), H2O+ (A-X) and H (4-2) transitions.

From the curve shape it is evident that there are three distinct thresholds. These correspond to different generation channels of excited hydrogen atoms in the electron-molecule reaction. Similar shape can be seen in case of other Balmer's series lines as well.

Acknowledgments

This work was supported by grant agency VEGA project nr. 1/0733/17; Slovak research and development agency project nr. APVV-15-0580.

This project has received funding from the European Union's Horizon 2020 research and innovation programme under grant agreement No 692335.

4. References

- [1] Feldman P D et al. 2015 *Astronomy and Astrophysics* **583** A8.
- [2] Bodewits D et al. 2016 *The Astronomical Journal* **152**, 130.
- [3] Danko M et al. 2013 *Journal of Physics B: Atomic, Molecular and Optical Physics* **46** 045203.
- [4] Filippelli A R et al. 1994 *Advances in Atomic, Molecular, and Optical Physics* **33** 1.
- [5] Orszagh et al. 2012 *Nucl. Inst. Meth. B* **279** 76.
- [6] Müller U et al. 1993 *Z. Phys. D* **25** 167.
- [7] Tsuji M et al. 1988 *Chem. Phys. Lett.* **147** 6.

THE PROTON AFFINITIES OF DIMETHYL PHTHALATE ISOMERS

Peter Papp, Bartosz Michalczuk, Ladislav Moravský, Štefan Matejčík

Department of Experimental Physics, Faculty of Mathematics, Physics and Informatics, Comenius University in Bratislava, Mlynská dolina F2, 84248 Bratislava, Slovakia

E-mail: peter.papp@uniba.sk

Three different isomers of dimethyl phthalate – DMP (ortho - isomer), dimethyl isophthalate – DMIP (meta) and dimethyl terephthalate – DMTP (para) were studied with Atmospheric Pressure Chemical Ionisation (APCI) and theoretically with quantum chemical methods. Using the Ion Mobility Spectrometry (IMS) the molecules were chemically ionized by reactant ions $H^+ \cdot (H_2O)_n$ ($n=3$ and 4). Clusters of ions $M \cdot H^+ \cdot (H_2O)_n$ with different degree of hydration ($n=0,1,2,3$) for different isomers were observed. The DFT and MP2 calculations of the structures and energies of the neutral and protonated isomers (for different conformers) were obtained and the corresponding proton affinities (PA) were calculated. In the case of DMP isomer, almost exclusive formation of $M \cdot H^+$ indicated conformer selectivity of the ionisation process.

1. Introduction

Phthalates are widely used as plasticizers in rigid polymers (PVC) [1] and can be found in many consumers products like toys, pharmaceuticals, food packaging, cosmetics and others. The contamination of the water and whole environment can be therefore dangerous, many of the phthalates are potentially risky for the human health. Therefore there is a need of development of analytical methods for detection of phthalates in the materials used as well as in the environment directly. Different analytical techniques have been involved in the investigation of phthalates, high performance liquid chromatography (HPLC) or gas chromatography - mass spectrometry (GC-MS) were used to determinate phthalates in industrial emissions and food samples [2, 3], HPLC–atmospheric pressure chemical ionization tandem mass spectrometry system (HPLC–APCI-MS/MS) [4], Liquid Chromatography–Atmospheric Pressure Chemical Ionization–Mass Spectrometry (LC-APCI-MS) [5]. Although there is a lot of data known about many compounds, some can be still lacking, or many of the analytical methods mentioned above can be complicated for sample preparation and time consuming for the analysis [6]. Recently in our group at Comenius University in Bratislava we have used for detection of the three dimethyl phthalate isomers the technique of Ion Mobility Spectrometry which has very fast response, high sensitivity and in many cases the samples can be measured directly without any special treatment. The same technique was already applied with Hagen [7] for the detection of dimethyl phthalate isomers in positive and negative polarity of IMS, and other authors but mostly in negative polarity only [8-10]. The positive polarity IMS results in combination with APCI measured with our group have revealed significant differences in IMS spectra of the isomers, the APCI of DMP isomers results in formation of protonated ions with different degree of hydration. For that reason theoretical calculations have been performed to evaluate the proton affinities of several conformers of the dimethyl phthalate isomers.

2. Experiment and Theory

The initial part of this work was performed experimentally with the IMS instrument with APCI source based on corona discharge in positive polarity at 700 mbars [11-13]. Volatile compounds are introduced into the spectrometer via a capillary inlet, as a drift gas zero air was used with residual water of ~20 ppm. The phthalates were supplied from Sigma-Aldrich with the following purities: dimethyl isophthalate 99%, dimethyl phthalate 99%, dimethyl terephthalate 99%.

Density functional method (DFT) was used to identify the ground state geometries and energies of all three studied phthalates, their neutral and protonated counterparts. The M06-2X/6-311G(2df,2pd) [14, 15] relative enthalpies, symmetries of the ground states were evaluated for three conformers of neutral

DMP, three conformers of neutral DMIP and two conformers of neutral DMTP. From the total energies of neutral and protonated compounds the corresponding PA were evaluated as the difference of the enthalpies of neutral and protonated counterpart.

3. Results and Discussion

The APCI process of phthalates in dehumidified ambient air was performed mostly with reactant ions (RI) $H^+(H_2O)_n$ ($n=3,4$) produced from positive corona discharge. The ionisation process takes place via proton transfer from the RI ($H^+(H_2O)_n$) to the phthalate molecule ($M \cdot H^+$) or cluster ($M_i \cdot H^+$), in case the PA of the molecule exceeds the PA of RI the proton transfer reaction is very fast. However there were observed many hydrated products, as a consequence of lower PA of the molecule than is the PA of RI. In that case products like $M \cdot H^+(H_2O)_m$ were formed, for which the hydronium bond energy $M-(H^+(H_2O)_m)$ ($m=1,2$) is larger than the bond energy $H^+(H_2O)-(H_2O)_n$. The IMS spectra confirmed the trend observed by Hagen [7] who also detected in the positive polarity significant differences in reduced ion mobilities, in the recent measurements the results were for DMP ($1.57 \text{ cm}^2\text{V}^{-1}\text{s}^{-1}$) on one side and for DMIP and DMTP (1.36 respectively $1.40 \text{ cm}^2\text{V}^{-1}\text{s}^{-1}$) on the other. In the case of DMP the dominant ion detected within monomer peak was $DMP \cdot H^+$ accompanied by weak $DMP \cdot H^+(H_2O)$, and also the dimers $DMP_2 \cdot H^+$ and $DMP_2 \cdot H^+(H_2O)$. On the other hand, in the spectrum of DMIP the pattern was completely different, with two strong monomer ions $DMIP \cdot H^+(H_2O)$ and $DMIP \cdot H^+(H_2O)_2$, but without the protonated ion $DMIP \cdot H^+$. The formation of the dimer ions including $DMIP_2 \cdot H^+$, $DMIP_2 \cdot H^+(H_2O)$ and the strongest ion present in the spectrum $DMIP_2 \cdot H^+(H_2O)_2$ was observed as well. Finally in the spectrum of DMTP were detected the following ions: $DMTP \cdot H^+$ and $DMTP \cdot H^+(H_2O)$ at comparable intensities accompanied by $DMTP \cdot H^+(H_2O)_2$, and a weak dimer ion $DMTP_2 \cdot H^+$. Unfortunately not all the PA of the measured compounds are known therefore we have performed DFT calculations to evaluate these quantities and check the hypothesis that the PA of molecule really exceeds the PA of RI.

We have applied density functional theory calculations of the PA using the M06-2X functional, which was used to identify the ground state geometries and energies of all three studied phthalates, their neutral and protonated counterparts. We have considered three conformers for DMP, three for DMIP and two for DMTP. The results are summarized in Table 1, the conformers DMP(1), DMIP(2) and DMTP(2) for each isomer separately are the energetically lowest ones. The corresponding geometries differing on the relative position of the C=O vs C-OCH₃ functional groups are in Fig. 1.

Tab. 1. The relative enthalpies $H_{rel} [meV]$ of neutral DMP, DMIP, DMTP and their protonated isomers calculated from M06-2X/6-311G(2df,2pd) ground state geometries, the MP2/6-311G(2df,2pd) values are only single point calculations. The proton affinities $PA [eV]$ are the differences of total enthalpies of two corresponding conformers, $PA(8.77 \text{ eV}) = DMP(1) - H^+DMP(1)$.

	M06-2X	MP2		M06-2X	MP2	PA
	$H_{rel} [meV]$	$H_{rel} [meV]$		$H_{rel} [meV]$	$H_{rel} [meV]$	$[eV]$
DMP(1)	259	224	H⁺DMP(1)	929	847	8.77
DMP(2)	268	236	H⁺DMP(2a)	664	591	9.05
			H⁺DMP(2b)	566	472	9.15
DMP(3)	315	276	H⁺DMP(3)	0	0	9.76
DMIP(1)	2	15	H⁺DMIP(1)	841	864	8.61
DMIP(2)	0	20	H⁺DMIP(2a)	730	717	8.72
			H⁺DMIP(2b)	800	837	8.65
DMIP(3)	14	36	H⁺DMIP(3)	666	658	8.80
DMTP(1)	11	3	H⁺DMTP(1)	861	839	8.60
DMTP(2)	8	0	H⁺DMTP(2)	867	828	8.59

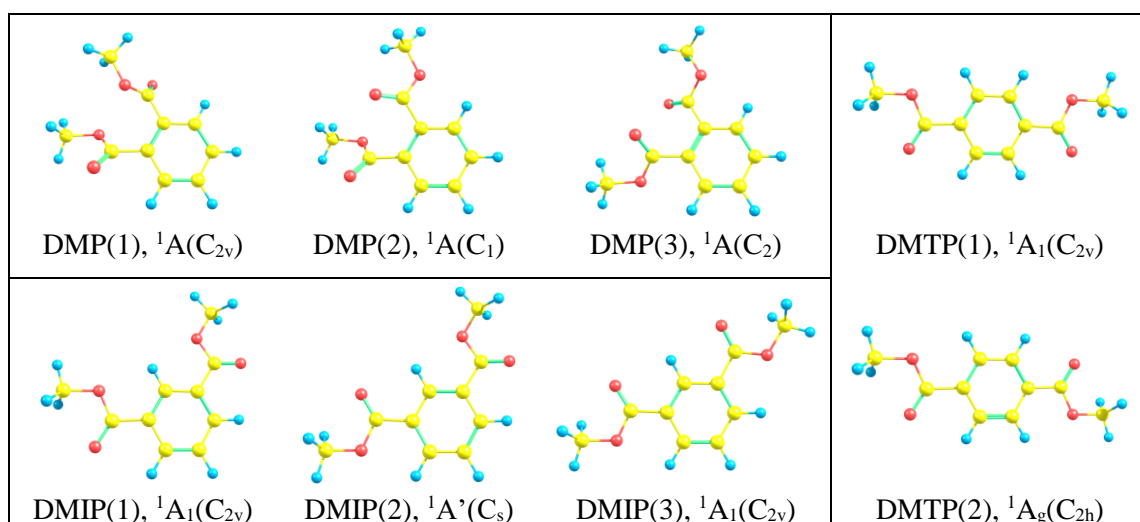


Fig. 1. The M06-2X/6-311G(2df,2pd) ground state geometries of different conformers of neutral DMP, DMIP and DMTP molecules. The final symmetry of the ground state with the multiplicity and point group in parenthesis is listed as well.

Proton attachment was considered to take place on the nonbonding electron pair of carboxylic oxygens, in each conformer there are two oxygens which may lead to identical (as for DMP(1)) or structurally different protonated product (as for DMP(2a) and DMP(2b)). This lead us to four protonated DMP, four protonated DMIP and two protonated DMTP conformers. Although the energetically lowest neutral molecule among all is the DMIP(2), the differences from the other conformers are very small either for the M06-2X or the single point MP2 results. However in the later the relative order of conformers has changed in favour of DMTP(2) to be the lowest, however the differences remained still in the order of tenths and in case of DMP hundreds of meV only.

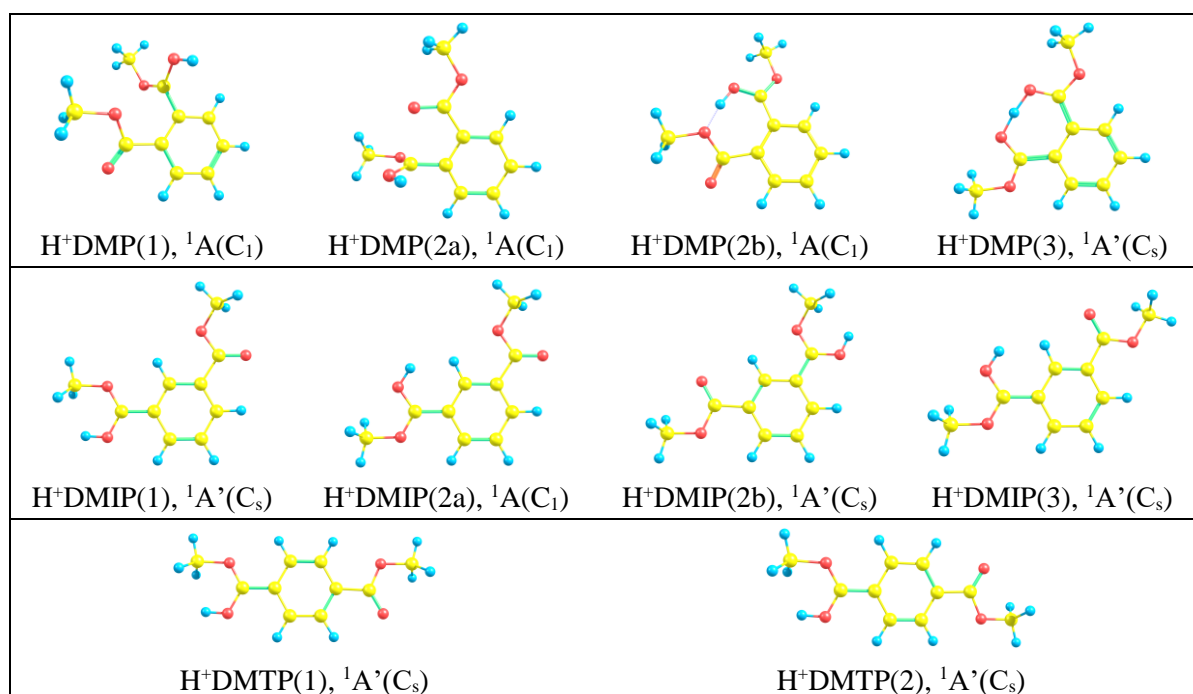


Fig. 2. The M06-2X/6-311G(2df,2pd) ground state geometries of different conformers of protonated DMP, DMIP and DMTP molecules. The final symmetry of the ground state with the multiplicity and point group in parenthesis is listed as well.

Among all the protonated structures the M06-2X energetically lowest $\text{H}^+\cdot\text{DMP}(3)$ was lower by more than several hundreds of meV from the other 9 structures, which is in excellent agreement with the single point MP2 results. All the calculated M06-2X proton affinities are summarized in Table 1, where the DMP(2) conformer has the highest proton affinity (9.76 eV), more than 1 eV higher than the other conformers and isomers. In the case of DMIP and DMTP the calculated PA values are in reasonable agreement with the experimental values of 8.74 eV for both isomers [16]. According to experimental PA of the water clusters (RI precursors), the proton binding energy for $\text{H}^+\cdot(\text{H}_2\text{O})_{3,4}$ is 9.32 and 9.64 eV, respectively [17]. Only the PA of conformer DMP(3) exceeds the proton bond energy of both RI and the proton transfer reaction is possible. These calculations and the experimental results indicate, that in case of DMP for RI $\text{H}^+\cdot(\text{H}_2\text{O})_{3,4}$ the ionisation is conformer selective and is leading to formation of protonated ion $\text{M}\cdot\text{H}^+$ for the conformer DMP(3).

4. Conclusion

Quantum chemical calculations were applied to obtain the proton affinities of different conformers of three dimethyl phthalate isomers and to explain the most recent atmospheric pressure chemical ionisation results. The IMS technique was used with reactant ions ($\text{H}^+\cdot(\text{H}_2\text{O})_{3,4}$) to study the ionisation of three isomers, DMP, DMIP and DMTP, showing that the separation was based on isomer and conformer selective ionisation process. All three isomers were separated mainly due to differences in hydration of the protonated monomer ions. Only for the DMP the present results indicate, that the ionisation process is conformer selective, resulting in $\text{DMP}\cdot\text{H}^+$ formation for DMP(3) monomer exclusively.

5. Acknowledgments

This project has received funding from the European Union's Horizon 2020 research and innovation programme under the Marie Skłodowska-Curie grant agreement No 674911 and from the European Union's Horizon 2020 research and innovation programme under grant agreement No 692335. This work was supported by the Slovak Research and Development Agency (contract no. APVV-0259-12 and APVV-15-0580) and the Slovak Grant Agency for Science (contract no. VEGA 1/0733/17 and VEGA 1/0417/15).

6. References

- [1] Schettler T 2006 *Int. J. of Androl.* **29** 134.
- [2] Fischer J et al. 1993 *Chromatographia* **37** 47.
- [3] Petersen J H and Breindahl T 2000 *Food Additives and Contam.* **17** 133.
- [4] Silva M J et al. 2003 *J. of Chromatography B* **789** 393.
- [5] Castillo M et al. 1997 *J. of Mass Spectrom.* **32** 1100.
- [6] Fernández-Amado M 2017 *Chemosphere* **175** 52.
- [7] Hagen D F 1979 *Anal. Chem.* **51** 870.
- [8] Poziomek E J and Eiceman G A 1992 *Environ. Sci. Technol.* **26** 1313–1318.
- [9] Barnett D A et al. 2000 *J. Mass Spectrom.* **35** 976.
- [10] Midey A J et al. 2013 *Analytica Chimica Acta* **804** 197.
- [11] Sabo M et al. 2015 *Anal. Chem.* **87** 7389.
- [12] Sabo M and Matejčík Š 2013 *Analyst* **138** 6907.
- [13] Sabo M and Matejčík Š 2012 *Anal. Chem.* **84** 5327.
- [14] Zhao Y and Truhlar D G 2006 *J. Phys. Chem. A* **110** 10478.
- [15] Zhao Y and Truhlar D G 2008 *Theor. Chem. Acc.* **120** 215.
- [16] Hunter E P and Lias S G, P.J. Linstrom and W.G. Mallard, Eds., NIST Chemistry WebBook, NIST Standard Reference Database Number 69, National Institute of Standards and Technology, Gaithersburg MD, 20899, (retrieved September 12, 2018)
- [17] Wróblewski T et al. 2004 *Czechoslovak Journal of Physics* **54** C747.

ELECTRON IMPACT EXCITATION OF HELIUM

Barbora Stachová, Juraj Országh, Štefan Matejčík

Department of Experimental Physics, Comenius University Bratislava, Slovakia

E-mail: stachovab@gmail.com

Optical emission spectroscopy is widely used analytical technique often for determination of the composition and concentration of compounds. The optical emission spectrum following electron impact excitation on He was studied in a crossed-beam experiment. Solely emissions of He I were detected, and relative cross sections of selected transitions were measured.

1. Introduction

Electron induced processes are common in various environments ranging from nature and space through laboratories to industry. Assessment of cross sections is necessary for plasma modelling, astrophysics, plasma physics, etc.

Helium is the second lightest element and the second most abundant in the known universe. It accounts for as much as 24 percent of the universe's mass. This element is also plentiful since it is a prime product of fusion nuclear reactions involving hydrogen. Helium is of particular interest, since it is frequently used in gas discharge plasmas including gas lasers, plasma-jets, in fusion research plasmas and so forth. In 1967, A. T. Jusick and others [1] used semi-empirical method for determining sets of collision cross sections for helium. The results for total excitation and ionization cross sections were evaluated using experimental angular distribution data, total cross section data, high-energy experimental generalized oscillator strengths, and theoretical optical oscillator strengths. The results for total excitation and ionization cross sections are also presented in a simplified empirical form that is more convenient for applications to electron loss calculation.

Experimental and theoretical data on cross sections of transitions between various neutral helium states were reviewed in 1978 by T. Fujimoto [2]. Therefore, the rate coefficients for excitation, de-excitation, ionization, three-body recombination and radiative recombination were investigated.

The study by F. J. de Heer in 1998 [3] was focused on previous assessment of collision strengths for excitation of He (1^1S). Due to the appearance of additional theoretical results the assessment was given within smaller error limits than before for the singlet levels, as well as for the lower triplet level.

In 2008, Yu. Ralchenko and others [4] assessed cross sections for the electron-impact excitation and ionization of ground state and excited helium atoms. The evaluated cross section data were presented by analytic fit functions, which preserved the correct asymptotic behaviour of the cross sections.

2. Experiment

Description of the apparatus

The crossed-beams technique has been used for the experiment. The electron-molecule interaction takes place in a vacuum chamber. Electron beam generated by trochoidal electron monochromator collides with a molecular beam of the sample formed by a capillary generating excited products. Subsequent deexcitation occurs, during which photons are emitted. These are reflected by a spherical mirror, which has focus in the centre of collision chamber and through the lens the photon signal (red in the Fig. 1.) is guided out of the vacuum chamber. The parabolic mirror focuses the light onto the entrance slit of the optical monochromator which filters the polychromatic light to the desired wavelength. Peltier cooled photomultiplier working in photon counting regime is used as a detector.

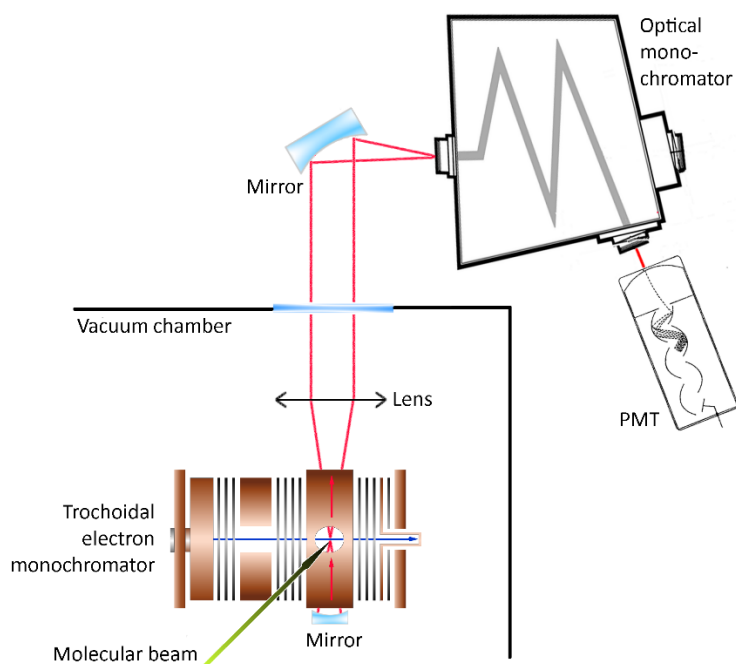


Fig. 1. The scheme of the experimental apparatus.

The energy resolution of the electron beam generated by trochoidal electron monochromator was approximately 0.5 eV and the absolute energy scale was calibrated according to the cross section curve of the nitrogen second positive system – transition (0,0) at 337 nm exhibiting relatively sharp maximum at 14.1 eV.

Spectrum was measured at several fixed electron energies. Wavelength calibration is given by the manufacturer of the monochromator. The intensity of the spectrum is corrected for apparatus sensitivity by multiplying the data by transmission function. This function was obtained by measurement of a heated tungsten filament and comparing this spectrum to the theoretical radiation of a black body and by measurement of continual radiation of hydrogen in the UV region of the spectrum.

Relative cross sections were measured at fixed wavelengths corresponding to the specific transitions and calibrated for the correct electron energy. Threshold electron energies are estimated as the interception of 2 fitted functions of the relative cross sections. The first fit corresponds to the region below the threshold energy – the background noise and the second fit corresponds to the slope of the cross section just above the threshold energy.

3. Experimental results

The spectrum of He in wavelengths within 250-700 nm was measured at 50 eV electron energy and it is shown in Fig. 2., Fig. 3. and Fig. 4. Spectrum was also measured at 23.5 eV, 24 eV, 24.5 eV and 25 eV electron energy and the results are compared in Fig. 5. These energies are close to the threshold energies of excitations-emission processes and the comparison of the spectra illustrated how significantly the electron energy influences the spectral emission. In the regions below 250 nm no significant line was detected and in the region, above 700 nm the sensitivity of the used photomultiplier decreases rapidly resulting in increased noise of the measured spectrum.

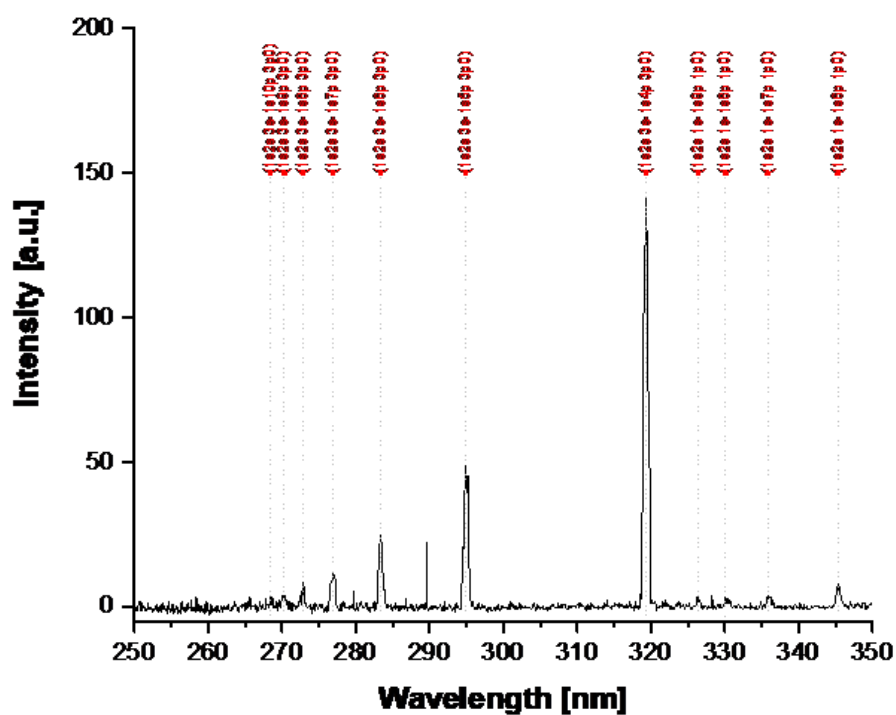


Fig. 2. Emission spectrum at 50 eV energy level within wavelengths 250-350 nm.

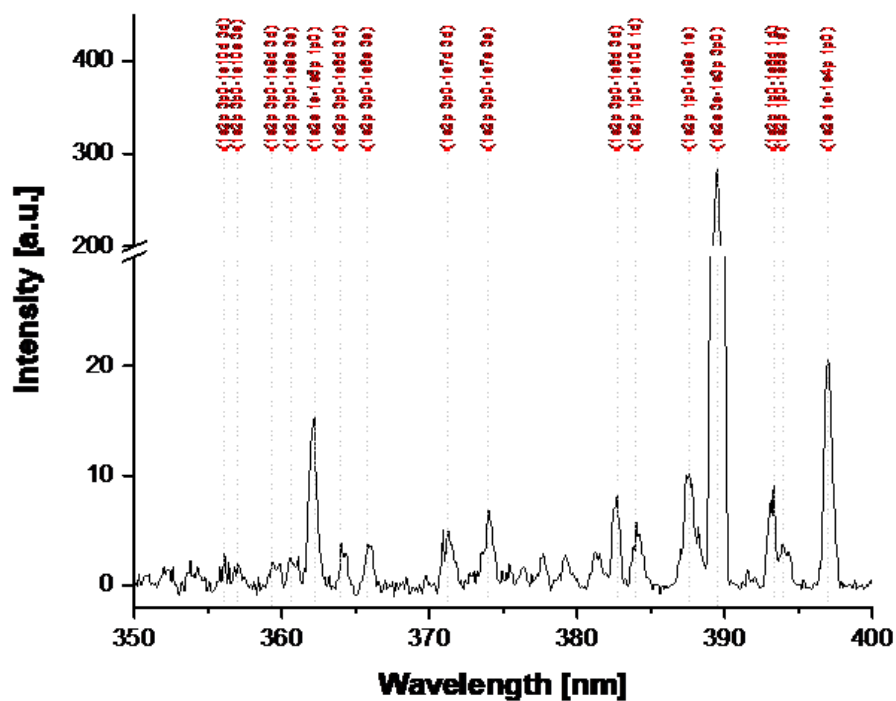


Fig. 3. Emission spectrum at 50 eV energy level within wavelengths 350-400 nm.

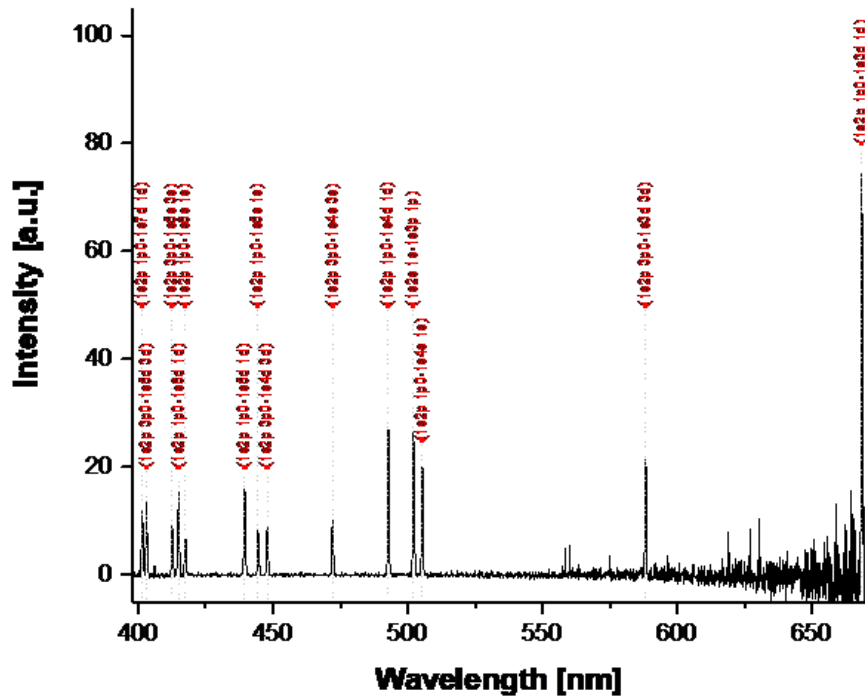


Fig. 4. Emission spectrum at 50 eV energy level within wavelengths 400-680 nm.

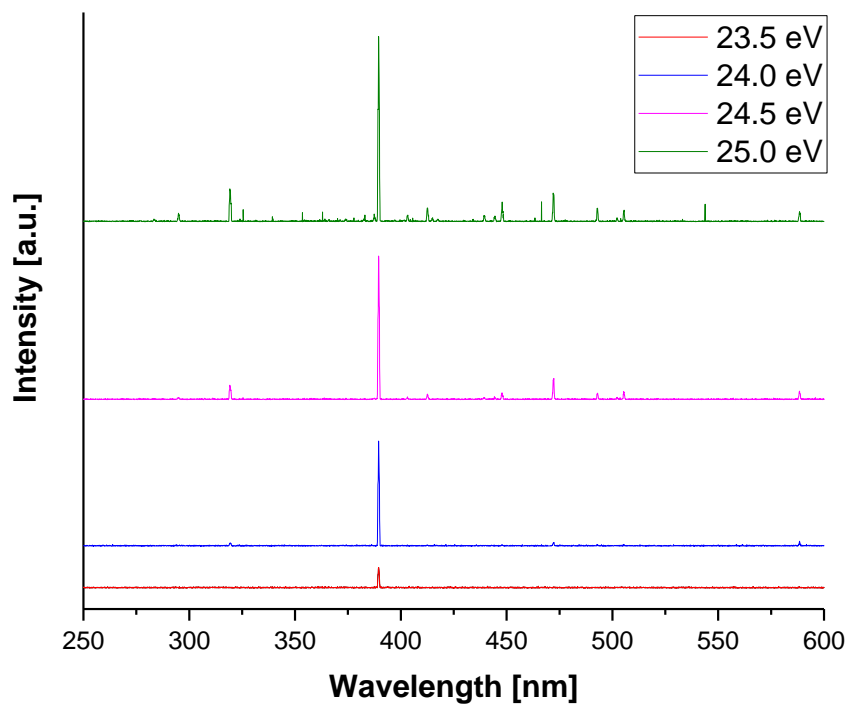


Fig. 5. Emission spectrum at different energy levels within wavelengths 250-600 nm.

Relative cross sections of excited fragments were measured for fixed wavelengths corresponding their emissions. The range of electron energy was 10-70 eV. Relative cross sections are processed graphically in figure 6 below.

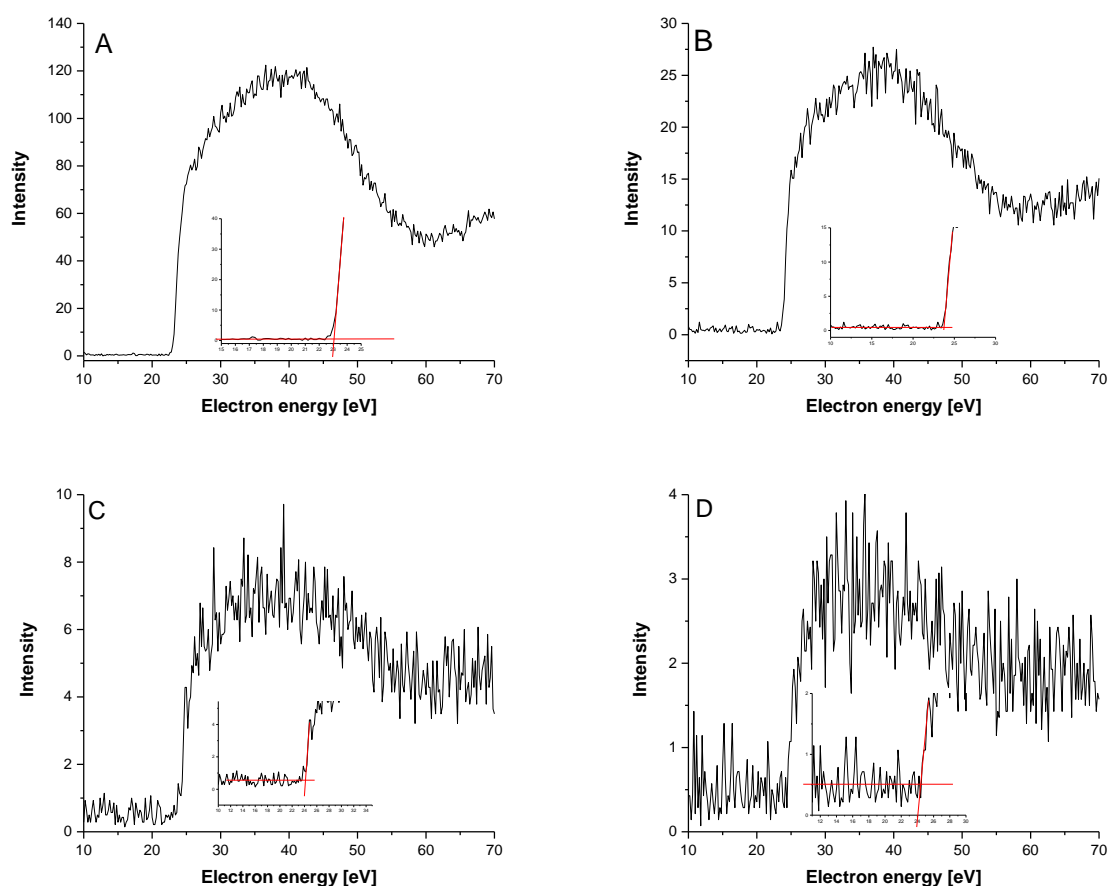


Fig. 6. Relative cross sections of (A) He I ($1s2s\ ^3s-1s3p\ ^3p^0$); (B) He I ($1s2s\ ^3s-1s4p\ ^3p^0$); (C) He I ($1s2s\ ^3s-1s5p\ ^3p^0$); (D) He I ($1s2s\ ^3s-1s6p\ ^3p^0$).

The acquired threshold energies for measured cross sections (tab. 1.) were compared to the values published in [5].

Tab. 1. Threshold energies acquired by fitting the experimental data.

	Determined threshold [eV]	Previously published [eV] [5]
He I ($1s2s\ ^3s-1s3p\ ^3p^0$)	23.06 ± 0.5	23.01
He I ($1s2s\ ^3s-1s4p\ ^3p^0$)	23.73 ± 0.5	23.71
He I ($1s2s\ ^3s-1s5p\ ^3p^0$)	24.16 ± 0.5	24.02
He I ($1s2s\ ^3s-1s6p\ ^3p^0$)	24.40 ± 0.5	24.20

Conclusion

The aim of this study was to measure the optical emission spectrum of He based on crossed-beam experiment. The spectrum was observed within the wavelength range from 250 nm to 700 nm at different electron energy levels. Spectral lines were identified and relative cross sections for some transitions were measured, as well as their threshold electron energies.

This represents only initial processing of collected data, further research will be performed to get more accurate spectra and absolute cross sections to help understand the behaviour of studied elements.

Acknowledgments

This work was supported by grant agency VEGA project nr. 1/0733/17; Slovak research and development agency project nr. APVV-15-0580.

This project has received funding from the European Union's Horizon 2020 research and innovation programme under grant agreement No 692335.

4. References

- [1] Jusick A T et al. 1967 Electron Impact Cross Sections for Atmospheric Species, *Journal of geophysical research* **72** 15.
- [2] Fujimoto T 1978 Semi-empirical Cross Sections and Rate Coefficients for Excitation and Ionization by Electron Collision and Photoionization of Helium, *IPPJ-AM* **18**.
- [3] De Heer F J 1998 Critically Assessed Electron-Impact Excitation Cross Sections for He (1'), *International Nuclear Data Committee, INDC(NDS)*-385.
- [4] Ralchenko Yu et al. 2008 Electron-impact excitation and ionization cross sections for ground state and excited helium atoms, *Atomic Data and Nuclear Data Tables* **94** 603–622.
- [5] Martin, W C 1960 Energy levels and spectrum of neutral helium ($^4\text{He I}$), *Journal of Research of the National Bureau of Standards – A. Phys. and Chem.* **64** 19.

LOW-TEMPERATURE PLASMA TREATMENT OF SELECTED CEREALS

Veronika Medvecká¹, Silvia Mošovská², Kitti Tóthová², Anna Mikulajová²,
Miroslav Zahoran¹, Anna Zahoranová¹

¹ Department of Experimental Physics, Faculty of Mathematics, Physics and Informatics, Comenius University in Bratislava, Mlynska dolina, Bratislava 842 48, Slovakia

² Department of Nutrition and Food Quality Assessment, Faculty of Chemical and Food Technology, Slovak University of Technology, Radlinského 9, 812 37 Bratislava, Slovakia

E-mail: veronika.medvecka@fmph.uniba.sk

Atmospheric pressure low-temperature plasma is prospective tool for decontamination, improvement of germination and growth of seeds. In our work, we studied the influence of atmospheric pressure low-temperature plasma on three types of cereals – wheat, barley and maize. Besides the growth parameters, the surface morphology and changes in chemical bonds were observed and also the qualitative characteristics were analysed.

1. Motivation

The low-temperature (LT) non-equilibrium plasma is the prospective alternative to high temperature or chemical processes for application in medicine and biotechnology for bio-decontamination, increase of biocompatibility or other surface modification of biological and non-biological material [1–3]. LT plasma generated at atmospheric pressure appears to be an effective and ecological tool for plasma treatment of various seeds for the purpose of decontamination/sterilization [4–6] and improvement of plant physiological parameters (speed of germination, biomass production, etc.) [7,8]. Conventionally applied wet chemical seed treatment often use toxic or aggressive chemicals [9–11]. Due to the reduction or complete removal of chemical agents the low temperature plasma is suitable alternative or pre-treatment method to conventionally used seed dressing.

The advantage of plasma sources working at atmospheric pressure is operation without requiring vacuum equipment. DCSBD generates non-thermal macroscopically homogeneous diffuse plasma in ambient air and it was successfully used for decontamination of wheat, maize, black peppercorn or almonds [12–14].

In our work, we analyzed the influence of cold atmospheric pressure plasma generated by Diffuse Coplanar Surface Barrier Discharge (DCSBD) [15] on the properties of three types of cereals – wheat, barley and maize depending on exposure time of samples in plasma. DCSBD generates macroscopically homogeneous low temperature diffuse plasma at atmospheric pressure with high surface power density of plasma without the need of any working gas [10,11]. The interaction DCSBD plasma with samples of wheat (*Triticum aestivum*), barley (*Hordeum vulgare*) and maize (*Zea mays*) was studied in term of changes in surface properties and qualitative characteristics.

2. Methods

In our work the atmospheric pressure ambient air plasma generated by Diffuse Coplanar Surface Barrier Discharge (DCSBD) was used for plasma treatment of three types of cereals samples - wheat (*Triticum aestivum*), barley (*Hordeum vulgare*) and maize (*Zea mays*). Plasma treatment of all types of samples was realized at atmospheric pressure in ambient air in dynamic regime. The DCSBD discharge was placed on vortex Biosan PSU-10i. Samples were treated at 330 rpm to ensure homogeneous treatment of seeds. The primary effect of plasma on surface properties was investigated. Water contact angle (WCA) representing wettability of seeds was measured after plasma treatment at various exposure times (10, 30, 60, 120, 180, 240 and 300 s) using Drop Shape Analysis DSA30

(Krüss, Germany). The changes in morphology of seeds were observed by Scanning Electron Microscopy Vega II SBH (Tescan, Czech Republic). The impact of low-temperature plasma on changes in chemical bonds on the surface of seeds was observed by using Fourier Transform Infrared Spectroscopy using Bruker Vector 22 FT-IR spectrometer with additional accessories Pike MIRacle™ in the range of 4500 to 500 cm⁻¹ during 20 scans, with 2 cm⁻¹ resolution using diamond crystal. The content of dry matter in grains was determined by gravimetric measurement before and after drying of samples to constant weight. The content of starch was estimated by Ewers standard method (STN 46 1011-37). The gas chromatography was used for the identification of fatty acid methyl esters. Their quantification was realized by ChemStation software. Oils were isolated from samples at laboratory temperature using hexane as extract agent to prevent oxidation by higher temperature.

3. Results and discussion

Diffuse Coplanar Surface Barrier Discharge was successfully used for the plasma treatment of the non-biological samples for the improvement of adhesion and increase surface energy and wettability. The similar effect occurs also by plasma treatment of biological samples. As from Fig. 1. (left), the exponential decrease of water contact angle on the surface of all grain types was observed. One of the related effects observed in plasma treated samples is the increase of water uptake of seeds, which can lead to better germination of seeds (Fig. 2 left). In Fig. 2 right, the optimal exposure time and observed improved germination of barley, wheat and maize is presented. SEM measurements realized on grains samples confirmed, that plasma treatment, even during the long exposure time, does not cause any degradation of surface morphology (Fig. 1 right).

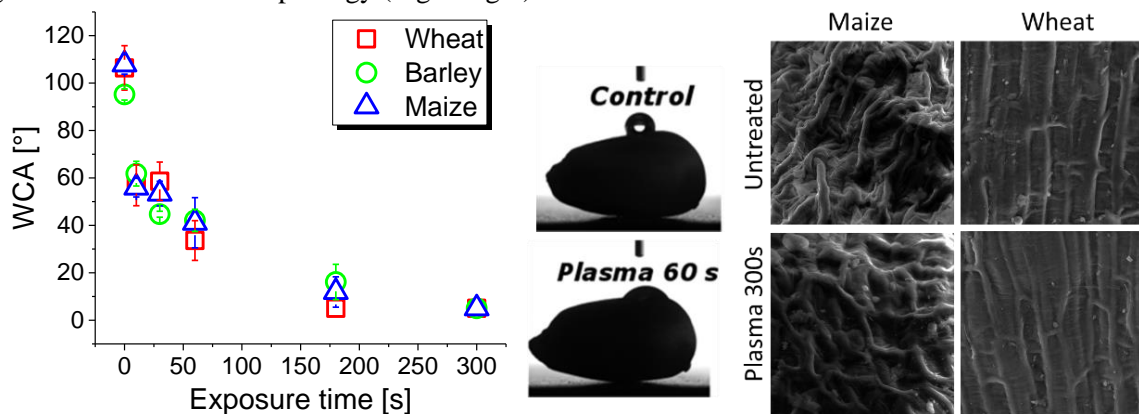


Fig. 1: Water contact angle in dependence on exposure time in plasma (left), the decrease of WCA after plasma treatment on maize seed and SEM pictures of maize and wheat seeds before and after plasma treatment (right)

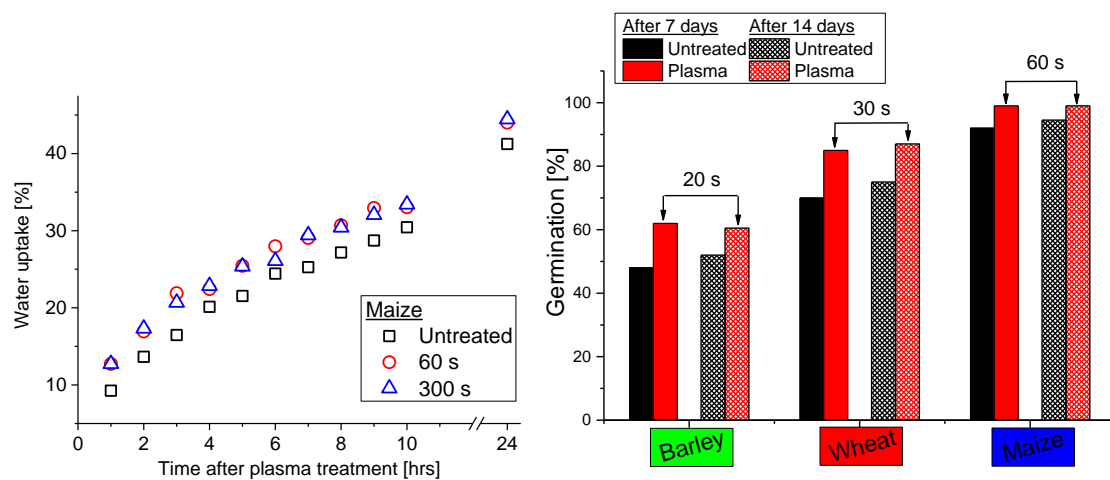


Fig.2: Comparison of water uptake (imbibition) of maize seeds before and after plasma treatment (left) and improvement of grain seeds germination after determined optimal exposure time in plasma (right)

The changes in chemical bonds caused by plasma exposure was analysed by ATR-FTIR spectroscopy (Fig. 3). On the reference samples, significant band in the interval 3000-3600 cm^{-1} and peak at 1650 cm^{-1} attributed to stretching and bending vibration of O-H groups, respectively, representing water, can be seen. The typical band of saccharides can be found in region 900-1200 cm^{-1} attributed to C-O, C-C, C-OH bonds and the significant peak of glycosidic linkage at around 1050 cm^{-1} . The lipids are present at 2800-3000 cm^{-1} by stretching vibration of C-H groups. In this region can be observed the main changes. Decrease of peaks indicates removal of lipids from the surface, which can contribute to the higher wettability of seeds surface.

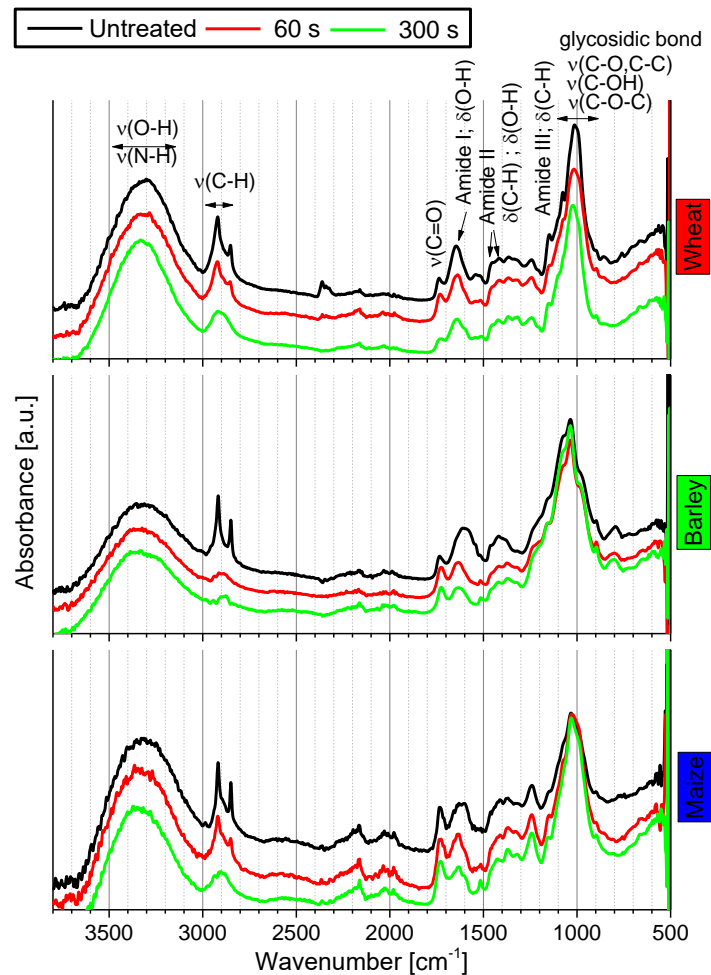


Fig. 3: ATR-FTIR analysis of grains surface before and after plasma treatment

Plasma generated by DCSBD was applied for inhibition and sterilization of various kind of bacterial or mycotic biocontamination. However, for use of plasma treatment in food industry, it is important to investigate the influence of plasma on qualitative characteristics and nutritional properties of grains. As we can see from Fig. 4, plasma can cause drying of samples. This effect is prospective in term of lower recontamination with low content of water in samples during storage.

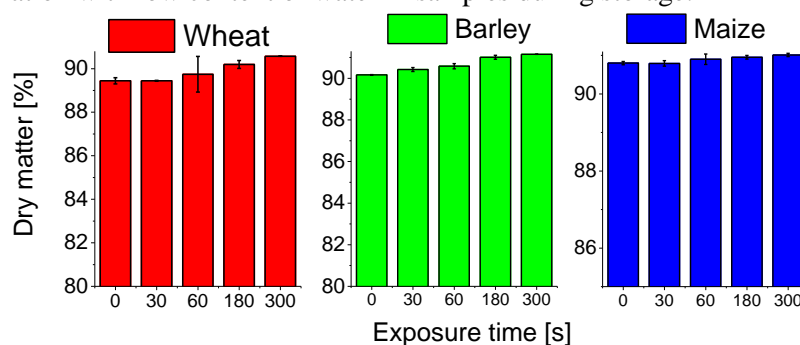


Fig. 4.: Dry matter of grains before and after plasma treatment in dependence of exposure time

The slight increase of starch content was measured after plasma treatment (Fig. 5 left), which can be related with the effect of water loss. The content of isolated oils also increased from 0.87 %, 1 % and 3.63 % in untreated samples of wheat, barley and maize, respectively, to 0.92 %, 1.09 % and 3.86 % after 300 s of plasma treatment. This effect can be also caused by decrease of water content in samples after exposure in plasma. Composition of fatty acid was not influenced by plasma treatment (Fig. 5 right)

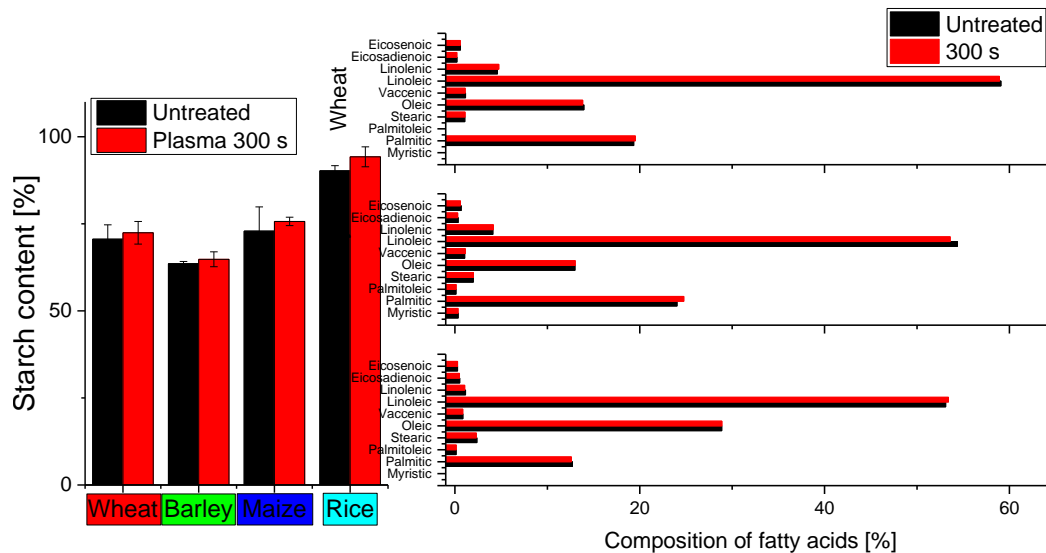


Fig. 5.: Content of starch (left) and composition of fatty acids in grains before and after plasma treatment (right)

4. Conclusion

Low temperature plasma is widely studied in bioapplications mainly in plasma medicine. However, LTP become very attractive for plasma treatment of biological material also in agriculture and food industry. Cereals are most common food in human and animal nutrition. We studied effect of LTP generated by DCSBD on the surface properties and nutritional characteristics of selected cereals – wheat, barley and maize. Besides the decontamination effect of plasma, which was intensively studied before and published in our previous work, we can reach improvement of germination in short exposure times. The changes in nutritional characteristics were detected after long exposure of samples in plasma, however, the changes were minimal.

Acknowledgement: This work was supported by the Slovak Research and Development Agency under the contract No. APVV-16-0216. This project has received funding from the European Union's Horizon 2020 research and innovation programme under grant agreement No 692335.

References

- [1] S Cheruthazhekatt, M Černák, P Slavíček, and J Havel *J. Appl. Biomed.* **8** 55 (2010).
- [2] G Fridman, G Friedman, A Gutsol, A B Shekhter, V N Vasilets, and A Fridman *Plasma Process. Polym.* **5** 503 (2008).
- [3] K Shimizu, H Fukunaga, and M Blajan *Curr. Appl. Phys.* **14** (2014).
- [4] M Selcuk, L Oksuz, and P Basaran *Bioresour. Technol.* **99** 5104 (2008).
- [5] C Hertwig, K Reineke, J J Ehlbeck, D Knorr, O Schlüter, and O Schlüter *Food Control* **55** 221 (2015).
- [6] D Butscher, D Zimmermann, M Schuppler, and P Rudolf von Rohr *Food Control* **60** 636 (2016).
- [7] D Dobrin, M Magureanu, N B Mandache, and M-D Ionita *Innov. Food Sci. Emerg. Technol.* **29** 255 (2015).
- [8] E Bormashenko, R Gryniov, Y Bormashenko, and E Drori *Sci. Rep.* **2** 3 (2012).
- [9] F Sgolastra, T Renzi, S Draghetti, P Medrzycki, M Lodesani, S Maini, and C Porrini *Bull.*

- Insectology* **65** 273 (2012).
- [10] L Maxim, J Van Der Sluijs, and J van der Sluijs *Seed-dressing systemic insecticides and honeybees* p 369 (2013).
- [11] M Greatti, A G Sabatini, R Barbattini, S Rossi, and A Stravisi *Bull. Insectology* **56** 69 (2003).
- [12] A Zahoranová, M Henselová, D Hudecová, B Kaliňáková, D Kováčik, V Medvecká, and M Černák *Plasma Chem. Plasma Process.* **36** 397 (2016).
- [13] S Mošovská, V Medvecká, N Halászová, P Ďurina, L Valík, A Mikulajová, and A Zahoranová *Food Res. Int.* **106** 862 (2018).
- [14] C Hertwig, A Leslie, N Meneses, K Reineke, C Rauh, and O Schlüter *Innov. Food Sci. Emerg. Technol.* **44** 242 (2017).
- [15] M Černák, D Kováčik, J Ráhel', P St'ahel, A Zahoranová, J Kubincová, A Tóth, and L Černáková *Plasma Phys. Control. Fusion* **53** 124031 (2011).

BIOLOGICAL ACTIVITY OF PLASMA MODIFIED PROTECTIVE LAYERS ON FAÇADE USING RF SLIT NOZZLE

Barbora Pijáková¹, Maja Korous¹

¹Department of Physical Electronics; Masaryk University; Kotlářská 267/2; 611 37 Brno-CZ

E-mail: barbora.pijakova@mail.muni.cz

Antifouling of surfaces frequently exposed to liquid environment is usually solved by photocatalytic or biocide agent incorporation. In our work, we present the possibility of combining the photocatalytic activity of titanium dioxide with non-wettability of UltraEverDry product layer. To enhance advantages of both reagents, we treated samples with argon/nitrogen or argon/octafluorocyclobuthan plasma generated by RF slit nozzle using 150 W power and 15 s treatment time. Biological activity was observed for *Chlorella kessleri* solution. Resulting layers containing titanium dioxide in combination with UltraEverDry after the modification with argon/octafluorocyclobuthan plasma exhibited excellent non-fouling properties even after 24 h exposure.

1. Introduction

Fouling of surfaces at terrestrial conditions is an important aspect of building degradation and service cost increase. Presence of the liquid environment in combination with the surface roughness enhance the possibility for impurities or microorganisms to adhere [1]. These processes can lead to formation of biofilm. To remove the biofilm, mechanical cleaning is necessary. One possible solution is viability inhibition of stucked microorganisms by incorporation of bio active agents, another one is to avoid the contact with liquids. The first one usually means addition of TiO₂ or biocides, whereas the second one is solved by preparation of non-wettable product [2,3,4].

In this work, we produce the protection layer on facade painting system by addition of TiO₂ anatase nanoparticles to fulfill the bioactivity criterion and superoleophobic agent UltraEverDry to create superhydrophobic surface. Consequently, as-prepared surface was treated using plasma slit nozzle to observe the additional effect on antifouling and photocatalytic properties. To sum up, TiO₂:UltraEverDry modified facade paint exhibited after plasma modification with argon/octafluorocyclobuthan plasma enhanced biological activity and fouling resistance even after 24h exposure in liquid environment with presence of *Chlorella kessleri* cells.

2. Experimental

2.1 Materials

UltraEverDry top coat by UltraTech was purchased from local dealer. Titanium dioxide in anatase form was kindly provided by Precheza. Façade paint FASAX was provided by Colorlak,a.s. .

2.2 Methods

2.2.1 Sample preparation

Stainless steel samples of size 70x25x0.8 mm were mechanically cleaned using surfactant solution and washed with deionized water. Subsequently, façade paint layer was applied with palette-knife, followed by spray coating of the one of three active reagent solutions. First consisted from titanium oxide nanoparticles (TiO₂, anatase) dispersed in acetone (5g/100ml), second contained UltraEverDry (UED) and the third was combination of UED/TiO₂ (TiO₂ – 5g/100ml). After drying of samples in ambient air for 15 h, plasma modification was implemented. The treatment was carried out using RF plasma slit nozzle operating at 13.56 MHz with applied power 150 W and treatment time of 15 s. Two different gas mixtures, Ar+N₂ (50 l/min + 0.5 l/min) and Ar+C₄F₈ (50 l/min + 0.3 l/min) were tested with variation of the distance between the sample surface and slit (10 mm - direct contact with afterglow and 30 mm - without direct contact). In addition to different gas composition, sample

storage in ambient air and admixture (N_2 or C_4F_8) atmosphere in desiccator were tested. Samples were prepared in triplicate. The list of the samples is stated in Tab. 1.

2.2.2 Surface testing and analysis

Confocal microscope Olympus LEXT OLS4000 3D Laser Measuring Microscope was used for macroscopic surface topography and roughness observation. 3D topography with magnification 20x and roughness of 1.5 mm profile, averaged from 4 measurements, were realized in laser mode.

Scanning electron microscope Tescan Mira3 including energy dispersive spectroscopy provided information about surface microstructure and bulk chemical composition of upper layer. 20 nm of Au/Pd covering was deposited on each sample to prevent charging.

Wettability measurement based on sessile droplet method was done using AdvexInstruments SeeSystem device and software. Deionized water droplet volume was 3μ . Resulting values are averaged from 5 measurements.

Fluorescence microscope Zeiss AxioImager A1 operating with IcC 1 Cam and filter set number 9 displayed the presence and viability of cells on the surface. Snapshots were created using exposition 270 ms with magnification 100x. The representative snapshot with the closest number of living/dead/dying cells to average value after the counting of cells on 10 snapshots for each sample.

2.2.3 Biological activity test

Methodology of biological activity testing is related to real terrestrial conditions. Samples were alternatively embedded into solution containing *Chlorella kessleri* cells followed by drying. The whole process took place with irradiation by aquarium fluorescent lamp GLO AquaGlo A-1587. Light intensity at the liquid level was 2200 lux. Concentration of microorganisms in 50% ZBB medium was stated to $100\,000 \pm 20\,000$ cells/ml. Solution was continually homogenized by magnetic stirrer with frequency 280 rpm. Samples were immersed 3 cm under the liquid level. The wet-process intervals were 1 h, 5 h and 18 h. Every immersion was followed by dry-process interval of 24 h. Before the immersion, water contact angle measurement and fluorescence microscopy shooting were realized. After the wet-process interval, fluorescence microscopy was done.

Tab. 1: Sample nomenclature and preparation differences

Sample	Reagent type (step 1)	Plasma modification (step 2)
FASAX	-	-
UED	UED	-
TiO ₂	TiO ₂	-
FH3	UED/TiO ₂	-
FH22	UED/TiO ₂	Ar+N ₂ ; h= 10 mm
FH22N	UED/TiO ₂	Ar+N ₂ ; h= 10 mm
FH22-	UED/TiO ₂	Ar+N ₂ ; h= 30 mm
FH22-N	UED/TiO ₂	Ar+N ₂ ; h= 30 mm
FH25-	TiO ₂	Ar+C ₄ F ₈ ; h= 30 mm
FH25-F	TiO ₂	Ar+C ₄ F ₈ ; h= 30 mm
FH26-	UED/TiO ₂	Ar+C ₄ F ₈ ; h= 30 mm
FH26-F	UED/TiO ₂	Ar+C ₄ F ₈ ; h= 30 mm
FH27-	TiO ₂	Ar+N ₂ ; h= 30 mm
FH27-N	TiO ₂	Ar+N ₂ ; h= 30 mm

3. Results and Discussion

3.1 Surface topography

3.1.1 SEM

Surface microstructure of chosen samples is on Fig. 1. Comparing the pristine façade with other layers, TiO₂ presence caused covering of formations from façade with aggregates. This was analogous for each sample with TiO₂ layer, with/without the plasma modification. Introducing the UED to upper layer is followed by appearance of smaller nanoparticles ($\approx 20 - 40$ nm). None of plasma modified samples exhibited any damage such as uncovering and surface melting of the UED nanoparticles or sintering. Plasma treatment can be considered as favourable technique of surface modification. EDX

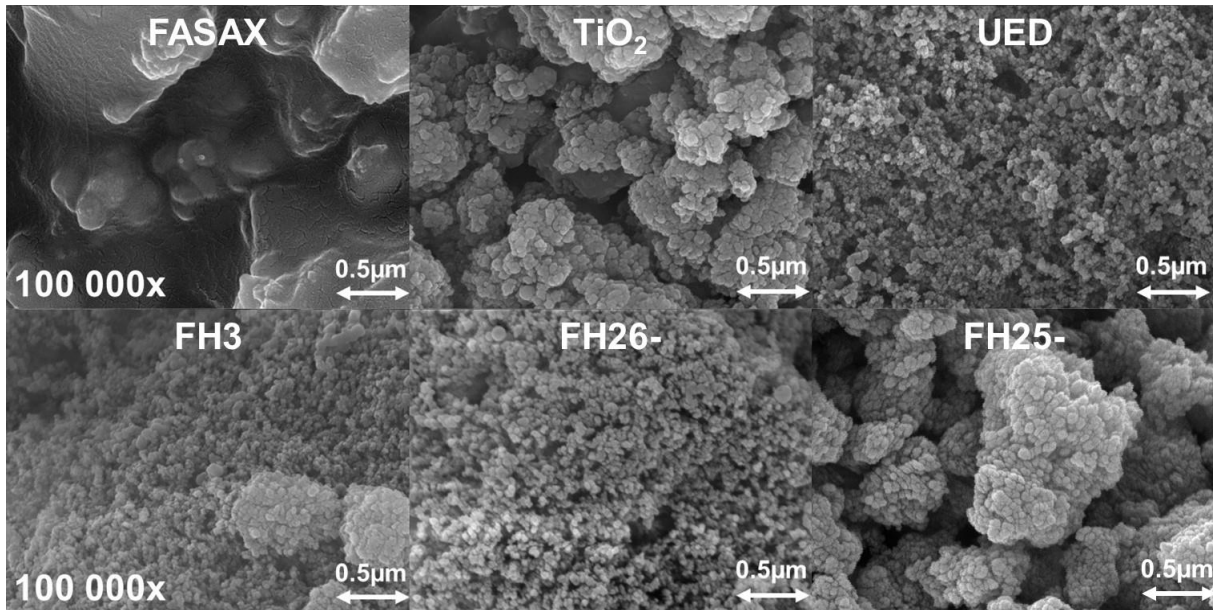


Fig. 1: SEM images of reference materials (FASAX, TiO₂, UED), UED/TiO₂ without plasma modification and after modification with C₄F₈ (FH3, FH26-) and N₂ modified TiO₂ (FH25-); magnification 100kx; SE detector

confirmed the production of new layers by the decrease of C content in comparison to façade followed by higher Si/F (4-13 at%/8-19at%), Ti (2-20 at%) and Si/F/Ti content for UED, TiO₂ and UED/TiO₂ samples, respectively. Higher fluorine content has a positive effect on surface wettability.

3.1.2 Confocal microscopy

Surface roughness value was the lowest for the pristine façade paint, 17 µm. After spray coating, layers without the presence of UED exhibited roughness under 30 µm. Applying UED resulted in increase of surface roughness to 30-40 µm. Surface roughness measurement did not show any direct dependence on plasma modification. High roughness is caused by coarse-grained façade paint and reagent tendency to aggregate in conjunction with spray deposition method.

3.2 Wettability

Wettability data of prepared samples show, that plasma modification using N₂ as the admixture with afterglow contact significantly reduces the water contact angle (WCA) in case of UED/TiO₂ samples. TiO₂ based sample types had very low WCA due to the used reagent. Combination of UED and TiO₂ without plasma treatment, plasma modified samples with C₄F₈ and plasma modified samples with N₂ without the contact with afterglow, exhibited very high initial WCA values.

During the biological activity tests, changes of WCA were connected to the change of surface roughness due to cell adhesion. In case of UED/TiO₂ unmodified samples and samples treated with C₄F₈, surface remained superhydrophobic, WCA > 150°, even after the whole testing period. To reach the necessary level of non-wettability, combination of UED/TiO₂ with C₄F₈ or pure UED can be chosen. Very high concentration of TiO₂ and N₂ modification suppress required attribute. Fig. 2 shows the average WCA values.

3.3 Fluorescence microscopy

Fluorescence microscopy offers the possibility to measure the approximate number of cells on the top of the surface. Using the setup mentioned in Experimental, we were able to distinguish viable cells and cells in bad living condition/dead cells. Viable cells are light and visible due to chlorophyll content presented as bright yellow formations on snapshots. On the other hand, less emitting dying cells appear red and smaller. To see the difference between references and the most effective FH26 and FH3, Fig. 3 contains representative snapshots for each interval of the test. After the calculation of the cell number for each sample, we observed visible trend for samples without ultrahydrophobic properties. After the wet-process interval, the number of cells increased because of easier adherence on wetted rough surface, followed in majority of samples by slight reduction of present cells and growth of the dead/dying cell number after the dry-process interval. Samples using UED/TiO₂ with C₄F₈ exhibited antifouling properties. This fact is caused by high WCA values, so prevention of the

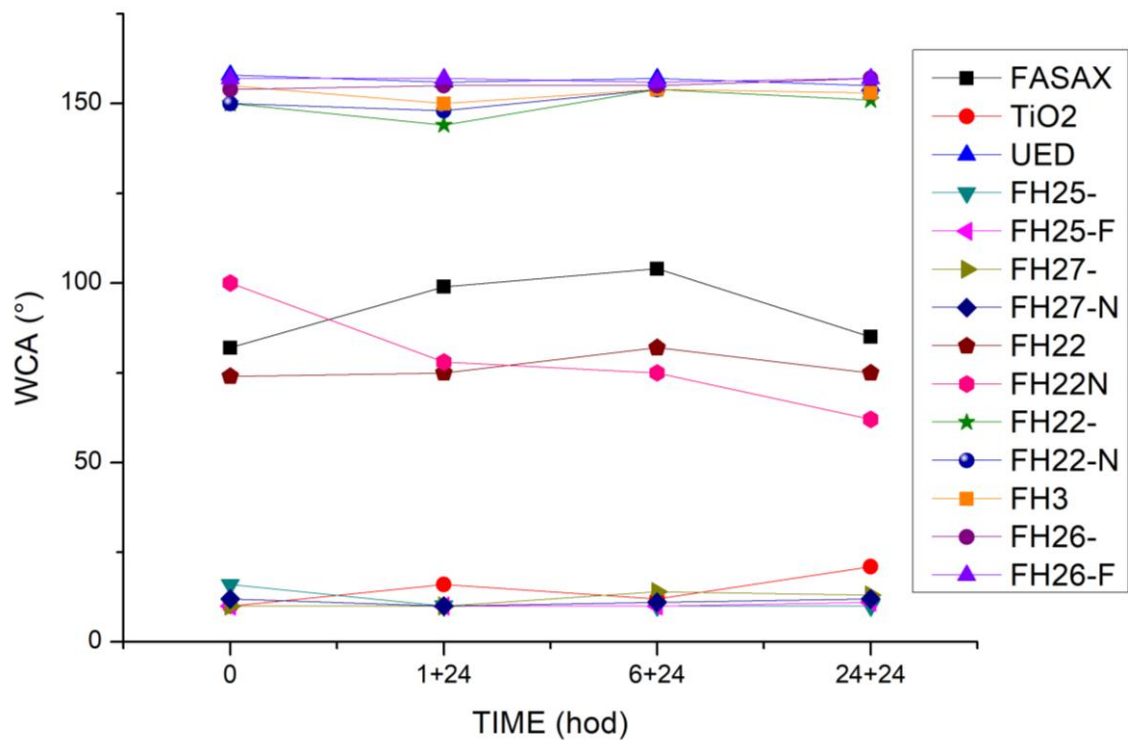


Fig. 2: WCA averaged values for the end of dry-process interval of biological activity testing

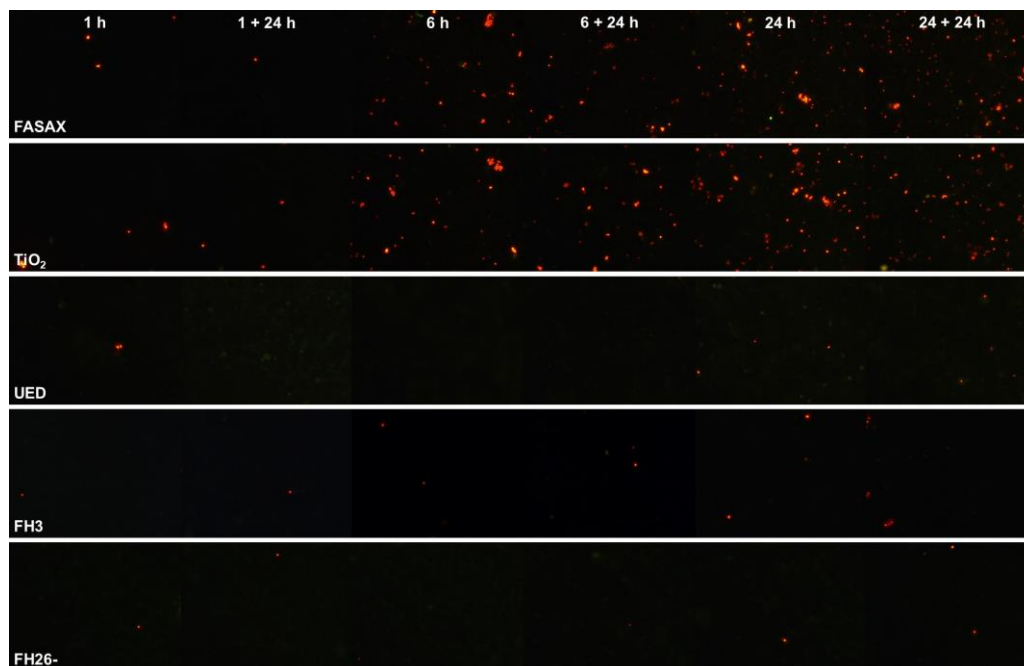


Fig. 3: Fluorescence microscopy representative snapshots for pristine façade FASAX, TiO₂, UED, plasma unmodified UED/TiO₂ and C₄F₈ modified UED/TiO₂; magnification 100x; exposition 270 ms; filter set n. 9

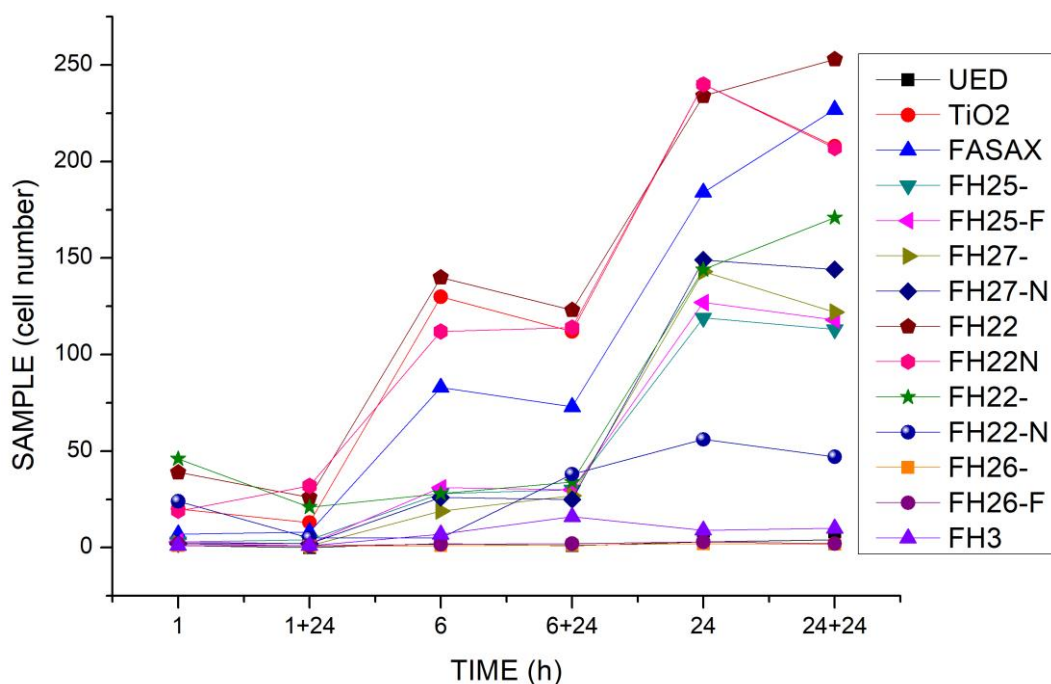


Fig. 4: Total number of adhered cells on the top of the surface measured after each wet/dry interval of biological activity test

contact with the liquid environment and secondly by presence of photocatalytically active TiO_2 which can reduce such small quantity of cells. Graph with averaged total cell number is presented on Fig. 4.

4. Conclusion

We successfully prepared protective layer on stainless steel substrate covered by façade paint by spraying of TiO_2 /UltraEverDry mixture with TiO_2 content 5 g/100 ml. Resulting product was modified by plasma treatment using RF plasma slit nozzle operating with power 150 W. Treatment time was stated for 15 s with gas composition of Ar 50 l/min and C_4F_8 0.3 l/min. As-prepared layer exhibited superhydrophobic properties with WCA $^\circ$, increased Si (+8 at%), F (+13 at%) and Ti (+7 at%) content and excellent antifouling properties after the 24 h in 50% ZBB solution containing *Chlorella kessleri* cells with concentration $100\,000 \pm 20\,000$ cells/ml.

5. Acknowledgement

This work was supported by Masaryk University, project number TE02000011 funded by Technology agency of Czech Republic, project number CZ.1.05/2.1.00/03.0086 funded by European Regional development Fund and project LO1411 (NPU) funded by Ministry of Education and Sports of Czech Republic.

6. Bibliography

- [1] Lampin M., Warocquier-Clerout R., Legris C., Degrange M., Sigot-Luizard M. F. 1997 *John Wiley & Sons, Inc. Journal of Biomeical Materials Research banner; vol. 36; iss. 1; p 99-108*
- [2] Banerjee I., Pangule R. C., Kane R. S. 2011 *John Wiley & Sons, Inc.; Advanced Materials vol 23; iss. 6; p 690-718*
- [3] Carp O., Huisman C. L., Reller A. 2004 *Elsevier Ltd.; Progres in Solid State Chemistry; vol. 32; iss 1-2; p 33-177*
- [4] Asahi R., Morikawa T., Ohwaki T., Aoki K., Taga Y., 2001 *American Association for the Advancement of Science, SCIENCE, vol. 293; iss 5528; p 269-271*

SURFACE MODIFICATION OF POLYPROPYLENE MEMBRANES BY PLASMA-INDUCED GRAFTING FOR THEIR APPLICATION AS SEPARATORS IN ALKALINE ELECTROLYSIS CELL

Lubomír Staňo, Michal Stano, Pavol Ďurina

Department of experimental Physics, Faculty of Mathematics, Physics and Informatics, Comenius University, Mlynská dolina F2, 84248 Bratislava, Slovak republic

E-mail: lubomir.stano@fmph.uniba.sk

Connection of alkaline water electrolyzers with intermittent renewable energy sources like wind power or photovoltaics in Power-to-Gas installations sets high requirements on inter-electrode separators in terms of low electrical resistance and gas separation efficiency. To achieve this, high wettability of separator membrane by the electrolyte is necessary. Present work is dedicated to hydrophilisation of porous polypropylene membranes by plasma-induced graft polymerization of acrylic acid (AAc) and their potential application as separators in alkaline electrolyzers. Low-pressure, capacitive-coupled, radio-frequency discharge at 13.0 MHz in argon or oxygen was used as a source of non-thermal plasma for membrane activation. The treatment was optimized for the creation of hydroperoxide functional groups which act as initiators for AAc graft polymerization. After modification, the electrical resistance of three types of studied membranes ranged from 30 m Ω cm² to 250 m Ω cm² and the purity of hydrogen and oxygen gases produced was above 99.86 %. Ageing tests were performed in 30 wt. % aqueous solution of potassium hydroxide at ambient and elevated temperature.

1. Introduction

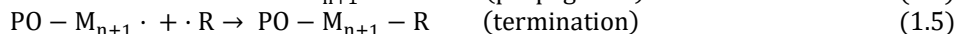
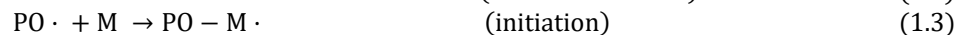
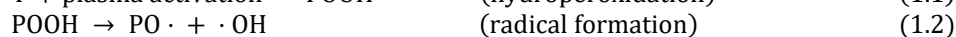
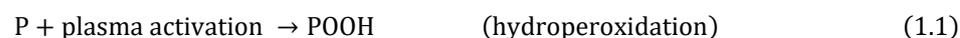
Alkaline water electrolysis is the mostly used electrolysis technology for large scale hydrogen production [1]. Its main advantage is no need for precious platinum group metals catalysts. An unavoidable component of the cell is an inter-electrode separator membrane. Its role is to separate anodic and cathodic cell compartments to prevent mixing of the produced hydrogen and oxygen. To ensure satisfactory performance, the membranes must be wettable by aqueous solution of potassium hydroxide (KOH) which is used as an electrolyte [2].

The measure of wettability is referred to the free surface energy, especially its polar component, which is responsible for surface adhesion to polar liquids such as KOH water solutions. Insufficient wettability (low surface energy) leads to adhesion of gas bubbles onto the separator with tendency to penetrate into pores. This leads into the reduction of active area for ion transfer and worsens the energy efficiency, resulting from the increase in cell ohmic resistance. Another consequence is the creation of H₂/O₂ gas mixtures which arise especially by dynamic power operation.

One of the mostly used separators today is Zirfon[®] which is a composite of PSF matrix doped with ZrO₂, serving as wettability enhancing additive. The composite is cast into 500-550 μ m thick membrane with 0.15 μ m average pore size [3]. However, high content of filler (85 wt.%) considerably contributes to the membrane cost and makes the membrane fragile, so that additional reinforcement by polyphenylene sulfide (PPS) fabric is necessary. Development of new separator materials is therefore an active area of research.

Wettability of thermoplastics can be improved, besides the other techniques, by grafting of polar group-containing monomers onto the polymer surface. Among many grafting monomers, acrylic acid (AAc) CH₂=CH-COOH is one of the most popular for hydrophilic surface modifications because of carboxylic functional groups which become intensively solvated in polar liquids. Grafting of AAc monomer proceeds by the interaction with radical situated on the treated surface of the substrate. The most common way of introducing radicals is plasma activation in low-pressure discharges in argon with subsequent exposition to air or activation in oxygen [5], which is accompanied by the creation of hydroperoxides on the polymer surface (P-OOH). Hydroperoxides are thermally unstable, hence they

undergo radical scissions. The formed radical ($\text{PO}\cdot$) act as active centre for graft polymerization when coming into contact with grafting monomer (M) of AAc present in liquid environment following the reactions 1.1 - 1.3 [6]. Until inhibited by another radical $\cdot\text{R}$ (eqn. 1.5), the $\text{PO-Mn}\cdot$ radical propagates the growth of grafted polymer chain (eqn. 1.4).



The study of plasma activation of porous PP membranes (Celgard 2500[®]) in low-pressure (50 Pa), microwave (2.45 GHz) discharge followed by liquid-phase grafting of AAc and their application as separators in alkaline NiCd batteries was already extensively studied [7].

In the present work we investigate alternative approach to create hydrophilic separators for alkaline electrolysis by plasma-induced graft polymerization of acrylic acid (AAc) on porous polypropylene membranes. We assume that filling of the pores by polyacrylic acid (pAAc) may notably reduce diffusion of produced hydrogen and oxygen and provide the membranes suitable for intermittent electrolyser operation.

2. Experimental

Samples preparation

Three types of PP membranes - PP nonwoven textile of 80 g/m² (referred to as PP 80) Celgard 2400 and PP 1 μm filter disc were cleaned by ultrasonic bath in methanol for 15 min., dried and kept under vacuum in dessicator until being used in experiments. Plasma reactor (volume of 14 700 cm³) with capacitive-coupled radio-frequency (RF) discharge was used for the sample activation. The distance between plan-parallel discharge electrodes of 80 mm diameter is set to 25 mm by polytetrafluorethylene (PTFE) support with the sample holder attached in the middle, as shown in the Fig. 1. The discharge was powered by Radio-frequency (RF) generator with symmetrical voltage outputs at frequency of 13.0 MHz. Prior to discharge ignition, the reactor chamber had been evacuated to a pressure below 10⁻¹ Pa. Working gas has been subsequently introduced to a pressure of 200 Pa (oxygen) or 100 Pa (argon) and maintained in flow regime (70 sccm). After activation in Ar plasma, the samples were exposed to ambient air for approximately 20 min to promote creation of hydroperoxides, while in the case of oxygen activation the samples were immediately grafted.

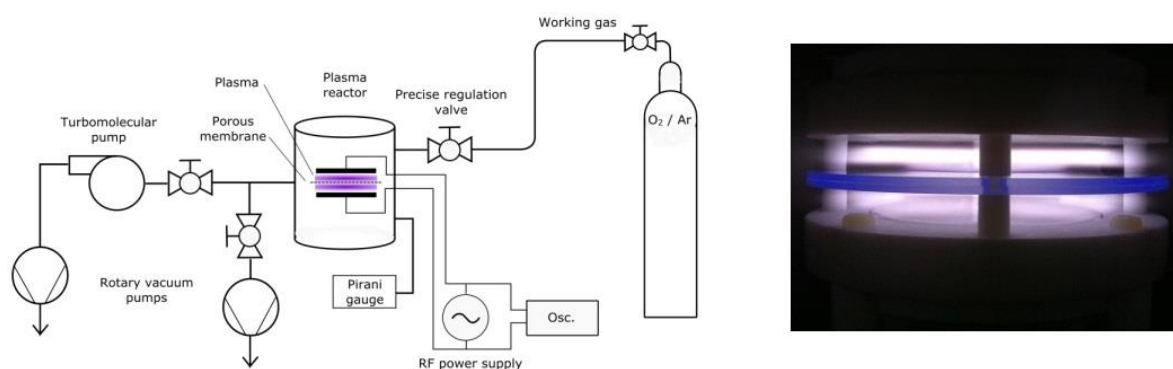


Fig. 1. Scheme of the apparatus for the activation of porous polymer membranes (left); photo of the RF discharge (right).

Grafting procedure was conducted in liquid phase. Acrylic acid per synthesis (> 99 %, Sigma-Aldrich) was vacuum-distilled to remove MEHQ stabiliser. Aqueous solution of AAc (20 vol.%) was poured into glass ampoules and deaerated by flushing with argon for 2 h. Activated samples were immersed in grafting solution, enclosed under Ar atmosphere and put into oven to maintain desired grafting temperature. Afterwards, the modified membranes were washed with 0.1 M KOH water solution for

24 h to dissolve pAAc homopolymer not covalently bound to the substrate and dried in ambient air at 50 °C. Different analyses were performed just after this procedure as well as during ageing tests. Before each analysis, the samples were washed twice in distilled water and dried in air.

Diagnostic methods

Concentration of hydroperoxides created on the polymer surface was quantified by a standard chemical analytical method based on a reaction with 2,2-Diphenyl-1-picrylhydrazyl (DPPH) dissolved in toluene [8]. It is a stable free radical which selectively reacts with $\cdot\text{OH}$ radicals coming from thermally-induced scissions of $-\text{OOH}$ functional groups. The amount of DPPH consumed was determined from Beer-Bouguer-Lambert law by measuring transmittance of the reagent solution (spectrophotometer Zeiss Nr. 776330) at $\lambda = 520$ nm.

Grafting Degree (GD) was determined gravimetrically and represents the weight content (wt.%) of pAAc on the grafted membrane.

Fourier-Transform Infrared Spectrometry (FTIR) was performed on Bruker Vector 22 using ATR (Attenuated Total Reflectance - single reflection) technique.

Electrical resistance of the separators was tested in four-contact electrolysis cell with a pair of planar nickel electrodes and a pair of self-constructed mercury-oxide (Hg/HgO) probe electrodes. Ohmic overvoltage created on the separator was determined by subtracting overvoltage measured without the separator from the overvoltage with separator at the same current density. The corresponding specific resistance per unit area was calculated from the slope of ohmic overvoltage as a function of cell current density.

The purity of gases produced in electrolysis cell (mutual electrode distance of 8 mm, active area of 13.8 cm²) was measured by a self-constructed thermal-conductivity detector (TCD). The gases enter TCD under atmospheric pressure after passing through bubblers which remove the remaining KOH aerosols and through dehydration cylinders. Measurement accuracy of the TCD determined from the calibration is ± 0.03 %.

3. Results

For argon and oxygen plasmas, applied voltages were 150 V and 320 V (peak-to-peak), respectively. Treatment gas flow rate was maintained at 70 sccm. Concentration of hydroperoxides on PP membranes formed by Ar and O₂ plasma activation was in order 10⁻⁹–10⁻⁸ mol/cm², see Fig. 2. It can be concluded that after O₂ plasma activation, the $-\text{OOH}$ concentration is higher as compared to Ar plasma at the same exposure time. We assume that this can be explained by the consumption of radicals formed during exposition to Ar plasma by crosslinking events until the sample is exposed to laboratory air. In O₂ plasma, this effect may play minor role because oxygen atoms/molecules are already present to promote peroxide formation. In addition, $-\text{OOH}$ formation after Ar plasma activation may be more dependent on air conditions (humidity etc.) during the experiments which is supported by wider error bars.

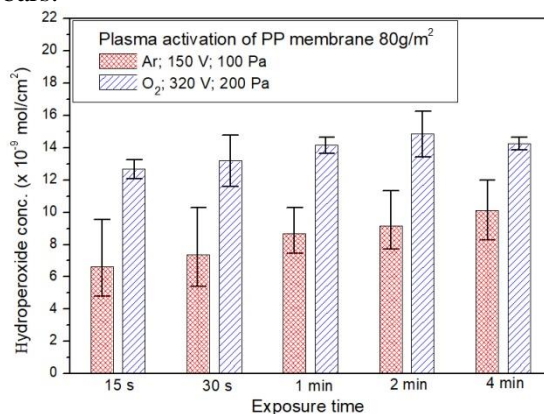


Fig. 2. Concentration of hydroperoxides per unit area formed on PP 80 membrane after exposure to argon and oxygen plasmas.

The samples prepared for grafting were activated as follows: 15 s for PP 80, 1 min for Celgard 2400 and 3 min for PP 1 μ m membrane. Drafting degree (see tab. 1) was determined just after grafting procedure. Structural analysis of the grafted and dried Celgard and PP 1 μ m membranes by SEM imaging is presented in Fig. 3. It can be seen that pores of Celgard became completely filled with pAAc while in the case of PP 1 μ m, pAAc coating of individual PP fibres is observed. Since pAAc swells and increases its volume intensively when immersed in KOH electrolyte we assume that the pores become blocked eventhough.

Ageing tests in 30 wt.% KOH at ambient temperature showed that membranes remain highly wettable even after 100-day storage with minor changes in GD. However, depletion of GD from 35 wt.% to 10 wt.% was observed when the storage was realised in 60 °C KOH for 50 days.

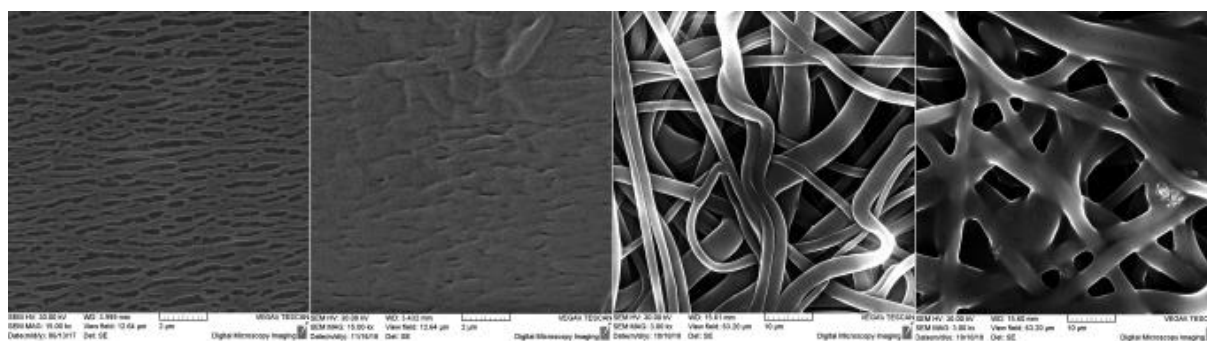


Fig. 3. SEM images of PP membranes. From the left: Celgard 2400 - virgin, Celgard 2400 - grafted (15kx magnification); PP 1 μ m - virgin, PP 1 μ m - grafted (3kx magnification); Electron energy 30 keV.

The prepared membranes were applied as separators in electrolysis cell. Figure 4 shows impurities of hydrogen and oxygen gases produced as a function of cell current density. It is evident that modified PP 80 used as separator at low-current density operation leads to much higher contamination of hydrogen and oxygen by respective foreign gas as compared to the two remaining membranes (PP disc 1 μ m and Celgard 2400). Moreover, fluctuations of gas impurity during pressure imbalances in the system were observed by using PP 80 which is in the contrary of very low electrical resistance (30 m Ω cm²). This is because of its high porosity (75 %) and above all, large average pore size.

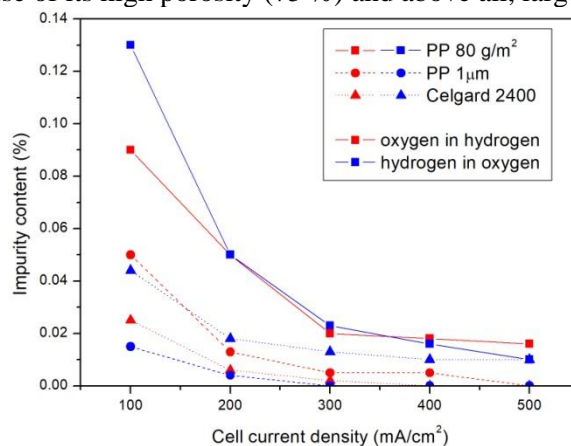


Fig. 4. Impurity of produced hydrogen and oxygen gases as a function of electrolysis cell current density.

It is generally known that in alkaline water electrolysis, oxygen impurity is higher than that of hydrogen because of higher diffusion of hydrogen in KOH electrolyte. When oxygen impurities are compared (Fig.4), the best result was obtained by using PP 1 μ m membrane. However, difference in electrical resistance between PP 1 μ m (250 m Ω cm²) and Celgard 2400 (52 m Ω cm²) is considerable. Because of major difference in membrane thickness, the corresponding specific resistance per unit volume of Celgard 2400 membrane is higher.

Table 1: Various parameters of the studied membranes and their comparison to commercial Zirfon^R membrane according to [9]. Pore size and porosity stated in the table are of virgin membranes, other parameters characterize membranes after grafting.

separator	pore size (μm)	porosity (%)	thickness (μm)	GD (wt. %)	resistance ($\text{m}\Omega\text{cm}^2$)	oxygen purity at 100 mA/cm^2 (%)
PP 80	-	75	450	3.2	30.2	>99.86
PP 1 μm	1 μm	65	600	45.7	250	>99.95
Celgard 2400	-	39	50	176	52	>99.98
Zirfon 550 LTP [9]	0.15 μm	50	550	-	270	-

4. Conclusion

The preliminary results presented in this work indicate that grafting of pAAc onto porous PP membrane represents a promising approach to prepare new separators for alkaline water electrolyzers. We find it important to emphasize that without the surface modification, polypropylene membranes are not applicable as separators at all, because of negligible retention of electrolyte. Grafting of pAAc leads to reasonable electrical conductivity which depends on initial membrane thickness, porosity and pore size. The highest grafting degree of 176 wt.% was achieved for Celgard 2400 membrane, while the highest oxygen gas purity produced by electrolysis was achieved when PP 1 μm was applied as separator. Application of PP 80 membrane in electrolysis cell led to gas purity fluctuations by changes in current density, therefore it was concluded to be not suitable for this purpose. In contrast, the performance of PP 1 μm was better in terms of gas separation efficiency while electrical resistance is almost an order of magnitude higher. The membranes remain hydrophilic in KOH electrolyte for at least 100 days at ambient temperature and 50 days at 60 °C. However, in order to prove suitability of the membranes for the desired application, longer ageing tests at elevated temperatures are necessary.

5. Acknowledgement

This work has received funding from the European Union's Horizon 2020 research and innovation programme under grant agreement No. 692335 and was supported by the Slovak grant agency Vega, project No. 1/0930/17.

6. References

- [1] G. Gahleitner, "Hydrogen from renewable electricity: An international review of power-to-gas pilot plants for stationary applications," *Int. J. Hydrog. Energy*, vol. 38, no. 5, pp. 2039–2061, Feb. 2013.
- [2] A. Godula-Jopek, *Hydrogen production: by electrolysis*. Weinheim, Germany: John Wiley & Sons, 2015.
- [3] P. Vermeiren, W. Adriansens, and R. Leysen, "Zirfon®: A new separator for Ni-H₂ batteries and alkaline fuel cells," *Int. J. Hydrog. Energy*, vol. 21, no. 8, pp. 679–684, 1996.
- [5] S. Saxena, A. R. Ray, and B. Gupta, "Graft polymerization of acrylic acid onto polypropylene monofilament by RF plasma," *J. Appl. Polym. Sci.*, vol. 116, pp. 2884–2892, 2010.
- [6] C. Oehr, M. Müller, B. Elkin, D. Hegemann, and U. Vohrer, "Plasma grafting—a method to obtain monofunctional surfaces," *Surf. Coat. Technol.*, vol. 116, pp. 25–35, 1999.
- [7] A. Ciszewski, I. Gancarz, J. Kunicki, and M. Bryjak, "Plasma-modified polypropylene membranes as separators in high-power alkaline batteries," *Surf. Coat. Technol.*, vol. 201, no. 6, pp. 3676–3684, Dec. 2006.
- [8] M. Suzuki, A. Kishida, H. Iwata, and Y. Ikada, "Graft copolymerization of acrylamide onto a polyethylene surface pretreated with glow discharge," *Macromolecules*, vol. 19, no. 7, pp. 1804–1808, 1986.
- [9] D. Burnat *et al.*, "Composite membranes for alkaline electrolysis based on polysulfone and mineral fillers," *J. Power Sources*, vol. 291, pp. 163–172, Sep. 2015.

ROLL-TO-ROLL ATMOSPHERIC PRESSURE PLASMA TREATMENT OF POLYAMIDE FOILS

Vlasta Štěpánová, Slavomír Sihelník, Petra Šrámková, Jana Jurmanová,
Dušan Kováčik

*CEPLANT, Department of Physical Electronics, Faculty of Science, Masaryk University,
Kotlářská 2, 611 37 Brno, Czech Republic
E-mail: vstepanova@mail.muni.cz*

The subject of this contribution is a hydrophilic ambient air plasma treatment of polyamide (PA) foils using diffuse coplanar surface barrier discharge with a concavely curved configuration of electrode system. The short plasma exposure time in the range of 0.5–2 s was sufficient for hydrophilization of foils. It was carried out also the comparison of discharge input power (400 W, 600 W) influence on water contact angle (WCA) values. A significant effect of plasma treatment on PA foils hydrophilicity increase was observed even after 0.5 s of treatment at the input power of 400 W when WCA was reduced from value 65° to 40°. The most significant wettability increase of PA surface was achieved after plasma treatment at a higher input power of 600 W. In this case, WCA decreased from value 65° to 28° after 2 s of plasma treatment. Even one month after the treatment the WCA values did not reach the initial values before treatment. No morphological changes were observed on the surface of PA foils after the plasma treatment.

1. Introduction and experimental

Polyamide foils belong among thermoplastic materials with poor hydrophilic properties that affect their wettability, adhesion, or printability, and for this reason, an improvement of surface properties is desirable. Besides chemical, thermal, or mechanical methods of surface modification, plasma treatment is widely used as an effective tool for surface modification of polymer materials without damaging the bulk material^[1]. One example is the use of dielectric barrier discharge at atmospheric pressure for durable hydrophilicity enhancement of polymeric substrates.^[2] Plasma treatment allows for improvement of dyeing mechanism, dye fixation and shorter dyeing times of polyamide fibres than with traditional dyeing methods.^[3] A significant increase in surface energy, improvement of bonding, and adhesion enhancement is often observed after plasma treatment of polyamide.^[4]

Diffuse coplanar surface barrier discharge (DCSBD)^[5] operating at atmospheric pressure has several applications in the treatment of nonwoven fabrics^[6,7], paper^[8], and polymers^[9–11]. The present study aimed to increase the hydrophilicity of polyamide (PA) foil surface by plasma treatment and to verify the stability of this effect in time. The DCSBD plasma source was applied to the surface of the PA foil for a short exposure time in the range of 0.5–2 sec. This plasma source was developed in a planar and later also in a concavely curved configuration of electrode system that allows for continuous roll-to-roll treatment of nonporous flexible materials^[12]. The plasma treatment of PA foils in this study was carried out in a laboratory reactor similar in principle to common roll-to-roll systems. It consists of a metal roller covered with rubber and a DCSBD unit with the concavely curved electrode system as shown in Fig. 1a and 1c. The significant features of the DCSBD plasma source have already been described previously^[5,7]. DCSBD generates non-equilibrium plasma in the form of a thin plasma layer with dimensions 8 cm × 20 cm (Fig. 1b) and with the effective thickness reaching value ~ 0.3 mm in ambient air. The frequency of supply voltage is usually in the range of 15–30 kHz and corresponding discharge input power from 400 W up to 700 W. The main feature of DCSBD plasma is its diffusiveness (Fig. 1b) and high plasma power density ~ 100 W/cm³. Several different distances (0.3 mm, 0.4 mm, 0.5 mm) between the sample and the ceramics of the DCSBD electrode system were studied. During the experiments, the PA foils treatment speed varied in the range of 4–16 cm/s depending on the exposure time (0.5 s, 1 s, 2 s). Also, the influence of two different input power values (400 W, 15 kHz; 600 W, 30 kHz) on the wettability change was studied. For evaluation of surface changes on PA foil surfaces after plasma exposure, the methods of surface analysis such as water contact angle (WCA) measurement and scanning electron microscopy (SEM) were used.

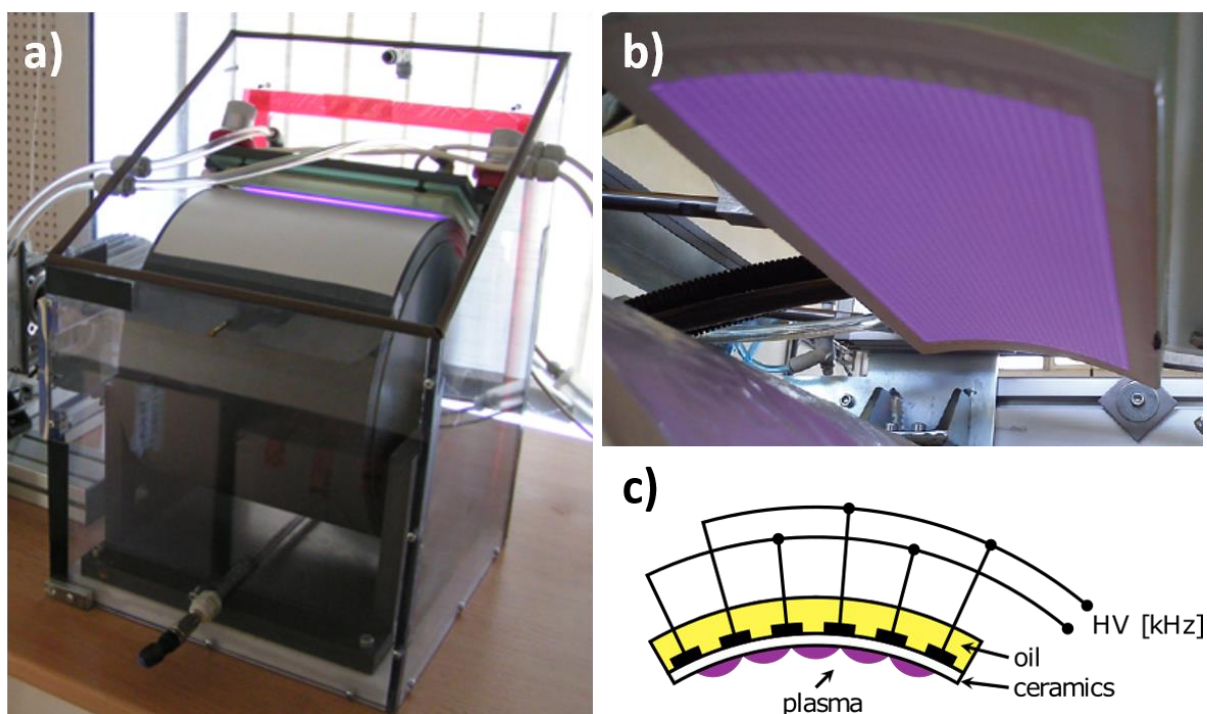


Fig. 1. DCSBD experimental setup, a) plasma reactor with installed DCSBD unit, b) DCSBD plasma generated in ambient air, c) a schematic diagram of a concavely curved DCSBD electrode system.

2. Results and discussion

As mentioned, the plasma treatment of the PA foils was carried out at several different distances of the sample from the ceramics of the DCSBD electrode system. The optimal and most effective distance of 0.3 mm was determined on the base of WCA measurements. This agrees with the claim that the effective thickness of DCSBD plasma for treatment of most nonconductive substrates is this value^[9,13]. An effect of plasma treatment was observable also in larger investigated distances between the samples and the ceramics, however, the effect was less significant.

Investigation of wettability changes immediately after plasma treatment and up to 1 month later (1, 5, 9, 14 and 30 days) was the main goal of this study. WCA of an untreated PA foil corresponds to the value of $65.4^{\circ} \pm 1.3^{\circ}$. Ten water drops were measured for each parameter (exposure time, input power, ageing time) and the presented WCA value is calculated as the average value. The influence of plasma exposure time on WCA values is presented in Fig. 2. It demonstrates that the WCA values measured immediately after DCSBD plasma treatment at the input power of 400 W were similar for all exposure times (approx. $38\text{--}40^{\circ}$). Differences in WCA values for various exposure times were observed during ageing of plasma treatment. After 5 days the WCA values differed by 5° for each exposure time, while after one month WCA was in the range of $56\text{--}58^{\circ}$ for all exposure times. WCA values did not reach the initial value even after one month from the treatment. Furthermore, the influence of higher discharge input power of 600 W was studied (Fig. 3). Plasma treatment at 600 W led to better results in PA foils wettability. The WCA values measured immediately after treatment decreased below 30° for exposure time 1 and 2 s. The effect of higher input power was evident also during ageing of treatment and led to the lower values of WCA. One month after treatment the WCA values increased only to values of $44\text{--}53^{\circ}$ depending on the exposure time.

The influence of discharge input power on hydrophilic plasma treatment of PA foils for 0.5 s exposure time is demonstrated in Fig. 4, in which WCA values measured on the treated surface at the input power of 400 W and 600 W are compared. The exposure time of 0.5 s and shorter is promising for plasma treatment of foils and other thin flexible substrates on the industrial level. As already pointed out, the positive effect of higher input power on WCA values is significant especially during ageing of plasma treatment. The value of WCA for plasma treated PA foil at input power of 600 W was 53° after one month from the treatment, which is lower than 58° for input power of 400 W.

More efficient hydrophilic treatment of the PA foils at higher discharge input power can be explained by the fact that plasma is characterized by higher power density and therefore more effective and stable treatment. Moreover, the plasma treatment using DCSBD is gentle, which was confirmed by SEM measurements carried out on the treated samples for all investigated exposure times and both values of discharge input power. No morphological changes were observed on the surface of PA foils after plasma treatment.

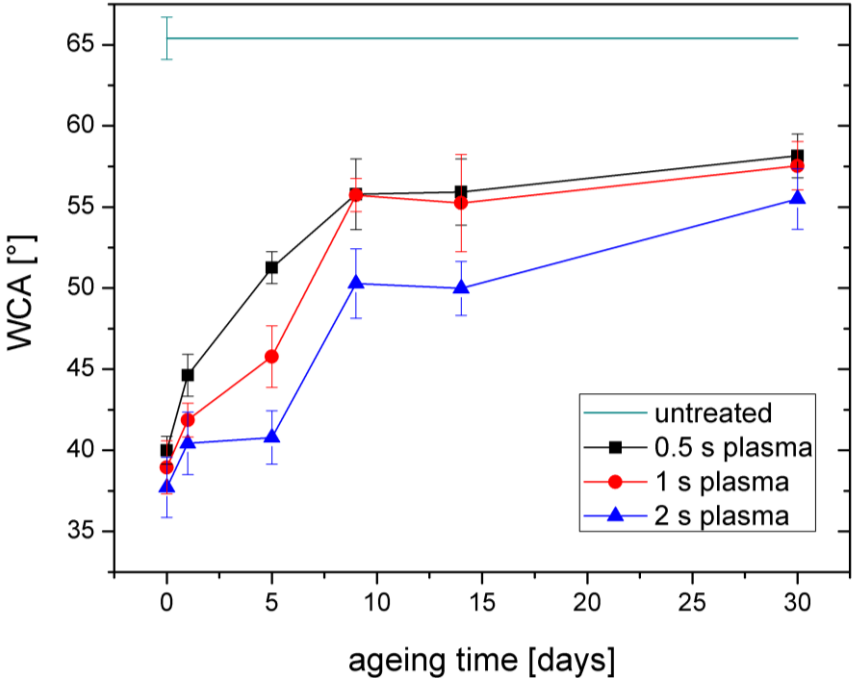


Fig. 2. WCA measured on PA foils after DCSBD plasma treatment in dependence on ageing time for different exposure times at discharge input power 400 W.

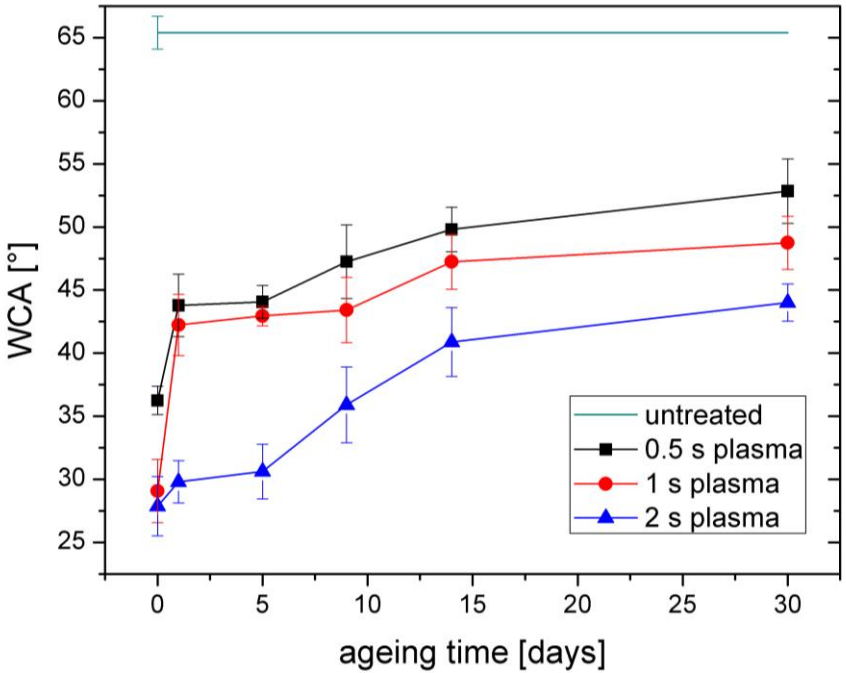


Fig. 3. WCA measured on PA foils after DCSBD plasma treatment in dependence on ageing time for different exposure times at discharge input power 600 W.

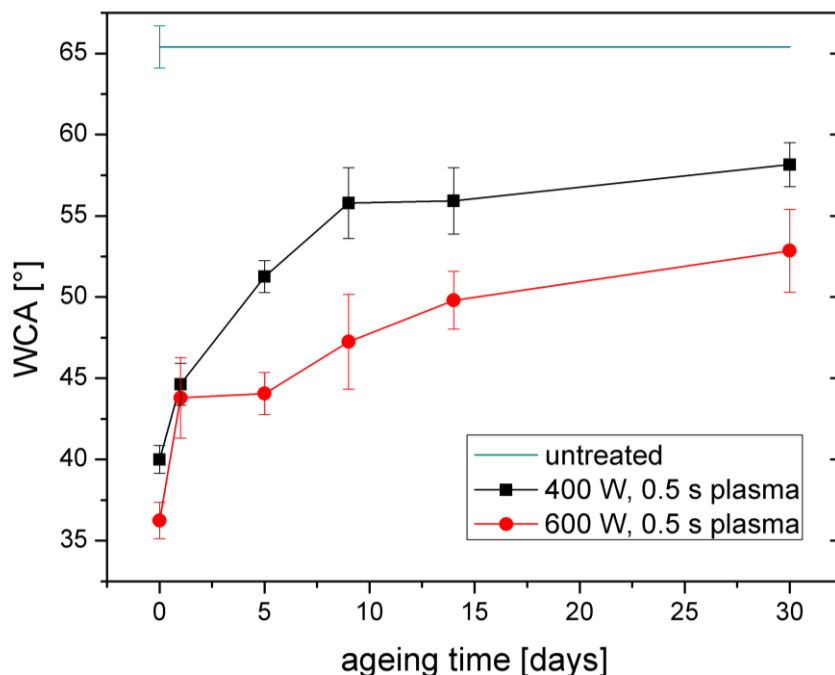


Fig. 4. Ageing comparison of DCSBD plasma treatment of PA foils for exposure time 0.5 s at discharge input power values 400 W and 600 W.

Based on the obtained results of WCA measurement we can compare the plasma treatment of polyamide foils carried out using the DCSBD with the concavely curved configuration of electrode system with the DCSBD consisting of the common planar configuration of electrodes^[9]. The larger errors of WCA values were calculated in case of PA foils treated with the DCSBD system with the planar configuration of electrodes^[9], whereas the error bars obtained from WCA measurement for PA foils treated using the DCSBD with the concavely curved electrodes were much smaller. It is an evident confirmation of higher homogeneity of plasma treatment using the DCSBD with the concavely curved system of electrodes in continuous regime (roll-to-roll) compared to the planar one. Setting the exact distance of the sample surface from DCSBD ceramics and ensuring the continuous movement of the sample are crucial parameters for homogeneous plasma treatment.

These preliminary results are promising and open the possibilities for continuous roll-to-roll plasma treatment of polymeric foils and other thin flexible substrates at high speed. Moreover, the research of DCSBD plasma treatment of PA foils is still ongoing including other analyses of the influence of plasma treatment on other surface properties. Surface chemistry will be studied via X-ray photoelectron spectroscopy and adhesion will be determined by a standard peel test. A comparative study of DCSBD and industrial corona treatment efficiency will be also carried out.

3. Conclusion

DCSBD represents a highly effective plasma source for fast, low-cost, and environmentally friendly treatment of polymers. Roll-to-roll treatment is suitable for in-line treatment of nonconductive flexible materials in large quantities. Plasma treatment already of the duration of 0.5 s resulted in a significant effect on the wettability of polyamide foil and led to its hydrophilization. The influence of discharge input power (400 W, 600 W) on WCA values was investigated, more significant wettability change was achieved using input power of 600 W. The DCSBD technology allows reaching shorter treatment time and increasing the treatment speed. Required treatment speed from polymer industry corresponds at least to the value of 30 m/min. Considering that the DCSBD technology is scalable using more plasma units together, it is possible to reduce the plasma exposure time and reach the required treatment time ~ 0.1 s.

Acknowledgement

This research has been supported by the project MUNI/31/63965/2018 funded by Masaryk University and project LO1411 (NPU I) funded by the Ministry of Education, Youth and Sports of the Czech Republic.

References

- [1] Hnilica J, Potočnáková L, Stupavská M, Kudrle V, 2014 *Appl. Surf. Sci.* **288**, 251.
- [2] Dubreuil M F, Bongaers E M, 2008 *Surf. Coat. Technol.* **202**, 5036.
- [3] Oliveira F R, Zille A, Souto A P, 2014 *Appl. Surf. Sci.* **293**, 177.
- [4] Novák I, Števiar M, Chodák I, 2006 *Monatshefte fur Chemie* **137**, 943.
- [5] Šimor M, Ráhel' J, Vojtek P, Černák M, Brablec A, 2002 *Appl. Phys. Lett.* **81**, 2716.
- [6] Kovacik D, Skacelova D, Slavicek P, Mikula M, Cernak M, 2014 *Surf. Modif. Technol.* XXVIII, Valardocs, Tampere, 385.
- [7] Černák M, Kováčik D, Ráhel' J, St'ahel P, Zahoranová A, Kubincová J, Tóth A, Černáková L, 2011 *Plasma Phys. Control. Fusion* **53**, 124031.
- [8] Skácelová D, Kováčik D, Homola T, Čech J, Černák M, 2016 *Atmos. Press. Plasmas*, Nova Science Publishers, Inc., 227.
- [9] Hanusová J, Kováčik D, Stupavská M, Černák M, Novák I, 2015 *Open Chem* **13**, 382.
- [10] Kelar J, Shekargoftar M, Krumpolec R, Homola T, 2018 *Polym. Test.* **67**, 428.
- [11] Kováčik D, Maxa J, Skácelová D, Kršková J, Stupavská M, Zahoranová A, Černák M, 2016 *Konf. PLASTKO*.
- [12] Shekargoftar M, Krumpolec R, Homola T, 2018 *Mater. Sci. Semicond. Process.* **75**, 95.
- [13] Černák M, Černáková L, Hudec I, Kováčik D, Zahoranová A, 2009 *Eur. Phys. J. Appl. Phys.* **47**, 22806.

LOW TEMPERATURE AIR PLASMA AND ITS EFFECT ON GERMINATION OF SOYA BEANS

Juliána Tomeková¹, Beáta Feilhauerová¹, Renáta Švubová²,

Ľudmila Slováková², Anna Zahoranová¹

¹*Department of Experimental Physics, Faculty of Mathematics, Physics and Informatics, Comenius University, Mlynská dolina F2, Bratislava 842 48, Slovakia*

²*Department of Plant Physiology, Faculty of Natural Sciences, Comenius University, Ilkovičova 6, Mlynská dolina B-2, Bratislava 842 15, Slovakia*

E-mail: juliana.tomekova@fmph.uniba.sk

The effect of low temperature plasma treatment on the germination of soya bean (*Glycine max*) seeds were studied in this contribution. Diffuse Coplanar Surface Barrier Discharge was used to generate low temperature plasma in ambient air at atmospheric pressure. The effect on soya beans germination was observed at various plasma exposures, to establish the optimal time. The optical emission spectroscopy method enabled us to determine rotational and vibrational temperature of the plasma components from the second positive system of nitrogen which dominated in the spectrum. Chemical composition of plasma gaseous products was investigated by Fourier Transform Infrared Spectroscopy.

1. Introduction

Low temperature plasma (LTP) is nowadays an actual point in application research. LTP contains many reactive species which affect the surface and may improve surface properties of various materials. The low temperature of heavy particles makes the plasma proper also for the treatment of sensitive material as polymers or biomaterial [1]. As many studies show, LTP has a positive effect on the seed germination, growth parameters or the decontamination effect on the biomaterial surface [2-4]. We used Diffuse Coplanar Surface Barrier Discharge (DCSBD) as a source of LTP for the treatment of soya beans and then we studied the influence on their germination. This type of plasma is created in thin layer on the ceramic surface [5].

Before the industrial use, it is needed to investigate the plasma properties, its chemical composition, concentrations or temperatures of reactive species. It is important for better understanding mechanisms of action of individual particles, which participate in changes of material properties. For plasma diagnostics, we used Optical Emission Spectroscopy (OES) and Fourier Transform Infrared Spectroscopy (FTIR).

2. Experimental

Diffuse Coplanar Surface Barrier Discharge

DCSBD, which we used as a source of LTP for the treatment of seeds, is composed of many parallel electrodes of 1.5 mm wide and 20 cm long placed in mutual distance of 1mm. Electrodes were embedded in dielectric material (Al₂O₃ 96% purity), cooled by oil flowing in cooling circuit. DCSBD was powered by AC high frequency sinusoidal voltage (14 kHz, up to 20 kV peak-to-peak) generated by LIFETECH VF 700 generator (from LIFETECH, s.r.o. Brno, Czech Republic). Schematic layout of DCSBD together with experimental set-up for treatment of seeds, OES and FTIR measurement is shown in Fig.1.

Plasma Treatment of Seeds

Soya bean seeds were treated in LTP of DCSBD discharge ignited in ambient air at atmospheric pressure at input power of 400 W and at the different exposure times: 30, 60, 90, 120 s. The DCSBD plasma panel was placed on the orbital shaker (PSU-10i, f. Biosan), which was used at the frequency 270 rpm

in order to achieve the movement of the seeds in plasma layer for the purpose of homogeneous treatment of the seeds.

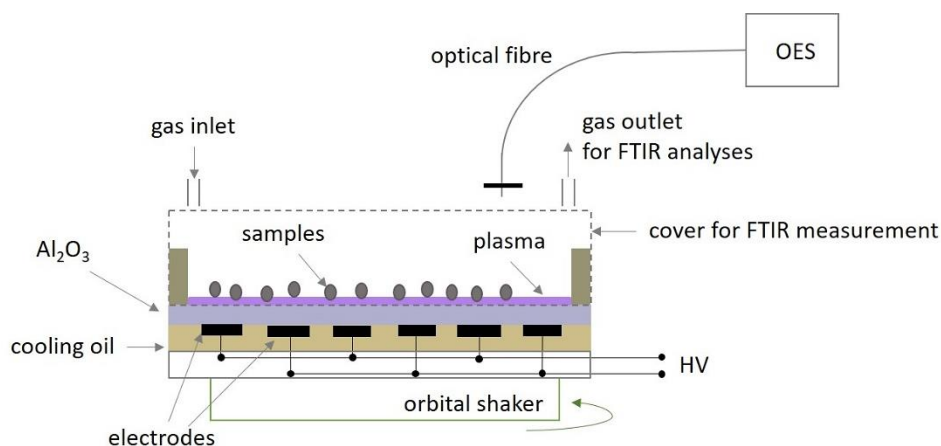


Fig. 1 Experimental set-up for plasma seed treatment, OES and FTIR measurements and scheme of DCSBD electrode system

Plasma Effect on Seed Germination

For estimation of plasma effect on vigor of soybean seeds, there were used 50 seeds, which were rolled in the sterile filter paper placed in glass pots and moistened with sterile deionized water. Seeds for germination were cultivated in the incubator at 24 °C in the dark for 5 days. The percentage of germination was calculated using the equation: final germination percentage = number of germinated seeds multiply by 100 and divided by total number of seeds. Germination potential was calculated as number of germinated seeds in 3 days divided by total number of seeds and multiplied by 100. Index of germination was calculated as a sum of germinated seeds on day x divided by days of germination.

OES of DCSBD plasma

Optical emission spectrum of DCSBD plasma was measured by the spectrometer AvaSpec 2048 TEC in spectral range 300-400 nm and with resolution 20 px/nm. Optical fibre mounted in a stand 6.3 cm above the dielectric surface collected optical radiation emitted from the plasma (from a circular area of 2.9 cm in diameter on the ceramics Al_2O_3) to the spectrometer connected with a computer (see Fig. 1). Spectrum was recorded by the programme AvaSoft and then analysed. Spectrum analysis included determination of vibrational and rotational temperature of the plasma. Vibrational temperature was calculated from relative intensities of the nitrogen peaks (0-2, 1-3, 2-4, 3-5 transition of second positive system of nitrogen $\text{N}_2(\text{C-B})$) by the programme Spectrum Analyzer 1.8 [6] and rotational temperature by the comparison of experimental and simulated 0-1 vibration transition of $\text{N}_2(\text{C-B})$ in software Specair 3.0 [7].

FTIR spectroscopy of gaseous content of the plasma

To find out the chemical composition of the plasma gaseous content, we used FTIR spectroscopy. FTIR spectrum was measured in range (4000-400) cm^{-1} , with resolution 2 cm^{-1} and 20 scans per sample, using Bruker Vector 22 FTIR spectrometer.

Ambient air from the room was carried by the compressor and passed through the flow meter into the DCSBD reactor chamber with 1.3 L volume (see Fig. 1) with flow rate 3 L/min. Subsequently, the gas from the chamber was carried for analysis through the tube and collected inside the gas cell (10 cm length and 31 cm^3 volume) situated in FTIR spectrometer, where the infrared radiation passed through the cell one time.

3. Results and discussion

Plasma Effect on Seed Germination

Germination, germination potential and index of germination measured on soya bean seeds showed an improvement at 30, 60, 90 s plasma treatment. At 120 s exposure time, only germination potential is better than reference (untreated) sample (see Fig. 2). The best results for ambient air plasma is at exposure time of 30 s. As shown by our previous experimental results (not published in this contribution) carried out in nitrogen and oxygen plasma at the same treatment times as it is in case of ambient air plasma, the best values of germination parameters were in case of 60 s treated seed sample. In case of 30 s ambient air plasma treatment, results showed the similar values of germination and index of germination than in nitrogen plasma, which shows better results than oxygen plasma. Therefore, the ambient air was chosen as working gas as the most advantageous alternative.

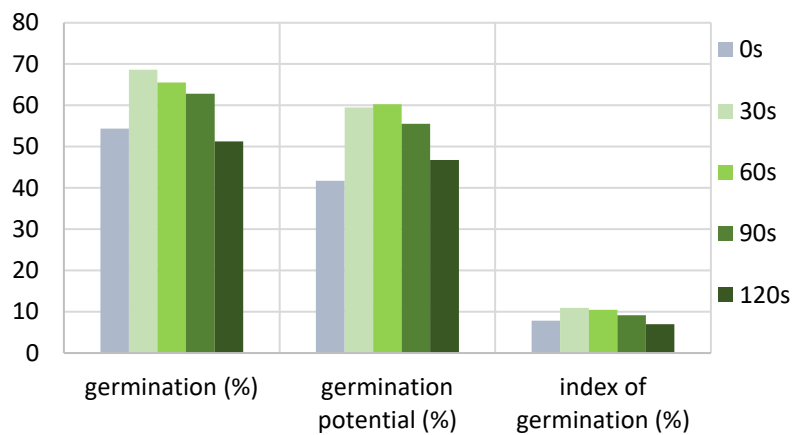


Fig. 2 Effect of LTP plasma, generated in ambient air at input power of 400 W, on germination, germination potential and index of germination of soya beans treated at different times (0, 30, 60, 90, 120 s)

OES of DCSBD plasma

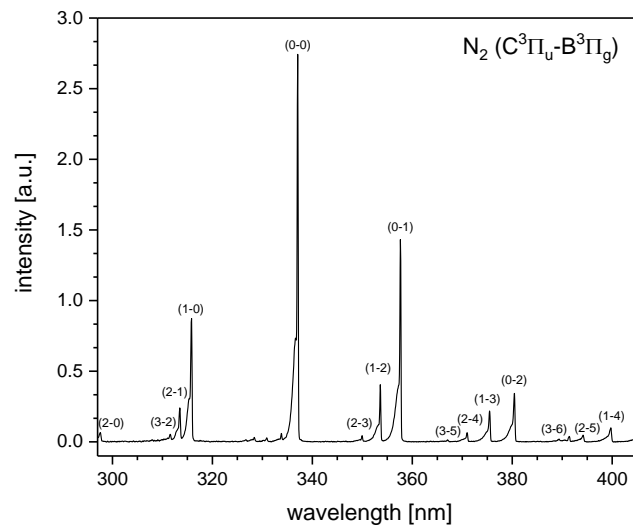


Fig. 3 Optical emission spectrum of DCSBD plasma generated in ambient air at input power of 400 W, second positive system of nitrogen $C^3\Pi_u - B^3\Pi_g$ is marked

Optical emission spectrum of DCSBD plasma is dominated by the second positive system of nitrogen $N_2(C^3\Pi_u-B^3\Pi_g)$, which transitions are marked in measured spectrum in Fig. 3. Non-equilibrium character of the plasma was confirmed by differences between values of vibrational and rotational temperatures. Vibrational temperature calculated from transitions 0-2, 1-3, 2-4, 3-5 reached the value $T_{\text{vib}} = 2800 \pm 250$ K and rotational temperature determined by simulation of 0-1 peak was $T_{\text{rot}} = 400 \pm 50$ K.

FTIR spectroscopy

FTIR spectroscopy of gaseous compounds from ambient air DCSBD plasma revealed the presence of various oxygen and nitrogen species (NO_2 , N_2O , NO , HNO_3 , HNO_2 , CO_2) and also water originating from air humidity [8-10]. The most intensive peak is NO_2 at 1630 cm^{-1} and then N_2O at 2235 cm^{-1} . Two more significant peaks of N_2O are visible at 590 cm^{-1} and 2915 cm^{-1} . Based on the smell during generating the plasma, ozone is also created in working gas but FTIR spectrum does not confirm its presence. We may therefore conclude that the concentration of ozone is less than can be detected by FTIR or ozone expires by some reactions. We tried to measure ozone concentration in synthetic air plasma which could be similar for ambient air plasma. In case of synthetic air plasma, we observed no ozone peak in optical absorption spectra at the same input power (400 W) what confirmed the FTIR measurement.

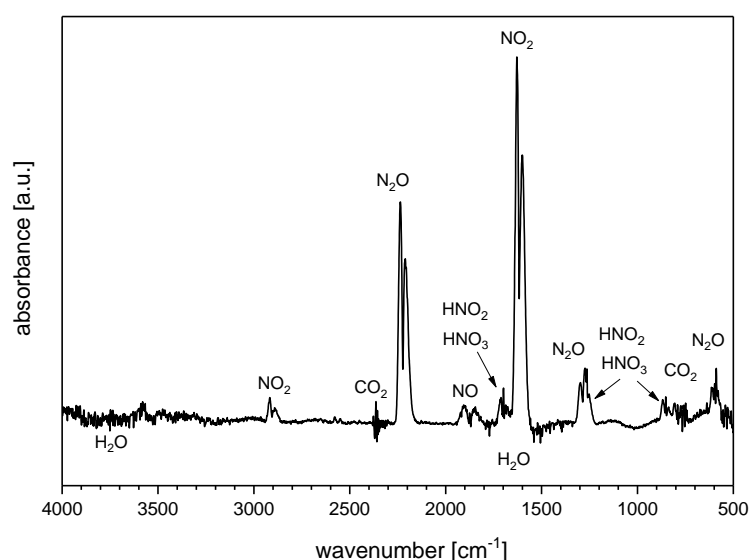


Fig. 4 FTIR spectrum of gas compounds of DCSBD plasma generated in ambient air at input power of 400 W

4. Conclusion

In this contribution the DCSBD plasma treatment of soya beans seeds, the important agricultural crop, was tested as an advantageous tool for germination improving. The best germination was reached at the treatment time of 30 s in ambient air at atmospheric pressure.

We performed also diagnostics of the plasma composition and properties using optical emission and absorption spectroscopy. As resulted from measured spectra, DCSBD plasma is non-equilibrium, with rotational temperature $T_{\text{rot}} = 400 \pm 50$ K and vibrational temperature $T_{\text{vib}} = 2800 \pm 50$ K. In FTIR spectrum of the gaseous products dominated NO_2 and N_2O , which temperature can be the temperature of the gas (\sim rotational temperature). Difference in conditions between the really seeds treatment and FTIR measurements is that in case of FTIR we used flow mode of ambient air (3L/min). Therefore, it could be useful to realise the plasma treatment at the same condition of flow mode and investigate if the

flow mode influence germination parameters. In comparison with experiments with oxygen and nitrogen plasma which results are not presented in this work, we observed that the highest values of germination and germination potential are in case of nitrogen plasma. Index of germination in nitrogen plasma is less than in case of ambient air plasma, but the difference is negligible (0,2 %). On the other hand, germination results after oxygen plasma treatment are worse than in case of ambient air plasma. From these aspects and results of our measurements we could predict that reactive nitrogen species or optical emission radiation improve germination parameters of the plasma treated seeds, but it is the topic for the next research.

5. Acknowledgement

This work was supported by the Slovak Research and Development Agency under the contract No. APVV-16-0216. This work is the result of the project implementation ITMS code 26240220042 supported by the Research & Development Operational Programme funded by the ERDF

6. References

- [1] Laroussi M. 2005 *Plasma Process Polym.* **2** 391
- [2] Henselová M, Slováková L, Martinka M, Zahoranová Z 2012 *Biologia.* **67** 490
- [3] Zahoranová A, Henselová M, Hudecová D et al. 2016 *Plasma Chemistry and Plasma Processing* **36** 397
- [4] Stolarík T, Henselová M, Martinka M et al. 2015 *Plasma Chemistry and Plasma Processing.* **35** 659
- [5] Černák M, Ráhel' J, Kováčik D et al. 2004 *Contributions to Plasma Physics* **44** 492
- [6] Navrátil Z, Trunec D, Smid R and Lazar L 2016 *Czechoslovak Journal of Physics* **56** B944
- [7] Laux CO (2002) Radiation and Nonequilibrium Collisional-Radiative Models. von Karman Institute Lecture Series 2002-07, Physico-Chemical Modeling of High Enthalpy and Plasma Flows, eds. D. Fletcher, J." M. Charbonnier, GSR Sarma, and T. Magin, Rhode-Saint-Genèse, Belgium.
- [8] Reuter S, Sousa J S, Stancu G D and Hubertus Van Helden J P 2015 *Plasma Sources Science and Technology* **24** 054001
- [9] Sivachandiran L and Khacef A 2017 *RSC Advances* **7** 1822
- [10] Gordon I E, Rothman L S, Hill C et al. 2017 *Journal of Quantitative Spectroscopy & Radiative Transfer* **203** 3

STRUCTURING OF POLYMETHYLMETHACRYLATE SUBSTRATES BY REDUCING PLASMA

Zlata Tučeková, Jakub Kelar, Zdeňka Doubková, Richard Krumpolec

R&D Centre for Low-Cost Plasma and Nanotechnology Surface Modifications,

Masaryk University, Kotlářská 267/2, 611 37 Brno, Czech Republic

E-mail: zlata.tucekova@mail.muni.cz

This contribution presents the results of plasma modification of rigid and flexible polymethyl methacrylate (PMMA) using Diffuse Coplanar Surface Barrier Discharge (DCSBD) generated in pure hydrogen at atmospheric pressure. After the several minutes of the plasma treatment, a time-dependent and plasma gap-dependent formation of nanoscale pillar-like structures was observed on rigid and flexible PMMA surface. The structuring and etching of substrates were investigated by a scanning electron microscopy. Atomic force microscopy revealed an increase of surface roughness in the order of 10.

1. Introduction

Plasma-induced etching and surface structuring of polymer substrates is capable to influence the wettability and surface morphology without the undesirable changes of the bulk and optical properties [1]. Surface etching of polymers has been studied to prepare superhydrophobic and superoleophobic surfaces for e.g. self-cleaning and bio- applications [2-5]. Usually, low-pressure plasma is reported to carry out polymer etching mostly in Ar, He, O₂ and fluorocarbon-containing gases [3,6-7]. The plasma generated at atmospheric pressure was recently tested in various gas mixtures for dry etching of different polymeric materials [8-12].

In this paper, the diffuse coplanar surface barrier discharge (DCSBD), capable of meeting the industrial requirements in reduction atmosphere, was used for surface etching and structuring by low-temperature (80°C) atmospheric pressure plasma [10]. The effect of DCSBD plasma generated in pure hydrogen, with high electron density of $\sim 1.3 \times 10^{16} \text{ cm}^{-3}$ and a mean electron temperature of approx. $19 \times 10^3 \text{ K}$ [13], was tested on one rigid and one flexible polymethylmethacrylate (PMMA) substrate.

2. Experimental

PMMA substrates - 2.0 mm thick sheet (CHO CHEN Ind. Co., Ltd, Taiwan) and 0.05 mm thin foil (DENZ BIO-MEDICAL GmbH, Austria), were treated with plasma generated by DCSBD plasma source. The plasma was generated on the area of $20 \times 8 \text{ cm}^2$ using high voltage generator VF700 (LIFETECH s.r.o., Czech Republic) with the frequency of 15 kHz and input power of 400 W. The samples were treated at a distance 0.2 mm from the DCSBD ceramics in a dynamic regime (samples were moved relative to the plasma).

The schematics of DCSBD as well as a picture of plasma generated by DCSBD in pure hydrogen can be seen in **Figure 1**. The plasma source was placed in the reactor chamber of volume approximately 2 l. The gas flow of pure hydrogen (99.998%, MESSER TECHNOGAS s.r.o., Czech Republic) was kept at 1 l/min during the plasma treatment.

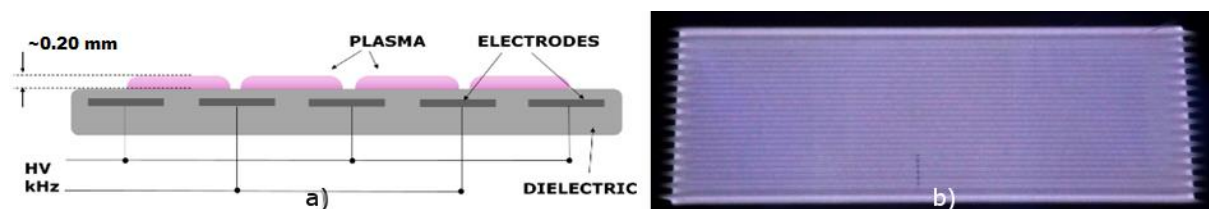


Fig. 1: a) Schematics of DCSBD plasma device and b) picture of DCSBD plasma in pure hydrogen [11].

The morphological changes of polymer surfaces were measured using Scanning Electron Microscope Mira3 (TESCAN s.r.o., Czech Republic) with accelerating voltage of 5 kV using secondary electron emission detector. To prevent charging of the polymer surface, the samples were coated with 10 nm of

Au/Pd composite layer. For etching rate estimation, the dimensions of PMMA foil edge (reference and treated) were measured. The changes in surface roughness were measured using Atomic Force Microscope NTEGRA Prima (NT-MDT, Russia) in a semi-contact mode.

3. Results and Discussion

The time-dependent change of the surface morphology of PMMA substrates before and after plasma modification in pure hydrogen (treatment time 5, 10 and 30 minutes) is shown in SEM micrographs (**Figure 2**). The change of the PMMA foil surface after 60 minutes of treatment with a different the plasma gap (or ceramics-substrate distance) from 0-0.7 mm is shown in **Figure 3**. The change of the RMS surface roughness of flexible and rigid PMMA measured by AFM is shown in **Table 1**.

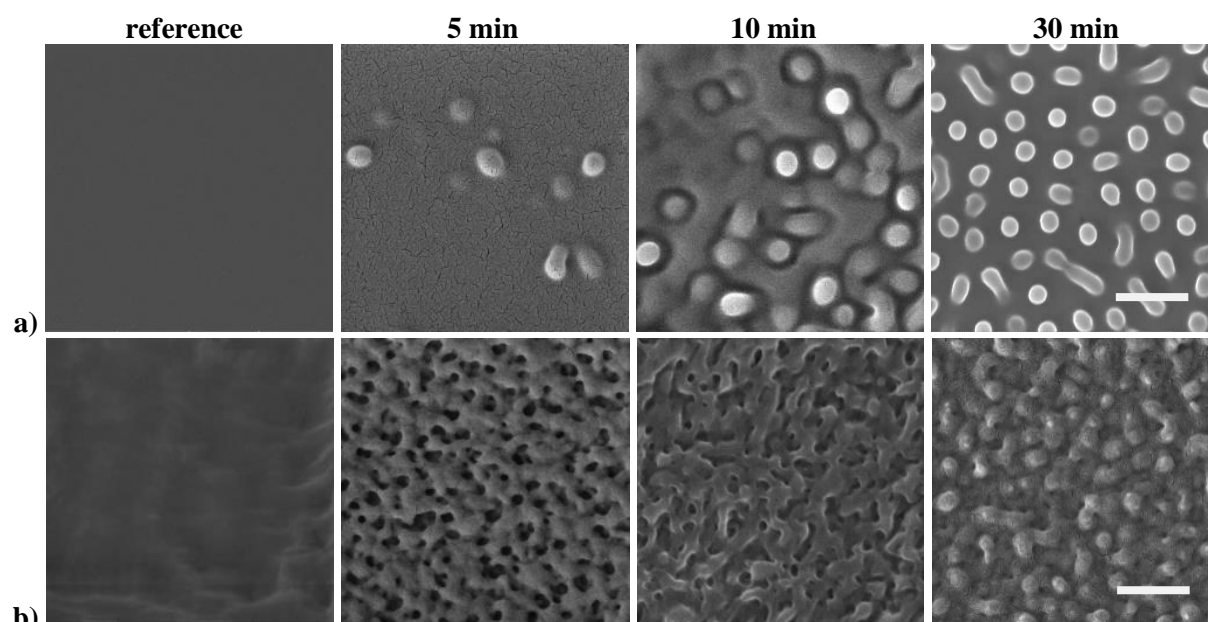


Fig. 2: SEM micrographs of the PMMA sheet (a) and foil (b) (from left to right) reference sample and samples 5, 10 and 30 min treated by DCSBD plasma generated in pure hydrogen (scale bar 1 μm).

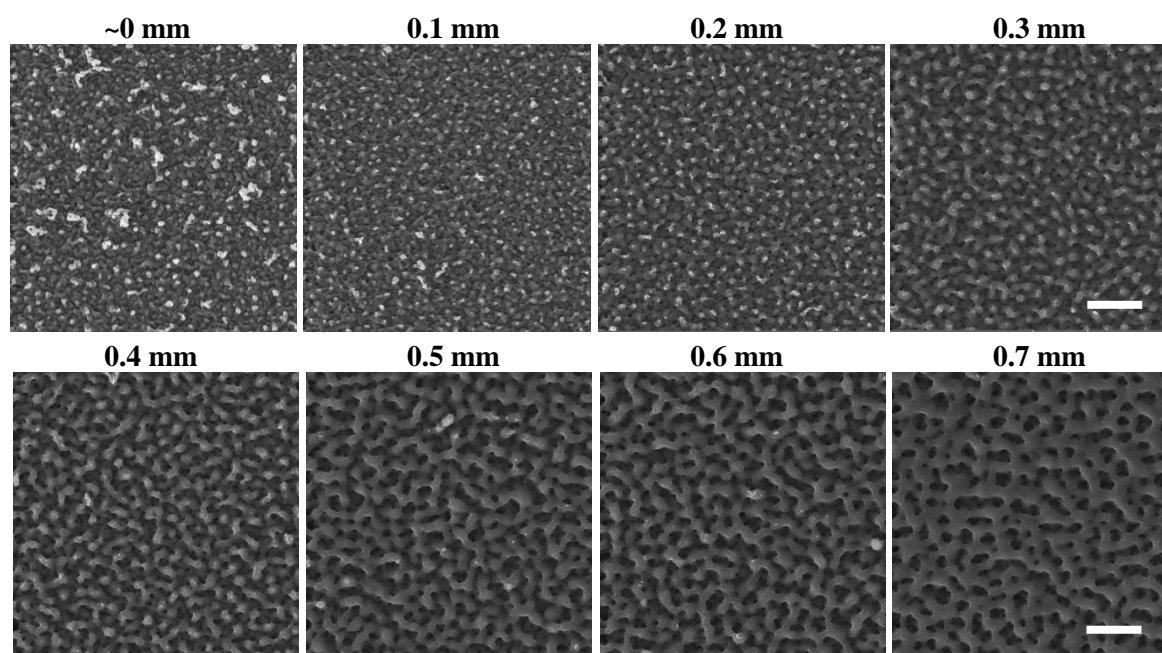


Fig. 3: SEM micrographs of the PMMA foil after 60 min treatment by DCSBD plasma generated in pure hydrogen (from left to right) with increasing plasma gap (scale bar 2 μm).

A time-dependent formation of pillar and dot like structures was observed after 5, 10 and 30 minutes of the plasma treatment in pure hydrogen. The authors in [2] observed similar effect on PMMA foil treated by low-pressure helium plasma.

As reported, small pillar structuring (called worm like chains) was revealed after short treatment times. The thicker grooves were formed after the further treatment with small pillars preserved on top. This similar time-dependent change of the structure was linked with melting process involving chain scission and etching effect.

The SEM micrographs in Figure 3 show a dependence of ceramics-substrate distance on flexible PMMA etching. The density of the structures decreased, and the diameter of their tops increased with increasing plasma gap. The distance-dependent etching effect of the reducing plasma is a reflection of active particles and plasma energy distribution above the DCSBD ceramics. The etching rate of flexible PMMA placed 0.2 mm above DCSBD ceramics was estimated to 48 nm.min⁻¹.

Tab. 1. The RMS roughness of flexible and rigid PMMA after the DCSBD plasma treatment in pure hydrogen (area 5×5 μm²).

Treatment time [min]	PMMA foil		PMMA sheet	
	Roughness [nm]	Δ [nm]	Roughness [nm]	Δ [nm]
0	3.6	0.2	1.7	0.6
5	25.6	0.1	14.3	4.1
10	28.6	5.9	18.1	3.3
30	82.1	1.7	67.1	3.8
60	86.0	6.2	-	-

The topological analysis of flexible and rigid PMMA substrate revealed similar tendencies of a roughness increase. After 10 minutes of DCSBD plasma treatment in pure hydrogen, the RMS average roughness value increased approx. ten times for both substrates. The maximum roughness on both PMMA was measured after 30 minutes of plasma exposure. The maximum value of roughness on the PMMA foil remained similar (within the result deviation) after the 60 minutes of the treatment.

Krumpolec et al. [10] reported that DCSBD hydrogen plasma achieved an efficient etching rate of several flexible polymer surfaces, such as polyethylene naphthalate (PEN), polyethylene terephthalate (PET) and polyimide (PI). Similar studies also revealed significant improvement of hydrophobic properties of the polymeric substrates after DCSBD plasma treatment in pure hydrogen [11-12]. As reported, the steep increase of a contact angle during the first 10 minutes of etching was observed and a maximum (plateau) was obtained after 30 minutes of the treatment. These results are in a good correlation with roughness increase and high etching rate of the PMMA surface measured in this work.

4. Conclusion

The effect of atmospheric pressure DCSBD plasma generated in pure hydrogen was studied on rigid and flexible PMMA substrate. The microscopic analyses showed the change of topology, etching and formation of submicron structures on both PMMA substrates. The distance- and time-dependent application of DCSBD hydrogen plasma is presenting a novel approach to precise etching and controlled structuring process of polymer substrates.

5. Acknowledgement

The authors would like to acknowledge financial support from the project LO1411 (NPU I), funded by Ministry of Education, Youth and Sports of the Czech Republic and from the project TJ01000327, funded by Technology Agency of the Czech Republic.

6. References

- [1] Ellinas, K. et al. 2016 *Chemical Engineering Journal*. 300 394.
- [2] Collaud Coen, M. et al. 2003 *Applied Surface Science*. 207 1–4 276.
- [3] Bormashenko, E. et al. 2013 *Applied Surface Science*. 270 98.

- [4] Tian, D. et al. 2013 *Chemical Society Reviews*. 12 5184-5209.
- [5] Tserepi, A. et al. 2016 *Plasma Chemistry and Plasma Processing*. 36 1 107.
- [6] Sainiemi, L. et al. 2011 *Advanced Materials*. 23 1 122.
- [7] Her, E.K. et al. 2013 *Plasma Processes and Polymers*. 10 5 481.
- [8] Fricke, K. et al. 2011 *Plasma Processes and Polymers*. 8 1 51.
- [9] Krumpolec, R. et al. 2017 *Surface and Coatings Technology*. 309 301.
- [10] Krumpolec, R. et al. 2017 *Proceedings of NANOCON 2017 - 9th International Conference on Nanomaterials - Research and Application, Brno*. 283.
- [11] Kelar, J. et al. 2018 *Conference proceedings of PLASTKO 2018, Zlín*. 6
- [12] Doubková, Z. et al. 2018 *Proceedings of NANOCON 2018 - 10th Anniversary International Conference on Nanomaterials - Research and Application, Brno*. 131.
- [13] PrysiashnyI, V. et al. 2014 *Contribution to Plasma Physics*. 54 138.

EFFECT OF COLD ATMOSPHERIC PRESSURE PLASMA TREATMENT ON SEED GERMINATION AND THE POTENTIAL GENOTOXIC IMPACT

Anna Zahoranová¹, Stanislav Kyzek², Lucia Hoppanová³, Veronika Medvecká¹, Juliána Tomeková¹, Ľudmila Holubová², Eliška Gálová²

¹*Department of Experimental Physics, Faculty of Mathematics, Physics and Informatics, Comenius University in Bratislava, Mlynská dolina, 842 48 Bratislava, Slovakia*

²*Department of Genetics, Faculty of Natural Sciences, Comenius University in Bratislava, Ilkovičova 6, Mlynská dolina, Bratislava, 842 15, Slovakia*

³*Institute of Biochemistry and Microbiology, Faculty of Chemical and Food Technology, Slovak University of Technology, Radlinského 9, 812 37 Bratislava, Slovakia*

E-mail: zahoranova@fmph.uniba.sk

Currently, the research in the field of applied plasma physics is intensively focused on the study of plasma utilisation in agriculture to improve the germination and growth parameters of plants. Cold atmospheric plasma generated in the ambient air is very suitable, it does not require any vacuum devices or expensive gases. This technique is both economical and environmentally friendly, but it is necessary to verify its safeness. Presented study investigates the effect of cold atmospheric pressure ambient air plasma treatment on germination improvement of maize (*Zea mays* L. *ssp.* *Mays*), pea (*Pisum sativum* L.) and barley (*Hordeum sativum* L.) seeds while maintaining the safety of the plasma treatment. The aim of our study was to verify the plasma impact on DNA damage. Plasma was generated by Diffuse Coplanar Surface Barrier Discharge (DCSBD) at atmospheric pressure in the ambient air, seeds were treated by plasma at the exposure times ranging from 60 to 300 s. The main plasma properties were estimated by electrical measurements and using the optical emission spectroscopy. The DNA damage was evaluated by the alkaline comet assay method. These results verify the safety of plasma application in agriculture at germination and growth enhancement.

1. Introduction

The cold atmospheric pressure (CAP) plasma generated in ambient air is of interest to the many biomedical, food and agriculture application. Her advantage is non-thermal character suitable for the treatment of thermosensitive biological materials. At the same time, plasma is the mixture of reactive species, ions, electrons, radiation, biologically active particles and there are many physical and chemical processes inside plasma volume and at contact with surface. Plasma interaction with the bio-objects has become a subject of the significant research effort in recent years. Many scientific teams are focused on the study of plasma interactions with cells, microorganisms, pathogens for example to sterilize or disinfect the surface, or to accelerate wound healing [1]. The results of scientific research suggest that plasma treatment has also a positive effect on the germination and the surface sterilization of the seeds. However, the potential genotoxic effect of plasma interaction with living objects (as well as plant seeds) is not yet fully studied and elucidated.

Our work is focused on the study of potential genotoxic effect of the CAP plasma treated seeds using the comet assay method. The comet assay is method used for a primary DNA damage detection in eukaryotic cells (single- and double-strand breaks) [2]. We try to compare the effect of CAP plasma generated in ambient air on maize, pea and barley seeds. The aim is to find if the plasma treatment at the time optimal for germination enhancement is safe from the genetics point of view and what is the level of DNA damage. Plasma parameter was evaluated by optical and electrical measurements.

The plasma treatment of all tested seeds was performed by a planar source of the low temperature plasma based on the Diffuse Coplanar Surface Barrier Discharge (DCSBD) [3], working at

atmospheric pressure and plasma was generated in ambient air. The plasma treatment was performed at the input power of 400 W, plasma exposure times varied from 60 s up to 300 s.

2. Experimental

DCSBD plasma source and treatment of seed

The plasma treatment of seeds has been carried out in the plasma reactor equipped with DCSBD plasma panel (Fig.1). Discharge was fed by high voltage source (LIFETECH, s.r.o., Brno, Czech Republic) providing AC signal with high voltage amplitudes up to 10 kV and frequency 15–18 kHz. The DCSBD plasma source generates thin (~ 0.3 mm) layer of diffuse, non-equilibrium plasma. The extremely high plasma volume power density of more than 100 W/cm³ results in the very short plasma processing times in order of seconds. In detail, DCSBD is described in [3, 4].

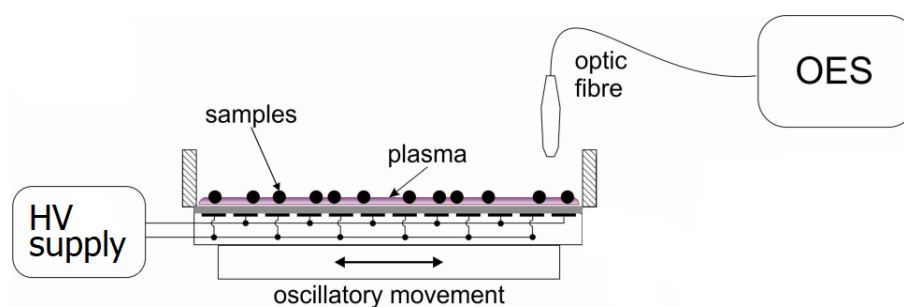


Fig. 1 Experimental set-up for DCSBD plasma treatment of seeds and OES measurement

The plasma treatment of seeds (200-250 pieces) was realised at input power of 400 W. The DCSBD plasma panel was placed and securely fixed to a laboratory orbital shaker to achieve a homogeneous treatment on the whole seeds surface. The seeds were evenly rotate in the plasma field on the ceramic surface at a rotary speed of the shaker of 270 - 330 rpm, depending on type of seeds. The plasma treatment times were in the range of 60 – 300 seconds. After the plasma treatment, seeds were exposed to ambient atmosphere for 24 hours before the biological experiments started.

Optical emission spectroscopy (OES) of DCSBD plasma was realized at the same conditions as in case of plasma seed treatment. Radiation emitted from the plasma was collected by the fibre situated in a distance of 6.3 cm above the dielectric surface. Spectrum of collected radiation measured by the spectrometer AvaSpec 2048 TEC in spectral range 300-400 nm was used to determine rotational and vibrational temperature of the plasma.

Seeds germination “*in vitro*”

Thirty seeds (maize, pea, barley) were placed into sterile Petri dishes with two layers of filter papers moisturized with sterile distilled water. During germination, sterile distilled water was added to the Petri dishes to maintain a constant moisture. The seeds were incubated at 25°C, 12 hrs light/12 hrs dark and 60% air humidity. After 5 days, the germination rate (GR, %) was calculated by the following equation (the radicle protrusion at 1 mm was recorded as the criterium for germination):

$$GR = \frac{SG}{ST} \times 100 \%$$

where GR – germination rate, SG – number of germinated seeds, ST – total number of seeds.

The vigor of seedlings was evaluated by the measurement of root lengths and shoot lengths of seedlings. Seedlings vigor index was calculated according to the Abdul-Baki and Anderson equation [5] in the following modification:

$$SV = \frac{(LR + LS) \times GR (treated\ seeds)}{(LR + LS) \times GR(untreated\ seeds)} \times 100\%$$

where SV – seedling vigor, LR – length of roots (mm), LS – length of shoots (mm), GR – germination rate.

Comet Assay Method

The potential genotoxic effect of CAP plasma treatment on maize, pea and barley seeds was investigated by the “comet assay” method. Single cell gel electrophoresis (SCGE, comet assay) is a method used for measuring of deoxyribonucleic acid (DNA) damage in eukaryotic organisms. Comet assay is an effective method for genotoxicity quantification of industrial chemicals, agrochemicals, biocides and pharmaceuticals. Cells with damaged DNA exhibit increased migration of the chromosomal DNA from the nuclei. The DNA, also called nucleoid, moves from the cathode to the anode during electrophoresis and the DNA then resembles comet. This method is applicable for detection of different DNA defects, like single- and double-strand breaks, crosslinks, apyrimidine and apurine sites [6].

3. Results and discussion

OES method was used to determine vibrational and rotational temperatures of the DCSBD plasma generated in ambient air at the input power 400 W. Vibrational temperature, calculated from the relative intensities of the second positive system of nitrogen, was $T_{\text{vib}} = 2800 \text{ K} \pm 250 \text{ K}$. Rotational temperature T_{rot} , determined by comparing the experimental and theoretical spectra simulated in the software Specair 3.0, was estimated at the value of $400 \text{ K} \pm 50 \text{ K}$. These results confirmed the strongly non-equilibrium character of DCSBD plasma.

As resulted from germination tests that were studied previously for maize, pea and wheat [7-10], the optimal treatment time that increases seed germination or improves growth properties depends on the type and condition of the seeds, its size and surface properties. The effect of CAP plasma treatment on maize, pea and barley seed germination rate (GR) varied with treatment time it is illustrated in Table I. If natural germination of studied seeds even without plasma treatment is high, there is not much change in germination rate observed after plasma treatment. For example, no significant response of changes of maize seeds germination was found at the treatment time of 60 seconds and 120 seconds in comparison to the control untreated maize, respectively. A greater reduction of 83% in the germination was observed at the exposure time of 240 seconds and after 300 seconds the germination rate dropped to the value of 7%. However, CAP plasma treatment of maize seeds also affected the characteristics of seedling growth, including root and shoot length. The seedling vigor index combines the growth parameters and germination rate, as it is summarised in Table. II. The response to a 60 second plasma exposure increased seedling vigor index by 32% compared to the untreated maize seeds. Higher exposure time of CAP plasma inhibited all the measured growth parameters.

Tab. I: Germination (GR) of maize, pea and barley seeds after plasma treatment using CAP plasma in ambient air, at the input power of 400W

Treatment time	0 s	60 s	120 s	180 s	240 s	300 s
maize	97%	100 %	96 %	69 %	18 %	7 %
pea	77 %	85 %	95 %	83 %	-	
barley	100 %	97 %	70 %	53 %	50 %	37 %

Tab. II: Seedlings vigor (SV) of maize, pea and barley seeds after plasma treatment using CAP plasma in ambient air, at the input power of 400W

Treatment time	0 s	60 s	120 s	180 s	240 s	300 s
maize	100 %	132 %	98 %	24%	2 %	0 %
pea	100 %	114 %	131 %	112 %	-	-
barley	100 %	116 %	73 %	52 %	39 %	11 %

Similarly, we have verified the optimal treatment time for pea and barley seeds. As resulted from Table I, the pea seeds have the increased germination compared to untreated seeds at plasma treatment times of 60 – 240 s. The barley seeds respond more sensitive to the plasma treatment time, which is probably due to the size of the seed and their surface properties. Seedlings vigor is increased at the treatment time of 60 s.

The effect of CAP plasma treatment on DNA damage of maize, pea and barley seeds studied using Comet Assay method was different (Table III). There was no significant DNA damage in maize seeds that were treated by plasma for 60, 90 and 120 sec compared to untreated seeds. The results of DNA damage observed in pea seeds was higher compared to maize seeds, but higher DNA damage was observed also in the negative control. Compared to negative control, there was no statistically significant increase in plasma treated seeds (60, 90, 120, 180 and 300 sec). But DNA damage in barley seeds after plasma treatment with exposition times from 60 to 300 sec was much higher than in pea or maize seeds. DNA damage of plasma treated barley seeds was statistically significant higher compared to negative control. We assume that this difference may be due to a higher sensitivity of barley seeds to plasma treatment, seed size and surface properties. For effective barley seed treatment to increase germination, shorter plasma exposure times (20-30 s) are enough.

Table III: DNA damage of various plant seedlings after plasma treatment (treatment times 0 – 300 s) of their seeds studied by comet assay, n.o. not observed

	0 s	60 s	90 s	120 s	180 s	300 s
maize	10.29	16.01 ± 3.01	13.57 ± 0.09	10.43 ± 3.12	n.o.	n.o.
pea	20.42 ± 2.01	19.83 ± 2.50	n.o.	23.25 ± 2.47	21.58 ± 5.13	23.95 ± 3.49
barley	12.91 ± 5.59	41.44 ± 7.62 ***	n.o.	n.o.	49.83 ± 12.15 *	51.69 ± 14.92 *

4. Conclusion

As resulted from our experimental study focused on the efficacy of CAP plasma treatment of maize, pea and barley seeds to increase germination and seedlings vigor, non-thermal plasma is suitable and effective already at short treatment time ranging of 60 – 120 s. The treatment time sufficient to improve the germination of barley seeds is only 20-30 seconds. We have verified the safety of plasma treatment regarding the possibility of DNA damage by the Comet Assay method. The DNA damage has been shown to be at the level of damage of control samples and therefore plasma treatment of seeds is safe method in verified cases.

5. Acknowledgement

This work was supported by the Slovak Research and Development Agency under the contract No. APVV-16-0216. This work is the result of the project implementation ITMS code 26240220042 supported by the Research & Development Operational Programme funded by the ERDF.

6. References

- [1] Laroussi M 2005 *Plasma Process. Polymers* **2**, 391.
- [2] Hartmann A, Agurell E, Beevers C et al 2003 *Mutagenesis* **18**:45–51.
- [3] Černák M, Černáková Ľ, Hudec I et al. 2009 *Eur. Phys. J. Appl. Phys.*, **47**, 22806).
- [4] Černák M et al 2011 *Plasma Phys. Control. Fusion*, **53**, 124031.
- [5] Abdul-Baki AA, Anderson JD 1973 *Crop Science* **13**:630–633
- [6] Collins AR 2004 *Mol Biotechnol* **26**:249–261.
- [7] Henselová M, Slováková Ľ, Martinka M, Zahoranová A 2012 *Biologia*.**67** 490.
- [8] Zahoranová A, Henselová M, Hudecová D et al. 2016 *Plasma Chem and Plasma Process* **36** 397
- [9] Stolárik T, Henselová M, Martinka M et al. 2015 *Plasma Chem and Plasma Process*. **35** 659
- [10] Zahoranová A, Hoppanová L, Šimončicová J, et al. 2018 *Plasma Chem Plasma Process* **38**:969

AGEING EFFECT OF PLASMA TREATED Al_2O_3 AND ZrO_2 CERAMIC POWDERS WITH RESPECT TO ELECTROPHORETIC DEPOSITION

Martina Ilčíková, Jozef Ráhel'

*Masaryk university, Faculty of Science, Department of Physical Electronics, Kotlářská 2,
611 37 Brno, Czech Republic*

E-mail: ilcikova@mail.muni.cz

Electrophoretic deposition (EPD) of plasma pre-treated Al_2O_3 and ZrO_2 powders results in ceramic layers of substantially improved deposit homogeneity. To evaluate the practical applicability of this phenomenon, we report on the magnitude and dynamics of undesired gradual deterioration on plasma treatment – the ageing effect. Powders samples were treated by diffuse coplanar barrier discharge and sequentially evaluated for their EPD performance for the time span of 30 days. The ageing effect has no detrimental effect on deposition rate at least for the first 14 days from the plasma treatment. During the whole testing period of 30 days, the improved coating uniformity remained unaffected.

1. Introduction

Electrophoretic deposition (EPD) is a technologically important coating process which involves charged particles dispersed in a colloid solution followed by their deposition to a substrate (electrode) by externally applied electric field [1]. Most of applications require formation of a homogenous deposit. To fulfill this requirement diverse types of chemical additives (stabilizers, dispersants etc.) have to be employed. These are a copious source of vexing problems caused by their health hazards issues, high cost, problematic hazardous waste disposal and/or corrosive character. Similarly to other cases, plasma treatment was successfully tested to be a suitable replacement of unwanted chemical additives [2]. The surface of ceramic powders was brought into the several tens of seconds lasting contact with non-thermal atmospheric pressure air plasma generated by dielectric barrier discharge (DBD). Resulting effect on EPD process can be summarized as follows:

1. The plasma treated powders deposited on the anode while material without the treatment ended up at the cathode
2. The suspension prepared from plasma treated powders had significantly lower electrical resistivity
3. Deposit created from suspension of plasma treated powders exhibited lower roughness compared to the as-received ones (Fig.1)
4. This effect is probably material-independent the same results were observed for alumina powders (Fig. 1. A) as well as for the zirconia powders (Fig. 1. B)

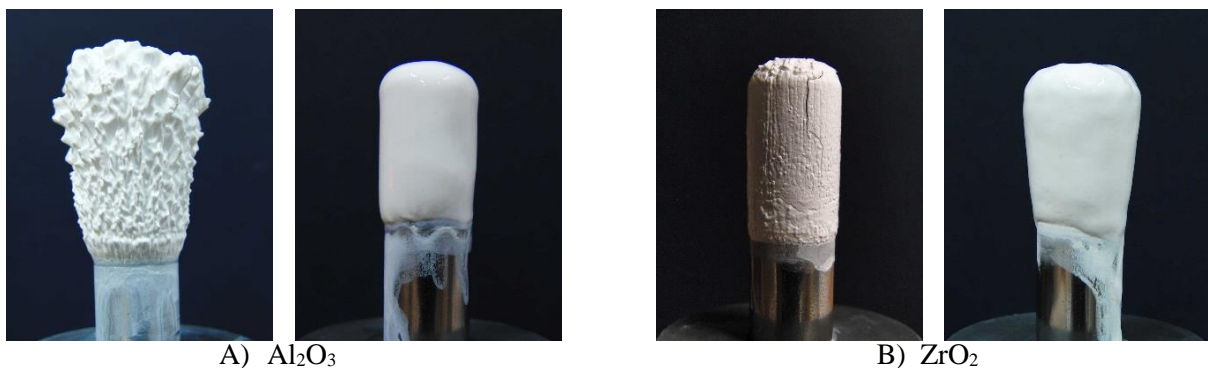


Fig.1 Improvement in roughness of deposit created from suspension containing A) Al_2O_3 as-received (left) and plasma treated (right) B) ZrO_2 as-received (left) and plasma treated (right).

It is a generally known fact that the weak spot of DBD plasma treatment is its ageing – gradual deterioration of obtained positive effect. In this contribution, the ageing dynamics and magnitude will be addressed.

2. Experimental setup

Two materials were studied in this work. Submicron α -alumina powders (Taimicron TM-DAR, Taimei Chemicals, Japan) and partially yttrium stabilized zirconia powder (TZ-3YS-E, Tosoh, Japan).

Plasma treatment was realized by Diffuse Coplanar Surface Barrier Discharge (shown at Fig. 2). The full description of DCSBD can be found elsewhere [3]. Powder material was put on the top of polymer mesh and sifted through it. Besides acting as a tool to doze the material into the discharge space, the mesh also prevented powder particles from escaping out of “plasma” space due to the present ionic wind. The treatment was done in ambient air at atmospheric pressure.

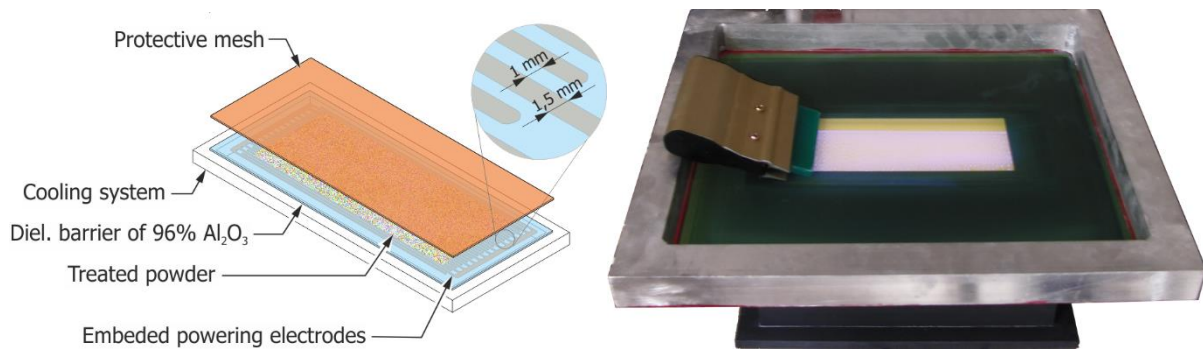


Fig.2 Schematic (left) and real (right) DCSBD setup used for plasma treatment of ceramics powders.

According to our previous research [4] the best EPD results were obtained for 30 sec treatment of 30 kHz driving frequency and 500 W input power. To minimize the influence of different air humidity (which affects the output of plasma activation significantly) the tested materials were treated all at once. Afterwards, the treated powder was left at the ambient air with no special storage condition.

The suspension was prepared from 15 wt% of powder material dispersed in 85 wt% of 2-propanol. To achieve a well dispersed suspension a double mixing system was used. Suspension was mixed mechanically by a glass stirrer (240 rpm), while being placed in an ultrasonic bath (SONOREX, Bandelin Digitec, Germany). After 30 minutes of mixing, 33 ml of suspension was poured into a coaxial deposition cell pictured in Figure 3.

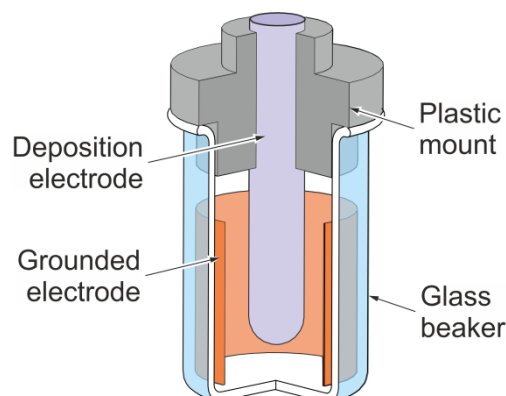


Fig.3 Schematic of deposition cell used for electrophoretic deposition of ceramics powders.

The powder was deposited on central stainless-steel cylinder at high-voltage potential supplied by DC power supply (HCP 1400-20000 MOD, Fug Elektronik, Germany). Outer coaxial electrode made of stainless-steel mesh was grounded. Total deposition time of 30 minutes was interrupted every 5 minutes to weigh the mass of deposit formed on electrode. During these measurements the suspension was repeatedly stirred to reduce the sedimentation effect.

3. Results

The results for both materials are shown in the graphs of Figure 4. In spite of using the same procedure before every deposition, the random effect of sedimentation during the mixing was observed. For better accuracy the results in the graphs shown in Fig.4 use the formula

$$\Delta m = \frac{M_{dep}}{M_{in} - M_{sed}} 100 \quad (1)$$

where M_{dep} states for deposited mass, M_{in} is total mass of initially dispersed powder and M_{sed} is mass of powder lost to the walls of mixing beaker.

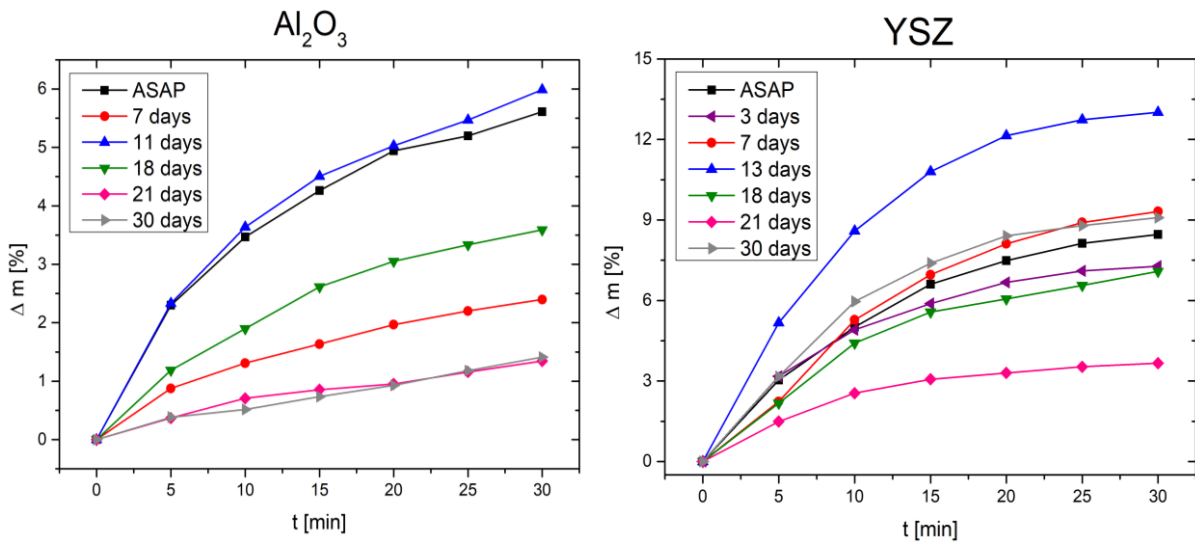


Fig.4 Ageing effect of plasma treated powders during EPD [4]. YSZ states for yttrium stabilized zirconia.

For alumina powders the results show (Fig. 4 left) that up to 11 days from the treatment the deposition rate remained unaffected. Afterwards, depositions showed decrease in deposited mass. Still, the plasma effect was present.

With respect to zirconia powders (Fig. 4 right) during the first 13 days, the ageing had either slightly negative or a positive effect on deposited mass. Afterwards, gradual degradation is observed, although at 30th day the original deposition rate was restored. We suppose, that these oscillations are chiefly due to the changes in ambient conditions of storage site. YSZ seems to be more sensitive to their changes than Al₂O₃ powders.

In spite of deposition decrease observed two weeks after the plasma treatment the positive effect of improved deposit homogeneity was still present. This is best illustrated in Fig. 5 which displays the quality of aged Al₂O₃ deposit.

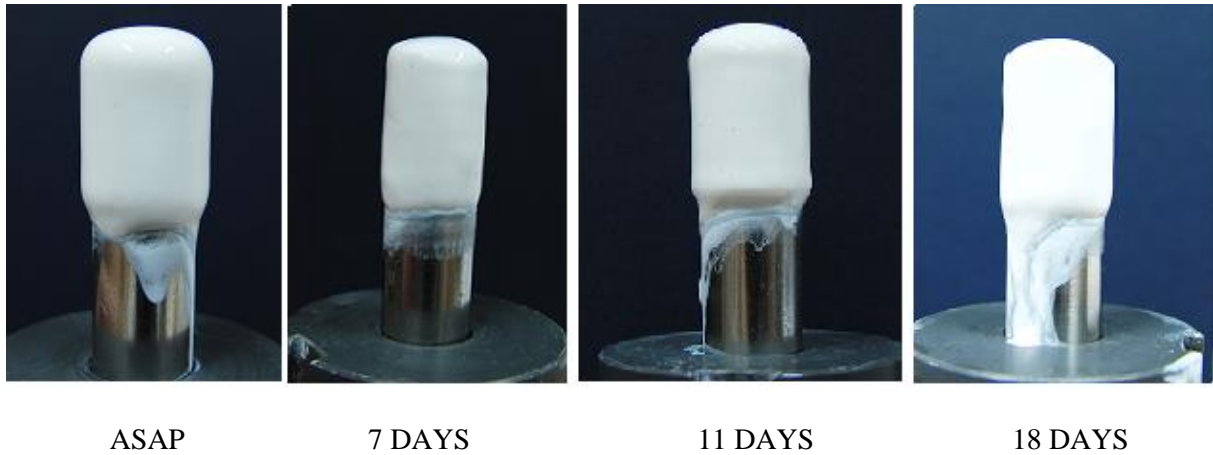


Fig.5 Ageing effect on Al_2O_3 layers prepared by EPD after plasma treatment.

4. Conclusion

EPD ageing effect of plasma treated ceramic powders was studied in this work. Within the first two weeks from the plasma treatment its detrimental effect on the deposition rate is negligible or even positive. A pair comparison between the YSZ and Al_2O_3 treatment ageing suggests, that YSZ powders are more sensitive to the nature of storage environment. After the first two weeks, gradual reduction of deposition takes place. In spite of the reduction of deposition rate, the deposition still keeps its anodic character. More importantly the homogeneous deposition remains unaffected for both types of powders (at least within the observed time span of 30 days). Since the homogeneous deposit is the main benefit provided by plasma pre-treated powders, it can be concluded, that the ageing of our plasma treatment has no technologically relevant adverse impact on EPD process.

5. References

- [1] Besra, L., Liu, M. “A review on fundamentals and application of electrophoretic deposition“, *Progress in Materials Science*, **52** (1), 2007, pp. 1-61.
- [2] Drdlík, D., Morávek, T., Ráhel', J. *et al.* “Electrophoretic deposition of plasma activated sub-micron alumina powder“, *Ceramics International*, **44** (8), 2018, pp. 9787-9793.
- [3] Šimor, M., Ráhel', J., Vojtek, P. *et al.* “Atmospheric-pressure diffuse coplanar surface discharge for surface treatments“, *Applied Physics Letters*, **81** (15), 2002, pp. 2716–2718.
- [4] Ilčíková, M. “The influence of plasma activated ceramic powders on electrophoretic deposition of fine-grained oxide ceramics“, *Master thesis*, Masaryk university, 2018.

DETECTION OF PHTHALATES BY ATMOSPHERIC PRESSURE CHEMICAL IONISATION ION MOBILITY SPECTROMETRY

Jana Hrdá¹, Ladislav Moravský¹, Bartosz Michalczuk¹, Štefan Matejčík¹

¹Comenius University in Bratislava, Faculty of Mathematics, Physics and Informatic, Department of Experimental Physics, Mlynska dolina F2 842 48, Bratislava, Slovakia

E-mail: hrda.jan@gmail.com

In this work we have studied three phthalate molecules, concretely dimethyl phthalate (DMP), diethyl phthalate (DEP) and dipropyl phthalate (DPP), using Ion Mobility Spectrometry (IMS) with ion source based on Atmospheric Pressure Chemical Ionisation (APCI). We determined IMS spectra for mentioned phthalates. This study also shows ability of APCI-IMS technique for separation of phthalates from prepared mixture.

1. Introduction

Phthalates are esters of phthalate acid and are widely used in many products of daily use, for instance building materials, furnishing, personal care products, cosmetics, food wrapping, coating of pharmaceuticals, medical devices or children's toys [1]. These chemical substances are additives to plastic products in order to modify their properties as durability, transparency and elasticity. One of main application is modification (plasticity) of polyvinyl chloride (PVC). Each year factories produce about hundred thousand tons of phthalates. These numbers are alarming, especially if we consider that phthalates can be easily released from the materials into the environment. Easy migration of phthalates species from products is caused by missing covalent bound with plastic materials [2]. Recent studies shown that some phthalates are toxic for animal's reproductive systems [3]. Phthalate esters are also suspected as endocrine disruptors for humans [4]. This fact should be main reason for developing a suitable analytical method, which can detect low concentration phthalates in sample. Ion Mobility Spectrometry (IMS) is a detection method with fast response, approximately few seconds after introduction of the investigated sample and high sensitivity for selected substances.

The first study of phthalates using IMS technique was done by Hagen. In this study detection of the DMP isomers in positive and negative polarity was demonstrated [5].

In this paper we present detection of three different phthalate molecules using IMS technique with ion source based on Atmospheric Pressure Chemical Ionisation. In contrast to earlier studies the experiments have been carried out at moderate temperature of 370K.

2. Experiment

Ion mobility spectrometer

Ion mobility spectrometer used in this work was constructed at Comenius University, Faculty of Mathematics, Physics and Informatics. Spectrometer is equipped with APCI ionisation source based on corona discharge (CD). The length of the drift tube was 11.93 cm and typical intensity of electric field inside of the drift tube was 671.8 V/cm. The IMS was operated slightly under atmospheric pressure, around 900 mbar and temperature 370 K. Purified air was used as the drift gas with flow of 1000 ml/min. The sample flow was controlled by a micro-splitter valve (Supelco) and flow rate was adjusted by a flow meter to 20 ml/min. With sample flow non-purified air was also constantly sucked into the reacting region of mobility spectrometer. The IMS was operated in reverse flow regime. All operation parameters of the IMS instrument are summarised in Table 1. The reduced mobility scale was calibrated by standard compound with well-known reduced mobility, namely 2,6-di-tert-butylpyridine (Sigma-Aldrich) with reduced mobility of $1.42 \text{ cm}^2\text{V}^{-1}\text{s}^{-1}$ [6].

IMS drift tube length	11.93 cm	Sample flow	20 ml/min
Intensity of electric field	671.8 V.cm ⁻¹	Shutter grid pulse width	40 μs
IMS operating pressure	~900 mbar	Shutter grid frequency	16 Hz
IMS operating temperature	370 K	CD current	10 μA
Drift gas flow	1000 ml/min		

Table 1. Parameters of IMS

Chemicals

In this work we studied 3 different phthalates, dimethyl phthalate (DMP), diethyl phthalate (DEP) and dipropyl phthalate (DPP). Molecular weight and the structure formulas for each phthalate are shown in Table 2. Samples were provided by Sigma-Aldrich with purity more than 98%.

The phthalates were placed into glass vials in liquid form (about 0.5g) and we waited at least 30 minutes to reach an equilibrium between gas and liquid. Afterwards we introduced vapours of the phthalates into the reaction region of the IMS device via thin capillary (ID 0.030''). The sample flow rate was pre-set by micro-splitter valve.

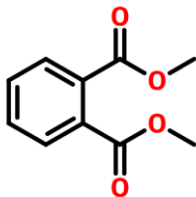
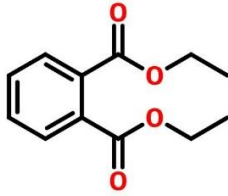
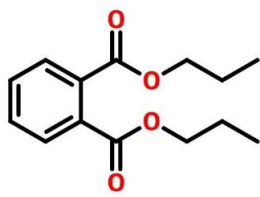
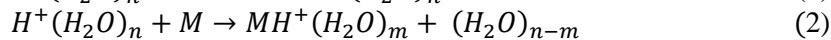
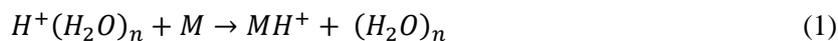
Phthalate	Molecular weight [g/mol]	Structural formula	Vapour pressure [Pa]
DMP $C_{10}H_{10}O_4$	194.18		0.8 (for 20°C)
DEP $C_{12}H_{14}O_4$	222.24		0.2779 (for 25°C)
DPP $C_{14}H_{18}O_4$	250.29		0.28 (for 20°C)

Table 2. Overview of analysed molecules

3. Results and discussion

Reactant ions (RI) were formed in the corona discharge of the purified and dehumidified laboratory air. The positive corona formed dominant reactant ions $H^+(H_2O)_n$ and secondary reactant ions are $NH_4^+(H_2O)_n$ and $NO^+(H_2O)_n$. Because of ions $H^+(H_2O)_n$ are more intense we are going to focus only on ion-molecule reactions with these RI. Analysed phthalate interacted with RI according following reactions:



Where M represents an analysed phthalate- DMP, DEP or DPP. The first reaction is more common for compounds with high proton affinity, PA of analysed molecule must be higher than PA of water cluster. Reaction (2) is typical for molecules with smaller PA than PA of $(H_2O)_n$ and also final product $MH^+(H_2O)_m$ must have larger binding energy than whole $H^+(H_2O)_n$ cluster.

DMP

In Figure 1. we present visualised ion mobility spectrum of DMP. Peak with reduced mobilities $2.22 \text{ cm}^2\text{V}^{-1}\text{s}^{-1}$ belongs to dominant reactive ions $H^+(H_2O)_n$ and peaks with reduced mobilities 2.37 and $2.50 \text{ cm}^2\text{V}^{-1}\text{s}^{-1}$ are assigned to minor reactant ions NH_4^+ and NO^+ .

Peak with reduced mobility $1.59 \text{ cm}^2\text{V}^{-1}\text{s}^{-1}$ is assigned to protonated DMP ion ($DMPH^+$).

DEP

The Figure 2. shows IMS spectrum of DEP. The peak with reduced mobility $1.43 \text{ cm}^2\text{V}^{-1}\text{s}^{-1}$ we assign to ion of $DEPH^+$.

DPP

Dipropyl phthalate DPP is displayed in Figure 3. The ion peak with the value of reduced ion mobility of $1.30 \text{ cm}^2\text{V}^{-1}\text{s}^{-1}$ we associate to DPP.

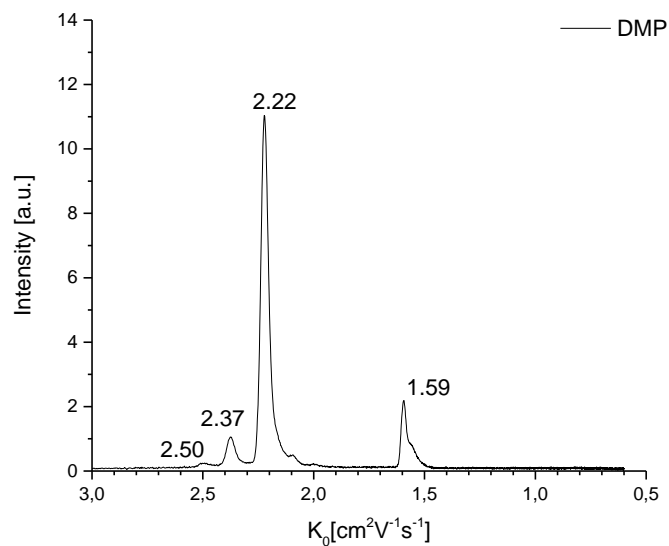


Figure 1. Ion mobility spectrum of DMP

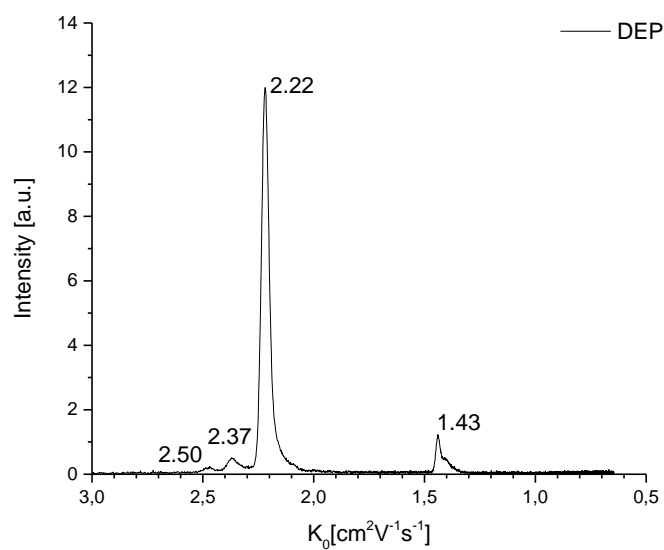


Figure 2. Ion mobility spectrum of DMP

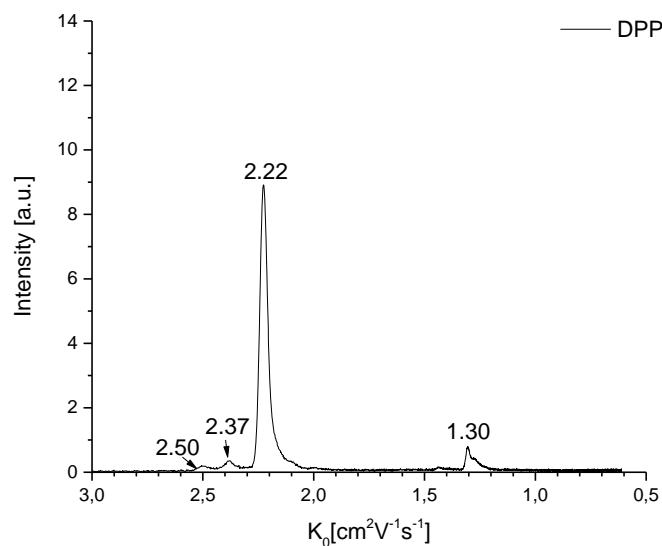


Figure 3. Ion mobility spectrum of DPP

Mixture of DMP, DEP and DPP

In this work we have tried to detect phthalates from a mixture of all three phthalates. The phthalates were placed into the glass vial (about 0.5 g each). Afterwards we have mixed sample by ultrasonic waves. After reaching the equilibrium between liquid and gaseous phases we have measured the IMS spectrum of the mixture.

The IMS spectrum is shown in Figure 4. In the spectrum we were able to detect ion peaks with reduced mobilities 1.59 and 1.43 cm²V⁻¹s⁻¹, which we associate to protonated ion of DMP and DEP. Peak with reduced mobility of 1.30 cm²V⁻¹s⁻¹, which belongs to DPP was detected only at low intensity. We assume that the low intensity of DPP is due to lower PA of DPP in comparison to DMP and DEP

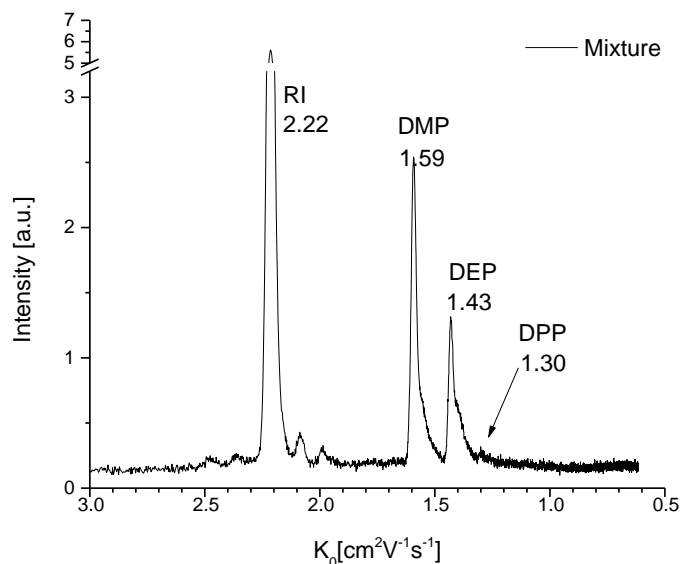


Figure 4. Ion mobility spectrum of mixture DMP, DEP, and DPP

4. Conclusion

We have used IMS equipped with APCI ion source for the detection of three phthalates- DMP, DEP and DPP. We have identified reduced ion mobility peaks for each molecule- $1.59 \text{ cm}^2\text{V}^{-1}\text{s}^{-1}$ for DMP, $1.43 \text{ cm}^2\text{V}^{-1}\text{s}^{-1}$ for DEP and $1.30 \text{ cm}^2\text{V}^{-1}\text{s}^{-1}$ for DPP. We have recorded IMS spectrum for the mixture of all three phthalates. We were able to detect all three analytes, however the response for DMP and DEP was stronger as response for DPP. This behaviour could be associated with the PA of the analytes.

5. Acknowledgment

European Union's Horizon 2020 research and innovation programme under the Marie Skłodowska-Curie grant agreement No 674911

Slovak Research and Development Agency Project Nr. APVV-15-0580 and the grant agency VEGA, project Nr. VEGA-15-089.

European Union's Horizon 2020 research and innovation programme under grant agreement No 692335

6. References

- [1] T. Schettler, "Human exposure to phthalates via consumer products," *International Journal of Andrology*, no. 29, pp. 134-139, 2006.
- [2] P. Gerbaux, J. D. Winter, R. Flammang, V. S. Nguyen and M. T. Nguyen, "Metastable dimethyl phthalate molecular ions: Does the loss of a methoxyl radical proceed with or without anchimeric assistance?," *International Journal of Mass Spectrometry*, no. 290, pp. 127-132, 2010.
- [3] U. Heudorf, V. Mersch-Sundermann and J. Angerer, "Phthalates: Toxicology and exposure," *International Journal of Hygiene and Environmental Health*, no. 210, pp. 623-634, 2007.
- [4] G. Latini, G. Knipp, A. Mantovani, M. L. Marcovecchio, F. Chiarelli and O. Söder, "Endocrine Disruptors and Human Health," *Mini-Reviews in Medicinal Chemistry*, no. 10, pp. 846-855, 2010.
- [5] D. F. Hagen, "Characterization of Isomeric Compounds by Gas and Plasma Chromatography," *Analytical Chemistry*, vol. 51, no. 7, pp. 870-874, 1979.
- [6] G. A. Eiceman, E. G. Nazarov and J. A. Stone, "Chemical standards in ion mobility spectrometry," *Analytica Chimica Acta*, no. 493, pp. 185-194, 2003.

ION MOBILITY SPECTROMETRY FOR RAPID QUANTATIVE ANALYSIS OF WHISKY LACTONE IN OAK WOOD

Bartosz Michalczuk¹, Ladislav Moravsky¹, Štefan Matejčík¹

¹*Department of Experimental Physics, Faculty of Mathematics, Physics and Informatics, Comenius University, Mlynska dolina F2, 842 48 Bratislava, Slovakia*
michalczuk@fmph.uniba.sk

Corona Discharge used in Ion Mobility Spectrometry (CD-IMS) as an Atmospheric Pressure Chemical Ionization source allows to detect compound (whisky lactone) present in whisky which is one of the main factors responsible for unique flavour of whisky. Mass spectrum and 2D map helped to assign peaks in IMS spectrum with particular ions generated in reaction region.

1. Whisky Lactone

With the advancement in analytical techniques like gas chromatography and its coupling with mass spectrometry many compounds present in whisky have been detected. One of them is whisky lactone known also as 5-butylidihydro-4-methylfuran-2(3H)-one, which has aroma of celery, coconut or fresh wood. It is not only present in whisky but also in other alcoholic beverages that have been matured in oak barrels.¹ Sometimes it is used as a flavouring agent when is added to liquors. As whisky lactone is present in oak wood, barrel staves are classified in ten categories depending on the concentration of whisky lactone (first category should have concentration in range: 0-7 µg/g while tenth category: 63-70 µg/g) of course more of lactone in wood is desirable.² Vapor pressure is (1.5±0.09) Pa and (2.0±0.1) Pa for cis- and trans- isomer respectively which give concentration of 15-20 ppm in vapours at room temperature.³

2. Experimental and Results

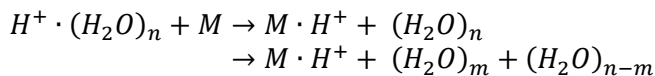
In our laboratory we have developed Corona Discharge Ion Mobility Spectrometry combined with orthogonal acceleration time of flight spectrometry technique (IMS-oaTOF)⁴ for high resolution separation of complex samples, isomeric compounds at very low concentrations. In table below operating parameters of IMS are summarized.

Table 1. Parameters of IMS used in experiment.

Operating Parameters	
IMS drift tube length	12.05 cm
Electric field intensity	665.5 V.cm ⁻¹
IMS operating pressure	700 mbar
IMS operating temperature	298 K
Drift gas flow	500 sccm
Sample gas flow	20 sccm
CD current	13 µA
Shutter grid pulse width	70 µs

In this study we present results for whisky lactone using IMS-MS setup.

In positive mode of IMS in corona discharge hydronium ions are responsible for Atmospheric Chemical Ionisation (APCI) of sample molecules. This process can be described by following reactions:



These reactions are valid only when proton affinity of M is higher than proton affinity (PA) of water clusters.⁵ At lower humidity protonation of analyte is possible but when water concentration is higher addition of hydronium ion to M can occur and even water clusters could be formed. PA for H₂O, H⁺(H₂O)₂, H⁺(H₂O)₃ is 697, 833 and 919 kJ/mol respectively. In case of whisky lactone IMS spectrum reveals two peaks with reduced mobilities 1,39 and 1,09 cmV⁻¹s⁻¹ (fig. 1). There is no literature data for proton affinity of whisky lactone so from just IMS spectrum it is impossible to conclude whether peaks correspond to protonated or heavier ions.

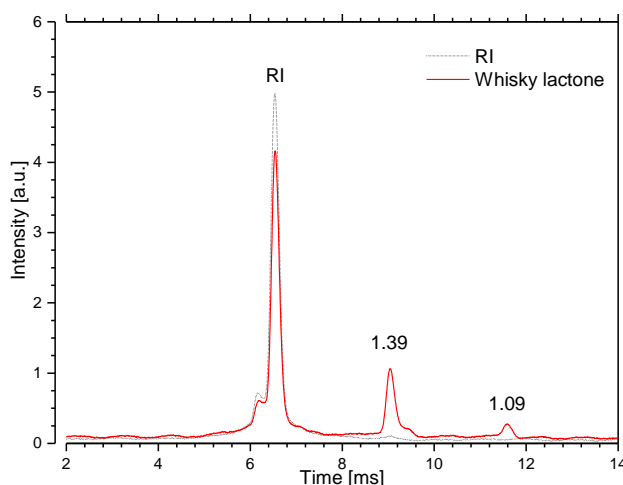


Fig. 1 The ion mobility spectra for reactant ions (RI) - dotted line and whisky lactone.

Combination of IMS with MS allows to identify peaks from IMS spectrum. As it is clear presented in Fig. 2, mass spectrum of whisky lactone shows three major peaks with $m/z = 157$, 175 and 313 Da which correspond to protonated molecule ($M \cdot H^+$), addition of hydronium ion ($M \cdot H_3O^+$) and protonated dimer ($M_2 \cdot H^+$) respectively. Finally, 2D map shows that monomer ions are related to peak with $1,39$ cmV⁻¹s⁻¹ and dimer ion with $1,09$ cmV⁻¹s⁻¹ peak in IMS spectrum. Presence of protonated monomer indicate that proton affinity for whisky lactone is higher than PA of water.

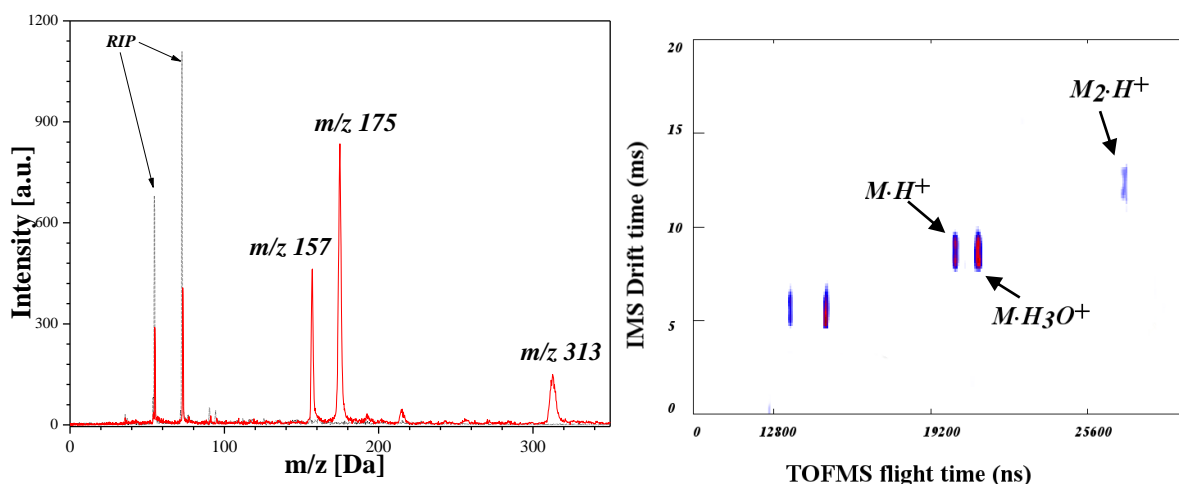


Fig. 2 MS spectrum of whisky lactone (left) and 2D map (right).

By this study we have demonstrated that IMS technique is sensitive enough to measure samples like whisky lactone even at very low concentrations. In this case limit of detection is about 50 ppb. Comparing whisky lactone levels in oak wood measured by IMS with curve obtain for reference sample allows to state to which category wood sample should be assign. That kind of measurements have been done already by MaSa Tech Company. ⁶

3. Acknowledge

This research has been supported by:

- European Union's Horizon 2020 research and innovation programme under the Marie Skłodowska-Curie grant agreement No 674911.
- European Union's Horizon 2020 research and innovation programme under grant agreement No 692335
- Slovak Research and Development Agency (contract no. APVV-0259-12 and APVV-15-0580)
- Slovak Grant Agency for Science (contract no. VEGA 1/0787/18 and VEGA 1/0417/15).

4. References

- [1] K. Y. M. Lee, A. Paterson, J. R. Piggott, and G. D. Richardson, "Measurement of Thresholds for Reference Compounds for Sensory Profiling of Scotch Whisky†," *Journal of the Institute of Brewing*, vol. 106, no. 5, pp. 287–294, 2000.
- [2] J. R. Piggott, "Whisky, Whiskey and Bourbon: Composition and Analysis of Whisky," in *Encyclopedia of Food and Health*, Elsevier, 2016, pp. 514–518.
- [3] D. Simmons and J. Chickos, "Enthalpy of vaporization and vapor pressure of whiskey lactone and menthalactone by correlation gas chromatography," *The Journal of Chemical Thermodynamics*, vol. 110, pp. 65–70, Jul. 2017.
- [4] M. Sabo and Š. Matejčík, "Corona Discharge Ion Mobility Spectrometry with Orthogonal Acceleration Time of Flight Mass Spectrometry for Monitoring of Volatile Organic Compounds," *Analytical Chemistry*, vol. 84, no. 12, pp. 5327–5334, Jun. 2012.
- [5] S. M. Collyer and T. B. McMahon', "Proton Affinity of Water. A Scale of Gas-Phase Basicities Including Ethylene and Water from Ion Cyclotron Resonance Proton Transfer Equilibria Measurements," p. 3.
- [6] M. Sabo, K. Jatzová, and M. Gregorová, "Fast Quantification of Whisky Lactone in Oak Wood by Advanced Ion Mobility Spectrometer - AIMS," p. 2. www.masatech.eu

IONIZATION AT ATMOSPHERIC PRESSURE USING KEV ELECTRON SOURCE

Matúš Sámel, Michal Stano, Miroslav Zahoran, Štefan Matejčík

*Faculty of Mathematics, Physics and Informatics, Comenius University, Mlynská dolina F2,842 48
Bratislava, Slovakia*

E-mail: Stefan.Matejcik@fmph.uniba.sk

In this work, we present the results of our experimental study focused on positive as well as negative ion current measurements using an electron source operating at atmospheric pressure. The electron source generates electrons with kinetic energies of several keV and could be used as replacement for β -radiation-based ionization sources for Atmospheric Pressure Ionisation (API) in Ion Mobility Spectrometry (IMS) or Mass Spectrometry (MS)

1. Introduction

Electron guns are devices used to generate electron beams, they are therefore used in plenty of applications, such as ion sources in MS, electron welding, electron microscopy and many others. The electron guns are operated in vacuum, because electrons interact with the gas and causing ionisation, excitation reactions and subsequent thermalisation at atmospheric pressure, thus cannot be as easily accelerated as in vacuum. Most common source of the electrons at atmospheric pressure is a photocathode irradiated by UV light of suitable wavelength [1]. Recently, vacuum electron guns with nanomembrane vacuum-atmosphere interface (window) of 300 nm thickness were developed, which allows transport of keV electrons from vacuum to atmosphere [2 - 4]. Such electron sources are suitable replacements for radioactive ion sources based on β radiation and could be applied for API in MS, IMS or other analytical methods at atmospheric pressure (e.g. excitation fluorescence) [5].

In this work, we present results of our experimental study of the Source of Electrons at Atmospheric Pressure (SEAP) based on 100 and 150 nm thick Si_3N_4 membranes with area of 1×1 mm used as vacuum-atmosphere separator which can withstand atmospheric pressure difference.

2. Experiment

Fig. 1 depicts the experimental setup of measurements of ion currents in the positive and the negative mode. The SEAP emits free electrons from heated tungsten filament floating at high negative potential in the range from 2 to 10 kV. The electrons are accelerated to grounded electrode with the Si_3N_4 membrane of given thickness. If the kinetic energy of the electrons was high enough (typically in the order of 10^3 eV) they are able to penetrate through the membrane. Positive as well as negative ions are produced by interactions between transported electrons with ambient air at atmospheric pressure. Produced ions subsequently drift in the applied electric field of 1 kV/cm of selected polarity to the shielded collector 1 cm apart from the ceramic membrane. Diameter of the shielded collector was 2 cm. Measured ion current was amplified by a transimpedance amplifier and subsequently converted to digital form and saved by a connected PC. During all measurements we have applied a constant electron emission current of $10 \mu\text{A}$ passing through the shielding electrode. This emission current was measured by the ammeter connected between the current source and the high voltage source.

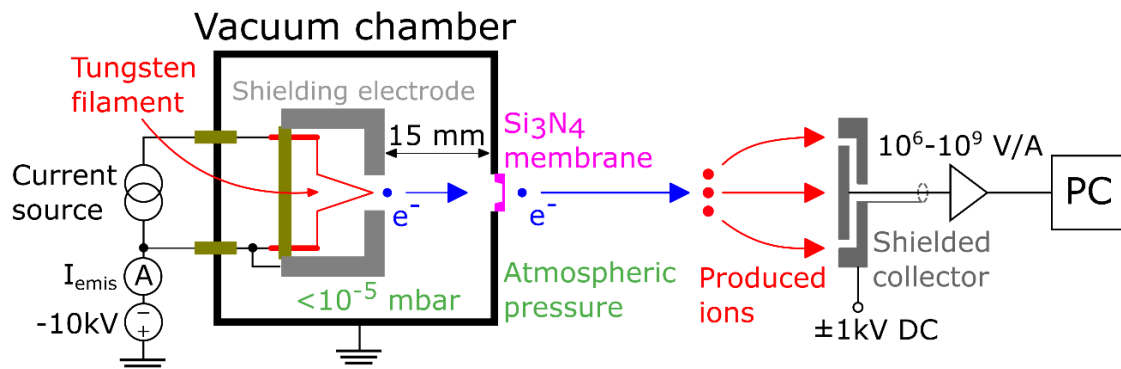


Fig. 1. Experimental setup of positive and negative ion current measurements at atmospheric pressure.

3. Results

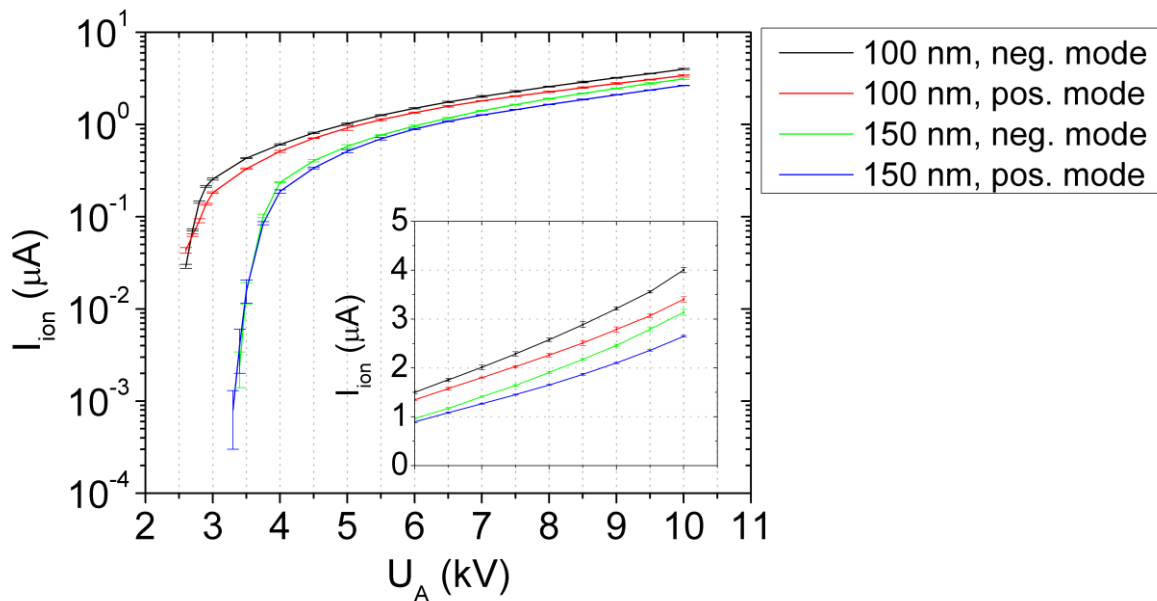


Fig. 2. The ion current I_{ion} measured for the positive and the negative mode as a function of acceleration voltage U_A generated by the SEAP in air at atmospheric pressure using 100 and 150 nm thick Si_3N_4 membranes. Small linear-scale subplot shown in bottom-right corner displays in more detail behaviour of the measured curves at higher energies.

Measured positive and negative ion currents using the membranes of both thicknesses are shown as in Fig. 2. The SEAP was able to produce first ions in both polarities at acceleration voltages U_A of circa 2.6 and 3.4 kV using 100 and 150 nm membranes, respectively. We can observe only negligible differences between positive and negative mode for both membranes at lower U_A . Further increase of U_A led to a significant increase of produced ion currents in all four cases and differences between modes started to be more prominent. We can more easily notice an increase of the differences at higher U_A in small subplot shown in bottom-right corner of Fig. 2. Positive ion currents reached 3.5 and 2.5 μA at 10 kV for 100 and 150 nm, respectively. In the negative mode, detected currents were 4 and 3 μA for the membranes at the same acceleration voltage. Due to short penetration depth of the electrons in air at atmospheric pressure (just 2 mm of 8.6 keV electrons [3]) we placed the ion collector 1 cm apart from the membrane to make sure that we were measuring only negative ion current.

The SEAP presented in this work achieved parameters, which make it a suitable atmospheric pressure ion source for IMS and MS techniques. The SEAP parameters make it especially suitable replacement of β -radiation-based ionization sources such as ^{63}Ni or ^3H which are widely used in the IMS community. The mechanism of ionisation is identical with the β -radiation ion sources, however, the APEG does not contain radioactive substances and is able to achieve high ion currents.

4. Acknowledgement

This work was supported by the Slovak Research and Development Agency, project Nr. APVV-15-0580, the grant agency VEGA, project Nr. VEGA-15-089 and the Comenius University Grant Nr. UK/39/2018. This project has received funding from the European Union's Horizon 2020 research and innovation programme under grant agreement number 692335.

5. References

- [1] J. Urquijo-Carmona; J. Phys. D: Appl. Phys. 16 (1983), 1603-1609.
- [2] F. Gunzer, A. Ulrich, W. Baether; Int. J. Ion Mobil. Spec. 13 (2010), 9-16.
- [3] P. Cochems, J. Langejuergen, A. Heptner, S. Zimmermann; Int. J. Ion Mobil. Spec. 15 (2012), 223-229.
- [4] P. Cochems, M. Runge, S. Zimmermann; Sensors and Actuators A: Physical 206 (2014), 165-170.
- [5] A. Ulrich, T. Heindl, R. Krücken, A. Morozov, C. Skrobol, J. Wieser; Eur. Phys. J. Appl. Phys. 47 (2009), 22815.

VELOCITY MAP IMAGING TECHNIQUE AND THE DISSOCIATION PROCESSES IN $W(CO)_6$ AND $Fe(CO)_5$ NEGATIVE IONS

¹M Pinteá and ²NJ Mason

¹ School of Physical Sciences, The Open University, Milton Keynes, MK7 6AA, UK

² School of Physical Sciences, The Open University, Milton Keynes, MK7 6AA, UK; School of Physical Sciences, University of Kent, Canterbury, CT2 7NH, UK

Tungsten hexacarbonyl and iron pentacarbonyl are two of the common precursors suggested for Focused Electron Beam Induced Deposition (FEBID), one of the new methods being explored by the nanotechnology industry to build sub-10nm structures. As a further continuation of the research study on FEBID molecules the Velocity Map Imaging (VMI) technique has been used in the study of the $Fe(CO)_5$ (Figure 1) and $W(CO)_6$ compounds.

In this presentation first results on Dissociative Electron Attachment to tungsten hexacarbonyl will be presented. This research is a stepping stone to refining the electron beam induced deposition process by giving the essential details on this molecules, such as cross sections, kinetic energies, angular distributions. Malli L. Gulzari et al.[3], Rosenberg G. et al. [4], Neustetter M. et al. [5], Thon R. et al. [6] DEA yields ligand breakage of the compound with the following negative fragments formed from the parent molecule: $W(CO)_5^-$, $W(CO)_4^-$, $W(CO)_3^-$, $W(CO)_2^-$, $W(CO)^-$.

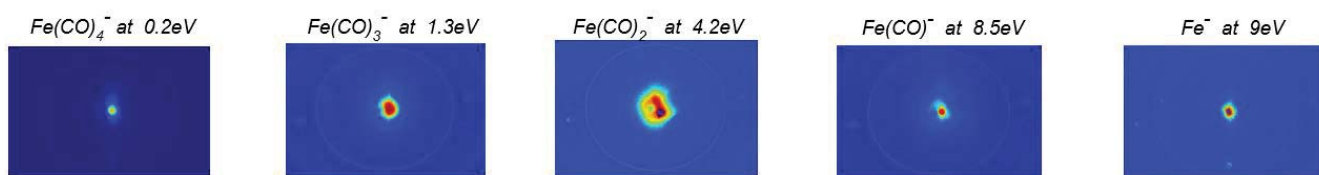


Figure 1. Iron pentacarbonyl VMI

Studies of the dissociation process bombarded with anions of Cl^+ and F^+ have been published by Martin S. et al. [1], Nicholas A Roberts et al. [2] determining the kinetic energy and energy distribution for each dissociation channel.

The mass spectrum presented by these authors is in good agreement with those derived from our ToF (Time – of – Flight) spectrometer.

This work is part of the ELENA Horizon 2020 Training Network, www.elena-eu.org was developed as a European Initiative to support the emerging nanotechnology market and as a response to the increasing demand in this field.

References:

- [1] Martin S. et al., J. Chem. Phys. 134, 034304 (2011)
- [2] Nicholas A Roberts et al., Nanotechnology 24 415301 (2013)
- [3] Malli L. Gulzari, J. Chem. Phys 144, 194301 (2016)
- [4] Rosenberg G. et al., Phys. Chem. Chem. Phys., 15, 4002 (2013)
- [5] Neustetter M. et al., The Journal of Chemical Physics 145, 054301 (2016)
- [6] Thon R. et al., J. Phys. Chem. A, 117, 8145 – 8156 (2013)

STUDY ON ATMOSPHERIC MICROPLASMA WITH TRANSMISSION LINE RESONATORS DRIVEN BY MICROWAVE

Ju Young Park^{1,2} and Jun Choi^{1*}

¹ *Advanced Forming Process R&D Group, Korea Institute of Industrial Technology, Korea*

² *Department of Electrical Engineering, Pusan National University, Korea*

E-mail: junchoi@kitech.re.kr

This work describes the design of two-parallel-wire transmission line resonator (TPWR) driven by microwave power. The TPWR was composed of a two-parallel-wire transmission line that uses air as a dielectric. The resonator was designed and fabricated to operate around 1 GHz and characterized by measuring rotational temperature, electron excitation temperature and electron density. The rotational temperature was determined by comparing the experimental results with the simulated spectrum of the OH band and the electron excitation temperature was calculated by the Boltzmann plot method. The rotational temperature was similar between the simulated and experimental values at 750 K. The calculated electron excitation temperature was 0.76 eV. The electron density was calculated using a method based on Stark broadening of the line, which was about $6.6 \times 10^{14} \text{ cm}^{-3}$.

1. Introduction

Non-thermal atmospheric-pressure plasmas (APPs) have been interested as a potential solution for material handling, surface treatment and biomedicine [1]. The microwave-excited (ME) APP has higher electron and reactive species density, lower discharge voltage and higher particle temperature than plasmas operating at low frequencies [2]. In addition, the device for the ME-APP has a long operational lifetime and low sheath voltage [3]. The ME-APP source can be a resonant by transmission lines (TL) and consequently is possible to operate with high power efficiency [4]. However, the TL resonators are difficult to manufacture because of its complicated structure. Therefore, the resonator needs to be adjusted after assembly. In order to manufacture the ME-APP effectively, the configuration of the device must be simplified. This work describes the design of two-parallel-wire transmission line resonator (TPWR) to generate atmospheric microplasma in argon. The TPWR operates at resonance with a length of a quarter wavelength when the operating frequency is ~ 1 GHz. Finally, the characteristics of TPWR such as electron excitation temperature, rotation temperature and electron density were analyzed through measurement using optical equipment.

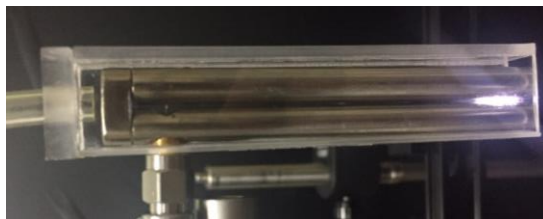


Fig. 1. ME-APP in argon by TPWR.

2. Design of the TPWR

The TPWR was short-circuited at one end and electrically open at the other end, based on the power feeding point. The resonator has two electrodes of the same length in parallel and uses the air as a dielectric. The characteristic impedance (Z_0) of the TPWR was determined by the distance between the centers of the two electrodes and the diameter of an electrode. The Z_0 was set to 50Ω and the resonator was designed to be powered by a subminiature type A (SMA) connector. The parameters obtained by the numerical solution method were analyzed by software COMSOL Multiphysics, which is based on the finite element method. In the simulation, the reflection coefficient at the resonant frequency was

measured at the position of the feeding point. Then, it was compared with the calculated by COMSOL. The optimization was performed by changing the position of the SMA connector to find the point where the maximum electric power is transferred. The electric field intensity at the open end of the resonator was calculated to be $10 \times 1.14 \text{ V}\cdot\text{m}^{-1}$ when the position of the SMA connector was 5.4 mm and the input power was 0.01 W. The input power applied to plasma is defined as the difference between the incident power and the reflected power from the end of the plasma. The feeding point of TPWR was theoretically calculated at 3.0 m but the simulation result shows that the optimum point of feed point is 5.4 mm. In conclusion, the feeding point of the fabricated device was determined to be 5.6 mm after tuning and the plasma of the TPWR was generated at the open end with the highest electric field intensity.

3. Experimental setup and results

The experimental setup of the TPWR was composed with a signal generator and a linear RF power amplifier. The incident and reflected power were monitored using bi-directional coupler, power sensor and power meter. The TPWR was covered with an acrylic case to supply Ar gas. The emission spectrum of TPWR was measured using a spectrometer in the wavelength range of 200 to 900 nm. Analysis of the results showed that the strongest peak was the second positive system of the nitrogen (N_2) band at 337.1 nm and many N_2 lines, Ar atomic lines and oxygen lines were observed. The rotation temperature was determined by comparing the spectrometer measurement results with the OH band spectrum of the simulation. The OH band was most suitable for the spectrum measured at 750 K. The electron excitation temperature was calculated by the Boltzmann plot method using the Ar peaks, where the calculated result was 0.76 eV. The electron density was determined using the atomic hydrogen peak of the Balmer transition line at 486.13 nm (H_β line). The Balmer transition line was calculated as a Stark broadening using the Voigt profile obtained from van der Waals broadening and Doppler broadening. The Voigt function was used to compare the results and the electron density calculated using GKS theory or Gig-Card theory was $6.6 \times 10^{14} \text{ cm}^{-3}$ [5].

4. Conclusion

The TPWR generates plasma with Ar and microwave power. The device has two-parallel-transmission lines and enables stable plasma generation with narrow gap electrodes. The rotation temperature was measured at 750 K. The electron excitation temperature and electron density were calculated to be 0.76 eV and $6.6 \times 10^{14} \text{ cm}^{-3}$, respectively. The electron density was similar to a typical microwave plasma. The results of the electron excitation temperature and the rotational temperature indicate that the plasma generated by the TPWR is a non-thermal plasma.

5. References

- [1] Al-Shamma'a A I et al., 2002 *IEEE Transactions on Plasma Science* **5** 7525581.
- [2] Gregorio J et al., 2015 *Journal of Applied Physics* **118** 08335
- [3] McKaY K et al., 2010 *The European Physical Journal D* **60** 497.
- [4] Choi J et al., 2009 *Plasma Sources Science and Technology* **18** 025029.
- [5] Hrycak B et al., 2010 *The European Physical Journal D* **60** 609.

NOZZLE-TYPE PLASMA ION SOURCE WITH HIGH ION FLUX FOR ION SURFACE INVESTIGATIONS

Faro Hechenberger¹, Lorenz Ballauf¹, Paul Scheier¹

¹Universität Innsbruck

Institut für Ionenphysik und Angewandte Physik

E-mail: faro.hechenberger@uibk.ac.at

For ion surface collision experiments, operating at low vacuum pressures, but with high ion currents is the key to obtain good results. This efficiently reduces impurity contributions. In order to meet these criteria, we developed a plasma ion source. The Plasma is ignited in a high-pressure cavity (50-300 mbar), that is separated from the vacuum apparatus by a small aperture/nozzle (50-100 μm). For producing positive ions, the anode is the tip of a spark plug, the cathode is the nozzle itself, separated by 0.1 to 0.7 mm. The plasma parameters are typically in the range of $U_{\text{plasma}} = 200\text{-}500$ V with I_{plasma} from 0.5 to 10 mA. This characterizes the discharge as a glow discharge [1].

At chamber pressures of 10^{-5} mbar, we observe a low-current-low pressure regime, with ion currents of $I_{\text{FC}} = 10$ μA , also characterized by higher U_{plasma} . When the pressure inside the cavity is raised, the emission of the plasma into the UHV becomes much more efficient, leading to ion currents of up to 3 mA at chamber pressures just below 1×10^{-3} mbar. U_{plasma} drops to ~ 240 V. Here we review theoretical considerations and the assembly and commissioning of a plasma ion source suitable for the described application.

1. Construction details

One concern of ion surface experiments is the low projectile flux to the surface. For many m/z -selected projectiles (D^+ , N^+), the surface current decreases to 1 to 2 nA using electron impact ion sources. We intend to increase this current by 1 to 3 orders of magnitude, using the new plasma ion source. It is inspired by a micro plasma source [2]. Using a skimmer and differential pumping, it will be possible in the new experiment (SurfTOF) to have high ion currents with low pressures in the surface chamber.

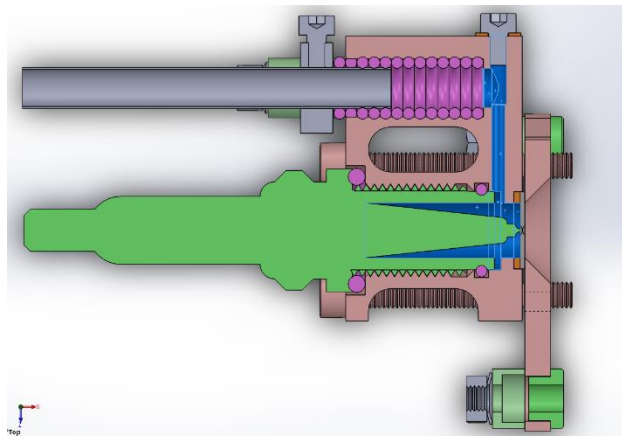


Figure 1. Cut view of the 3D CAD model of the plasma ion source utilizing a spark plug (green). The high pressure side is marked in blue, it is connected to the gas inlet (grey), insulated by a stack of O-rings (purple), in order to avoid ignition of a plasma at the wrong place. The tip of the spark plug (anode) points toward a small nozzle (few μm diameter) which is used as a cathode. The plasma ignites between the tip and the nozzle. Outside of the nozzle the pressure drops to 10^{-5} to 10^{-3} mbar (low pressure side).

The setup (see Fig.1) consists of a spark plug (anode), a $75\mu\text{m}$ aperture nozzle (cathode) and a gas inlet, which is insulated against both, anode and cathode, in order to float the source to high electrical

potentials, allowing to set the surface impact energy in the intended use. For the first measurements, it is important to know the pressure-distance (pd) characteristics [3].

In addition to the dimensions of the cathode and the distance between anode and the cathode, our findings imply that the shape of the aperture does not affect the current voltage behaviour. Using the plasma ion source depicted in Fig. 1 the plasma characteristic including ion currents and different types of plasma regimes at low pressures will be investigated. In the first prototype (Fig. 2), the same geometry was quickly implemented using mostly 3D-printed parts (SLA technique).

With a pressure controller (MKS Series), the chamber pressure was used as a feedback signal, in order to precisely regulate the primary pressure. Different pressure regimes were investigated and it was seen that there is a threshold pressure, which suddenly ejects the plasma into the UHV.

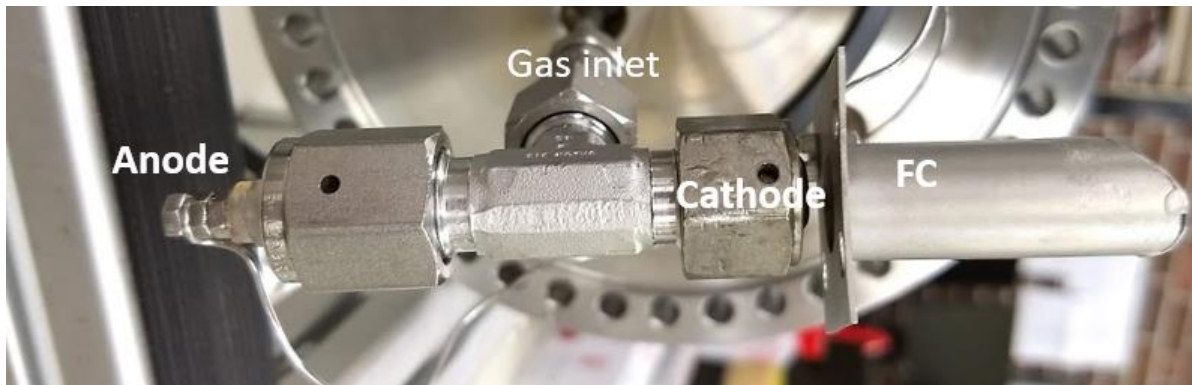


Figure 2. A closer look in the first test setup. The cathode can use any type of nozzle diameters. For the measurements the $3\ \mu\text{m}$ nozzle was not good. Highest currents were obtained with $150\ \mu\text{m}$. The transition started at chamber pressure of 1.2×10^{-4} mbar and up to half of the plasma current at the faraday cup (FC). Plasma ignition was achieved at roughly 500 V. A Faraday cup which was insulated against the cathode was placed behind the aperture and the ion current on the cup was determined as a function of the potential on the cup. Results are shown in Fig. 3.

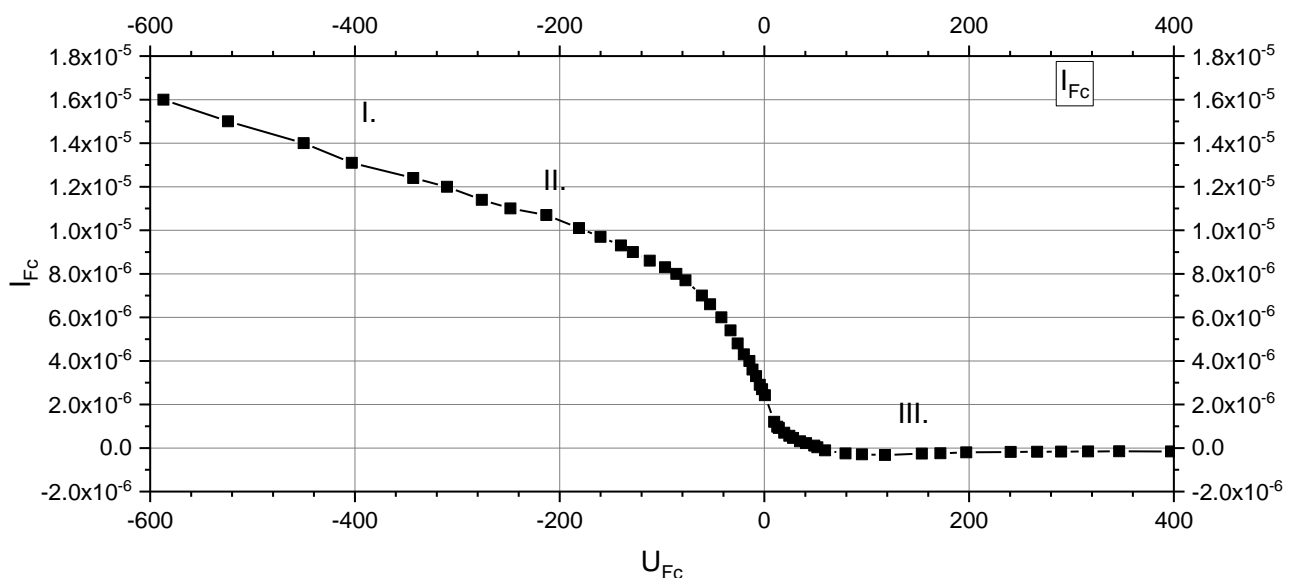


Figure 3. The retarding field analysis shows the ion current on the Faraday cup behind the aperture of the cathode as function of the potential on the cup. The plasma current was 3 mA with 640 V, which leads to a stable plasma over all measurements. The used nozzle was $50\ \mu\text{m}$ at a vacuum pressure of 4×10^{-5} mbar. As no suppression of secondary electrons was implemented, the ion current does not seem to saturate for negative bias, which is an artifact (Zone 1).

In Fig. 3 we kept the plasma stable and varied the potential on the faraday cup. We can divide this plot in 3 regions: Region I shows a combination of the current on the faraday cup in

combination with secondary electrons. As seen in Fig. 2 we did not use any secondary electron suppression that would have flattened the curve. Region II can be assigned as the positive ions hitting the faraday cup. At about -220 V, there should be the maximum of positive ions without any secondary electrons. Region III. can then be assigned as the negative ions or electrons which were attracted by the positive potential of the faraday cup. This suggests that some ions are accelerated through the plasma sheath. There are negative charge carriers emitted, the most at 120 V.

The actual setup (Fig. 1) has now been tested and seems to perform like the prototype (Fig. 2).

2. Acknowledgement

Our work is supported by Friedrich Schiedel Foundation for Energy Technology 259564, “Reaktive Ionen-Oberflächenstöße”. Austrian Science Fund (FWF) W1259-N27 „DK-ALM“. This work has been carried out within the framework of the EUROfusion Consortium and has received funding from the Euratom research and training programme 2014-2018 and 2019-2020 under grant agreement No 633053. The views and opinions expressed herein do not necessarily reflect those of the European Commission. Financial support has also been provided by KKKÖ (Commission for the Coordination of Fusion Research in Austria at the Austrian Academy of Sciences (ÖAW))

3. References

- [1] Conrads, H, and M Schmidt. “Plasma Generation and Plasma Sources.” *Plasma Sources Science and Technology* 9, no. 4 (November 1, 2000): 441–54. <https://doi.org/10.1088/0963-0252/9/4/301>.
- [2] Schoenbach, Karl H, Ahmed El-Habachi, Wenhui Shi, and Marco Ciocca. “High-Pressure Hollow Cathode Discharges,” n.d., 11.
- [3] Stoffels, E, A J Flikweert, W W Stoffels, and G M W Kroesen. “Plasma Needle: A Non-Destructive Atmospheric Plasma Source for Fine Surface Treatment of (Bio)Materials.” *Plasma Sources Science and Technology* 11, no. 4 (November 1, 2002): 383–88. <https://doi.org/10.1088/0963-0252/11/4/304>.

COMBUSTION EXHAUST CLEANING USING TRANSITION ELECTRIC DISCHARGE

Vladimír Held¹, Marcela Morvová²

¹*Faculty of Mathematics, Physics and Informatics, Comenius University, Mlynska dolina F2, 84248 Bratislava, Slovakia*

²*Division of Environmental Physics, Faculty of Mathematics, Physics and Informatics, Comenius University, Mlynska dolina F2, 84248 Bratislava, Slovakia*
E-mail: held5@uniba.sk

Pollution caused by fossil fuel combustion and industrial production is an increasing threat not only to the environment (ozone depletion, acid rain, smog) but also to global warming and climate change. Not negligible is the influence on human health. The commercial methods such as absorption, separation and catalysis have the disadvantage of high investment cost as well as high operating costs. In recent decades the research of non-thermal plasma as a technique for pollution removal due to its lower costs and greater efficiency increases. For the commercial use of this method, it is necessary not only to enlarge the system, but also to optimize the ratio of efficiency to energy cost. It is also important that final purification products and intermediates are safe to environment and human health and eventually reusable. In this paper we present the influence of non-thermal plasma on exhaust produced by a two stroke benzine fuelled engine.

1. Introduction

Plasma consists of molecules, atoms, electrons, ions, metastables and radicals. It can be found in two generic states where all of these components are in equilibrium in the sense that the temperatures of all the components are about the same - thermal plasma or the state where neutral particles, ions and electrons differ – non-thermal plasma. Non-thermal plasma can be generated by various electrical discharges, where the most of energy is consumed to produce and accelerate electrons than to heat the ions and gas. The electrons have sufficient energy to cause ionization, dissociation and produce excited states, reactive particles as radicals and metastable from the surrounding gas. These particles can react with other gas particles through plasma chemical reactions at room temperature [1,2]

The first applied technique was the use of an electron beam. Electrons are produced in a vacuum, accelerated by an electric field, and then passed through a thin film into a chamber containing gas at atmospheric pressure. The electrons activate the gas in which chemical reactions inside pollutants occur, what is the bases of removal process. By this method, it is possible to remove molecules such as NO_x, SO_x and VOC. However, the disadvantage is the price of high-pressure accelerators, the need of vacuum and the Xray hazard [1-4].

Another possibility of non-thermal plasma application is the use of dielectric barrier discharge. The energy is supplied by an alternating current high voltage source with a frequency from 10 Hz to 100 kHz. One or both of the electrodes are covered by a dielectric layer to prevent the dc operation or the transition to the arc discharge. The discharge is initiated by a large number of micro discharges producing electrons and reactive particles. DBD was first used in ozone production but later much work was done in purification of toxic substances such as NO_x, VOC, etc. The system needs electrode cooling and is sensitive on particles inside inter electrode space. As the distance between electrodes is small, the system is sensitive on vibrations. The operating costs is high, what is disadvantage for practical use. [5,6]

As another method of producing non-thermal plasma usable for pollution control is pulsed power discharge. Due to the very short high voltage pulses between the electrodes is possible to generate a large number of high energy electrons with energies of 1-10eV. These electrons can ionize and dissociate the purified gas, thereby achieving a high efficiency of pollutant purification [1,7].

As the last of the methods we refer the dc current spontaneously pulsed discharge stabilized by the external resistor. In discharge gap with non-homogeneous electric field according to the value of the resistor several types of discharge are formed:

- streamer corona,
- prevented spark,
- spontaneously pulsing transition discharge,
- high pressure continuous discharge. [8,9].

We have also used spontaneously pulsing transition discharge with applied resistance $5,4 \text{ M}\Omega$ and small internal capacity of discharge gap in our experiments [10]. This type of discharge is characterized by the formation of pulsing discharge filaments. One or both electrodes have a small radius of curvature. The schematic arrangement is illustrated in Figure 1. The discharge begins with formation of streamer which, upon reaching the second electrode causes an electrical breakdown with short duration limited by the discharging of internal capacity C . When the discharge gap capacity is fully discharged, the discharge extinguishes because of high resistance of gap. The capacity is recharged by high voltage source and the discharge pulse forms again. The periodicity of spontaneous pulses depends on the composition of gas, external resistance R , capacity of the gap and reached values 1-10 kHz [8].

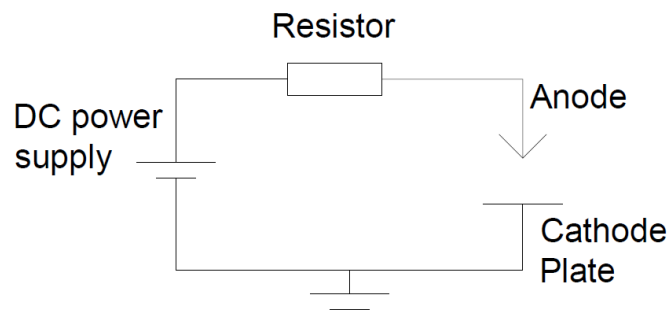


Fig.1. Simple schematic of circuit.

Our goal was to inspect the influence of non-thermal plasma generated by spontaneously pulsing transition discharge on exhaust produced by two stroke engine. Simple electric reactor was developed and used as a gas cell for FTIR analysis.

2. Experimental setup

The experimental setup is illustrated in Fig. 2. Plasma was generated by direct current electric discharge in spontaneously pulsing transition discharge mode. As high voltage source we used unregulated variable power supply with step up transformer. Current limiting resistor value of resistance

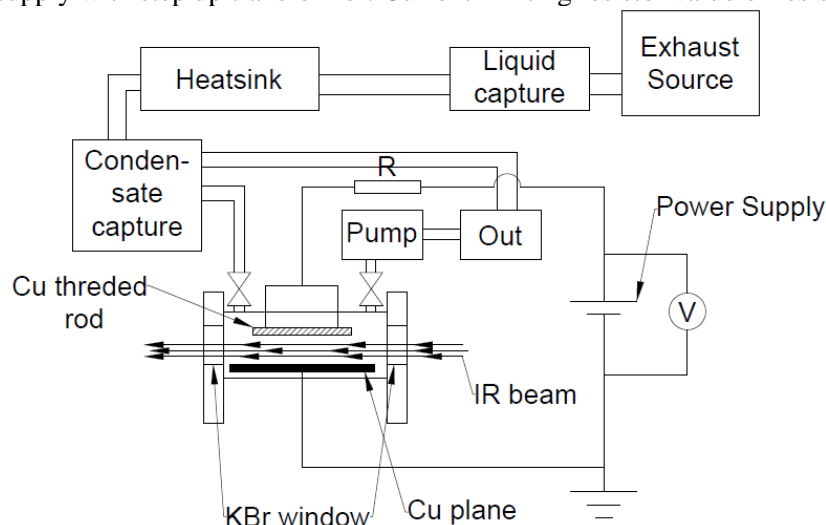


Fig. 2. Experimental setup

was $R = 5,4M\Omega$. Developed discharge reactor consisted of plexiglass tube with 42mm inner diameter, 4mm in thickness and 135mm in length. Geometry of electrical reactor was 8mm diameter threaded copper rod (stressed electrode) and 1mm thick copper plane in 10mm distance. On each side of discharge reactor tube was KBr window. Reactor was sealed from both sides. This type of reactor has an advantage, because isokinetic sampling is no longer necessary for proper measurement. As exhaust source we used two-stroke engine which was directly connected to pipeline of whole system. Since we were using commercial engine, we had to take into account incomplete combustion. Liquid capture and condensate capture tank were integrated into the system for extraction of unburned fuel. Before each measurement, exhaust was let to flow through whole system for a sufficient period of time. This ensure that residual gas e.g. air was extracted from the gas cell. Subsequently gas cell was evacuated and sample was sucked into the cell after opening valve. Composition of the gas was measured using FTIR spectrometer (Shimadzu IR-Affinity 1S). We investigate the composition of gas both before discharge and after discharge in order to discover influence of non-thermal plasma on exhaust produced by two stroke engine.

3. Results and discussion

Figure 3 shows IR spectrum of gas sample before and after discharge. From spectrum scanned before exposure of exhaust gas to plasma we can see its composition. We can see presence of CO_2 , CO , CH_4 and VOCs, although we could not see the trace NO_x gases as they were minor gas component. IR absorption bands of NO_x were overlapped by bands of other components with higher concentrations. At $2250-2290\text{ cm}^{-1}$ R branch of vibration-rotational band of radical $-NCO$ was observed. It was impossible to determine species corresponding to bands at region from $900-1250\text{ cm}^{-1}$. After exposure to plasma, spectrum of gas changed. Bands in region near 3000 cm^{-1} vanished. This can be expressed as result of oxidation of VOC and its decomposition as well as oxidation of CO in region at $2030-2230\text{ cm}^{-1}$. Acetylene removal can be also seen after discharge action. Outcome of these oxidation processes was the increase in concentration of CO_2 which we have observed as increase of absorbance at regions $3550-3750\text{ cm}^{-1}$, $2290-2390\text{ cm}^{-1}$ and $630-700\text{ cm}^{-1}$, as well as at regions $3000-3700\text{ cm}^{-1}$ and $1500-1700\text{ cm}^{-1}$ due to formation of water and OH radicals.

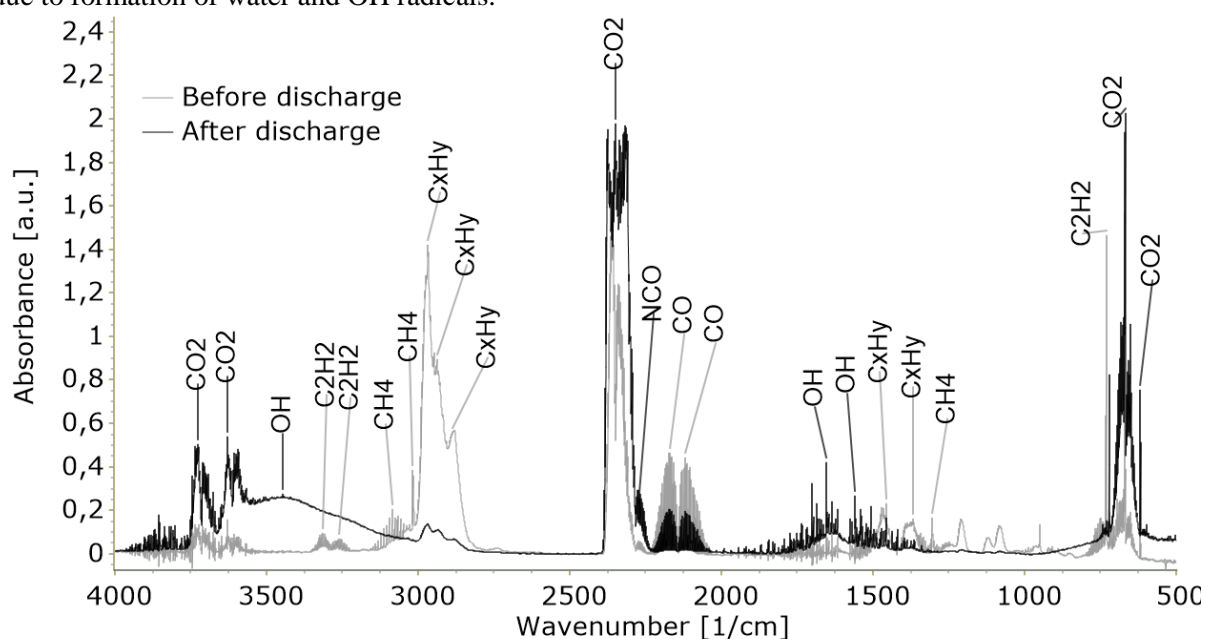


Fig. 3. IR spectrum of exhaust gas before and after 2 min discharge treatment obtained by FTIR spectroscopy measurement. (12kV, 10mm gap).

In region at $2250-2290\text{ cm}^{-1}$ is an indication of NCO radical formation. This evolution is related with excited state $N_2A^3\Sigma^+$ and CO_2 or CO decomposition [12].

4. Conclusion

Influence of non-thermal plasma generated by dc electric discharge in spontaneously pulsing transition discharge mode on exhaust was studied. Real exhaust gas was treated by spontaneously pulsing discharge in threaded rod to plane geometry at 12kV voltage. FTIR spectroscopy measurements showed decomposition of VOCs, oxidation of CO and formation of NCO radical which is important in CO₂ removal in plasma reactor. Our work demonstrated that use of dc electric discharge in spontaneously pulsing transition discharge mode is suitable method for air pollution control.

5. Acknowledgments

This project has received funding from the European Union's Horizon 2020 research and innovation programme under grant agreement No 692335.

We would like to thank to doc. Karol Hensel for his advice and also for providing us FTIR spectrometer for our measurements.

6. References

- [1] Matsumoto T, Wang D, Namihira T and Akiyam H 2012 Non-Thermal Plasma Technic for Air Pollution Control, in Air Pollution - A Comprehensive Perspective *InTech*.
- [2] Chang J S 2008 Physics and chemistry of plasma pollution control technology *Plasma Sources Science and Technolog. Vol 17 No 4*.
- [3] Licki J, Chmielewski A G, Pawelec A, Zimek Z, Bigos A 2013 *Journal of power technologies. Vol 93 No 5* 300.
- [4] Chmielewski A G and Licki, J 2008 *Nukleonika.. Vol 53* 61.
- [5] Kogelschatz U, Eliasson B, Egli W 1997 *Journal de Physique IV Colloque. Series C4 07* 47.
- [6] Kogelschatz U 2003 *Plasma Chemistry and Plasma Processing. Vol 23* 1.
- [7] Wang D, Akiyama H and Namihira T 2010 Pulsed Discharge Plasma for Pollution Control *InTech*.
- [8] Janda M, Machala Z, Niklová A and Martišovitš, V 2012 *Plasma Sources Science & Technology. Vol 21 No 4*.
- [9] Staack D, Farouk B, Gutsol A and Fridman A 2005 *Plasma Sources Science and Technology. Vol 14 No 4*.
- [10] Janda M, Machala Z, Dvonč L, Lacoste D and Laux C O 2014 *Journal of Physics D: Applied Physics. Vol 48 No 3*
- [12] Morvova M, Hanic F and Morva I 2000 *Journal of Thermal Analysis and Calorimetry. Vol 61* 273
- [13] Linstrom P.J. and Mallard W.G, *NIST Chemistry WebBook, NIST Standard Reference Database No 69*
- [14] Menges F 2018 Spectragryph - optical spectroscopy software, *Version 1.2.10*.

INTERFEROMETRIC ANALYSIS OF PRESSURE FIELDS AROUND NANOSECOND DISCHARGES IN WATER

Petr Hoffer, Václav Prukner, Jiří Schmidt, Milan Šimek

Institute of Plasma Physics of the CAS

E-mail: hoffer@ipp.cas.cz

Spatially resolved pressure field around nanosecond discharges produced in deionized water by fast rise-time positive high-voltage pulses (duration of 10 ns and amplitude of +100 kV) on a point electrode was investigated by means of picosecond laser interferometry. The Mach-Zehnder interferometer with 2nd harmonic of Nd:YAG laser was used in the experiments. The changes of the liquid refractive index, which is a well-known function of pressure, produced a shift of fringes in interference pattern projected by the interferometer and acquired by the CCD camera. Observation of the interference patterns was possible only at a certain minimum distance (approx. 0.3 mm) from the discharge filaments, where gradients of the refractive index of liquid were sufficiently weak. Closer to the discharge, the gradients were so strong that the diagnostic laser beam was diverted away from the field of view of the projecting lens, and thus, the interference pattern could not be produced.

1. Introduction

Generation of shockwaves by spark discharges in liquid water is a well-known phenomenon with important practical application (e.g. in shockwave lithotripsy). However, shockwaves are generated also by low current corona-like discharges. In the case of discharges emanating from positive electrode, non-luminous *primary streamers* are often the initial phase of plasma propagation in water, which can, but need not start to propagate from an initial gas bubble with plasma streamers inside. The launch of primary streamers is triggered, when local electric field is of the order of $100 \text{ MV}\cdot\text{m}^{-1}$ [1]. Propagation of primary streamers is accompanied by a phase transition, occurrence of microbubbles, and their hydrodynamic expansion. Primary discharges have hemispherical bush-like appearance, where the edges of the individual streamers can be clearly resolved (their channel diameters were measured to be 3-10 μm [2]), and propagate along radial directions at relatively low velocities (often subsonic, but some may reach even several kilometers per second) producing spherical shockwaves. Therefore, the initial disturbance has approximately spherical shape. Adjacent electric field may initiate next discharges or gas bubbles in the liquid and thus elongate the streamers plasma channel. The process stops when the breakdown voltage of the gaseous channel becomes higher than the voltage along the channel or when the electric field at the active tip of one of the streamer becomes so high that *secondary streamers* can be formed [3] [1] [4]. The secondary streamers are much more luminous, and often start out of the primary streamers. However, it is possible to create conditions where secondary streamers takes are produced directly. Secondary streamers have a filamentary structure (channel diameters larger than that of the primary streamers, roughly in the 5–25 μm range), and propagate much faster than the primary streamers. Upper limit of the propagation velocity of secondary streamers is not known; it commonly ranges from a few kilometers per second to about $500 \text{ km}\cdot\text{s}^{-1}$ (depending on voltage used and on electrode geometry) [2]. Field induced dissociation and ionization of molecules in the bulk liquid are considered as mechanisms for secondary streamer propagation, because electric field around secondary streamer heads reaches $2 \text{ GV}\cdot\text{m}^{-1}$ [1]. The ion mobility in the liquid vapour in the streamer channel gives drift velocities of the order of $10^3 \text{ m}\cdot\text{s}^{-1}$ for heavy ions and $10^5 \text{ m}\cdot\text{s}^{-1}$ for protons, the main product of the water dissociation and ionization. The vaporization at the tip of a streamer head thus also takes place due to charged particle flow from the discharge plasma in the streamer channel (fast energy input into the water volume). This argument is based on the fact, that the discharge input energy is consistent with the energy required to vaporize the volume of water contained in the streamer channels [5]. Since the mechanism of the Townsend breakdown in water vapour is independent on the water conductivity, the streamer velocity also does not depend on the water conductivity.

Pressure distribution around positive secondary streamers was studied in more detail in [1] by means of Mach-Zehnder interferometry. Evaluation of fringe shifts in produced interference patterns of the streamer surroundings leads to the desired pressure profile, since the fringe shift represents a phase shift due to deviations of the liquid refractive index, which is a known function of the liquid pressure at a given temperature. Streamers can be recognized by the conical shape (Mach cone) of the shock front evolving from them. At driving voltage of 20 kV, the peak pressure of the shock front, when it reached radius of 35 μm , was 46 MPa. A reproduction of the detected pressure field required 2–3 ns pressure pulses with amplitudes of up to 3 GPa.

Another approach to shock-front pressure evaluation was described in [6], where high-speed shadowgraphy was utilised to the shock-front speed measurement. The shock-front speed was directly related to the shock-front pressure. At 15 kV of the driving voltage, the maximum shock velocity was determined to 4.2 $\text{km}\cdot\text{s}^{-1}$, which, according to the authors, corresponded to 5.8 GPa of initial pressure of the plasma channel. Although the regression was performed at constant liquid density, this value was comparable to that obtained in [1].

The main purpose of experiments described in this work is to develop suitable setup for the pressure field measurement in vicinity of nanosecond positive corona-like discharges produced in distilled water.

2. Experimental setup

The experimental setup of the second experiment is depicted in the Fig. 1a. The pulsed power supply was FID nanosecond pulser, which produced pulses 100 kV/10ns. The pulsed source was connected to the needle electrode, where corona streamers were produced. Deionised water ($\sim 1 \mu\text{S}/\text{cm}$) was used as working liquid. The compact discharge chamber is sketched in Fig. 1b. The concept of Mach-Zehnder interferometer was applied to detect the pressure field. The Katana 05 (Ofive) laser, producing pulses 532 nm/30 ps/4 nJ was used to produce probe and reference beams. The 12 bit CCD SensiCam (PCO) camera was used as detector. The diameter of the output window and the output beam-splitter of the interferometer was 50 mm.

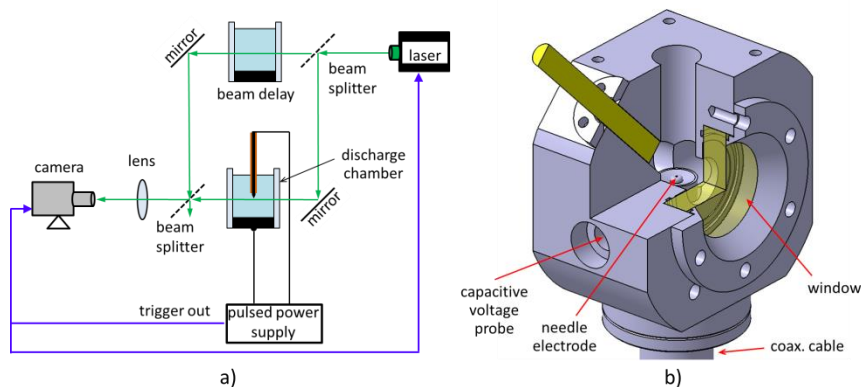


Fig. 1. Experimental setup.

3. Results

Generally, optical interferometry is based on interference of reference (direct) and measuring (propagating through the analyzed optical inhomogeneity) light rays with different phases. The phase shift is caused by their propagation through regions with different refraction indexes. The interference can be constructive or destructive, which leads to creation of bright and dark regions on the plane, where they interfere (CCD chip of the camera). When mirrors and beam splitters of the interferometer are adjusted appropriately and when both the reference and measuring beams propagate through optically homogeneous environment, then the interference pattern contains parallel fringes only [7] with adjustable pitch. Any optical inhomogeneity in one of interfering beams results in a shift of fringes; this shift can be used for evaluation of the phase shift in each point of the interference pattern.

Since interferograms provide information about deviations of the refractive index inside an inhomogeneity, it is possible to calculate profile of liquid density and hence, the appropriate pressure profile. Examples of interference patterns captured in recent experiments are shown in Fig. 2.

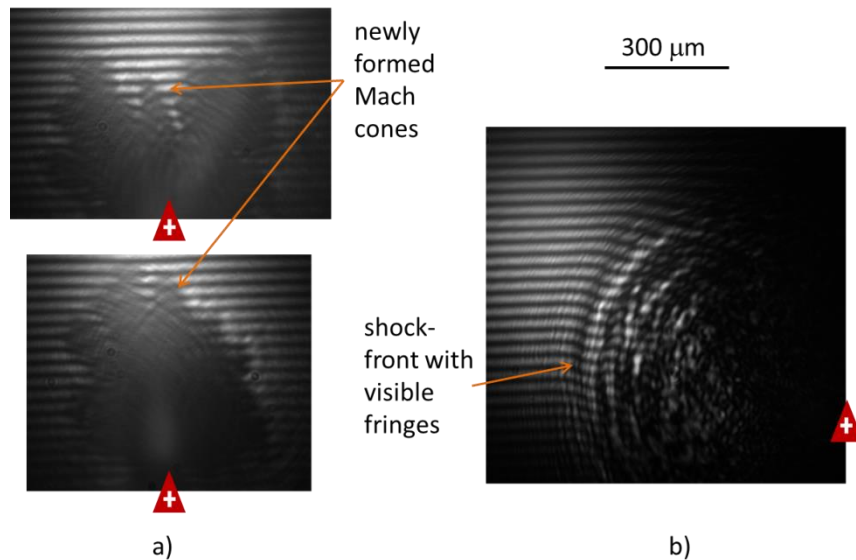


Fig. 2. Examples of captured interferograms; a) interferograms captured early after the discharge initiation (shockwave area is opaque), b) interferogram capturing expanded shockwave. The red triangle indicates position of the positive needle electrode.

Interference patterns captured just after the discharge initiation (Fig. 2a) show opaque areas with no visible fringes. This means that the measuring laser beam was bent outside of the field of view of the optical system by very strong refractive index gradients, and the interference pattern could not be created. This indicates presence of extremely strong shock waves. Fig. 2b shows an interference pattern captured 220 ns after the discharge initiation, where the produced shockwave had expanded, and thus, its pressure decreased. Therefore, the beam bending was weaker, and the interference pattern could have been observed. Analysis of these interferograms is now in progress.

In the future, we will try to improve the interferometer for avoiding the mention issue with the shockwave opacity. The fast schlieren method will also be used for possible result comparison.

Acknowledgement

This work was supported by the Czech Science Foundation under project No. 18-04676S.

4. References

- [1] W. An, K. Baumung and H. Bluhm, "Underwater Streamer Propagation Analyzed from Detailed Measurements of Pressure Release," *J. Appl. Phys.*, vol. 101, p. 053302(10), 2007.
- [2] J. F. Kolb, R. P. Joshi, S. Xiao and K. H. Schoenbach, "Streamers in Water and Other Dielectric Liquids," *J. Phys. D: Appl. Phys.*, vol. 41, p. 234007 (22), 2008.
- [3] P. Bruggeman and C. Leys, "Non-thermal Plasmas in And in Contact with Liquids," *J. Phys. D: Appl. Phys.*, vol. 42, p. 053001(28), 2009.
- [4] V. Y. Ushakov, *Impulse Breakdown of Liquids*, Heidelberg: Springer-Verlag, 2007.

- [5] I. V. Lisitsyn, H. Nomiya, S. Katsuki and H. Akiyama, "Thermal Processes in a Streamer Discharge in Water," *IEEE Transactions on Dielectrics and Electrical Insulation*, vol. 6, pp. 351-356, 1999.
- [6] I. Marinov, S. Starikovskaia and A. Rousseau, "Dynamics of plasma evolution in a nanosecond underwater discharge," *J. Phys. D: Appl. Phys.*, vol. 47, p. 224017 (10pp), 2014.
- [7] B. Gross, Měření vysokých teplot, Praha: SNTL, 1962.

ELECTRON-INDUCED SECONDARY ELECTRONS IN LOW-PRESSURE CAPACITIVELY COUPLED RADIO-FREQUENCY PLASMAS

Benedek Horváth¹, Julian Schulze^{2,3}, Zoltán Donkó¹, Aranka Derzsi^{1,3}

¹*Institute for Solid State Physics and Optics, Wigner Research Centre for Physics, 1121 Budapest, Konkoly-Thege M. 29-33, Hungary*

²*Institute for Electrical Engineering, Ruhr-University Bochum, 44801 Bochum, Germany*

³*Department of Physics, West Virginia University, Morgantown, WV 26506, USA*

E-mail: horvathb95@gmail.com

We investigate the effects of secondary electrons (SEs) induced by electrons on the discharge characteristics in low-pressure single-frequency capacitively coupled plasmas (CCPs) by Particle-in-Cell/Monte Carlo Collisions (PIC/MCC) simulations. In a recent work, such SEs (δ -electrons) were found to have a remarkable influence on the plasma parameters in argon at 0.5 Pa and 6.7 cm gap between SiO₂ electrodes [1]. Here we study the impact of δ -electrons on the ionization dynamics and plasma parameters at various pressures and voltage amplitudes, assuming different SE yields for ions (γ -coefficient). The voltage amplitude, the gas pressure and the value of the γ -coefficient affect the role of δ -electrons in the ionization dynamics. While their effect is most striking at low pressures, high voltage amplitudes and high γ -coefficients, in the whole parameter regime investigated here the realistic description of the electron-surface interaction changes significantly the computed plasma parameters compared to results based on a widely used simple model for the description of the electron-surface interaction.

1. Introduction

Capacitively coupled plasmas (CCPs) are widely used in plasma processing applications such as the deposition in solar cell manufacturing, the etching in the semiconductor industry, as well as in medicine for surface treatment [2]. The Particle-in-Cell simulation method combined with Monte Carlo type treatment of collision processes, known as the PIC/MCC numerical technique [3], is a powerful method for the self-consistent kinetic description of such low-pressure CCPs. By tracing “superparticles”, representing a large number of real plasma particles, PIC/MCC simulations make it possible to follow the spatio-temporal evolution of discharge characteristics and to obtain information about various plasma parameters in a very efficient way. While the description of the gas phase has become more and more accurate (by the increase of the number of particle species and collision processes), in PIC/MCC simulations of capacitively coupled plasmas (CCPs), several simplifications are common regarding the plasma-surface interactions. In the description of the interaction of electrons with boundary surfaces, the most wide-spread simplifications are: (i) the electron reflection is completely neglected, or a constant value (typically 0.2 [3]) for the electron reflection coefficient is assumed, irrespectively of the discharge conditions; (ii) the secondary electron emission (SEE) due to electron impact is not taken into account, and (iii) the effects of the electrode material and surface conditions on these processes are not accounted for. However, electron-induced secondary electron emission is a phenomena that has been studied a lot because of its important role in several different systems, such as scanning electron microscope [4] and stationary plasma thrusters [5-10]. Experimental data suggest that the SE yield depends on the energy of the primary electron (PE) beam. The σ relative SE yield (the ratio of the SE flux and the PE flux) as a function of the PE energy, ε , results in curves with similar shape for different surface materials: at low energies of the PEs σ increases rapidly with ε , reaches a maximum value σ_{max} at a PE energy ε_{max} , then slowly decreases towards high PE energies. While the general shape of $\sigma(\varepsilon)$ is the same for all surface materials, the σ_{max} and ε_{max} values vary over a wide range: σ_{max} is smaller than 2 for most metals and can reach values higher than 10 for some oxides, while ε_{max} takes values between about 100 and 1000 eV, depending on the material [11-12]. The SE yield is influenced by the properties of the surface, as well as the angle of incidence of the PEs: σ_{max} and ε_{max} are significantly increased for oblique impact [12]. In many cases phenomenological models are used for the description of electron-induced SEE [11-17]. In this work we use such a phenomenological model [12, 17] to describe the electron-surface interaction in PIC/MCC simulations of CCPs. An algorithm was developed by

Sydorenko [18] to implement this model into a PIC/MCC simulation code. Following his basic ideas we also implemented an algorithm for the electron-induced SEE to our PIC/MCC code according to the phenomenological model.

2. Model and discharge conditions

The calculations are based on an electrostatic Particle-in-Cell code complemented with Monte Carlo treatment of collision processes (PIC/MCC) [19-21]. The code is one-dimensional in space and three-dimensional in velocity space. The plane, parallel and infinite electrodes are separated by a distance of $L = 6.7 \text{ cm}$. The discharges investigated are geometrically symmetric. The electrodes are assumed to be identical, made of SiO_2 with the same surface conditions, hence characterized by the same electron emission and particle reflection properties. The discharge gas is argon, the temperature of the gas is 400 K. One of the electrodes is grounded, while the other one is driven by the voltage waveform

$$V(t) = V_0 \cos(2\pi f t). \quad (1)$$

The discharges investigated here are all single-frequency CCPs, and $f = 13.56 \text{ MHz}$ in all cases. The driving voltage amplitude is varied between 100 V and 1500 V, while the gas pressure is between 0.5 Pa and 3 Pa.

For describing the interaction of the electrons colliding with the electrode we use two different models in this work:

- *Model A* assumes that the electrons hitting the electrode surface are elastically reflected with a constant probability of 0.2 [3], independently on their energy and angle of incidence. Electrons escaping from the electrode material are neglected. This approach has been used frequently in PIC/MCC simulations of low-pressure CCPs.

- *Model B* is a realistic description of the electron-surface interaction that was introduced in [1]. It assumes that the total SE yield consists of three components: elastically reflected PEs, inelastically reflected PEs and electron-induced SEs (true SEs, δ -electrons).
$$\sigma = \eta_e + \eta_i + \delta, \quad (2)$$

where η_e is the elastic reflection yield, η_i is the inelastic backscattering yield and δ is the electron-induced SE yield. The characteristics of the surface are taken into account via material specific input parameters, such as the maximum emission at normal incidence, the energy of the primary electron at maximum emission etc. A detailed description of this approach is given in [1].

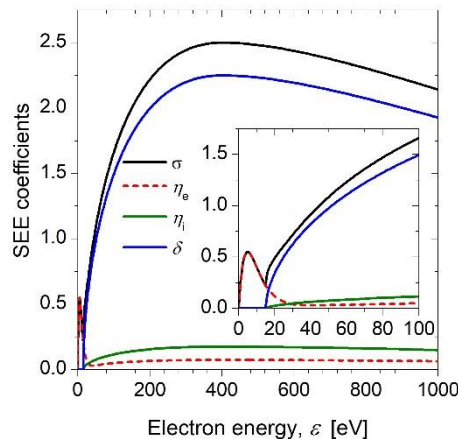


Fig. 1. The total electron induced secondary electron emission coefficient (σ) and the partial emission coefficients of the elastic reflection (η_e), inelastic backscattering (η_i), and electron induced secondary electron emission (δ) as a function of the incident electron energy, ε , at normal incidence for SiO_2 surfaces [1].

The total and partial electron emission coefficients are shown for a SiO_2 surface in figure 1, at normal incidence. For the ion induced SEE coefficient, γ , we use constant values in the simulations, varied between 0 and 0.4. Since our main goal was to describe the effect of electron-induced SEs, it is

appropriate to use a simple model for the ion-induced SEE. With the use of different γ values, it is possible to simulate several different discharge conditions.

3. Results

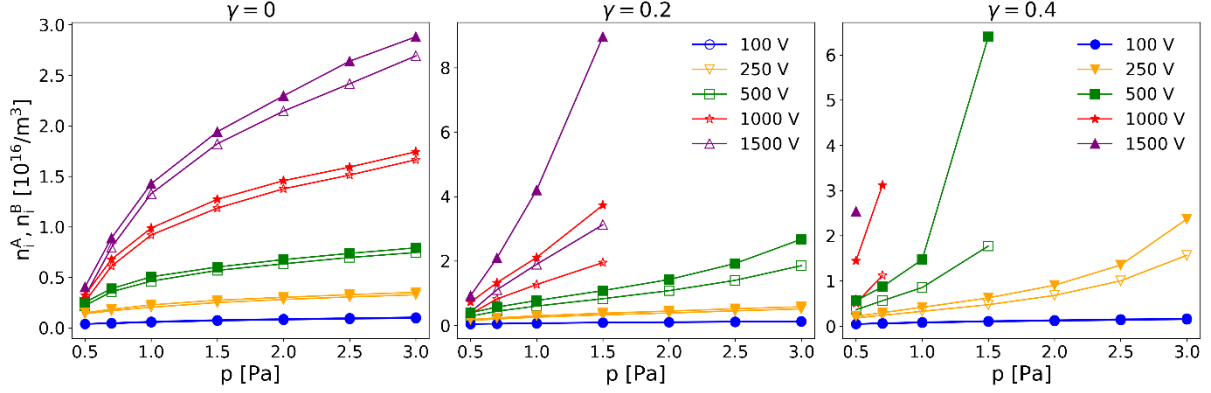


Fig. 2. The central ion densities obtained from model A and model B, n_i^A (open symbols) and n_i^B (filled symbols), respectively, as a function of the gas pressure, for different driving voltage amplitudes and various values of the ion-induced SEE coefficient: $\gamma = 0$, $\gamma = 0.2$, $\gamma = 0.4$ [22].

Figure 2 shows the central ion densities obtained from model A and model B, n_i^A and n_i^B , respectively, as a function of the gas pressure, for different driving voltage amplitudes and various values of the ion-induced SEE coefficient: $\gamma = 0$, $\gamma = 0.2$, $\gamma = 0.4$. Both models show, for all V_0 and γ values an increase of the central ion density with increasing gas pressure. For a given value of the pressure, the driving voltage amplitude and the γ coefficient, the plasma density obtained is always higher with model B compared to model A. The difference between the results obtained from the two models gets more and more significant at higher voltage amplitudes and higher values of the ion-induced SEE coefficient (γ).

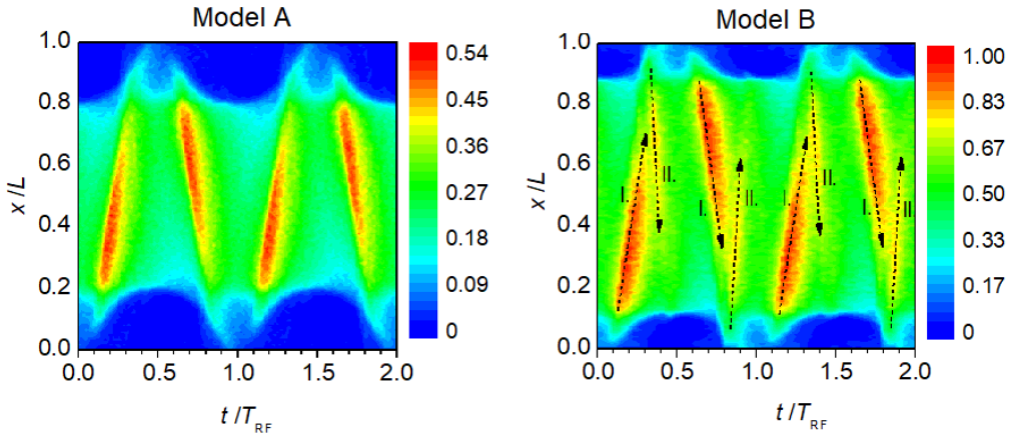


Fig. 3. Spatio-temporal distribution of the total ionization rate obtained from model A and model B at 0.5 Pa pressure, 1000 V driving voltage amplitude and $\gamma = 0.4$ ion-induced SEE coefficient. The colour scales are given in units of $10^{20} \text{ m}^{-3} \text{ s}^{-1}$ [1].

In [1] a detailed analysis of the simulation results obtained using models A and B at 0.5 Pa, 13.56 MHz, 1000 V, 6.7 cm electrode gap, $\gamma = 0.4$ was presented. For these discharge conditions model B resulted in about 2.75 times higher plasma density than model A, and completely different electron power absorption and ionization dynamics were obtained in the two different models for the same discharge conditions. Figure 3 shows the spatio-temporal plots of the total ionization rate (number of ionizations occurring per unit time and volume) obtained from models A and B. The simulation based on model A shows discharge operation in the classical α -mode, where the ionization is dominated by the electrons that are accelerated at the expanding sheath edge; one beam of energetic electrons is generated at both

electrodes during a RF period at the time of sheath expansion, which propagates through the bulk at low pressures and causes ionization. In the simulations based on model B, however, two beams of energetic electrons are found at both electrodes during a RF period, and consequently, two separate maxima in the spatio-temporal distribution of the ionization rate were observed at both electrodes during a RF period [1]: (i) strong ionization at the expanding sheath edge (beam I) and (ii) additional ionization during sheath collapse (beam II, weaker compared to beam I). These beams are shown by arrows in figure 3. The beams II were found to be mainly composed of δ -electrons, which play a key role also in the α -mode ionization at the expanding sheath edge (beams I) [1]. Some information about the composition of these beams can be seen in figure 4, which shows the δ -electron flux from the powered electrode and the contribution of bulk electrons, δ -electrons and γ -electrons to this SE flux. Panel (c) corresponds to the same set of simulation results also shown in figure 3.

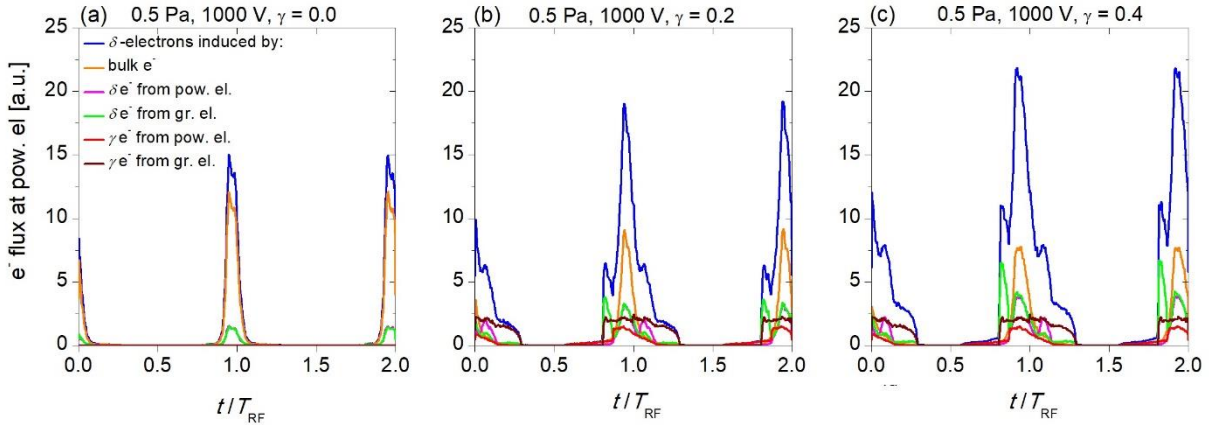


Fig. 4. δ -electron flux from the powered electrode and the contribution of bulk electrons, δ -electrons and γ -electrons (each differentiated to two components according to which electrode they originate from) to this SE flux, obtained from model B for 0.5 Pa, 1000 V and different values of the ion-induced SEE coefficient: (a) $\gamma = 0$, (b) $\gamma = 0.2$, (c) $\gamma = 0.4$ [22].

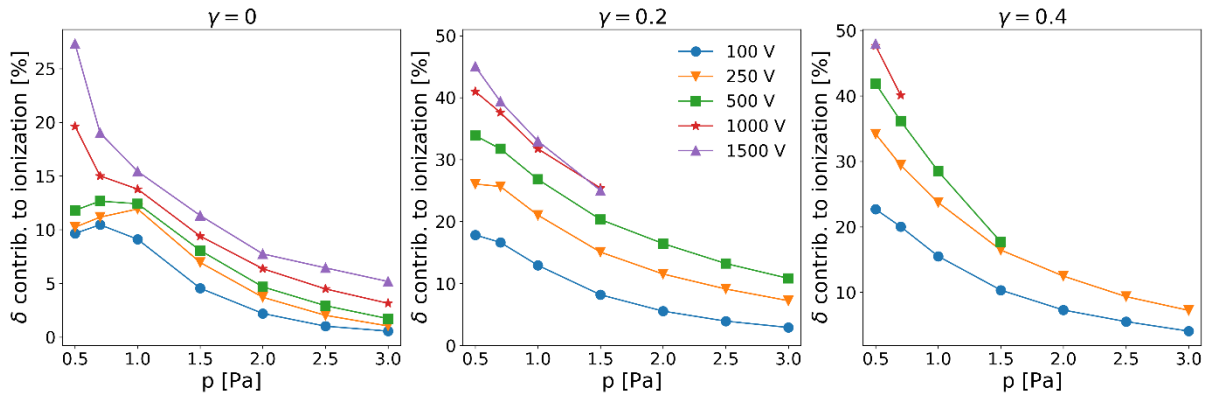


Fig. 5. The contribution of δ -electrons to the total ionization obtained from model B, as a function of the gas pressure, for different driving voltage amplitudes and various values of the ion-induced SEE coefficient: $\gamma = 0$, $\gamma = 0.2$, $\gamma = 0.4$ [22].

Figure 5 shows the contribution of δ -electrons to the total ionization obtained from model B as a function of the gas pressure, for different voltage amplitudes and for different values of γ . We note that the term bulk electrons refers to all the electrons that are not created at the electrodes, i.e. that are neither γ - nor δ -electrons. Thus, the electrons created in ionization collisions between the γ - or δ -electrons and the atoms of the background gas are also considered bulk electrons. As a result, the effect of δ -electrons on the ionization dynamics is even larger than what can be concluded based on figure 5. A large number of bulk electrons are generated by δ -electrons via ionization, which can also induce significant ionization. At $\gamma = 0$, the contribution of δ -electrons to the ionization decreases with increasing the gas pressure at a given voltage amplitude and γ , except the case of low voltage amplitudes ($V_0 \leq 500$ V). For the lowest

voltage amplitude of $V_0 = 100$ V, the contribution of δ -electrons to the ionization first increases with the gas pressure (below 1 Pa, reaching a maximum contribution of about 11 %), then decreases towards higher gas pressures, reaching less than 1 % for the highest pressure of 3 Pa. A similar trend can also be observed for voltage amplitudes of 250 V and 500 V. Under such conditions, the collisional multiplication of the emitted δ -electrons is not efficient. By slightly increasing the gas pressure (up to 0.7 Pa), the contribution of δ -electrons to the ionization increases due to the more frequent collisions. However, as the pressure is even further increased, the flux of electron-induced SEs from the electrodes decreases due to the decrease of the incident electron energy, but the multiplication of these δ -electrons becomes more and more efficient. Since all the electrons that originate from this multiplication are considered bulk electrons, the larger portion of the beam will consist of bulk electrons, by definition. As a consequence of these effects, the contribution of δ -electrons to the ionization strongly decreases, while that of bulk electrons strongly increases with the pressure. A similar scenario, i.e. a decrease of the contribution of δ -electrons to the ionization with the gas pressure, is found at high voltage amplitudes as well at $\gamma = 0$. However, at high voltage amplitudes, the highest contribution of δ -electrons to the ionization is found at the lowest pressure of 0.5 Pa (27 % at $V_0 = 1500$ V). At 0.5 Pa, a large flux of δ -electrons from the electrodes is induced by bulk electrons at the time of sheath collapse at high voltage amplitudes (see figure 4 (a) for 1000 V). This large flux of δ -electrons and the ionization induced by these electrons compensates the negative effect of the less efficient multiplication of δ -electrons at low pressures on the ionization dynamics. Note that besides δ -electrons, γ -electrons also have a crucial role in the ionization dynamics. It is obvious that these electrons can enhance the ionization directly via their collisional multiplication. In addition, γ -electrons can induce the emission of δ -electrons from the electrode material, which also generate ionization and can be multiplied efficiently in electron avalanches in the sheaths. This latter effect is most pronounced at higher voltage amplitudes and pressures, and it is only described in the realistic model (B).

4. References

- [1] Horváth B, Daksha M, Korolov I, Derzsi A and Schulze J 2017 *Plasma Sources Sci. Technol.* **26** 124001.
- [2] Lieberman M A and Lichtenberg A J 2005 *Principles of Plasma Discharges and Materials Processing* 2nd edn. (New York: Wiley-Interscience); Makabe T and Petrovic Z Lj 2006 *Plasma Electronics: Applications in Microelectronic Device Fabrication* (London: Taylor & Francis).
- [3] Kollath R 1956 *Encyclopedia of Physics* Vol. XXI, ed. Flügge S (Berlin, Springer) p 264
- [4] Thornton P R 1968 *Scanning Electron Microscopy, Applications to Materials and Device Science* (London: Chapman and Hall)
- [5] Gascon N, Dudeck M and Barral S 2003 *Phys. Plasmas* **10** 4123
- [6] Sydorenko D, Smolyakov I A, Kaganovich I D and Raitsev Y 2006 *Phys. Plasmas* **13** 014501
- [7] Kaganovich I D, Raitsev Y, Sydorenko D and Smolyakov I A 2007 *Phys. Plasmas* **14** 057104
- [8] Taccogna F, Longo S, Capitelli M and Schneider R 2009 *Appl. Phys. Lett.* **94** 251502
- [9] Lafleur T, Baalrud S D and Chabert P 2016 *Phys. Plasmas* **23** 053502
- [10] Boeuf J-P 2017 *J. Appl. Phys.* **121** 011101
- [11] Seiler H 1983 *J. Appl. Phys.* **54** R1–18
- [12] Vaughan J R M 1989 *IEEE Transactions on Electron Devices.* **36** 1963
- [13] Bruining H 1954 *Physics and Applications of Secondary Electron Emission* (New York: Pergamon, McGraw-Hill)
- [14] Dekker A J 1958 Secondary electron emission. *Solid State Physics* ed F Seitz and D Turnbull vol 6 (New York: Academic) pp 251–315
- [15] Gopinath V P, Verboncoeur J P and Birdsall C K 1998 *Phys. Plasmas* **5** 1535
- [16] Barral S, Makowski K and Peradzynsky Z 2003 *Phys. Plasmas* **10** 4137
- [17] Vaughan J R M 1993 *IEEE Transactions on Electron Devices.* **40** 830
- [18] Sydorenko D 2006 PhD thesis (University of Saskatchewan, Saskatoon, Canada).
- [19] Donkó Z 2000 *J. Appl. Phys.* **88** 2226
- [20] Donkó Z 2001 *Phys. Rev. E* **64** 026401
- [21] Maric D, Hartmann P, Malovic G, Donkó Z and Petrovic Z Lj 2003 *J. Phys. D.* **36** 2639
- [22] Horváth B, Schulze J, Donkó Z and Derzsi A 2018 *J. Phys. D. Appl. Phys.* **51** 355204

PROTON TRANSFER REACTION – MASS SPECTROMETRY AND ITS APPLICATIONS TO HOMELAND SECURITY: DETECTION OF COCAINE AND ITS METABOLITES

David Olivenza-León¹, Peter Watts¹, Fraser Reich², Chris A. Mayhew^{1,3}

¹*School of Physics and Astronomy, University of Birmingham, Edgbaston, Birmingham, B15 2TT, UK*

²*KORE Technology Ltd, Cambridgeshire Business Park, Ely, Cambridgeshire, CB7 4EA, UK*

³*Institute for Breath Research, University of Innsbruck, Rathausplatz 4, 6850 Dornbirn, Austria*

E-mail: D.OlivenzaLeon@bham.ac.uk

Abstract

Proton Transfer Reaction Mass Spectrometry (PTR-MS) is an ideal analytical tool for use in homeland security owing to its high sensitivity, good selectivity, real-time capabilities, and its ability to detect a wide range of threat agents. In the following we present a PTR-MS investigation of cocaine and related compounds using a thermal desorption unit. The experimental work is supplemented by quantum chemical calculations, which are used to help interpret the results.

1 Introduction

PTR-MS has already proved to be a useful tool for the detection of drugs. It has successfully been used to detect rape drugs even when mixed in drinks [1] and ion-molecule processes can be manipulated to differentiate between isomeric substances [2]. Cocaine is one of the most consumed illicit drugs. A recent study has shown that only the use of cannabis is higher than that of cocaine [3]. Often, cocaine users are heavy drinkers of alcohol. When both cocaine and ethanol are present in the bloodstream, the metabolite cocaethylene is produced in the body [4], which in itself is a recreational drug.

Law enforcement agencies need to rapidly detect cocaine or similar compounds rapidly and with a high level of confidence. One real time analytical technique that can provide this is PTR-MS. To be able to use this instrument in the field, we first need to determine and understand the protonation and fragmentation processes that cocaine and related compounds undergo as a function of the key operational parameter, namely the reduced electric field, which is the ratio of the electric field strength to the gas number density in the drift (reaction) tube. Here we present a study of the reactions of cocaine, methyl ecgonine and cocaethylene with hydronium ions as a function of the drift tube voltage and the reduced electric field.

2 Experimental Details

2.1 Proton Transfer Reaction Mass Spectrometry

PTR-MS is a soft chemical ionisation mass spectrometry technique that uses hydronium ions (H_3O^+) as analytical probes for the real-time and rapid detection of generally volatile organic compounds (VOCs) in low concentrations, with applications to health, environmental and security sciences [5]. A schematic diagram of the PTR-ToF-MS instrument used in this study (Kore Technology Ltd.) is shown in Fig. 1. Its operation is as follows: hydronium is generated in the glow discharge source which is then injected into the drift tube, where it interacts with the buffer gas containing trace amounts of the compound of interest. At low reduced electric fields protonated water clusters are also produced, namely $H_2O.H_3O^+$ and $(H_2O)_2.H_3O^+$ are the only ones with any significant intensity. These may react by proton transfer if the proton affinity of the relevant compound is greater than about 830 kJ mol^{-1} . The proton transfer reaction occurs in the drift tube, which comprises a set of electrodes that generate an electric field that delivers collisional energy to the ions involved in the process. Energy gained by the reagent and product ions in the drift field may result in new or enhance fragmentation of the protonated analyte, through collisional processes which may help in the identification of the compound.

The protonation of an analyte M takes place if the proton affinity of M is higher than that of water (691 kJ/mol), via the reaction:



After the protonation and any subsequent fragmentation either immediately following the proton transfer or subsequentially through collisional processes has occurred, the transfer lenses guide a fraction of the ions from the drift tube in to the time-of-flight mass spectrometer, where the detection of the product ions takes place by means of a microchannel plate detector.

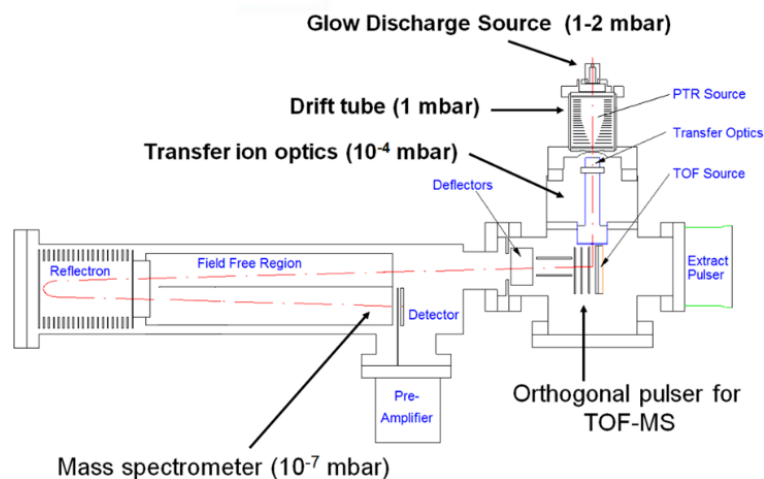


Fig. 1. Schematic diagram of a PTR-MS instrument courtesy of KORE Technology Ltd.

2.2 Thermal Desorption Unit

Although highly sensitive, PTR-MS is based on the volatility of the targeted chemicals, which can raise difficulties when searching for compounds with low volatilities. These include compounds such as illicit drugs and explosives and hence special procedures need to be adopted to get solid compounds into the vapour phase.

In this study, we have used a thermal desorption unit (TDU, Fig.2) developed by KORE Technology Ltd. in conjunction with a PTR-MS instrument. Full details of the TDU have already been described and its application to detecting solid explosives illustrated [6]. In brief, a carrier gas is preheated to the same temperature as the jaws of the TDU (up to 200 °C). The TDU's jaws make a high-quality circular seal onto a PTFE swab, so that the gas is forced to flow through the swab vaporising and sweeping out any trace solid compounds that have been deposited. This desorbs the analyte into the heated inlet line of the PTR-MS instrument and through into the drift tube.

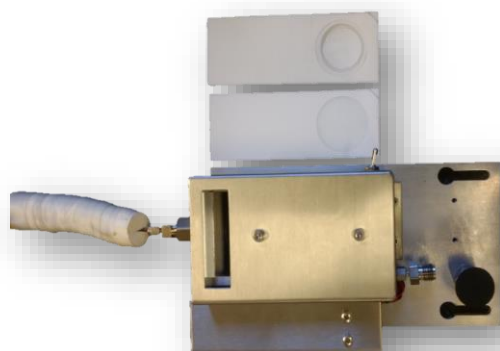


Fig. 2. Picture of the TDU connected to the inlet pipe of the PTR-MS instrument with some swabs next to it.

3 DFT Calculations

These were conducted using Gaussian09W and GaussView05 for Windows. All calculations used the B3LYP hybrid functional and the 6-31 + G(d,p) basis set. These yield a proton affinity of 933 kJ/mol and 1013 kJ/mol respectively for the protonation sites 1 and 2 of cocaine (see figure 3a) and 906 kJ/mol and 996 kJ/mol respectively for the protonation sites 1 and 3 in the case of methyl ecgonine (see figure 3b). The proton affinities of the main protonation sites of cocaethylene have not yet been calculated.

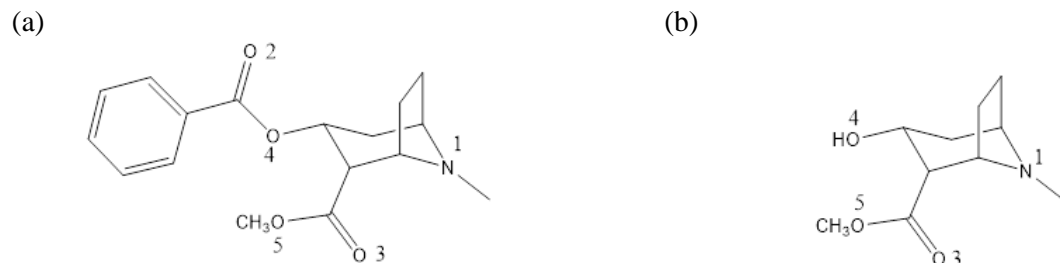


Fig. 3. Molecular structure of (a) cocaine and (b) methyl ecgonine. The possible protonation sites of cocaine and methyl ecgonine are indicated.

4 Results

4.1 Cocaine (C₁₇H₂₁NO₄)

The calculated proton affinity of cocaine is higher than that of any water clusters, and hence (H₂O)_n (n = 1, 2, 3) will react via proton transfer processes, which are sufficiently exothermic to facilitate dissociative proton transfer. However, we have found that the protonated parent is the dominant product ion for all reduced electric field values investigated (figure 4). This is followed by a product ion at m/z 182.12, which results from the loss of benzoate. Other notable product ions are at m/z 272.13 caused by the elimination of methanol from the protonated parent. Protonated benzoic acid is also detected at m/z 123.04 and benzoyl⁺ at m/z 105.03. Furthermore, the protonated pyrrolidine ring is found at m/z 82.07. This is in reasonable agreement with another earlier PTR-MS study [7], where the ions at m/z 182.12, m/z 272.13 and m/z 304.15 were reported, but not the ones we have found at m/z 82.07, m/z 105.04 and m/z 123.04. Furthermore, the previous study only reported results at 120 Td. Our study is much more extensive, by investigating reaction processes over a reduced electric field from 30 Td up to 250 Td.

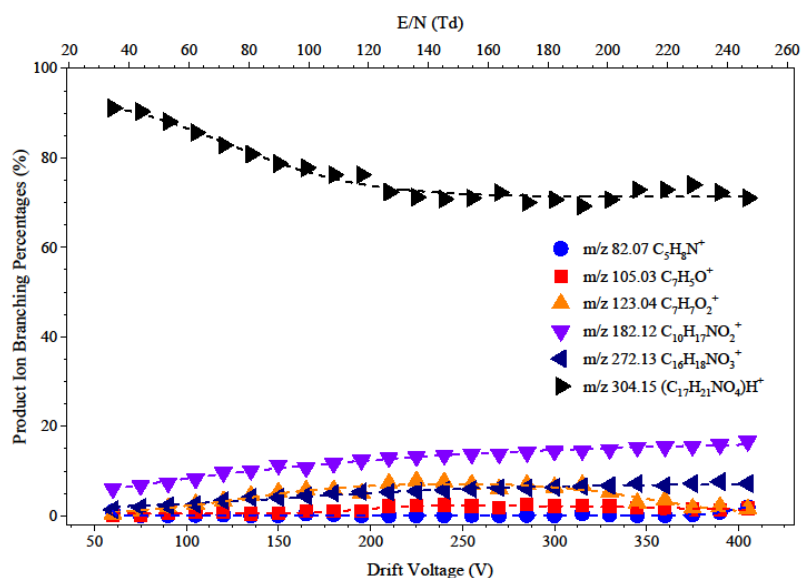


Fig. 4. Product ion distribution plot resulting from the reaction of (H₂O)_nH₃O⁺ (n = 0, 1, 2) with cocaine as a function of the drift voltage and the reduced electric field.

4.2 Methyl ecgonine (C₁₀H₁₇NO₃)

Methyl ecgonine is usually formed through pyrolysis when crack cocaine is smoked, and then this is metabolised in the body to ecgonidine. As found for cocaine, the protonated parent at m/z 200.13 is the

most intense product ion (figure 5). Other relevant product ions are found at m/z 82.07, m/z 168.10 and m/z 182.12, corresponding to the protonated pyridine ring, the loss of methanol from the protonated parent and the loss of water from the protonated parent, respectively.

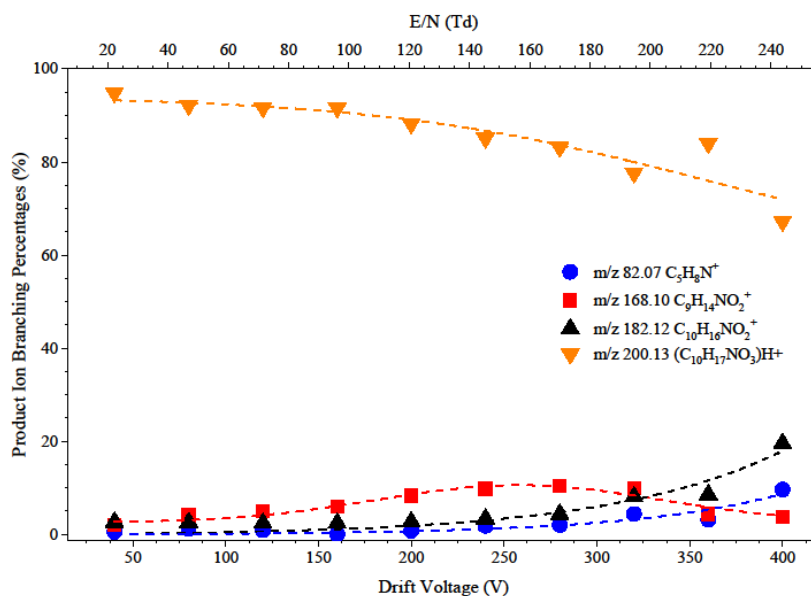


Fig. 5. Product ion distribution plot resulting from the reaction of $(\text{H}_2\text{O})_n\text{H}_3\text{O}^+$ ($n = 0, 1, 2$) with methyl ecgonine as a function of the drift voltage and the reduced electric field.

4.3 Cocaethylene ($\text{C}_{18}\text{H}_{23}\text{NO}_4$)

Cocaethylene is a metabolite of cocaine that is formed in the liver through transesterification when cocaine and ethanol coexist in the blood.

The PTR-MS results are shown in figure 6. The dominant product ion is the protonated parent at m/z 318.17. Ions resulting from the loss of benzoate and surprisingly ethanol, rather than ethene, from the protonated parent are found at m/z 196.13 and m/z 272.13, respectively. This is currently being investigated by DFT studies.

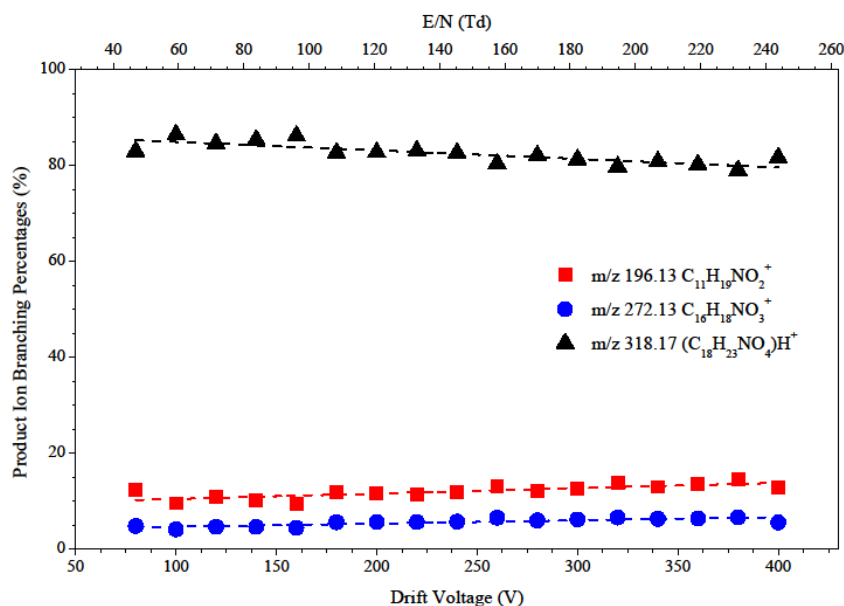


Fig. 6. Product ion distribution plot resulting from the reaction of $(\text{H}_2\text{O})_n\text{H}_3\text{O}^+$ ($n = 0, 1, 2$) with cocaethylene as a function of the drift voltage and the reduced electric field.

5 Conclusions

A PTR-ToF-MS equipped with a thermal desorption unit has been used to study the product ions resulting from the reaction of cocaine, methyl ecgonine and cocaethylene with hydronium ions and associated water clusters as a function of the drift tube voltage/reduced electric field. The loss of an alcohol is common to the three compounds reported here – loss of methanol in cocaine and methyl ecgonine and ethanol in cocaethylene. Also, the loss of benzoate is common to the compounds, we are therefore currently extending our studies to benzoic acid and related compounds. Further studies will include analogous compounds to the ones shown here, including benzoylecgonine and methyl ecgonidine.

6 Acknowledgments

This project was supported by the IMPACT ITN which is in turn supported by the European Union's Horizon 2020 research and innovation programme under the Marie Skłodowska-Curie grant agreement No 674911.

7 References

- [1] Jürschik S, Agarwal B, Kassebacher T, Sulzer P, Mayhew C, Märk T. 2012. *Journal of Mass Spectrometry*. 47(9):1092-1097
- [2] Lanza M, Acton W, Jürschik S, Sulzer P, Breiev K et al. 2013. *Journal of Mass Spectrometry*. 48(9):1015-1018
- [3] Mastroianni N, López-García E, Postigo C, Barceló D, López de Alda M. 2017. *Science of The Total Environment*. 609:916-926
- [4] McCance-Katz E, Price L, McDougle C, Kosten T, Black J, Jatlow P. 1993. *Psychopharmacology*. 111(1):39-46
- [5] Ellis A, Mayhew C. 2013. *Proton transfer reaction mass spectrometry*. John Wiley & Sons
- [6] González-Méndez R, Reich D, Mullock S, Corlett C, Mayhew C. 2015. *International Journal of Mass Spectrometry*. 385:13-18
- [7] Agarwal B, Petersson F, Jürschik S, Sulzer P, Jordan A et al. 2011. *Analytical and Bioanalytical Chemistry*. 400(8):2631-2639

SURFACE DBD BASED JET SYSTEM FOR IN-LINE PROCESSING OF SOLID AND LIQUID PARTICLES

Václav Prukner and Milan Šimek

Institute of Plasma Physics v.v.i., Department of Pulse Plasma Systems, Academy of Sciences of the Czech Republic, Za Slovankou 3, 182 00 Prague, Czech Republic

E-mail: prukner@ipp.cas.cz

Novel SDBD based jet system suitable for in-line processing of solid and liquid particles was designed and tested. The system can be used to deposit plasma polymers, modify/activate surfaces or produce plasma activated water. The SDBD micro-discharges are typically produced by a burst of four sine-waves ($f_{AC} = 5$ kHz) applied at a fixed repetition frequency. Feasibility of in-line treatment of various materials is demonstrated in the case of cellulose nanocrystals.

1. DBD-based jet system

Most of the non-LTE atmospheric pressure plasma jets, which are currently investigated for novel applications, are based on electrode configurations promoting generation of active plasma region in the volume of working gas.

Recently, we have proposed and developed a concept of a surface DBD-based jet for processing solid and liquid materials. The electrode geometry is formed by a pair of concentric ring electrodes. Smaller discharge exposed high-voltage electrode is deposited on the surface of MACOR glass-ceramic disk with a hole drilled in its centre. Grounded back electrode is embedded inside the disk and separated from the powered electrode by approximately 0.5 mm thick dielectric layer. The dielectric surface with powered electrode is closed inside cylindrical chamber containing two tangential gas inlets and one quartz window. Working gas is injected symmetrically through the two tangential inlets. Resulting whirlwind influences microdischarges propagating on the ceramic surface above the back electrode towards the central orifice. Induced vortex flow passes the discharge zone expelling discharge transients and products out of the chamber through an axial orifice in the form of the jet spinning around its axis.

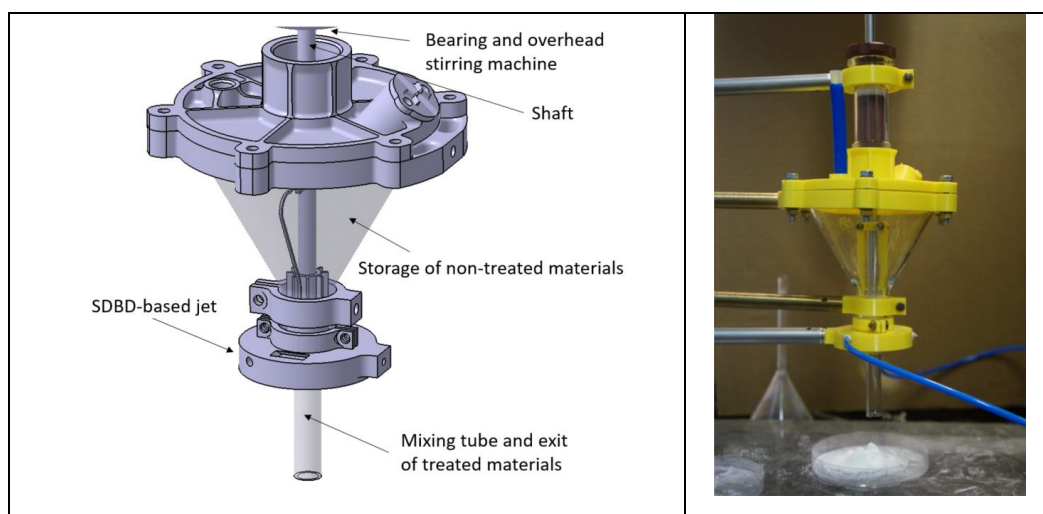


Fig. 1. Schematics (left) and snapshot (right) of the SDBD based atmospheric pressure in-line processing system

2. In-line processing

Feasibility of the in-line treatment of various materials is actually under investigation using cellulose nanocrystals and nanofibers. The SDBD-based jet setup was modified to allow continuous delivery and passage of cellulose nanocrystals/nanofibers through the jet orifice with subsequent collection of treated samples in the downstream region (Fig.1). In-line treatment times of tens of seconds appear to be sufficient to modify surface of nanocellulose materials for further processing and use.

The reactor is powered by an AC high-voltage power supply composed of the TG1010A Function Generator (TTi), Powertron Model 250A RF Amplifier and a high-voltage step-up transformer. The micro-discharges were produced by a burst of four sine-waves ($f_{AC} = 5$ kHz) applied at a fixed repetition frequency of $f_M = 1$ kHz (figure 2). The reactor was fed by synthetic air through a Bronkhorst *HI-TEC* model mass-flow controller (flow rate $Q = 1$ l min⁻¹).

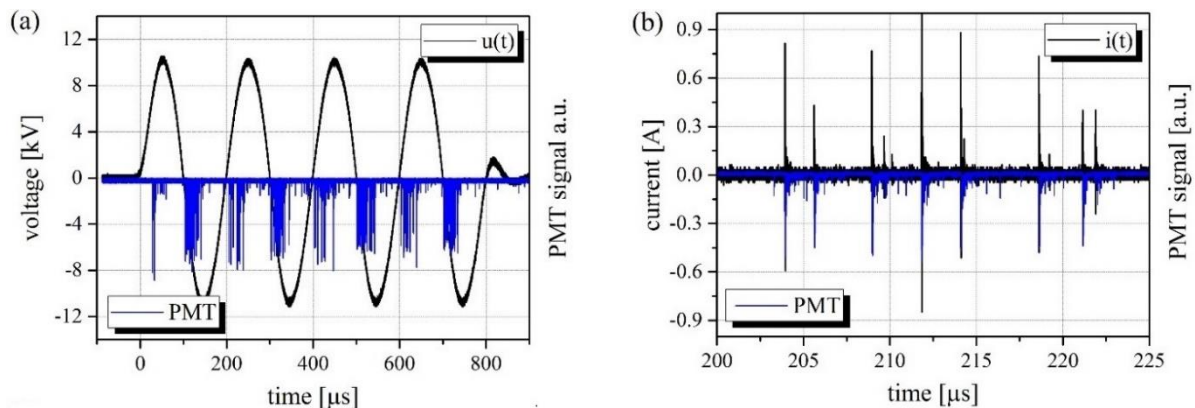


Fig. 2. Typical electrical characteristics (a) voltage and PMT signal for burst of 4 sin-waves, (b) current and PMT signal for 1 sine wave

3. Conclusions

Feasibility of an in-line treatment of various materials is actually under investigation. The concept was verified by treating cellulose nanocrystals and nanofibers. The SDBD-based jet setup was modified to allow continuous delivery and passage of cellulose nanocrystals/nanofibers through the jet orifice with subsequent collection of treated samples in the downstream region. Up to now, the most promising applications seem to be those related to surface cleaning and activation, deposition of plasma polymers [1], organic farming [2], treatment and modification of nanocrystals/nanofibers, and activation of liquid water.

Acknowledgement

This work was supported by KONNECT-009 project.

4. Reference

- [1] Gordeev I., Šimek M., Prukner V., Artemenko A., Kousal J., Nikitin D., Choukourov A., Biederman H.: Deposition of Poly(Ethylene Oxide)-Like Plasma Polymers on Inner Surfaces of Cavities by Means of Atmospheric-Pressure SDBD-Based Jet. *Plasma Processes and Polymers* **13** [8] (2016) 823-833.
- [2] Ambrico P. F., Šimek M., Morano M., De Miccolis Angelini R.M., Minafra A., Trotti P., Ambrico M., Prukner V., Faretra F.: Reduction of microbial contamination and improvement of germination of sweet basil (*Ocimum basilicum* L.) seeds via surface dielectric barrier discharge. *Journal of Physics D-Applied Physics* **50** [30] (2017)

DISSOCIATIVE ELECTRON ATTACHMENT TO 4-BROMOBIPHENYL MOLECULE

N. L. Asfandiarov¹, S. A. Pshenichnyuk¹, R. G. Rakhmeyev¹, R. F. Tuktarov¹,
N. L. Zaitsev¹, A. S. Vorob'ev², J. Kočišek³, J. Fedor³, A. Modelli^{4,5}

¹ Institute of Molecule and Crystal Physics UFRC RAS, October Avenue 151, 450075 Ufa, Russia

² Moscow Institute of Physics and Technology, Institutskiy Pereulok 9, 141700 Dolgoprudny, Moscow Region, Russia

³ Department of Dynamics of Molecules and Clusters, J. Heyrovský Institute of Physical Chemistry Academy of Sciences of the Czech Republic, Dolejškova 3, 18223 Prague 8, Czech Republic

⁴ Dipartimento di Chimica "G. Ciamician", Università di Bologna, Via Selmi 2, 40126 Bologna, Italy

⁵ Centro Interdipartimentale di Ricerca in Scienze Ambientali, Università di Bologna, via S. Alberto 163, 48100 Ravenna, Italy

E-mail: n.asfandiarov@gmail.com

Electron attachment to the 4-bromobiphenyl (4BrB) molecule and the decay channels of its molecular anion were investigated by means of Dissociative Electron Attachment (DEA) Spectroscopy with two different spectrometers. The first apparatus is equipped with a static magnet mass analyzer (Ufa group), the second one with a quadrupole mass filter (Prague group). The dominant DEA channel at low electron energy leads to formation of Br⁻ negative fragments. Long-lived ($\tau_a=40$ μ s at the temperature of 80 °C) molecular negative ions were detected only in the Ufa experiment. We explored the involved potential energy surfaces and found that the molecular anion has two distinct structures with the C-Br distances of 1.92 Å and 2.8 Å. The statistical model based on the Arrhenius approximation fully explains the experimental observations and sheds light on the earlier anion dissociation kinetic studies in solution.

1. Results and discussion

The results obtained by Prague and Ufa groups are presented in Figure 1.

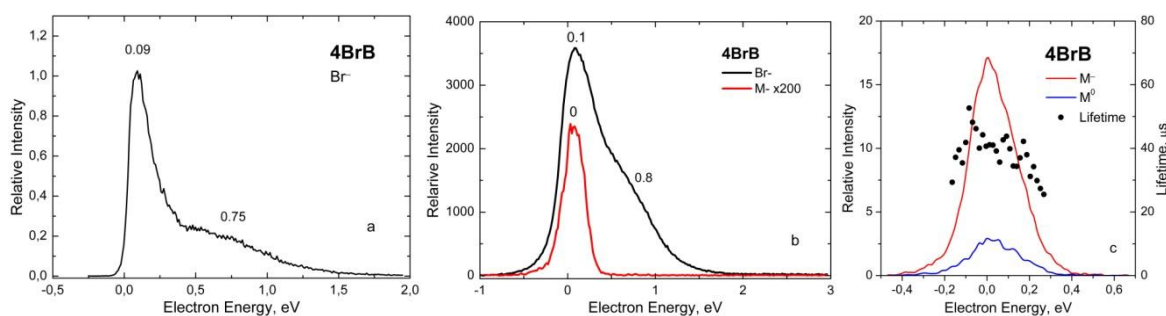


Fig. 1. a) Br⁻ negative current from 4BrB obtained using the high-resolution quadrupole mass analyzer, Prague group; b) Br⁻ yield (black line) and M⁻ yield multiplied by 200 (red line) from 4BrB, Ufa group; c) relative M⁻ (red line) and M⁰ (blue line) yields, and autodetachment lifetime τ_a (black dots, right scale), Ufa group.

The decay of a parent anion is a statistical emission process, where the excess energy (energy of incoming electron + electron affinity) is stored in the vibrational degrees of freedom. The autodetachment lifetime is connected to the gas phase EA_a as:

$$\tau_a = \tau_0 \cdot \exp\left[\frac{N \cdot EA_a}{EA_a + NkT + \varepsilon}\right], \quad (1)$$

where the time τ_0 is the inverse of the frequency factor; $N = 3n - 6$ is the number of internal degrees of freedom, NkT the vibrational energy storage of the target molecule, k the Boltzmann constant, T the temperature in Kelvin of the target molecule (ionization chamber temperature), and ε the kinetic energy of an incoming electron. From a physical point of view, the pre-exponential factor τ_0 represents the time of anion motion on the reaction coordinate (from the anion geometry to that of the neutral molecule). The value of τ_0 depends on the anion structure, and may vary from $\sim 1 \cdot 10^{-13}$ s for

naphthoquinone derivatives [1] to $\sim 5 \cdot 10^{-13}$ s for benzene derivatives [2]. Equation (1) may be transformed into the following form and using experimentally determined τ_a it can be used for quantitative evaluation of EA_a [3]:

$$EA_a = \frac{\ln(\tau_a/\tau_0) \cdot (NkT + \varepsilon)}{N - \ln(\tau_a/\tau_0)}. \quad (2)$$

All the parameters of eq. (2), except τ_0 , are known. The first evaluation of EA_a can be obtained using $\tau_0 = 5 \cdot 10^{-13}$ s, the value previously used for nitrobenzene derivatives [2]. Below we will try to improve this approximation. The other parameters are the following: $\tau_a = 40$ μ s; $N = 60$; $k = 8.617 \cdot 10^{-5}$ eV/K; $T = 353$ K; $\varepsilon = 0.0$ eV, leading to $EA_a = 0.79$ eV. This is in strong contrast with the calculations of Takeda et al. [4] who predicted a negative EA_a of -0.221 eV at the B3LYP/3-31G(d) level and measured a fast rate $k_d = (3.2 \pm 1.0) \cdot 10^{10}$ s $^{-1}$ for the dissociation of 4BrB^- . When we repeat their B3LYP calculations (geometry optimization of the anion starting from the geometry of the neutral) with larger basis set, we obtain EA_a s of 0.11 eV with the 6-31G+(d) basis set and 0.33 eV with the 6-311G++(d,p) basis set, taking into account zero point vibrational energy (ZPVE) corrections. The latter value is still much lower than that obtained from the present experimental data. This discrepancy can be explained upon closer inspection of the involved potential energy surface.

There are several key structures that determine mutual position of the anion and neutral terms, see Figure 2 and Table 1. We take the energy of the optimized 4BrB neutral geometry as the origin. The energy difference between the neutral and anion (both optimized) structures is the adiabatic electron affinity (EA_a).

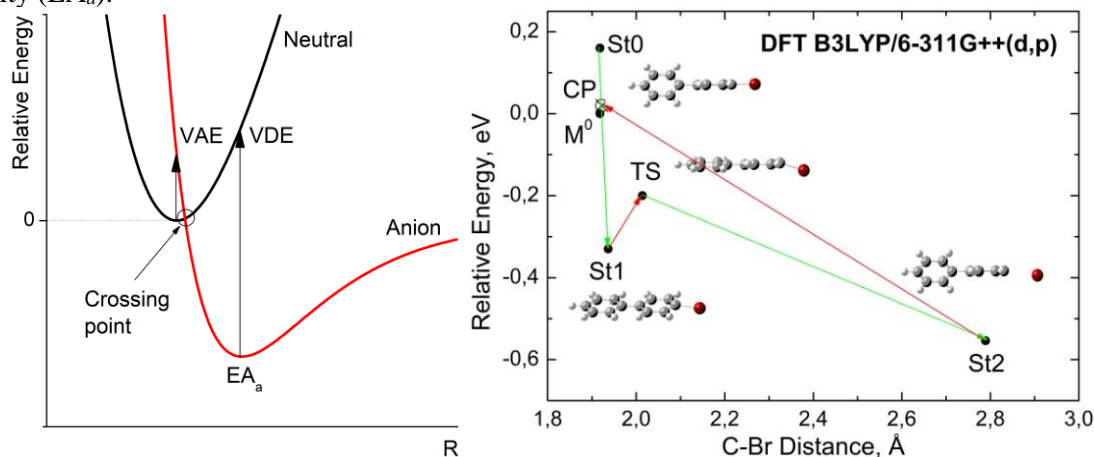


Figure 2. Left: molecule and anion electronic term intersection for the case of negative vertical and positive adiabatic EA_a [1]. $VAE = -EA_v$ means Vertical Attachment Energy, VDE means Vertical Detachment Energy. Right: overview of the relative energy changes associated with the electron-induced geometry transformation of the 4BrB anion according to B3LYP/6-311G++(d,p) calculations taking into account ZPVE correction. St_0 refers to the anion with the geometry of the neutral molecule, St_1 to the anion in its optimized geometry with a coplanar structure; TS is the (out-of-plane) transition state; St_2 denotes the optimized twisted anion structure. CP means crossing point. Exothermic transitions are shown by green arrows, endothermic ones by red arrows.

The calculated results can be improved taking into account corrections for zero-point vibrational energies [5,6]. This approach is valid only for equilibrium geometry of a system: the initial neutral molecule M^0 and two equilibrium anion states St_1 , St_2 . Reliable evaluations of vertical attachment energies (VAEs) can be obtained scaling with a linear equation the virtual orbital energies (VOEs) supplied by B3LYP/6-31G(d) calculations [7,8]. This procedure, using the equation given in [8], leads to $VAE = 0.16$ eV. The anion state labeled St_0 is unstable with respect to electron detachment and out-of-plane bending of the Ar-Br bond and rotation around the Ar-Ar-bond, in line with negative values calculated for the corresponding vibrational frequencies. As a result, the torsional vibration ν_2 leads to fast coplanarity of the two rings, to give the anion structure St_1 close to the point group C_{2v} . Delocalization of the excess negative charge on both the phenyl rings favors this coplanar structure. Electron autodetachment and geometry relaxation of the temporary St_0 species into the stable St_1

anion (see Figure 2) are in competition until the anion reaches the crossing point (CP) with the term of the neutral. This St1 anion state corresponds to a local minimum of the anion potential energy, associated with a positive $EA_a=0.33$ eV, see Figure 1. This St1 anion state is more stable than the corresponding neutral state (St1⁰) with the same geometry, being thus metastable with respect to autodetachment. Its detachment lifetime can be evaluated using equation (1): $\tau_a(\text{St1})\sim 6\cdot 10^{-9}$ s.

Table 1. Computed B3LYP/6-311G++(d,p) geometries, total energies (with ZPV corrections), charge distributions and SOMO nature of anion structures.

Structure	$r_{\text{C-Br}}$, Å	$\theta_{\text{Ar-Br}}$, °	$\phi_{\text{Ar-Ar}}$, °	Energy, eV	q_{Br} , e ⁻	SOMO
Neutral	1.918	0.0	41.10	0.0 (0.0)	-0.185	$\pi^* b_1$ LUMO
Vertical anion St0	1.918	0.0	41.10	0.16 ¹ (VAE)	-0.355	$\pi^* b_1$
Crossing point	1.922	-	-	~0.01	-	$\pi^* b_1$
Adiabatic anion St1	1.956	10.04	1.58	-0.33	-0.345	$\pi^* b_1$
Transition state	2.014	18.4	8.0	-0.20 ²	-0.352	$\pi^* b_1 + \sigma^*_{\text{C-Br}}$
Adiabatic anion St2	2.787	7.5	37.92	-0.55	-0.761	$\sigma^*_{\text{C-Br}}$
Dissociation limit	∞	0.0	42.31	-0.23 (0.27) ³	-1.0	$\sigma^*_{\text{C-(Br)}}$

¹ Estimated using scaling equation $\text{VAE}=0.8065\cdot\text{VOE}+0.9194$ eV [8].

² Estimated from experimental k_d [4].

³ Estimated from experimental bond dissociation energy [9].

The most stable anion structure St2 has an unusually long C-Br distance 2.787 Å. The phenyl rings are not coplanar and the bromine atom has a large negative charge -0.761. Therefore the St2 species can be considered as a complex between a bromine anion and a polarized radical $\text{Br}^- \cdots \text{C}_{12}\text{H}_9$ [5]. Figure 2 clearly demonstrates that the electron detachment process from St1 and St2 is impossible until the anion returns to the vicinity of the crossing point. Obviously, the crossing point is somewhat higher in energy than the neutral molecule. It would not be a big mistake to assume that the crossing point energy does not exceed $E_{CP}=0.01\text{-}0.02$ eV, see Figure 2. This conclusion is consistent with the fact that molecular NIs are observed at thermal electron energies. At the beginning of the discussion, we estimated the EA using formula (2), without taking into account the energy of the crossing point. Let us return to the evaluation of EA_a from the lifetime of the molecular NI. The mean autodetachment time from the global potential minimum St2 can be described using a slightly modified Arrhenius equation (3), provided the activation energy $AE_{AD}=EA_a+E_{CP}$ is known. A pre-exponential factor $\tau_0=5\cdot 10^{-13}$ s seems reasonable for the 4BrB anion [2].

$$\tau_a = \tau_0 \cdot \exp \left[\frac{N \cdot (EA_a + E_{CP})}{EA_a + NkT + \varepsilon} \right]. \quad (3)$$

Solving this equation for EA_a , we get:

$$EA_a = - \frac{-N \cdot E(CP) + \ln(\tau_a/\tau_0) \cdot NkT + \ln(\tau_a/\tau_0)\varepsilon}{-N + \ln(\tau_a/\tau_0)} = 0.78 \text{ eV}, \quad (4)$$

where $\tau_a=40$ μs , $E_{CP}=0.01$ eV, $\varepsilon=0$ eV.

The same consideration can be used for evaluation of the anion dissociation rate constant. The corresponding dissociation time is

$$\tau_d = \tau_0 \cdot \exp \left[\frac{N \cdot DE}{EA_a + NkT + \varepsilon} \right] = 14 \cdot 10^{-6} \text{ s}, \quad (5)$$

where $\tau_0=500\cdot 10^{-15}$ s, $EA_a=0.78$ eV, $DE=0.745$ eV. The DE value corresponds to the dissociation limit $DL=-0.035$ eV and is very close to EA_a .

The process of molecular anion decay can be described in the framework of appropriate kinetic equations [10]. The intensity of the M^- signal as a function of electron energy can be evaluated with the following equation [10]:

$$M^-(u) = \int_0^\infty \{ \sigma(q) \cdot e^{-[k_a(q) + k_d(q)] \cdot t_{fl}} \} \cdot f(q, u) dq, \quad (6)$$

where $k_a=1/\tau_a$ and $k_d=1/\tau_d$ are the detachment and dissociation rates, t_{fl} is the time of M^- flight from the moment of anion formation to the moment of its detection, $f(u)$ is the electron energy distribution in a

given experiment. For the Ufa and Prague spectrometers $f(u)$ are ~ 0.4 and ~ 0.1 eV, respectively. The intensity of Br^- as a function of electron energy:

$$\text{Br}^-(u) = \int_0^\infty \left\{ \sigma(q) \cdot \frac{k_d(q)}{k_a(q) + k_d(q)} \cdot \left[1 - e^{-(k_a(q) + k_d(q)) \cdot t_{ext}} \right] \right\} \cdot f(q, u) dq, \quad (7)$$

where t_{ext} is the M^- extraction time from the ionization chamber of the Ufa mass spectrometer or M^- incoming into the quadrupole mass filter of the Prague machine. The time windows of the Ufa and Prague mass spectrometers are the following: time-of-flight $t_{fl}=37 \mu\text{s}$ and $t_{fl}=100 \mu\text{s}$ for the Ufa and Prague apparatus, respectively, $t_{ext}=10 \mu\text{s}$ (Ufa) and $t_{ext}=20 \mu\text{s}$ (Prague).

As to the energetic, the exact energies obtained by DFT calculations for the energy of St2 and the dissociation limit (listed in Table 1) do not provide satisfactory M^- and Br^- relative intensities when used kinetic equations (6) and (7). This might be caused by a high (exponential) sensitivity of the model to these values and by the uncertainties in the determination of the experimental time window, especially in case of the Prague experiment. We have thus varied some of these values as the parameters, their final set listed in Table 2 leads to the results shown in Figure 3. Here, the DE stands for the dissociation energy with respect to the St2 energy. It is easy to see that Figures 1 and 3 are very similar.

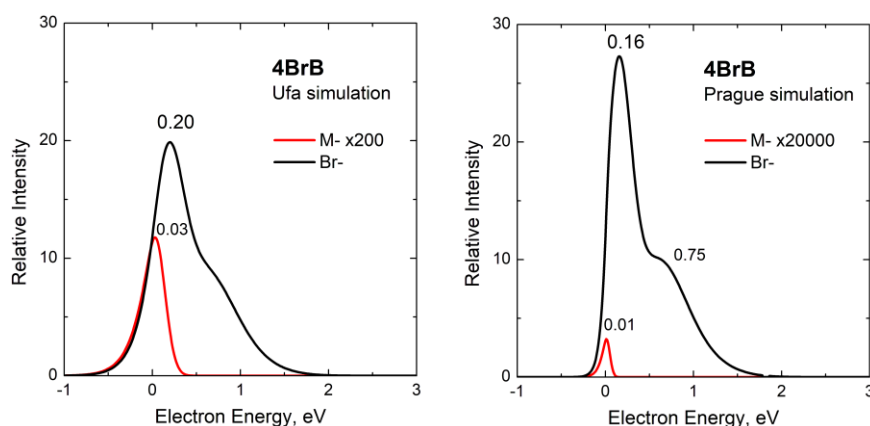


Figure 3. Simulation of the anion yields obtained in different experimental conditions by means of kinetic equations. The static magnet mass analyzer spectra, Ufa group, are shown in the left panel, the quadrupole mass filter spectra, Prague group, are shown in the right panel.

Table 2. VOs obtained with B3LYP/6-31G(d) calculations, scaled VOs, FWHM and peak amplitudes A for the electron capture cross section model, see text.

Orbital	VOE, eV	SVOE, eV	fwhm, eV	A, relative units
$\pi^* b_1$	0.541	1.36		
$\sigma^*_{\text{C-Br}}$	0.010	1.24 ¹		
$\pi^* a_2$	-0.174	0.78	0.82	2.5
$\pi^* a_2$	-0.391	0.60	0.59	5.0
$\pi^* b_1$ LUMO	-0.938	0.16	0.275	7.5

¹ Scaling according to ref. [11]: $\text{VAE}(\sigma^*_{\text{C-Br}}) = 0.79 \cdot \text{VOE} + 1.228$.

It can be noted that for the case of time windows $t_{ext}=10 \mu\text{s}$ and $t_1=37 \mu\text{s}$ for the static magnet mass analyzer the relative intensities of Br^- and M^- differ by ~ 300 times, see left panel in Figure 6. For the case of the quadrupole mass filter, where $t_{ext}=20 \mu\text{s}$ and $t_1=100 \mu\text{s}$, this difference exceeds $6 \cdot 10^4$ times. As a result, the molecular NI in the Ufa experiment is “visible”, while it is “invisible” in the Prague experimental conditions. This does not mean that one of these spectrometers provide us with incorrect data, it just means that DEA spectra can be different in different experimental conditions. Simultaneous detection of the parent and fragment ions at the same energy region is possible when the detachment time τ_a and dissociation time τ_d are comparable with t_{ext} and t_{fl} of an experimental setup. When the dissociation rate constant k_d is large (τ_d is short) and the detachment constant k_a is small (τ_a is long), the DEA results will be independent on experimental setup time-windows.

2. Conclusions

DEA to the 4Br-biphenyl molecule was investigated by means of two different experimental equipments: a DEA spectrometer with a quadrupole mass filter (Prague group) and a DEA spectrometer with a static magnet mass analyzer (Ufa group). The results obtained were analyzed using DFT calculations and an Arrhenius statistical model. It is concluded that the dissociation rate (k_d) previously reported in the literature for the production of Br^- negative fragments is in fact the rate of transition between two anion structures of the molecular anion. This prediction explains the previously observed correlation of k_d with the activation energy obtained with DFT calculations. We evaluated the adiabatic EA associated with formation of the most stable anion state to be 0.78 eV, based on the measured molecular anion lifetime of 40 μs at 0 eV.

We estimated the quite different Br^- and M^- ion yields in the Ufa and Prague experiments are explained using kinetic equations to describe detachment and dissociation processes. The model explains the observed difference, as no M^- ions were detected in the Prague experiment with a quadrupole mass filter. The present results demonstrate the high importance of inclusion of experimental conditions into the interpretation of DEA data.

3. Acknowledgments

NLA, SAP and RGR thank to Russian Foundation for Basic Research, Grant # 18-03-00179. J.F. acknowledges the support from Czech Science Foundation grant no 17-04844S. AM thanks the Italian Ministero dell'Istruzione, dell'Università e della Ricerca for financial support.

4. References

- [1] N. L. Asfandiarov, S. A. Pshenichnyuk, A. S. Vorob'ev, E. P. Nafikova, Y. N. Elkin, D. N. Pelageev, E. A. Koltsova, A. Modelli. *Rapid. Commun. Mass Spectrom.* **28**, 1580 (2014).
- [2] N. L. Asfandiarov, S. A. Pshenichnyuk, A. S. Vorob'ev, E. P. Nafikova, A. Modelli. *Rapid. Commun. Mass Spectrom.* **29**, 910 (2015).
- [3] N. L. Asfandiarov, M. V. Muftakhov, S. A. Pshenichnyuk, P. Papp, M. Danko, M. Lacko, J. Blaško, Š. Matejčík, A. Modelli. *J. Chem. Phys.*, **147**, 234302 (2017).
- [4] N. Takeda, P. V. Poliakov, A. R. Cook, J. R. Miller. *JACS*, **126**, 4301 (2004).
- [5] R. Schürmann, K. Tanzer, I. Dąbkowska, S. Denifl, I. Bald. *J. Phys. Chem. B*, **121**, 5730 (2017).
- [6] T. Sommerfeld, M.C. Davis, *J. Chem. Phys.*, **149**, 084305 (2018).
- [7] A. Modelli. *J. Phys. Chem. A*, **109**, 6193 (2005).
- [8] A. M. Scheer, P. D. Burrow. *J. Phys. Chem. B*, **110**, 17751 (2006).
- [9] E. C. M. Chen, K. Albyn, L. Dussack, W. E. Wentworth. *J. Phys. Chem.*, **93**, 6827 (1989).
- [10] D. Luckhaus, M. Quack. *Encyclopedia of Chemical Physics and Physical Chemistry*. J. H. Moore, N. D. Spencer Eds., Pub.: Institute of Physics, 2001, Vol. I.
- [11] S. A. Pshenichnyuk, N. L. Asfandiarov, and P. D. Burrow, *Russ. Chem. Bull.* **56**, 1268 (2007).

STABILITY OF DISCHARGES THERMOMETRY BASED ON THE EMISSION OF $2PS$, NO_γ , AND HIR SYSTEMS

Peter Čermák¹

¹*Department of Experimental Physics, Faculty of Mathematics, Physics and Informatics, Comenius University in Bratislava, Mlynská dolina F-2, 842 48 Bratislava, Slovakia*

E-mail: cermak@fmph.uniba.sk

The goal of this study is to investigate the possibility of direct retrievals of discharge parameters (e.g. rotational temperature) from the recorded emission signal without the use of external calibration sources. The idea is to treat both the X and Y calibration as an unknown parameter together with other variables describing the discharge. A common iterative cycle is then applied to find their optimal values to best fit the experimental data. The latter approach is tested on a set of simulations involving nitrogen second positive ($2PS$) and Herman-infrared (HIR) and NO_γ systems.

1. Introduction

The modeling of ro-vibrational electronic transitions present in the emission spectra is a key ability to extract the information about energy distribution within different states of species in the discharge. These data represent an important diagnostic tool, which helps us to understand the physics and chemistry of low-temperature non-equilibrium discharges.

For instance, the slow vibrational-translational relaxation, the phenomenon allowing the existence of non-equilibrium discharges could be perturbed by various external parameters such as humidity or the presence of different types of impurities [1, 2]. To understand and quantify this behavior, we need to have access to the vibrational populations of the different electronic states present in the discharge.

The second important phenomenon, broadly exploited in the spectroscopy of the non-equilibrium discharges, is the fast translational-rotational relaxation, which allows the gas temperature (T_g) to be measured optically, by considering it equal to the rotational temperature (T_{rot}) retrieved from the emission spectra [3]. If this thermalization condition is fulfilled, the rotationally resolved optical spectroscopy of the vibrational bands is capable of providing critical information for various plasma studies or applications.

2. Scope of the work

In our previous paper [4], we reported on the first application of the N_2 Herman-infrared (HIR) ro-vibrational model for the metrology of the atmospheric-pressure dielectric-barrier discharge. Based on our work in the UV part of spectra [5], we have developed a fitting algorithm which allows determining automatically both the rotational temperature and the sensitivity of the detection scheme directly from the recorded discharge spectrum without any need of pre-calibration. In the Ref. [4] the results from here mentioned $2PS$, NO_γ , and HIR systems were compared and a first-order Monte Carlo type of analysis of the models was performed to quantify the stability regarding the sensitivity calibration process.

This work aims to continue in this direction and investigate to what extent a complete sensitivity function could be retrieved from the fit. In the previous study, the variability of testing conditions was limited by the conditions given by the experiment (both the discharge and the detection scheme). In the present case, the issue is circumvented by using "virtual" - simulated signals. It is a very similar approach, we applied already in case of CO_2 absorption spectra [6], where a close-to-real simulation of its absorption spectra allowed to benchmark new fitting algorithm.

Here, to find optimal conditions where the discharge parameters could be retrieved from the spectra together with the apparatus function a series of virtual experiments was performed (Fig. 1.). First, for a

given set of initial parameters, the emission spectra was synthesized. Secondly, the spectra were convoluted with various apparatus functions including noise. Thirdly, the simulated signals were repeatedly fitted with different initial conditions by program designed in the LabVIEW environment. Finally, the resulting parameters, including their errors and correlations, were compared with the input data-sets and optimal conditions for the operation was identified.

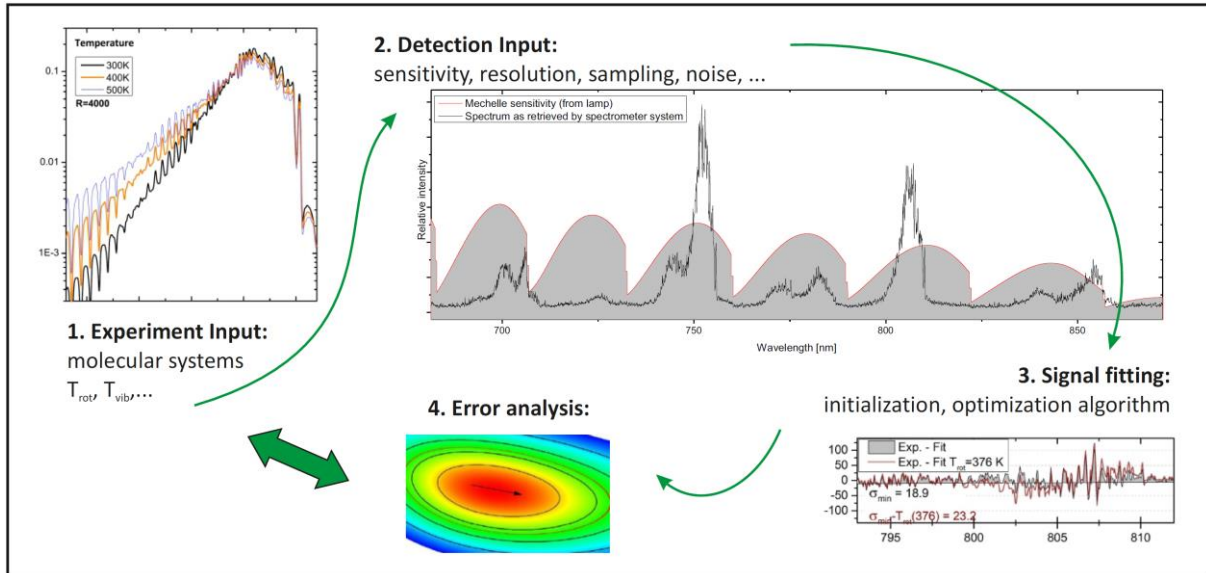


Fig. 1. Scheme of applied methodology

Acknowledgments

This project has received funding from the European Union's Horizon 2020 research and innovation programme under grant agreement No 692335 and from the Scientific Grant Agency of the Slovak Republic (project number 1/0465/19).

3. References

- [1] Ono R, Teramoto Y and Oda T 2009 *Plasma Sources Sci. Technol.* **19** 015009
- [2] Komuro A, Ono R and Oda T 2010 *Plasma Sources Sci. Technol.* **19** 055004
- [3] Bruggeman P J, Sadeghi N, Schram D C and Linss V 2014 *Plasma Sources Sci. Technol.* **23** 023001
- [4] Čermák P, Anušová A, Rakovský J, Martišovič V and Veis P 2018 *Plasma Sources Sci. Technol.* **27** 055009.
- [5] Rakovský J, Krištof J, Čermák P, Kociánová M and Veis P 2011 *WDS'11 Proceedings of Contributed Papers, Part II*, 257-262.
- [6] Hovorka J, Čermák P and Veis P 2017 *Laser Phys.* **27** 055701

THE EFFECT OF CATALYST ON OZONE AND NITROUS OXIDE PRODUCTION IN DIELECTRIC BARRIER DISCHARGE

Kalev Erme¹, Indrek Jõgi¹

¹*Institute of Physics, University of Tartu, W. Ostwaldi str. 1, 50411 Tartu, Estonia*
E-mail: kalev.erne@ut.ee

The aim of the present study was to investigate the influence of oxygen percentage, temperature and the addition of TiO₂ catalyst on the production of ozone O₃ and nitrous oxide N₂O by DBD. For this purpose, a flow-through system was used with a mixture of O₂ and N₂ with the total flow rate of 1 L/min directed through the DBD reactor in coaxial configuration. The specific input energy was up to 300 J/L. The oxygen fraction was varied in the range of 1-80%. In experiments with TiO₂ catalyst, the TiO₂ powder was pressed on the inner surface of the reactor. The experiments were carried out at 20°C and 100°C. The production of O₃ slightly decreased with the increase of temperature while the production of N₂O increased. The production efficiency of O₃ increased with O₂ percentage while the production efficiency of N₂O had a maximum at approximately 20% of O₂. The presence of TiO₂ considerably increased the production efficiency of N₂O production. The O₃ production efficiency was enhanced by TiO₂ at 20°C and degraded at 100°C.

1. Introduction

Nitrogen containing discharges produce various excited N₂ molecules and N atoms. These nitrogen species have an important role in a number of chemical processes and in the case of O₂:N₂ mixtures result in the production of different nitrogen oxide species, most notably N₂O and N₂O₅ [1]. Furthermore, they contribute to the production of ozone [2]. Nitrogen oxides are unwanted by-products in ozone generators, but they may also be valuable commodities. The production of nitrogen oxides is interesting from the viewpoint of N₂ fixation which is the first step in fertilizer production [3]. Nitrogen oxides may also be important in plasma-medicine [4].

Non-thermal plasma devices are often used for the production of ozone and the same devices could also be used for the production of nitrogen oxides. Unfortunately, the efficiency of the production of nitrogen oxides by non-thermal discharges remains relatively low [5]. It has been shown that the efficiency of various plasma-chemical processes can be improved by the presence of a catalyst [3].

The aim of the present contribution was the investigation of O₃ and N₂O production by non-thermal plasma devices in O₂ and N₂ mixtures with a wide range of O₂ fraction. The effect of reactor temperature and presence of TiO₂ catalyst without additional metal loading was also investigated.

2. Experimental setup

Measurements were carried out with a flow-through type coaxial home-made volume barrier discharge device with the length of 8 cm and the gap width of 1.2 mm (Fig. 1) described more thoroughly in our earlier paper [6].

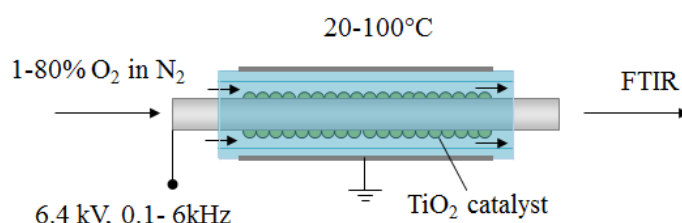


Fig. 1. Coaxial DBD reactor with catalyst.

The gas stream was directed through the reactor by mixing variable concentrations of oxygen (1-80%) with nitrogen by the use of Alicat Scientific flow controllers. The total flow rate was kept at 1 slm. Sinusoidal voltage with frequencies between 100 Hz to 6 kHz was applied on the electrodes with a

power source consisting of a sinusoidal voltage generator, power amplifier and a transformer. The input electrical power was determined by the method of Lissajous figures [6-7]. The specific input energy, SIE, was determined by dividing the input power by the flow rate of the gas. The concentrations of nitrogen oxides and ozone were measured by directing the exhaust gas of plasma reactor through the absorption cell which was placed into FTIR spectrometer Interspec 2020. The length of the absorption cell was 10 cm. The concentrations of O₃ and N₂O were obtained from the absorption bands by fitting procedure where the synthetic spectra of these bands were calculated on the basis of line intensity data available in the HITRAN database [8].

3. Results and discussion

An example of the FTIR spectra obtained in the case of 20% O₂ at 20°C without the presence of catalyst is shown in Fig. 2. The spectra contained bands corresponding to O₃, N₂O, HNO₃ and N₂O₅. The bands corresponding to NO and NO₂ were not detectable. The O₃ concentration was determined from the band with the maximum at 1055 cm⁻¹ and N₂O concentration from the band with the maximum at 2233 cm⁻¹.

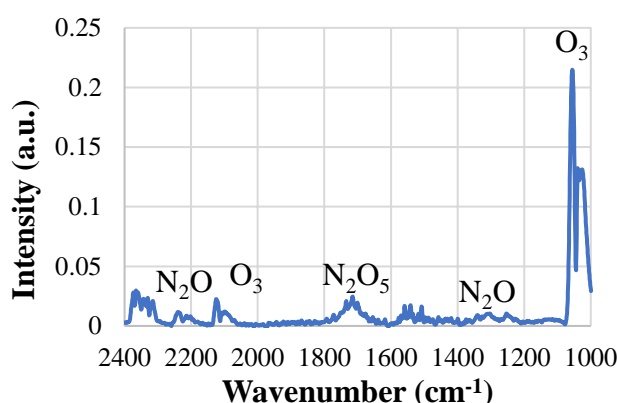


Fig. 2. FTIR spectra obtained in case of 20% O₂ mixture at 244 J/L without the presence of catalyst. The temperature was 20°C.

Examples of the SIE dependent concentrations of O₃ and N₂O calculated from the intensities of the FTIR bands are shown in Fig. 3 and 4. At a fixed SIE value, the concentration of O₃ monotonically increased with the increase of O₂ content, while the concentration of N₂O had a maximum which depended on the presence of catalyst.

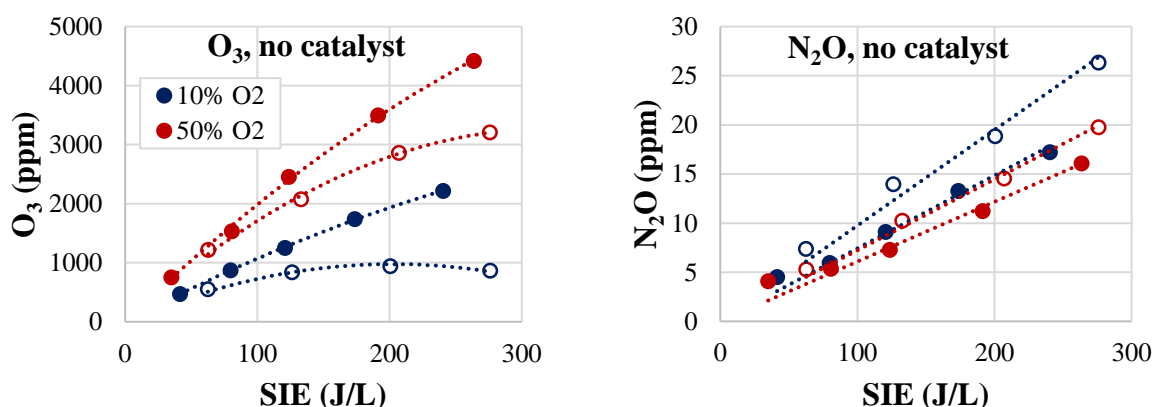


Fig. 3. Concentrations of O₃ and N₂O as functions of SIE at different O₂ fractions without catalyst at 20°C (filled circles) and 100°C (empty circles).

At low SIE values below 50 J/L, the O₃ concentration was independent of temperature, whereas at higher SIE values, the O₃ concentration decreased at 100°C (Fig. 3). In case of N₂O, the increase in temperature resulted in the growth of the N₂O concentration. The presence of catalyst slightly increased the O₃

production at 20°C (Fig. 4) while degraded O₃ production at 100°C (not shown). In case of N₂O, the catalyst increased the production at both temperatures whereas the increase was especially pronounced at low O₂ fractions (Fig. 4).

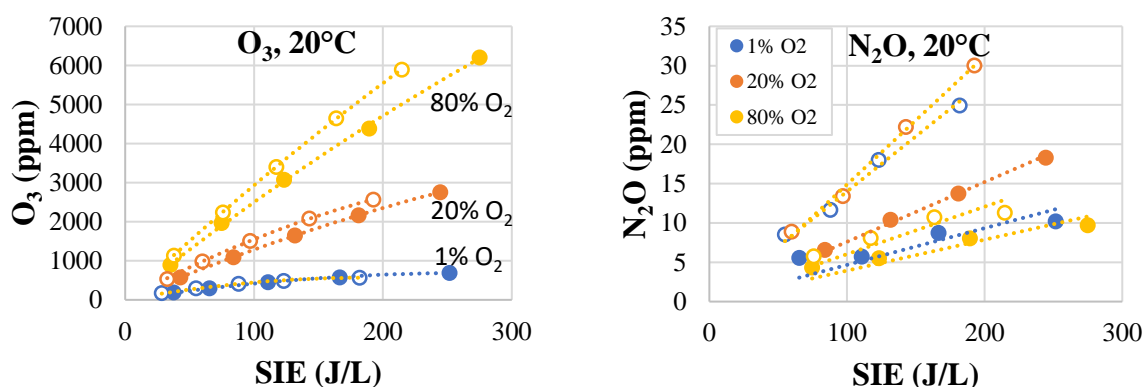


Fig. 4. The concentrations of O₃ and N₂O as a function of SIE at different O₂ fractions at 20°C without (filled circles) and with (empty circles) catalyst.

The concentration of O₃ is a sublinear function of SIE. At sufficiently low SIE values, the O₃ production is determined by the efficiency of O radical production, G_O , and the produced O₃ is proportional to SIE: $[O_3] = G_O \cdot SIE$ [2,9]. With the growth of SIE, the decomposition of O₃ caused by the increasing temperature and NO_x concentration becomes more important [2] and this results in the deviation of O₃ production from the linear function. The deviation effect was more important at higher temperatures (not shown). The presence of catalyst resulted in a somewhat increased O₃ production, compared to the case without catalyst. In the present study, the O₃ dependence on SIE was fitted by a quadratic function $ax - bx^2$. The slope a at low SIE values was used to estimate the O radical production efficiency G_O .

The O radical production efficiency G_O at different O₂ fractions, temperatures and in the presence of catalyst is shown on Fig. 5. The efficiency increased monotonically with O₂ fraction. As expected, the efficiency was somewhat higher at room temperature, when compared to 100°C. The efficiency obtained without catalyst in 20% O₂ mixture was comparable to the efficiency obtained in our earlier study for similar volume barrier discharge reactor [9] and for a surface barrier discharge reactor [10]. At room temperature, the presence of the catalyst resulted in the increase in O radical production efficiency, whereas at 100°C the catalyst decreased the production efficiency. The temperature activation of O₃ decomposition on TiO₂ surface was also observed in our earlier study, where O₃ was produced from O₂ by DBD and the catalyst was placed downstream from the DBD reactor. The enhancement of ozone production by TiO₂ has also been observed by Pekárek *et al* [11].

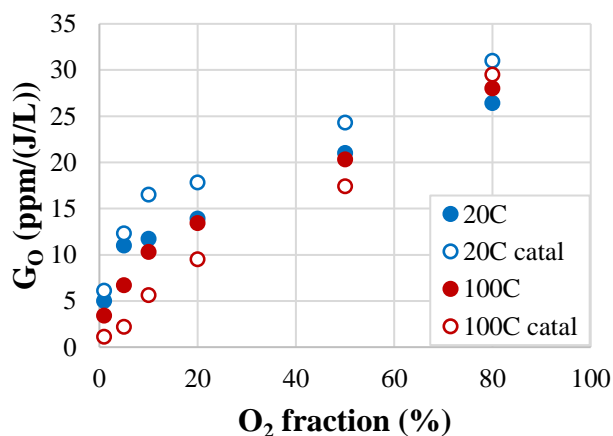


Fig. 5. O₃ production efficiency as a function of O₂ fraction at different temperatures, without (filled circles) and with (empty circles) the presence of catalyst.

The slope of the linear dependence of N₂O concentration as a function of SIE gives the N₂O production efficiency. Fig. 6 shows the N₂O production efficiency as a function of O₂ fraction at two different temperatures, with and without the catalyst. The efficiency obtained without the catalyst is comparable to the efficiencies in other studies [1,12]. The presence of the catalyst increased the efficiency more than twofold. The increase was more pronounced at low O₂ fractions.

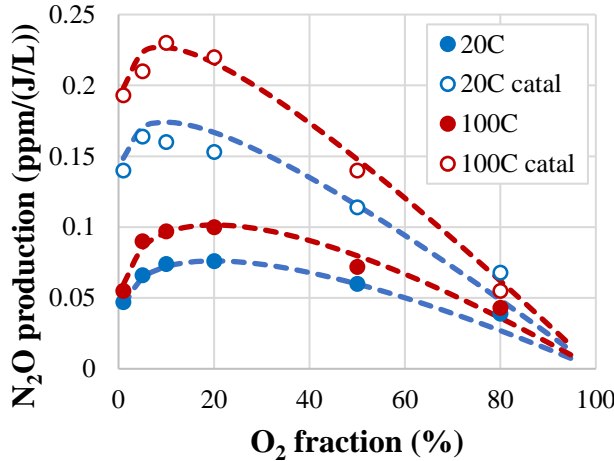


Fig. 6. N₂O production efficiency as a function of O₂ fraction at different temperatures and with and without the presence of catalyst.

According to several studies [1,12], N₂O is produced by the impact of N₂(A) and O₂. However, other studies have suggested the N₂O production through the N₂(X,v) + O₂(a) → N₂O + O(¹D) with v ≥ 15 [13]. In both cases, the linear dependence on SIE could be obtained when N₂^{*} is produced with uniform efficiency along the tube and the main loss channel of N₂^{*} is the production of N₂O with the impact of either O₂ or O₂(a) which does not depend on the SIE value. In addition, the impact of either O₂ or O₂(a) should also be the main loss channel for N₂^{*}. In such case, the production of N₂O can be described according to following function:

$$[N_2O] = G_{N_2O} SIE; G_{N_2O} = \kappa \frac{k_{N_2^*}}{e_0 v_d E/N} \frac{[N_2]}{N}$$

Here, κ is the fraction of energy used by electrons, $k_{N_2^*}$ is the rate coefficient of N₂^{*} production by electron impact, v_d is the drift velocity of electrons and E/N is the reduced electric field coefficient. According to the formula for G_{N_2O} , the efficiency should decrease at increasing O₂ fraction due to smaller availability of N₂. This decrease is observable at O₂ fractions above 20 %. The increase of G_{N_2O} at smaller fractions of O₂ may be related to the changes in reduced electric fields which also affect the drift velocities and production rate coefficients of N₂^{*}. The curves on Fig. 6 are calculated by assuming that the product of $\frac{k_{N_2^*}}{v_d E/N}$ is an exponent of O₂ fraction, and a reasonably good fit with experiments is obtained.

The abrupt increase of N₂O production in the presence of catalyst could be caused by several reasons. One option could be the increase of E/N which may further increase the production of N₂^{*} responsible for the production of N₂O. Another possibility to explain the increased efficiency of N₂O production is the inclusion of additional reactions on the catalyst surface. The reactions may include the adsorbed oxygen species which react with N₂ or nitrogen species which react with O₂.

4. Summary

In the observed range of SIE values, the O₃ dependence on SIE was sublinear, whereas N₂O dependence was a linear function of SIE. The production efficiencies of O₃ and N₂O obtained from the slope of dependence on SIE were strongly dependent on the O₂ fraction in the gas. The O₃ production efficiency is a monotonically increasing function of O₂ fraction, whereas the N₂O production efficiency has a maximum. Without the catalyst, the maximum efficiency was obtained at 20% of O₂ fraction, whereas with the catalyst the efficiency was highest at 5-10% of O₂ fraction.

The catalyst increased the production efficiency of O₃ at room temperature and decreased the efficiency at 100°C. The production efficiency of N₂O increased two to three times in the presence of the catalyst and the increase was especially notable at low O₂ fractions. The decreased production efficiency of ozone at higher temperature is attributable to O₃ decomposition on the catalyst. The increased production efficiency of N₂O in the presence of catalyst could be caused by changing electric field E/N which increases N₂^{*} yield or by surface reactions taking place on the catalyst surface.

5. Acknowledgements

The study was co-financed by Estonian research agency project PUT585.

6. References

- [1] Kogelschatz U and Baessler P 1987 *Ozone Sci Eng* **9** 195.
- [2] Kogelschatz U, Eliasson B and Hirth M 1988 *Ozone Sci Eng* **10** 367.
- [3] Patil B S, Wang Q, Hessel V and Lang J 2015 *Catal Today* **256** 49.
- [4] Janda M, Martišovits V, Hensel K and Machala Z 2016 *Plasma Chem Plasma Process* **36** 767.
- [5] Bogaerts A and Neyts E C 2018 *ACS Energy Lett* **3** 1013.
- [6] Jõgi I, Bichevin V, Laan M, Haljaste A and Käämbre H 2009 *Plasma Chem Plasma Process* **29** 205.
- [7] Manley T C 1943 *J Electrochem Soc* **84** 83.
- [8] Rothman L S et al 2009 *J Quantum Spectrosc Radiat Transfer* **110** 533.
- [9] Jõgi I, Erme K, Levoll E and Stamate E 2017 *J Phys D Appl Phys* **50** 465201.
- [10] Šimek M, Pekárek S and Prukner V 2012 *Plasma Chem Plasma Process* **32** 743.
- [11] Pekárek S, Mikeš J, Beshajová Pelikánová I, Krčma F and Dzik P 2016 *Plasma Chem Plasma Proc* **36** 1187.
- [12] Yuan D, Wang Z, Ding C, He Y, Whiddon R and Cen K 2016 *J Phys D Appl Phys* **49** 455203.
- [13] Fraser M E, Tucker T R, Piper L G and Rawlins W T 1990 *J Geophys Res* **95** 18611.

INVESTIGATION OF THE ELECTROSPRAYED WATER MICRODROPLETS USING OPTICAL IMAGING METHODS

Mostafa Hassan¹, Mário Janda¹, Zdenko Machala¹

¹*Faculty of Mathematics, Physics and Informatics, Comenius University, Bratislava, Slovakia*

E-mail: Mostafa.Hassan@uniba.sk

Two optical imaging methods for investigating electrospayed water microdroplets interacting with atmospheric air corona discharge plasma were tested: double planar laser beam technique and fast camera imaging. The size distributions of the sprayed microdroplets measured by the two methods did not correlate well due to the lower limit of the camera imaging method. For 13 kV applied across 15.8 mm gap, the most abundant microdroplets were with size 20-30 μm . Further work is needed to improve the spatial resolution of the two methods and be able to detect droplets below 20 μm .

1. Introduction

Because of producing large quantities of reactive oxygen and nitrogen species (RONS) that seem to be the most efficient biocidal agents in bio-decontamination by plasma, atmospheric air plasmas generated in contact with water become a great interest in the plasma decontamination community [1]. Plasma activation of liquid droplets of a few to hundreds of microns size address transport limits where the higher surface area to volume ratio enables for rapid solvation of plasma activated species while small volume enables rapid mixing even if only by diffusion [2]. The transport phenomena of various RONS which have various Henry's law solubility coefficients are determined by the water droplet size or layer thickness. An efficient way of producing Plasma activated water is applying water electro spray to fine aerosol droplets through the active plasma region, which results in an efficient transfer of gaseous RONS into water [3]. So, it is important to study the transport mechanism of the plasma reactive species into water droplets of various sizes, as well as the liquid chemistry to better understand the relevant effects of plasmas in liquids or the activity of plasma activated water. Our approach presented here is focused on measuring and controlling the electro-sprayed water droplet size and density. We employ various optical imaging methods. Understanding the plasma reactive species transport into the water as a function of the microdroplet size and density is our key objective with applications in biomedicine, environmental sciences and agriculture. Scarce numerical modeling studies [4,5] of plasma induced RONS transport processes into water will be then supported by experimental measurements.

2. Experiment Setup

The experimental setup is shown in Fig. 1 consists of a high voltage power supply and syringe pump which passes the deionized water (with conductivity $<3 \mu\text{S/cm}$) through a plastic tube with a flow rate 0.1 mL/min into a stainless-steel needle (nozzle) electrode with the outer diameter 0.7 mm, opposite to a stainless-steel rounded wire grounded electrode, with a gap distance 15.8 mm. Two diode laser beams (red and green) pass through cylindrical lenses, become planar and then intersect with the droplets sprayed from the needle electrode. The red laser is 5.6 mm below nozzle and above the green laser, which is 10.5 mm below nozzle. The output signals of the laser beams are detected using photodetectors and processed by a digital oscilloscope TEKTRONIX TBS2104. The droplets passing through the two planar laser beams cause a signal decrease, which is proportional to the shaded area of the beam signal on the photodetectors.

A digital camera type CASIO EXILIM is used as complementary imaging of the droplets, with typical record parameters 60 fps (frame per second) shutter speed 40,000 (exposure time $1/40000 \text{ s} = 25 \mu\text{s}$). In order to improve the spatial resolution of the camera, the droplets are illuminated with a strong white LED and the image of droplet shades is magnified using a convex lens and projected onto a white paper screen. The photos are then processed and analyzed by some software Microsoft Office Picture Manager and GIMP.

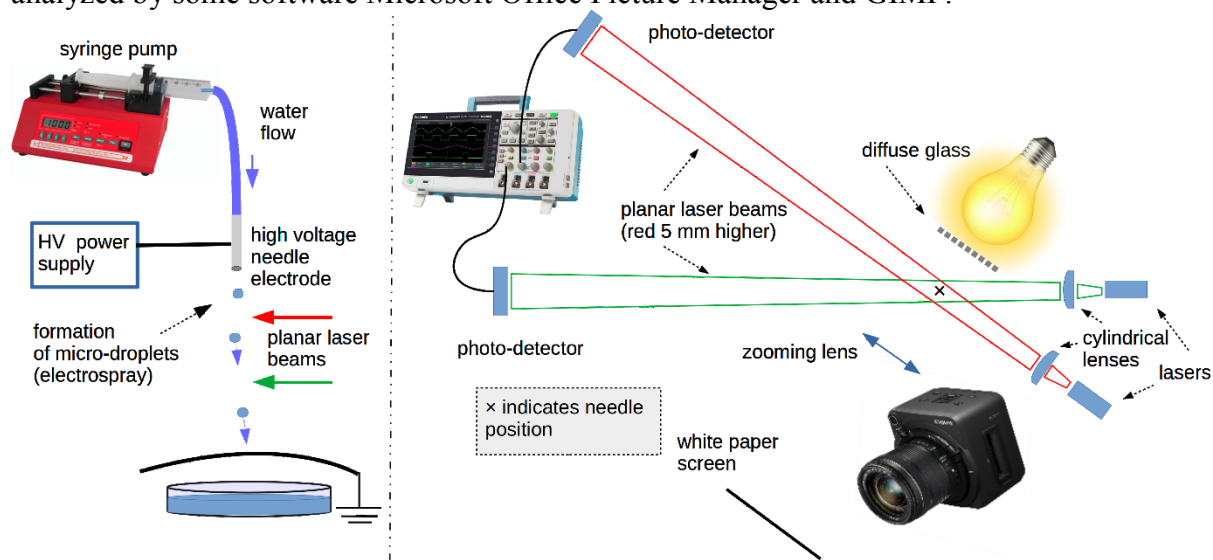


Fig. 1. Experimental Setup.

3. Results and Discussion

The electrospayed water microdroplets were measured at several applied positive voltages (5-13 kV) on the needle electrode using the two parallel laser beams and the camera. The horizontal width of the microdroplets was calculated from the laser shading signal, as well as from the photograph sequences. The measured “apparent” vertical height of the droplets is strongly affected by their speed versus the temporal resolution of the laser systems and camera exposure time, as they propagate by accelerated motion in the vertical electric field between the electrode. The visualization of microdroplets by the fast camera was used to calculate the width of the microdroplets and the recorded photos also help us to understand the laser signal waveforms.

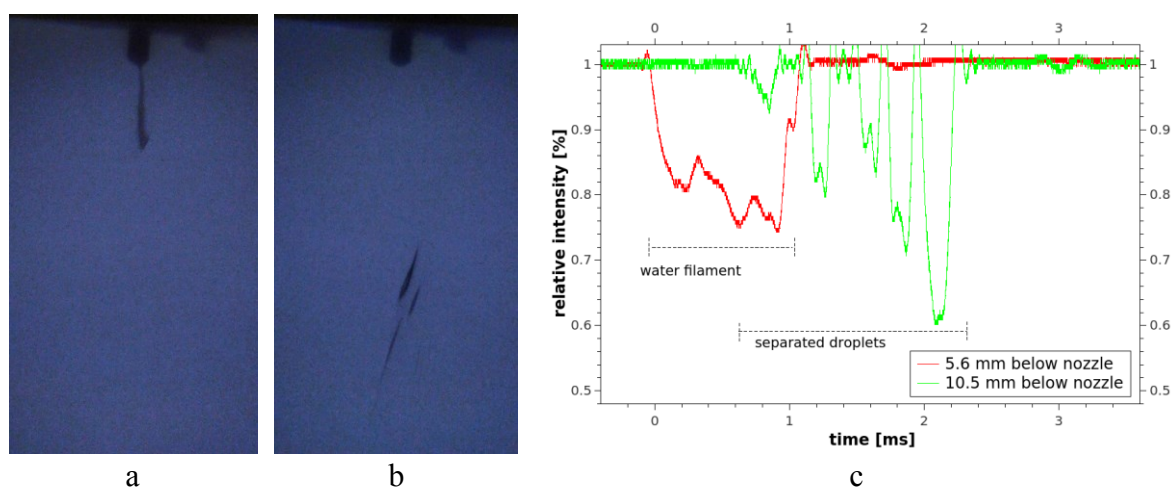


Fig. 2. Microdroplets photographs (exposure time 25 μs) and corresponding laser beam signals at 13 kV.

Fig. 2a shows the formation of the water filament at the needle nozzle. After the detachment, the filament splits into several microdroplets with widths (38-93) μm as shown in Fig. 2b. The process of filament elongation and the subsequent formation of droplets can be observed on the temporal evolution of the lasers' intensities I , as shown in Fig. 2c. The intensity of the upper red laser (5.6 mm below nozzle) decreases as the water filament passes through this planar laser and this intensity decrease is more or less constant for a time interval ~ 1 ms. The signal from the lower laser (~ 10.5 mm below the nozzle) is different. The filament separation and formation of droplets can be observed as several sharp signal drops in the laser intensity. The individual drops with different minimum values correspond to the microdroplets with different sizes. The smallest (in width) and the fastest microdroplet appears first, while the biggest and the slowest is the last one.

The diameter d of these droplets is estimated based on the following assumptions. The relative decrease of light intensity $\Delta I/I_0$ is directly proportional to the ratio of droplet shadow size S and the detector active area A . The active area of detectors is given by horizontally oriented optical slit with length $s_l = 3$ mm and the slit width $s_w = 100 \mu\text{m}$ or $150 \mu\text{m}$, for green and red laser detectors, respectively. We also consider the horizontal divergence of the planar beams. Due to this divergence, the shadow of the droplets is zoomed in a horizontal plane by a factor $z_f = 4.7$ or 3.8 , for the green and red laser, respectively. We further assume ideal spherical droplets.

Due to the horizontal zoom, the shadow of spherical droplets should be elliptical, with the area

$$S = \pi/4 \times z_f \times d^2 \quad (1)$$

For droplets with $d < s_w$, we can thus estimate d using the following formula

$$d = (4/\pi \times A/z_f \times \Delta I/I_0)^{1/2} \quad (2)$$

The shadow of larger droplets is never entirely projected onto the detector entrance slit. For $d > 4s_w$, we can consider the covered area to be rectangular with area $S = s_w \times z_f \times d$. For droplets with $d \in \langle s_w, 4s_w \rangle$, we introduced a correction factor c_f so that we can finally estimate the size of droplets as

$$d = A/(z_f \times s_w) \times \Delta I/I_0 + c_f \quad (3)$$

The c_f decreased linearly from maximum value (for $d = s_w$) down to 0 for $d = 4s_w$. The maximum value of c_f was chosen so that for $d = s_w$ formulae (2) and (3) give the same result. In practice, we first estimated the diameter of all droplets using eq (2). Then we calculated new diameter for droplets with $d > s_w$ by eq (3) without the correction factor. Next, we added c_f to meet the criterion mentioned above. Next, we recalculated the diameter of droplets with $d > s_w$ using formula (3) with the appropriate correction factor.

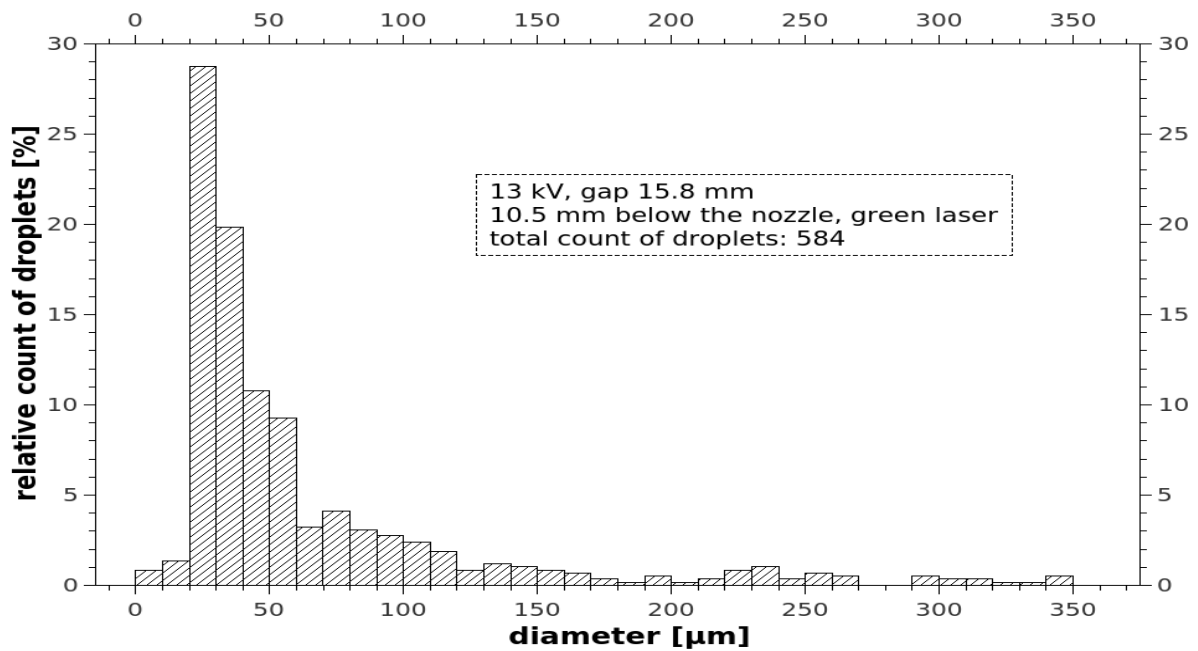


Fig. 3. Droplet size distribution measured by lower green laser 10.5 mm below nozzle, 13 kV.

After analysis of several waveforms, we were able to create a histogram showing the droplet size distribution. Fig. 3 shows the droplet size distribution as measured by the lower green laser in electro spray at 13 kV, with the glow corona discharge. We assume that due to the sensitivity limit, our method underestimates the number of droplets with diameter below 20 μm and that the detection limit is slightly below 10 μm. The most abundant are droplets with $d = 20\text{-}30\ \mu\text{m}$.

In order to verify the reliability of this technique we compared the obtained droplet size distribution with that measured from the camera image sequences as shown in Fig. 4. However, based on the camera images, the most abundant droplets are with $d = 50\text{-}120\ \mu\text{m}$. We assume that our current camera imaging set-up does not allow us to correctly detect all droplets with diameter below ~50 μm. With the aperture fully opened, our depth of field is narrow, and the image of the droplets is sharp enough only if they do not deviate from the focusing plane. With smaller aperture, we are unable to detect anything with the exposure time as short as 25 μs, due to insufficient illumination and longer exposure times make elongated droplet images as they move in the electric field. We thus cannot reliably compare the results obtained by the two presented techniques now.

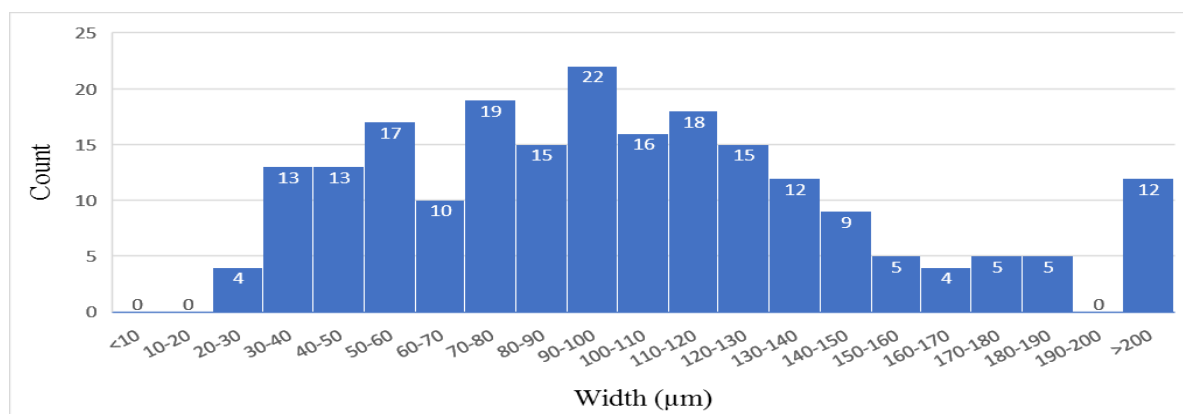


Fig. 4. Size distribution of microdroplets measured from photographs at 13 kV, total count of droplets: 214.

4. Conclusions

We developed and tested two optical imaging techniques for measuring sizes of electrosprayed microdroplets in order to control the droplet size distribution when studying plasma-liquid interactions and RONS transport from plasma into water. Theoretically, the detection limit of our double planar laser beam technique for online monitoring of microdroplets is $\sim 10 \mu\text{m}$, but we can reliably recognize only droplets with sizes starting from $\sim 20 \mu\text{m}$. The camera imaging technique we used for the same electrosprays did not demonstrate a sufficient sensitivity to correlate with size distributions measured by laser beams. We further assume that we can still improve the detection limit of our laser technique if we effectively decrease the width of the detection area by the additional entrance slit from current 3 mm down to 1.5 mm. However, we still need to find suitable independent method to verify the measured distributions.

Acknowledgments

This work was supported by Slovak Research and Development Agency APVV-17-0382 and Slovak Grant Agency VEGA 1/0419/18, and Faculty of Mathematics, Physics, and Informatics, Comenius University Bratislava.

5. References

- [1] Branislav Pongráč: *Study of the Electrospraying Effect of Water in Combination with Atmospheric Pressure Corona Discharge 2014 DOCTORAL THESIS*, Comenius University Bratislava.
- [2] Adamovich I, Baalrud S D, Bogaerts A, et al. 2017 The 2017 Plasma Roadmap: Low temperature plasma science and technology *J. Phys. D. Appl. Phys.* **50** 323001
- [3] Machala Z, Tarabová B, Sersenová D, Janda M and Hensel K 2019 Chemical and antibacterial effects of plasma activated water: correlation with gaseous and aqueous reactive oxygen and nitrogen species, plasma sources and air flow conditions *J. Phys. D. Appl. Phys.* **52** 034002
- [4] Kruszelnicki J, Lietz A M and Kushner M J 2017 *INTERACTION BETWEEN ATMOSPHERIC PRESSURE PLASMAS AND LIQUID MICRO-DROPLETS** *International Conference on Plasmas with Liquids (ICPL 2017) ed P Lukeš and K Koláček, Prague (Czech Republic), p 37*
- [5] Verlact C C W, Van Boxem W and Bogaerts A 2018 Transport and accumulation of plasma generated species in aqueous solution *Phys. Chem. Chem. Phys.* **20** 6845–59

INFLUENCE OF SOLUTION PROPERTIES AND GAS ADDITION ON HYDROGEN PEROXIDE PRODUCTION BY A NOVEL PLASMA SOURCE GENERATING DC NON-PULSING DISCHARGE IN LIQUIDS

Zdenka Kozáková¹, František Krčma¹, Aneta Možíšová¹, Anastasia Dürrová¹

¹Faculty of Chemistry, Brno University of Technology, Purkyňova 464/118, 612 00 Brno, Czech Republic

E-mail: kozakova@fch.vut.cz

The paper evaluates concentration of hydrogen peroxide produced by a novel pin-hole plasma source in electrolyte solutions with or without gas addition. An effective production rate of hydrogen peroxide is decreased by the increased argon as well as oxygen flow rate through the plasma region. Further, it is enhanced by higher solution conductivity while it is decreased in the strongly basic conditions with the highest pH values.

1. Introduction

Nowadays there are many different electrode configurations ensuring discharge generation directly in the liquid phase. A very high electric field value is usually necessary for the initiation of the breakdown. Typical electrode configurations are point to plane [1, 2], coaxial [3] or pin-hole systems [4, 5]. All discharges in the liquid phase are usually supplied by pulsing high voltage both in the direct current and alternating current regimes up to the microwave excitation region [6, 7]. This paper presents results obtained by a recently developed electrode system based on the pin-hole discharge configuration that was patented in the Czech Republic [8]. The discharge is generated by a DC non-pulsing voltage in various electrolyte solutions giving different pH values. Thus the previously published detailed characteristics of this plasma source [9] are extended by chemical experiments focused on hydrogen peroxide determination in the dependence on solution properties and gas addition.

2. Experimental setup

The electrode system consisted of two electrodes [9]. The main electrode was constructed by a tungsten wire (diameter of 1.0 mm) which was inserted into a dielectric cylindrical rod made of Macor ceramics with outer diameter of 10 mm and with one conical end. An orifice with the diameter of 1.2 mm was made in the ceramics along its longitudinal axis. A small gap of 1 mm was kept between the end of the wire electrode and the end of the dielectric rod. An outer glass tube served as a holder and as a gas inlet. The second electrode was a planar plate made of platinum with dimensions of 20x100 mm². Both electrodes were immersed in a vessel containing 500 ml of electrolyte solution with initial conductivity of 300 or 1000 μS/cm. The used electrolyte set the initial pH of the solution on 5 (NaH₂PO₄), 9 (Na₂HPO₄) or 11 (Na₃PO₄) and its value remained constant during the treatment. Addition of two gases (argon and oxygen) with flows in the range of 10–50 ml/min was studied. The system was supplied by DC non-pulsing high voltage up to 2 kV with the positive polarity on the main electrode. The discharge itself showed self-pulsing operation [9] giving the mean input power from the range of 50–150 W.

Production of chemical active species was represented by hydrogen peroxide formation. Concentration of hydrogen peroxide was determined by a standard colorimetric method using a specific titanium reagent [10]. Based on the linear increase of H₂O₂ concentration during the discharge treatment, an effective production rate $\eta_{H_2O_2}$ in mg/kJ was calculated according to the following equation:

$$\eta_{H_2O_2} = \frac{a \cdot M_{H_2O_2} \cdot V}{P} \quad (1)$$

where a is the coefficient of the linear dependence of H₂O₂ concentration in time (in mol/L·s), $M_{H_2O_2}$ is the molecular weight of H₂O₂ (34 g/mol), V is the treated volume (in L) and P is the input power (in W).

3. Results

As the previous results [9] indicated significantly higher production of hydrogen peroxide when positive polarity was applied on the main electrode, presented results are also focused on this configuration. An influence of pH and solution conductivity set by the chosen electrolyte is demonstrated in Fig. 1. Concentration of hydrogen peroxide produced during the discharge in a phosphate solution with initial conductivity of 1000 $\mu\text{S}/\text{cm}$ is compared for acidic (pH 5) or basic (pH 9 and 11) conditions (Fig. 1 left). H_2O_2 concentrations obtained after 3 minute plasma treatment are from 0.9 to 1.3 mmol/l. These results are similar to our previous studies carried out in the diaphragm discharge configuration [4] or others in the point to plane pulsed supplied configurations [1]. According to the effective production rate $\eta_{\text{H}_2\text{O}_2}$, lower pH values supports H_2O_2 formation ($\eta_{\text{H}_2\text{O}_2} = 2.4 \text{ mg}/\text{kJ}$) while it is more than twice decreased in strongly basic conditions (pH 11: $\eta_{\text{H}_2\text{O}_2} = 0.9 \text{ mg}/\text{kJ}$). It is evident that higher concentration of hydroxyl anions given by the higher pH value shifts the reaction of hydrogen peroxide formation back to the original hydroxyl radicals.

Decreasing the initial conductivity of all electrolyte solutions from 1000 to 300 $\mu\text{S}/\text{cm}$, the effective production rate is almost four times lower (Fig. 1 right). This phenomenon is typical for our novel plasma system [9], but it is in contrary to previously studied configurations such as the diaphragm discharge [5] or the point to plane electrode geometry [7].

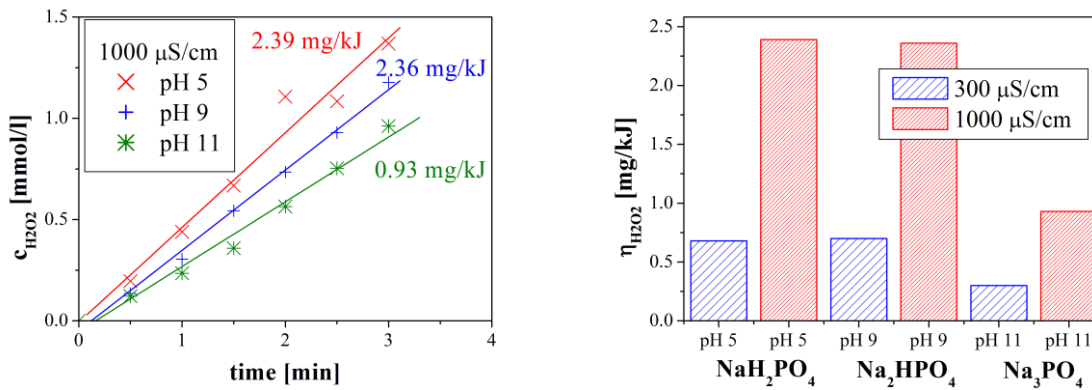


Fig. 1. Left: Concentration of hydrogen peroxide during the discharge treatment of electrolyte solutions with different pH. Right: Comparison of H_2O_2 effective production rate for different pH and initial solution conductivity.

An influence of the gas addition into the plasma region is demonstrated in Fig. 2. It is obvious that hydrogen peroxide effective production rate is significantly decreased by the argon addition although the smallest flow rate of 10 ml/min is used and it is further decreasing by the increasing flow rate (Fig. 2 left). Comparing both studied gases, argon as an inert gas and oxygen as a reactive gas, the influence of their addition into the system is similar (Fig. 2 right). Both of them substantially decrease the H_2O_2 effective production rate and this decrease is higher at the acidic conditions (pH 5). An explanation of the negative influence of the gas addition on the hydrogen peroxide formation could be an irregular discharge operation due to the presence of gas bubbles in the plasma region which also decreases the possibility of particles collisions in the liquid phase.

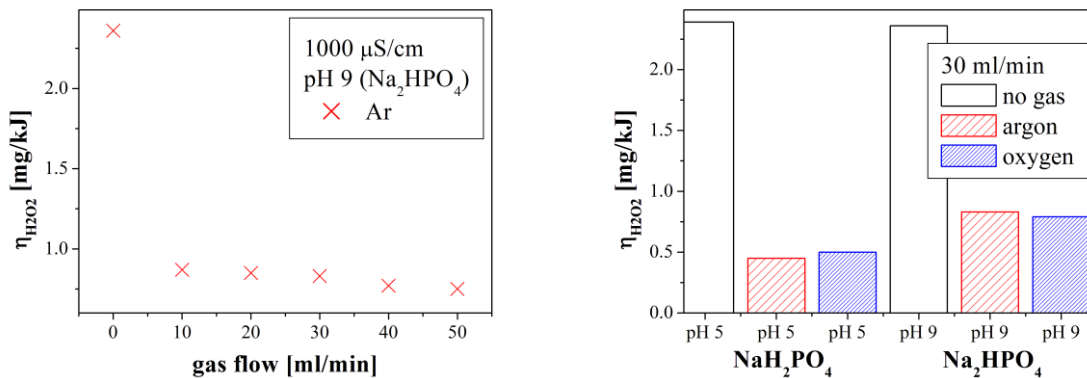


Fig. 2. Left: Influence of argon flow rate on the H_2O_2 effective production rate. Right: Comparison of H_2O_2 effective production rate for different gas addition and pH.

4. Conclusions

Hydrogen peroxide is formed by our novel plasma source in electrolyte solutions with different pH values and initial conductivities. The effective production rate of hydrogen peroxide reaches values of about 2.4 mg/kJ (NaH_2PO_4 electrolyte, pH 5, 1000 $\mu\text{S}/\text{cm}$) and it is significantly decreased by the increasing pH value as well as by the decreasing solution conductivity. Especially the effect of solution conductivity is substantially different in our plasma source comparing to other electrode systems. Addition of gas flowing through the plasma region significantly decreases the H_2O_2 effective production rate no matter which gas, inert argon or reactive oxygen, is used.

5. References

- [1] Kirkpatrick M J and Locke B R 2006 *Ind. Eng. Chem. Res.* **45** 2138.
- [2] Ruma, Lukeš P, Aoki N, Špetlíková E, Hosseini S H R, Sakugawa T and Akiyama H 2013 *J. Phys. D: Appl. Phys.* **46** 125202.
- [3] Šunka P, Babický V, Člupek M, Fuciman M, Lukeš P, Šimek M, Beneš J, Locke B R and Majcherová Z 2004 *Acta Phys. Slovaca* **54** 135.
- [4] Stará Z and Krčma F 2005 *Acta Physica Slovaca* **55** 515.
- [5] Krčma F and Stará Z 2002 *Proc. of ECAMPIG XVI*, Grenoble, 47.
- [6] Locke B R, Sato M, Šunka P, Hoffmann M R and Chang J S 2006 *Ind. Eng. Chem. Res.* **45** 892.
- [7] Lukeš P 2001 *PhD Thesis* Institute of Plasma Physics, Prague.
- [8] Krčma F 2015 *Jet system for plasma generation in liquids* Czech Republic Patent CZ 305304 B6.
- [9] Krčma F, Kozáková Z, Mazánková V, Horák J, Dostál L, Obradović B, Nikiforov A and Belmonte T 2018 *Plasma Sources Sci. Technol.* **27** 065001.
- [10] Eisenberg G M 1943 *Ind. Eng. Chem., Anal. Ed.* **15** 327.

THE ROLE OF OXYGEN AND CARBON DIOXIDE ON DISCHARGE INITIATED CHEMISTRY IN TITAN RELATED ATMOSPHERE AT RELEVANT TEMPERATURES

František Krčma, Stanislav Chudják

Brno University of Technology, Faculty of Chemistry, Purkyňova 118, 612 00 Brno, Czech Republic

E-mail: krcma@fch.vut.cz

The chemical processes initiated by electrical discharges in prebiotic atmospheres became a hot topic during the last decade because of extensive discovering of exo-planets. The biggest atmospheric data collection is about Saturn's moon Titan atmosphere that is composed mainly from nitrogen and methane at low temperature of about 94 K. The presented contribution gives the first measurement of the main compounds formed in glow discharge at atmospheric pressure in nitrogen-methane gaseous mixture containing traces of oxygen and carbon dioxide at the relevant temperature. Results show very complex chemistry in these mixtures leading to the formation of currently considered direct life precursors like formamide.

1. Introduction

Laboratory mimic studies of processes running in the exo-planetary atmospheres became a hot topic during the last years because many exo-planets were discovered very recently. Moreover, the successful space missions like Cassini-Huygens bring a huge number of data from the in situ observations that are impossible using earth techniques [1-3]. The main interest is focused on the search of life traces or life molecular precursors and consequent discovering the possible ways leading to the life origins formation. The majority of studies were carried out in the Titan's atmosphere up to know because there are many in situ available data and its atmosphere seems be very similar as Earth's before life creation [3-5]. The exo-planetary atmospheric processes are very complex and can be initiated mainly by UV and VUV radiation and particles fluxes coming from the space or by electrical discharges in the planetary atmospheres. The planetary scale processes can be simulated by laboratory experiments using various discharges: corona and DBD conditions are similar as the St. Elmo's fire, spark and arc relates to lightning, and corona and glow conditions are similar to conditions in aurora borealis. Nearly all laboratory studies up now were carried out at ambient temperatures that are not fully reflecting real planetary conditions. The presented study gives the first results obtained by glow discharge generated in the Titan like atmosphere (nitrogen-methane mixture) in the flowing regime at the liquid nitrogen temperature [5-6].

2. Experimental

The experiment was carried out in the simple glass reactor (see Fig. 1) equipped by a pair of tungsten rod electrodes (diameter of 1 mm) in distance of 1 mm. The glow discharge was operating at the current of 25 mA (corresponding power was of 10 W). Reactor was placed into Dewar vessel fill able by liquid nitrogen up to level 2 above the electrode system. The gas mixture composition was controlled by Bronkhorst MCFs. Used gasses were of the following purities: Nitrogen 99.999%, methane 99.95%, oxygen 99.5% and CO₂ of alimentary quality. Four mixtures were used for the current experiments: pure nitrogen with flow of 200 Sccm, nitrogen with addition of 5 Sccm of methane and the same mixture enriched by oxygen or CO₂ with flows of 1 Sccm. Pressure in the reactor was kept as atmospheric. The exhaust gas analysis was examined by proton transfer reaction time of flight (PTR-TOF) mass spectrometry allowing continual in situ complex analysis of the discharge exhaust gas. Advantage of this technique is immediate response and simultaneous detection of all compounds with proton affinity higher than proton affinity to water molecules. Thus it is not sensitive on any of the gasses in the reaction mixture. Unfortunately, there is impossible to distinguish isomers. Whole line (made of PTFE and stainless steel) to PTR-TOF mass spectrometer was heated up to 80 °C to avoid discharge products condensation. Experiment was completed following the scheme:

- 1) -300 s start of reaction mixture flow
- 2) 0 s start of measurement

- 3) 60 s discharge turn on
- 4) 300 s starting reaction vessel cooling
- 5) 1200 s discharge off
- 6) 1500 s end of vessel cooling
- 7) 2100 s start of reactor heating by hair drier
- 8) 2400 s end of reactor heating by hair drier
- 9) 2700 s nitrogen (99.999%) high flow of 5 Slm purge flow on
- 10) 3000 s end of experiment

Reactor was not opened or cleaned between experiments, so some contamination (mainly by some deposited material on electrode surfaces) was possible.

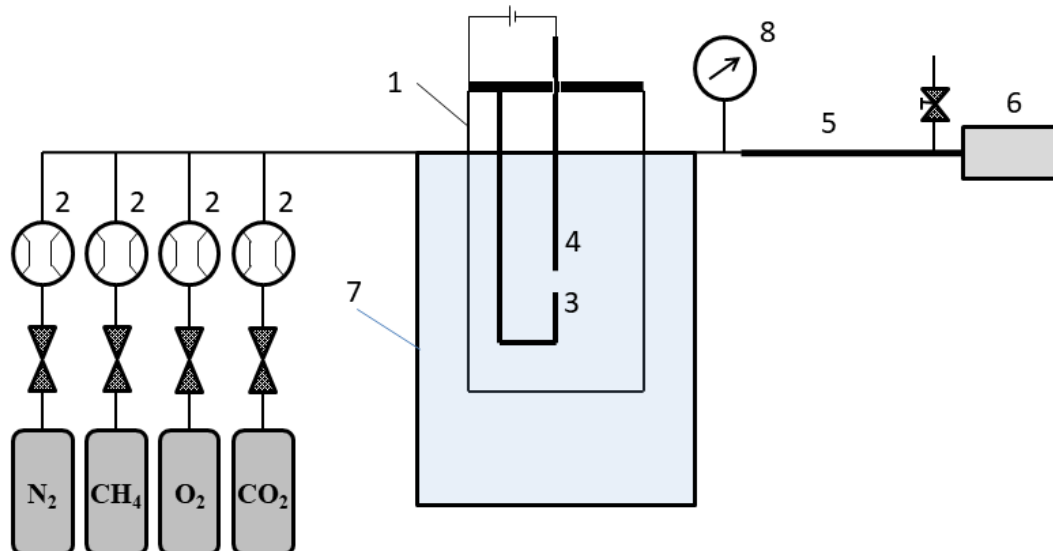


Fig. 1. Scheme of the experimental set up: 1 – Pyrex glass reactor vessel; 2 – mass flow controller; 3 – cathode; 4 – anode; 5 – heated exhaust gas sampling line; 6 – proton transfer reaction time of flight mass spectrometer; 7 – liquid nitrogen vessel; 8 – membrane manometer.

3. Results

The time profiles of concentrations for the selected compounds are given in Figs. 2-5. The hydrogen cyanide (Fig. 2) and acetonitrile (Fig. 3) are the main compounds formed by the discharge in nitrogen-methane mixtures [7, 8]. Both these compounds reach during the discharge operation and later evaporation of condensed discharge products the saturation limit of the device and thus there are rather complicated to relate them to appropriate kinetic processes. The ammoniac (NH_4^+) was impossible to detect because its mass is nearly the same as of H_2O^+ (formed in PTR-TOF ionization discharge source) and the device resolution is about 1000, only. Their concentration time dependence clearly follows the experimental scheme. The initial increases of their concentrations after the discharge turn on in generally independent on the reaction gas mixture. In couple of ten seconds after starting the reactor vessel cooling, the concentrations drop down due to compounds trapping on the frozen reactor wall and only a small part of formed species can continue to the PTR-TOF. When discharge is stopped concentrations rapidly decrease. This decrease is the same in case of hydrogen cyanide at all conditions but differs in case of acetonitrile. This can be explained that this specie is further oxidized when oxygen containing gas is presented in the reaction mixture. The increase of all concentrations in the case of oxygen containing mixture could not reflect discharge/cooling effect because it is observed just at the moment of discharge turn off and there is no delay necessary for the species transfer from reactor to PTR-TOF (it is about 12 s at these experimental conditions). The later concentrations increase (after 1500 s) reflects reactor vessel spontaneous heating followed by the evaporation of condensed species. Also at this experimental period the further oxidation of acetonitrile is probable. Besides the main formed compounds many tens of other species were identified [7, 8]. The benzene and formamide were selected to present here, only. The first one represents the cyclic hydrocarbons that are important for the synthesis of more complicated organic compounds; formamide is known as the precursor of nuclear acids basis components that can be formed thermally.

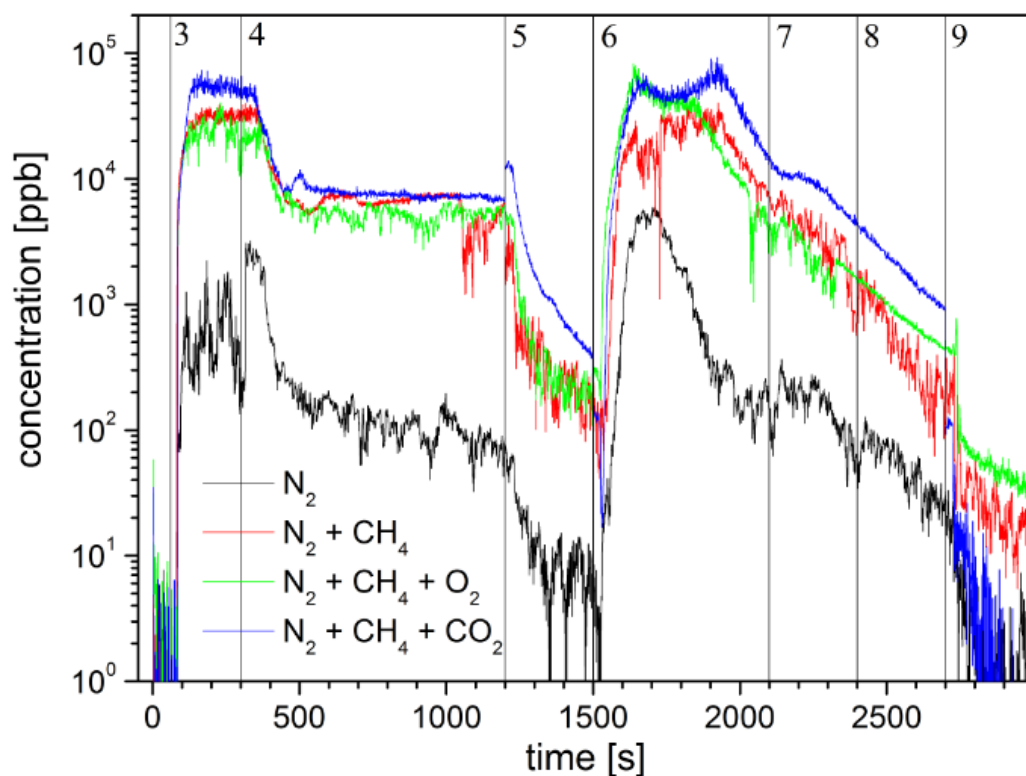


Fig. 2. Concentration of hydrogen cyanide during the experiment. The vertical lines indicate experimental setting points given in experimental section. Note that saturation limit for the used detection technique is about 60 000 ppb for this compound.

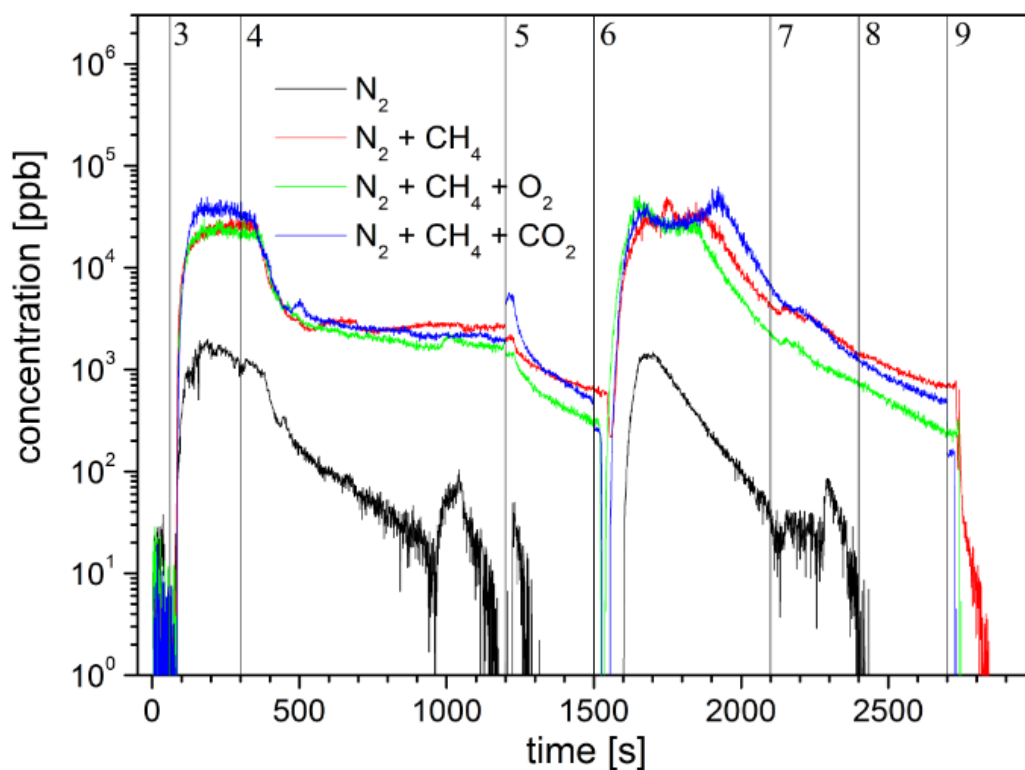


Fig. 3. Concentration of acetonitrile during the experiment. The vertical lines indicate experimental setting points given in experimental section. Note that saturation limit for the used detection technique is about 60 000 ppb for this compound.

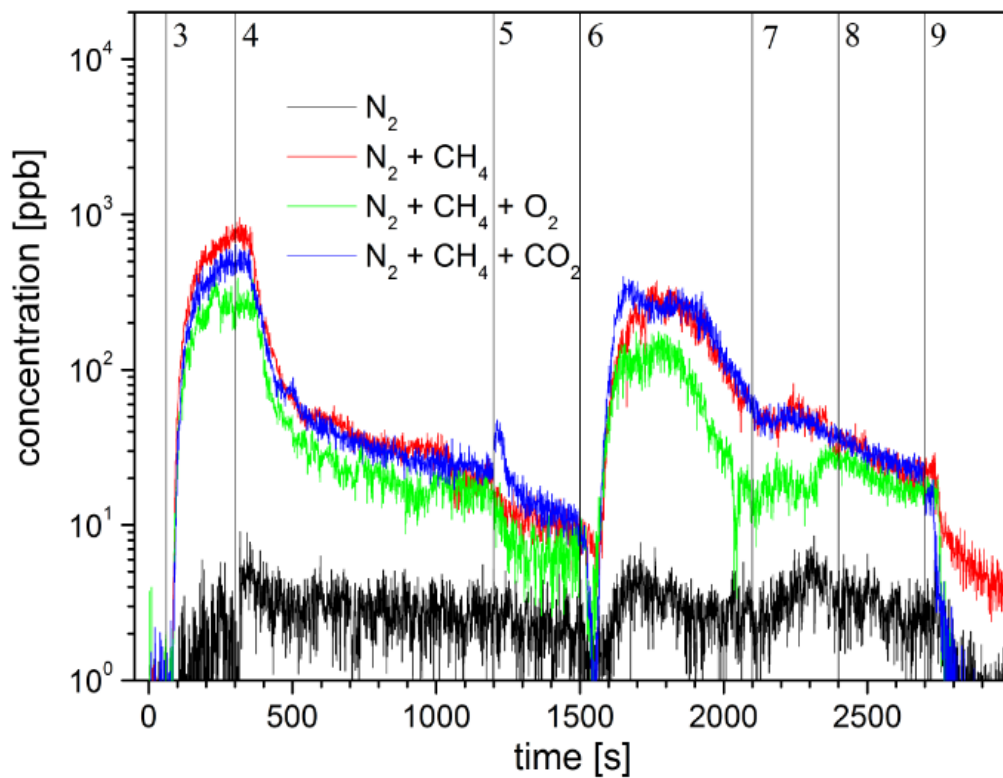


Fig. 4. Concentration of benzene during the experiment. The vertical lines indicate experimental setting points given in experimental section.

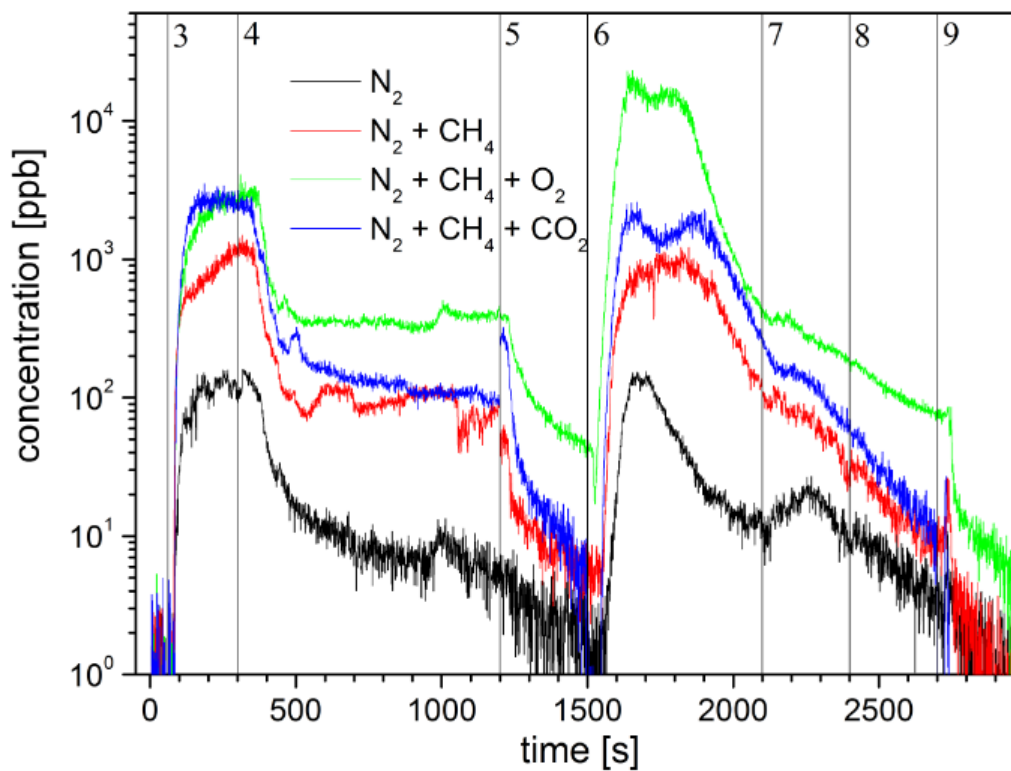


Fig. 5. Concentration of formamide during the experiment. The vertical lines indicate experimental setting points given in experimental section.

The benzene formation is significantly quenched by the presence of oxygen atoms in the reaction mixture. On the other hand, formamide formation is supported by oxygen presence because this molecule contains oxygen in its structure. It is important to note that formamide is formed by discharge also in the case when no additional oxygen is added into the reaction mixture, so even small traces from nitrogen and methane pressure cylinder together with some oxygen adsorbed on wall are sufficient for its remarkable production.

4. Conclusion

The presented contribution brings the first experiments obtained in the Titan like atmosphere at relevant temperature. The shown pilot experimental data demonstrated the critical role of the small oxygen containing impurities was observed mainly in the formation of formamide that is known as a nuclear acids bases compounds precursor. The detailed further experiments will be done to verify the role of discharge operation power and duration as well as role of impurities and surface reactions, especially at the low temperature.

5. References

- [1] J. M. Bernard et al. *Icarus* 185 (2006) 301
- [2] J. M. Bernard et al. *Proc. Sec. Eur. Workshop on Exo-Astrobiology* (2002) 623
- [3] H. Imanaka et al. *Icarus* 168 (2004) 344
- [4] R.E. Johnson, et al. *Icarus*, 271 (2016) 206
- [5] J.A. Kammer, et al. *Planetary and Space Science*. 88 (2013) 92
- [6] T. Tokano. *Icarus*. 289 (2017) 133
- [7] L. Töröková et al. *Eur. Phys. J. – Appl. Phys.* 71 (2015) Art. No. 20806
- [8] L. Töröková et al. *Contr. Plasma Phys.* 55 (2015) 470

INVESTIGATE SURFACE STRUCTURE OF MOLYBDENUM SPUTTERING TARGETS BY LOW ENERGY ION-SURFACE COLLISIONS

Felix Duensing¹, Stefan Raggl¹, Manuel Drost¹, Paul Scheier¹

¹Institut für Ionen- und Angewandte Physik, Universität Innsbruck
E-mail: felix.duensing@uibk.ac.at

Using a focused argon beam to simulate plasma-surface interactions, we investigate ion-surface collisions, similar to conditions in DC magnetron sputtering. Investigating the commonly used molybdenum target material, the secondary electron emission coefficients in areas with different molybdenum lattice orientation as well as on boundaries between grains are measured under controlled conditions.

1. Motivation

DC Magnetron sputtering is a common method to apply thin films of a material onto surfaces. Typically the target surface is biased negatively, therefore, the positively charged argon ions, produced by the magnetron sputtering source, get accelerated towards the target surface. Subsequently, target atoms are ejected due to sputtering and are adsorbed on a substrate surface. To understand the influence of the targets micro-structure in detail, a setup was built, to control the energy of the ion-surface collision and the position of the ion beam with respect to the target. By measuring the secondary electron emission coefficient (SEEC, γ), one gets detailed information about target structure and its possible influence during DC magnetron sputtering processes.

2. Method

In the setup, argon (Ar) gas is introduced into a small volume and ionized via electron bombardment. Through a small opening the Ar^+ is accelerated into the chamber. With several lenses the beam gets further accelerated and focused onto the target surface with an energy of 450 eV. The beforehand simulated beam width could be verified to 104 μm and 117 μm in x- and y-direction, respectively. The SEEC γ (eq. 1) is calculated by the current measured on the target itself and the Faraday cup covering the target. A xy-stage with nanometre accuracy moves the target relative to the beam, which is used to address different areas on the target.

$$\gamma = \frac{i_{FC}}{i_T - i_{FC}} \quad i_{FC} = \text{current on Faraday cup}, \quad i_T = \text{current on target} \quad (1)$$

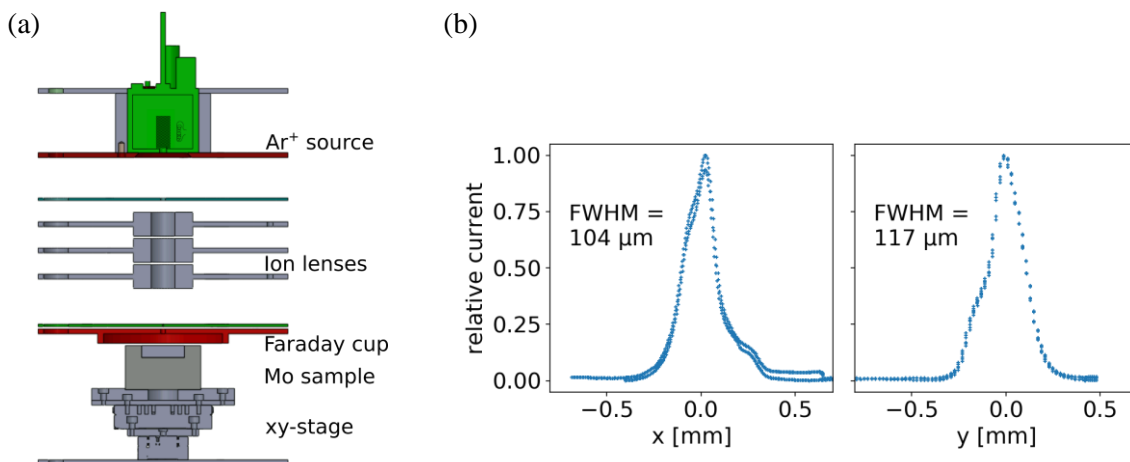


Fig. 1. (a) Schematic setup. Positively charged argon ions are accelerated and focused via electrostatic lenses onto a molybdenum target sample. Secondary electrons are measured via a Faraday cup. A high

precision xy-stage moves the sample relative to the ion beam. (b) Beam profile in x- and y-direction at the position of the molybdenum target sample surface position.

3. Structure of the molybdenum samples

Depending on the manufacturing process, the grain size of one lattice orientation varies in orders of magnitude. The dependence of the SEEC on grain size as well as on the lattice orientation and on the grain boundary is investigated.

4. Results

Results of the shown revised setup will be given on the conference. A former setup with a beam width of 1.45 mm was used to confirm the proof of concept. Fig. 2 shows values of γ measured on a molybdenum target along one direction. The blue dotted lines show the possible boundaries between the grains. Due to the large beam width its not completely clear, if the signal change comes from adsorption of gas compounds, impurities of the molybdenum target, or from the grain boundaries. With the new setup it is possible to distinguish between different structures and measuring on or off a boundary.

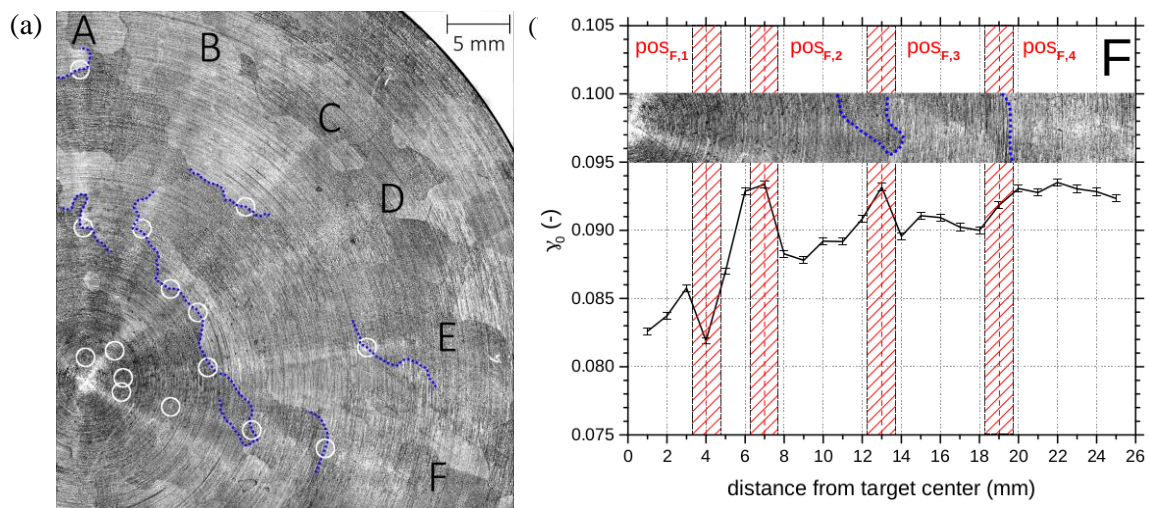


Fig. 2. (a) Light optical micrograph of the molybdenum target. Taken from [1]
 (b) SEEC values γ measured on the target. Taken from [1]

5. References

[1] Raggl, S. (2018). *Experimental Plasma Analysis of DC Magnetron Sputtering Processes* (Doctoral dissertation), University of Innsbruck.

PLASMA ACTIVATED WATER GENERATED BY TRANSIENT SPARK AIR DISCHARGE: CHEMICAL PROPERTIES AND APPLICATION IN SEED GERMINATION AND PLANT GROWTH

Gervais Blondel Ndiffo Yemeli, Katarína Kučerová, Zdenko Machala

Faculty of Mathematics, Physics and Informatics, Comenius University, 84248 Bratislava, Slovakia

E-mail: GBN.yemeli@fmph.uniba.sk

Abstract: Cold plasmas generated by electrical discharges in air at ambient temperature and atmospheric pressure generate reactive oxygen and nitrogen species (RONS) that in contact with water generate the plasma activated water (PAW). PAW produced by pulsed discharge electrospray was chemically analysed and its effects on maize seed germination and growth were investigated. Higher RONS concentrations in PAW resulted in enhanced germination and plant growth.

Cold plasma, electrospray, plasma activated water, reactive oxygen and nitrogen species.

1. Introduction

Cold plasma generated by electrical discharges in air at atmospheric pressure may cause strong oxidation and antimicrobial effects and induce other beneficial effects in food processing and agriculture [1-3]. This plasma is an efficient source of radicals and reactive species often coupled with the effects of electric fields and radiation, and opens up many new applications, especially in disinfection and sterilization, juice pasteurization, stimulation of seed germination and plant growth [4, 5]. It has shown immense potential as a simple, safe, and environmental friendly alternative to various chemical processes used in the food processing and agriculture [6]. These properties have led researchers to study the action of this plasma on aqueous solutions in general and water in particular. Its action on water has given very positive results with the in situ generation of highly reactive species in contact at the gas-water interface, thus generating the reactive oxygen and nitrogen species in this water [1]. In this study we evaluated the effect of two water flow rates and electrospray method through two needles on the chemical composition of plasma activated water generated by transient spark discharge and investigated the effect of PAW produced on the germination and growth of maize. Positive effects of similar PAW prepared by transient spark air discharge in water circulation system have been reported on wheat seeds [7].

2. Materials and methods

a- Plasma device and PAW preparation procedure

i- The experimental setup for DC-driven transient spark discharge in point-to-plane geometry is shown in Fig. 1. The discharge was generated in ambient air through the water-spray system configuration. Two high voltage (HV) hypodermic hollow needle electrodes enabled us to inject water through the discharge zone with constant flow rates (0.5 and 1.0 mL.min⁻¹), and the water was electro-sprayed through the active zone of the discharge and then collected under the metallic mesh. The inter-electrode spacing from the HV needles to the grounded mesh electrode was usually kept around 8 mm. The discharge voltage was measured by a HV probe Tektronix P6015A. The discharge current was measured by a Rogowski current monitor Pearson Electronics 2877. The current and voltage signals were processed by a digitizing 200 MHz oscilloscope Tektronix TDS 2024.

ii- Maize (*Zea Mays L. var Saccharata*) seeds were used to investigate the PAW effect on germination and plant growth (in vitro and in vivo), using two flow rates 0.5 and 1.0 mL.min⁻¹ (PAW 0.5 and PAW1.0 respectively) and the effect of long-lived reactive oxygen and nitrogen species (RONS) concentrations was evaluated.

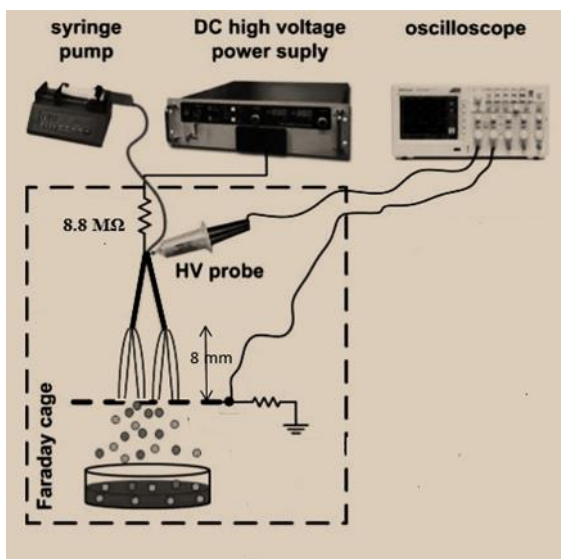


Fig. 1. The experimental setup with electro-spray of water through two needles and two parallel transient spark discharges

b- Performed water analysis

The detection of reactive species (hydrogen peroxide, nitrites/nitrates) was performed by UV/VIS absorption spectroscopy colorimetric methods (Shimadzu UV-1800 Spectrophotometer) as follows:

i- Determination of hydrogen peroxide (H_2O_2): H_2O_2 reacts in the presence of sodium azide (NaN_3 to remove interacting nitrites) with a reagent titanil oxysulphate (TiOSO_4) and the resulting yellow product with a maximum absorption (407 nm), is directly proportional to the concentration of H_2O_2 .

ii- Determination of nitrite and nitrate (NO_2^- and NO_3^-):

Nitrite reacts with Griess reagents and produces a peak of azo purple product at an absorption maximum (540 nm), which is proportional to the concentration of NO_2^- . Nitrates are converted to nitrites by nitrate reductase and measured as above.

iii-The change of pH in plasma treated water was measured by pH probe (WTW 3110)

c- Seed procedure

i- *In vitro* tests

Seeds of maize (*Zea Mays L. var Saccharata*) were soaked during 6 h in tap water or PAWs. After that 10 seeds were placed in petri dishes (90 mm diameter) containing two layers of filter paper and moisturized with 5mL of tap water or PAWs. Germination was performed at $24 \pm 2^\circ\text{C}$ in darkness for 3 days. All experiments were made with 4 replicates and during germination tap water or PAWs were added to each petri dish every other day to maintain constant moisture.

ii- *In vivo* tests

Seeds were sown in experimental pots (100 ml) containing soil. Each pot was watered with tap water or PAWs to keep the constant moisture level of soil. The plants were cultivated for 7, 10 and 14 days in controlled growth conditions: $23 \pm 2^\circ\text{C}$, a 12 h light/12 h dark.

d- Statistical Analysis

Differences among different treatments were evaluated using the one-way analysis of variance (ANOVA). Results were significant at $*P < 0.05$; $**P < 0.01$. Values are expressed as a mean \pm standard deviation (SD).

3. Results and Discussion

a- Transient spark discharge parameters

The typical voltage and current waveforms of the positive TS discharge in 8 mm gap with electro spray of water are shown in Fig. 2. The typical pulse repetition frequency ~ 1 kHz and pulse duration ~ 25 ns. Transient spark was operated with water electro spray flow rates 0.5 and 1 mL/min.

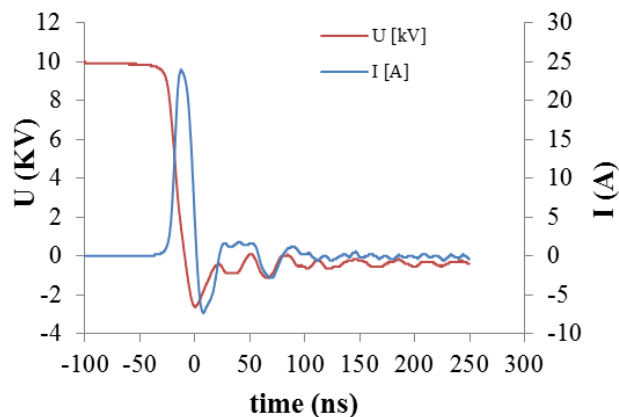


Fig. 2. The typical voltage and current pulse waveforms of the transient spark with water electro spray

b- RONS concentrations and pH in water and PAW

As shown in Fig. 3a, reactive oxygen and nitrogen species were detected in the control with the concentrations of 0.0, 0.0 and 235.6 μM respectively for hydrogen peroxide (H_2O_2), nitrite (NO_2^-) and nitrate (NO_3^-). The chemical analysis showed an increase of RONS concentrations in the plasma activated water. The concentrations of treated water are 449.6, 1075.1, 1578.9 μM , respectively, for H_2O_2 , NO_2^- and NO_3^- for PAW 0.5 and 317.2, 575.1, 848.2 μM , respectively, for hydrogen peroxide, nitrite and nitrate for PAW 1.0. Fig. 3b shows a slight difference of pH between the control and plasma activated waters.

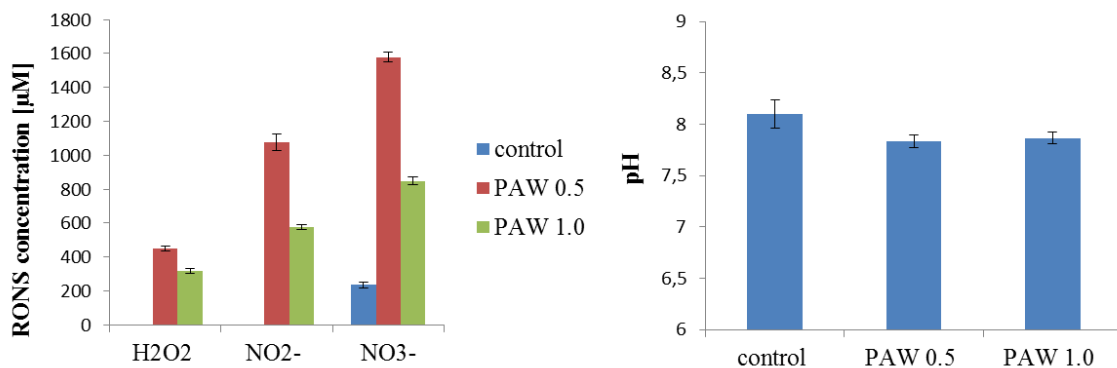


Fig. 3. a)- Hydrogen peroxide (H_2O_2), nitrite (NO_2^-), and nitrate (NO_3^-) concentrations in the PAW b)- pH measured in water before and after plasma treatment.

c- “*In vitro*” seed germination test (petri dishes)

Fig. 4a shows the results of the germination rate of maize after one day, in the figure the germination rate was 87.5, 100% and 95.8 for the Control, PAW 0.5, and PAW 1.0, respectively, and there was significant a difference between the control and PAW 0.5. The improvement effect of PAW was 14.28 and 9.52 %, respectively, for PAW 0.5 and PAW 1.0. Figs. 4b and 4c show the root and shoot length after 6 days of seed cultivation with PAW. The maximum enhancement 1.09 times and 1.37 times, respectively, for the root and shoot length is obtained with PAW 0.5. The fresh weight of seedling after 6 days was 302.7 and 321.3 mg for the control and PAW 0.5, respectively, as shown in Fig. 4d.

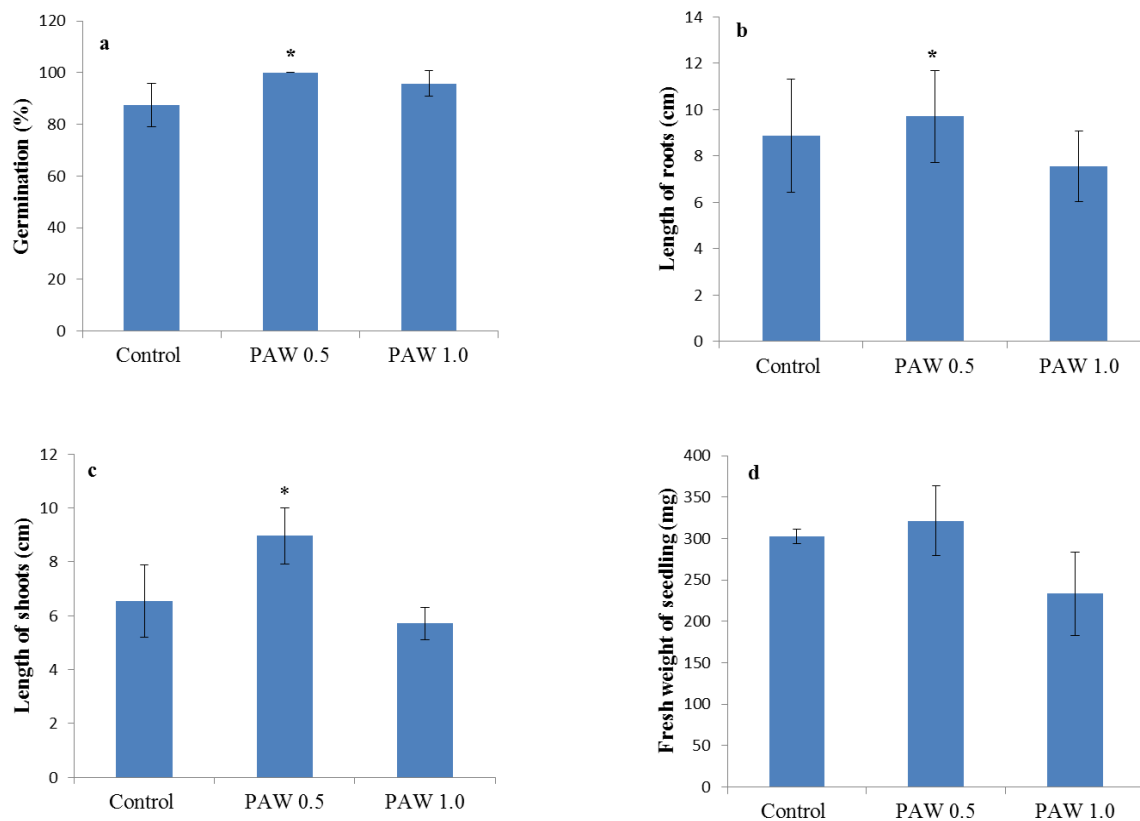


Fig. 4. a) Germination rate of maize after 1 day, b, c and d) root length, shoot length and fresh weight of seedling after 6 days of seed cultivation.

d- “*In vivo*” plant growth (sowed in the soil)

As can be seen in Fig. 5, the best plant growth enhancement results were obtained for the plants watered with PAW compared to control. The higher results have been reached with PAW 0.5 where the concentration of RONS was higher than in PAW 1.0. For instance the plants length for PAW 0.5 was 2.1, 1.8 and 1.3 times higher, respectively, on day 7th, 10th and 14th as compared to control.

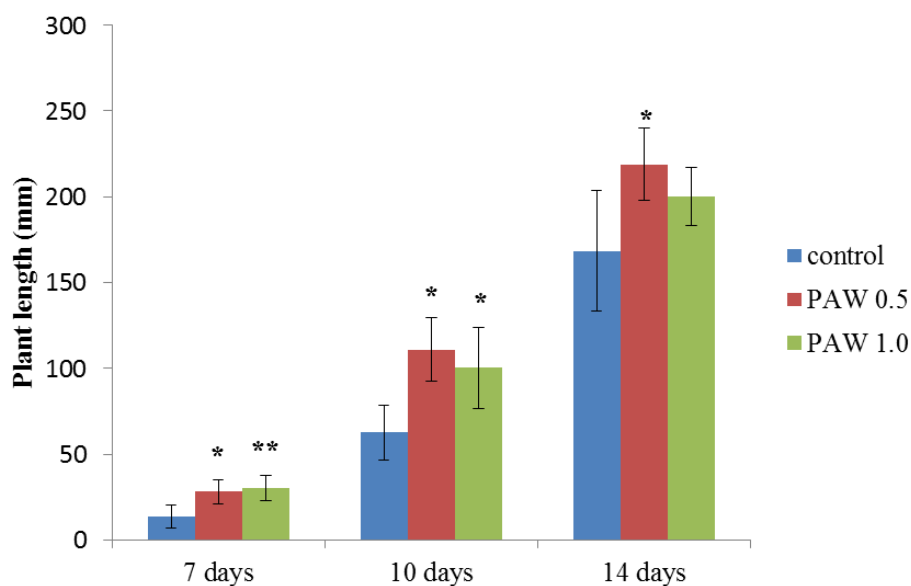


Fig. 5. Plant length of maize after 7-14 days of sowing in soil

4. Conclusion

The plasma activation of water treated by the transient spark discharge at ambient air and atmospheric pressure induces chemical changes in the water mostly dominated by production of hydrogen peroxide, nitrate and nitrite. We investigated the effects of PAW on maize seed germination and plant growth. The following conclusions are obtained:

The concentration of RONS depends of water flow rate during the plasma treatment.

PAW induces higher germination rate and enhances the plant length; the stronger effect was obtained for PAW 0.5 with higher RONS concentrations.

The long lifetime species in PAW are probably responsible for the growth enhancement.

5. Acknowledgements

This work was supported by Slovak Research and Development Agency APVV-17-0382, Slovak Grant Agency VEGA 1/0419/18 and FMFI extraordinary scholarship.

6. References

- [1] Machala Z et al., 2013 *Plasma Processes and Polymers* **10** 649-659.
- [2] Niemira B A et al., 2012 *Annu. Rev. Food Sci. Technol.* **3** 125-14.
- [3] Zahoranová A et al., 2018 *Plasma Chemistry and Plasma Processing* **38** 969-988.
- [4] Gomez-Ramirez A et al., 2017 *Sci Rep* **7** 5924.
- [5] Gautam D et al., 2017 *Food Science and Technology* **83** 127-131.
- [6] Sarinont T et al., 2017 *MRS Advances* **2** 995-1000.
- [7] Kucerova K et al., 2018 *Plasma Proc. Polym* doi.org/10.1002/ppap.201800131, accepted.

TETRAFLUOROMETHANE (CF₄) DECOMPOSITION USING ARGON/WATER PLASMA TORCH

M. Hlina, O. Zivny, A. Maslani, A. Serov, M. Hrabovsky

*Plasma Chemical Technologies Department, Institute of Plasma Physics AS CR, v.v.i,
Za Slovankou 1782/3, 182 00 Prague, Czech Republic
E-mail: hlina@ipp.cas.cz*

A DC plasma torch producing argon/water plasma with a very high enthalpy was used for the decomposition of tetrafluoromethane (CF₄). The effects of the power of the torch, the dilution of treated gas by N₂ and the addition of H₂ were investigated. The efficiency of the decomposition of CF₄ reaches high values within all conditions.

1. Introduction

The extreme growth of a semiconductor industry leads to the growth of the by-production of unwanted species such as perfluorinated compounds as well, therefore, an efficient way how to treat them has been studied. Perfluorinated compounds are due to their effective absorption of radiation over wide areas potent greenhouse gases with extremely long lifetime [1]. CF₄, which was chosen as a model substance, is a very stable molecule with very high bond strength. C–F bond is the strongest single bond in organic chemistry [2].

The combustion of perfluorinated compounds is probably the most developed method of their decomposition, however, thermal plasma carries high energy and is able to decompose CF₄ completely even without the addition of other gases convenient for the reactions leading to the decomposition [3]. Nonetheless, the recombination of CF₄ is possible then, so the addition of H₂ to the process was studied on this account as well.

2. Experimental

The simplified scheme of a plasma torch with DC supply used as the energy source for the decomposition of CF₄ is shown in Fig. 1. The plasma torch involves the combination of arc stabilization by gas (cathode part), where the cathode is protected against oxidation by Ar flow, followed by water stabilization of the arc. Water is injected tangentially to the arc chamber of the torch and forms a vortex that surrounds the electric arc. An anode is a water cooled rotating copper disc.

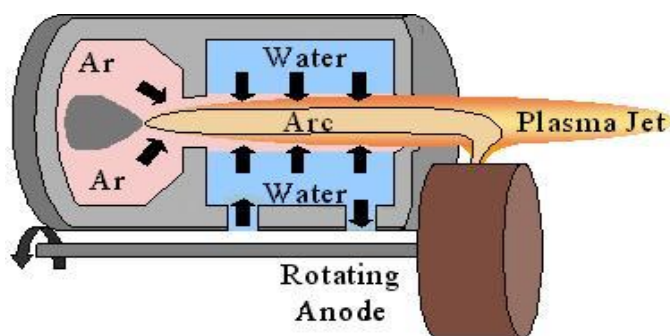


Fig. 1 Schema of the argon/water DC plasma torch.

Produced plasma reaches extreme values such as very high bulk temperature together with a low mass flow rate (typically around 0.3 g/s of H₂O + 0.2 g/s of Ar), however, due to combined stabilization, wide range of plasma properties can be adjusted [4]. The plasma torch is mounted to the side of a cylindrical reactor in a horizontal position. The reactor is made of stainless steel. The entering part of the reactor is 30 cm wide and 60 cm long. There is an intermediate water cooled part connecting the entering part and further tubing. The intermediate part is 25 cm wide and 30 cm long. Then, the flow

of produced gases enters stainless steel tubing equipped with a thermometer and a sodium hydroxide scrubber for HF trapping. Sampling for composition measurements is performed in the upper part of the scrubber. A quadrupole mass spectrometer Pfeiffer Vacuum Omnistar GSD 301 with direct inlet was used as a main gas analyzer. A freezing unit is placed between the mass spectrometer and the sampling probe to avoid water condensation and the damaging of the mass spectrometer.

3. Results and discussion

The arc power was set to 20 or 40 kW during experiments and CF₄ flow rates ranged from 0.5 to 10 standard litre per minute (slm). The temperatures of produced gases entering the scrubber were higher when a higher power was set up and due to endothermic characteristics of the decomposition process, even when the lower flow rates of reactants were set as well. Typical temperature values were 60 to 180 °C.

The rate of the decomposition of CF₄ (g/s) depends on the flow rate of CF₄ added to the process evidently, the higher flow rate, the higher rate of the decomposition, and higher power leads to higher rate of the decomposition as well. It can be seen in Fig. 2.

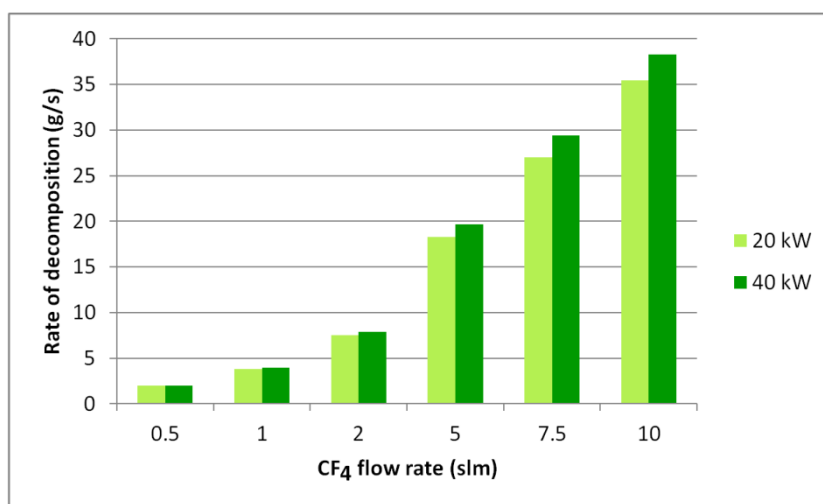


Fig. 2 Dependence of the amount of decomposed CF₄ on the flow rate of CF₄ and the plasma torch power.

The decomposition efficiency of CF₄ is defined by this equation:

$$EFF_{dec} = \frac{CF_4IN - CF_4OUT}{CF_4IN} \times 100 \quad (1)$$

, where CF₄IN and CF₄OUT are the amount of CF₄ added to the reactor and the amount of CF₄ leaving the reactor, respectively. Fig. 3 shows that complete decomposition occurs when the lowest CF₄ flow rate entered the reactor even for 20 kW. 40 kW was able to completely decompose the flow rates of CF₄ up to 5 slm, but even the highest flow rate of CF₄ was decomposed by efficiency over 90 and 97 % for the powers of 20 and 40 kW, respectively.

Such high values of decomposition efficiency compel to compare the energetic demand of the process with other experiments, ideally those using thermal plasma. The demand is high, but still comparable with other similar experimental utilities [5].

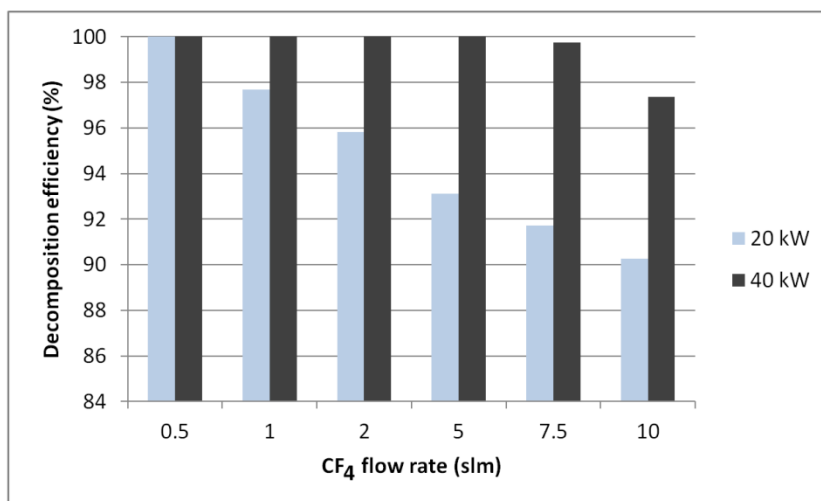


Fig. 3 Dependence of the decomposition efficiency on the flow rate of CF₄ and the plasma torch power.

Plasma is consisted of H₂O partially (dissociated and ionized) that participated in the decomposition reactions, however, decomposition efficiency can be enhanced by the addition of other reactive species such as H₂ for example:



The dependence of the decomposition efficiency on the flow rate of added H₂ and the plasma torch power is in the Fig. 4. The flow rate of CF₄ was set to 20 slm. Maximum decomposition efficiency is achieved for the H₂ flow rates of 15 and 20 slm that roughly matches with 1:1:1 ratio on the left side of equation 2.

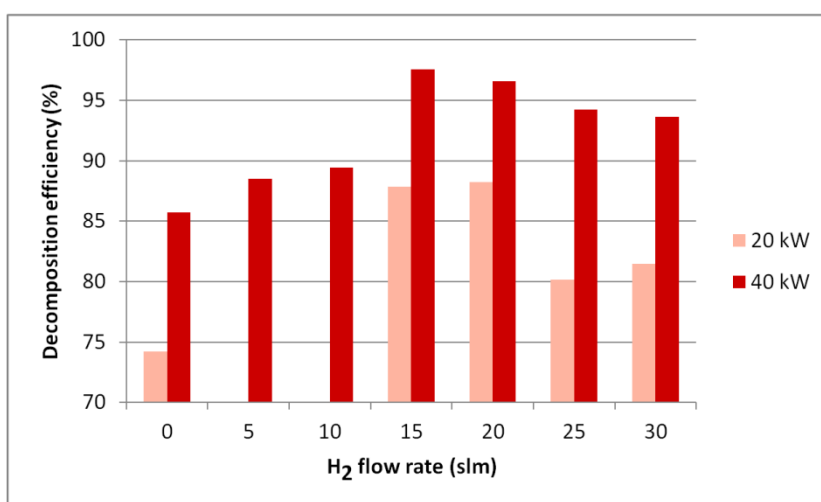


Fig. 4 Dependence of the decomposition efficiency on the flow rate of added H₂ and the plasma torch power. The flow rate of CF₄ was 20 slm.

The increase of the H₂ flow rate did not lead to the formation of CH₄, nevertheless, increasing H₂ concentration in gases leaving the reactor was observed.

CF₄ to be decomposed is usually diluted by other gases in real industry conditions. Such a dilution negatively influences the efficiency of decomposition due to the fact that the diluting gases carry away the energy needed for the decomposition process. The effects of the dilution up to 99 % (for the lowest flow rate of CF₄) are summarized in Fig. 5, 6.

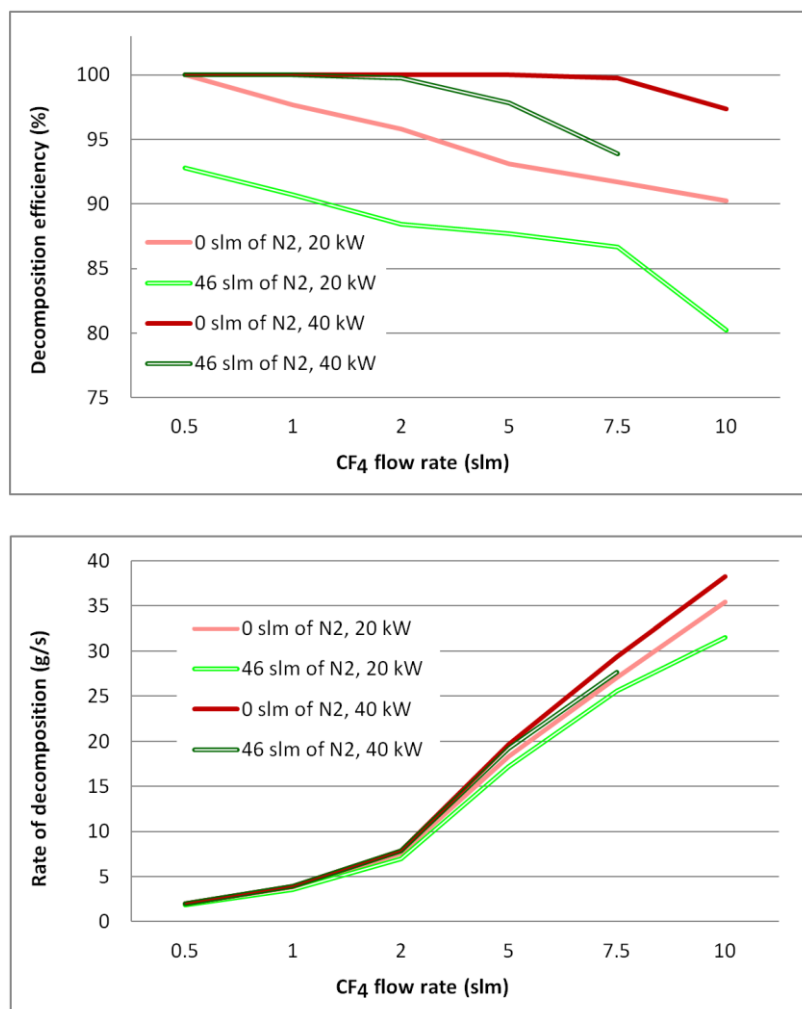


Fig. 5, 6 Dependences of the decomposition efficiency and the amount of decomposed CF₄ on the flow rate of decomposed CF₄ (0.5 – 10 slm) and added N₂ (approximately 46 slm) and the power of the torch.

It can be seen that the dilution by N₂ (46 slm) negatively influences the decomposition efficiency and the rate of decomposition. This influence is much more significant for lower power, however, the lowest calculated value of the decomposition efficiency was above 80 %.

This work was supported by the Czech Science Foundation under project No. GC17-10246J.

3. References

- [1] Kanno S, Tamata S and Kurokawa 2004 *American Chemical Society Meeting* 227.
- [2] O'Hagan D 2008 *Chemical Society Reviews* 37 2.
- [3] Oh S M and Park D W 2000 *Korean J. Chem. Eng.* 17 299.
- [4] Hrabovsky M, Kopecky V, Sember V, Kavka T, Chumak O, Konrad M 2006 *IEEE Trans. on Plasma Science* 34 1566.
- [5] Choi S, Lee H S, Kim S, et al. 2008 *1st International Conference on Microelectronics and Plasma Technology* 55 5.

SURFACE MODIFICATIONS OF POLYMER FOR VARIABLE APPLICATIONS

Zdenka Kolska¹, Monika Benkocka¹, Viktorie Neubertova¹, Vaclav Svorcik²,
Alena Reznickova², Katerina Kolarova²

¹Faculty of Science, J. E. Purkyně University in Ústí nad Labem, České mládeže 8, 400 96 Ústí nad Labem, Czech Republic

²Department of Solid State Engineering, Institute of Chemical Technology, Technická 5, 16628 Prague, Czech Republic

E-mail: zdenka.kolska@ujep.cz

Polymers are well known and useful for their excellent bulk properties. They are frequently employed in industry, biotechnology, tissue engineering studies, medicine, etc. However, the inert nature of most polymer surfaces may limit their use. Our research is focused to develop variable modification approaches to improve surface properties of different polymers for many applications. By these ways we are able to prepare new nanocomposite materials as a luminophores, surfaces with antimicrobial properties and/or surface for better adhesion and proliferation of cells.

1. Introduction

The inert nature of many polymers limits their wider usage, especially in e.g. tissue engineering. Surface chemistry, polarity, roughness and morphology strongly influence cell adhesion, proliferation and they are important for many potential applications of polymers in medicine and related fields [1-2]. Many modification techniques have been developed (not only by our team) to improve surface properties of polymers, like plasma treatment, UV-radiation, laser treatment, activation by chemical way with Piranha solutions and subsequent grafting of variable chemical compounds. These approaches are expected to provide new materials of excellent surface properties for potential usage in many fields, like optics, electronics, medicine, etc.

In our research we firstly activate the polymer surfaces and subsequently we grafted variable chemical compounds. The surface activation is provided by (i) plasma treatment, (ii) UV-radiation, (iii) laser treatment or (iv) by the so called Piranha solutions of different compositions. The preactivated surfaces are subsequently grafted with (i) borane clusters for luminescent properties or for antimicrobial activation [3-4], or by (ii) amino-acids or other chemical compound for better cell adhesion and proliferation [5-6].

Surface properties changed significantly and were studied using various methods, by X-ray photoelectron spectroscopy, electrokinetic analysis, goniometry, atomic force microscopy, BET analyses, UV-Vis spectroscopy, scanning electron microscopy, etc.. Representatives of unmodified and modified polymers were used antimicrobial properties and/or for *in vitro* study of adhesion and proliferation of cells.

2. Experimental

Materials

Many polymers in the form of foils supplied by Goodfellow Ltd., UK were used in this study: polyethyleneterephthalate (PET), cellulose, polytetrafluoroethylene (PTFE), polyvinyl fluoride (PVF), polyvinylidene fluoride (PVDF), polystyrene (PS), poly *L*-lactic acid (PLLA), high density polyethylene (HDPE) and low density polyethylene (LDPE). For subsequent grafting the following compounds were employed: 2-aminoethanol (OH-(CH₂)₂-NH₂), 2-aminoethanethiol (cysteamine, HS-(CH₂)₂-NH₂), ethanediamine (DIA), *D*-alanin, octenidine, different borane clusters, etc.

Used analytical methods

Properties of all samples, pristine polymers, polymers activated by the plasma, UV-radiation, laser treatment or Piranha solutions and/or subsequently grafted with tested chemical compounds were characterized using different methods. Surface chemistry was characterized by X-ray photoelectron spectroscopy, chemistry and polarity by electrokinetic analysis and by goniometry, roughness and

morphology by atomic force microscopy, scanning electron microscopy, surface area and porosity by BET and BJH analyses.

Selected materials were tested also for antimicrobial activity for *E. coli* and *S. Epidermidis* colony and for algae inhibition growth. Also tests for cell adhesion and proliferation were performed for selected samples.

3. Results and discussion

All of used method for characterizations confirmed the changes in surface chemistry, polarity, roughness, morphology, wettability, surface area and porosity before and after (i) surface activation by the plasma, UV-radiation, laser treatment or Piranha solutions and/or (ii) subsequent grafting with tested chemical compounds.

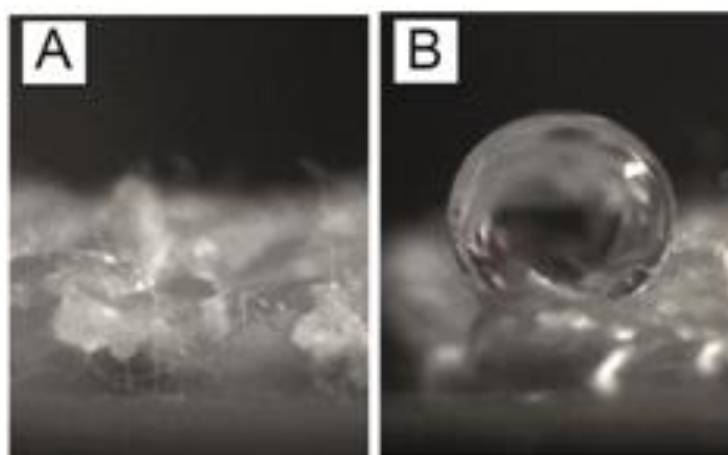


Fig. 1. Cellulose surface wettability before (A) and after (B) plasma treatment [7].

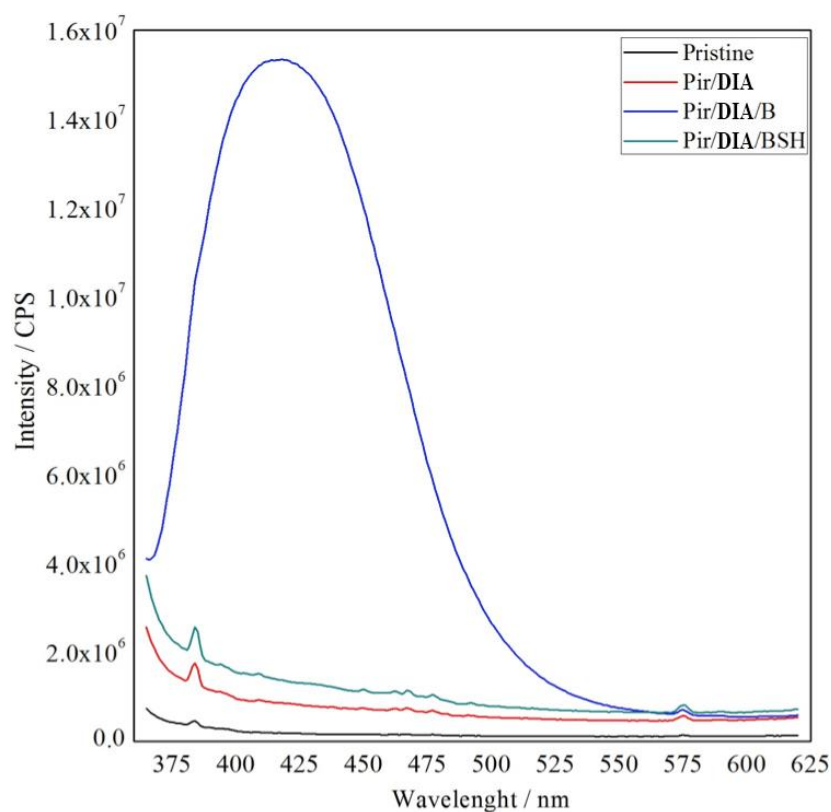


Fig. 2. UV-Vis spectra for polymer (unmodified = pristine, black line), activated by Piranha solution and grafted with amino-compound (DIA, red line) and subsequently with borane clusters (B, blue line) or (BSH, green line) [3,8].

Acknowledgement

This work was supported by the GACR project No. 17-00885S.

4. References

- [1] Townsend J S and Tiyard H T 1912 *Proc. of the Royal Society of London. Series A* **87** 357.
- [1] Reisinger B, Fahrner M, Frischauf I, Yakunin S, Svorcik V, Fiedorowicz H, Bartnik A, Romanin C, and Heitz J 2010 *Appl. Phys. A* **100** 511.
- [2] Goddard J M, Hotchkiss J H 2007 *Prog. Polym. Sci.* **32** 698.
- [3] Benkocká M, Lupínková S, Matoušek J, Kolářová K, Kolská Z 2018 *RSC Adv.* **8** 15001.
- [4] Benkocká M, Kolářová K, Matoušek J, Semerádtová A, Šícha V, Kolská Z 2018 *Appl. Surf. Sci.* **441** 120.
- [5] Kolska Z, Reznickova A, Nagyova M, Slepickova Kasalkova N, Sajdl P, Slepicka P and Svorcik V 2014 *Polym. Degrad. Stabil.* **101** 1.
- [6] Slepicka P, Siegel J, Lyutakov O, Slepickova K N, Kolska Z, Bacakova L, Svorcik V 2018 *Biotechnol. Adv.* **36(3)** 839.
- [7] Vosmanska V, Kolarova K, Rimpelova S, Svorcik V. 2014 *Cellulose* **21(4)** 2445.
- [8] Benkocká M, Lupínková S, Knapová T, Svorcik V, Matousek J, Kolska Z 2019 *Mater. Sci. Eng. C-Mater* (accepted 28.11.2018).

THE EFFECT OF LOW-TEMPERATURE PLASMA TREATMENT OF SEEDS OF SELECTED CROPS ON GERMINATION AND ITS BIOLOGICAL ACTIVITY IN EARLY GROWTH

Pavel Kriz^{1,4}, Andrea Bohata², Pavel Olsan³, Zbynek Havelka³, Monika Strejckova², Petr Bartos³, Petr Spatenka⁴

¹Department of Applied Physics and Technology, Faculty of Education, University of South Bohemia, 370 01, Ceske Budejovice, Czech Republic

²Department of Plant Production, Faculty of Agriculture, University of South Bohemia, 370 05, Ceske Budejovice, Czech Republic

³Department of Agricultural Machinery and Services, Faculty of Agriculture, University of South Bohemia, 370 05, Ceske Budejovice, Czech Republic

⁴SurfaceTreat, Inc., Na Lukach 669, CZ-511 01 Turnov, Czech Republic

E-mail: kriz@pf.jcu.cz

Plasma has been used to sterilize surfaces for medical purposes for many years. Currently the possibility of using plasma to sterilize surfaces of thermally sensitive materials, such as plastics or biological materials, has been studied intensively. In this field plasma discharge treatment can be used as an alternative method for Integrated Plant Protection. The effect of Gliding Arc plasma discharge on the germination rate, early growth and healthy status of treated seeds is presented. Barley, wheat, rapeseed and poppy were used as model crops.

1. Introduction

Plants may be endangered by pathogens transportable by seeds or pathogens that survive in the soil [1] at the beginning of cultivation. Conventional seed protection involves chemical treatment. However, this method has negative effects on other organisms and the environment. For this reason, scientists are focusing on the development of alternative ways of plant protection against diseases and pests [2]. Currently, the Integrated Pest Management Directive [3] is applied, which favors biological, physical and other non-chemical methods of treatment against chemical seed treatment methods. The Directive aims to provide effective protection in the form of alternative seed treatment against the harmful organism.

Low temperature plasma (LTP) is the source of many highly reactive particles such as reactive molecules of oxygen, ozone, nitrogen and/or hydroxyl radicals [4,5]. LTP is already being used in healthcare for sterilization of the medical devices or for disposal of hazardous biological material [6,7]. In the past few years, this technology has also been applied in agriculture. Some of the first applications concerning breaking the dormancy of *Chenopodia* seed after plasma treatment were published by Šerá [8,9]. The plasma discharge has also positive effect on the inhibition of spores on the surface and inside the seeds [10], on germination of seeds [11], or on disinfection of the fruit surface [12]. Hence, physical treatment by LTP could be intended as one of the alternative methods of seed protection.

This paper describes the effect of plasma treatment on the germination of selected model cereals and oil plants.

2. Experiment

The certified seed of four types of crops, including two cereals and two representatives of oilseeds were tested as model samples. Spring wheat (*Triticum aestivum* L.), variety Tercia from Selgen breeding company, JSC and spring barley (*Hordeum vulgare* L.), variety Bojos from the Limagrain Central Europe Cereals, LLC were used as the representatives of cereals. Winter rape (*Brassica napus* L.), variety Cortes from Selgen breeding company, JSC and spring poppy (*Papaver somniferum* L.), variety Opex from Oseva Pro, LLC were selected as the representatives of the oilseeds.

The seeds were treated by plasma discharge of the Gliding Arc type generated in the plasma head between two divergent stainless steel electrodes with a minimum gap of 3 mm. The plasma head was

powered by a high-voltage power supply with power input of 1.3 kW operating at frequency 50 Hz. The ignited discharge was blown out by a working gas flow from the space between the electrodes toward the treated sample. The compressed air was used as a carrier gas. The gas flow was maintained at 30 SCFH (35 SCFH = 1.00 Nm³/h) by the OMEGA FL-2008 rotameter. The distance between the edge of the plasma head and the treated surface of the seeds was set to 6 cm for cereals, or to 10 cm in case of oilseeds due to their higher thermal sensitivity.

The treatment process was performed out in a batch mode and the weight of one treated seed sample was 150 g. The treatment time of each dose was 4 minutes, for the poppy seed the treatment time was only 1 minutes. To ensure the homogeneity of the process, seeds were blended during the treatment in a mixing device with 50 rpm. Samples were randomly taken for further analysis after the treatment.

The germination of cereals and oilseeds was monitored every day within one week. The germination took place at (20±1) °C in the dark air-conditioned room. Several replicants were prepared, each of them with 100 seeds for every crop variant.

Furthermore, selected seed parameters such as, germination energy, root length index, sprout length index, plant height index, plant development index, or root count was monitored for all crops after seven days of the test. The germination energy is the ratio of the number of seeds that germinated in three days in the examined sample. Plant development indices were evaluated by specially created scales (see Table 1). At the same time, the percentage of healthy plants without the presence of fungal diseases was determined.

The germination and all observed early growth parameters were determined statistically for each replicant of every crop. The effect of plasma treatment on the variance of data was tested by the *F*-test of the equality of two variances at a significance level of 0.95, and Student's *t*-test at the same level of significance compared the arithmetic mean values of the treated and untreated variants of the same crop and their significant differences were determined. Critical *F*-test values for wheat and rape were 5.05, and 2.74 for barley and poppy. In the case of Student's *t*-test the critical values for wheat and rape were 2.23, and 2.06 for barley and poppy. An adequate *p*-value was specified for every statistical test.

Tab. 1. Indices scales for seed early growth monitoring.

index	0	1	2	3	4
grain root index	seed is not germinated	length of root is at the most as long as of seed	length of root is 2× longer than of seed	length of root is 3× longer than of seed	length of root is 4× longer than of seed
rapeseed root index	seed is not germinated	root length up to 1 cm	root length up to 1 - 2 cm	root length up to 2 – 2.5 cm	root length greater than 2.5 cm
grain sprout index	seed is not germinated	sprout is longer than 0.3 cm but does not reach the length of the grain	length of sprout is 2× longer than of grain	length of sprout is 3× longer than of grain	length of sprout is 4× longer than of grain
rapeseed sprout index	seed is not germinated	seed is germinated, sprout length up to 0.5 cm; cotyledons may appear	seed is up to 1.5 cm high; cotyledons are fully developed, sometimes still trapped	seed is 1.5 to 3 cm high; cotyledons are released	Seed is longer than 3 cm
poppy index	seed is not germinated	seed is swollen; root appears	root fully developed; cotyledons appears; seedling is	cotyledons rear up, sticked together; height up to 1 - 2 cm	seedling grows; cotyledons released; height greater than 2 cm

			crunching; up to 1 cm high		
--	--	--	----------------------------	--	--

3. Results and discussion

Tables 2 - 5 summarize the results of germination test of all crops in the first seven days. The germination of plasma treated and untreated seeds of wheat and rapeseed was comparable and it reached about 97 % - 100 %. Either it is slightly lower for wheat or slightly higher for rapeseed where it even reached 100 % for treated seed surprisingly. So the plasma treatment of these seeds did not lead to the significant reduction of germination.

Some different situation was achieved for poppy seed and for barley. Poppy seed germinated in three days comparably for both variant but after that almost no other seed germinated for treated variant while untreated seed germination still weakly increased. Significantly different germination ($p = 0.000$) was observed for barley seed, where germination of treated seeds was approx. 7 % lower than for untreated one.

Tab. 2. Germination of wheat (*Triticum aestivum* L.); NA – not available.

wheat	untreated		treated		F-test	t-test
	mean	SD	mean	SD	p-value	p-value
1 st day	0.0	0.0	0.0	0.0	NA	NA
2 nd day	93.3	0.3	94.0	0.4	0.301	0.426
3 rd day	97.3	0.6	97.3	0.4	0.193	1.000
4 th day	98.2	0.5	97.5	0.4	0.460	0.508
5 th day	98.5	0.4	97.7	0.4	0.359	0.362
6 th day	98.8	0.4	97.7	0.4	0.484	0.240
7 th day	98.8	0.4	97.7	0.4	0.484	0.240

Tab. 3. Germination of barley (*Hordeum vulgare* L.).

barley	untreated		treated		F-test	t-test
	mean	SD	mean	SD	p-value	p-value
1 st day	16.0	0.4	16.4	0.2	0.470	0.622
2 nd day	96.7	0.4	89.7	0.4	0.129	0.000
3 rd day	97.0	0.3	90.0	0.3	0.110	0.000
4 th day	97.0	0.5	91.3	0.3	0.390	0.000
5 th day	98.2	0.4	91.3	0.3	0.196	0.000
6 th day	98.3	0.3	91.4	0.3	0.111	0.000
7 th day	98.5	0.3	91.4	0.3	0.064	0.000

Tab. 4. Germination of rapeseed (*Brassica napus* L.).

rapeseed	untreated		treated		F-test	t-test
	mean	SD	mean	SD	p-value	p-value
1 st day	35.0	1.1	33.3	1.5	0.407	0.311
2 nd day	96.5	0.5	95.0	0.3	0.253	0.004
3 rd day	98.5	0.4	98.8	0.3	0.322	1.000
4 th day	98.8	0.3	99.3	0.3	0.409	0.787
5 th day	99.2	0.2	100.0	0.0	0.103	0.086
6 th day	99.3	0.2	100.0	0.0	0.071	0.401
7 th day	99.3	0.2	100.0	0.0	0.071	0.401

Tab. 5 Germination of poppy (*Papaver somniferum* L.).

poppy	untreated		treated		F-test	t-test
	mean	SD	mean	SD	p-value	p-value
1 st day	87.0	0.9	88.0	0.4	0.375	0.504
2 nd day	93.0	0.4	92.7	0.4	0.113	0.744
3 rd day	93.2	0.4	93.5	0.4	0.083	0.794
4 th day	95.0	0.2	93.6	0.4	0.003	0.036
5 th day	95.3	0.2	93.7	0.4	0.011	0.019
6 th day	95.3	0.2	93.7	0.4	0.011	0.019
7 th day	95.3	0.2	93.9	0.4	0.011	0.031

Similarly inconsistent results can be observed in test of early growth. Table 6 shows that early growth of wheat is not significantly influenced by plasma treatment and all tested parameters are almost the same. Hence development of wheat seed is not sensitive for plasma treatment neither negatively or positively. The results of rapeseed are very similar (Table 7). It is obvious the plasma does not affect rapeseed early growth, however some difference is worth noting in healthy plants ratio. The amount of healthy plants is slightly higher after plasma treatment although it is still not statistically significant ($p = 0.073$).

Tab. 6 Early growth monitoring for wheat (*Triticum aestivum* L.).

wheat	untreated		treated		F-test	t-test
	mean	SD	mean	SD	p-value	p-value
root count	3.91	0.01	3.91	0.01	0.166	0.845
root length index	3.91	0.01	3.92	0.01	0.266	0.794
sprout length index	3.88	0.01	3.89	0.01	0.222	0.750
healthy plants	87.0	0.6	87.0	0.6	0.399	1.000

Tab. 7 Early growth monitoring for rapeseed (*Brassica napus* L.).

rapeseed	untreated		treated		F-test	t-test
	mean	SD	mean	SD	p-value	p-value
root length index	3.975	0.008	3.975	0.008	0.459	1.000
plant height index	3.977	0.007	3.972	0.008	0.400	0.766
healthy plants	97.2	0.3	98.3	0.2	0.225	0.073

Entirely opposite effect of plasma treatment was determined for barley seed (Table 8). Only number of roots is the same for both variants. All other parameters are decreased despite that sprout length index is not statistically significant ($p = 0.385$). But it could be caused due the high dispersion of the data. Even also the healthy plants ratio is about 6 % lower for plasma treated variant in comparison to untreated one.

Tab. 8 Early growth monitoring for barley (*Hordeum vulgare* L.).

barley	untreated		treated		F-test	t-test
	mean	SD	mean	SD	p-value	p-value
root count	4.21	0.03	4.21	0.02	0.330	0.965
root length index	3.82	0.02	3.61	0.04	0.006	0.002
sprout length index	3.70	0.03	3.62	0.03	0.059	0.385
healthy plants	96.8	0.4	90.5	0.3	0.201	0.000

Poppy seed showed rather contradictory development (Table 9). The plant development index of plasma treated variant was significantly decreased ($p = 0.019$). The data dispersion was also significantly different ($p = 0.001$). This behaviour can be explained by inhomogeneity of plasma treatment due to combination of some factors, such as small size of poppy seeds, higher distance between seeds and the plasma jet or shorter treated time. On the contrary healthy plant amount of plasma treated variant is slightly higher than for untreated one and its dispersion is lower as well but the statistical differences are not significant ($p = 0.693$ t -test, $p = 0.465$ F -test).

Tab. 9 Early growth monitoring for poppy (*Papaver somniferum* L.).

poppy	untreated		treated		F -test	t -test
	mean	SD	mean	SD	p -value	p -value
plant development index	3.55	0.01	3.40	0.04	0.001	0.019
healthy plants	75.5	0.9	76.2	0.5	0.465	0.693

Seed treatment by low temperature plasma of Gliding Arc discharge device was used to all model plant crops treatment. The influence of plasma on seeds germination and seedlings development was assessed only in a laboratory study. The only narrow selection from wide range of process parameters was used for plasma treatment. The germination test proved that low temperature plasma treatment can influenced not only the seed germination of all crops but also the development of all seedlings. Such results were previously obtained also by many authors [11,13,14,15,16], but each of them reported a different time of exposure of tested seeds with the same or a distinct plasma treatment technology.

The germination rate is a very important factor for evaluations of all single plasma treatments but, in some cases, the differences between individual variants are sometimes negligible and can be quite insignificant. For this reason, scales of seedlings development have been established. This bioassay is based on the characterization of the development and of the growth rate of roots and sprouts from treated seeds. A similar evaluation of the plasma treatment influence was used by [17,18,19]. The length of seedlings was measured in mentioned studies. The use of other indexes can, however, easily evaluate the differences between plasma and control variants and give thus the results faster than by measuring the plant parts of each individual seed, namely because of the high amount of individuals in the variants. In our experiments, we have found that seedlings from plasma treated seeds often developed differently in comparison with untreated seeds. The differences were expressed using early growth indexes, which strongly depends on the kind of treated seed. Sometimes plasma did not affect development indexes at all (wheat) or it changed them very little (rapeseed). On the other hand plasma treatment can lead to contradictory results in case of poppy seeds treatment or even it has negative impact on early growth of barley seeds.

It is evident that each of model plant react to the same plasma treatment differently. Some of obtained results are very promising to support this physical method of treatment. Moreover previously published articles support an idea of plasma treatment of seeds. For example, it was reported that plasma can have a positive effect on the inactivation of surface-borne microorganisms [14] and such a treatment led to an increase of the water uptake of *Cynara scolymus* L. seeds, and thus it raised the germination speed and, consequently, the seedlings development [19,20]. Therefore it is necessary to find out optimal process parameters for each plant separately to obtain maximal positive effect to germination or early growth.

4. Conclusions

LTP can be used for physical seed treatment. It influences either germination, early growth and/or healthy status of seeds. Due to wide range of plasma source and process parameters it is necessary to specify the optimal conditions of the treatment. Various types of seeds respond to plasma exposition differently. Considerable differences were found not only between groups of crop (cereals or oilseeds) but even between crops from the same group of plants.

Positive effect of plasma treatment can also be used in practical applications, for example, in the production of high-quality seeds. In this field the elimination of pathogens from the seed surface, the

wettability enhancement or the seed surface treatment for adhesion improvement of various protective layers are typical applications.

Acknowledgment

The work has been supported by Technology Agency of the Czech Republic in the framework of project TE02000177. The work has also been supported by Grant Agency of University of South Bohemia (GAJU), project number 094/2016/Z.

5. References

- [1] Sinclair J B 1993 *Pest Management Science* **37** 15–19.
- [2] Rebek E J, Frank S D, Royer T A, and Bográn C E 2012 *InTech*, Rijeka, Croatia 171.
- [3] Decree 205/2012 Coll. [on-line 13.10.2017]. <https://www.zakonyprolidi.cz/cs/2012-205>
- [4] Bogaerts A 2009 *Spectrochim. Acta, Part B* **64** 1266-1279.
- [5] Bußler S, Herppich W B, Neugart S, Schreiner M, Ehlbeck J, Rohn S and Schlüter O 2015 *Food Res. Int.* **76** 132-141.
- [6] Moisan M, Barbeau J, Moreau S, Pelletier J, Tabrizian M, and Yahia L 2001 *Int. J. Pharm.* **226**, 1.
- [7] Lee K, Paek K, Ju W, and Lee Y 2006 *J. Microbiol.* **44** 269.
- [8] Sera B, Sery M, Stranak V, Spatenka P, and Tichy M 2009 *Plasma Sci. Technol.* **11** 750.
- [9] Sera B, Stranak V, Sery M, Tichy M, and Spatenka P 2008 *Plasma Sci. Technol.* **10** 506.
- [10] Basaran P, Basaran-Akqul N and Oksuz L 2008 *Food Microbiology* **25** (4) 626-632.
- [11] Sera B, Spatenka P, Sery M, Vrchetova N and Hruskova I 2010 *IEEE Transactions on Plasma Science* **38** 2963–2968.
- [12] Perni S, Liu D W, Shama G and Kong M G 2008 *Journal of Food Protect.* **71** 302-308.
- [13] Pawlat J, Starek A, Sujak A, Kwiatkowski M, Terebun P and Budzeń M 2018 *Plasma Process. Polym.* **15** 2.
- [14] Stepanova V, Slavicek P, Kelar J, Prasil J, Smekal M, Stupavska M, Jurmanova J and Cernak M 2018 *Plasma Process. Polym.* **15** 2.
- [15] Zivkovic S, Puač N, Giba Z, Grubisić D and Petrović Z LJ 2004 *Seed Sci. Technol.* **32** 693.
- [16] Mildaziene V, Pauzaite G, Naucienė Z, Malakauskiene A, Zukiene R, Januskaitiene I, Jakstas V, Ivanauskas L, Filatova I and Lyushkevich V 2018 *Plasma Process. Polym.* **15** 59.
- [17] Sera B, Sery M, Gavril B and Gajdova I 2018 *Plasma Chem. Plasma Process.* **37** 207.
- [18] Dobrin D, Magureanu M, Mandache N B, and Ionita M D 2015 *Food Sci. & Emerg. Technol.* **29** 225.
- [19] Hosseini S I, Mohsenimehr S, Hadian J, Ghorbanpour M and Shokri B 2018 *Phys. Plasmas.* **25** 013525.
- [20] Puac N, Gherardi M, and Shiratani M 2018 *Plasma Process. Polym.* **15** 1.

EFFECT OF PLASMA ACTIVATED WATER ON LETTUCE

Katarína Kučerová¹, Mária Henselová², Ľudmila Slovákovič²,
Michaela Saganová², Karol Hensel¹

¹*Faculty of Mathematics, Physics and Informatics, Comenius University, Bratislava, Slovakia*

²*Faculty of Natural Sciences, Comenius University, Bratislava, Slovakia*

E-mail: katarina.kucerova@fmph.uniba.sk

The effect of plasma activate water (PAW) generated by transient spark discharge on lettuce was investigated and compared with the effect of H₂O₂ and/or NO₃⁻ synthetic solutions. The growth parameters, number and quality of leaves, fresh and dry weight, photosynthetic pigment content, photosynthesis rate and activity of antioxidant enzymes in above-ground parts and roots were measured.

1. Introduction

Cold plasma has potential to be used in various agricultural applications [1]. The majority of the studies deal with direct plasma treatment of seed for germination and growth improvement [2-5]. Besides, indirect plasma treatment, i.e. effect of plasma activated water (PAW) on seeds and plants has recently become of interest [6,7].

The cold plasma generated by the atmospheric pressure air discharges is a source of various reactive oxygen and nitrogen species RONS, namely [•]OH, H₂O₂, NO₂⁻, NO₃⁻ that may dissolve in water and change its chemical composition while producing PAW. The long lived species in PAW (H₂O₂, NO₂⁻, NO₃⁻) may act as signal molecules in plant metabolism or be a source of nutrients. Encouraged by our previous results on wheat [8], we studied the effect of PAW irrigation on lettuce plants and compared it with effect of H₂O₂ and/or NO₃⁻ synthetic solutions to understand the role of individual reactive species in PAW.

2. Experimental

The PAW was generated by DC driven self-pulsing transient spark (TS) discharge at atmospheric pressure in air. The TS discharge was produced in a reactor with tap water circulating through the discharge zone. The experimental setup is depicted in Fig 1a. The plasma reactor consisted of high voltage needle and grounded plane inclined electrode in mutual distance ~ 1 cm. The discharge was driven by positive DC power supply (Technix RS20-R-1200) and its electrical characteristics were monitored by high voltage probe (Tektronix P6015A) and Rogowski type current probe (Pearson Electronics 2877) connected to an oscilloscope (Tektronix TDS 1012). The typical amplitude of the applied voltage used in our experiments was U_{app} = 16 kV, amplitude of the breakdown voltage U_{br} = 10 - 13 kV, frequency of the discharge current pulses f ~ 2 - 3 kHz, amplitude of current pulses I_{max} = 6 - 8 A and average discharge power was ~ 6 W. The characteristic voltage and current waveforms of the TS discharge are depicted in Fig. 1b.

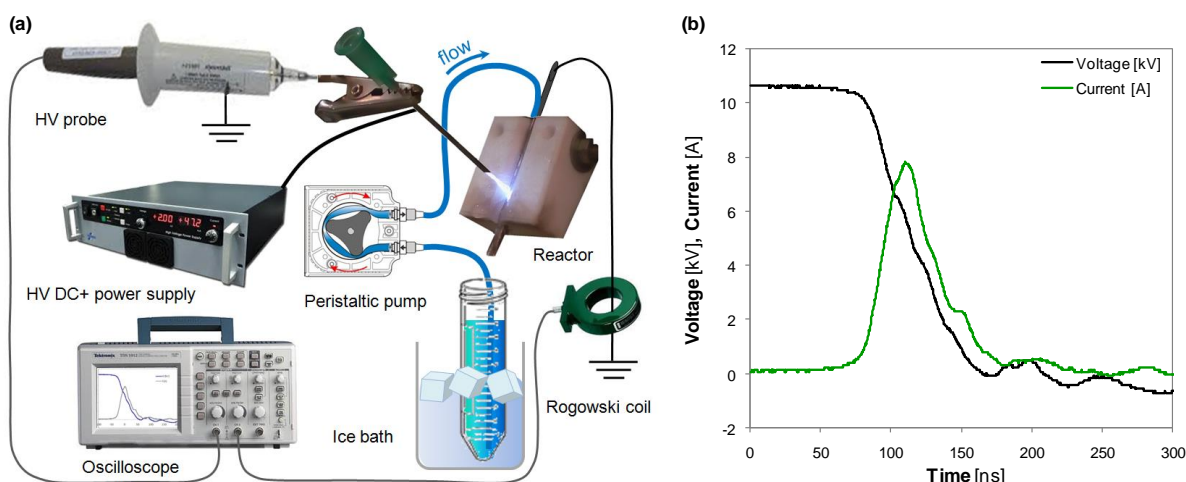


Fig. 1. The scheme of experimental setup (a) and characteristic voltage and current waveforms of self-pulsing transient spark (TS) discharge (b).

The PAW was produced from tap water as it is more physiological for plants than deionized water. Moreover tap water preserves the constant pH during the activation by discharge. The water flow rate through the discharge was 14 mL/min. The activation time was 1 min/mL (i.e. every 1 mL of water was activated for 1 min). The chemical composition of PAW was measured by established UV/Vis spectrophotometric methods to characterize the concentration of hydrogen peroxide H_2O_2 , nitrites NO_2^- and nitrates NO_3^- . The H_2O_2 concentration was determined by its reaction with titanyl ions of TiOSO_4 [9]. The NO_2^- and NO_3^- concentrations were determined by the commercial kit using Griess reagents (Cayman chemicals).

As a model plant was used lettuce (*Lactuca sativa* L. var. capitata cv. Král máje I). The plants were cultivated in pots with soil at controlled conditions: 24/18 °C (light-dark), light intensity $120 \mu\text{mol}\cdot\text{m}^{-2}\cdot\text{s}^{-1}$ and 12 hours photoperiod. Three weeks old plants were separated to one plant per pot and irrigated with PAW or with H_2O_2 and/or NaNO_3 synthetic solutions of various concentrations for 4 weeks (Tab. 1). The control plants were irrigated with tap water only.

Tab. 1. Concentration of H_2O_2 and NO_3^- in solutions used for plants irrigation

Name of solution	H_2O_2 [mM]	NO_3^- [mM]
Control - tap water	-	~ 0.02
PAW 1 min/mL	~ 0.42 ± 0.12	~ 0.85 ± 0.18
H_2O_2 I	0.4	-
H_2O_2 II	1.0	-
H_2O_2 III	10.0	-
NO_3^- I	-	0.85
NO_3^- II	-	2.0
NO_3^- III	-	20.0
Combination I	0.4	0.85
Combination II	10.0	20.0

The complex evaluation of growth parameters (number and quality of leaves, fresh and dry weight), photosynthetic pigments content, soluble protein content, rate of photosynthesis and activity of antioxidant enzymes of lettuce were performed. We also evaluated the visual appearance of the lettuce. The **fresh weight** of above-ground parts and roots of lettuce were measured separately. After drying at 60 °C packed into aluminum foil, also the **dry weight** were determined separately for above-ground parts and roots. The concentration of **photosynthetic pigments**, i.e. chlorophylls and carotenoids, in leaves were measured according to Lichtenthaler [10]. The measurement of **photosynthesis rate** was performed by infrared analyzer (CIRAS-2) based on rate of CO_2 exchange in dependence on light intensity (PAR - photosynthetic active radiation [$\mu\text{mol}\cdot\text{m}^{-2}\cdot\text{s}^{-1}$]). The **activity of antioxidant enzymes**,

namely superoxide dismutase (SOD), catalase (CAT), guaiacol peroxidase (G-POX) and ascorbate peroxidase (APX) were measured according to standardized assays and normalized to soluble protein content in sample. The data are presented as mean values \pm standard deviation. The one-way analysis of variance (ANOVA) and subsequent multiple range test by least significance difference method (LSD) were performed to judge the differences between groups. The different lower case letters represent significant difference at $p < 0.05$.

3. Results

To understand the effect of PAW on lettuce it is necessary to know its composition. In the presented experiments we irrigated the lettuce with 1 min/mL PAW. Immediately after the activation the PAW had pH ~ 7.5 and concentration of RONS were ~ 0.42 mM H_2O_2 , ~ 0.38 mM NO_2^- and ~ 0.85 mM NO_3^- . The effect of PAW on lettuce was compared with the effect of H_2O_2 and/or NO_3^- synthetic solutions. Several solutions of the same and also higher concentrations of H_2O_2 and/or NO_3^- than those in the PAW were prepared and used (Tab. 1).

Lettuce plants irrigated with PAW had similar number of leaves, but differed in leaf size compared to control (Fig. 2). Plants irrigated with synthetic solution containing NO_3^- had slightly higher number of green than senescent leaves compared to control. The high concentration of H_2O_2 negatively affected the appearance of plants. However, in combination with high NO_3^- concentration the positive effects of NO_3^- prevailed, as plants with proper nutrition can better handle stress.



Fig. 2. The representative lettuce plants irrigated with PAW (left) and with tap water (right).

The fresh and dry weight represents the amount of biomass produced by the plant. The dry weight of above-ground parts of lettuce irrigated with PAW was higher compared to control. With increasing concentrations of H_2O_2 and NO_3^- in synthetic solution also the dry weight of above-ground part of lettuce increased (Fig. 3). The NO_3^- is main source of nitrogen for plant production of proteins and nucleic acids, therefore can be consider as a main PAW component responsible for weight increase. On the other side, H_2O_2 can take part in weight increase through the process of plant tissue lignifications.

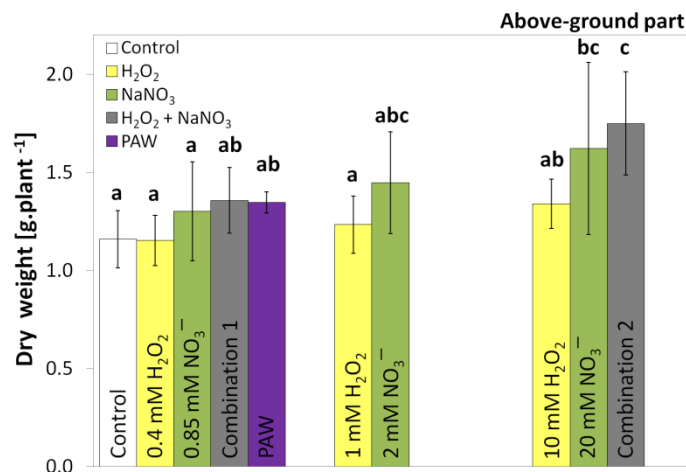


Fig. 3. Dry weight of above-ground part of lettuce irrigated with PAW, synthetic solutions of various concentration of H₂O₂ and/or NO₃⁻ and control irrigated with tap water.

Concentrations of photosynthetic pigments (chlorophylls and carotenoids) were higher in plants irrigated with PAW compared to control (Fig. 4). Chlorophylls are closely connected to photosynthesis rate, that PAW also positively affected (Fig. 5). The NO₃⁻ itself had stimulative effect on pigments, however H₂O₂ did not have. The NO₃⁻ as a source of nitrogen can contribute to the chlorophyll production in plants, unlike H₂O₂.

The activity of antioxidant enzymes reflects the level of oxidative stress that plant is facing. Here, we present the results of the SOD activity as one representative of the enzymes that are part of complex specialized system protecting plant cells against oxidation. SOD is intracellular antioxidant that decomposes O₂⁻ to H₂O₂. The PAW can be a potential source of oxidation as it contains various reactive oxygen species and free radicals. However, we measured decrease activity of antioxidant enzymes in PAW irrigated plants compared to control (Fig. 6). It indicates that PAW did not increase the oxidative stress in plant cells. To compare the effect with the effect of synthetic solutions, the activity of antioxidant enzymes decreased with NO₃⁻ concentration and increased with H₂O₂ concentration in above-ground part and root of lettuce (Fig. 6). The H₂O₂ can contribute to elevated oxidative stress by its oxido-reduction potential. However, the high oxidative stress could be also the result of nutrient deficit; therefore NO₃⁻ could decrease the antioxidant enzymes activity through its nutrient function.

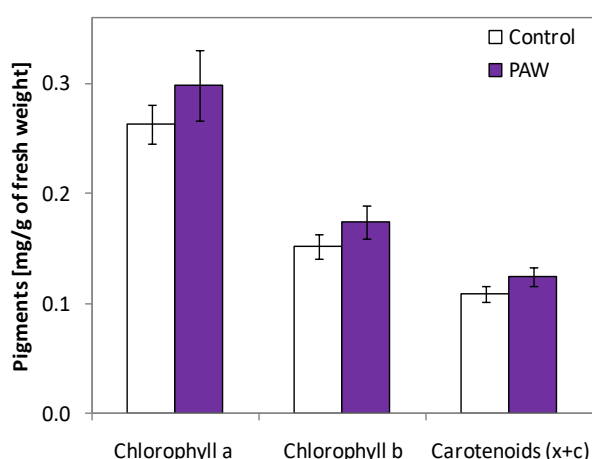


Fig. 4. Photosynthetic pigments content in above-ground parts of lettuce irrigated with PAW compared to control irrigated with tap water.

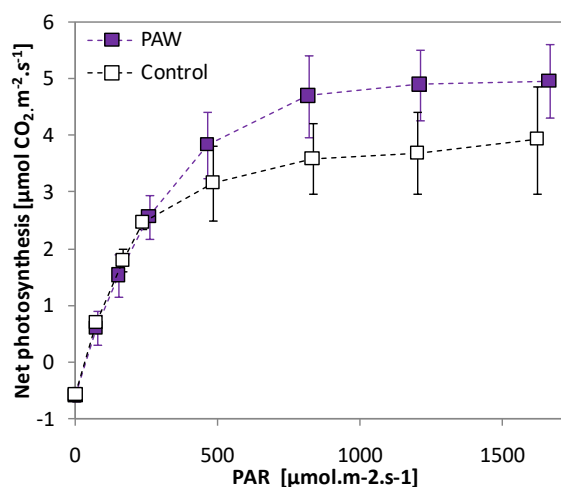


Fig. 5. Rate of photosynthesis in above-ground parts of lettuce irrigated with PAW compared to control irrigated with tap water.

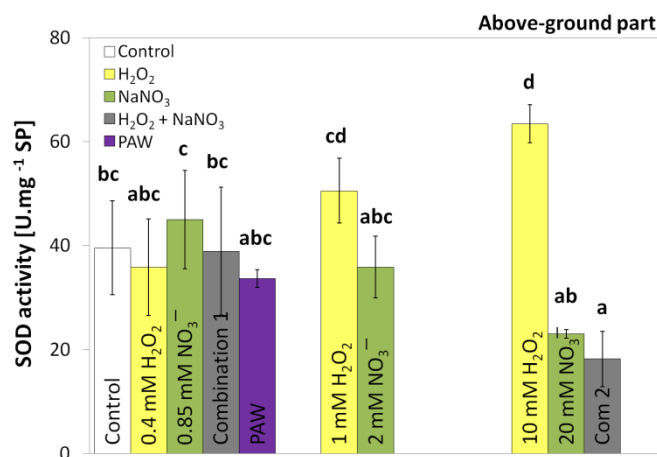


Fig. 6. Activity of superoxide dismutase (SOD) in the above-ground part of lettuce irrigated with PAW, synthetic solutions of various concentration of H₂O₂ and/or NO₃⁻ and control irrigated with tap water.

4. Conclusion

The effect of PAW generated by transient spark discharge on growth and important physiological and biochemical parameters of lettuce plants were investigated. The PAW effect was compared and correlated to the effect of H₂O₂ and/or NO₃⁻ synthetic solutions.

Lettuce irrigated with PAW in comparison to lettuce irrigated with chemically equivalent synthetic solution (Combination 1) had similar dry weight of above-ground part and root. However PAW induced higher photosynthetic pigment content, higher photosynthetic rate and lower activity of antioxidant enzymes.

The NO₃⁻ mainly contributed to the increase of dry weight, photosynthetic pigments content, rate of photosynthesis and overall better appearance of plants. The H₂O₂ induced increase of dry weight and antioxidant enzyme activity. Despite positive results obtained with the use of the PAW, the mechanism of its effect on plants is rather complex and need to be further studied.

This work was supported by Slovak Research and Development Agency APVV 0134-12 and APVV 17-0382 grants and Scientific Grant Agency VEGA 1/0419/18.

5. References

- [1] Puač N Gherardi M Shiratani M 2017 *Plasma Process Polym.* **15** e1700174.
- [2] Zhou Z Huang Y Yang S Chen W 2011 *Agric Sci.* **2** 23.
- [3] Henselová M Slovákova E Martinka M Zahoranová A 2012 *Biologia* **67** 490.
- [4] Zahoranová A Henselová M Hudecová D Kaliňáková B Kováčik D Medvecká V Černák M 2016 *Plasma Chem Plasma Process.* **36** 397.
- [5] Štěpánová V Slavíček P Kellar J Prášil J Smékal M Stupavská M Jurmanová J Černák M 2018 *Plasma Process Polym.* **15** e1700076.
- [6] Sivachandiran L Khacef A 2017 *RSC Adv.* **7** 1822.
- [7] Maniruzzaman M Sinclair A J Cahill D M Wang X Dai X J 2017 *Plasma Chem Plasma Process.* **37** 1393.
- [8] Kučerová K Henselová M Slovákova E Hensel K 2018 *Plasma Process Polym.* e1800131.
- [9] Eisenberg G M 1943 *Ind. Eng. Chem.* **15** 327.
- [10] Lichtenhaler H K 1987 *Methods Enzymol.* **148** 350.

DIAGNOSTICS OF THIN LAYERS ON Si SUBSTRATE BY CF-LIBS USING VUV AND UV-NIR SPECTRAL RANGES

A. Marín Roldán¹, S. Manzoor¹, J. Krištof^{1,2}, P. Veis¹

¹*Department of Experimental Physics, Faculty of Mathematics, Physics and Informatics, Comenius University, Mlynská dolina F2, 84248 Bratislava, Slovak Republic*

²*Graduate School of Science and Technology, Department of Optoelectronics and Nanostructure Science, Shizuoka University, Johoku, Hamamatsu, Shizuoka 432 8561, Japan*

E-mail: pavel.veis@fmph.uniba.sk

Calibration Free-Laser Induced Breakdown Spectroscopy (CF-LIBS) is a well-established method for the elemental analyses. As it can be seen in the literature, it is usually performed in the UV-NIR (230–975 nm) spectral range. Although, some elements have problems to be detected and quantified by this method in this classical spectral range. Thus, enlarging the spectral range until the VUV part (114–295 nm), allow to add more suitable points (related to spectral lines) to the Saha-Boltzmann plot, leading to a more precise electron evaluation temperature and subsequently, to a more precise quantification. In this work silicon has been selected as substrate for thin layers analysis as it has several spectral lines ranging from VUV to NIR. A MoS₂/Si nanosheets sample has been used as an example of thin layer material for the analysis. VUV and UV-NIR LIBS measurements have been simultaneously performed using a vacuum chamber filled with helium (13 mbar) and two different spectrometers.

1. Introduction

Laser induced breakdown spectroscopy (LIBS) technique is commonly used for the characterization of materials [1-4]. The detection and quantification of light elements by CF-LIBS is sometimes challenging because most of their spectral lines appear in the vacuum UV (VUV) range (from 115 nm to 200 nm) [1, 5-7]. The main goal of this work is to prove the clear advantage of using VUV and UV-NIR simultaneously for CF-LIBS measurements. For this reason, a pure silicon sample has been selected for performing the measurements as silicon is easily detectable in both VUV and UV-NIR spectral ranges and could be used as a substrate for the deposition and analysis of thin film materials [5, 8]. The enlargement of the spectral range becomes crucial for the improvement in the electron temperature (T_e) evaluation leading a more accurate quantification of Mo, S and Si by CF-LIBS method.

2. Experiment

Molecule of oxygen strongly absorbs in the VUV spectral range (< 200 nm). For this reason, all the measurements were performed in a vacuum chamber under 13 mbar helium atmosphere. A Q-switched Nd:YAG laser operating at the 4th harmonic (266 nm, CFR, Quantel, 80 mJ) has been used. A quartz lens (175 mm) focused the laser beam onto the surface of the sample through a quartz window of the vacuum chamber. Two spectrometers were used simultaneously: Echelle spectrometer (ME5000, Andor Technology, resolution = 4000, range 230–975 nm) coupled with an iCCD camera (iStar DH743, Andor Technology, temporal resolution 5 ns) and VUV spectrometer (234/32VM, McPherson, $f = 20$ cm, 2400 grooves/mm, resolution = 1000, range 114–295 nm) coupled with the iCCD camera (iStarDH740 for VUV–UV, Andor technology, temporal resolution 5 ns). The emission light from the plasma was focused by an MgF₂ lens (75 mm) to the optical fibre in the case of echelle spectrometer, and through an MgF₂ window from the side of the plasma plume in the case of VUV spectrometer. Both spectrometers have been calibrated: the echelle spectrometer by using black/grey body radiation method and the branching ratio method for the VUV range in both spectrometers [9]. Delay (D) and the gate width (G) times were set to 500 ns (D=G). The employed experimental setup has been already described in detail at [1].

3. Results and discussion

A simultaneous VUV and broadband UV-NIR LIBS analysis of a silicon substrate has been performed in this work. Silicon substrate has been chosen because it could be used for the deposition of thin layers with elements with problems to be measure in the classical UV-NIR range, helping with the evaluation of the electron temperature. As it was mentioned before, the many spectral lines can be in the SB plot, the better accuracy of the slope (related to the T_e).

Figure 1a shows the experimental LIBS spectra for pure Si substrate and MoS₂ nanosheets deposited on Si substrate ranging from 115 to 138 nm and from 177.5 to 188 nm. The first region shows the most intense S I-II lines. Some Si II-III lines are also observable in the first region in addition to N I and H I lines. The second region of the spectra shows S I and Si I-II lines. All these spectral lines are observable in the VUV spectral range, and can help for the T_e evaluation from the SB plot.

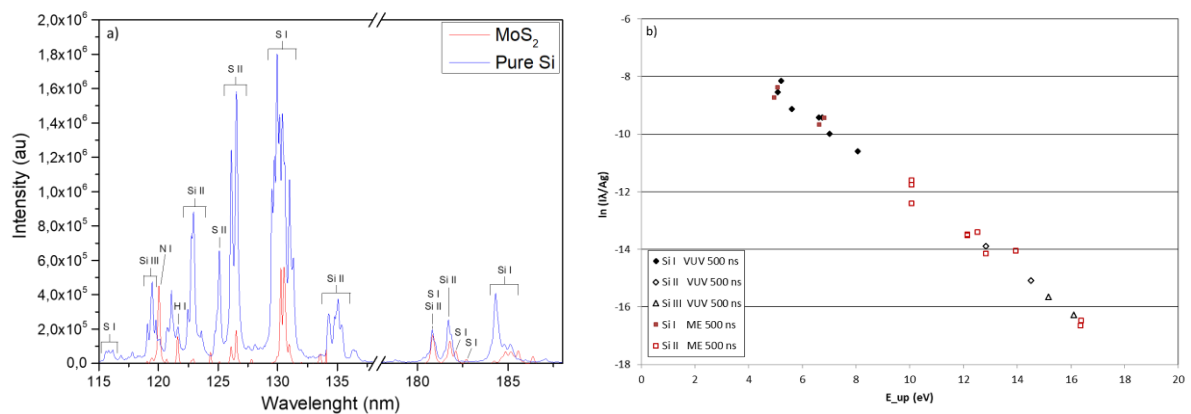


Figure 1: (a) experimental LIBS spectra for pure Si substrate and MoS₂ nanosheets deposited on Si substrate, (b) Boltzmann plot for Si I-III spectral lines (D=G: 500 ns).

Applying the Saha-Boltzmann (SB) equation, the electron temperature of the plasma can be obtained. Each point in the Boltzmann plot is obtained from the SB equation using the intensity of the spectral lines, considered as the area under the peak in the spectra. The n_e is calculated using the Stark broadening of H _{α} line at 656 nm, being $1.95 \cdot 10^{16} \text{ cm}^{-3}$ for 500 ns. Performing a linear fitting in the Boltzmann plot of all Si I-III in the same graph, the electron temperature is obtained from the inverse of the slope (see Figure 1b for delay 500 ns). For this reason, the higher number of experimental spectral lines included in the Boltzmann plot implies that a more precise temperature evaluation can be made from its slope. The obtained T_e from the fitting of the Boltzmann plot was 1.37 eV for 500 ns. As it can be observed, the Local Thermodynamic Equilibrium is reached at 500 ns.

This work characterizes the plasma plume of silicon substrate by simultaneous VUV and classical UV-NIR LIBS analysis. The enlargement of the LIBS spectral range down to VUV range improves the precision of the T_e evaluation, crucial for the quantification of the rest of the elements contained in the sample, and sometimes not so detectable in the classical UV-NIR range, such as Mo and S.

4. Conclusion

This work presents an improvement in the evaluation of the T_e from Boltzmann plot for a silicon substrate, using simultaneous VUV and UV-NIR measurements at 500 ns under helium atmosphere. The improvement lye on the enlargement of the spectral range, providing access to more suitable spectral lines for the Boltzmann plot. The extended range of spectral lines decreases the error in the fitting and subsequently in the slope (T_e evaluation). This is crucial for the quantification of elements by CF-LIBS method.

Acknowledgments:

This work would like to thank the support by the Slovak Research and Development Agency (APVV-15-0641 and APVV-16-0612) and by the Scientific Grant Agency of the Slovak Republic (VEGA-1/0903/17).

5. References

- [1] P. Veis, A. Marin-Roldan, and J. Kristof, "Simultaneous vacuum UV and broadband UV-NIR plasma spectroscopy to improve the LIBS analysis of light elements," *Plasma Sources Science & Technology*, vol. 27, p. 18, Sep 2018.
- [2] R. Fantoni, S. Almaviva, L. Caneve, F. Colao, A. M. Popov, and G. Maddaluno, "Development of Calibration-Free Laser-Induced-Breakdown-Spectroscopy based techniques for deposited layers diagnostics on ITER-like tiles," *Spectrochimica Acta Part B-Atomic Spectroscopy*, vol. 87, pp. 153-160, Sep 2013.
- [3] A. Marin-Roldan, S. Manzoor, S. Moncayo, F. Navarro-Villoslada, R. C. Izquierdo-Hornillos, and J. O. Caceres, "Determination of the postmortem interval by Laser Induced Breakdown Spectroscopy using swine skeletal muscles," *Spectrochimica Acta Part B-Atomic Spectroscopy*, vol. 88, pp. 186-191, Oct 2013.
- [4] F. S. Marzizarani, S. Z. Shoursheini, H. S. Mahdavi, and S. Pashaei-Adl, "The effect of self absorption correction using internal reference on determining heavy metals concentration by laser induced breakdown spectroscopy," *Int. J. Opt. Photonics*, vol. 8, pp. 23-30, 2014.
- [5] J. Bockova, A. M. Roldan, J. Yu, and P. Veis, "Potential use of surface-assisted LIBS or determination of strontium in wines," *Applied Optics*, vol. 57, pp. 8272-8278, Oct 2018.
- [6] M. A. Khater, J. T. Costello, and E. T. Kennedy, "Optimization of the emission characteristics of laser-produced steel plasmas in the vacuum ultraviolet: Significant improvements in carbon detection limits," *Applied Spectroscopy*, vol. 56, pp. 970-983, Aug 2002.
- [7] M. A. Khater, "Features of VUV emission from plasmas generated by nanosecond laser pulses in air," *Optics and Laser Technology*, vol. 54, pp. 315-320, Dec 2013.
- [8] A. M. Roldán, J. Krištof, and P. Veis, "Simultaneous VUV and UV-NIR CF-LIBS Analysis of Light Elements " in *WDS'18 Proceedings of Contributed Papers: Part III - Physics*, Prague, 2018, pp. 162-167.
- [9] A. M. Daltrini and M. Machida, "Modified branching ratio method for absolute intensity calibration in VUV spectroscopy," *Ieee Transactions on Plasma Science*, vol. 33, pp. 1961-1967, Dec 2005.

ANTIBACTERIAL EFFECTS OF PLASMA ACTIVATED WATER COUPLED WITH ELECTROPORATION

Robin Mentheour¹, Barbora Tarabová¹, Zdenko Machala¹

¹*Faculty of Mathematics, Physics and Informatics, Comenius University, Bratislava, Slovakia*

E-mail: robin.mentheour@gmail.com

Transient Spark discharge operated in atmospheric air with water electrospray, with nanosecond high energy pulses, demonstrated strong and fast antimicrobial effects when bacteria are directly exposed to the discharge. It can also activate water which keeps its antibacterial properties for a few hours after plasma treatment. However, the antibacterial effects of plasma activated water are weaker than in direct exposure. Preliminary experiments shown here are focused to understanding the role of strong electric fields in the overall plasma action to bacterial cells and the effect of electroporation induced by high electric field in combination with chemical effect of plasma activated water.

1. Introduction

Operative bacterial infections are still responsible for several thousand deaths per year, requiring the use of disposable medical equipment or more reliable sterilization. Transient Spark (TS) discharge induced by several kilovolts drop during 20 ns and driving a current of several tens of amperes demonstrated a significant antibacterial effect when combined with water electrospray [1]. However, the mechanisms have not been clearly identified yet. Previously we observed significant bacteria reduction after direct exposure of *E. coli* bacterial suspension to TS with electrospray compared to only Plasma Activated Water (PAW) produced by TS with water electrospray. The difference between the results may be due to short lived reactive oxygen and nitrogen species (RONS)..., which were clearly identified as having strong antibacterial effects. However, their extremely short life time limits their detection in the liquid and makes their storage impossible, which also limits a precise estimate of their effects. On the other hand, the electric field between the electrode and the grounded metal grid is a good candidate to explain the enhanced antibacterial effects. Cell membrane can be affected by electric field that may open pores in the cell membrane. This is also known as the electroporation or electro-permeabilization and can lead to antibacterial effects [2, 3]. As electroporation also increases the cell porosity, it allows penetration of RONS produced by the TS plasma into the cell interior. This may result in a high cell mortality compared to the separated effects of the electric fields or the PAW.

Applying a high electric field moves the lipid bilayer of the cell membrane; which expands the membrane pore size depending on the length of the pulse and the electric field intensity. Pulses of several millisecond with a voltage of several tens of millivolts across the cell membrane can pass the membrane. For exposures of seconds to several minutes with tens of kV/m the small molecules can pass through the membrane pores and even damage the cell. If the position of lipids, organized in a double layer, is modified a little, the effect is reversible. Otherwise the lipids cannot be rearranged, the effect is then irreversible and leads to cell death.

Electro-sprayed droplet size and evaporation increase the complexity of the investigation because plasma species are created from the air plasma and from the water. The objective of the experiments presented here is to investigate the effect of the increase of the antibacterial effect due to PAW when it is coupled with the electroporation.

2. Materials and methods

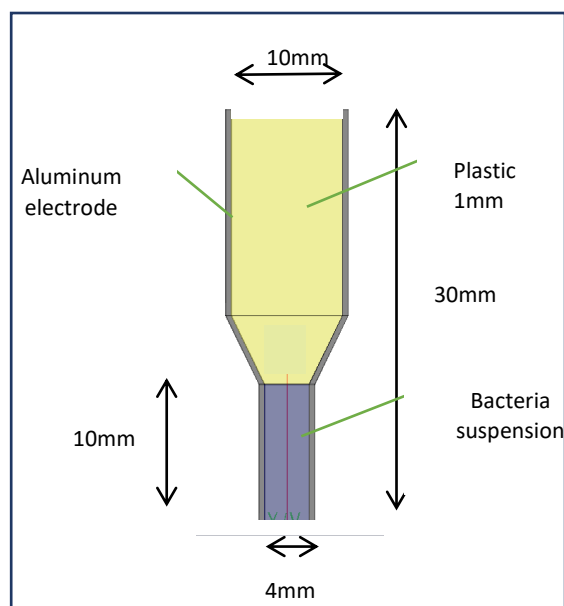
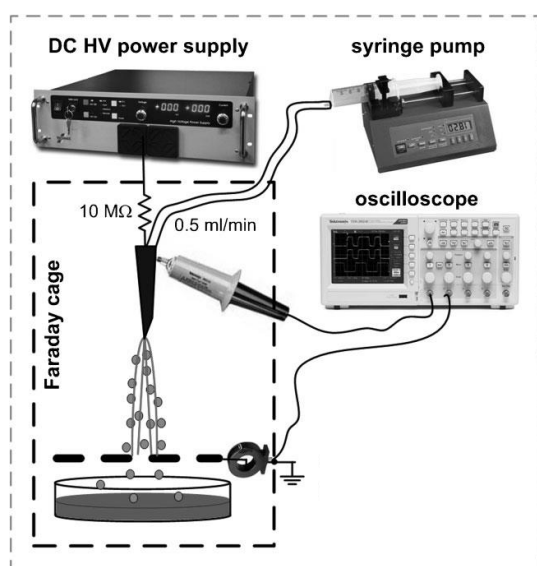


Figure 1. The experimental setup with electro-spray of water. [4] Figure 2. Electroporation cuvette

Plasma Activated Water (PAW) is created by electro-spraying of deionized water (DW) through the cold plasma produced by TS discharge. DW is injected by a syringe pump with the flow rate 0.5 ml/min through a high voltage (HV) needle placed 1 cm from a metal grid grounded through a 1Ω resistor. We trigger the discharge only when DW drops from the needle. The PAW is collected in a small Petri dish placed below the grid. When HV is applied on the needle, it induces the TS discharge between the needle and the grounded grid. Voltage is measured by a HV probe Tektronix P6015A connected to the needle. Maximum voltage was 15 kV (experiment A-B) and 17 kV (exp C. Current is measured as the voltage drop across 1Ω resistance between the grid and the ground, typically with pulses of 27-30 A (experiment A-B) or 40 A (experiment C). The electrical parameters were recorded by oscilloscope Tektronix TDS 2024C that measured the frequency of the discharge pulses, which is related to the applied voltage. This frequency is maintained at 1 kHz (± 200 Hz). We used a $10\text{ M}\Omega$ protection resistor on the output of the HV generator.

experiment	Pulse Voltage (kV)	Pulse Current (A)	Pulse Length	Pulse Frequency	EP time treatment	Number of Pulses
A	7.8(DW) 4.2(PAW)	-	$1\mu\text{s}$	100Hz	1s	100
B	2.0	5.0	200ns	1kHz	90s	90 000
C	1.0	4.5	200ns	1kHz	90s	90 000

Table 1 : Electroporation experiment parameters

Electroporation (EP) experiment: 1ml of bacterial suspension ($300\mu\text{l}$) in DW (3ml) or PAW is collected and is placed into the sterile electroporation cuvette. It is a 30 mm high plastic cuvette filled only in the bottom narrowed area (10 mm high and 10 mm wide),where is a 4 mm gap between two aluminum tape electrodes. The cuvette is decontaminated before use by being fully filled by isopropyl alcohol and a overnight UV exposure. Cuvette was flushed off thrice by sterilized DW, a pipette

mixing was done. Pulses with 100Hz frequency and 1 μ s duration are applied from *Behlke HTS 301-03GSM* pulser driven by a 5V pulse signal from Textronix AFG2021 generator. The pulsed voltage was measured by a HV probe Tektronix P6015A.

For the electroporation alone, Table 1 the output voltage of the HV power supply was fixed at 10kV but due to the certain conductivity of the suspension we measured 7. V

max value and 300ns time constant of the voltage decay for the suspension bacteria-DW,

For the combined effect at 7 min after mixing PAW with bacteria, the pulses are applied on the cuvette electrodes. and 4.2kV and 100 ns time constant for the mixture PAW-bacteria, respectively.

Three experimental settings were tested:

A-experiment was carried out with a 1 μ s pulses on the cuvette input electrode: we applied 100 pulses at a 100 Hz frequency. However, considering the experiment duration we fixed only the generator voltage at 10 kV and the voltage measured on the cuvette depended of the media, 4.5 kV for PAW and 8 kV for DW.

The B-experiment was carried out with a 200 ns, 2 kV pulses ($E=5kV/cm$) and 11 A on the cuvette input electrode applied during 90 s at a 1 kHz frequency. Pulse duration is limited by water conductivity that limits the voltage drop at 200-500 ns exponential decay time constant and the minimum length of pulses 200 ns allowed by the pulser.

C-experiment:200 ns, 1 kV pulses, 5 A, 1 kHz. The only difference between C and B-experiment was the exposure time on PAW and the pulses were only 1 kV in C. PAW is produced at a frequency of 1 kHz but for a higher voltage of 17 kV and current 40 A. The gap between electrodes for preparing PAW was still around of 1 cm, nevertheless a little difference can explain these different characteristics.

Bacteria decontamination. Gram-negative bacteria *Escherichia coli* (ATCC 25922) of initial population 10^7 colony forming units (CFU) per ml were growing in the overnight culture in a sterile liquid nutrient (Lauria-Bertani broth, Biolab) at 37°C. Bactericidal effects were observed on bacterial suspension prepared from overnight culture diluted in DW or PAW (i.e. DW treated by TS discharge with electrospray). Immediately after treatment by PAW or EP bacteria were diluted by serial 10-fold dilutions and cultivated on agar plates (Lauria-Bertani agar, Biolab) during 22-24h at 37°C. Then CFUs were counted on the Petri dishes. Usually 4-6 agar plates from each sample was used to be statistically relevant. Replication of the experiments must be done to confirm our results to be statistically stronger.

3. Results and discussion

Fig. 3 shows the survival of *E. coli* bacteria treated by electroporation, PAW or their combined effect, for three experiments A, B and C with different pulse parameters described above. All three experiments are processed with 4 different sample types : control, electroporation (EP) only, PAW only, and PAW combined with EP. EP only slightly reduced the bacterial population (52% survived in A, all bacteria dead in B so it is close to 0%, and 33% in C) against respectively 83% in A 49% in B and 73% in C. PAW effect is even stronger - in A incubation time was 15 min and only 1.4% of bacteria survived, i.e. 1.9 log reduction, in B this effect was the strongest : 0.06% survived (3.2 log reduction) due to longer incubation time (30 min) and a probable overheated sample of the electroporation with PAW due to the high current. In C we observed 15% of survived (0.8 log reduction). The combined effect was the strongest, as we expected: combination of EP and PAW seems to facilitate penetration of PAW RONS into the cells through cell membrane pores induced by EP. The effect correlates with the PAW only effect (in all A, B, C - please note that in B, the combined EP+PAW effect resulted in complete bacteria sterilization, confirming the dominant effect of RONS in bacterial killing by air plasmas, in agreement with [1]-[2]-[3] and other authors. Moreover, electroporation has an effect on the bacteria survival and it is increased by the effect of PAW. Pulse duration, electric fields magnitude, number of pulses are known to increase the number of cells pores

and pore size and consequently increase the effect of antibacterial agent RONS molecules present in PAW.

Temperature may have increased in all experiments, but we measured it only for the C experiment by EU 620-2343 thermometer. Temperature 52 °C was measured in PAW+EP case and 34°C in EP+DW case. Temperature 52 °C might have negatively affected the bacterial population. Viscosity of the bilayer is already changing at such temperatures, which may influence the reaction of the bacteria with PAW and the electric field, making them more fragile. A cooling system should be added in the future. Nevertheless, a more precise temperature measurement, with a thermal camera, will be done to be sure of the temperature during the experiments

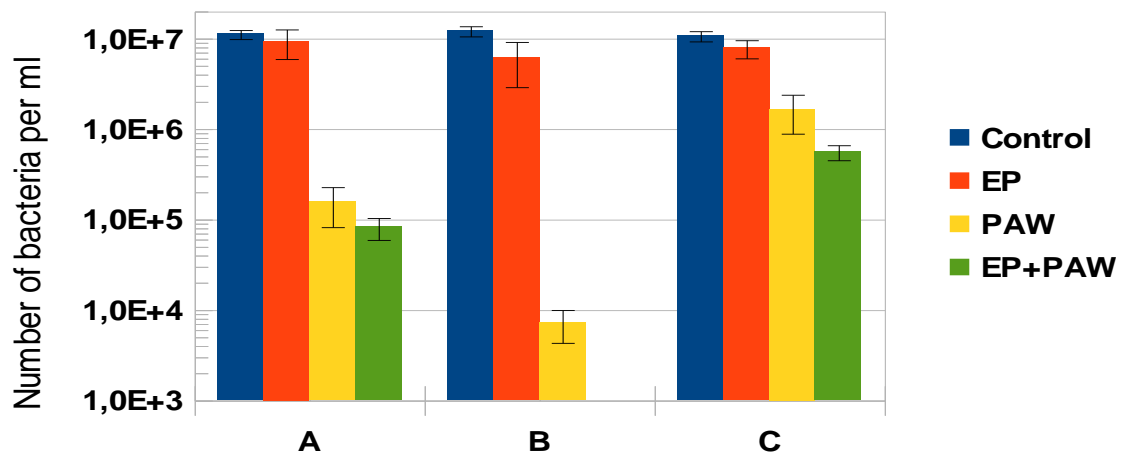


Figure 3: Number of bacteria per ml after treatment. (A) 100 pulses of 10 kV at 100Hz. PAW prepared by TS 15kV, 1 kHz, 27 A, 15min incubation; (B) 2kV, 5A, 200ns pulses at 1kHz operated during 90s, PAW prepared by TS 15 kV, 1 kHz, 27A, 30min incubation;(C)1 kV,4.5 A, 200ns pulses at 1kHz during 90s,PAW 17 kV, 1 kHz, 40 A,15min incubation. Error bars are expressed as the standard deviation of bacteria colonies grown on multiple petri dishes.

We used DW for preparation of bacterial suspensions to increase the pulse length, limit the voltage drops which trigger high currents that increase temperature. However, since DW has very low osmotic pressure, it affects the bacteria cells to increase their volume to balance the low osmotic pressure of their environment. This phenomenon could make the cell membranes more fragile and could influence bacterial survival, especially after combination of EP and PAW.

4. Conclusion

In simple preliminary experiments, we tested the effects of electroporation, PAW and their combination on *E. coli* bacterial cells. The electroporation seems to contribute to the antibacterial effect induced by PAW: the combined EP+PAW effect resulted in the strongest bacterial reduction during our experiments. The issue of short-lived species also remains to be discussed for plasma application. However, local temperature increases in some experiments could be in part responsible of antibacterial effect. Further experiments and/or simulations are needed to set up better experiments to identify the dominant effects of plasma induced bacterial inactivation, as well as the coupling of different agents in bacterial decontamination.

5. Acknowledgment

This work was supported by Faculty of Mathematics, Physics and Informatics, Comenius University, Bratislava, and Slovak Research and Development Agency APVV-17-0382.

6. References

- [1] Machala Z, Chládeková L and Pelach M 2010 *J Phys D Appl Phys* **43** 222001
- [2] Machala Z, Tarabová B, Hensel K, Spetlikova E, Sikurova L and Lukeš P 2013 *Plasma Process. Polym.* **10** 649–659
- [3] Machala Z, Tarabová B, Sersenova D, Janda M, Hensel K 2018 *J Phys D: Appl Phys* **52** 034002
- [4] Dower W J, Miller J F and Ragsdale C W. 1988 *Nucleic Acids Research* 16
- [5] Kolb J F and Stacey 2012 in *Plasma for bio-decontamination, medicine and food security*, NATO Science for Peace and Security Series A - Chemistry and Biology, Springer, eds: Z. Machala, K. Hensel, Y. Akishev. 365
- [6] P.E. HERNANDEZ & P. LOPEZ-LORENZO 1984 *Journal of Applied Bacteriology* **56**, 175-177

NON THERMAL PLASMA APPLICATION IN ANTIMICROBIAL CONDITIONING OF MUNICIPAL WASTES

Joanna Pawłat¹, Katarzyna Wolny-Koładka²,
Piotr Terebun¹, Michał Kwiatkowski¹

¹Laboratory of Plasma Technology and Renewable Energy, Institute of Electrical Engineering and Electrotechnologies, Electrical Engineering and Computer Science Faculty, Lublin University of Technology, Nadbystrzycka 38A, 20-618 Lublin, Poland

²Department of Microbiology, Faculty of Agriculture and Economics, University of Agriculture in Krakow, al. Mickiewicza 24/28, 30-059 Kraków, Poland
E-mail: askmik@hotmail.com

Conditioning of municipal wastes for fuel production is a troublesome process. This work describes antimicrobial potential of non thermal plasma against microbial contamination of wastes. However, achieved results are promising, there is a need to conduct further research and optimize proposed process in order to limit re-growth of the microorganisms.

1. Introduction

The antimicrobial properties of low-temperature plasma are investigated by many research groups for medicine, food industry and environmental technology [1-9]. Reactive forms of oxygen and nitrogen, and UV radiation are the factors having impact on the stability of cells. In this study small scale experiment of mixed municipal waste hygienisation was conducted in order to prepare safe and stable [10] waste material used for the production of refuse-derived fuel (RDF).

2. Experimental set-up

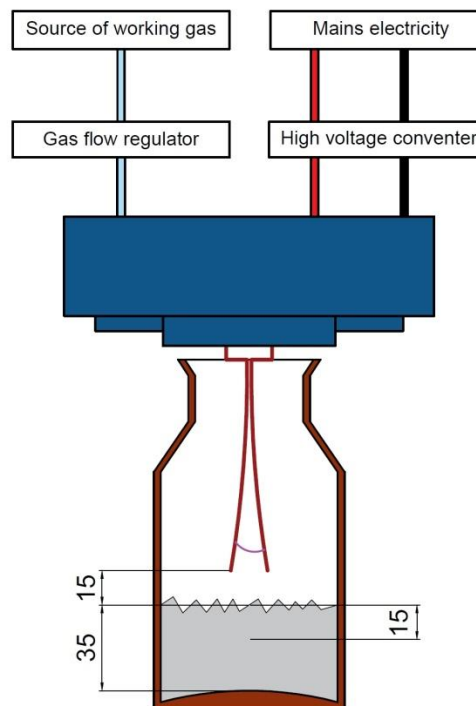


Fig. 1. Experimental setup.

Gliding arc discharge reactor with 10.4 cm long copper electrodes was selected for the tests. Distance between the electrodes in the upper part was 5 cm and in the lower part 3 mm.

Parameters of power supply system for plasma reactor were as follows: 52 VA of apparent power drawn from power grid, 612 V of RMS voltage (secondary windings) and 50 Hz frequency (primary and secondary windings of the transformer).

The real mixed waste was received from “EKO-BIOMASA” Sp. z o.o. and divided onto 15 g roughly equalized portions. Non-thermal plasma was used for waste treatment for 5, 10 and 15 min in triplicates. The air flow in the reactor was 480 l/h.

3. Results and conclusions

Plasma treated samples (no. 1-5 min, no.2-10 min, no.3-15 min) and sample no.4 as untreated control were investigated. It could be observed that the number of vegetative bacteria greatly exceeded the number of endospores. A strong decreasing trend with the treatment time was observed in the case of the number of vegetative bacteria (Fig.2) but the results are not clear for endospores (Fig. 3) capable of producing protective structures in order to survive under unfavorable conditions.

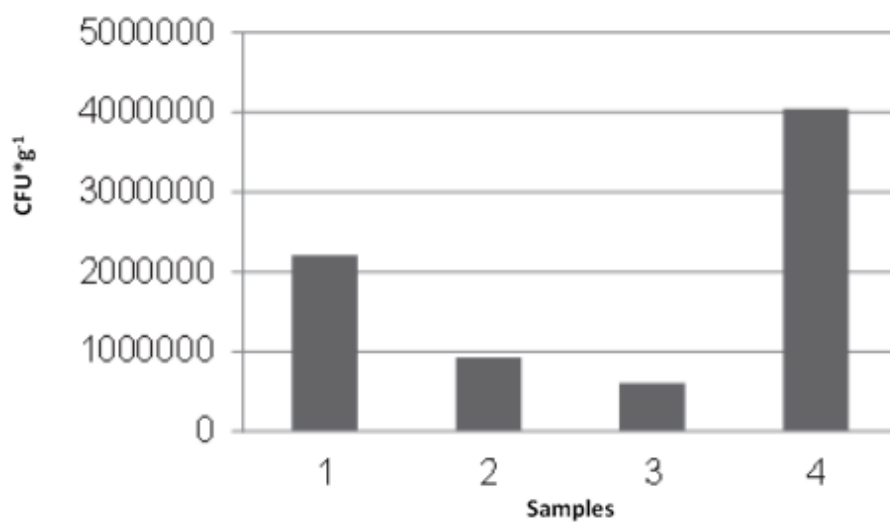


Fig. 2. Number of vegetative bacteria.

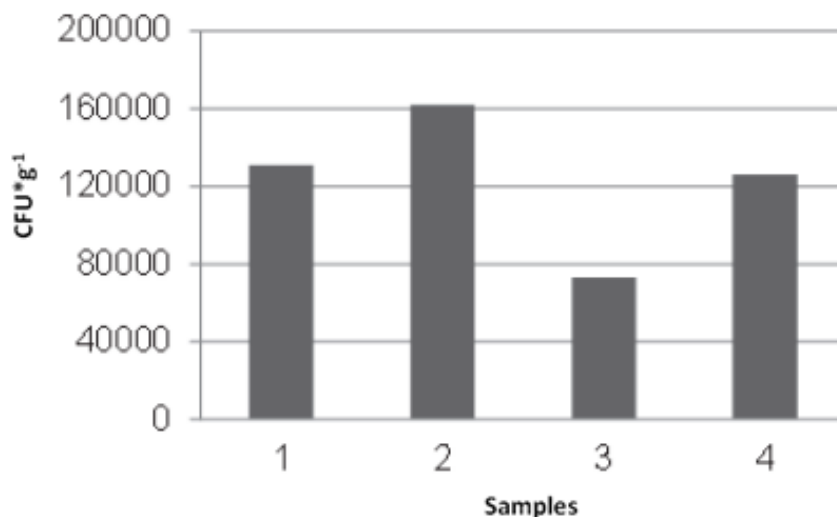


Fig. 3. Number of endospores.

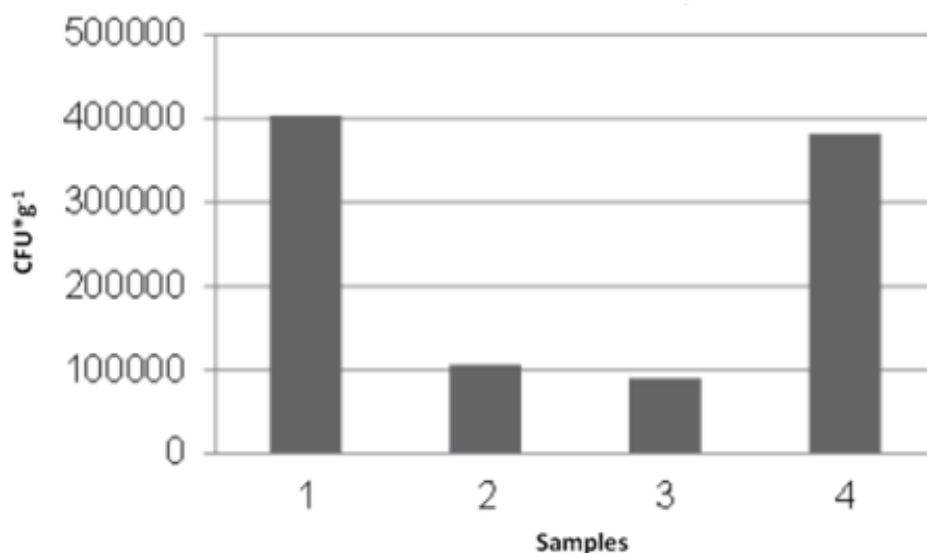


Fig. 3. Number of mold fungi.

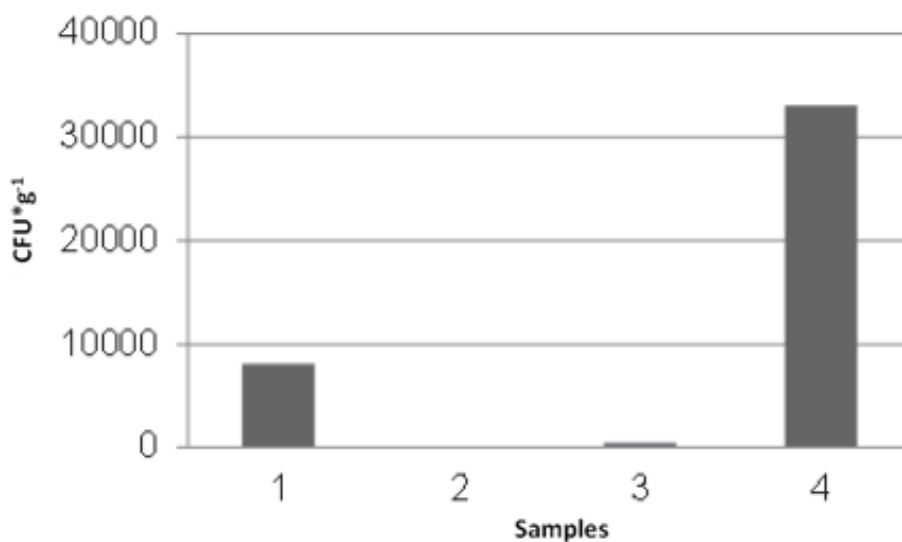


Fig. 4. Number of *Salmonella* spp.

After short 5 min. plasma treatment, the number of mold fungi (Fig. 3) and *Salmonella* bacteria (Fig.4) increased in comparison to the control group, which was strongly undesirable stimulation effect. Longer treatment time caused decrease of colony count and effectively decontaminated the wastes from *Salmonella* bacteria. However, the process requires further optimization. Plasma reveals rather surface activity and it is recommended to implement mechanical mixing of the waste to increase the efficiency of the hygienisation in the future.

4. References

- [1] Hensel K, Kučerová K, Tarabová B, Janda M, Machala Z, Sano K, Mihai C, Gorgan L, Jijie R, Pohoata V, Topala I 2015 *Biointerphases* **10(2)** 029515.
- [2] Lukes P, Dolezalova E, Sisrova I, Clupek M 2014 *Plasma Sources Sci. Technol.* **23(1)** 015019.
- [3] Moisan M, Barbeau J, Crevier M, Pelletier J, Philip N, Saoudi B 2002 *Pure Appl. Chem.* **74(3)**, 349.
- [4] Bourke P, Ziuzina D, Han L, Cullen P, Gilmore B 2017 *J Appl Microbiol* **123** 308.
- [5] Brisset J-L, Pawłat J 2016 *Plasma Chem. Plasma Process.* **36(2)** 355.

- [6] Czernichowski A, Lesueur H 1991 *First Annual INEL, Idaho Falls, USA*.
- [7] Pawłat J, Diatczyk J, Stryczewska H 2011 *Przegląd Elektrotechniczny* **87(1)** 245–248.
- [8] Dasan B, Onal-Ulusoy B, Pawłat J, Diatczyk J, Sen Y, Mutlu M 2017 *Food Bioproc Tech* **10(4)**, 650.
- [9] Pawłat J, Kwiatkowski M, Terebun P, Murakami T 2016 *IEEE Trans. Plasma Sci.* **44(3)** 314.
- [10] Wolny-Koładka K, Malinowski M, Sikora A, Szymonik K, Pelczar G, Wawrzyniak-Turek K 2016 *Infrastruktura i Ekologia Terenów Wiejskich* **4(1)** 1099.

ANTIBACTERIAL PROPERTIES OF SILVER COATED REGENERATED CELLULOSE

Petr Slepíčka¹, Nikola Slepíčková Kasálková¹, Kateřina Kolářová¹, Zdeňka Kolská², Václav Švorčík¹

¹Department of Solid State Engineering, The University of Chemistry and Technology, 166 28 Prague, Czech Republic

²Faculty of Science, University of J. E. Purkyně, 40096, Ústí nad Labem, Czech Republic
E-mail: vaclav.svorcik@vscht.cz

The paper is focused on study and characterization of surface properties of regenerated cellulose after plasma modification, which significantly affects its physical and chemical properties such as wettability, surface chemistry and surface morphology. Depending on the selected parameters, such as the plasma exposure time of the substrate, its aging and the sputtering time with silver, the modified material was studied different analytical methods. An ablation of the substrate was determined gravimetrically. Changes in surface roughness were detected by atomic force microscopy (AFM) and chemical changes were studied with X-ray spectroscopy (XPS). Silver nanolayers were sputtered on the activated substrate and the antibacterial properties of these layers were studied. We have determined the aging period for surface treated under different exposure time, gravimetric analysis has show almost linear mass loss with plasma treatment time, the surface roughness slightly decreases with the action of plasma. XPS analysis revealed that the oxygen content increased due to higher reactivity of the surface of the modified cellulose. Antibacterial tests has shown that the silver layer sputtered on plasma activated regenerated cellulose significantly reduces the colonies of both *E. coli* and *S. epidermidis*.

1. Introduction

The inert nature of many polymers limits their wider usage, especially in e.g. tissue engineering. Antibacterial surface can be considered as surface of any material in form of foil, granule or other specific type that can be used to limit the growth and proliferation of bacteria. Bacteria adaptation on the surface and its adhesion with subsequent multiplication on the surfaces of substrate materials can lead to a wide range of health problems, where expensive cleaning processes have to be applied. Bacterial may exist in several environments, such as water-cooled air conditioning systems and have been also considered as the key factor in the phenomenon of bio corrosion, when cells attached to e.g. metallic surfaces lead to the corrosion of the material through the formation of 'pits' [1-5].

Herein we present simple but effective approach for construction on antibacterial cellulose surface based on combination of plasma exposure followed by simple sputtering of thin silver nanolayer. This technique can be also realized in large-fabrication scale in industry, and was confirmed to be successful for inhibition of both *Gram-positive* and *Gram-negative* bacteria, even after very short time of interaction.

2. Experimental

Materials and modification

For experiments we used regenerated cellulose foils (thickness 90 μm , density 1.44 g cm^{-3}) supplied by Goodfellow Ltd. The samples were modified in diode plasma discharge on Balzers SCD 050 device for 10-240 s, using DC Ar plasma (gas purity was 99.997 %, power 8 W). Process parameters were: Ar flow 0.3 l s^{-1} , Ar pressure 10 Pa, electrode area 48 cm^2 , the inter-electrode distance of 50 mm, chamber volume 1000 cm^3 . The silver layers were deposited from a silver target (99.999 %) by means of diode sputtering technique (BAL-TEC SCD 050 device). Typical sputtering conditions were: room temperature (RT), time 30 and 150 s, total argon pressure of about 5 Pa, electrode distance of 50 mm and current of 20 mA.

Used analytical methods

Contact angle was determined by goniometry using static water drop method. The measurements of the advancing water contact angle (error 5 %) were performed using glycerol and distilled water on 6

different positions using the Surface Energy Evaluation System (SEE System, Advex Instruments, Czech Republic). Surface morphology was examined with atomic force microscope Dimension ICON (Bruker Corp.). ScanAsyst mode in air was used for determination. Silicon Tip on Nitride Lever SCANASYST-AIR with spring constant 0.4 N/m was used. The presence of the oxygen and carbon in the modified cellulose surface layer was proved by X-ray photoelectron spectroscopy (XPS). An Omicron Nanotechnology ESCAProbeP spectrometer was used. The X-ray source was monochromated at 1486.7 eV and the measurement was performed with the step of 0.05 eV. The antimicrobial activity of the prepared cellulose samples was determined by a drop test using *Gram-negative* bacteria *Escherichia coli* (*E. coli*, DBM 3138) and *Gram-positive* bacteria *Staphylococcus epidermidis* (*S. epidermidis*, DBM 2179). The bacterial strain of *E. coli* was diluted with fresh PBS buffer at a concentration of 2×10^4 cells per mL. The bacterial strain of *S. epidermidis* was diluted with fresh PBS buffer at a concentration of 4×10^4 cells per mL. The plates were incubated for 24 hours at RT for *E. coli* and 37°C for *S. epidermidis*. The number of colonies of both cultures was evaluated by colony forming units (CFU), each sample being performed in a triplet.

3. Results and conclusion

We have determined the aging time for plasma treated regenerated cellulose for different times of exposure and power 8 W to be 336 hours. Gravimetric study of the effect of plasma exposure revealed the decrease of cellulose weight due to the ablation to be almost 1.2 % for plasma power 8 W and 240 s. During plasma exposure the oxygen concentration on cellulose surface increases, which is very important for consequent silver metallization. Plasma modification induced the decrease of surface roughness of plasma modified cellulose, the structure of amorphous cellulose is disrupted. The simple combination of plasma treatment and silver sputtering results in construction of effective antibacterial surface both for *Gram-positive* and *Gram-negative* bacteria.

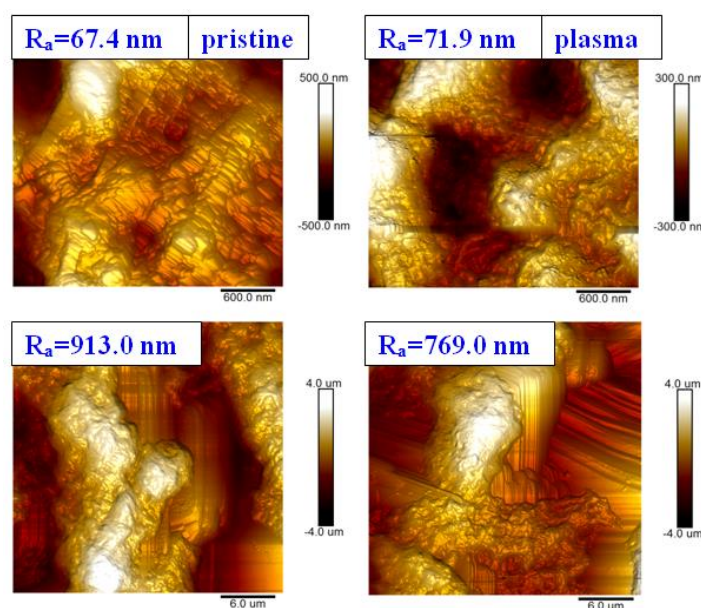


Fig. 1. Surface morphology and roughness for pristine (left) and plasma modified with 8 W and 240 s (right) cellulose samples. Inspected squares are 3x3 (up) and 30x30 μm² (down)..

Acknowledgement

This work was supported by the GACR project No. 17-00885S.

4. References

- [1] Slepíčka P, Siegel J, Lyutakov O, Slepíčková Kasálková N, Kolská Z, Bačáková L and Švorčík V 2018 *Biotechnol. Adv.* **36** 839-855.
- [2] Vosmanská V, Kolářová K, Rimpelová S, Kolska Z and Švorčík V 2015 *RSC Adv.* **5** 17690-17699.
- [3] Slepíčka P, Neděla O, Sajdl P, Kolská Z and Švorčík V 2013 *Appl. Surf. Sci.* **B 285** 885–892.
- [4] Kolářová K, Vosmanská V, Rimpelová S and Švorčík V 2013 *Cellulose* **20** 953–961.
- [5] Elashnikov R, Slepíčka P, Ulbrich P, Švorčík V, Lyutakov O 2017 *Mater. Sci. Eng. C* **72** 293–300.

NON-THERMAL PASTEURIZATION OF FRESH APPLE JUICE BY COLD AIR PLASMAS

Barbora Tarabová¹, Andrea Žilková¹, Francesco Tampieri², Ester Marotta², Cristina Paradisi², Marco Krewing³, Julia E. Bandow³, Zdenko Machala¹

¹Faculty of Mathematics, Physics and Informatics, Comenius University, Bratislava, Slovakia

²Department of Chemical Sciences, University of Padova, Padova, Italy

³Applied Microbiology, Biology and Biotechnology, Ruhr University, Bochum, Germany

E-mail: tarabova@fmph.uniba.sk

Cold air plasma (CAP) generated by the transient spark discharge in air was successfully tested for non-thermal pasteurization of fresh apple juice. Inactivation of model pathogens of bacteria and yeasts and extended shelf-life time of the juice were achieved. Minimal effects of CAP treatment on juice chemical and sensory properties (i.e. color, pH, degradation of important juice components, chemical composition) were observed. Successful inactivation of peroxidase enzyme typically responsible for the undesirable juice browning was achieved. By comparing two systems of juice treatment – the static (batch) system was evaluated as more efficient for bacterial inactivation and less affecting the juice properties compared to the electro-spray system.

1. Introduction

Conventional methods for inactivation of food borne pathogens are based on thermal treatments, typically referred to as pasteurization. Particularly ultra-high temperature (UHT) processes lead, beside the sterilization, to the loss of food quality (nutrition values, vitamin content, changes in sensory properties, such as taste or color). A growing customers' demand for long-lasting fresh products requires the concept of the “minimal processing”. Therefore in recent years, new technologies that can achieve the required level of sterilization and safety without thermal input have been investigated – e.g. pulsed electric field, high pressure, ultrasound, etc [1]. Non-thermal (cold) plasmas known for their bactericidal properties achieved without excessive heat requirement are predetermined for application in sterilization/pasteurization of fresh food and food packaging [2-3].

The objective of this work was to test the use of cold air plasma (CAP) generated by the transient spark discharge in two different systems for the non-thermal pasteurization of freshly squeezed apple juice. We also focused on chemical, nutrient and sensory properties of CAP treated apple juice.

2. Experimental set-up and methods

Transient spark discharge (TS) in positive polarity in direct contact with the juice was generated in ambient air at atmospheric pressure in two different set-ups depicted in Fig. 1. TS discharge is characterized as a self-pulsing repetitive streamer-to-spark transition with very short duration (<100 ns) of spark current pulses (repetitive frequency ~1 kHz) [4]. Both set-ups are based on the point-to-plane geometry using sharp hollow needle as the high voltage (HV) electrode. In the electro-spray system (ES), juice flowed directly through the HV needle with flow rate 1mL/min. Due to the applied HV, the effect of the electro-spraying of the juice to the micrometric size droplets occurred. ES set-up enabled the direct contact of the active discharge zone with the sprayed droplets of the juice. Static system (SS) is based on the batch treatment by the discharge generated directly over the juice surface, in which the grounded electrode was submerged with the treatment conditions 1min per 1 mL of the juice.

Freshly squeezed apple juice (cultivar Ontario) was stored in the freezer at -20°C and defrost immediately before plasma treatment. We performed experiments focused on:

- inactivation rate of model pathogens by CAP, where juice was inoculated by bacteria *Escherichia coli* ATCC 25922 or yeasts *Saccharomyces cerevisiae* S228C (initial concentration ~10⁶-10⁷ CFU/mL);
- effects of CAP treatment on the shelf-life time of juice when containing only its native pathogens.

The pathogen inactivation rate and the spoilage rate were evaluated by the classical thermostatic cultivation and was followed up to 28 days post CAP treatment. During this period, the juice was stored in the fridge at 4°C to simulate the typical behaviour of consumers.

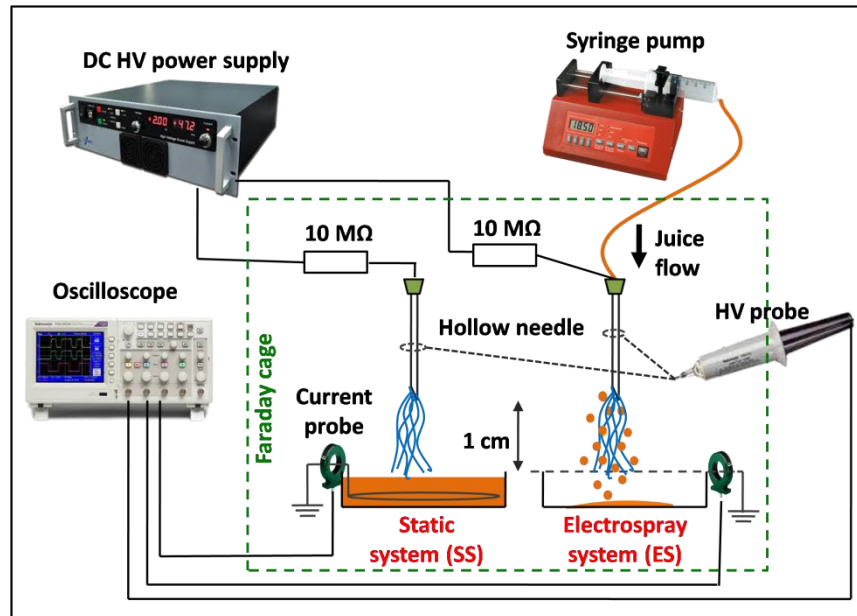


Fig. 1. Experimental set-up of air transient spark discharge in static SS and electrostatic ES system for juice treatment.

We also focused on the effects of cold plasma on the chemical, nutrient and sensory properties of the CAP treated juice, such as changes of pH, conductivity; colour changes measured by juice transmittance; concentrations of nitrites/nitrates ($\text{NO}_2^-/\text{NO}_3^-$) and hydrogen peroxide (H_2O_2) measured by colorimetric methods; changes of °Brix degree (dissolved sugar content measured by refractive index). The potential chemical changes of juice composition due to the presence of reactive oxygen and nitrogen species (RONS) formed by CAP were evaluated. The most typical juice components including polyphenols, organic acids and sugars, and their CAP induced degradation products were investigated by means of HPLC coupled to UV-VIS, mass spectrometry (MS) and refractive index (RI) detectors. Activity of the peroxidase (POD) enzyme responsible for the natural browning of fruit juices was evaluated.

3. Effects of CAP on pathogen inactivation and spoilage rate of fresh juice

The juice contaminated with model pathogens (*E. coli* or *S. cerevisiae*) was treated in both systems (ES and SS). The efficiency of cold plasma treatment on the inactivation rate (population growth) was followed up to 26-28 days post CAP treatment. In both systems, the initial relatively low (< 1 log) inactivation of *E. coli* bacteria immediately post CAP treatment was followed by a significant decrease of bacterial load within the first 2 days post plasma (~ 3 -5 log) that reached further complete inactivation, which remained up to 26 days (Fig. 2). The efficiency of CAP treatment on yeast *S. cerevisiae* remained quite low over the period of 28 days (~ 1 log), slightly higher for the SS system (not shown). However the high initial yeasts concentration ($\sim 10^6$ CFU/mL) surpasses by several orders of magnitude the possible natural contamination and therefore much stronger effect can be expected for lower yeast concentration.

Freshly squeezed apple juice may contain its native pathogens (different strains of yeasts and bacteria were detected) responsible for the spoilage of the juice, which primarily affect its shelf-life time. Our preliminary experiments indicated no bacterial or yeast growth up to 26 days post treatment in natural juice treated in both plasma systems and refrigerated at 4°C although both treated and control untreated samples were under detection limit.

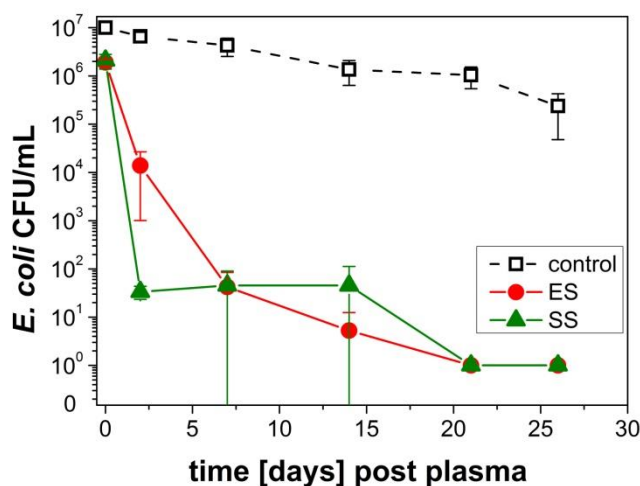


Fig. 2. The time evolution of the inactivation rate of the CAP treated juice contaminated by *E. coli*.

4. Analysis of CAP treated juice chemical, sensory and nutrient properties

Cold air plasmas generated in direct contact with liquids typically induce chemical changes and formation of reactive oxygen and nitrogen species (RONS) in these liquids. Some of the abundant long-lived RONS, especially $\text{NO}_2^-/\text{NO}_3^-$ or H_2O_2 may be harmful for human health in high doses and their content in food products is regulated. For example the acceptable daily intake (ADI) per kilogram human body weight is 0-3.7 mg NO_3^- and 0-0.06 mg NO_2^- ions. Fig. 3 shows that the concentrations of measured NO_2^- and NO_3^- in CAP treated juice were significantly lower after 24 hours post plasma treatment than the ADI of NO_2^- and NO_3^- per average 60 kg human assuming exaggerated 1L/day juice consumption.

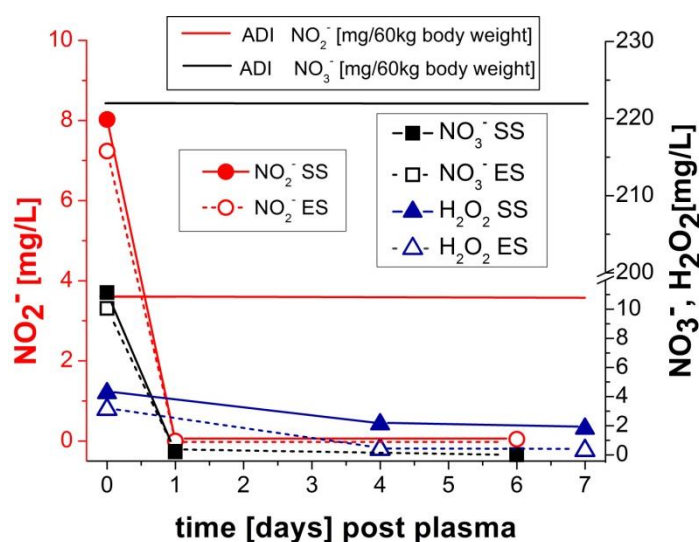


Fig. 3. NO_2^- , NO_3^- and H_2O_2 concentrations measured in CAP treated juice compared to the ADI doses calculated to an average human of 60 kg body weight. The shown measured and ADI values are directly comparable assuming that an average human consumes 1L of the juice daily.

CAP treatment and RONS formed in CAP treated liquids are known for inducing chemical changes resulting in changes of pH, conductivity or degradation of the organic chemical compounds. Native apple juice contains many organic components including sugars, organic acids and polyphenols known as antioxidants or vitamins. Representative components from each group (i.e. sugars – fructose, glucose and sucrose; organic acids – malic, citric and ascorbic acid; polyphenols – chlorogenic acid,

phloridzin and epicatechin) have been tested for possible degradation by CAP treatment [5]. These compounds were CAP treated separately as aqueous solutions and all together in the fresh juice. The results show that in control experiments these compounds undergo reactions when they are CAP treated individually in aqueous solutions at the same concentration as found typically in the juice, leading to their hydroxylated and nitrated products. For instance in Fig. 4 are shown UV-chromatograms of non-treated phloridzin solution and its detected nitrated and hydroxylated degradation products after CAP treatment.

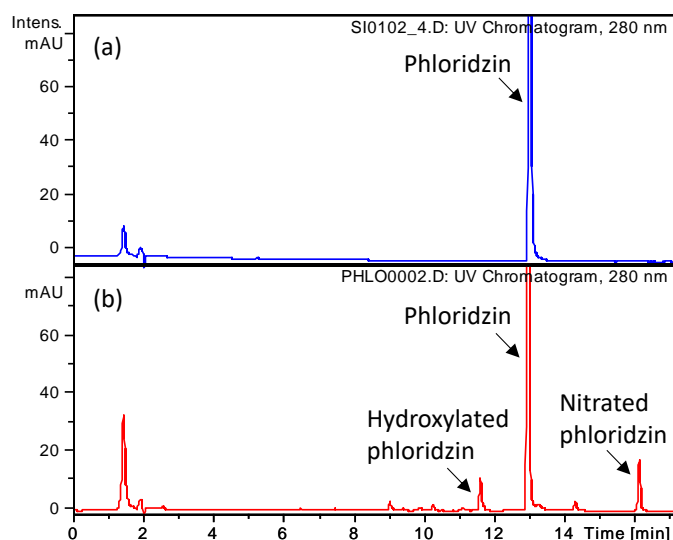


Fig. 4. UV chromatograms (280 nm) of (a) non-treated and (b) ES treated phloridzin solution.

In contrast, phloridzine seemed to remain unaffected in similarly CAP treated fresh juice as can be seen in Fig. 5. This can be attributed to the fact, that although high concentrations of RONS may be formed in the CAP treated juice, the competition by numerous juice components for the same reactive species limits the effect on each individual substance. We were also able to successfully detect all aforementioned components in the fresh juice and determine the percentage of their decomposition (not shown).

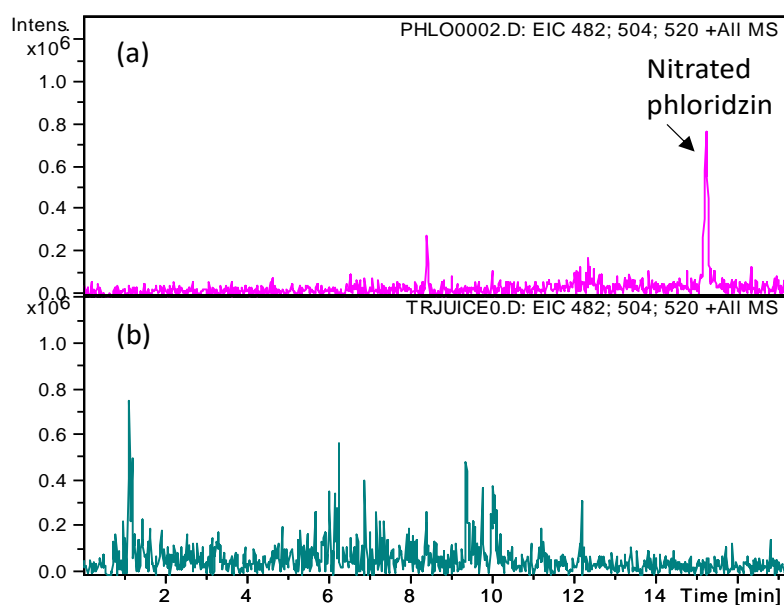


Fig. 5. Extracted ion chromatograms of the signals ($[M+H]^+$ m/z 482, $[M+Na]^+$ m/z 504, $[M+K]^+$ m/z 520) due to nitrated phloridzin (a) in ES treated phloridzin solution and (b) in ES treated juice.

We also detected no significant changes of pH (3.28→3.19), conductivity and °Brix degree in CAP treated juice. The measured transmittance slightly decreased indicating very mild darkening of the juice due to direct CAP treatment. Peroxidase as one of the enzymes responsible for the undesirable browning (oxidation) and the loss of the juice quality [6] was successfully inactivated. The remaining activity of POD in juice treated in SS system was about 29 % and 47% in ES system.

5. Summary

Cold plasma of the transient spark discharge in air was demonstrated as a promising alternative food processing technique for non-thermal pasteurization of fresh apple juice. Preliminary results showed a significant decontamination rate of pathogens, and shelf lifetime extension up to 26 days. It was shown that the juice quality was not significantly affected by the CAP treatment, i.e. minimal changes of chemical composition (degradation of organic acids, polyphenols, sugars), pH and color were detected. Successful inactivation of peroxidase enzyme known for the undesirable juice browning was achieved.

This work was supported by the Slovak Research and Development Agency APVV-17-0382 and APVV-0134-12, Comenius University in Bratislava, University of Padova (PRAT 2014, Grant CPDA147395/14), and by German Research Foundation (JEB(PAK728)).

6. References

- [1] Minimal processing technologies in the food industry 2002 edited by Ohlsson T and Bengtsson N Woodhead Publishing Limited CRC press ISBN 0-8493-154-2.
- [2] Niemira B A 2012 *Annual Review of Food Science and Technology* **3**.
- [3] Thirumdas R, Sarangapani C and Annappure U S 2014 *Food Biophysics* **10**.
- [4] Machala Z, Tarabova B, Sersenova D, Janda M and Hensel K 2019 *Journal of Physics D: Applied Physics* **52**.
- [5] Eisele T A and Drake S R 2005 *Journal of Food Composition and Analysis* **18**.
- [6] Surowsky B, Fischer A, Schlueter O and Knorr D 2013 *Innovative Food Science and Emerging Technologies* **19**.